VERÖFFENTLICHUNGEN
des Instituts für Geotechnik
der Technischen Universität Bergakademie Freiberg

Herausgeber: H. Konietzky

Heft 2016-2

45. Geomechanik-Kolloquium

Freiberg • 11. November 2016

Freiberg 2016

Veröffentlichungen des Instituts für Geotechnik der TU Bergakademie Freiberg

Herausgeber: Prof. Dr.-Ing. habil. Heinz Konietzky

Anschrift: TU Bergakademie Freiberg
Institut für Geotechnik
Gustav-Zeuner-Straße 1
09596 Freiberg
Telefon: 03731 39-2458
Fax: 03731 39-3638
E-Mail: ifgt@ifgt.tu-freiberg.de
Internet: http://tu-freiberg.de/fakult3/gt/

Herstellung: SDV Direct World GmbH
Printed in Germany

ISSN 1611-1605

Table of contents

More papers

Die Schienenneubaustrecke Dresden-Prag – Geologische/geotechnische Untersuchungen als Grundlage einer anspruchsvollen Verkehrsinfrastrukturplanung

New Railway Line Dresden-Prague – Geological/ Geotechnical Investigations as the Basement for an Advanced Transport Infrastructure Planning

Sabine Kulikov, Ottomar Krentz,
SAXON STATE AGENCY OF ENVIRONMENT, AGRICULTURE AND GEOLOGY (LfULG)
Pillnitzer Platz 3 | 01326 Dresden Pillnitz
Thomas Frühwirt
TU Bergakademie Freiberg, Institut für Geotechnik
Gustav-Zeuner-Str. 1 | 09599 Freiberg

Abstract

The new high speed rail line Dresden-Prague is considered to be one of the most important railway projects in Central Europe linking Germany and the Czech Republic with a cross border tunnel through the Ore Mountains. It is a vital part of the Orient / East-Med Corridor of the Trans-European Transport Network, which connects the North and Baltic Sea ports and economic centers in Southeast Europe. The newly planned railway line will both serve passenger transport and increase the capacity for freight transport.

The new railway line passes through a complex geological and hydrological situation in the Ore Mountains on both sides of the tunnel portal. The dominant civil structure on this new railway line will be the Cross Border Base Tunnel with a length of 26.53 km. The tunnel is designed as twin tube tunnel according to international rescue and safety regulations. The tunnel length at the German side will be 15.10 km and 11.43 km at the Czech side. As determined in the actual study the tunnel will pass through sensitive geological and hydrogeological zones that need to be investigated in great detail.

Zusammenfassung

Zwischen der Tschechischen Republik und dem Freistaat Sachsen ist es ein erklärtes Ziel, die Schienenverbindung zwischen Dresden und Prag, die durch das Elbtal führt und einen Engpass darstellt, für die künftigen Anforderungen an ein steigendes Güterverkehrsaufkommen und kürzere Reisezeiten im Personenfernverkehr zu verbessern. Dafür soll die Streckenführung aus dem Elbtal heraus ins Osterzgebirge verlegt werden, welches durch einen ca. 27 km langen, Sachsen und Tschechien verbindenden Tunnel, durchfahren werden soll.

Für dieses anspruchsvolle Infrastrukturvorhaben unterstützt der Sächsische Geologische Dienst des Landesamtes für Umwelt, Landwirtschaft und Geologie (LfULG) in Zusammenarbeit mit der Technischen Universität Bergakademie Freiberg (TUBAF) das Staatsministerium für Wirtschaft, Arbeit und Verkehr (SMWA) seit 2012 bei den planungsvorbereitenden Aufgaben mit Detailkenntnissen über den regionalen geologischen Bau des Untergrundes.

Die enge Zusammenarbeit zwischen SMWA, Planungsbüro, LfULG und TUBAF führten zu einer Verbesserung der geologisch/geotechnischen Grundlagen, der Optimierung des Trassenverlaufes sowie einer Ausweisung von Risikofaktoren und -bereichen.

1 Einführung

Zwischen der Tschechischen Republik und dem Freistaat Sachsen ist es ein erklärtes Ziel, die Schienenverbindung zwischen Dresden und Prag für die künftigen Anforderungen an ein steigendes Güterverkehrsaufkommen und kürzere Reisezeiten im Personenfernverkehr zu verbessern (Fig. 1).

Durch die Streckenführung außerhalb des Elbtals soll die Reisezeit im Personenfernverkehr zwischen Dresden und Prag auf unter 1 Stunde reduziert, die Kapazität für den Güterverkehr deutlich gesteigert, die Lärmbelastung entlang der Bestandsstrecke reduziert sowie eine hochwassersichere Trassenführung erreicht werden [1].

Fig. 1: Eisenbahn-Neubaustrecke Dresden-Prag im TEN-V-Korridor Orient / Östliches Mittelmeer

Seit dem Jahre 2012 unterstützt das Landesamt für Umwelt, Landwirtschaft und Geologie (LfULG) das Staatsministerium für Wirtschaft, Arbeit und Verkehr (SMWA) bei den Planungsarbeiten mit Detailkenntnissen über den regionalen geologischen Bau des Untergrundes in Zusammenarbeit mit der Technischen Universität Bergakademie Freiberg (TUBAF) durch die FuE-Vorhaben „Geophysikalische Untersuchungen an der Struktur Börnersdorf/Osterzgebirge zur Klärung der tektonischen Situation" sowie eine "Geologische 3D-Modellierung der Neubaustrecke Dresden-Prag".

Die enge Zusammenarbeit zwischen SMWA, Planungsbüro, LfULG und TUBAF im Rahmen der laufenden Studie führten zu einer Verbesserung der geologischen Grundlagen, der Optimierung des Trassenverlaufes sowie einer Ausweisung von Risikofaktoren und -bereichen.

Im Folgenden werden ein kurzer Abriss der geologisch/geotechnischen sowie tektonischen Verhältnisse im Streckenverlauf gegeben sowie die durchgeführten Untersuchungen und deren Ergebnisse vorgestellt.

2 Charakterisierung der geplanten Trasse

Der Trassierungskorridor beginnt südlich von Dresden in der Stadt Heidenau. Dort erfolgen der Anschluss der Neubaustrecke an die Bestandsstrecke und die Ausleitung der Neubaustrecke aus dem Elbtal in Richtung Pirna-Zehista. Nach der Querung des Seidewitztals bei Zehista folgt der Trassenkorridor dem Lohmgrundrücken unter Umgehung des Bahre- und des Gottleubatals mit den Kurbädern in Berggießhübel und Bad Gottleuba. Danach führt der Trassenkorridor in Richtung Grenze zwischen dem Freistaat Sachsen und der Tschechischen Republik. Der Korridor führt auf tschechischer Seite weiter durch den Bereich am Berg Špičák bis nach Chlumec und danach zum nächsten Bahnhof in Ústí nad Labem.

Die Neubaustrecke zwischen Heidenau und Ústí nad Labem hat eine Gesamtlänge von ca. 42.8 km. Der Abschnitt von Heidenau bis zur Staatsgrenze wird 22.16 km lang sein (Fig. 2). Wesentliche Elemente sind 2 Brückenbauwerke und 2 Tunnelbauwerke. Wichtigstes Hauptelement wird der ca. 27 km lange grenzüberschreitende Erzgebirgsbasistunnel. Der Tunnel wurde nach den aktuellen EU-Rettungs- und Sicherheitsvorschriften für Tunnelbauwerke mit 2 eingleisigen Röhren konzipiert. Die Tunnellänge wird auf der deutschen Seite 15.10 km und auf der tschechischen Seite 11.43 km betragen. [1]

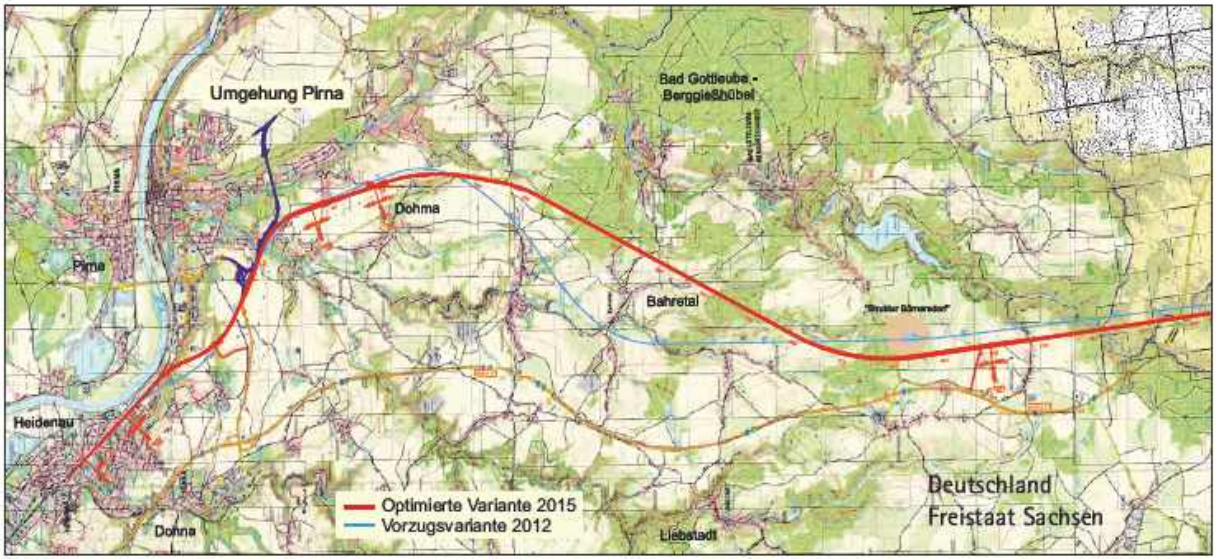

Fig. 2: Lageplanausschnitt mit optimiertem Streckenabschnitt im Freistaat Sachsen

3 Geologie im Trassenverlauf

Durch die frühzeitige Zusammenarbeit mit dem Sächsischen Geologischen Dienst (Abteilung Geologie des LfULG) konnten bereits im Zuge der ersten Voruntersuchungen zur Trassenführung geologische "Brennpunktbereiche" lokalisiert und die Trassierung angepasst werden. Ausführlich wird darauf unter <http://www.nbs.sachsen.de/12176.html> in „Technische Beurteilung wesentlicher Bauwerke nach verschiedenen Kriterien“ eingegangen.

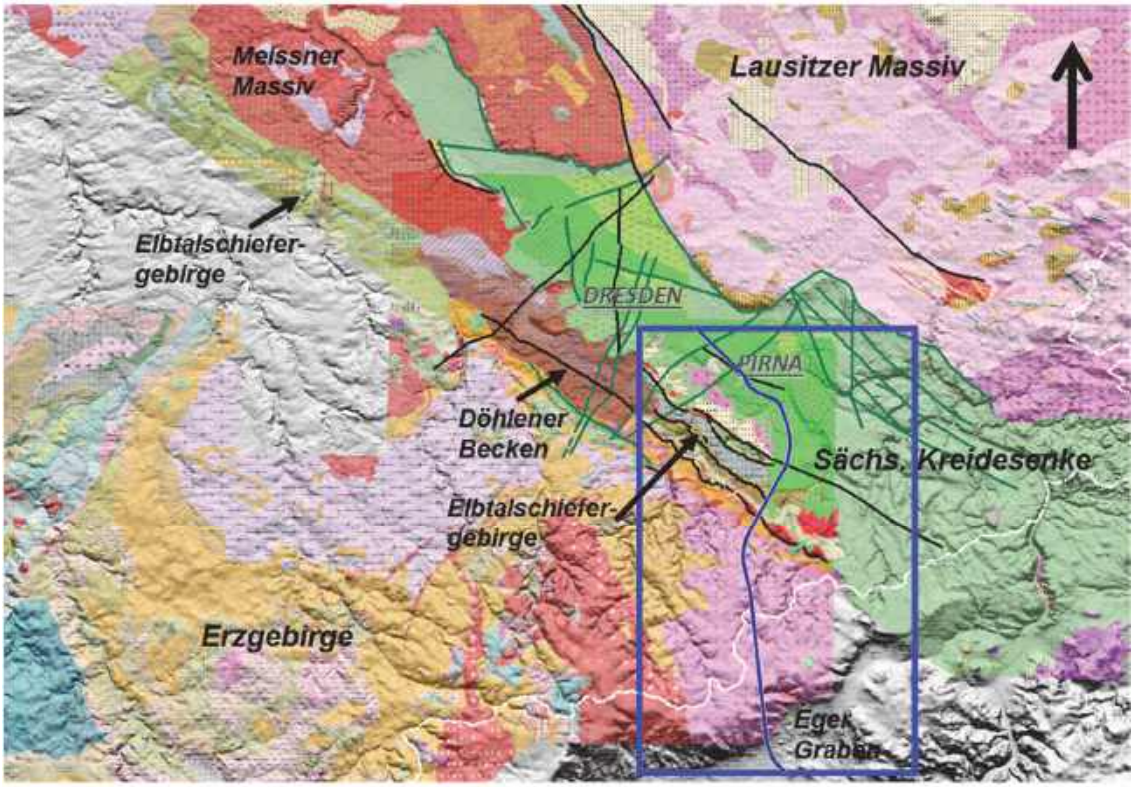

Fig. 3: Geologische Übersichtskarte von Sachsen mit NBS-Trassenführung

Die Übersichtsdarstellung in Fig. 3 zeigt die wesentlichen geologischen Komplexe in Sachsen. Nachfolgend werden die im Trassenverlauf anzutreffenden Gesteinskomplexe betrachtet.

Bezogen auf die Trasse der Schienenneubaustrecke werden im Wesentlichen drei große Gesteinskomplexe durchlaufen (Fig. 3):

- Im Norden bis etwa Trassen-km 10 die **Kreideablagerungen** mit Sandsteinen und Ton-Mergelsteinen, die am Trassenanfang von Auenablagerung der Elbe überlagert werden.
- Das **Elbtalschiefergebirge** von Trassen-km 10 - 14 mit einem kleinräumigen Wechsel von Grauwacken, Tonschiefern, Phylliten, Tuffen, Diabas und Kalksteinen.
- Den Bereich der **Erzgebirges** mit Gneisen von Trassen-km 14 - 32.

Komplikationen mit erhöhtem Untersuchungsaufwand sind im Bereich der tektonischen Störungsbereiche zu erwarten (vgl. Fig. 4).

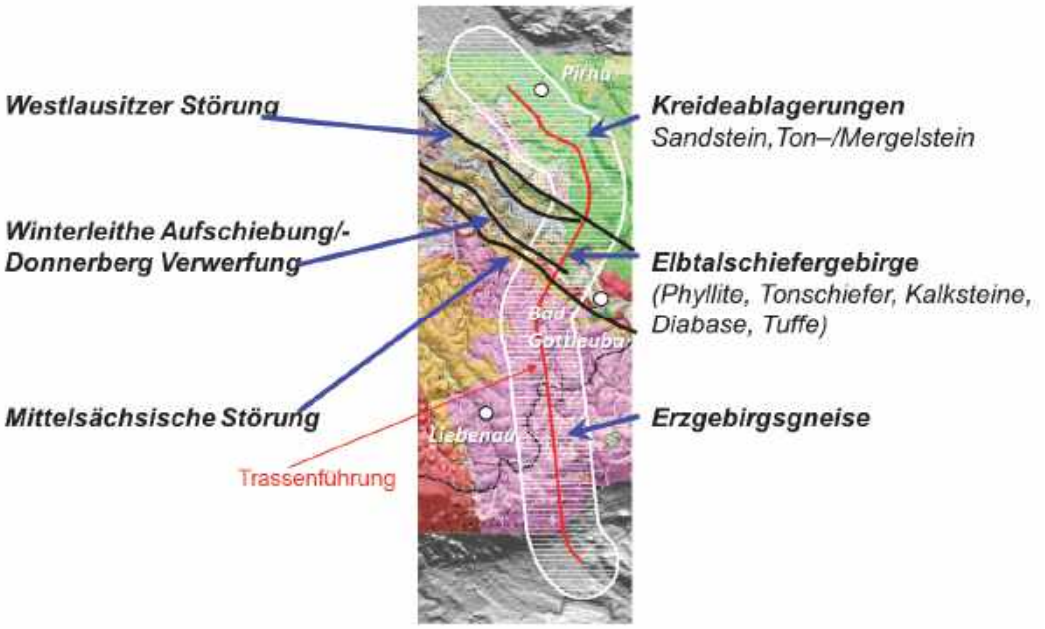

Fig. 4: Übersichtsdarstellung der im Bearbeitungsgebiet bekannten Hauptstörungen und vorherrschenden Gesteinskomplexe

Die wichtigsten Hauptstörungen im Elbtalschiefergebirge verlaufen Nordwest-Südost (Fig. 4). Weitere Störungen, insbesondere im Gneis-Areal, sind in dieser Übersicht nicht dargestellt. Geologische Störungen sind besonders für den Tunnelbau von Bedeutung, weil sie häufig Gesteinswechsel markieren, ihr Umfeld aufgelockert und tektonisch zerrüttet sowie der Gesteinsverband gestört ist (infolge der tektonischen Beanspruchung) und abschnittsweise häufig eine erhöhte Wasserführung zu verzeichnen ist.

Durch das LfULG wurde in Vorbereitung der weiterführenden Arbeiten zur EUKOM-Studie des SMWA ein Übersichtsschnitt entlang des Trassenverlaufes erstellt, in den neben den Informationen aus den geologischen Karten, das tektonische Inventar, die Ergebnisse der geophysikalischen Untersuchungen, die Analyse tiefer Altbohrungen sowie Daten eines tschechischen Berichtes zur Geologie im Grenzbereich einflossen (Fig. 5).

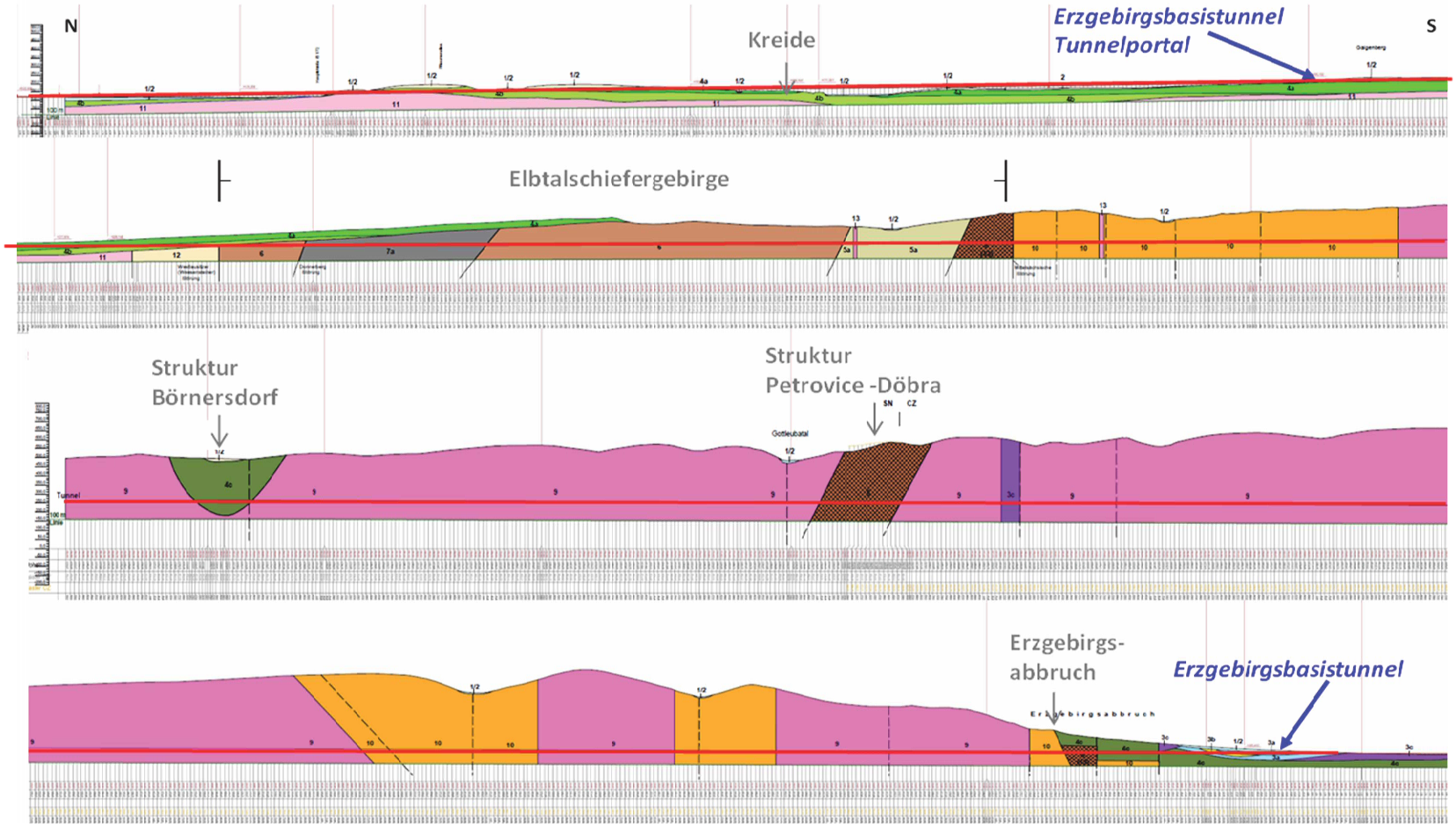

Fig. 5: Geologischer Schnitt im Trassenverlauf

4 Gesteinsphysikalische Untersuchungen (Studienarbeit am Institut für Geotechnik)

In Vorbereitung des Aufbaus eines Sächsischen Kennwertinformationssystems, das für Infrastrukturvorhaben nutzbar sein soll, wurden die im Trassenverlauf zu durchörternden Gesteine betrachtet. Dabei erfolgten umfangreiche Recherchearbeiten im rohstoffgeologischen Archiv des LfULG in Freiberg, wobei die wesentliche Aufgabe darin bestand, die Unterlagen der in der Nähe liegenden Steinbrüche aufzuarbeiten und Kennwerte zu sammeln. Parallel dazu wurden auch Literaturwerte zur Ersteinschätzung und Gutachten aus dem geologischen Archiv des LfULG herangezogen. Außerdem wurden vom Gesteinsmechanischen Labor des Instituts für Geotechnik der TU-BAF Laborergebnisse recherchiert und Kennwerte zusammengefasst [2].

Probenahme
Zusätzlich zur Datenrecherche erfolgte nach deren Abschluss und Festlegung potentieller Risikogesteine (Gesteine mit wenig vorhandenen Kennwerten sowie Gesteine weiträumiger Verbreitung), im August 2015 eine Probenahme an ausgewählten Gesteinen, die im Trassenverlauf erwartet werden.

Zu den ausgewählten Risikogesteinen zählten im ersten Untersuchungsabschnitt die Weesensteiner Grauwacke und der Quarzit, die aufgrund ihres hohen Quarzgehalts einen hohen Verschleiß an sämtlichen Bohr- und Schneidwerkzeugen erwarten lassen. Da insgesamt 17.837 km Tunnel im Gneis aufgefahren werden, wurde auch dieser ausgewählt. Ebenfalls untersucht wurde der in Linsen vorkommende Kalkstein.

Recherche und Auswertung von rohstoffgeologischen Unterlagen im LFULG
Tagebaucharakteristik

- Angaben zur Geologie/Geotechnik
- Angaben zu geomechanischen Gesteinskennwerten
- Recherche zu Verfüllungsmöglichkeiten für Tunnelausbruchmaterial anhand vorliegender Planfeststellungsunterlagen (Statusprüfung für die Nachnutzung)

Laboruntersuchungen im gesteinsmechanischen Labor der TUBAF
Probenahme / Laboruntersuchungen

- Auswahl besonders interessierender Gesteine im Trassenverlauf, für die kaum Kennwerte vorlagen
- Festlegung der Probenahmepunkte und Probenahme
- Herstellung der Probenkörper
- Durchführung der Laboruntersuchungen

Die ausgewählten Gesteinsproben wurden hinsichtlich Druckfestigkeit, Spaltzugfestigkeit, Abrasivität und Scherfestigkeit im gesteinsmechanischen Labor der TUBAF untersucht (Fig. 6).

Fig. 6: Übersicht über durchgeführte gesteinsmechanische Laboruntersuchungen

Im Nachgang wurden im LfULG vom Restprobenmaterial Schliffe angefertigt und eine petrographische Analyse der Gesteinsproben durchgeführt, um eventuelle Zusammenhänge zwischen dem Gesteinsgefüge und den geomechanischen Untersuchungen herstellen zu können.

5 Geophysikalische Untersuchungen an der Struktur Börnersdorf (FuE-Vorhaben)

Für die Untersuchung und Klärung des tektonischen Inventars der Struktur Börnersdorf, die als Kreidevorkommen mitten im Gneisgebiet eine geologische Besonderheit darstellt, wurden durch die TUBAF folgende Untersuchungsmethoden angewandt.

Geophysikalische Untersuchungen

- Gravimetrie
  Messung der Dichteunterschiede (Gesteinsgrenzen)
- Geomagnetik
  Ermittlung der magnetischen Eigenschaften (magmatische/sedimentäre Gesteine)
- Geoelektrik
  Ermittlung des spezifischen Widerstandes (Wasserführung, Störungen)
- Seismik
  Ermittlung Wellengeschwindigkeit/Dichte in größerer Tiefe (Gesteinsgrenzen, Störungen)

Die Auswertung der geophysikalischen Ergebnisse ergab, dass es sich bei der Struktur Börnersdorf um eine 500 x 600 m große, ca. 300 m tiefe kesselförmige Struktur handelt. Diese Struktur, die von Störungen begleitet wird, lag ursprünglich genau auf der geplanten Tunneltrasse. Aufgrund der bisher ungeklärten Entstehungsgeschichte der Kreidesenke im Gneis und des noch wenig bekannten Störungsinventars sowie zur

Minimierung des bautechnischen Risikos wurde die Trasse nach Westen verlegt, da sich im Osten die Talsperre Gottleuba befindet (Fig. 7).

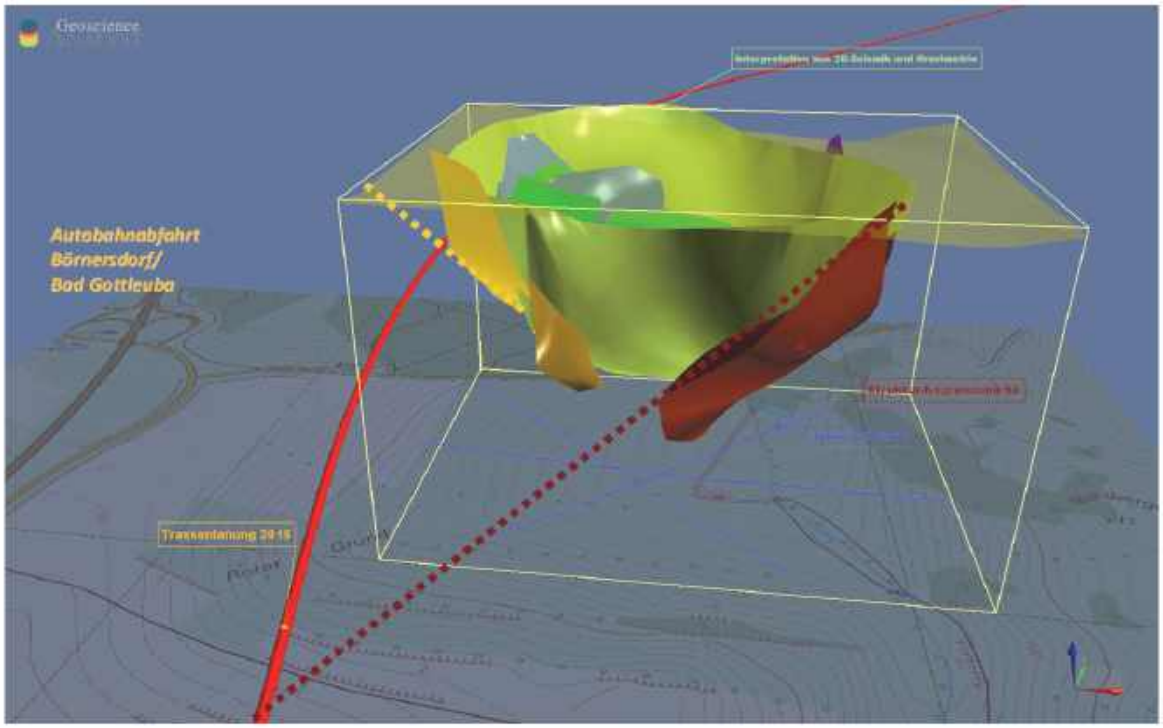

Fig. 7: Auswertung und Interpretation der Ergebnisse der seismischen Untersuchungen

6 Geologische 3D-Modellierung

Anlass für die 3D-Modellierung waren Wirtschaftlichkeitsbetrachtungen im Rahmen der EUKOM-Studie für die Eisenbahnneubaustrecke. Die Schwerpunktgebiete wurden auf der Grundlage der geplanten Bauwerke und der zu erwartenden geologischen/hydrogeologischen sowie tektonischen Situation und der Beeinflussung durch andere Infrastrukturobjekte ausgewählt (Fig. 8).

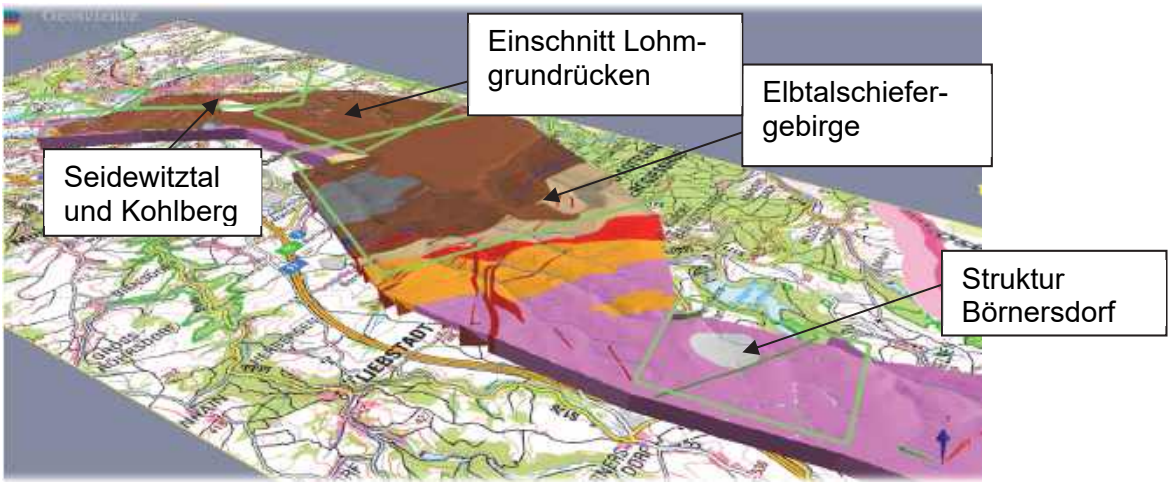

Fig. 8: Schwerpunktgebiete für die 3-D-Modellierung

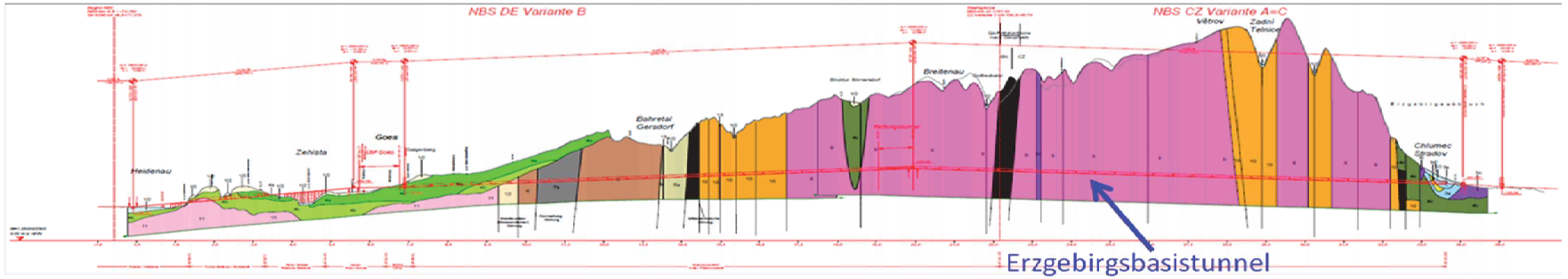

Fig. 9: Lageplan mit Streckenabschnitt im Freistaat Sachsen

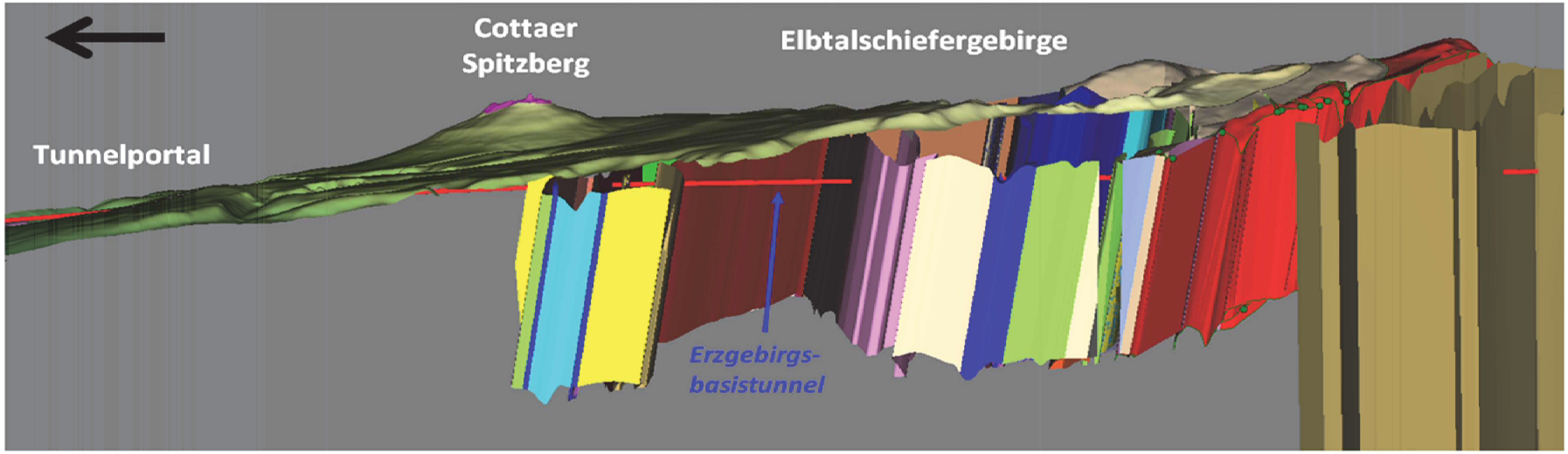

Fig. 10: Ausschnitt aus dem 3-D-Modell (Elbtalschiefergebirge)

Besonders komplex stellt sich die Situation im Elbtalschiefergebirge dar, wo neben dem kleinräumigen Gesteinswechsel und den bekannten Hauptstörungen mit einer Vielzahl untergeordneter Störungen zu rechnen ist (Fig. 9).

Die Komplexität der geologischen Situation veranschaulicht der 10-fach überhöhte Schnitt (Fig. 10), der die geplanten Bauwerke enthält.

7 Ergebnisse und weiterführende Arbeiten

Im Rahmen der EUKOM-Studie wurde somit anhand vorhandener Unterlagen ein erstes geologisches Übersichtsmodell geschaffen, das zum einen Grundlage für eine geotechnische Vorbetrachtung der geplanten Bauwerke sowie eine überschlägige Massenbilanzierung und Wirtschaftlichkeitsbetrachtung war, und zum anderen eine Optimierung des Trassenverlaufs und der Gradiente ermöglichte (Fig. 11, Fig. 12). Weiterhin wurden Schwerpunktbereiche für weiterführende Arbeiten aufzeigt.

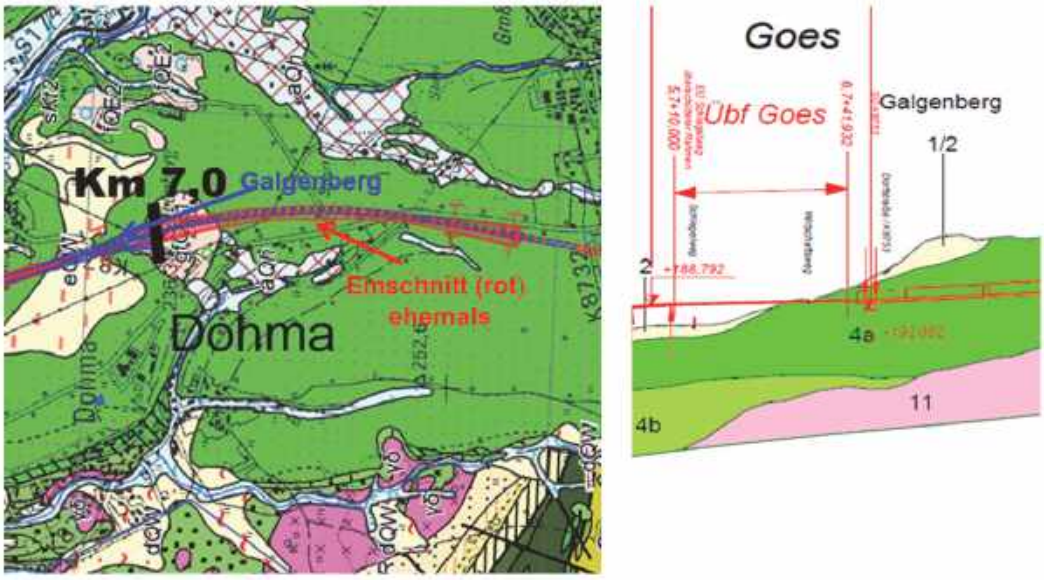

- ➔ Tieferlegung der Gradiente und Verlegung des Tunnelportals
- ➔ deutliche Verkürzung des Einschnittes auf den Bereich Galgenberg (> 1 km auf ca. 250 m) durch Verlängerung des Tunnels und Erhalt des historischen Eisenbahntunnels Cotta
- ➔ Minimierung der offenen Böschungen im Lockergestein

Fig. 11: Optimierung der Gradientenführung

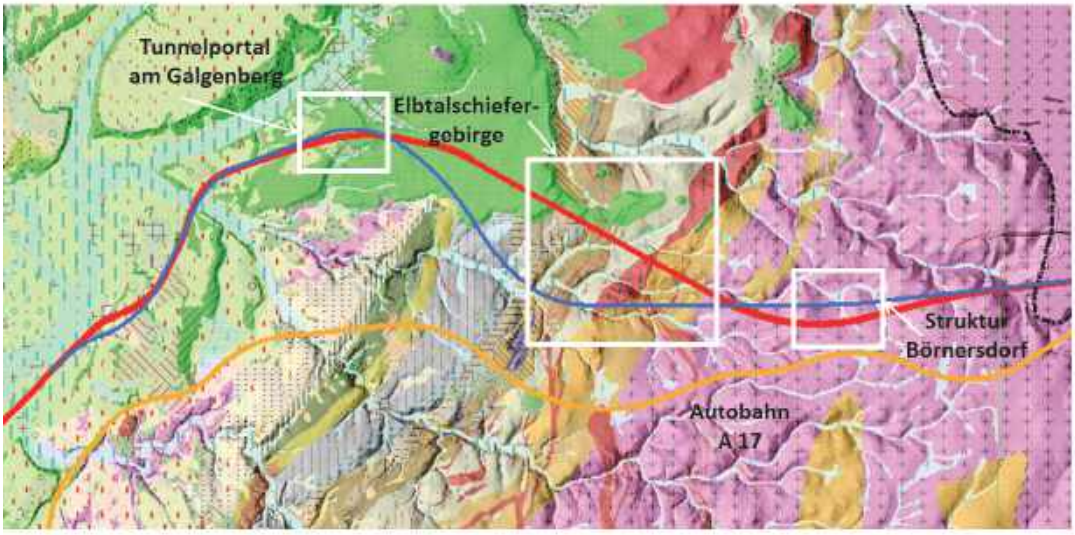

Fig. 12: Optimierung des Trassenverlaufes

Im Rahmen eines europäischen INTERREG V-Projektes ist geplant, durch die geologischen Dienste von Sachsen (als Partner des SMWA) und Tschechien ein grenzübergreifendes geologisches 3D-Modell zu erarbeiten und mittels geophysikalischer Untersuchungen große grenzüberschreitende Störungsstrukturen zu untersuchen (Fig. 13). Gleichzeitig soll mit dem Projekt eine intensive hydrogeologische sowie geologisch/tektonische Kartierung markanter Störungsbereiche im Einflussbereich der Talsperre Gottleuba erfolgen.

Weiterhin erfolgt in Zusammenarbeit mit dem SMWA eine Fortführung der geophysikalischen Arbeiten im Umfeld der Struktur Börnersdorf.

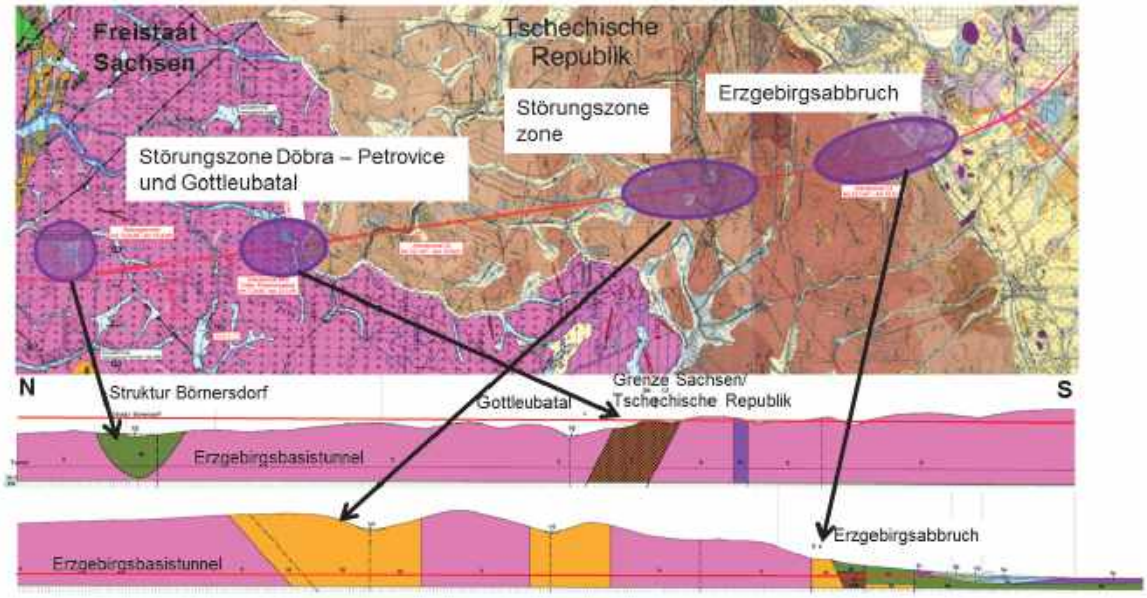

Fig. 13: Schwerpunktgebiete weiterführender Untersuchungen

Die Einbeziehung des geologischen Dienstes in diesem frühen Stadium der Planung, noch vor dem eigentlichen Planungsbeginn, hat sich als überaus hilfreich für die Erstellung der EUKOM-Studie erwiesen.

Am 29. April 2016 wurden gemeinsam mit dem Verkehrsministerium der Tschechischen Republik in Usti nad Labem die Studienergebnisse zur Schienenneubaustrecke Dresden-Prag vorgestellt und die Gründungsdokumente für den Europäischen Verbund für Territoriale Zusammenarbeit „Eisenbahnneubaustrecke Dresden–Prag EVTZ“ unterzeichnet – den ersten Verbund dieser Art in Deutschland.

Quellen

[1] Eisenbahn-Neubaustrecke Dresden-Prag (Internetpräsentation des Sächsischen Staatsministeriums für Wirtschaft und Arbeit) http://www.nbs.sachsen.de/index.html

[2] LfULG: Geophysik und 3D-Modellierung im Osterzgebirge, Voruntersuchungen zur Neubaustrecke Dresden–Prag, Abschlussbericht zu den FuE-Vorhaben zur EUKOM-Studie, Dezember 2015

Rock Mechanics in the Swedish Nuclear Waste Disposal Program

Felsmechanik im schwedischen nuklearen Endlagerprogramm

Diego Mas Ivars
Swedish Nuclear Fuel and Waste Management Co, Stockholm, Sweden
Eva Hakami
Geosigma AB, Stockholm, Sweden
Harald Hökmark
Clay Technology AB, Lund, Sweden

Abstract

The design, construction and safety assessment of a final repository for spent nuclear fuel is a unique and demanding project with strict requirements. This paper focuses on the rock mechanics aspects. It presents the current understanding, which has crystalized in the present site-descriptive model. The rock mechanics processes of importance for the repository design and safety assessment and the current understanding based on the analyses performed to date are also summarized. This is an iterative process in which new data and novel or updated methodologies are incorporated, when judged appropriate, to improve our understanding and our engineering and predictive capabilities with the objective of increasing our confidence and complying with the posed requirements.

Zusammenfassung

Design, Aufbau und Sicherheitsbewertung von Endlagern für Kernbrennstoffe ist ein einzigartiges und anspruchsvolles Projekt mit strengen Voraussetzungen. Der folgende Beitrag konzentriert sich auf die Aspekte der Felsenmechanik. Er präsentiert das aktuelle Verständnis, das sich im gegenwärtigen ortsbeschreibenden Modell kristallisiert hat. Basierend auf durchgeführten Betrachtungen, werden die felsenmechanischen Prozesse, die für das Design des Endlagers, die Sicherheitsbewertung und das aktuelle Verstehen wichtig sind, vorgestellt. Das ist ein sich wiederholender Prozess, in dem neue Daten und neuartige oder aktualisierte Methoden nach ihrer Beurteilung berücksichtigt werden. So kann das Verständnis und die Vorhersage mit dem Ziel verbessert werden, unser Vertrauen zu vergrößern und die angenommenen Voraussetzungen zu erfüllen.

1 Introduction

The Swedish Nuclear Fuel and Waste Management Co (SKB) is in charge of handling and safe disposal of nuclear waste in Sweden.

More than 30 years of research have led to the KBS-3 method for the final disposal of spent nuclear fuel. This method is based on three protective barriers which perform two safety functions: isolation and retention. The spent nuclear fuel is encapsulated in copper canisters with a cast iron insert. Embedded in bentonite clay for isolation and mechanical protection, the canisters are deposited in vertical deposition holes in the floor of horizontal tunnels at a depth of around 500 m in crystalline bedrock (Figure 1). The deposition tunnels are also backfilled with bentonite and sealed with concrete plugs. Rock caverns, transport and main tunnels are backfilled and a top sealing is put in place after the disposal is completed.

Identifying, understanding, conceptualizing and bounding the main rock mechanics aspects that can influence the construction of the repository and the performance of the barrier system in the short-, mid- and long term is of critical importance for the safe geological disposal of nuclear waste.

This paper focuses on rock mechanics aspects, including coupled thermo-mechanical and coupled hydro-mechanical mechanisms when required. The first part of the paper describes the methodology, results and lessons learned from the site-descriptive modelling (SKB, 2008), which is used as input for repository design (SKB, 2009a) and long-term safety assessment (SKB, 2011). The second part focuses on the status of the knowledge regarding the key rock mechanics aspects influencing the performance of the KBS-3 method.

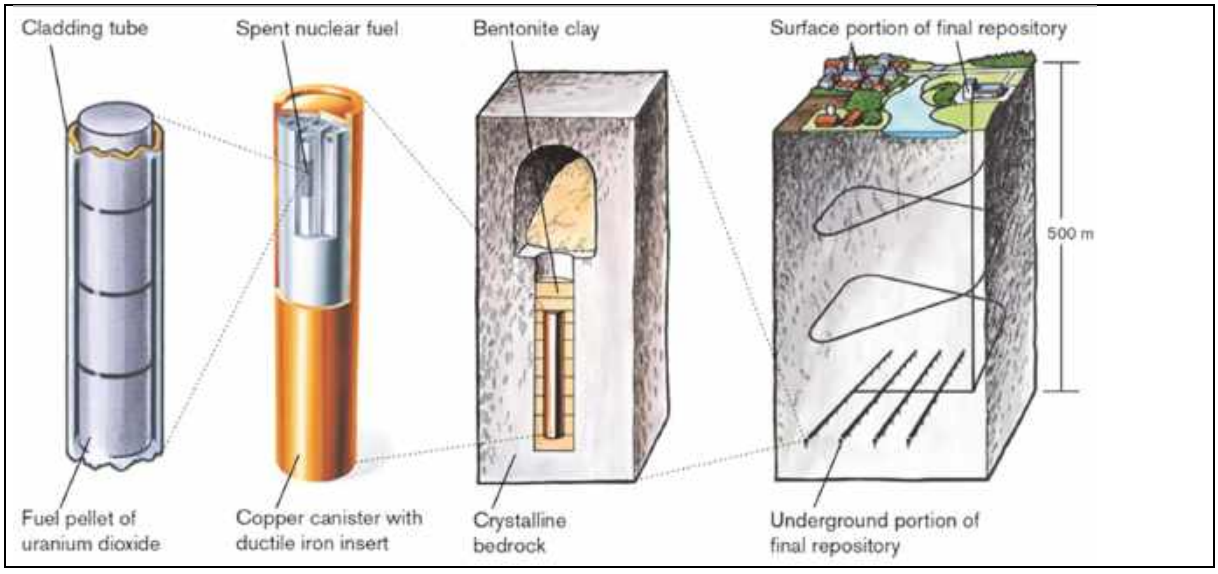

Figure 1. The KBS-3 concept for disposal of spent nuclear fuel (SKB, 2011).

2 Site-descriptive modelling

Within the siting process for the future repository three different areas in Sweden were investigated with a comprehensive investigation program and geological modelling. After this phase one of the sites, Forsmark, was selected by SKB as the most suitable for the continued investigations and planning (SKB, 2008). In this paper focus will be on the Forsmark site but general rock mechanics understanding has been gained from all sites, including results from experiments at the underground Hard Rock Laboratory at Äspö.

The site description of the future site has been worked out and described in several versions of modelling, and the latest description for the Forsmark site can be found in (SKB, 2008). The aim of the description is to provide all information needed in the design work and in the safety assessment. The processes involved are complex and interconnected, the geological understanding is the basis for understanding the mechanical processes which in turn are a factor in the hydrogeological changes and the transport processes from repository up to the biosphere. The geochemical understanding of the site is a main component to the safety assessments as well. The time scales involved for a nuclear waste repository means that different issues are raised compared to ordinary rock engineering projects, in particular issues coupled to the heat generated by the waste, and this complexity demands an extraordinary close cooperation between geo-disciplines in the project.

The site description modelling work carried out has been based on extensive field investigations. Apart from surface mappings at the Forsmark site, totally 23 cored boreholes and 38 percussion drilled holes were drilled, providing totally about 17 500 m drill core. These boreholes were extensively used by all the different disciplines, including borehole investigations of different kinds and rock sampling for laboratory studies (SKB, 2008).

2.1 Geology

The main rock types in Forsmark are granite to granodiorite, metamorphic, medium-grained or aplitic (roughly 75 % of volume), pegmatitic granite to pegmatite (13 %), amphibolite and other mafic rocks (5 %), granodiorite to tonalite and fine- to medium-grained granite. The geological properties of these rock types are described in detail in (Stephens et al., 2007).

The classification of rock types was made both on an optical inspection during mapping and through the composition determined from modal analyses and from the silica density values. An important implication of this observation was that silicate density measurements in the geophysical logs can provide a continuous assessment of at least the composition of the bedrock along boreholes. The quartz content in the metagranite, which strongly dominates the area, ranges between 24 % and 46 %. The silica density of this rock type is 2,656 kg/m^3. The quartz-rich character of the bedrock has particularly important consequences for its thermal and mechanical properties.

The target area for the repository was divided into major rock domains in which the composition of rock types were similar. This division is shown in Figure 2. The two

main domains RFM029 and RFM045 have similar general rock type distribution where the difference is that in the latter the granite is commonly affected by albitization and more fine-grained. This alteration gives rise to an increased content of quartz and a marked decrease in the content of K-feldspar, relative to equivalent unaltered rocks.

To describe the site structurally a deterministic model was built for the deformation zones (Stephens and Simeonov, 2015). This model is illustrated in Figure 3, and more details about the methodology applied to arrive at the model can be found in (Fox et al., 2008). In the following rock mechanics description the rock mass outside the deformation zones ("rock domains") and the rock mass inside the deformation zones were treated separately, and given separate description and parameters. But the geometrical division for the deformation zones, based on geological observations primarily, was kept the same throughout the project between different disciplines.

The geological description further includes a Discrete Fracture Model (DFN), currently mainly based on core logging and outcrop mapping data, which gives the fracture sets of each domain and the intensity and distribution of each fracture set (SKB, 2008).

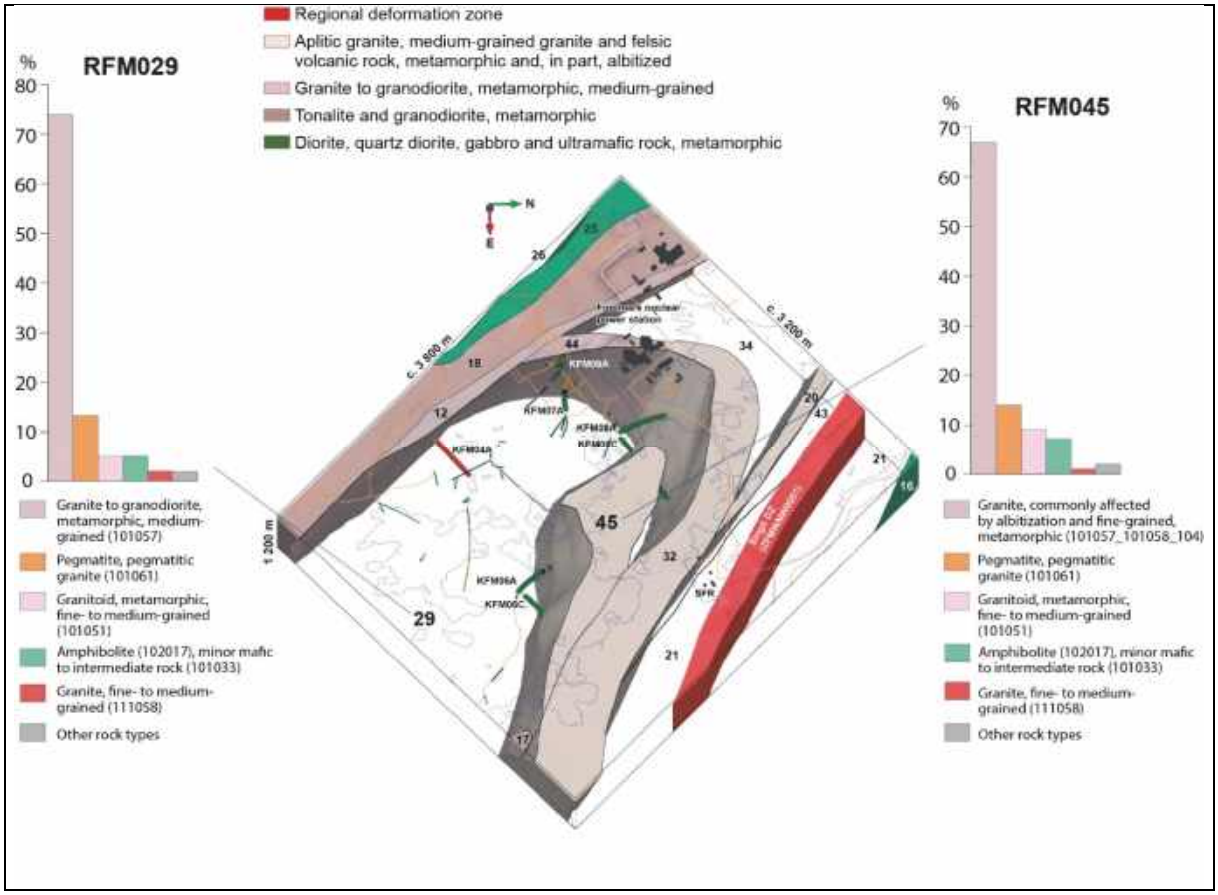

Figure 2. Rock domains, (SKB, 2008).

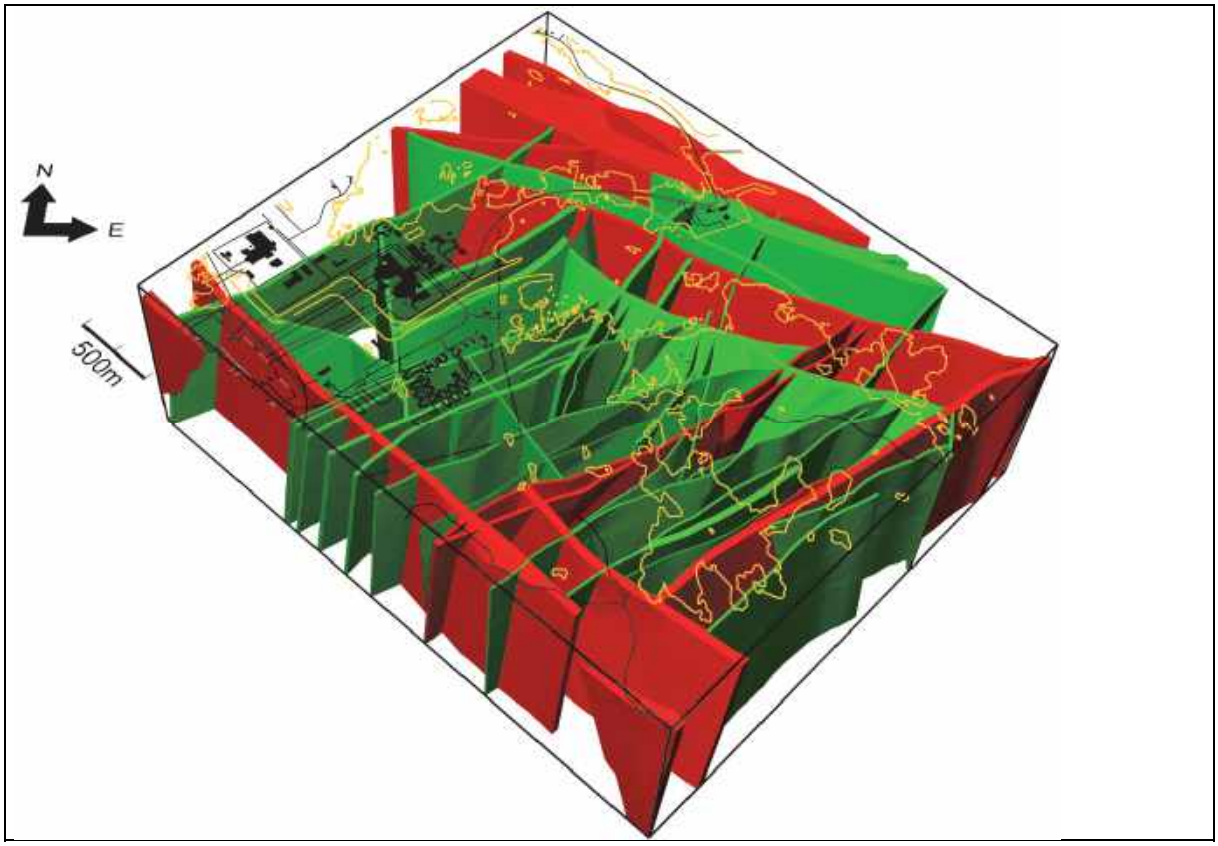

Figure 3. Three-dimensional model for vertical or steeply dipping deformation zones inside the local block model. Zones marked in red have a trace length at the surface longer than 3,000 m. Zones marked in green are less than 3,000 m in length (Stephens and Simeonov, 2015).

2.2 Rock mechanical properties

Intact rock

The intact rock mechanical properties were described by assigning deformation and strength parameters to each rock *type*, i.e. not to a rock *unit* with "mixed" rock types. This choice was made since the scale of many mechanisms of interest in the near field of a deposition hole will be smaller than the bodies of rock with constant rock type. At deposition hole scale the properties of a single rock type will thus probably often determine the mechanical behaviour. Further, the mechanical properties variation was expected to follow the rock type division, primarily.

Uniaxial, triaxial and indirect tensile tests (Brazilian tests), according to ISRM recommendations, were the basis for the parameter determination. Test equipment and procedures are described in e.g. Jacobsson (2007). The number of samples was kept relatively high to ensure that the natural variation, spatially and with depth, would be possible to evaluate. The results shown in Figure 4 demonstrate how the spread among rock types is significant and also that a certain variation exists within the main rock type. A gentle trend with depth is seen in the strength results for the main rock type, in particular observable for the tensile strength (Figure 5). For the other rock types the number of samples was not enough to study depth dependence.

The final summary of the intact rock properties is presented in Table 1. The description was chosen to be made with a mean value and a standard deviation for a normal distribution, which should be truncated with the minimum and maximum values also given in the table. The understanding of the properties were further described by estimating a value for the uncertainty. This value is the uncertainty for the mean value of the distribution (and not the range covering the whole expected distribution of values). Also the number of samples tested with respect to each parameter is given in Table 1. It may be noted that for the most common rock type, denoted 101057, the variation was quite small with 3 MPa as the standard deviation in the descriptive model.

Table 2 gives the estimated values of the constant mi included in Hoek-Brown's failure criterion and estimated cohesion and friction angle based on Mohr-Coulomb's criterion. The values given for the constant m_i correspond to normal values for granite, while the cohesion and friction angle correspond to values of very strong rock (Hoek, 2007).

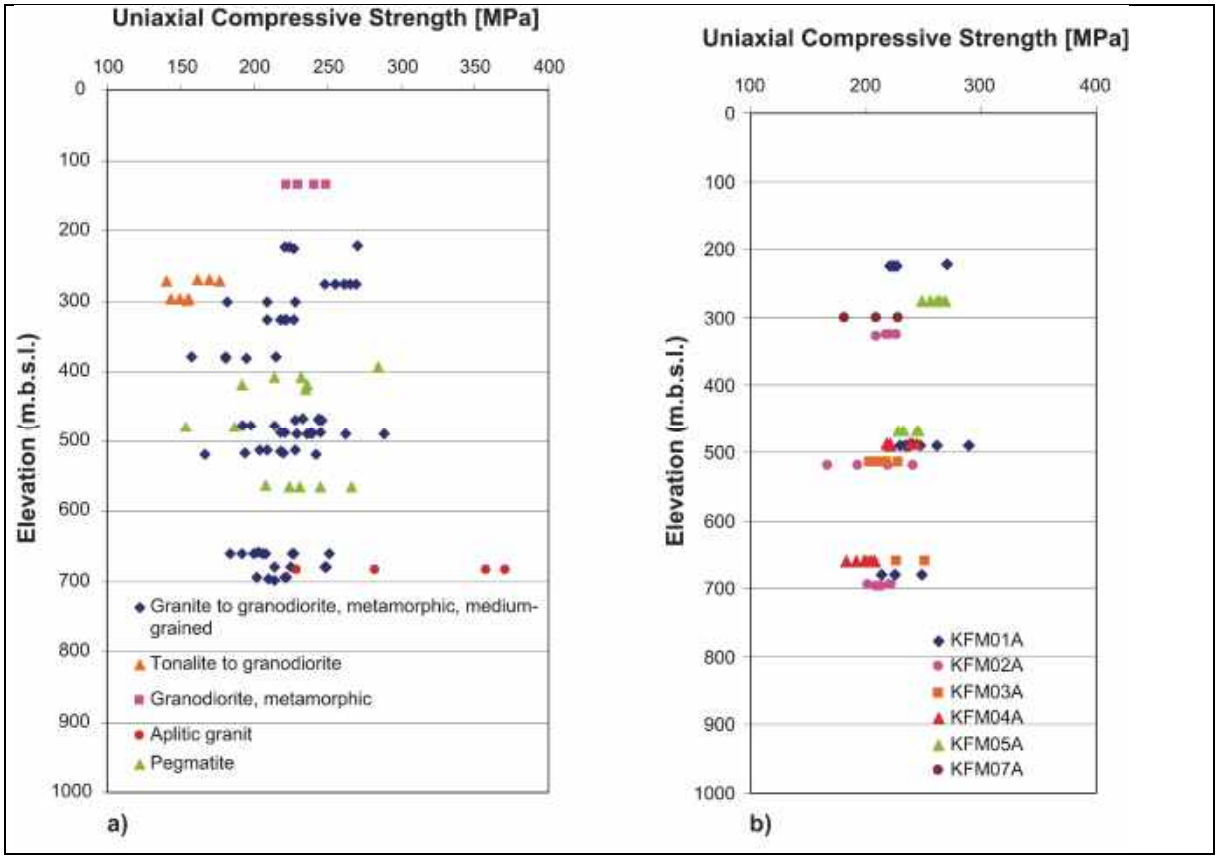

Figure 4. The uniaxial compressive strength (UCS) versus depth for(a) all rock types and (b)all samples in the main rock type, granite to granodiorite, sorted by borehole (Glamheden et al., 2007).

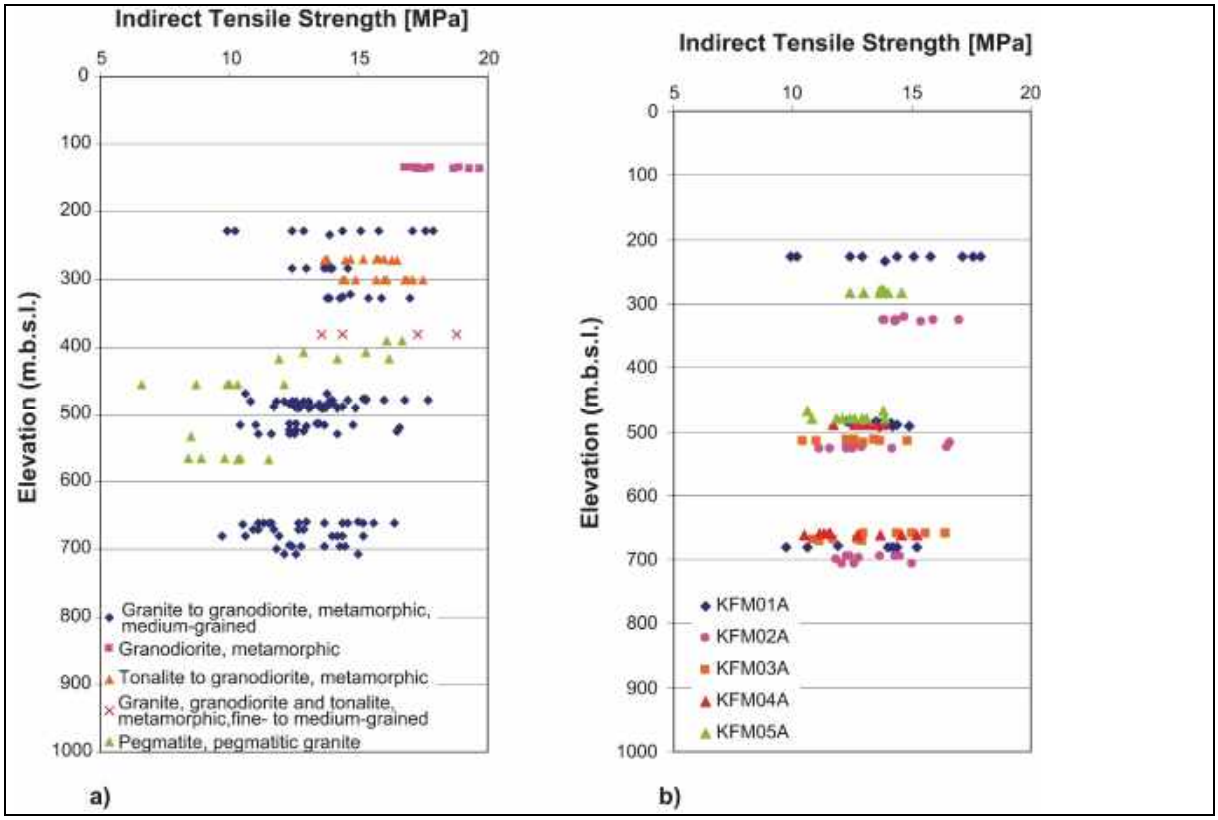

Figure 5. Results from laboratory, indirect tensile tests, on samples from the Forsmark site, presented for (a) all rock types, and b) presented for only the most common rock type at the site, granite to granodiorite, sorted by borehole (Glamheden et al., 2007).

The estimated microcrack volume for samples of the main rock type indicates that the mickrocracking due to stress relaxation and mechanical effects during the drilling is moderate in Forsmark. The evaluated microcrack volume corresponds to 5 – 10 % of the measured mean porosity. Furthermore, the results show a linear increase of the crack volume with depth in the samples from borehole KFM01A, while the depth dependency is indistinct for samples from borehole KFM02B (Figure 6). This is in compliance with the minor trend seen in tensile strength.

The geological features that occur in the target area seem to have little influence on the strength and deformation properties of the intact rock. The laboratory results on samples inside or in the vicinity of deformation zones are in the same range as the results on samples taken in the host rock outside deformation zones. These findings are in accordance with the geological description of the deformation zones being composed of mainly sealed fractures.

Table 1. Summary of deformation and strength properties for intact rock in domains RFM029 and RFM045 (Glamheden et al., 2007).

RFM FFM Rocktype	Number of samples	E [GPa] Mean/st dev Min–max *Uncertainty of mean*	ν Mean/st dev Min–max *Uncertainty of mean*	UCS [MPa] Mean/st dev Min–max *Uncertainty of mean*	σ_{ci} [MPa] Mean/st dev Min–max *Uncertainty of mean*	Number of samples *For tensile* 	σ_t [MPa] Mean/st dev Min–max *Uncertainty of mean*
RFM029 FFM01 101057	47	76/3 69–83 *± 1%*	0.23/0.04 0.14–0.30 *± 4%*	226/28 157–289 *± 4%*	116/23 60–187 *± 7%*	82	13/2 10–18 *± 2%*
RFM029 FFM01 101061	10	75/3 71–80 *± 3%*	0.30/0.03 0.26–0.35 *± 6%*	228/21 192–266 *± 6%*	121/12 100–140 ± 9%	11	12/3 8–16 *± 13%*
RFM029 FFM03 101057	13	75/3 71–80 *± 2%*	0.23/0.03 0.16–0.27 *± 7%*	220/13 203–251 *± 3%*	118/7 105–127 *± 4%*	30	14/2 10–17 *± 5%*
RFM029 FFM03 101054	4	72/3 70–76 *± 4%*	0.29/0.04 0.25–0.34 *± 13%*	150/6 143–155 *± 4%*	–	10	16/1 14–18 *± 4%*
RFM029 PDZ 101057	4	77/1 77–79 *± 1%*	0.22/0.02 0.20–0.24 *± 8%*	205/33 166–242 *± 16%*	105/22 85–134 ± 35%	10	13/2 11–17 *± 9%*
RFM045 FFM06 101058	5	83/3 80–86 *± 3%*	0.27/0.03 0.25–0.31 *± 8%*	310/58 229–371 *± 16%*	169/29 125–200 *± 15%*	–	18

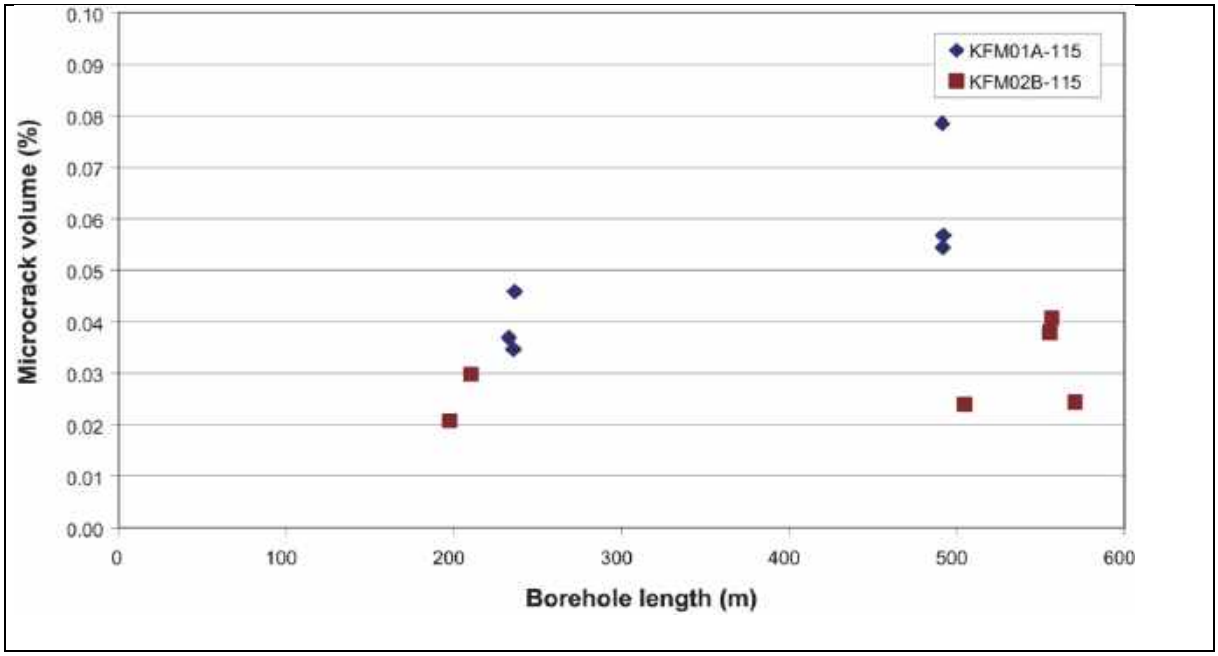

Figure 6. Measured micro crack volumes versus sampling level (borehole length) (Jacobsson, 2007).

Table 2. Estimated mean values of constant m_i included in Hoek-Brown's criterion and mean values of the cohesion and friction angle of Mohr-Coulomb's criterion for intact rock in domains RFM029 and RFM045.

Rock domain	Facture domain	Rock type	Number of samples	m_i	c [MPa]	ϕ [°]
RFM029	FFM01	Granite to granodiorite, metamorphic, medium-grained 101057	86	28	28	60
RFM029	FFM01	Pegmatite, pegmatitic granite 101061	15	18	33	56
RFM029	FFM01	Granite, granodiorite and tonalite, metamorphic, fine- to medium-grained 101051	4	46	19	63
RFM029	FFM03	Granite to granodiorite, metamorphic, medium-grained 101057	25	28	27	60
RFM029	FFM03	Tonalite to granodiorite, metamorphic 101054	8	13	25	51
RFM029	PDZ	Granite to granodiorite, metamorphic, medium-grained 101057	4	37	24	62
RFM045	FFM06	Granite, metamorphic, aplitic 101058	5	29	30	60

Fractures

The fracture properties were tested through laboratory tests on drill core samples. These small scale samples were moulded into concrete fixtures. These samples were submitted to normal loading / unloading tests to estimate normal stiffness and to direct shear tests under constant normal load to estimate shear stiffness, shear dilation and shear strength. These laboratory methods are described in detail in Jacobsson (2007). A summary of the results is presented in Table 3. A similar format for the description of properties as used for the intact rock is also used for the fractures. The test show results that were expected compared to what is found in the literature for small fractures. The scale effect of the fracture properties is an area that has not been investigated further within the current site-descriptive model.

Table 3. Summary, and selection, of properties determined from direct shear tests for the fracture domains (Glamheden et al., 2007).

Fracture domain	Peak friction (°)	Peak cohesion (MPa)	Normal stiffness, K_N (GPa/m)	Shear stiffness, $K_{S5.0}$ (GPa/m)	Dilatancy angle, ψ_5 (°)
	Mean/std. dev. **Min–max** ***Uncertainty of mean***	**Mean/std. dev.** **Min–max** ***Uncertainty of mean***	**Mean/std. dev.** **Min–max** ***Uncertainty of mean***	**Mean/std. dev.** **Min–max** ***Uncertainty of mean***	**Mean/std. dev.** **Min–max** ***Uncertainty of mean***
FFM01	36.6/2.9 29.3–42.0 *± 2.9%*	0.8/0.3 0.2–1.3 *± 13.7%*	656/396 159–1,833 *± 22.0%*	26/9 7–46 *± 12.6%*	7.7/2.7 2.5–13.7 *± 12.8%*
FFM02	36.4/2.5 34.4–40.0 *± 6.7%*	0.5/0.4 0.2–1.0 *± 78.4%*	248/165 115–483 *± 65.2%*	26/4 21–31 *± 15.1%*	2.2/0.5 1.6–2.6 *± 22.3%*
FFM03	37.0/1.7 34.2–39.0 *± 3.0%*	0.6/0.2 0.3–0.9 *± 21.8%*	293/193 152–734 *± 43.0%*	31/7 23–43 *± 14.8%*	3.1/2.1 0.5–6.3 *± 44.3%*
FFM04	32.0/3.3 28.5–35.0 *± 11.7%*	0.9/0.4 0.6–1.4 *± 50.3%*	1,385/283 1,072–1,624 *± 23.1%*	16/5 12–22 *± 35.4%*	6.6/1.3 5.4–7.9 *± 22.3%*
FFM05	37.0/1.8 35.7–38.2 *± 6.7%*	0.8/0.2 0.7–0.9 *± 34.7%*	599/57 559–639 *± 13.2%*	20/7 14–25 *± 48.5%*	8.8/0.1 8.7–8.8 *± 1.6%*
DZ	35.3/2.4 32.5–38.4 *± 4.2%*	0.8/0.5 0.0–1.7 *± 38.7%*	662/729 167–2,445 *± 68.3%*	26/9 7–41 *± 21.5%*	5.7/4.3 1.0–13.0 *± 46.8%*

Rock mass

The rock mechanics site-descriptive model utilises two modelling approaches to estimate the rock mass properties, an empirical and a theoretical approach. The empirical characterisation of the rock mass was carried out on 5 m long borehole sections, using the Q and RMR classification systems and the methodology is presented in (Andersson et al., 2002, Röshoff et al., 2002). A more comprehensive compilation of the results from the rock mass characterisation is provided in (Glamheden et al., 2007). Results from rock mass characterisation of the major deformation zones Singö and Forsmark are provided in (Glamheden et al., 2008).

The empirical indices were used with empirical relationships to estimate rock mechanics parameters.

The “theoretical” approach was also aiming at the same mechanical parameters using the DFN model as a starting point. Numerical modelling with discontinuous rock mass was conducted. The properties of intact rock and fractures, as previously presented, where used as input to the numerical models. The mechanical properties of the rock mass were then determined from numerical “compression tests” of simulated rock

mass volumes (Staub et al., 2002; Olofsson and Fredricksson, 2005; Glamheden et al., 2007).

The results from both the empirical and the theoretical approaches were finally compared and a "harmonized" value that was judged to best represent the predicted behaviour of the rock mass was chosen (Table 4). Variation in parameters was estimated by studies of the effect of variation in the input data to the two approaches (i.e. sensitivity analyses). The fairly consistent results from the two approaches are encouraging, but the final verification of methodology and parameters will be available only when the excavations is started and there are possibilities to measure the actual responses of the rock mass.

Table 4. Suggested rock mechanics properties of the rock mass (Glamheden et al., 2007).

Rock domain	**Empirical approach**		**Theoretical approach**		**Harmonized values**	
Properties of the rock mass	**Mean/std. dev.** **Min–max** ***Uncertainty of mean***		**Mean/std. dev.** **Min–max** ***Uncertainty of mean***		**Mean/std. dev.** **Min–max** ***Uncertainty of mean***	
	FFM01	**FFM06**	**FFM01**	**FFM06**	**FFM01**	**FFM06**
Deformation modulus [GPa]	72/8 39–76 *± 1%*	70/12 40–81 *± 3%*	69/4 59–79 *± 2%*	68/5 56–81 *± 3%*	70/8 39–79 *± 2%*	69/12 40–81 *± 3%*
Poisson's ratio	0.23/0.03 0.12–0.30 *± 1%*	0.23/0.04 0.12–0.33 *± 3%*	0.24/0.03 0.19–0.33 *± 5%*	0.3/0.03 0.23–0.37 *± 4%*	0.24/0.03 0.12–0.33 *± 5%*	0.27/0.04 0.12–0.37 *± 4%*
Uniaxial compressive strength (Hoek and Brown) [MPa]	92/27 23–153 *± 3%*	95/32 30–149 *± 7%*	No values	No values	92/27 23–153 *± 3%*	95/32 30–149 *± 7%*
Friction angle (Mohr-Coulomb) [°]	50/2 32–52 *± 0%*	50/2 43–53 *± 1%*	53/2 50–56 *± 2%*	52/2 47–57 *± 2%*	51/2 32–56 *± 2%*	51/2 43–57 *± 2%*
Cohesion (Mohr-Coulomb) [MPa]	27/4 12–35 *± 1%*	27/4 18–34 *± 3%*	21/6 5–42 *± 13%*	18/6 1–40 *± 15%*	24/5 6–42 *± 13%*	23/5 1–40 *± 15%*
Tensile strength [MPa]	2.4/1.0 0.6–5.0 *± 3%*	2.3/1.0 0.6–4.0 *± 8%*	No values	No values	2.4/1.0 0.6–5.0 *± 3%*	2.3/1.0 0.6–4.0 *± 8%*

In-situ rock stress

Direct stress measurements have been carried out in several different measurement campaigns. Both overcoring and hydraulic methods have been used. Major efforts to improve these methods have been made. Figure 7 shows the stress magnitude results

from the overcoring measurements in different boreholes in the Forsmark area. A general trend with increasing magnitudes can be noted, but there is a considerable spread in the values.

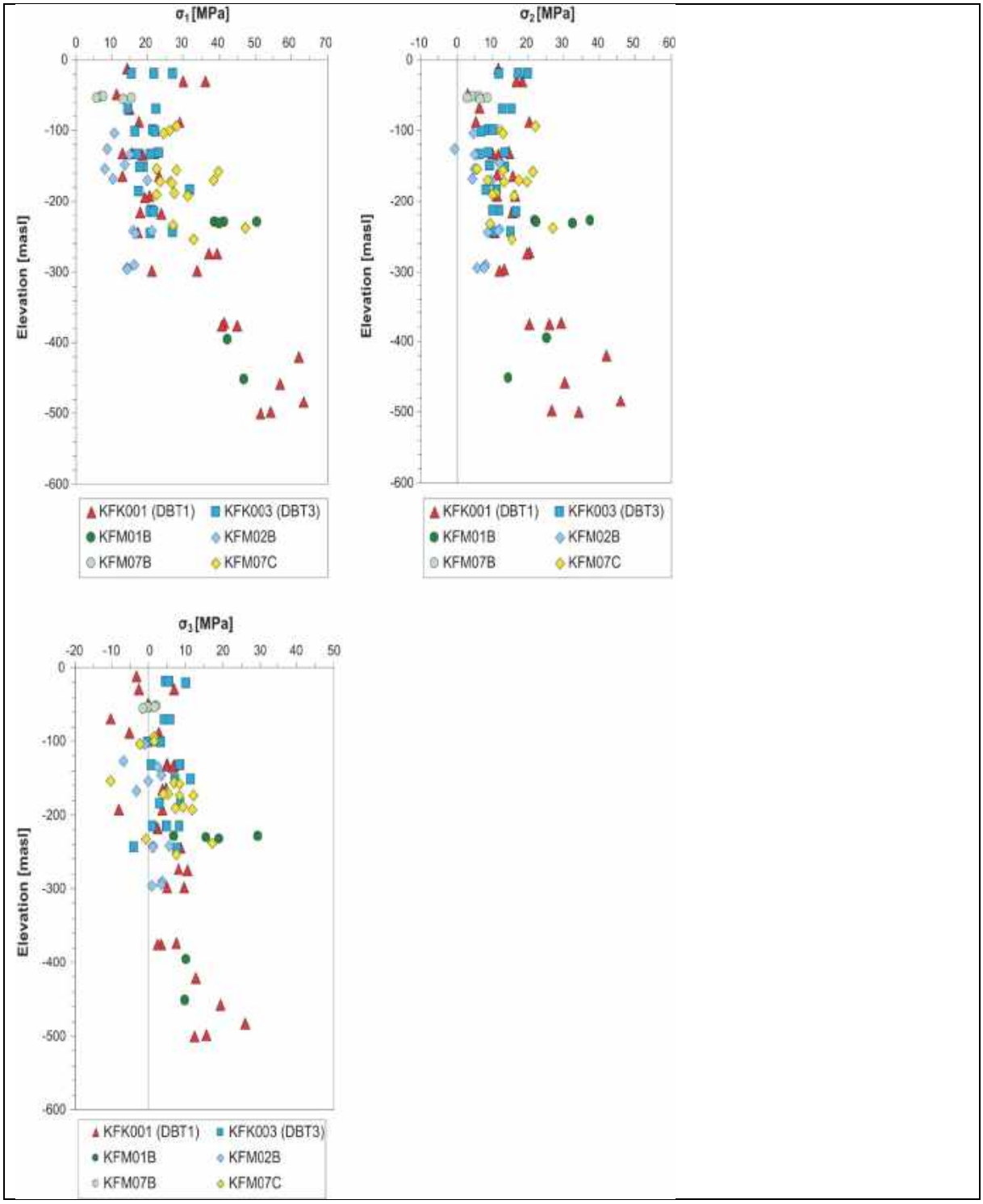

Figure 7. Measurement data from overcoring. Major, intermediate and minor principal stress magnitude.

A comparison between the results from overcoring measurements and hydraulic measurements is made in Table 5, and it can be concluded that the difference is significant. The conclusion from the stress measurements is that there is a remaining uncertainty regarding the stress magnitudes and therefore conservative approaches have been taken in the design and safety assessment work. Further research and development work is ongoing on this regard.

The in-situ stress orientation, on the contrary, is judged to have a quite small uncertainty. This is based both on the overcoring data and the borehole breakout studies. The latter has shown very consistent results, irrespective of boreholes and depths (Figure 8). Also the micro fallouts (borehole sections were full breakouts are not developed but small fallouts are observed on opposite sides of the holes) have the same consistent direction.

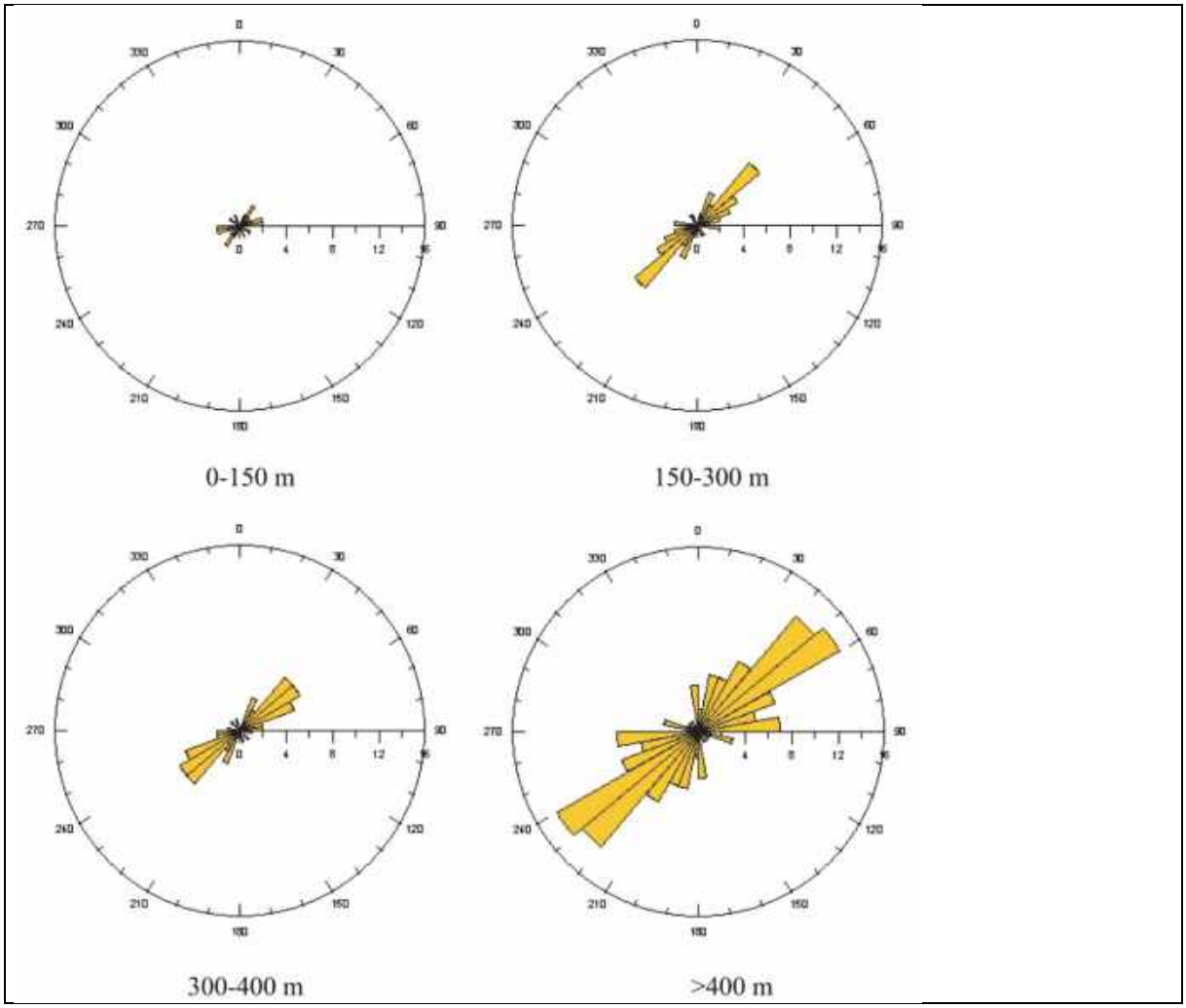

Figure 8. Rose diagram showing the orientation of the “classical” breakouts in 12 boreholes from the Forsmark site, at different depth intervals in boreholes. The number of breakouts is 11 in the interval 0-150 m, 27 between 150-300 m, 29 between 300-400 and 75 for depths >400 m. From (Glamheden et al., 2008).

Table 5. Comparison of the horizontal and vertical stress magnitudes at 400 and 500 m depth. The values by Martin (2007) are based primarily on overcoring data whereas the values by Ask et al, (2007) are based on hydraulic fracturing and hydraulic testing of pre-existing fractures (Glamheden, et al., 2007).

Depth (m)	Maximum horizontal stress (MPa)	Trend (deg)	Minimum horizontal stress (MPa)	Trend (deg)	Vertical stress (MPa)
(Martin, 2007)					
400	38.7 ±5.8	145 ±15	20.4 ±4.0	55	10.6 ±0.2
500	41.0 ±6.2	145 ±15	23.2 ±4.6	55	13.2 ±0.3
(Ask et al., 2007)					
400	19.2 ±0.7	124 ±6	9.3 ±1.1	34	10.4
500	22.7 ±1.1	124 ±6	10.2 ±1.6	34	13.0

2.3 Thermal properties

The thermal properties of rock samples were obtained from laboratory tests. In the modelling work, to keep the lithological simulations manageable, the rock types were grouped into thermal rock classes (TRC) within which the thermal and lithological properties were similar Table 6 gives the division into TRC and the mean thermal conductivity from laboratory tests for each rock type. The distribution of the testing results for each TRC are also presented in Figure 9. It can be noted that generally the thermal conductivity (TPS) of the rock is fairly high, about 3.7 W/(m K), but a minor part of the target volume, the TRC51A-C, has a wide range of values with some of them lower than 2.5 W/(m K). Low thermal conductivity volumes are of particular interest because they will give the largest temperatures close to the deposited canister when it is placed in this rock. According to the design requirements, the temperature must be kept below 90 degrees for a canister location to be acceptable and therefore it was also of interest to simulate how the distribution of the thermal bodies could be expected to turn out at the site. Examples of 2D visualisations of the realisations of thermal conductivity (slices in xz-plane) are shown in Figure 10.

Table 6. Division of rock types into TRCs for domain RFM029 (SKB, 2008).

TRC	Rock name/code	Mean thermal conductivity (TPS), (W/(m·K))	Composition, mode of occurrence, etc.	Proportions of rock types from geological model 2.2, (%)
57	Granite to granodiorite, 101057	3.68	Felsic composition, group B rocks.	74
	Granite, aplitic, 101058	3.85		1
51	Granite, granodiorite and tonalite, 101051	2.85	Felsic to more intermediate compositions, group A and C rocks.	5
	Felsic to intermediate volcanic rock, 103076	2.54		< 1
61	Pegmatite, pegmatitic granite, 101061	3.33	Felsic composition, group D rocks. Late tectonic dykes, segregations, veins.	13
	Granite, 111058	3.47		2
17	Amphibolite, 102017	2.33	Mafic composition, group B rocks. Dykes and minor bodies or lenses.	4
	Diorite, quartz diorite and gabbro, 101033	2.28		< 1

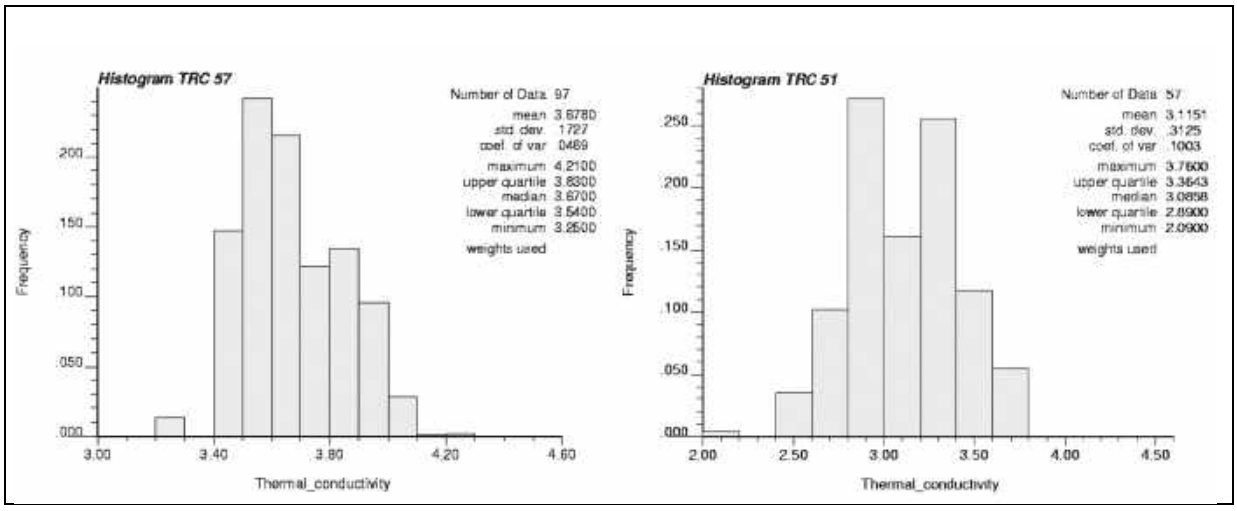

Figure 9. Histograms of thermal conductivity derived for TRC57 and TRC51 (SKB, 2008).

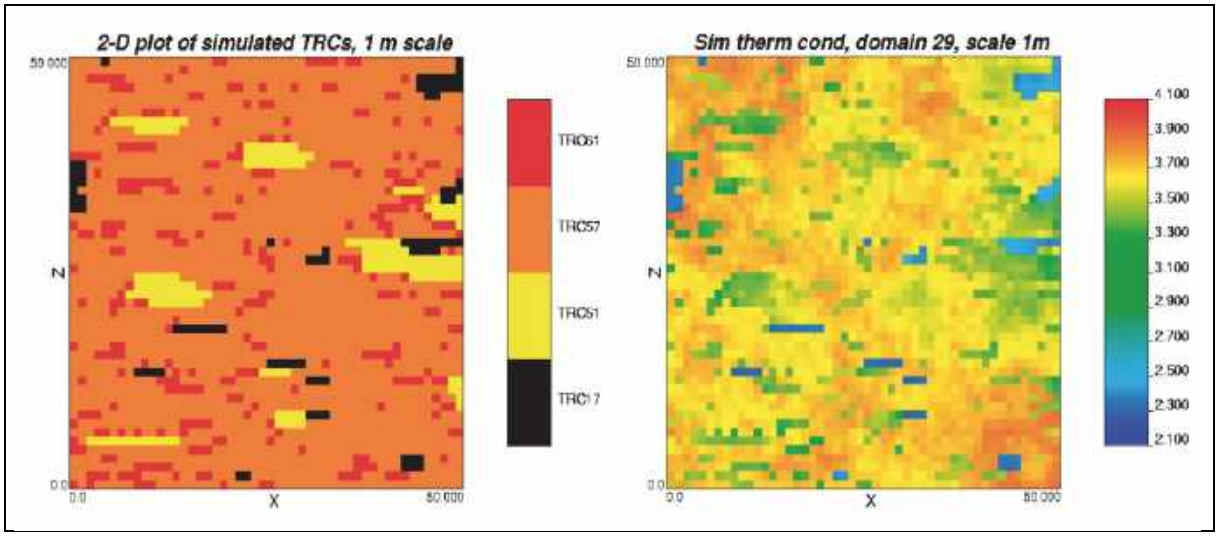

Figure 10. Example 2D visualizations of the lithological simulations (left) and the corresponding realization of thermal conductivity (right) for domain RFM029 (Internal) simulated at the 1 m scale. Slices in xz-plane (SKB, 2008).

3 Rock mechanics aspects

In this section the handling of a number of rock mechanics issues of particular potential importance to the performance assessment and to repository layout decisions are briefly described. For some of the issues the uncertainties are very large and the handling must be based on schematic input assumptions to ensure sufficient margins to critical conditions. This is, for instance and in particular, the case for the seismic reactivation issue described in one of the sections below. The probability of large future earthquakes in the Forsmark region is extremely small and uncertain. The details, even important ones, of a possible future earthquake, e.g., the stress drop, the magnitude etc., are obviously also extremely uncertain. For the thermomechanical evolution of the repository host rock, in contrast, the essential input parameters are reasonably well known, i.e., the initial heat power and power decay of the spent fuel and the thermal and thermomechanical properties, as described in Section 2 above, of the Forsmark rock mass. Regardless of the degree of uncertainty, it is essential to develop an understanding of the different rock mechanics issues and to ensure and also demonstrate, as attempted below for a number of issues, that that understanding is adequate for layout decisions and risk analysis.

3.1 Spalling

Stress-induced brittle failure, spalling, in the walls of openings in highly stressed crystalline rock is a process of potential concern for the Swedish nuclear waste repository. Spalling in the walls of the deposition holes could, depending on scope and extent, mean permeability changes that need to be accounted for in the safety assessment. At AECL's URL in Manitoba, spalling has been found to result in progressive development of borehole-notches of depths corresponding to tens of percent of the borehole radius, cf. e.g. Read and Martin (1992). Andersson and Söderhäll (2001) found no evidence of any corresponding damage at any position in SKB's HRL in Äspö. Chryssantakis et al. (2003) back-analysed convergence measurements performed during excavation of a 5 m diameter TBM tunnel in the Äspö HRL and concluded that

the rock mass response had been essentially elastic. Not observing any indications of damage to Äspö HRL underground openings after excavation analogous to those observed in AECL's URL is a logical consequence of the significantly lower in situ stress level at Äspö. At the Forsmark site, however, the in situ stresses are higher, albeit not as high as in AECL's URL in Manitoba. A few years after deposition of the heat-generating canisters, the near field stress level at Forsmark will be significantly increased and eventually exceed the in situ stress level in AECL's URL, meaning that spalling in the walls of deposition holes will be a realistic possibility even if deposition tunnels will be oriented in parallel with the major horizontal stress in order to minimize tangential stresses in tunnels and deposition holes (cf. text on layout below). Improving the understanding of the spalling process and the possible implications of exceeding the spalling strength in SKB deposition holes has been concluded to be an issue that needs attention.

One aspect of particular interest is related to an observation made in the mine-by-tunnel test in AECL's URL: While spalling resulted in a notch being developed in the region of maximum tangential stress in the tunnel roof, the presence of tunnel muck on the floor appeared to have inhibited the development of a notch in the corresponding, identically stressed, floor position (Martin and Read, 1992), indicating the possibility that a low support pressure, significantly smaller than the swelling pressure of a saturated (or partly saturated) bentonite buffer, might be sufficient to suppress spalling in highly stressed SKB deposition holes. Two field experiments, APSE and CAPS, were conducted at Äspö HRL to establish spalling strength estimates relevant to fractured rock and to explore the potential of low support pressures to suppress spalling. Both experiments were carried out in vertical boreholes, drilled in the rounded floor of the TASQ tunnel which is oriented perpendicular to the major horizontal stress, i.e., under maximized stress conditions. In both experiments the rock was heated to increase the tangential stresses further.

In the APSE (Äspö Pillar Stability Experiment) a full scale deposition hole was drilled in the highly stressed floor and then stabilized by means of a 700 kPa internal pressure applied in a large water-filled rubber bladder (Andersson, 2007). In a second hole, drilled at one meter distance from the stabilized hole, spalling occurred as a result of excavation from a depth of approximately 0.5 m down to 2 m below the tunnel floor. Later, when the pillar between the two holes was heated, the spalled zone propagated down to 5 m depth. Still later, under steady state thermal stress conditions, the confining bladder pressure was slowly ramped down in 50 kPa steps. Extensive acoustic activity on the confined side of the pillar was not observed until the bladder pressure had been reduced to 150 kPa. The test procedure, the results of the different numerical analyses performed before, during and after the test and the conclusions of the APSE field test are described and reported in detail by Andersson (2007). One important result is that the spalling strength was found to be about 57% of the unconfined compressive strength. Another important result is that a confining pressure of only 150 kPa appeared to suppress, or at least significantly limit, spalling in the walls of the full scale APSE hole.

The tangential stresses in Forsmark deposition holes will increase fast after deposition of the heat-generating canisters (Figure 11). The spalling strength will typically be

reached between 0.1 and 10 years after deposition, assuming it to be 57 % ±5 % of the uniaxial compressive strength. The time-scale for the development of a bentonite swelling pressure that is sufficient to stabilize the walls of the deposition holes, i.e., on the order of 150 kPa, is very uncertain and will vary within very wide ranges between holes. The CAPS experiment (Counterforce Applied to Prevent Spalling) was initiated to explore to what extent the unsaturated bentonite pellets filling out the annular space between compacted bentonite blocks and rock would stabilize the walls of dry deposition holes and contribute to suppress spalling (Glamheden et al., 2010). Four pairs of 0.5 m diameter, 4 m deep holes separated by 0.7 m pillars were drilled in the rounded and highly stressed floor in a segment of the TASQ tunnel. Four heating tests were performed, each involving one pair of holes. In two of the tests the walls were supported by dry pellets filled in the annular space between heater and rock, while the walls were left unsupported in two tests. Laboratory tests were made to determine the mechanical properties of the intact TASQ tunnel rock and the pellets material, and to estimate the pressure exerted on the rock wall by the pellets (Glamheden et al, 2010). When the holes were cleared and checked for occurrences of spalling in the walls after completion of the tests, breakouts and tendencies of notch formation were found in open holes as well as in holes that had been supported during heating. Although the results were concluded to have been influenced by spatial rock strength variabilities and differences in water inflow, breakout volumes and breakout depths appeared to have been larger in open holes than in confined holes. One of the supported holes was left un-cleared to be sealed and checked, by means of an injection test, for permeability changes in the wall section subjected to the highest tangential stresses. The injection test gave no indications of any increased permeability, meaning that the pellets filling appeared to have suppressed the progression of the failure effectively merely by keeping potentially detaching rock slabs in place.

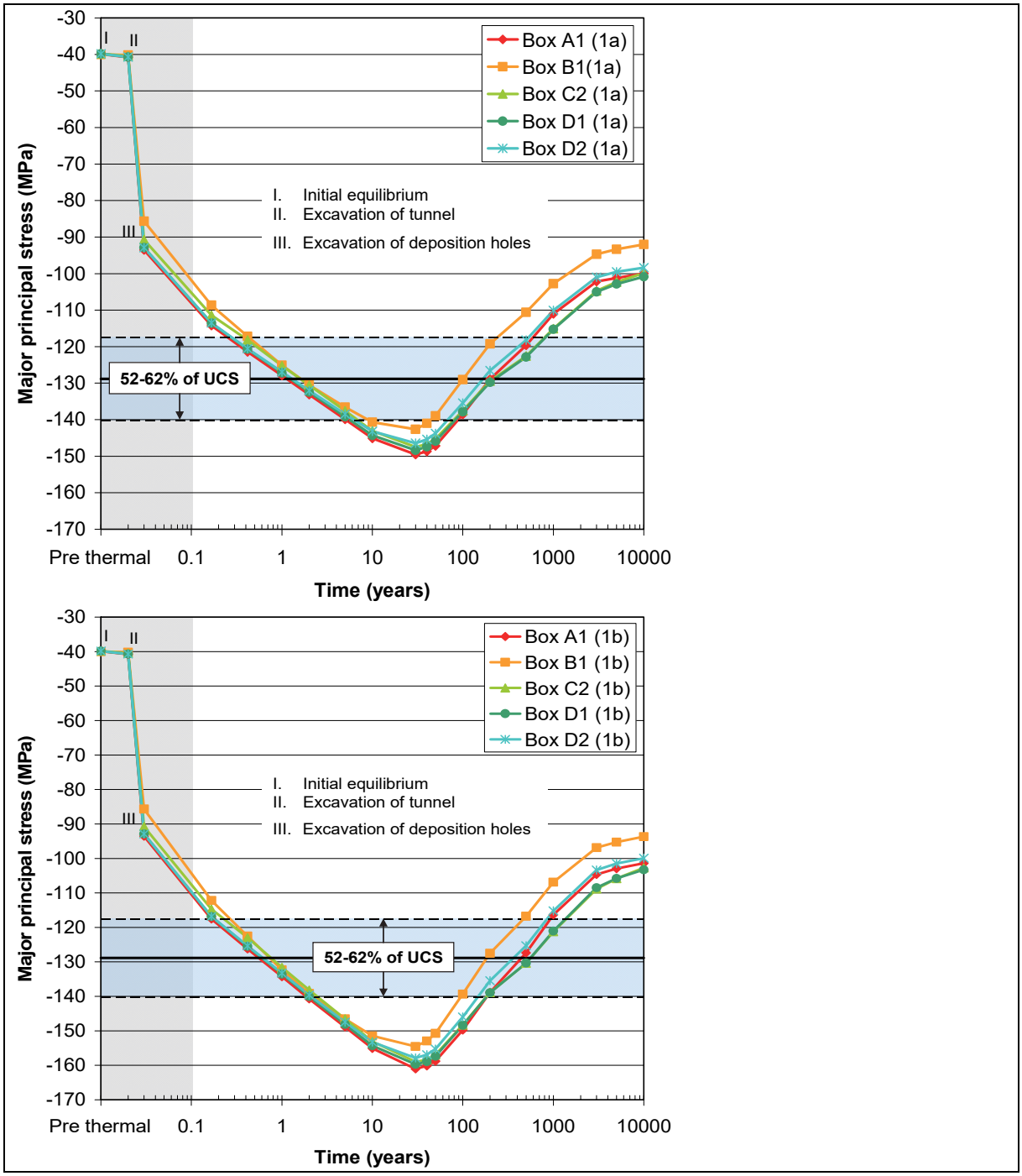

Figure 11. Evolution of tangential rock wall stress at canister mid-height. Left: Mean nearfield rock temperature. Right: Highest nearfield rock temperature calculated according to the models established for the spatial variability of the heat transport properties in the Forsmark bedrock (Hökmark et al., 2010).

3.2 Fracture reactivation due to seismic events

The Baltic Shield is a seismically stable region, subjected to a slow horizontal tectonic compression related to the North Atlantic ridge-push process and to slow glacial rebound. The largest historical earthquakes in Sweden is the 1904 magnitude 5.4 Koster (or Oslofjorden) event (Bungum et al., 2009). In historical time no earthquakes of magnitude larger than 4 are known to have occurred within 200 km distance from the Forsmark site (Bödvarsson et al., 2006). Under present day stress conditions, large earthquakes occurring within a few kilometres distance from the Forsmark repository are therefore, if not completely excluded, very unlikely. Towards the end of the last glaciation, however, large earthquakes did occur in the northern parts of the Shield in response to the disappearance of the stabilizing ice cover (SKB, 2011), meaning that, given the time scale relevant for the safety assessment, the potential impact of seismic events on the performance of the repository yet needs attention. In addition, thermally induced stresses may trigger earthquakes on potentially unstable deformation zones in the period of increased rock temperatures some thousand years after deposition. Therefore, no canister positions within certain respect distances from deformation zones that could host large earthquakes are allowed. The remaining concern is that rock fractures located further away from the earthquake zone may reactivate and slip in response to stress waves and stress redistribution and possibly damage intersected canisters (SKB, 2011). At present canisters sheared 50 mm or more count as failed. The reactivation problem has been addressed in several numerical studies, all aiming at finding reasonably realistic upper bound estimates of induced, secondary, shear displacements along differently oriented host rock fractures located at different distances from an earthquake fault (Fälth et al., 2010; Fälth et al., 2015; Fälth et al., 2016). The numerical studies are all based on the dynamic logic of the distinct element code 3DEC (Itasca, 2013) and include numerous simulation cases with explicitly modelled, rupturing deformation zones and surrounding host rock fractures. Figure 12 shows a compilation of results from 22 3DEC models, each with 120 fractures located at different distances from the gently dipping ZFMA2 Forsmark deformation zone, assumed to rupture under endglacial stress conditions (Fälth et al., 2016). The 22 models correspond to 22 differently oriented fracture sets. The fractures are perfectly planar and have diameters of 300 m. Tests with models with more realistic assumptions regarding the fracture geometry, the rupture arrest at the fault edges, the seismic efficiency, etc., have shown that the secondary displacements in Figure 12 are likely to be very considerable overestimates.

In the safety assessment, the handling of the seismic risk is based on the concept of critical fractures, i.e., fractures that potentially could reactivate and slip by 50 mm or more, and the concept of critical positions, i.e., canister positions within the central parts of such fractures, i.e., where induced displacement actually may exceed the 50 mm damage limit. The final bounding risk estimate in SR-Site is based on the 3DEC modelling results reported by Fälth et al. (2010) and methods devised by Munier (2010) to account for the Forsmark fracture population. Results of numerical work carried out during the last few years, e.g. (Fälth et al., 2015) and (Fälth et al., 2016), has indicated that the SR-Site safety margins are likely to be unnecessarily large (cf. text on results presented in Figure 12), meaning that it might be worthwhile to re-evaluate layout restrictions associated with seismic risks. To actually pave the avenue for a more efficient use of the rock volume available for the repository more work is however necessary,

for instance on the style of rupture arrest in margins of the ruptured fault area. More work is also needed to explore how different geometrical disturbances, e.g. undulations, steps, etc., will contribute to limit induced slip along reactivated fractures (Lönnqvist and Hökmark, 2015).

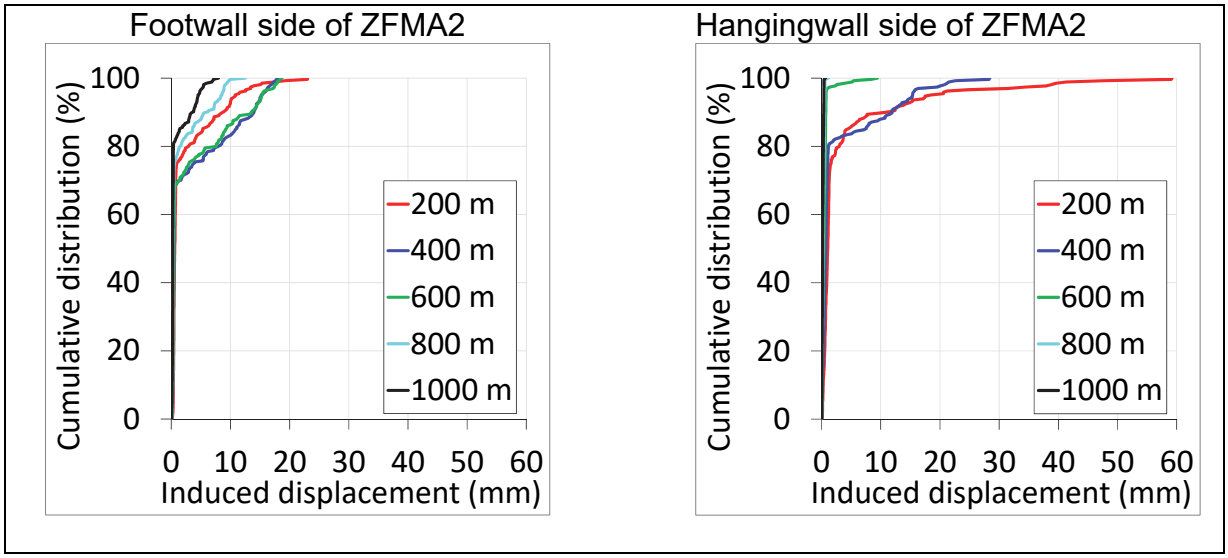

Figure 12. Cumulative plots of secondary displacements on differently oriented fractures at different distances from a gently dipping rupturing Forsmark fault. In total 2640 fractures are included. Note that the repository will be located on the footwall side of the fault. From (Fälth et al., 2016).

3.3 Repository layout

The principles of the Forsmark repository layout are shown in Figure 13. Deposition tunnels are parallel or subparallel with the major horizontal stress in order to limit the tangential stresses in the roofs and floors of the tunnels and, consequently, also the tangential stresses in the walls of the deposition holes. The size and shape of the deposition areas are determined by constraints set up regarding the maximum tunnel length, 300 m, and the smallest distance, 100 m, allowed between canisters and deformation zones with trace lengths of 3,000 m or more, cf. text on fracture reactivation above. Canister positions intersected by deterministic deformation zones are rejected. The repository is required to hold 6000 canisters, but to cover for losses of canister positions due to unacceptable water inflows or intersections with large fractures, the layout has a gross capacity of about 7,800 canister positions, allowing for about 23 % of the positions to be rejected (SKB, 2008). All thermomechanical analyses conducted within the SR-Site safety assessment, and described here in the following, are based on a layout version allowing for loss of only 13 % of the positions, i.e., a layout with a slightly denser average heat production.

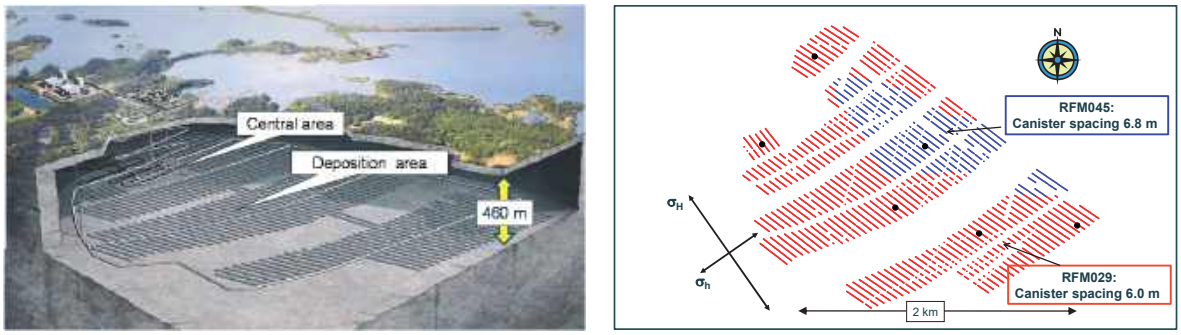

Figure 13. Left: Position of repository at 460 m depth close to the Forsmark power plant. Right: repository layout. Red and blue dots correspond to canisters deposited at 6.0 and 6.8 m distance, respectively, from each other. The layout version shown here has 6900 canister positions to allow for loss of 900 positions. In the latest layout version the southernmost deposition area has been extended to allow for about 1800 positions to be lost (SKB, 2009a). In the large scale thermal and thermomechanical models described in the following, lost (rejected) positions are evenly distributed within the repository footprint. The black dots represent locations picked for nearfield analyses in high resolution local thermomechanical models.

3.4 Thermo Mechanical evolution

Over the years, and at different stages of the concept development, site selection process and layout work, numerous studies have been conducted to assess the thermal and thermomechanical evolution of the repository host rock on different scales. These studies include early analytical work with schematic assumptions regarding layout and rock mass properties (e.g. Claesson and Probert, 1996a; Claesson and Probert, 1996b; Probert and Claesson, 1997a; Probert and Claesson, 1997b) as well as numerical simulations based on actual data, e.g. Forsmark repository site data and the layout shown in Figure 13 (Hökmark et al., 2010). The distinct element code 3DEC (Itasca, 2013) has been the main tool for the numerical simulations. Some of the modelling efforts have aimed at establishing layout details, i.e., the spacing between canisters required to meet the criterion set up for the maximum canister temperature (Hökmark et al., 2009). The canister spacing actually established for the Forsmark rock domains (SKB, 2009c) is based on the thermal data described in section 2.3 above. The thermomechanical numerical work carried out within the SR-Site context include 3DEC models at the repository scale (length x width x height = 8 x 7.4 x 3.1 km^3), at the tunnel (medium) scale (l x w x h = 198 x 200 x 200 m^3) and on the nearfield scale (l x w x h = 42 x 40 x 50 m^3).

Figure 14 shows the repository scale temperature evolution at the Forsmark site as calculated by Hökmark et al. (2010) using the thermal logic of the 3DEC code. The canisters are deposited in the sequence roughly indicated by the arrows in the leftmost contour plot, in total six thousand canisters at a rate of one canister every three days, giving a 50 year duration of the deposition phase. Thirteen percent of the around 6900 canister position were assumed to be lost. Figure 15 shows the associated stress evolution along a vertical scanline intersecting the central deposition area. Here time zero is when deposition takes place at the position intersected by the scanline. Figure 16 shows the heave of the Forsmark ground surface following the thermal expansion of the rock mass as obtained from the same large scale 3DEC model. Perhaps most importantly: the large scale model results are used to define boundary conditions for a

number of tunnel scale and nearfield scale models at different locations within the repository footprint (cf. Figure 13, right). Figure 17 shows examples of boundary displacements imposed on tunnel scale and nearfield scale models to account for the local effects of the large scale thermally induced rock mass expansion and subsequent contraction as obtained from the large scale 3DEC model.

In coarsely discretized repository scale 3DEC model such as the one described above, the repository openings i.e., deposition tunnels and deposition holes are not explicitly modelled and the heat-generating canisters are represented by simple point sources. To capture spatial temperature and stress variations adequately, a number of small and finely discretized tunnel scale and nearfield scale models are analysed, each corresponding to a specific location within the repository footprint, cf. Figure 13, right). To capture the heat flux distribution around individual deposition holes, vertical arrays of point sources were combined to mimic the heat output from cylindrical canisters. Figure 18 shows result examples from one tunnel scale model (left) and one nearfield scale model (right).

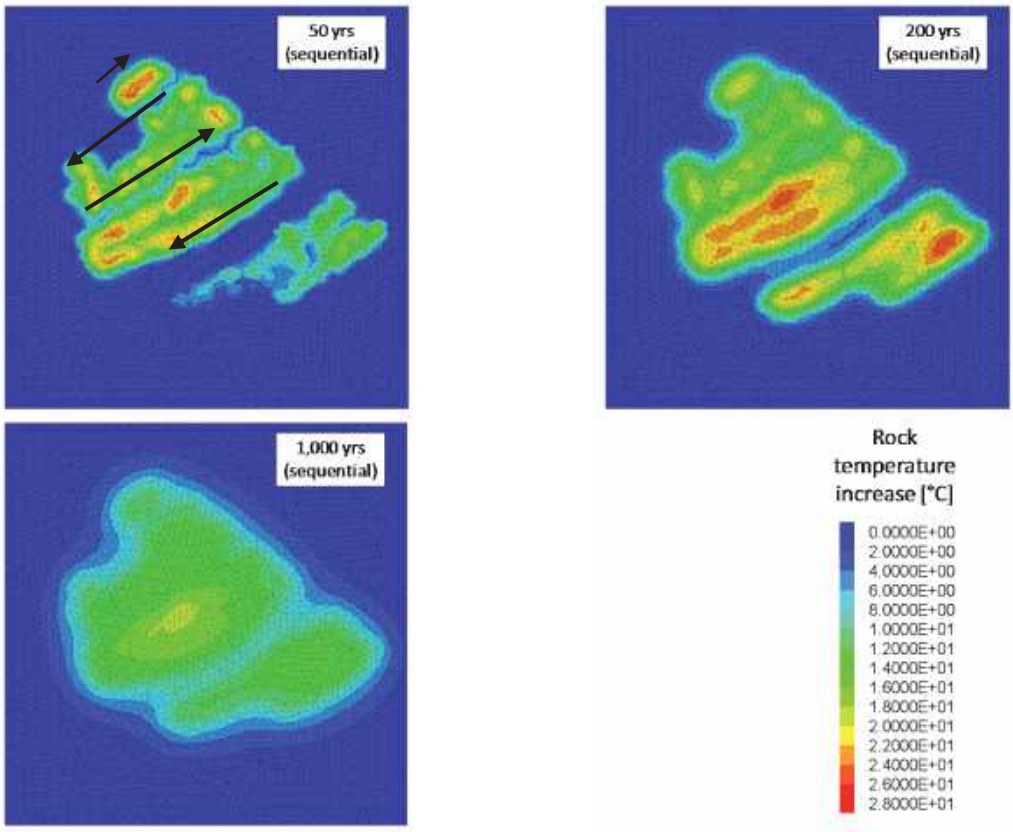

Figure 14. Temperatures in repository horizon 50, 200 and 1000 years after start of deposition, assuming one canister to be deposited every three days. In total 6000 canisters are deposited giving a 50 year duration of the deposition phase. The deposition sequence is indicated by the arrows in the left contour plot. From Hökmark et al., (2010).

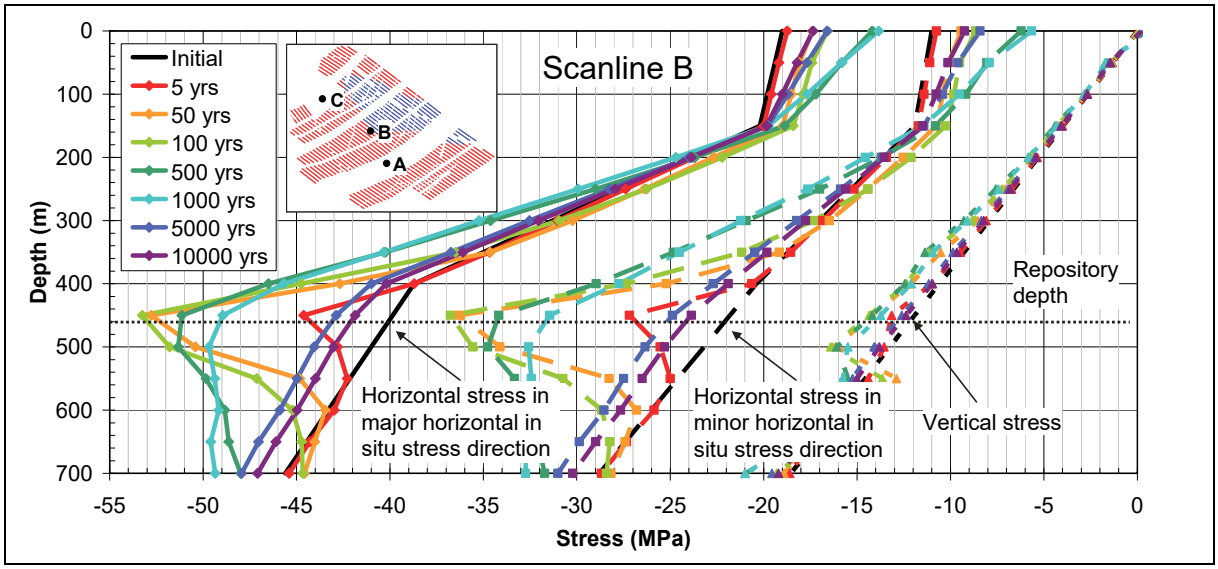

Figure 15. Stress along a vertical scanline intersecting the central deposition area (from Hökmark et al., 2010).

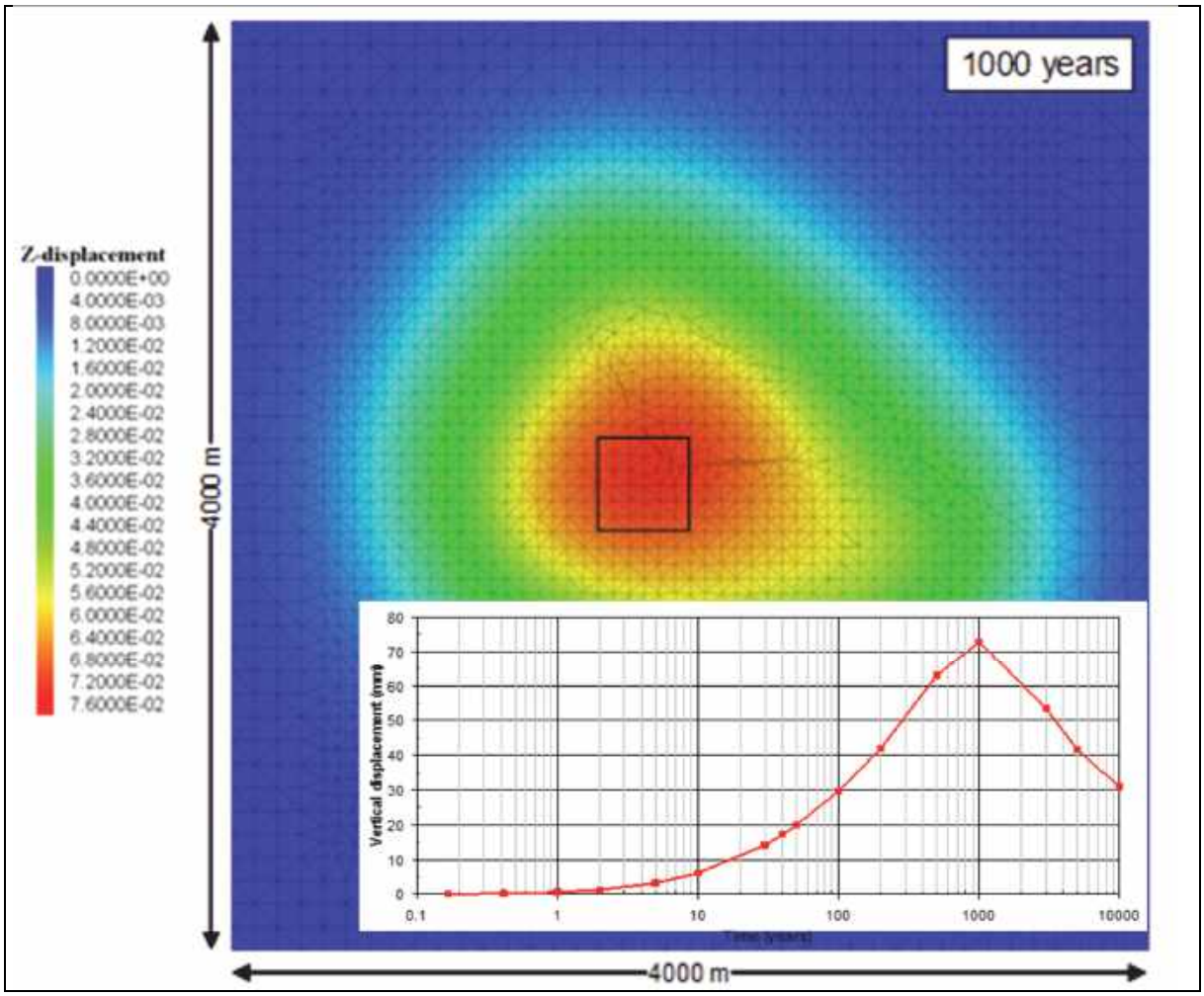

Figure 16. Heave of ground surface. The insert shows the temporal heave evolution averaged over the central quadratic area indicated in the colour plot.

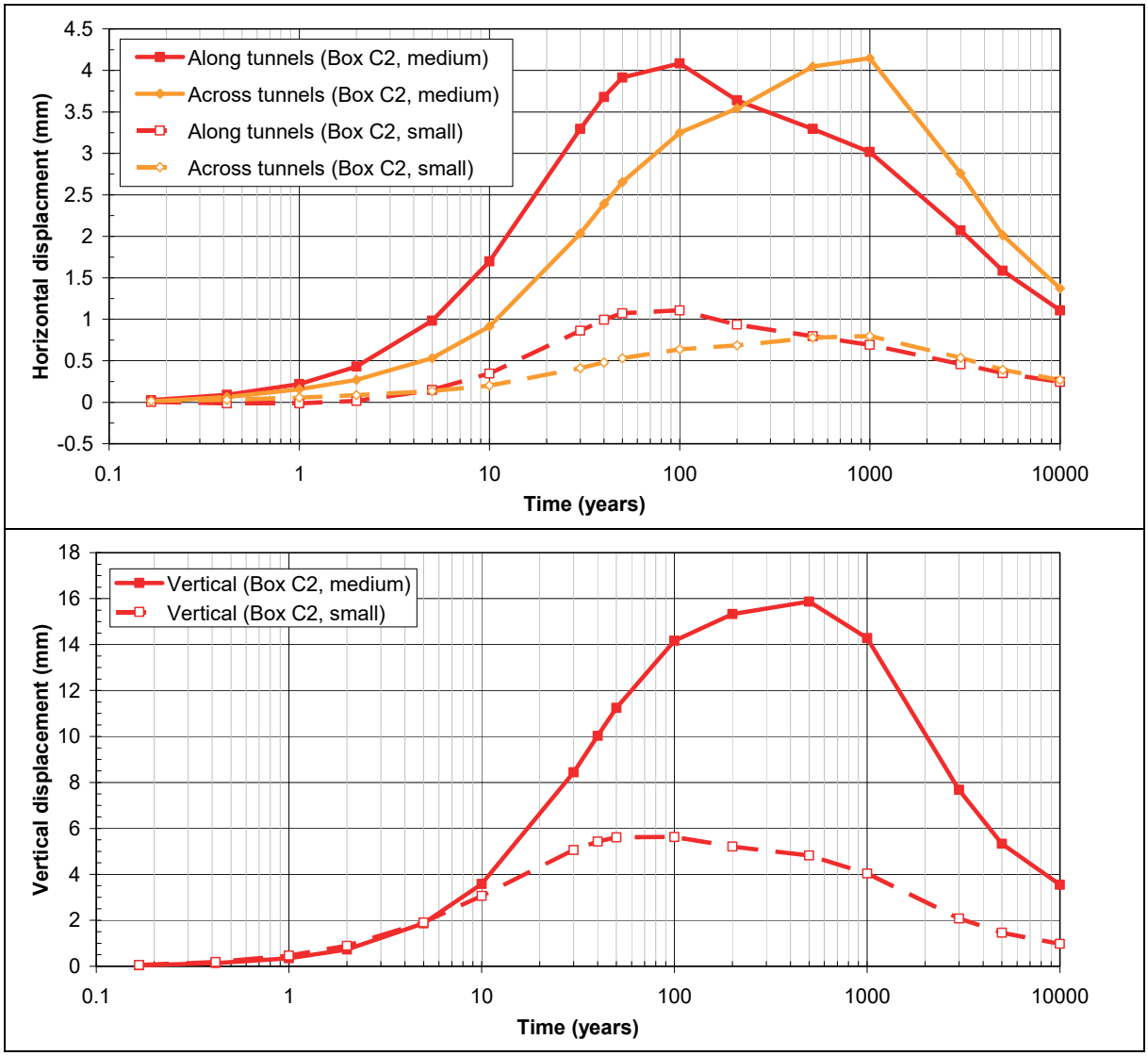

Figure 17. Examples of large scale model results translated into boundary conditions for medium scale and small scale model boxes located at different positions within the repository footprint.

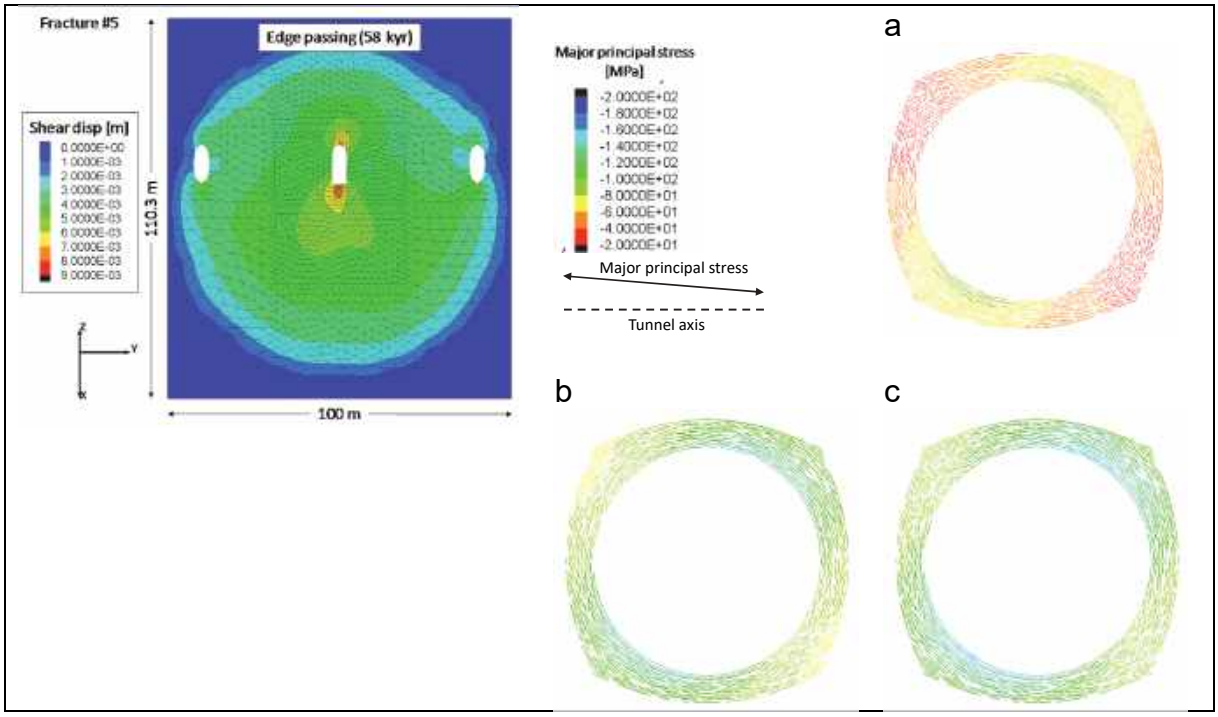

Figure 18. Left: result example from medium sized near field model. The contour plot shows total shear displacements along a 100 m diameter gently dipping fracture, accumulated during the thermal phase and a following glacial phase. The glacial phase includes the period of increased instability during ice retreat, i.e. when the edge of the ice cover passes over the site. From (Hökmark et al., 2010). Right: result example from small scale near-field model of Box A1 deposition hole, showing rock wall stresses at canister mid-height after excavation (a) and after 50 years of heating assuming mean (b) and maximum (c) rock wall temperature, cf. Figure 11. From (Hökmark et al., 2010).

3.5 Glaciation, permafrost, hydraulic jacking

The safety analysis must account also for the possible effects of future glaciations. The time scale and the evolution of the ice thickness are, as a base case, assumed to be similar to those of the previous, Weichselian, glaciation. The impact of the Weichselian ice cover on the stresses in the upper crust has been analysed numerically by Lund et al. (2009) using the ice reconstruction established by Näslund (2006) and trying various earth models, i.e., combinations of elastic crust models and viscoelastic models of the underlying mantle (Figure 19). The glacial stresses resulting from the earth model giving the best fit with sea level data from the Baltic (Whitehouse, 2006) and with current day vertical and horizontal velocities (Lidberg et al., 2007), are used as input to the modelling of the Forsmark rock response to glacial load cycles conducted for the SR-Site safety assessment, e.g. (Hökmark et al., 2010). The time of ice retreat, i.e., when the vertical stresses are reduced fast in direct response to the disappearance of the ice load, whereas the horizontal excess stresses associated with crustal flexure remain, is, given the in situ reverse faulting stress regime, a period of potential instability for the Forsmark host rock and in particular for gently dipping deformation zones and fractures. In consequence, the seismic analyses conducted by Fälth et al., (2015) and Fälth et al., (2016) focus on endglacial earthquakes occurring on verified local gently dipping Forsmark deformation zones; cf. section on fracture reactivation.

The horizontal glacial stresses will obviously increase the tangential stresses in the walls of the deposition holes substantially. As opposed to the thermal phase however, the bentonite buffer will be fully saturated in all deposition holes and exert pressures of several MPa on the walls. As outlined in the section on spalling, much smaller pressures, on the order of 100 kPa, have been concluded to suppress or limit spalling in KBS-3 deposition holes considerably. For the glacial phase with fully saturated deposition holes spalling is not considered to be an issue.

An additional concern associated with glacial cycles is the possibility of hydraulic jacking, i.e., pore pressures may increase and exceed the fracture normal stress, causing the fracture to dilate and its transmissivity to increase very considerably. Hydraulic jacking may affect not only the flow patterns and the transport capacity of the rock mass, but also the rock mass stability, meaning that it is essential for the safety assessment that safe bounding estimates of the maximum jacking depth can be made. Lönnqvist and Hökmark (2013) identified two glacially-related jacking scenarios (Figure 20):

1. High water pressures are generated in the melt zone under an ice sheet advancing over a permafrost layer. If the permafrost layer can be assumed to be effectively impermeable, the melt zone pressure could theoretically propagate long distances to regions outside the ice-covered area and jack open horizontal fractures.
2. Long time periods of high water pressures in the ice/bed interface of a warm-based ice will give increasing pressures also at large depths. Depending on the speed of ice retreat and the rock mass permeability at different depths, the residual increased pore pressures may be sufficient to jack open horizontal fractures when the ice load has disappeared.

Both scenarios were analysed by Lönnqvist and Hökmark (2013) using combinations of analytical and numerical methods. For the case of an ice advancing over an impermeable permafrost layer (Figure 20, left) a 200 m jacking depth was concluded to be a safe bounding estimate. If the distance between ice front and melt zone would be according the SR-Can reference case, jacking would be confined to the top few meters. For the case of a retreating ice (Figure 20, right), the residual excess pore pressures would be sufficient to generate hydraulic jacking down of 50 - 75 m, provided that the ice/bed interface water pressure everywhere is assumed to be at maximum, i.e., approximately equal to the total ice load, for the duration of the ice-covered period.

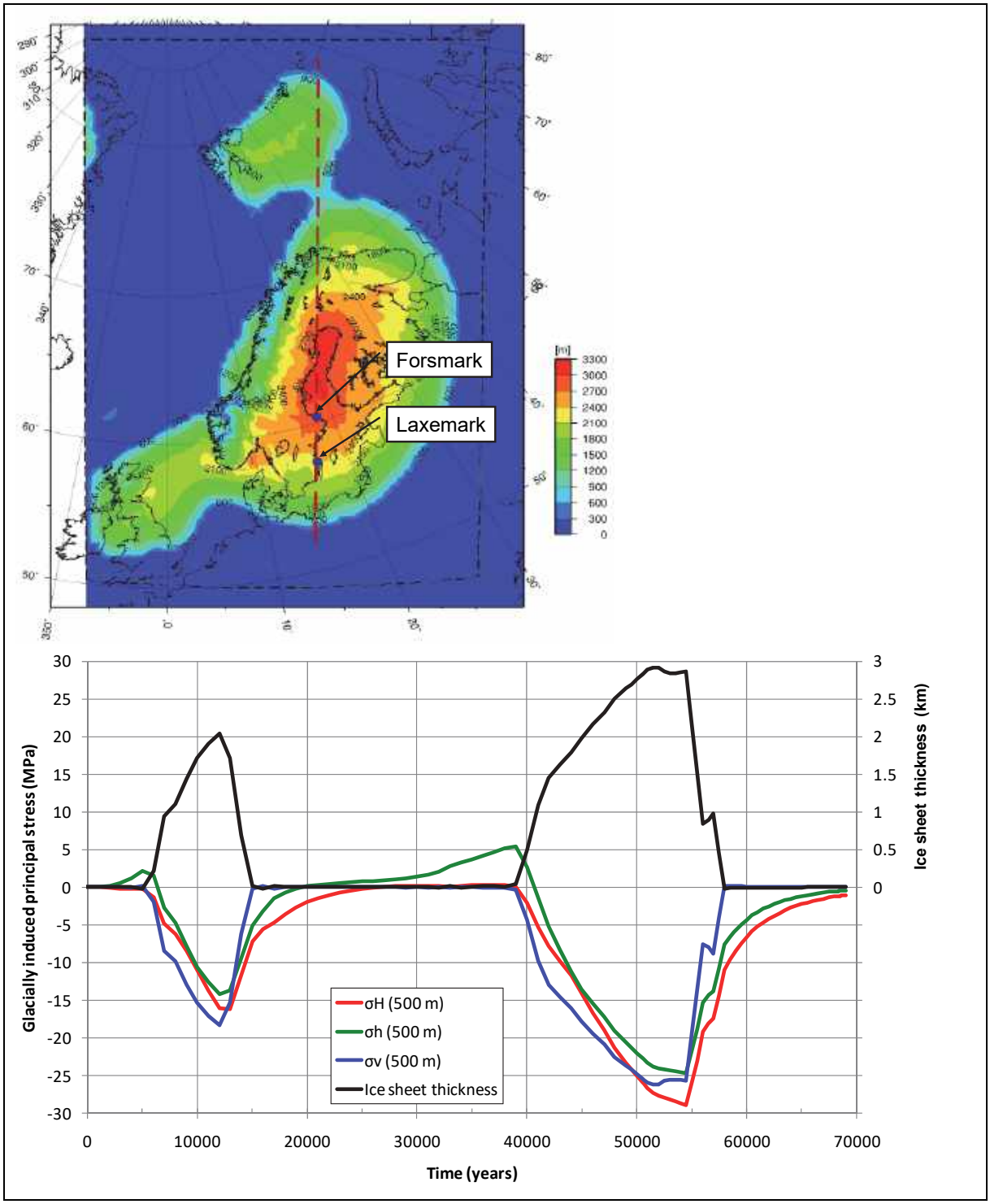

Figure 19 Left: Wechselian ice thickness at time of maximum ice sheet extent. Modified from (Lund et al. 2009). Right: Temporal evolution of ice thickness and glacial stress components at Forsmark as calculated by Lund et al., (2009). Compression is negative. Note that the vertical stress drops in direct reponse to the load reduction after the glacial maxima, whereas parts of the horizontal coponents remain for long times. From (Hökmark et al., 2010).

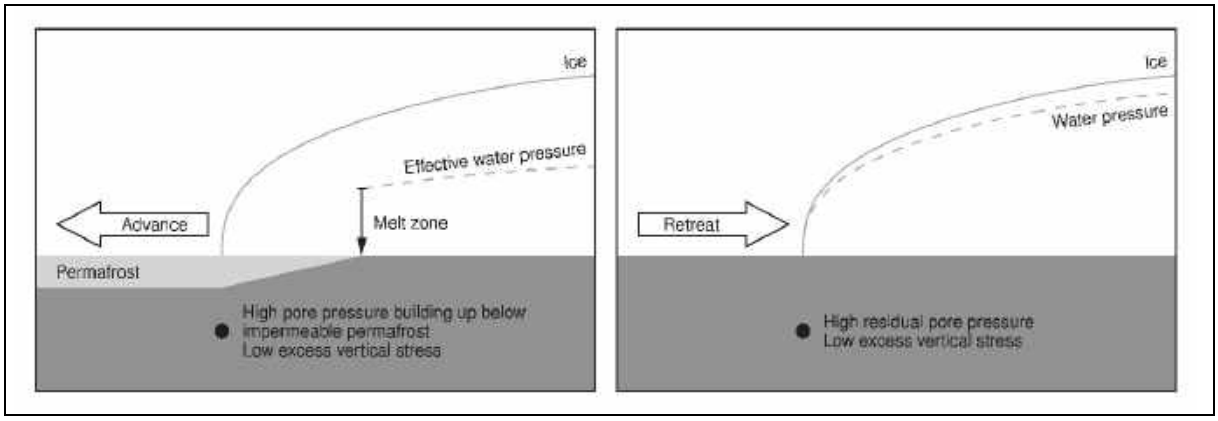

Figure 20. Schematics of glacial scenarios that theoretically could generate pore overpressures sufficient to jack open horizontal fracture in the region below the ice margin. From (Lönnqvist and Hökmark, 2013).

3.6 Transmissivity change in near- and far–field due to thermal load and glaciation

The glacial phase as well as the thermal phase will include changes in both normal and shear stresses on the fractures and deformation zones that control the flow patterns in the Forsmark host rock. Figure 21 (left) shows two models applied to estimate fracture transmissivities (solid lines) as function of the effective fracture normal stress. Both models are based on the notion of fracture mechanical apertures being exponentially dependent on that stress, and that hydraulic apertures (dashed lines) in turn are functions of the mechanical apertures. Model A (red) represents an upper bound estimate of the sensitivity to normal load changes, whereas model B (blue) can be regarded as a best estimate, cf. Hökmark et al., 2010, for details. Here e_0 and T_0 are the initial hydraulic apertures and transmissivities, respectively, while e and T are corresponding quantities at normal stress σ_n. The parameters e_r (residual aperture), e_{max} (maximum aperture) and α are used to calibrate the model to be consistent with normal stiffness data and actual transmissivity estimates. The relative transmissivities in Figure 21 (left) are normalized to a 20 MPa effective normal stress. Figure 21 (right) shows relative transmissivities for five fractures explicitly modelled at 450 m depth in the Forsmark medium scale 3DEC models. Here the transmissivities are normalized individually to the in situ effective normal stresses on the five differently oriented fractures. For the transmissivities to increase by one order of magnitude for fractures at repository depth it takes very substantial stress reductions even assuming the upper bound stress sensitivity model (A).

Figure 22 shows examples of transmissivity effects of a glacial load cycle as calculated by Hökmark et al. (2010). Instances of time are given according to the time-scale in Figure 19, right. For the vertical fractures considered here the transmissivity increases at the time preceding the arrival of the advancing ice front, i.e., during the forebulge period. For the worst case stress-transmissivity model (A), the transmissivity increases by around 80% if the ice approaches the site over an impermeable permafrost layer as described above for the hydraulic jacking scenario, cf. Figure 20 (left). In all other cases transmissivity changes are modest.
Constant stiffness hydromechanical direct shear tests on lab scale granite joint samples subjected to initial normal loads of 4 MPa reported by Olsson (1998) gave reduced

transmissivities for shear displacements smaller than 5-6 mm and increased transmissivities for larger displacements. Esaki et al. (1999) conducted shear flow tests on rock fractures using equipment specifically developed for the purpose and reported transmissivity increases of between one and two orders of magnitude also for joint samples subjected to much higher normal stresses than those applied by Olsson (1998). Whether or not transmissivity changes, caused by shearing of Forsmark fractures under the high normal stresses at repository depth, would be large and systematic enough to be accounted for when estimating the hydrological response of the repository rock mass to different loading scenarios is a complicated question that may need additional attention. Effects of gouge production, for instance, could be important but are difficult to estimate. In addition, mainly the central parts of large fractures would slip by amounts larger than 5 mm, meaning that transmissivity effects of fracture displacements, in contrast to transmissivity effects of changes in normal load are likely too local and varying. In (Hökmark et al. 2010) the transmissivity effects of fracture shear displacements were suggested to be sufficiently small and unsystematic compared to the effects of normal load changes to be neglected.

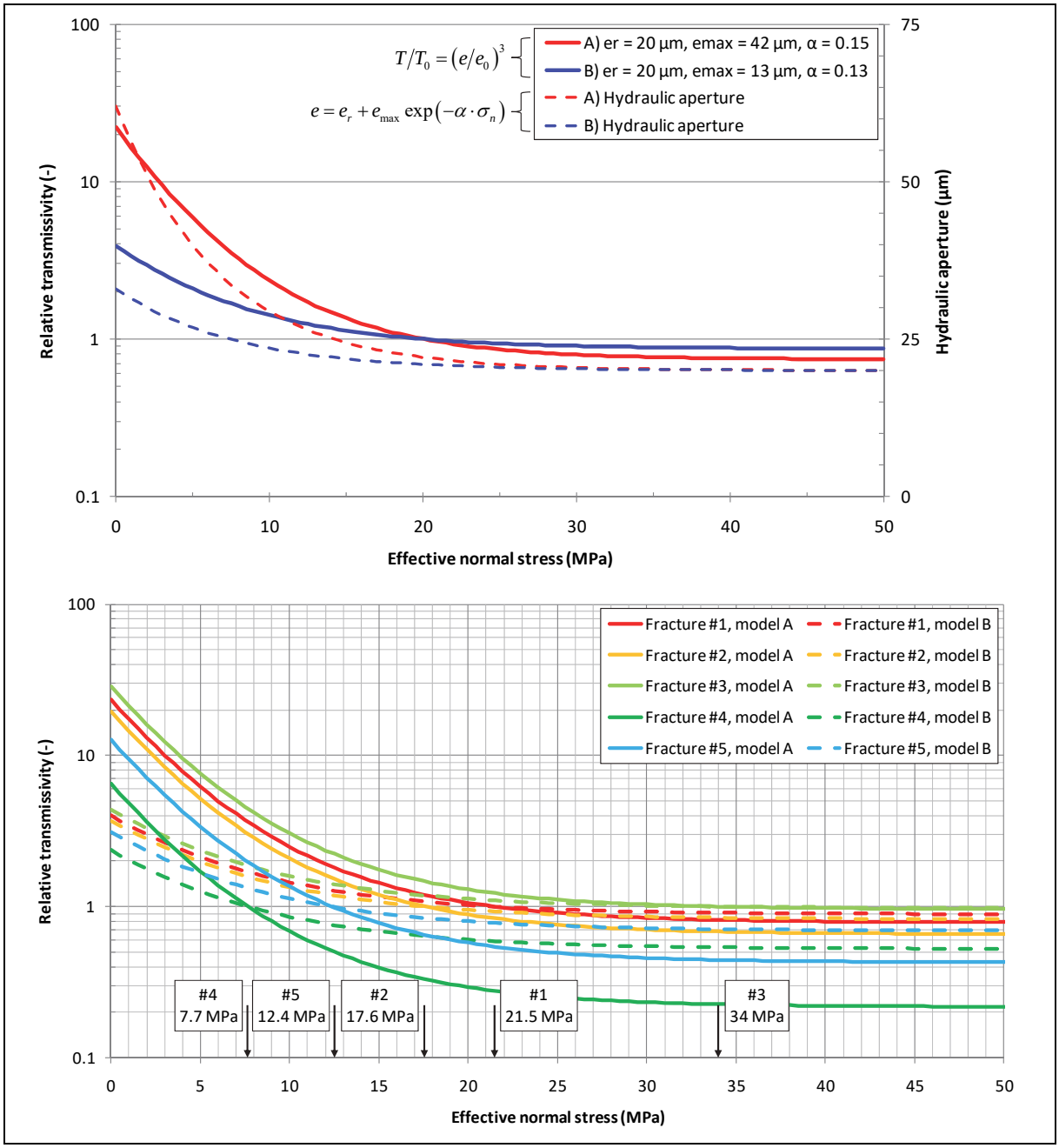

Figure 21. Above: Principles of stress-transmissivity models. Below: Stress-transmissivity models applied to five differently oriented fractures at repository depth. From (Hökmark et al., 2010).

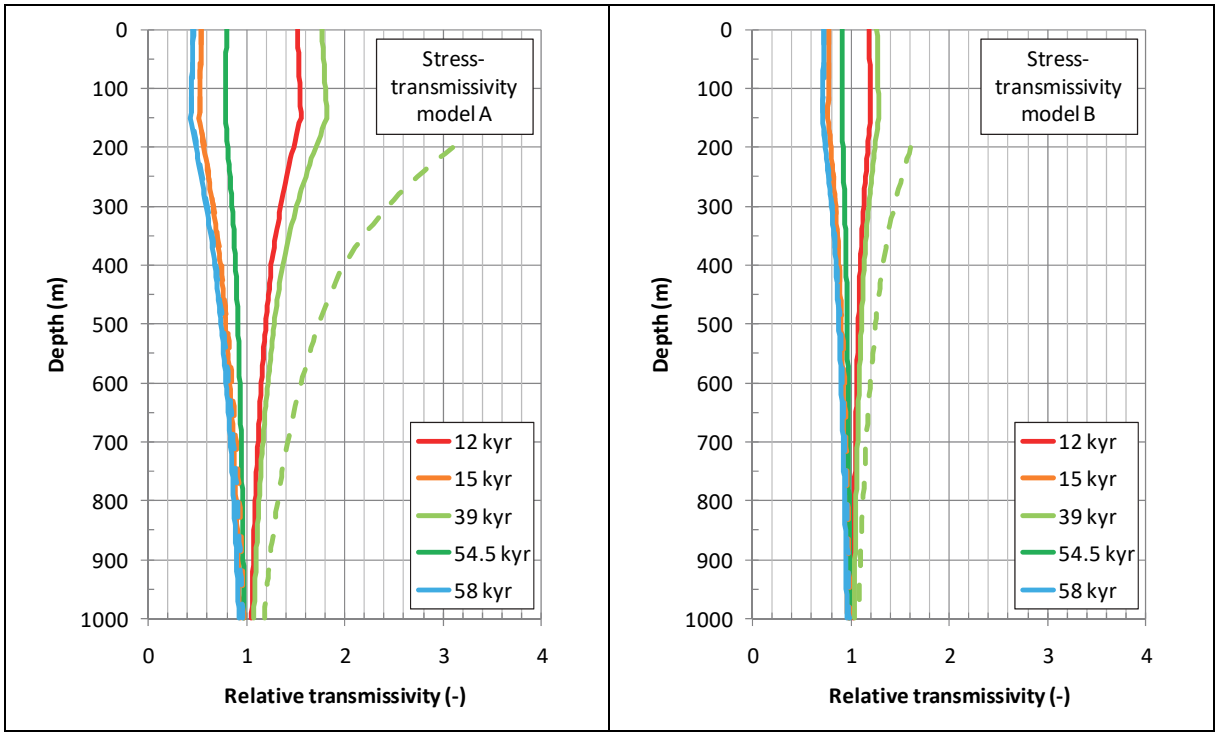

Figure 22. Relative transmissivity of vertical fractures oriented normally to the minor horizontal stress. Transmissivities increase during forebulge periods (12 kyr and 39 kyr). Dashed lines represent cases with excess pore pressures. The discontinuity of the stress gradients at 150 m depth is due to details in the in situ stress model. From Hökmark et al. 2010.

4 Discussion and Conclusions

A final repository for spent nuclear fuel is a project of unique character. The engineering design is subject to strict requirements (SKB, 2009b) and the safety assessment encompasses the next million years (SKB, 2011). Complex behaviour and coupled processes as well as long term phenomena (e.g. glaciation cycles) have to be considered. This implies a truly multidisciplinary approach in which specialists in different fields have to cooperate at a level never required before. Therefore the amount of field and laboratory data and the effort performed in data analysis and modelling is outstanding. Nonetheless, uncertainty cannot be avoided and therefore the site-descriptive model is continuously under development as new data and improved understanding of the site is incorporated into it. The site characterisation should continue until the reliability and confidence of the site-descriptive model has reached such a level that the body of data and understanding are sufficient for the purpose of safety assessment and repository engineering, or until the body of data shows that the rock at the site does not satisfy the predefined requirements. It is necessary therefore to continuously evaluate the new data in the light of what we already know and to assess the uncertainty and the confidence on the modelling (Andersson et al. 2013).

For some of the aspects mentioned in this article there is yet no absolute answer. This is why all the analyses presented in this paper regarding different rock mechanics aspects and their impact in the engineering and the safety assessment of the repository are conducted in a conservative, redundant and iterative manner, trying to find reason-

able bounds. The latest developments in rock mechanics and related fields are followed in a daily basis by SKB and developments of methodologies and techniques are also driven by SKB in several fronts. Some of the areas where there is ongoing research are:

- Fracture mechanical parameters. In cooperation with Posiva and NWMO, a large scale field test has been conducted and the effect of constant normal stiffness conditions during laboratory shear testing of fracture samples has been investigated in the POST (i.e. fracture parameterisation for repository design and post-closure analysis) project (e.g. Valli et al., 2016; Valli and Hakala, 2016; Siren et al., 2016; Jacobsson, 2016). Effect of large scale undulation in shear behaviour of fractures is being investigated by Lönnqvist and Hökmark (2015).
- Seismically induced fracture reactivation. Work is being conducted to arrive at less schematic, but yet defendable, ways of arriving at upper bound estimates of secondary slip along host rock fractures. This work includes modelling of more realistic rupture processes and development of more realistic descriptions of fault inhomogeneity and fault edges.
- Fundamental research on spalling phenomena. Fundamental studies with emphasis on microstructure have been performed (e.g. Potyondy et al., 2009; Potyondy, 2010; Lim et al., 2012; Lan et al., 2012; Nicksiar and Martin, 2013; Lan et al., 2013). A large number of laboratory tests with different specimen sizes and measurement of the deformation with strain gauge and digital image correlation (DIC), and acoustic emission have been performed. The preliminary results have been summarized in Jacobsson et al. (2015) and Jacobsson and Lindqvist (2015).
- Rock mass behaviour characterization. An updated theoretical (analytical and numerical) approach for the estimation of rock mass properties is being developed in cooperation with Posiva and NWMO (e.g. Darcel et al., 2015).
- Effect of tunnel excavation by blasting on the surrounding rock mass. The research focus is on conventional emulsion explosives and the influence of blast design on the fracturing. Field tests include mapping of blast fractures in slots excavated in the tunnel wall and floor at several sites including Äspö HRL, (Ittner et al., 2014; Ittner and Bouvin 2015; Ittner et al., 2016). Applications can be found in design for smooth blasting, contour quality control and limitation of Excavation Damage Zone (EDZ).

All these lines of research are still active. Safety assessment and design concepts are revised and updated in regular intervals in the light of the improved understanding to prove compliance with the requirements. During the following years new lines of research will be defined as the need arises. When new or improved techniques and methodologies are judged mature and appropriate, they will be incorporated into the site characterization, safety analysis and engineering design processes.

5 References

Andersson C and Söderhäll J, 2001. Rock mechanical conditions at the Äspö HRL A study of the correlation between geology, tunnel maintenance and tunnel shape. SKB R-01-53. Svensk Kärnbränslehantering AB, Stockholm.

Andersson J, Christiansson R, Hudson J, 2002. Site investigations. Strategy for Rock Mechanics Site Descriptive Model. SKB TR-02-01 Svensk Kärnbränslehantering AB.

Andersson J C, 2007. Äspö Hard Rock Laboratory. Äspö Pillar Stability Experiment, Final report. Rock mass response to coupled mechanical thermal loading. SKB TR-07-01, Svensk Kärnbränslehantering AB, Stockholm.

Andersson J, Skagius K, Winberg, A, Lindborg T and Ström A, 2013.Site-descriptive modelling for a final repository for spent nuclear fuel in Sweden. Environ Earth Sci (2013) 69:1045–1060. DOI 10.1007/s12665-013-2226-1.

Ask D, Cornet, F, Brunet, C and Fontbonne, F, 2007. Stress measurements with hydraulic methods in boreholes KFM07A, KFM07C, KFM08A, KFM09A and KFM09B. Forsmark site investigation. SKB P-07-206, Svensk Kärnbränslehantering AB.

Bungum H, Pettenati F, Schweitzer J, Sirovich L, Faleide J I, 2009. The 23 October 1904 Ms 5.4 Oslofjord earthquake: reanalysis based on macroseismic and instrumental data. Bulletin of the Seismological Society of America, 99, pp 2836-2854.

Bödvarsson R, Lund B, Roberts R and Slunga R, 2006. Earthquake activity in Sweden. Study in connection with a proposed nuclear waste repository in Forsmark or Oskarshamn. SKB R-06-67. Svensk Kärnbränslehantering AB.

Claesson J and Probert T, 1996. Temperature field due to time-dependent heat sources in a large rectangular grid - Derivation of analytical solution. SKB TR-96-12, Svensk Kärnbränslehantering AB, Stockholm.

Claesson J and Probert T, 1996b. Thermoelastic stress due to a rectangular heat source in a semi-infinite medium - Derivation of an analytical solution. SKB TR-96-13, Svensk Kärnbränslehantering AB, Stockholm.

Chryssanthakis P, Tunbridge L and Christiansson R, 2003. Numerical modelling in 3D of the TBM/ZEDEX tunnels at Äspö, Hard Rock Laboratory and comparison with in-situ measurements. Proceedings of Underground Construction Conference, London.

Darcel C, Davy P and Le Goc R, 2015. Onkalo POSE experiment - Effective elastic properties of fractured rocks. Posiva 2015-17. Rep., Posiva Oy, Eurajoki, Finland.

Esaki T, Du S, Mitani Y, Ikusada K, Jing L, 1999. Development of a shear-flow test apparatus and determination of coupled properties for a single rock joint. International Journal of Rock Mechanics and Mining Sciences 36 (1999) 641-650.

Fox A, La Pointe P, Hermansson J, and Öhman J, 2008. Statistical geological discrete fracture network model. Forsmark modelling stage 2.2. Updated 2008-12. SKB R-07-46, Svensk Kärnbränslehantering AB, Stockholm.

Fälth B, Hökmark H and Munier R, 2010. Effects of large earthquakes on a KBS-3 repository. SKB TR-08-11, Svensk Kärnbränslehantering AB, Stockholm.

Fälth B, Hökmark H, Lund B, Mai PM, Roberts R and Munier R, 2015. Simulating earthquake rupture and off-fault fracture response: application to the safety assessment of

the Swedish nuclear waste repository. Bull Seism Soc Am. 2015;105:134–151http://dx.doi.org/10.1785/0120140090.

Fälth B, Hökmark H and Lund B, 2016. Simulation of co-seismic secondary fracture displacements for Different earthquake rupture scenarios at the proposed nuclear waste repository site in Forsmark. International Journal of Rock Mechanics & Mining Sciences 84 (2016) 142–158.

Glamheden R, Fredriksson A, Röshoff K, Karlsson J, Hakami H and Christiansson R, 2007. Rock mechanics Forsmark. Site descriptive modelling Forsmark stage 2.2. SKB R-07-31, Svensk Kärnbränslehantering AB, Stockholm.

Glamheden R, Lanaro F, Karlsson J, Lindberg U, Wrafter J, Hakami H and Johansson M, 2008. Rock mechanics Forsmark. Modelling stage 2.3. Complementary analysis and verification of the rock mechanics model. SKB R-08-66, Svensk Kärnbränslehantering AB, Stockholm.

Glamheden R, Fälth B, Jacobsson L, Harrström J, Berglund J and Bergkvist L, 2010. Counterforce applied to prevent spalling. SKB R-10-37, Svensk Kärnbränslehantering AB, Stockholm.

Hakami E and Christiansson R, 2012. Using induced borehole breakout as a method for stress orientation determination in hard crystalline rocks. Eurock 2012.

Hoek E, 2007. Practical rock engineering, updated. Notes that are available on the site www.rocscience.com.

Hökmark H, Lönnqvist M, Kristensson O, Sundberg J and Hellström G, 2009. Strategy for thermal dimensioning of the final repository for spent nuclear fuel. Version 1.0. SKB R-09-04, Svensk Kärnbränslehantering AB, Stockholm.

Hökmark H, Lönnqvist M and Fälth B, 2010. T-H-M issues in repository rock. Thermal, mechanical, thermo-mechanical and hydro-mechanical evolution of the rock at the Forsmark and Laxemar sites. SKB TR-10-23, Svensk Kärnbränslehantering AB, Stockholm.

Itasca. 2013. 3DEC – 3-Dimensional Distinct Element Code, User's Guide. Itasca Consulting Group Inc., Minneapolis, USA

Ittner H, Lehtimäki T and Christiansson R, 2014. Design and control of the EDZ for a deep repository in crystalline rock. Rock engineering and Rock Engineering and Rock Mechanics: Structures in and on Rock Masses. Paper presented at ISRM International Symposium EUROCK 2014,Vigo, Spain.

Ittner H and Bouvin A, 2015. Investigation of blast damage from string emulsion in the wall and floor of two experimental tunnels in Äspö HRL Paper presented at ISRM International Symposium Eurock 2015 , Salzburg, Austria.

Ittner H, Åkeson U, Christiansson R, Olsson M and Johansson D, 2016. Recent Swedish Studies on the Extent of Blast Damage after Excavation Paper presented at World Tunnel Congress 2016, San Francisco, United States.

Jacobsson L, 2007. Boreholes KFM01A and KFM02B. Micro crack volume measurements and triaxial compression tests on intact rock. Forsmark site investigation. SKB P-07-93. Svensk Kärnbränslehantering AB.

Jacobsson L, Glamheden R, Hakami E and Olofsson I, 2012. Rock mechanics laboratory testing in SKB site investigation program. Eurock 2012.

Jacobsson L, Appelquist K and Lindqvist JE, 2015. Spalling experiment on hard rock specimens, Rock Mechanics Rock Engineering 48(4), pp. 1485-1503. DOI: 10.1007/s00603-014-0655-0.

Jacobsson L and Lindqvist JE, 2015. Laboratory investigation of stress gradient effect at spalling experiments on granite, The 13th International Congress of Rock Mechanics ISRM 2015, Montreal, Canada. (Extended abstract & Poster).

Jacobsson L, 2016. Parametrisation of Fractures - Direct Shear Tests on Calcite and Breccia Infilled Rock Joints from Äspö HRL Under Constant Normal Stiffness Condition. Working report 2016-19. Eurajoki: Posiva Oy.

Lan H, Martin C D and Hu B, 2010. Effect of heterogeneity of brittle rock on micromechanical extensile behavior during compression loading. Journal of Geophysical Research 115. doi:10.1029/2009JB006496.

Lan H, Martin C D and Andersson J C, 2013. Evaluation of in situ rock mass damage induced by mechanical-thermal loading. Rock Mechanics and Rock Engineering 46, 153–168.

Lidberg M, Johansson J M, Scherneck H-G and Davis J L, 2007. An improved and extended GPS-derived velocity field of the glacial isostatic adjustment (GIA) in Fennoscandia. Journal of Geodesy, 81, pp 213-230.

Lim S S, Martin C D and Åkesson U, 2012. In-situ stress and microcracking in granite cores with depth. Engineering Geology 147–148, 1–13.

Lund B, Schmidt P and Hieronymus C, 2009. Stress evolution and fault stability during the Weichselian glacial cycle. SKB TR-09-15, Svensk Kärnbränslehantering AB (SKB) Stockholm Sweden.

Lönnqvist M and Hökmark H, 2013. Approach to estimating the maximum depth for glacially induced hydraulic jacking in fractured crystalline rock at Forsmark, Sweden. Journal Of Geophysical Research: Earth SurfaceE, VOL. 118, 1–15, doi:10.1002/jgrf.20106.

Lönnqvist M and Hökmark H, 2015. Assessment of method to model slip of isolated, non-planar fractures using 3DEC. ISRM Congress 2015 Proceedings - Int'l Symposium on Rock Mechanics - ISBN: 978-1-926872-25-4.

Martin D, 2007. Quantifying in situ stress magnitudes and orientations for Forsmark. Forsmark stage 2.2. SKB R-07-26. Svensk Kärnbränslehantering AB.

Munier R, 2010. Full perimeter intersection criteria. Definitions and implementations in SR-Site. SKB TR-10-21. Svensk Kärnbränslehantering AB.

Nicksiar M and Martin C D, 2013. Crack initiation stress in low porosity crystalline and sedimentary rocks. Engineering Geology 154, 64–76.

Näslund J-O, 2006. Ice sheet dynamics, in Climate and climate related issues for the safety assessment SR-Can. SKB TR-06-23, Svensk Kärnbränslehantering AB, Stockholm, Sweden.

Olofsson I and Fredriksson A, 2005. Strategy for a numerical Rock Mechanics Site Descriptive Model. Further development of the theoretical/numerical approach. SKB R-05-43, Svensk Kärnbränslehantering AB, Stockholm, Sweden.

Olsson R, 1998. Mechanical and hydromechanical behaviour of hard rock joints. A laboratory study. Ph.D. Thesis, Department of Geotechnical Engineering, Chalmers University of Technology, Sweden.

Potyondy D, Ekneligoda T and Fälth B, 2009. Simulating spalling, phase II: Preliminary feasibility assessment. Itasca Consulting Group, Inc., Report to Svensk Kärnbränslehantering AB (SKB, Swedish Nuclear Fuel and Waste Management Company), Stockholm, Sweden, ICG08-2502-5F, January 2009.

Potyondy D O, 2010. A Grain-Based Model for Rock: Approaching the True Microstructure. In: Proceedings of Bergmekanikk i Norden 2010 — Rock Mechanics in the Nordic Countries 2010 (Kongsberg, Norway, June 9–12, 2010), pp. 225–234. C.C. Li, G. Grøneng, R. Olsson and S. Engen, Eds. ISBN: 978-82-8208-017-0. Norwegian Group for Rock Mechanics, 2010.

Probert T and Claesson J, 1997a. Temperature field due to time-dependent heat sources in a large rectangular grid. Application for the KBS-3 repository, SKB TR-97-27, Svensk Kärnbränslehantering AB, Stockholm.

Probert T and Claesson J, 1997b. Thermoelastic stress due to a rectangular heat source in a semi-infinite medium. Application for the KBS-3 repository. SKB TR-97-26, Svensk Kärnbränslehantering AB, Stockholm.

Read RS and Martin CD, 1992. Monitoring the excavation-induced response of granite. In Tillerson and Waversik, editors, Proc. 33rd U.S. Symp. on rock mechanics, Santa Fe, pp 201-210. A.A Balkema, Rotterdam.

Röshoff K, Lanaro F, Jing L, 2002. Strategy for a Rock Mechanics Site Descriptive Model. Development and testing of the empirical approach. SKB R-02-01, Svensk Kärnbränslehantering AB.

Siren T, Christiansson R, Lam T, Hakala M, Valli J, Mas Ivars D and Mattila J, 2016. Parametrisation of Fractures – Final report, To be published as Posiva Report 2016 (In prep.) Eurajoki: Posiva Oy.

Staub I, Fredriksson A and Outters N, 2002. Strategy for a Rock Mechanics Site Descriptive Model. Development and testing of the theoretical approach. SKB R-02-02, Svensk Kärnbränslehantering AB, Stockholm.

Stephens MB, Fox A, LA Pointe P, Simeonov A, Isaksson H, Hermansson J and Öhman J, 2007. Geology Forsmark. Site descriptive modelling Forsmark Stage 2.2. SKB R-07-45, Svensk Kärnbränslehantering AB.

Stephens MB and Simeonov A, 2015. Description of deformation zone model version 2.3, Forsmark. SKB R-14-28, Svensk Kärnbränslehantering AB, Stockholm.

SKB, 2008. Site description of Forsmark at completion of the site investigation phase. SDM-Site Forsmark. SKB Technical Report TR-08-05, Svensk Kärnbränslehantering AB, Stockholm.

SKB, 2009a. Underground design Forsmark. Layout D2. SKB R-08-116, Svensk Kärnbränslehantering AB, Stockholm.

SKB, 2009b. Design premises for a KBS-3V repository based on results from the safety assessment SR-Can and some subsequent analyses. SKB TR-09-22, Svensk Kärnbränslehantering AB, Stockholm.

SKB, 2009c. Site engineering report Forsmark. Guidelines for underground design Step D2. SKB R-08-83, Svensk Kärnbränslehantering AB, Stockholm.

SKB, 2011. Long-term safety for the final repository for spent nuclear fuel at Forsmark main report of the SR-Site project. SKB TR-11- 01, Svensk Kärnbränslehantering AB, Stockholm.

Valli J and Hakala M, 2016. Parametrisation of Fractures – Model Generation Methodology and Prediction Calculations. To be published as Working Report 2016. Eurajoki: Posiva Oy.

Valli J, Hakala M, Suikkanen J, Heine J, Simelius C and Mattila J, 2016. Parametrisation of Fractures – PUSH Test Execution and Back-analysis. To be published as Working Report 2016. Eurajoki: Posiva Oy.

Whitehouse P, 2006. Isostatic adjustment and shoreline migration. In: Climate and climate-related issues for the safety assessment SR-Can. SKB TR-06-23, Svensk Kärnbränslehantering AB, pp 68–92.

Tightness of Salt Rocks and Fluid Percolation

Dichtheit von Salzgesteinen und Fluidperkolation

Wolfgang Minkley, Dieter Brückner, Christoph Lüdeling
IfG – Institut für Gebirgsmechanik GmbH
Leipzig, Friederikenstr. 60

Abstract

This paper summarises the current knowledge regarding the tightness and integrity of salt rocks in general and rock salt in particular, based on lab tests, in-situ investigations and natural analogues concerning long term fluid inclusion. Pressure-driven percolation is the most important failure mechanism responsible for loss of integrity of salt rock barriers at fluid pressures higher than the minor principal stress which acts as the percolation threshold. Only after overcoming this threshold, pressure-driven opening and interconnection of flow paths along grain boundaries in salt rocks begins and induces a directed percolation in the direction of the major principal stress. In laboratory experiments it could be shown that fluid transport through the polycrystalline rock salt without overcoming the percolation threshold, as postulated for high temperature and pressure, is not possible.

Zusammenfassung

Im Beitrag wird der aktuelle Kenntnisstand zur Dichtheit und Integrität von Salzgesteinen auf der Grundlage von Laborversuchen, in situ Tests und natürlicher Analoga zum Einschlussvermögen von Fluiden in Salzgesteinsformationen wiedergegeben. Druckgetriebene Perkolation ist der entscheidende Versagensmechanismus für einen Integritätsverlust von Salzgesteinsbarrieren bei Fluiddrücken, welche die minimale Hauptspannung als wirkende Perkolationsschwelle überschreiten. Im Ergebnis experimenteller Untersuchungen kann die bei hohen Temperaturen und Drücken postulierte Durchlässigkeit polykristalliner Salzgesteine durch Fluidbenetzung der Korngrenzen, ohne dass eine Perkolationsschwelle zu überwinden ist, nicht bestätigt werden.

1 Introduction

Salt rocks are generally considered to be impermeable to fluids, i.e. liquids and gases. This notion is supported by a large number of laboratory experiments as well as natural analogues (Minkley and Knauth 2013, Minkley et al. 2015a). In a large-scale technical application of this impermeability, hydrocarbons and other gases are stored in caverns leached into salt formations in depths ranging from a few hundred metres to two kilometres. Solution mining caverns exist down to three kilometres without brine migration between neighbouring caverns (van Heekeren et al., 2009).

Impermeability also implies that salt rocks possess unique barrier properties. Saliferous barriers play a key rôle in underground disposal of toxic (Schade 2008) and radioactive waste (Robert et al. 2012). Both bedded (Minkley 2009) and domal salt has been considered as a suitable repository host rock for heat-generating nuclear waste (Bracke et al. 2013).

It has been claimed in Lewis and Holness 1996 that salt rocks become permeable in depths greater than three kilometres, based on measurements of the dihedral angles between grain boundaries in a halite-brine two-phase system. Permeabilities are supposed to be similar to sandstone, in the range of 10^{-13} to 10^{-16} m^2. More recently, the hypothesis has been put forward that salt rocks can lose their tightness even in smaller depths by a process called deformation-assisted fluid percolation (Ghanbarzadeh et al. 2015).

2 Theoretical Background: Wetting and Dihedral Angle

We briefly recap the argument of (Lewis and Holness 1996, Ghanbarzadeh et al. 2015). The equilibrium state in a two-phase system consisting of halite and brine is characterised by the dihedral angle between the grain surfaces. This angle is in turn determined by the ratio of the surface energies of the crystals, γ_{ss}, and the fluid-crystal interface, γ_{sf}, via the relation

$$\cos\left(\frac{\Theta}{2}\right) = \frac{1}{2}\frac{\gamma_{\mathrm{ss}}}{\gamma_{\mathrm{sf}}}. \qquad (1)$$

The angle Θ is supposed to control the connectivity of the pore space: For $\Theta > 60°$, the pores are isolated, while for $\Theta < 60°$, there will be a connected network of pores and channels along the grain edges. Hence, in the latter case, the rock mass should allow fluid permeation without a percolation threshold at any porosity (see Figure 1). For a porosity of 0.1 %, Lewis and Holness (1996) estimate a permeability of 10^{-16} m^2.

The dihedral angle Θ is a thermodynamic quantity depending on pressure and temperature, since it results from a minimisation of the total surface energies. From this observation and laboratory investigations of the dihedral angle, (Lewis and Holness 1996) have constructed a simple diagram (see Figure 2) showing regions in p-T space, and by extension depth ranges, where rock salt is supposedly permeable (white), impermeable (dark grey) or in a transition zone (light grey). Specifically, in the dark region, any fluid permeation requires the fluid pressure to exceed a percolation threshold,

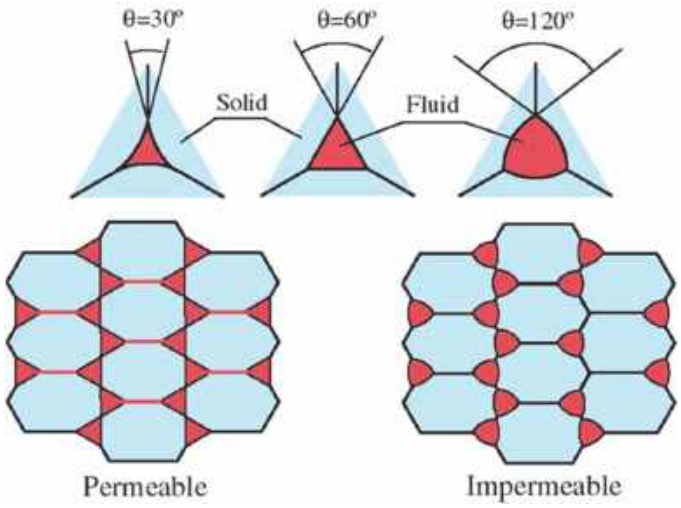

Figure 1: Sketch of the claimed relation between dihedral angle and permeability (from http://www.geosci.usyd.edu.au/users/prey/Granite/Diedre.JPG)

while in the white region, permeabilities similar to sandstone are expected, without any percolation threshold pressure.
Since there is very little experimental or in situ data available for conditions in the white region, it was necessary to check whether the postulated permeability transition occurs or not.

3 Hypothetical Consequences for Waste Disposal in Salt Rocks

According to the discussion in Section 2, the connectivity of brine-filled pores in salt rocks, and thus the permeability, is controlled by temperature and pressure. For a nuclear waste repository in depths less than a kilometre, local temperatures can exceed 200 °C for intermediate timescales. Hence, Figure 2 indicates that the rock surrounding the repository will become permeable, and the temperature gradient can create a fluid-enriched porous zone in the repository horizon (Lewis and Holness 1996).

Ganbarzadeh et al. (2015) postulate an additional mechanism of fluid transport, dubbed deformation-assisted percolation, that can induce a fluid permeability in rock salt even for dihedral angles $\Theta > 60°$ and porosities below 1 %, such hat the hydraulic barrier between repository and ground water loses its integrity.

4 Experimentally Verified Criteria for Tightness of Salt Rocks

The hypotheses discussed in Sections 2 and 3 are not supported by experiments such as permeability measurements and are in contradiction to practical experiences for barrier integrity in salt and potash mining as well as cavern storage.

In the course of their geological genesis, salt rocks have been compacted and dehydrated over millions of years. With porosities of the order of one to 0.1 percent, they are, with the exception of local fluid intrusions, not a two-phase system of salt and brine.

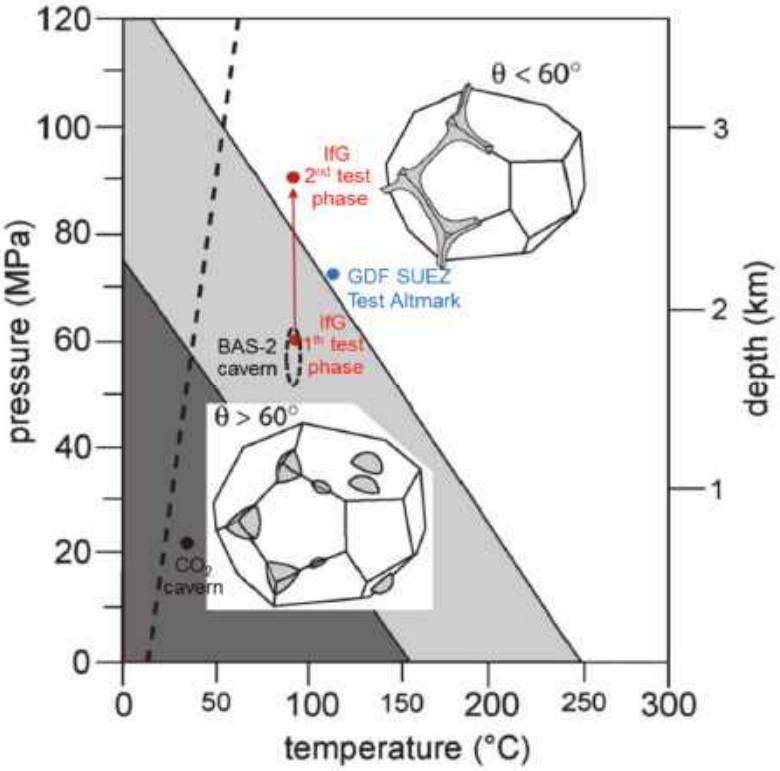

Figure 2: Pressure – temperature diagram following Lewis & Holness (1996). Test condition for lab and in situ tests indicated by red, blue and black color are added.

Cohesive and adhesive forces act along the fused grain boundaries, and contaminants only permeate the rock mass by solid diffusion, i.e. extremely slowly.

In situ, undisturbed salt rocks are impermeable to liquids and gases. Due to the visco-plastic behaviour, the undisturbed stress state is almost isotropic. Hence, the shear stresses along the grain boundaries essentially vanish, and the normal stress is given by the lithostatic pressure. Under these conditions, there is no connected pore space in the rock mass. The remaining pore space almost exclusively consists of isolated single pores at grain boundary vertices.

Salt rocks can lose their impermeability if some connectivity is created, i.e. by the generation of interconnected pores or fractures, due to mechanical or hydraulic loads:

- *Tensile loads can create fractures if the local tensile strength (adhesive inter-grain bonds) is exceeded →* ***Tensile stress criterion***
- *Under shear loads, plastic failure is associated with volume increase (dilatancy) due to formation of inter- and intragranular microcracks →* ***Shear strength criterion (dilatancy criterion)***
- *A fluid can open up grain boundaries if its pressure exceeds the normal pressure and adhesive strength (fluid-pressure driven percolation) →* ***Minimal stress criterion (fluid pressure criterion)***

The mechanical strength of rock salt can generally occur in the vicinity of excavations, i.e. close to disposal rooms in a repository: Shear loads are induced around drifts and in structural elements such as pillars, and tensile loads can occur along the contour of excavations.

The minimal stress criterion, on the other hand, is the most important criterion for the integrity of a geological barrier, because thermomechanically or geomechanically induced stress redistributions can change the stress state far away from the excavations. In particular, the minor principal stress can be decreased at the top of the salt formation until it falls below the ground water pressure, so that fluid percolation can start. Note that the minimal stress criterion is more severe for shallower excavations since lithostatic stress grows faster with depth than the ground water pressure.

5 Fluid Pressure Driven Percolation

The generation of flow paths by fluid pressure is a result of the polycrystalline microstructure of salt rocks. On the microscopic level, salt rocks are a discontinuous mesh of impermeable salt grains fused at their boundaries. Fluid pressure can generate a fluid connectivity, i.e. open up flow channels along the grain boundaries (see Figure 3), if the pressure exceeds the percolation threshold p_c, given by the normal stress (bounded by the minor principal stresss σ_{min}) and adhesive grain bonding (tensile strength $\sigma_{tensile}$) (Minkley et al. 2012),

$$p_c = f \cdot (\sigma_{\min} + \sigma_{\text{tensile}}). \qquad (2)$$

Here $f \leq 1$ represents a factor yet to be determined.

Physically, this implies that percolation, i.e. the generation of a connected network of flow paths, requires the compensation of normal stress and adhesive contact forces in the polycrystalline salt rock. The normal stress on the grain boundaries varies with the

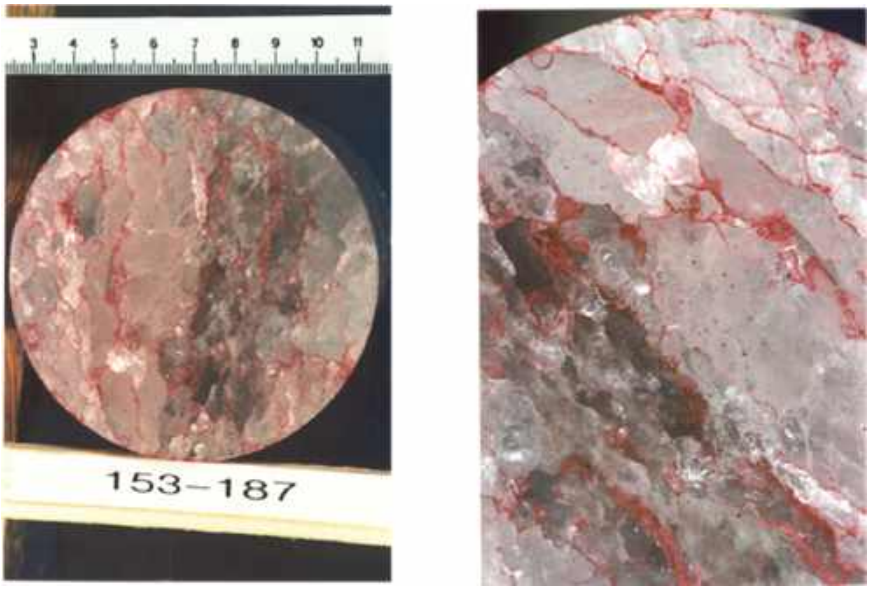

Figure 3: Discrete fluid flow along grain boundaries after the percolation threshold has been exceeded (fluid dyed red).

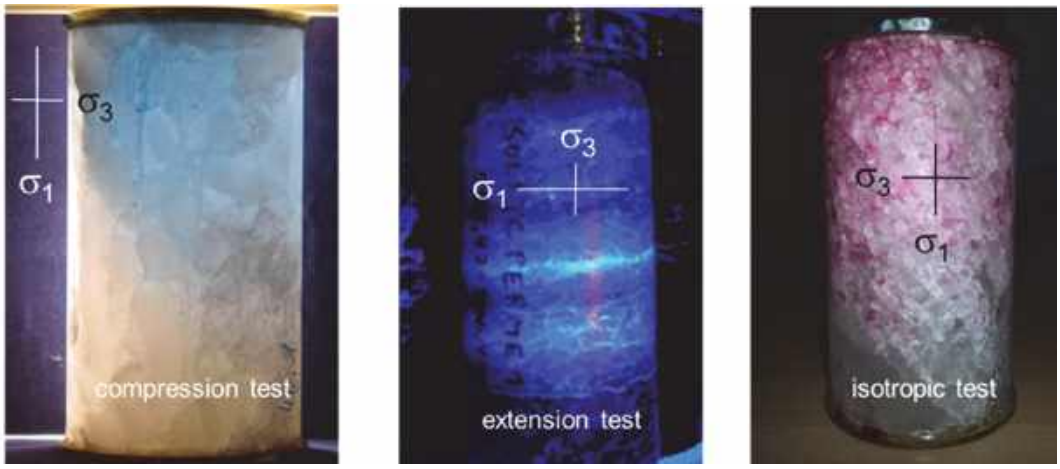

Figure 4: Directed percolation in the external stress field: Anisotropic stress fields (left and centre panels) lead to fluid flow in the direction of the major principal stress. Isotropic stress fields (right panel) imply isotropic flow.

orientation, but is bounded from below by the minor principal stress – hence the name minimal stress criterion. Impermeability is lost if the attacking fluid pressure is higher than the percolation threshold p_c.

If the threshold is exceeded, percolation starts and fluid migrates through the rock in a directed way: Grain boundaries with lower normal stress, i.e. with contact normals in the direction of the minor principal stress, are opened preferably, so that the overall motion proceeds in the direction of the major principal stress (Minkley et al., 2013), as shown in Figure 4. Thus, pressure-driven percolation is a directed process determined by the stress field, seeking the path of least resistance along the grain boundaries (see Figure 4 and Figure 5), which is generally orthogonal to the minor principal stress.

The name percolation is chosen in accord with the mathematical field of percolation theory which analyses the question under which (microscopic, stochastic) conditions macroscopically connected structures in lattices are generated. In the problem at hand,

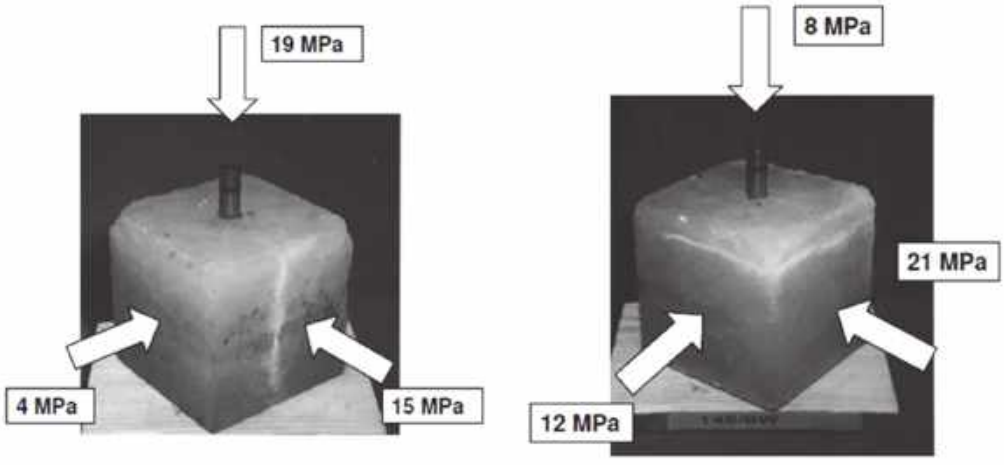

Figure 5: Directed percolation in truly triaxial stress fields.

the structures correspond to the connected flow paths across a rock mass, i.e. the fluid connectivity between distant points, while the local properties essentially are the normal stresses. Percolation in polycrystalline salt rocks is the pressure-generated opening and interconnection of grain boundaries in a preferred direction determined by the stress field. A key result is that there is no connectivity if the fluid pressure is below a threshold value.

This threshold, verified in laboratory experiments, was also confirmed in numerous in-situ tests, see Table 1.

Table 1: Percolation thresholds in salt rocks from in-situ tests

Test (Source)	Depth (m)	Test volume (m^3)	Pressure medium	Percolation threshold (bar)	Threshold gradient (bar/m)
IfG Springen, Large-diameter borehole (Minkley et al., 2013)	340	50	Air	68	0,200
Cavern S102 (Bannach & Klafki, 2009)	400	13600	Brine	83,7	0,198
IfG Bernburg, Test cavern (Brückner et al., 2003)	459	25	Brine	89	0,194
IfG Bernburg, Borehole (Minkley et al., 2013)	560	0,05	Nitrogen	126	0,225
GDF Borehole test EZ58 (Durup, 1994)	871	7	Nitrogen	206	0,237
GDF Cavern EZ53 (Berest & Brouard, 2003)	950	7500	Brine	130	0,137
Etzel Cavern K102 (Staudtmeister & Rokahr, 1994)	830	233000	Brine	182	0,220
Cavern BAS-2 (van Heekeren et al., 2009)	2533	210000	Brine	542	0,205
GDF SUEZ Altmark test (Wundram, 2014)	3096	2,1	Drilling fluid	718	0,232

Table 1 lists the fluid pressure at the point of loss of impermeability, i.e. the percolation threshold, and the depth of the test site. Hence, one can easily compare the minimal principal stress at the fluid injection point, which is basically given by the lithostatic pressure. In Figure 6, we have plotted the percolation threshold versus the depth – the measurements are well approximated by the overburden pressure with average densities between ρ = 2.1 t/m^3 and 2.35 t/m^3, corresponding to pressure gradients from 0.206 bar/m to 0.23 bar/m. A few tests show lower percolation thresholds, presumably due to a decrease in the minor principal stress caused by nearby excavations. Generally, however, tests in depths from 300 m to 3100 m, test volumes from less than a cubic metre to more than 200 000 m^3 and several different test fluids show that the percolation threshold at which the salt rocks lose their tightness closely correlates with the minor principal stress. In undisturbed salt rocks, the minor principal stress is given by the lithostatic pressure.

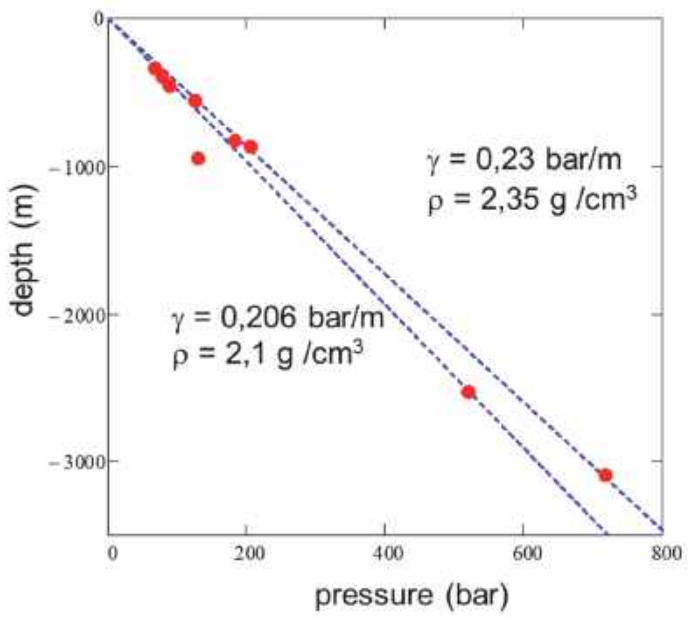

Figure 6: Percolation thresholds from in-situ tests versus depth (see Table 1).

As an example from Table 1, we take a closer look at the integrity test of cavern BAS-2 (see Figure 7), in a depth between 2500 m and 3000 m (van Heekeren 09).

The rock temperature was measure to be 97°C. According to the reasoning in Section 2 (see Figure 2), the cavern parameters are located in the transition region where a connected fluid network starts to form and tightness is not maintained.

After cavern abandonment, brine pressure at the cavern roof reached 95 % of the lithostatic pressure in four years, and slowly rose further towards it. Pressure build-up is limited by percolation along the grain boundaries as lithostatic pressure is approached, due to opening of discrete flow paths. Surface subsidence above the cavern has practically stopped, indicating that equilibrium has been reached between the brine pressure and the rock stress. This large-scale in-situ test confirms that, even under very high temperatures and stresses, the tightness of salt rocks is lost by pressure-driven percolation only when the minor principal stress, i.e. the percolation threshold, is reached.

Numerous experiments in the laboratory and in situ have shown that there is no capillary sealing pressure (Durup 1994). Rather, the percolation threshold is just given by Equation (2). The test results discussed in this Section indicate that the factor f in Equation (2) is close to one. This is consistent with the maximal pressure for cavern storage, which is generally set to $p_{max} \leq 0.9\ \sigma_{min}$, including a factor of safety (Schreiner et al. 2010).

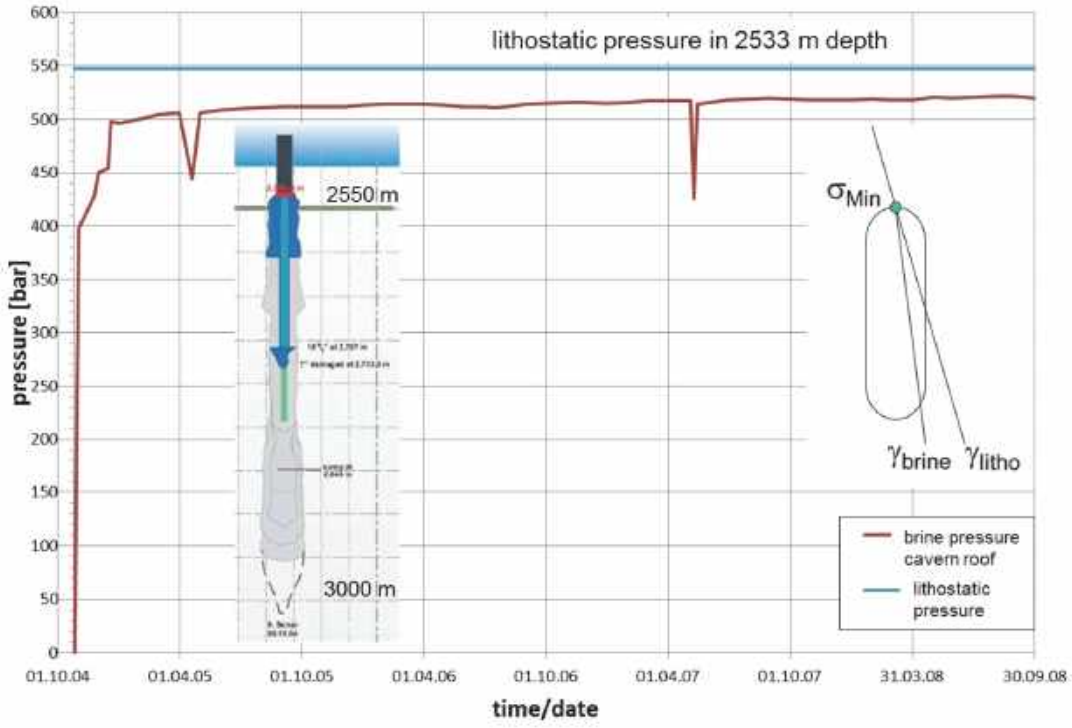

Figure 7: Brine pressure in the roof of the abandoned cavern BAS-2 (van Heekeren 2009).

6 Integrity Loss of Saliferous Barriers

Salt rock barriers preferably lose their integrity in regions where extensional strains are induced and thus the minimal stress can be lowered below the fluid pressure. For example, convergence and subsidence can cause extensions over mining edges and lower the minor principal stress (Figure 8) in the salt back.

As the visco-elasto-plastic simulations show in Figure 8 show that due to the minimal stress criterion, barrier integrity is not generally compromised in the areas of minimal barrier thickness, but rather over the mining edges: The difference in subsidence over the mine and over the pillar causes an extension zone where the minor principal stress is decreased. Pressure-driven percolation starts if the minor principal stress falls below the attacking fluid pressure. Since the minor principal stress is roughly horizontal, the percolation proceeds towards the excavations.

In salt and potash mining around the world, this failure mode has led to a loss of integrity of saliferous barriers in salt and potash mining, and for low-depth mines also to sinkholes at the surface (Minkley et al., 2015c), e.g. Berezniki I and Solikamsk II in Russia (2007 and 2014), Weeks Island Mine in the US (1992) or the K2 mine in Canada (1985).

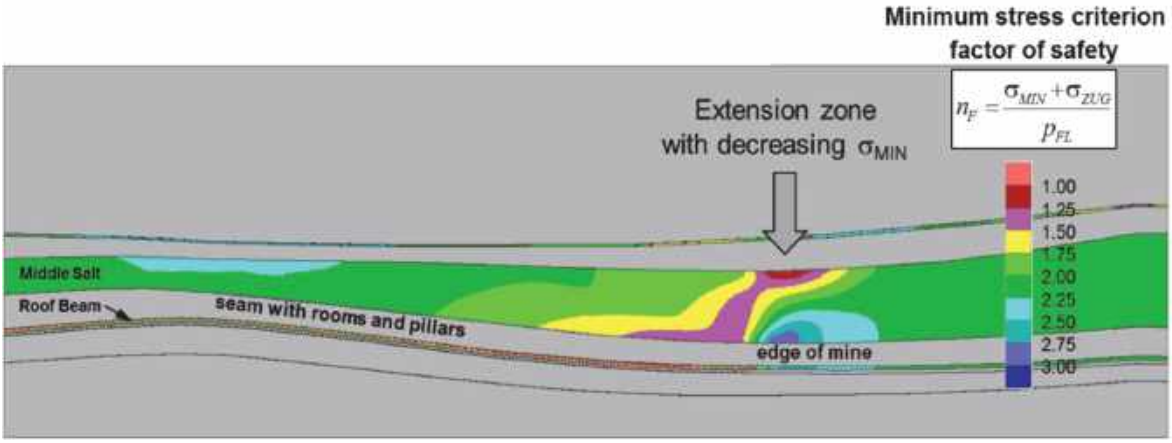

Figure 8: Extensional strain over a mining edge. Minor principal stress and factor of safety for percolation are decreased.

The IfG has conducted coupled hydraulic-mechanical simulations of the Berezniki I mine, including the discontinuous microstructure of the salt rocks (Figure 9). Integrity loss occurred over the edge of the two-level mine at the shaft safety pillar. Over the mine, surface subsidence reached up to 3.7 m, and the resulting extensions over the pillar edge lowered the minor principal stress below the ground water pressure. Subsequently, the brine pressure has opened flow paths along grain boundaries in the 90 m barrier. Once the brine reached the excavation, unsaturated water followed and dissolved the salt back, finally causing the sinkhole when the overburden could no longer bridge the resulting cavity.

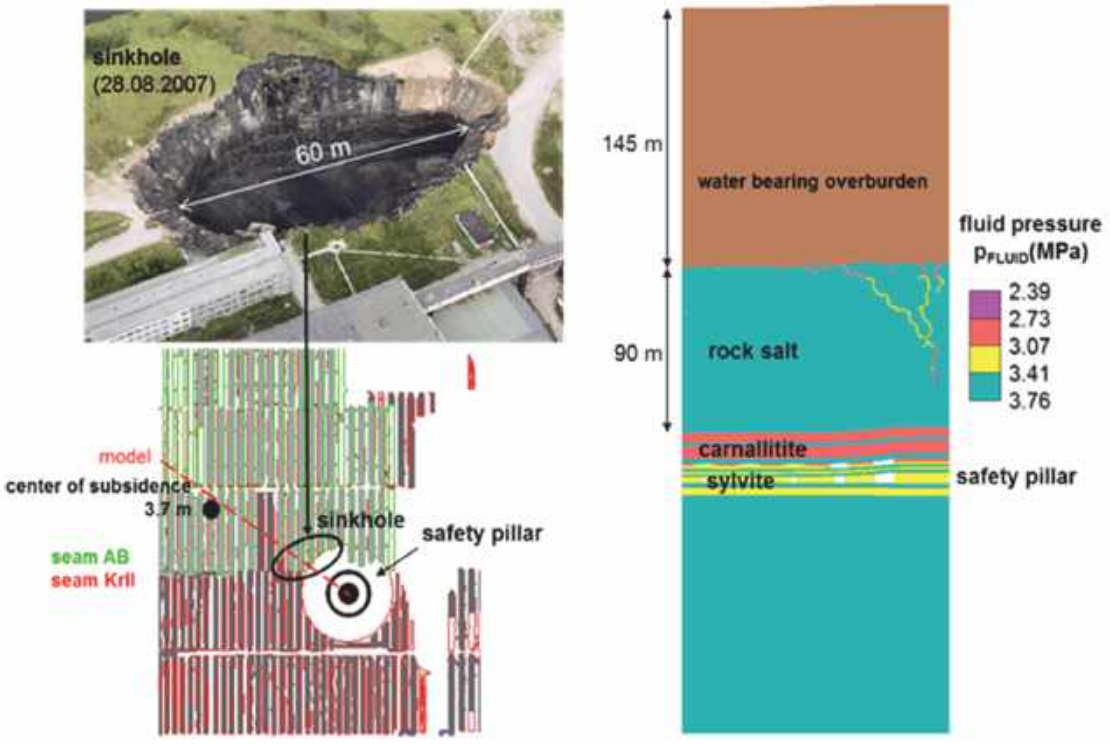

Figure 9: Sinkhole over Berezniki I mine and coupled hydraulic-mechanical simulation showing the percolation over the hard edge at the shaft safety pillar.

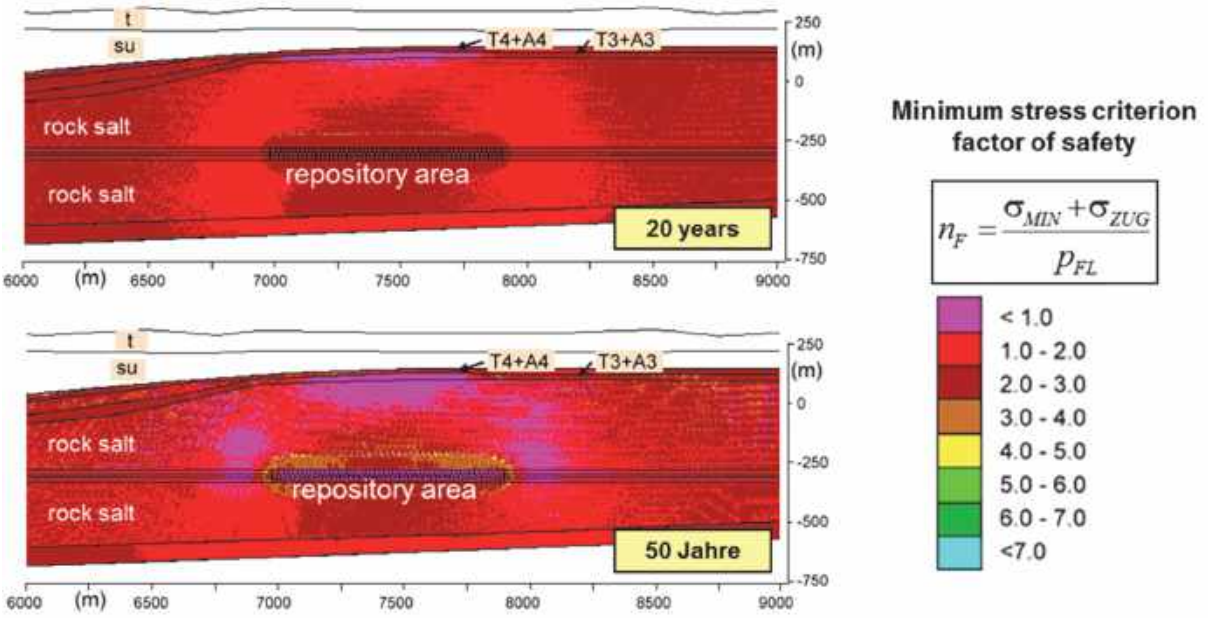

Figure 10: Temporary violation of the minimal stress criterion (violet regions) due to the thermal extension around a waste repository in bedded salt.

The flooding of the Solikamsk II mine in 2014 could be predicted from simulations in 2005 that showed a violation of the minimal stress criterion throughout the saliferous barrier (Minkley et al., 2005).

7 Proof of Barrier Integrity in Waste Disposal

A mined repository for heat-generating waste at first induces convergence and the associated strains around the excavations, similar to a production mine. After waste emplacement, temperatures rise and the overlying strata lift up due to thermal expansion, leading to extensions at the top of the barrier. From a mechanical point of view, it is irrelevant whether extensions are caused by subsidence or thermal uplift – in any case they lower the minor principal stress. The relevant question for barrier integrity simply is whether the minimal stress criterion is violated, i.e. whether the minor principal stress is lower than the fluid pressure. Hence, the tightness of the salt rock barrier in disposal of heat-generating waste has to be analysed with respect to thermomechanically induced stresses and the external hydraulic loads.

Thermal expansion due to the waste-generated heat induces additional stress in the host rock, with deviatoric loads up to $5\ \mathrm{MPa}$. The associated uplift in the overburden is of the order of a few metres and can reach up to the surface. The largest effects on the integrity of the barrier occur some decades after the end of the emplacement process.

As an example, Figure 10 shows the temporary violation of the minimal stress criterion for the case of a repository mine in bedded rock salt (Minkley 2009). For a quantitative assessment of the integrity and tightness of the barrier, however, the simple minimal stress criterion is not sufficient. Rather, coupled thermal-hydraulic-mechanical (THM)

simulations of pressure-driven percolation in the anisotropic stress field around the excavations are required.

Simulations performed in the framework of the preliminary safety assessment for the Gorleben repository (Vorläufige Sicherheitsanalyse Gorleben, VSG) show the principal mechanisms that cause temporary local violations of the integrity of the geological barrier (Minkley and Knauth 2013). Heating and uplift alter the stress state throughout the salt dome. At the top of the salt, the minor principal stress consequently is reduced due to the extension. The region where the minor principal stress falls below the brine pressure, and where thus pressure-driven percolation can proceed due to a violation of the minimal stress criterion, reaches more than hundred metres below the salt top in the simulations.

Subsequently, creep processes continuously reduce the area where the minimal stress criterion is violated, even though the uplift continues. Hence, the largest thermomechanical-hydraulic violations of the barrier are to be expected within the first hundred years after emplacement. Thus, anthropogenic influences on the barrier are most pronounced in the first century; later, the geological barrier is again dominated by the natural geological conditions that have maintained the integrity of rock salt barriers for millions of years.

8 Rock Salt Tightness: Natural Analogues

Salt rocks can locally contain large amounts of fluids. In almost every salt or potash mine, local volumes of brine or gases are tapped by the excavations, encompassing fossil fluids, brines remaining from salt mineral conversion or fluids that have migrated into the salt from surrounding rocks by tectonic, volcanic or halokinetic processes. Fluids can be stored in fractures, on the grain boundaries or in cavities in the salt rocks.

In the Werra potash district, CO_2 has been injected into the salt by tertiary volcanic activity (approximately 20 million years ago). The gas is still trapped on grain boundaries or in cavities as gas or in the supercritical phase. A gas outburst, by far the world's largest, occurred in the Unterbreizbach mine on 1 October 2013 (see left panel of Figure 11). The potash seam Thuringia in a depth of 900 m is composed of carnallitite here. Temperature and lithostatic pressure (T = 31°C, p = 220 bar) imply that the CO_2 was supercritical and trapped in a cavity of a volume of approximately 100 000 m^3 in the rock salt above the seam. The explosive decompression of the gas to atmospheric pressure generated about 40 million m^3 of CO_2 that left the mine through the shaft Unterbreizbach II in a distance of 7 km.

Similar fluid intrusions have been reported from mining districts around the world (see e.g. right panel of Figure 11). In the Weeks Island salt Dome, gas outbursts (hydrocarbons) created cavities of up to 45 000 m^3 (Davisson 2009).

In these examples, fluids were contained in large cavities. Due to the discontinuous microstructure of polycrystalline salt rocks, however, the majority of fluid intrusions is actually bound to the grain surfaces.

The largest gas-salt outburst, i.e. an outburst of mineral-bound gas, in the Werra district, expelled 100 000 tons of salt and 2 million cubic metres of CO_2 (Salzer 1991): The gas-bearing sylvinite was exposed and unloaded by the drill-and-blast mining operations, and the CO_2 underwent a phase transition from liquid to gas, with a large associated volume increase (approximately 500-fold). The high pressure on the grain boundaries fragmented the rock and pneumatically expelled the debris. Such gas outbursts have been triggered in a controlled way in a dedicated mining scheme (so-called *Weitungsbau*).

Similar phenomena are known from other salt formations: The large majority, i.e. usually more than 90 % by volume, of the hydrocarbons found in the *Hauptsalz* of the Gorleben salt dome are stored in intercrystalline pores and grain faces (BGR 2011). The hydrocarbon-bearing Klodawa salt formation in Poland was generated by local overpressure in the hydrocarbons that hydraulically fractured the salt rocks (Burliga & Czechowski, 2010). The so-called *Schnitte* (sections), long straight CO_2-bearing zones are fluid-pressure generated fractures created by dynamical overpressures in eruptions during tertiary volcanism.

As a final example, we consider the South Oman Basin (Kukla et al. 2011). Here, the compaction of oil-bearing carbonatic wall rocks in large depths (anhydrite and dolomite,

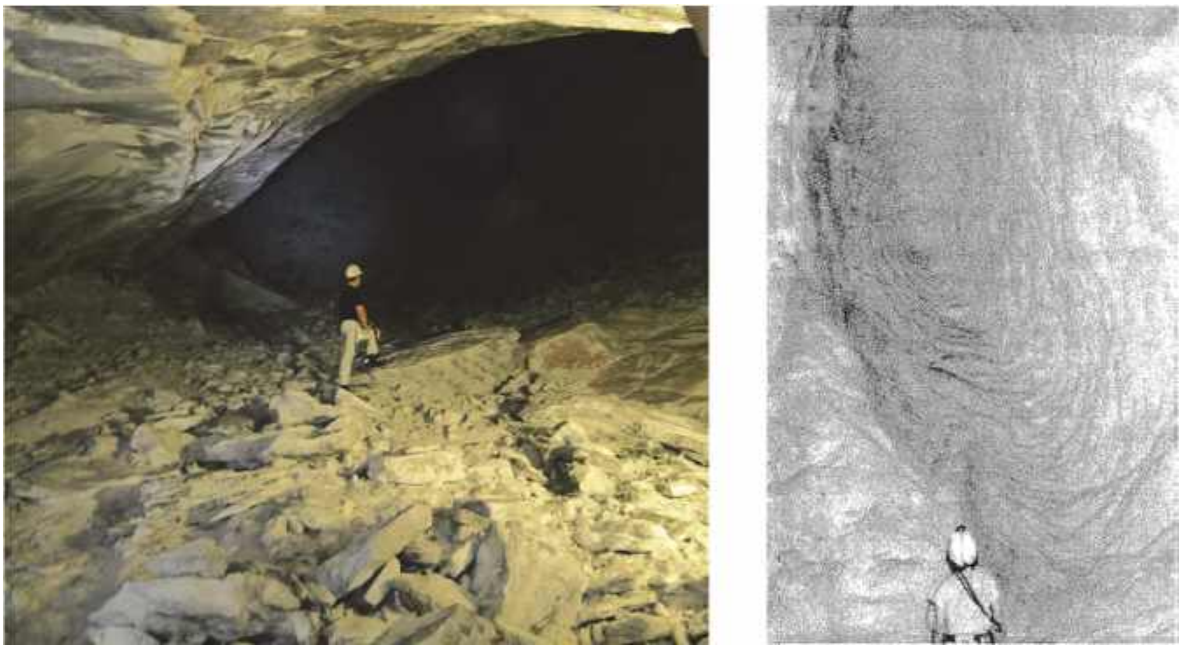

Figure 11: Outburst cavities. Left panel: Supercritical CO_2 in the Unterbreizbach mine (100 000 m^3), right panel: Hydrocarbon outburst in the Weeks Island salt dome (Davisson 2009).

the so-called stringers) raised the oil pressure above the minor principal stress in the adjacent rock salt and injected the oil into the salt by pressure-driven percolation.

Fluids can migrate from their host rocks into salt formations only if their pressure exceeds the percolation threshold, i.e. the minor principal stress. Halokinetic processes can move the trapped fluids over large distances by salt dome uplift and associated intradomal deformations and recrystallisations (Schramm 2007), so that the fluids are far away from their original host rocks. The notion of deformation-assisted percolation used in this context (Ghanbarzadeh et al. 2015) describes a process acting over geological timescales rather than a fluid transport mechanism of interest for the one million years relevant for waste disposal.

The natural analogues discussed in this section can be considered as geological long-term experiments that demonstrate the tightness of the rock salt and the integrity and isolation potential of saliferous barriers over millions of years.

9 Laboratory Tests of Percolation at High Pressure and Temperature

The IfG conducted laboratory experiments to test the hypotheses regarding percolation at high temperature and pressure discussed in Sections 2 and 3. The experiments were performed on rock salt from the Zechstein deposit in Germany. The cylindrical rock salt specimens had dimensions of 192 x 96 mm (height × diameter). Specimens were installed in the triaxial chamber and a constant temperature of 95°C was maintained, the stress state was isotropic throughout the test. Nitrogen gas pressure was applied at a borehole at the upper end of the specimen; flow was measured at the bottom end via a sinter plate.

In a first test phase, axial stress and confining pressure were increased to 60 MPa. To prove the tightness of the rock salt specimens under these temperatures and pressure conditions, gas pressure was applied at the upper end surface of the test specimen. Nitrogen pressure was increased in two steps to 100 bar and later to 190 bar. For both pressure levels, no gas flow was detected at the lower end surface of the specimen.

In a second phase, confining pressure and axial stress were increased to 90 MPa. Again, gas pressure was applied over a couple of hours in multiple steps up to a pressure level of 190 bar (see Figure 12). Even with this increased stress level and the temperature of 95°C, no gas flow could be detected: The rock salt specimen remained impermeable.

We can compare the test conditions with the pressure-temperature diagram of Lewis and Holness (1996) as discussed in Section 2 (see Figure 2). The first experimental stage is in the transition region (light grey) where rock salt should not be impermeable anymore but there is no full grain boundary wetting. The increase of stress to 90 MPa at a temperature of 95°C reaches the white region where the dihedral angle falls below 60° and the wetted grain boundary network should be fully connected. Lewis and Holness (1996) hypothesize a permeability similar to sandstone for these conditions.

The experimental tests do not confirm this prediction. Hypotheses derived solely from measurements of the dihedral angle in synthetic two-phase systems of halite and brine (Ghanbarzadeh at al. 2015) are thus not supported by observation. On the contrary, experiments show that rock salt is impermeable even under these high pressures and temperatures, in accord with previous experiments at lower stresses and temperatures.

10 Limits of Simple Wetting Trigonometry

The surface energy of crystalline solids cannot be expressed by a simple vector of surface tension (Cmiral et al. 1998). There is no simple relation for the balance of surface energies at anisotropic gain boundary vertices, and the equilibrium at the contacts of three or more grains or phases is not yet sufficiently understood theoretically. The simple relation (1) only applies if the crystalline anisotropy is negligible, an assumption not satisfied by real polycrystals.

Measurements of the dihedral angle only partially characterise the fluid distribution in in-situ rocks (Laporte and Provost 2000). A quantitative determination of the fluid transport properties by measurements of permeability and percolation threshold is always required.

In salt formations, the stress state is almost isotropic due to the viscoplastic behaviour of salt rocks; deviatoric stresses are in the range of 1 or 2 MPa. Hence, the stress state is far below the dilatancy boundary, and microcracks cannot form. Due to adhesive forces and lowered surface energy (Minkley 1989), the grain boundaries form a fused network impermeable to fluids. Since porosities are in of the order of 0.1 % to 1 %,

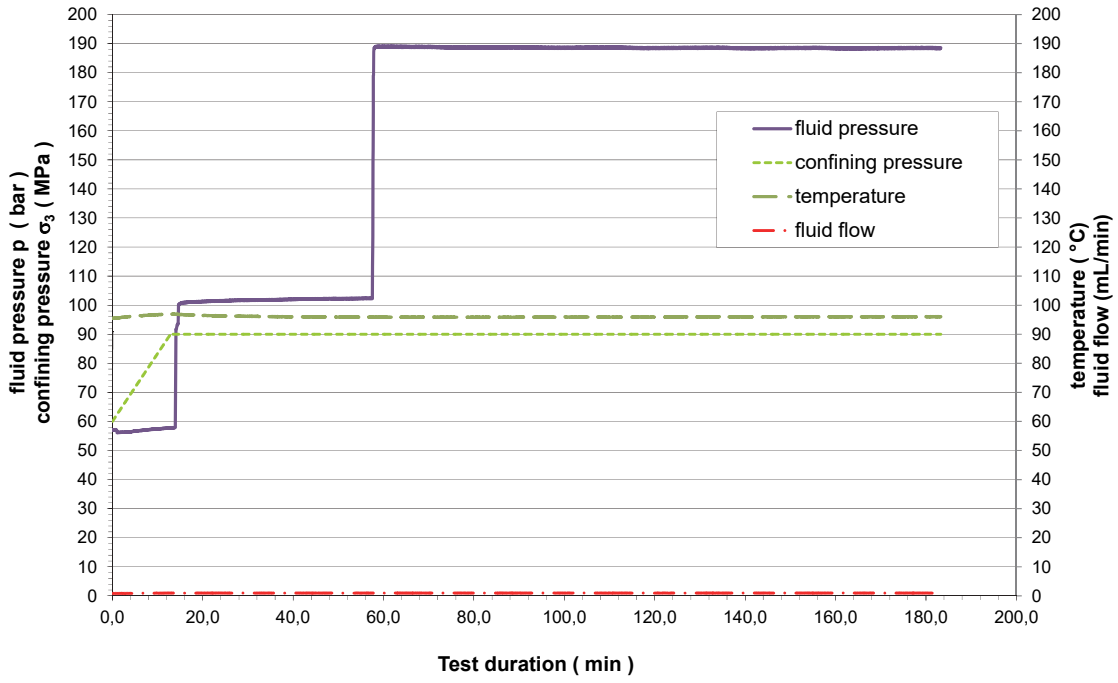

Figure 12: Permeability test. Isotropic pressure 90 MPa, temperature 95°C. Nitrogen pressure was increased from 60 bar via 100 bar to 190 bar. No gas flow was observed throughout the test.

fluids are stored in isolated pores without interconnection. Salt rocks, which have been almost completely dehydrated in their geological evolution, do not form a halite-brine two-phase system.

Under these stress conditions, salt rock barriers can lose their integrity only by pressure-driven percolation: The attacking fluid has to overcome the normal stress and adhesive forces on the grain boundaries (percolation threshold) to create connected fluid pathways (see Sections 5 and 6).

11 Conclusions

Experiments on a natural rock salt specimen under an isotropic stress up to 90 MPa and a temperature of 95°C showed no permeability up to fluid pressures of 19 MPa.

Pressure and temperature conditions were in a region where, according to hypotheses based on the dihedral angle in two-phase systems of brine and halite, the fluid along the grain boundaries should form a completely connected network. Permeabilities of the polycrystalline salt rock were postulated to be high, similar to sandstone. Based on measurements of the dihedral angle in synthetic rock salt generated by compaction of granular salt, it was claimed that rock salt loses its impermeability under high temperature and pressure, regardless of its low porosity or water content, and fluid flow becomes possible without a percolation threshold.

First experiments on natural rock salt do not support this hypothesis. Further tests are required to obtain reliable and verifiable results and a solid understanding based on a broad experimental database. In the research project KOSINA (2016), which aims to develop a concept for a generic repository mine for heat-generating nuclear waste in bedded salt in Germany, a systematic laboratory program regarding rock salt permeability under high stresses and temperatures is planned. In particular, experiments with large fluid pressures are intended to show that the minor principal stress acts as the percolation threshold even under extreme boundary conditions. If no permeability can be detected under high stresses and temperatures in natural rock salt, the theory discussed above is falsified.

Existing knowledge indicates that natural rock salt loses its tightness only if the fluid pressure exceeds the minor principal stress, i.e. the percolation threshold, even under high stress and temperature. Only in in this case, grain boundaries can be opened and a connected fluid network can be created in the polycrystalline salt rock. This process, denoted by pressure-driven percolation, led to the loss of integrity of saliferous barriers in salt and potash mining several times.

Fluid intrusions found in salt formations, both in bedded and domal salt, form natural analogues for the barrier function of rock salt. Fluids can be stored in cavities of up to 10^5 m^3 and prove the impermeability of saliferous barriers in geological long-term experiments. Hence, a fluid percolation in rock salt without a percolation threshold contradicts the in-situ observations. An abandoned brine production cavern in a salt formation (depth ranging from 2500 m to 3000 m) provides an experimental confirmation of the minor principal stress as percolation threshold. Thus we conclude that for pressures below the minor principal stress, polycrystalline salt rocks are impermeable.

Bibliography

BGR (2010): Berücksichtigung der Kohlenwasserstoff-Vorkommen im Hauptsalz des Salzstockes Gorleben. Bundesanstalt für Geowissenschaften und Rohstoffe Hannover.

Bracke, G., Fischer-Appelt, K., Noseck, U., Wolf, J. (2013): The current status of a safety case for heat-generating radioactive waste disposal in salt in Germany. Natural Analogues for safety case of repositories in Rock Salt, OECD 2014, 75-83

Brückner, D., Lindert, A., Wiedemann, M. (2003): The Bernburg Test Cavern – A Model Study of Cavern Abandonment. SMRI Fall Meeting, 5-8 Okt. 2003, Chester, UK, pp. 69-89

Cmiral, M., Fitz Gerald, J. D., Faul, U. H, Green, D. H. (1998): A close look at dihedral angles and melt geometry in olivine-basalt aggregates: a TEM study. Contrib. Mineral Petrol 130, 336 – 345, Springer Verlag

Davison, I. (2009): Faulting and fluid flow through salt. Journal of the Geological Society Lon-don, Vol. 166, 205 – 216

Durup, J. G. (1994): Long-Term Test for Tightness Evaluations with Brine and Gas in Salt. SMRI Research and Development Project Report No. 94-0002-S

Ghanbarzadeh, S., Hesse, M. A., Prodanovic, M., Gardner, J. E. (2015): Deformation-assisted fluid percolation in rock salt. Science, Vol. 350, ISSUE 6264, 1069 – 1072

Heekeren, H., Bakker, T., Duquesnoy, T., de Ruiter, V., Mulder, L. (2009): Abandonment of an extremely deep Cavern at Frisia Salt. SMRI Spring 2009 Technical Conference, 27 - 28 April, Krakow, Poland

Holness, M. B. (2006): Melt-Solid Dihedral Angles of Common Minerals in Natural Rocks.Journal of Petrology, Vol. 47, N^{o}. 4, 791 – 800

KOSINA (2016): Konzeptentwicklung für ein generisches Endlager für wärmeentwickelnde Abfälle in flach lagernden Salzschichten in Deutschland sowie Entwicklung und Über-prüfung eines Sicherheits- und Nachweiskonzeptes. GRS, BGR, DBE TEC, IfG: För-derkennzeichen 02E11405C

Kukla, P.A., Reuning, L., Becker, S., Urai, J.L., Schoenherr, J. (2011): Distribution and mechanisms of overpressure generation and deflation in the late Neoproterozoic to early Cambrian South Oman Salt Basin. Geofluids 2011 – Blackwell Publishing Ltd.

Lewis, S., Holness, M. (1996): Equilibrium halite-H_2O dihedral angles: High rock-salt perme-ability in the shallow crust? Geology, May 1996, N^{o} 5, 431-434

Laporte, D., Provost, A. (2000): Equilibrium geometry of a fluid phase in a polycrystalline aggregate with anisotropic surface energies: Dry grain boundaries. Journal of Geophysical Research, Vol. 105, N^{o} B11, 25,937 – 25,953

Minkley, W. (1989): Festigkeitsverhalten von Sedimentgesteinen im post-failure-Bereich und Gebirgsschlagerscheinungen. Proc. Int. Symp. Rock at Great Depth, Pau. Vol. 1, pp. 59 - 65

Minkley, W. (2009): Final Disposal in Rock Salt and Barrier Integrity. Proceedings of the Eu-ropean Commission TIMODAZ-THERESA Int. Conferene, Luxembourg, 29.Sept. – 01. Oct. 2009, 105-121, European Union 2012, ISBN 978-92-7926057-5

Minkley, W., Mühlbauer J., Naumann, D., Wiedemann, M. (2005): Prognose der dynami-schen Langzeitstabilität von Grubengebäuden im Salinar unter Berücksichtigung von Diskontinuitäts- und Schichtflächen. (FKZ: 02 C 0892). IfG, Leipzig, 30.07.2005

Minkley, W., Knauth, M., Wüste, U. (2012): Integrity of salinar barriers under consideration of discontinuum-mechanical aspects. Mechanical Behavior of Salt VII, Paris, France, 16-19 April 2012, 469 – 478, Taylor & Francis Group, London, ISBN 978-0-415-62122-9

Minkley, W., Knauth, M. (2013): Integrity of rock salt formation under static and dynamic im-pact. Natural Analogues for Safety Cases of Repositories in Rock Salt. Salt Club Workshop Proceedings, 5-7 September 2013, Braunschweig, Germany, Radioactive Waste Management, NEA/RWM/R(2013)10, March 2014, 177-195

Minkley, W., Knauth, M., Brückner, D. (2013): Discontinuum-mechanical behaviour of salt rocks and the practical relevance for the integrity of salinar barriers. ARMA, 47th US Rock Mechanics Symposium, San Francisco, CA, USA, 23-26 June 2013. Paper ARMA 13-388

Minkley, W., Knauth, M., Fabig, T., Farag, N. (2015a): Stability of salt caverns under consideration of hydro-mechanical loading. Mechanical Behavior of Salt VIII, Rapid City, USA, 26-28 May 2015, 217 – 227

Minkley, W., Knauth, M., Brückner, D., Lüdeling, C. (2015b): Integrity of saliferous barriers for heat-generating radioactive waste – natural analogues and geomechanical requirements. Mechanical Behavior of Salt VIII, Rapid City, USA, 26-28 May 2015, 159 -170

Minkley, W., Mühlbauer, J., Lüdeling, C. (2015c): Dimensioning principles in potash and salt mining to achieve stability and integrity. ARMA, 49th US Rock Mechanics Symposium, San Francisco, CA, USA, 28 June -1 July 2015. Paper ARMA 15-698

Robert, J. M., Sevougian, S. D., Leigh, C. D., Hansen, F. D. (2012): Towards a Defensible Safety Case for Deep Geologic Disposal of DOE HLW and DOE SNF in Bedded Salt. SANDIA REPORT SAND2012-6032, Sandia National Laboratories Albuquerque, New Mexico and Livermore, California

Salzer, K. (1991): Die Beherrschung von Gas-Salzausbrüchen im Kalibergbau des Thüringi-schen Teils des Werrareviers. Kali 91 - Second international Potash Technology Con-ference, Hamburg, May 26-29

Schade, H. W. J. (2008): Reverse mining – The development of deep geologic isolation of hazardous (chemotoxic) waste in Germany and its international prospects. Geological Society of America Reviews in Engineering Geology XIX, 23-30

Schramm, M. (2007): Vorkommen natürlicher Gase im Salz. Workshop der GRS, Berlin, 17. – 18. April 2007, 157-166 (GRS-242)

Schreiner, W., Lindert, A., Brückner, D. (2010): IfG Cavern Design Concept - Rock-mechanical aspects for the development and operation of rock salt caverns, SMRI Fall 2010 Technical Conference Leipzig, 03.-06. Oct. 2010, 68 – 81

Staudtmeister K., Rokahr R. (1994): Pressure Build-Up Test in the Etzel K 102 Cavern. SMRI Research Project Report No. 98-5-SMR

Fracturing processes for brittle rocks – a numerical study

Rissausbreitungsprozesse in spröden Gesteinen - eine numerische Studie

Xiang Li[a], Heinz Konietzky[b], Xibing Li[a]

[a] School of Resources and Safety Engineering, Central South University, Changsha 410083, Hunan, China

[b] Chair for Rock Mechanics, Geotechnical Institute, TU Bergakademie Freiberg, Gustav-Zeuner-Str. 1, 09596 Freiberg

Abstract

Numerical modeling schemes are proposed considering material heterogeneity and initial microflaws at the element scale based on the physical observations of fracturing processes in brittle rocks. Linear elastic fracture mechanical theory is adopted to define the mechanical conditions of a microcrack within each element, where failure criterion based on stress intensity factor is introduced. The kink model and wing crack propagation model are developed to describe the initiation and growth of microcracks. Numerical simulations are implemented under distinct loading types, where factors influencing model response are studied. Typical fracture patterns are observed under distinct external loadings. The numerical models are able to reproduce the fracturing process of heterogeneous brittle rocks spatially and temporally. The simulation results have shown good agreement with laboratory observations. Conclusions were drawn and possible future work is discussed for the improvement of the current model.

Zusammenfassung

Es wird ein numerisches Berechnungsschema basierend auf Beobachtungen von Rissprozessen in spröden Gesteinen vorgestellt, das Heterogenität des Materials und initiale Mikrorisse auf elementarer Skala verwendet. Die Theorie der Linear Elastischen Bruchmechanik wird adaptiert, um Mikrorisse in jedem Element abzubilden, wobei Versagenskriterien auf Basis der Spannungsintensitätsfaktoren angewendet werden. „Kink-, und Wing-Crack“-Modelle wurden entwickelt, um die Rissinitiierung und -ausbreitung zu beschreiben. Numerische Simulationen unter verschiedenen Belastungssituationen wurden durchgeführt, wobei der Einfluss verschiedener Faktoren untersucht wurde. Typische

Rissmuster wurden unter spezifischen Belastungen beobachtet. Die numerischen Modelle sind in der Lage, den Rissausbreitungsprozess in heterogenen und spröden Materialien räumlich und zeitlich abzubilden. Die Simulationsergebnisse zeigen gute Übereinstimmung mit Laborergebnissen. Schlussfolgerungen und potentielle weitere Arbeiten zur Verbesserung der Modelle werden diskutiert.

1. Introduction

The existence of microflaws (microcracks) in rocks, such as pores, voids and mineral grain boundaries etc., is known to have significant influence on the mechanical behavior [1]. In fact, the inelastic response of such quasi-brittle materials including rock, concrete and ceramic under load is explained by the microcracking process involving initiation, propagation and coalescence of microcracks [2]. The coalesced microcracks finally form macroscopic fractures which lead to the loss of loading bearing capacity and the eventual failure of the material. The above mentioned process is observed and widely acknowledged in both short and long term inelastic deformation and fracturing mechanisms of brittle rock [3-6]. Considerable constitutive models have been established to investigate the failure process of rock. These models are generally divided into phenomenological models [e.g. 7, 8] and micromechanics-based models [e.g. 9-16]. Phenomenological models are characterized by empirical internal variables and can be calibrated to fit the experiments. However, the physical mechanisms of the fracturing process are not accounted for, whereas micromechanical based models are able to consider micro-mechanisms such as microcrack growth together with microscopic kinetics.

In this study, 2D micromechanical numerical models are established to simulate both time dependent and time independent fracturing processes, up to the formation of final macroscopic failure (macroscopic tensile crack or shear band) of brittle rock. It is assumed in this modelling approach that the final failure of the rock is the result of the partially parallel growth and coalescence of many initially existing microcracks at the grain size level, rather than the growth of one or only a few single cracks. We base our model on the linear elastic fracture mechanical theory (LEFM) [e.g. 17, 18], considering heterogeneity. For the time dependent fracturing process, stress corrosion and Charles theory are adopted to describe the subcritical growth of microcracks. The simulation scheme is developed for cohesive granular material such as rocks, which consists of mineral grains of different shape, size, and mechanical properties, like strength and stiffness.

2. Numerical modeling approach

We establish our numerical model through extensive use of the internal program language FISH in commercial code FLAC [19]. The model is divided into elements (zones) of uniform size, to represent the heterogeneity in rock material at grain scale. A detailed discussion about prescribing heterogeneity in the model is given in section 2.1 and 2.2.

2.1 Heterogeneity in macroscopic model

As an ensemble of distinct minerals and cementitious materials, natural rock is well accepted as a heterogeneous material [9, 20], where the properties vary in different locations at grain size scale. The mechanical response of rock sample

is greatly influenced by this material discontinuity together with structural heterogeneities, such as grain sizes and initial microflaws. Such mechanism can be viewed from the dispersion of strength data of distinct rock samples obtained in lab tests. To represent the heterogeneity in rock, we adopted the statistical approach where one or many mechanical properties are spatially described at the micro scale (zone level) in a stochastic manner. Specifically, we assign the Young's modulus and Poisson's ratio for each zone stochastically following Weibull distribution [21]. This scheme is illustrated in Fig. 2, where the distinct gray scale in each zone represents distinct Young's modulus and Poisson's ratio values (Fig. 2(b)). The Weibull probability density function is written as

$$\mathrm{f(x)} = \frac{b}{a}\left(\frac{x}{a}\right)^{b-1} e^{-(x/a)^b}, \tag{1}$$

where x denotes a random variable (mechanical property Young's modulus or Poisson's ratio in this study); a denotes scale parameter, which was assigned with the mean value of the mechanical property; b denotes shape parameter (b > 0). Specifically, when b is given the value of 1 and 2, the Weibull distribution becomes Exponential distribution and Rayleigh distribution, respectively. Shape parameter b represents the level of heterogeneity: when b increases, the values of random variable x become more concentrated within a narrow range, which means x values are more homogeneous; when b decreases, the values of x become more scattered in a wide range, which means they are more heterogeneous. This feature can be seen from the probability density of Young's modulus and Poisson's ratio with different shape parameters (Fig. 1).

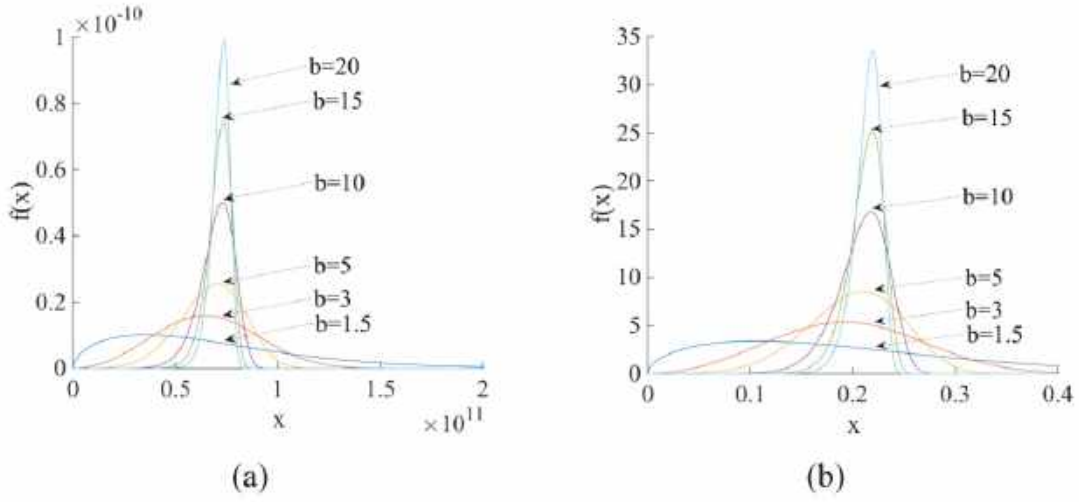

Figure 1 Probability density function of (a) Young's modulus with scale parameter a = 7.38e10 Pa, and (b) Poisson's ratio with scale parameter a = 0.22 with different shape parameter b

The structural heterogeneity of rock is implemented by including initial microcracks in the model. We define stochastically an initial microcrack in each zone with the microcrack's length and orientation following certain distributions (uniform or normal distribution) (Fig. 2 (b)). In this paper, the orientation is described as the angle between initial microcrack plan and abscissa. The uniaxial load applied on the model is perpendicular to abscissa.

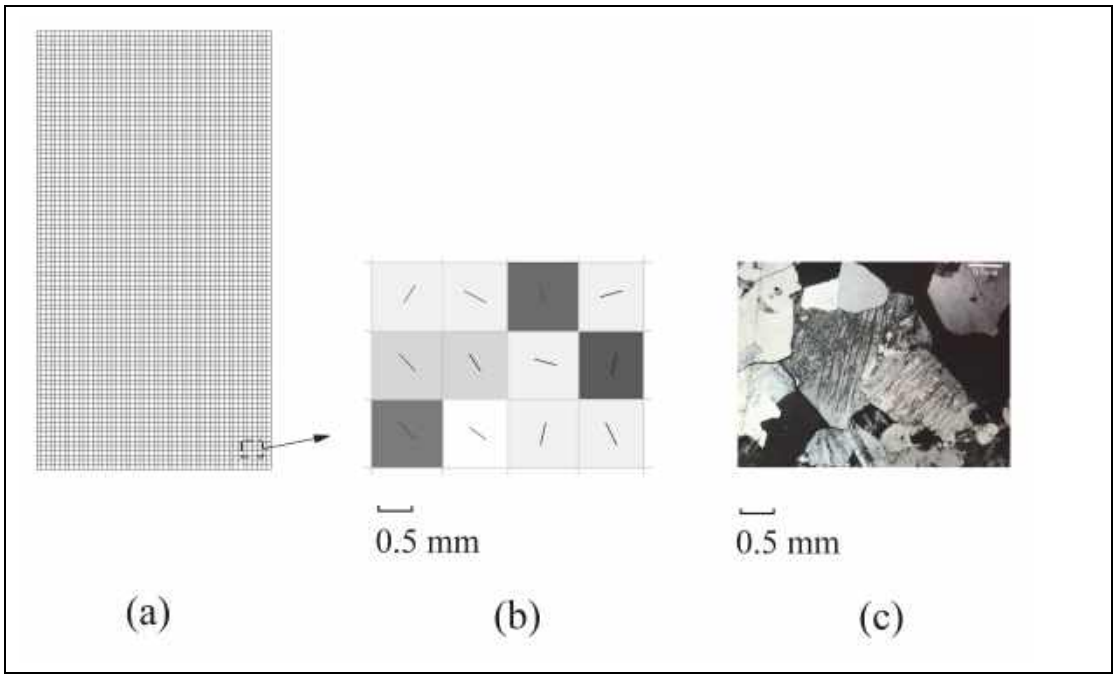

Figure 2 Illustration of heterogeneity in the numerical model (a) Example of numerical model layout; (b) Zoomed in view of certain small area of the model showing the heterogeneity by mechanical properties and initial microcracks at the micro scale; (c) Photomicrograph of granite under cross-polarized light [22]

2.2 Time independent constitutive model

Mohr–Coulomb constitutive law is adopted in the numerical simulation, and we employ failure criterion based on stress intensity factor of the microcrack concerning each zone of the model. Although mechanical properties are heterogeneous for distinct zones, the material is considered homogeneous and isotropic inside each specific zone. This feature makes it applicable to practice linear fracture mechanics theory on the initial microcrack within one zone [3]. Classical linear elastic fracture mechanics assumes that the crack propagates ultrasonically when the stress intensity factor K reaches a critical value. Accordingly, our fracture criterion based on the stress intensity factor can be described: failure of one zone occurs when the stress intensity factor at the tip of the microcrack within the zone reaches the critical value, so-called fracture toughness K_C. Otherwise the crack is determined stable and the zone remains not failed. This means one singular zone reflects linear elastic mechanical behavior before failure state, and when $K \geq K_C$, the post-failure regime is applied by assigning

residual strength values to this zone, which leads to elasto-plastic stress redistributions at macro scale in the model. The interaction between microcracks is realized by the stress redistribution caused by the failed zone containing a microcrack at critical state to other zones containing microcracks at stable state. Naturally, the zones in the vicinity of the failed zones are more influenced by the stress redistributions.

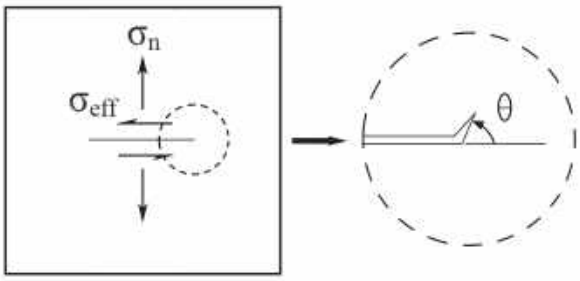

Figure 3 Kink of initial microcrack under mixed-mode loading

It is known that a crack can experience three types of loading in a 3-dimensional body, Mode I, II and III loading, corresponding to normal loading, in-plane shear loading and out-of-plane shear loading, respectively. A cracked body may be subjected to any one of these modes, or a combination of more than one mode (mixed-mode condition) [17]. In this study, analyses are carried out on 2D models. Only mixed-mode condition caused by Mode I and II are considered since Mode III loading does not existed under 2D conditions. Consider one zone of the model where the initial microcrack is subjected to mixed-mode loading, as seen in Fig. 3. In this case, the stress field is characterized by K_I and K_{II}. Under mixed-mode loading, the crack kinks at an angle from its original crack plane by initiation. It is well accepted that the crack tip kinks to the direction where maximum circumferential stress is found [23]. The circumferential stress near the crack tip is expressed as [17]:

$$\sigma_{\theta\theta}(r,\theta) = \frac{K_I}{\sqrt{2\pi r}} cos^3\left(\frac{\theta}{2}\right) - \frac{K_{II}}{\sqrt{2\pi r}} 3\, cos^2\left(\frac{\theta}{2}\right) \sin\left(\frac{\theta}{2}\right). \quad (2)$$

Where r denotes the distance ahead of the crack tip; θ denotes the angle from its original crack plane. The kink angle θ_1 at maximum circumferential stress is obtained by:

$$\tan\left(\frac{\theta_1}{2}\right) = -\frac{2K_{II}/K_I}{1+\sqrt{1+8(K_{II}/K_I)^2}} \quad (3)$$

It is considered that $K_I > 0$ for opening crack, so the kink angle θ_1 has an opposite sign to K_{II}. Especially, when the crack is under pure Mode I loading (K_{II} = 0), θ_1 becomes zero and crack propagates along its original plane. When the

crack is under pure Mode II loading ($K_I = 0$), the value for θ_1 is 70.5° [24]. Assuming normal stress on the main crack is σ_n, effective shear stress on the crack is expressed as:

$$\sigma_{eff} = \begin{cases} \tau & (\sigma_n \geq 0) \\ \frac{\tau}{|\tau|}(|\tau| - \mu|\sigma_n|) & (\sigma_n < 0) \\ 0 & if \ \ |\tau| - \mu|\sigma_n| < 0 \end{cases}, \tag{4}$$

where τ denotes the shear stress on the main crack; μ denotes the friction coefficient. The Mode I and Mode II stress intensity factors are expressed by:

$$K_I = \sigma_n \sqrt{\pi a}, \tag{5}$$

$$K_{II} = \sigma_{eff} \sqrt{\pi a}\ , \tag{6}$$

where a denotes half crack length. The stress intensity factor at the tip of the kink is obtained from K_I and K_{II} [17]:

$$K(\theta_1) = K_I \left[\frac{3}{4}\cos\left(\frac{\theta_1}{2}\right) + \frac{1}{4}\cos\left(\frac{3\theta_1}{2}\right)\right] - \frac{3}{4}K_{II}\left[\sin\left(\frac{\theta_1}{2}\right) + \sin\left(\frac{3\theta_1}{2}\right)\right]. \tag{7}$$

If main initial microcrack is subjected to tensile normal stress and $K(\theta_1) \geq K_{IC}$, tension failure occurs to the zone. If main initial microcrack is subjected to pure Mode II loading and $K(\theta_1) \geq K_{IIC}$, shear failure occurs to the zone. Since microcrack lengths and orientations are different for distinct zones, the obtained stress intensity factor values are also distinct, even under the same stress conditions. The heterogeneity level of initial microcracks can also be altered by changing parameters of the distribution functions for initial microcrack lengths and orientations.

2.3 Time dependent microcrack growth scheme

It is assumed by classical LEFM that the crack propagates when the stress intensity factor K reaches the fracture toughness K_C. Otherwise the crack will remain stable. However, microcrack developing phenomena are observed in brittle material under long-term loading when stress intensity factor is lower than the critical limit [25-30]. This time dependent fracturing process is called subcritical crack growth [31-33], and can be explained by the theory of stress corrosion [18]. We include subcritical microcrack growth scheme in each zone of the numerical model to study the time dependent fracture process, where the relation between crack growth velocity and stress intensity factor is described by Charles equation, a power law most commonly adopted to characterize subcritical crack growth [34, 35]:

$$v = v_o K^n exp\left(\frac{-u}{RT}\right), \tag{8}$$

where v denotes the crack growth velocity; u_o denotes a material constant; K denotes the stress intensity factor; n denotes the stress corrosion index; u denotes the activation energy; T denotes the absolute temperature and R denotes the gas constant (Boltzmann constant). By defining $C = u_o exp(-u/(RT))$ as a rock-specific parameter, Charles equation (Eq. 8) is simplified to:

$$v = CK^n. \tag{9}$$

In the time dependent microcrack growth model scheme, the initial model setup is the same as for the time independent model introduced in Section 2.2 considering material heterogeneity at the micro scale and a microcrack in each zone. We continue executing the static analysis in FLAC, where a “timestep” is taken for each calculation cycle around the loop, and grid or zone variables (e.g. stresses) are updated from known values that remain fixed within this cycle. For example, within a calculation cycle, new stresses are calculated for each element with the set of velocities already calculated, while the newly calculated stresses do not affect the velocities. This process is justified by the fact that the inherent “timestep” in FLAC is so small that information cannot physically pass from one element to another in that interval [19]. We obtain the real time for subcritical crack growth by including a real time span value as a parameter in each calculation cycle. In view of the nature of static analysis mentioned above, it is reasonable to assume that the inherent small “timestep” exists only for realizing the static analysis, and is negligible in the subcritical crack growth time scale. More discussion about setting real time span value conforming to static analysis is given in reference [36].

2.4 Wing crack propagation scheme

It is observed that cracks under load typically propagate forming wing cracks. The exact calculation of the stress intensity factor of wing crack was given in the work of Nemat-Nasser and Horii [37] and Horii and Nemat-Nasser [38]. Based on their work a modified wing crack propagation scheme was developed by Baud et al. [24], where a curved wing crack is represented by a straight one, so that calculation of the stress intensity factor at the wing crack tip is easier (faster) in terms of computational effort, as is seen in Fig. 4. The scheme determines further wing crack propagation after the initial kinking by assuming that the wing crack propagates in the direction of the maximum local stress intensity factor KI at the wing crack tip ($K_{II} = 0$). However, K_I value at the wing crack tip is obtained by contributions from both normal stress on wing crack and shear stress on initial main crack.

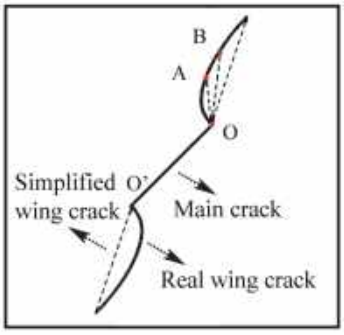

Figure 4 Simplification scheme of wing crack propagation (modified from Baud et al. [24])

Specifically, when the normal stress on the crack is compressive, the local stress intensity factor at wing crack tip is composed of K_{ISO}, the component of stress intensity factor derived from the two wing cracks from the initial main crack tips, and K_{SLI}, the component of stress intensity factor derived from the sliding of the initial main crack subjected to the same stress condition [24]:

$$\mathrm{K} = K_{SLI} + K_{ISO} = -3\sigma_{eff}\sqrt{\frac{a + l_{eq}}{\pi}}\left[\sin\left(\frac{a}{a + l_{eq}}\right)\right]^{-1}\sin\theta\cos\frac{\theta}{2} +$$

$$\frac{1}{2}[(\sigma_V + \sigma_H) + (\sigma_V - \sigma_H)\cos 2(\theta + \beta)]\sqrt{\pi l}, \qquad (10)$$

where σ_{eff} denotes the effective shear stress on the initial main crack ($|\sigma_{eff}| = |\sigma_T| - \mu|\sigma_N|$), while σ_T and σ_N denotes shear and normal stress on the initial main crack, respectively. μ denotes the coefficient of friction; σ_V denotes the vertically applied major principal stress; σ_H denotes the horizontally applied minor principal stress; l denotes the length of each wing crack; β denotes the main crack's orientation to the abscissa; θ denotes the angle between the main crack and the wing crack. $l_{eq} = (9/4)l\cos2(\theta/2)$ denotes the wing crack's equivalent length (Baud et al. [24]). The term "ISO" (isolated) and "SLI" (sliding) are used for K_{ISO} and K_{SLI} only to differentiate their respective origins in the superposition technique.

In the above mentioned condition, the crack is assumed to be closed and compressive normal load on main crack does not contribute to the local stress intensity factor value at the wing crack tip. Thus, a component derived from the compressive normal stress on the main crack does not exist in Eq. 10 [24]. However, if the initial main crack is subjected to tensile normal load, the crack is considered open. In addition to the equivalent stress intensity factor derived from wing cracks (K_{ISO}) and shear stress on the main crack (K_{SLI}), tensile normal stress on the main crack also contributes to the local K value at the wing crack tip. In this case, we extend the expression of the local stress intensity factor at wing crack tip by including an additional component, the equivalent

Mode I stress intensity factor (K_{TEN}), accounting for the tensile normal stress on the main crack:

$$\mathrm{K} = K_{SLI} + K_{ISO} + K_{TEN} = -3\sigma_{eff}\sqrt{\frac{a+l_{eq}}{\pi}}\left[\sin\left(\frac{a}{a+l_{eq}}\right)\right]^{-1}\sin\theta\cos\frac{\theta}{2} +$$

$$\frac{1}{2}[(\sigma_V+\sigma_H)+(\sigma_V-\sigma_H)\cos 2(\theta+\beta)]\sqrt{\pi l}+\sigma_N\sqrt{\pi a}\left[\frac{3}{4}\cos\left(\frac{\theta}{2}\right)+\frac{1}{4}\cos\left(\frac{3\theta}{2}\right)\right] \quad (11)$$

where σ_{eff} denotes the effective shear stress on the initial main crack. Since the crack is considered open, it equals shear stress on the initial main crack σ_T. σ_N denotes the normal tensile stress on the main crack. K_{TEN} denotes the equivalent Mode I stress intensity factor from the tensile normal stress on the main crack. Anderson [17] also introduced a similar superposition method, where the local stress intensity factor at the kink tip was calculated by summing equivalent Mode I stress intensity factors obtained from normal and shear stresses on main crack, corresponding to K_{TEN} and K_{SLI} in this paper, respectively. However, as only kinking condition was considered, the component of local stress intensity factor from wing crack was not included in Anderson's work [17].

For each initial microcrack in our model, we combine the above-mentioned simplified wing crack propagation scheme with subcritical crack growth scheme in a stepwise manner. Specifically, the microcrack growth velocity is obtained by Charles equation (Eq. 9) with the local stress intensity factor calculated using the superposition technique introduced above (Eq. 10 or Eq. 11), and crack length described by the simplified wing crack propagation scheme (Fig. 4). Considering an initial microcrack "OO'" within one zone of the model under a constant load, the calculation scheme is described as follows: In each calculation cycle (one time span), the stresses on the crack are calculated and the stress intensity factor is obtained according to the current crack state. Whether the zone is failed or not is then determined by consulting the failure criteria: 1. whether the current microcrack size has reached the zone; 2. whether the microcrack's fracture toughness has been reached. If the zone fails by one or both of these criteria, post failure regime is applied to this zone, and the calculation process moves on to the next zone. Otherwise, the microcrack propagation velocity is obtained according to Charles equation (Eq. 9). By multiplying the current velocity and the real time span value assigned to the step, the newly propagated wing crack length is obtained. The initial microcrack has propagated from tip "O" to point "A", and Curve "OA" is the newly formed wing crack (Fig. 4), which is simplified by straight line "OA". Local stress intensity factor $K_I(A)$ is then calculated knowing the length of initial microcrack, representative wing crack (straight line "OA") and their corresponding orientations, where specific superposition strategy (Eq. 10 or Eq. 11) is chosen according to the normal stress state on the main crack. This current $K_I(A)$ value is used to calculate

crack propagation velocity using Charles equation (Eq. 9) for the next cycle. Thus, both stress condition and microcrack condition are ‘‘updated’’ for this zone and ready for the next calculation step. This process goes on until the crack propagation halts under updated stress condition, or the critical crack state is reached and causes failure to the zone. The calculation cycle iterates itself through all the zones within each step of FLAC. After certain steps, the failed zones coalesce and form ‘‘macroscopic fractures’’. It is assumed that the model fails when “macroscopic fractures” penetrate the model, and the lifetime (time to failure) is obtained as cumulative time span values from the calculation cycles up to failure.

3. Numerical realizations

In this chapter, numerical simulation results are presented. Especially, fracture patterns are studied of models under distinct loading types. Factors influencing the results, such as the initial crack lengths and level of heterogeneity, are also discussed.

3.1 Numerical model under distinct loadings

The numerical model is established in rectangular shape with the dimension of 50 mm $\times$ 100 mm, and is divided into 5000 zones with each zone 1 mm^2 (1 mm $\times$ 1 mm) in size (Fig. 2 (a)). The parameters used in the numerical model are chosen from reference [14], where 73.8 GPa and 0.22 are given as scale parameters in the Weibull distributions for Young’s modulus and Poisson’s ratio, respectively. The initial friction angle for the zones of the model is 30º, and 0.0005 m is assigned as the mean length for the initial microcracks following normal distribution. The orientations of microcracks follow uniform distribution (ranging from 0º to 360º), and normal distribution with the mean orientation of 45º. As is introduced in the previous section, the material heterogeneity is reflected by assigning mechanical properties to each zone of the model stochastically, while within each specific zone, the material is regarded as homogeneous. Thus the choice of zone size associates with the material heterogeneity of the whole model. The effect of zone size on the mechanical response (Fig. 5) and fracture pattern (Fig. 6) of the numerical model is investigated. Tests are carried out on numerical model divided by 1250 zones, 1800 zones, 5000 zones, 12800 zones and 20000 zones, respectively. The external load is applied in a displacement controlled loading mode. As is shown in Fig. 6, with a larger zone size, fewer zones are needed to represent the model, which results in less distinctiveness of the mechanical properties than if a smaller zone size is chosen and more zones are adopted for the model. This feature can also be seen in Fig. 5, where the stress strain curve of model divided by more zones (20000 zones) displays non-linearity more obviously than by less zones (1250 zones). It is also worth noticing that, the strength of the model does not present obvious pattern with different zone sizes (Fig. 5). In fact, the difference between the

obtained strength values is rather negligible, where the gap between the extreme strength values accounts for 2.6% under compression and 6.2 % under tension.

Uniaxial compressive and tensile loads are applied on the numerical model with 5000 zones (with each zone 1 mm ×1 mm in size) in a displacement controlled loading mode. In each calculation cycle, a displacement of $0.25e^{-9}$ m is applied to the grid points at the top and bottom of the model in tension tests. In compression tests, the displacement in each cycle is $0.5e^{-9}$ m, where the lateral displacement is confined only for gridpoints at the top and bottom of the model. Numerical results after 180000 cycles under tension and 400000 cycles under compression are obtained. The macroscopic fracturing process can be seen from the state of the model at distinct loading stages (Fig. 8), which correspond to the positions in the stress strain curves shown in Fig. 7. It is observed from Fig. 8 that under compression, failed zones (damage locations) gradually coalesce and form shear bands as external load ascends. Tensile fractures are also observed formed by the zones failed in tension along the loading direction at later stages of fracturing process (Fig. 8 e, f, d', e', f'). Under tension, macroscopic tensile fracture is formed perpendicular to the direction of the external tensile load (Fig. 8 g~l, g'~l'). Comparison has been made between models with distinct initial crack orientation distributions: the macroscopic fractures are formed by more scattered failed zones if the initial crack orientations are randomly distributed (higher level of heterogeneity) (Fig. 8 (a) a~f, Fig. 8 (b) g~l), while the failed zones are more concentrated and form smooth macroscopic fractures if the initial crack orientations are normally distributed (lower level of heterogeneity) (Fig. 8 (a) a'~f', Fig. 8 (b) g'~l'). To study the influence of material heterogeneity on the numerical results, we assign the model with distinct shape parameters (b=3, 5, 10, 15 and 20) for Young's modulus as well as Poisson's ratio. For each specific shape parameter, the model state where 200 zones failed under compression and 50 zones failed under tension are shown in Fig. 10. The locations of the failed zones are more concentrated as b value ascends (less heterogeneous). Take compressive loading case as an example: 200 zones failed at rather dispersed locations when the heterogeneity level is comparatively high (Fig. 10 (a) b=3, 5), while at lower heterogeneity levels, preliminary shapes of the macroscopic fractures have already been formed by the zones failed within a concentrated region (Fig. 10 (a) b=10, 15, and 20). In the loading processes, the stress strain curves develop linearly before any zone fails, and show non-linear feature when failure of the zones start to occur before the strength of the specimen has been met (Fig. 7, Fig. 9). This feature is more clearly seen in compressive loading cases where the shape parameter becomes smaller (higher level of material heterogeneity) as seen in Fig. 9 (a). Also worth noticing is that the strength and elastic modulus of the model descend as material heterogeneity gets greater, which is the case for both loading types (Fig. 9).

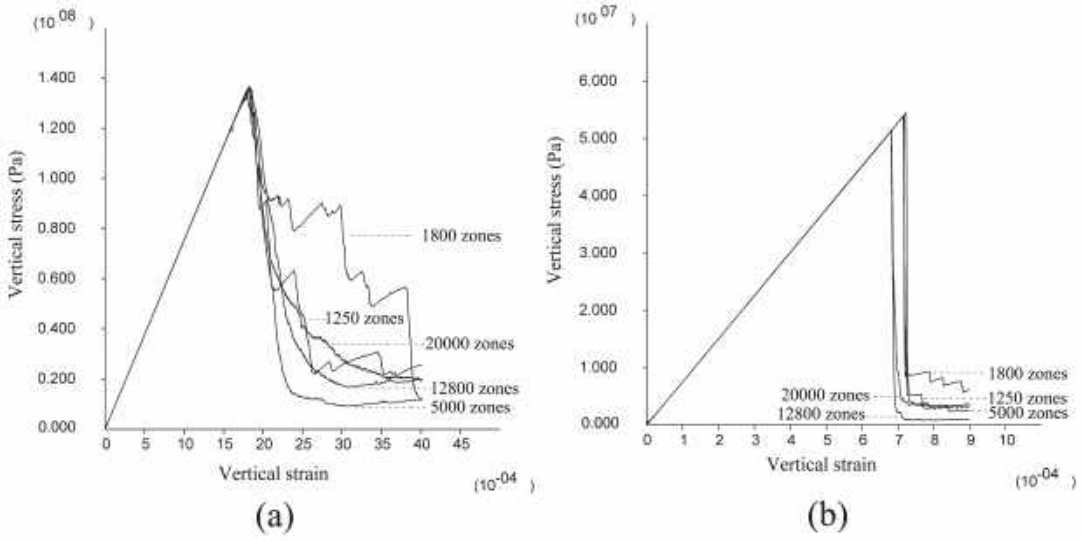

Figure 5 Stress strain curves for uniaxial test on models with different number of zones: (a) under compression, (b) under tension

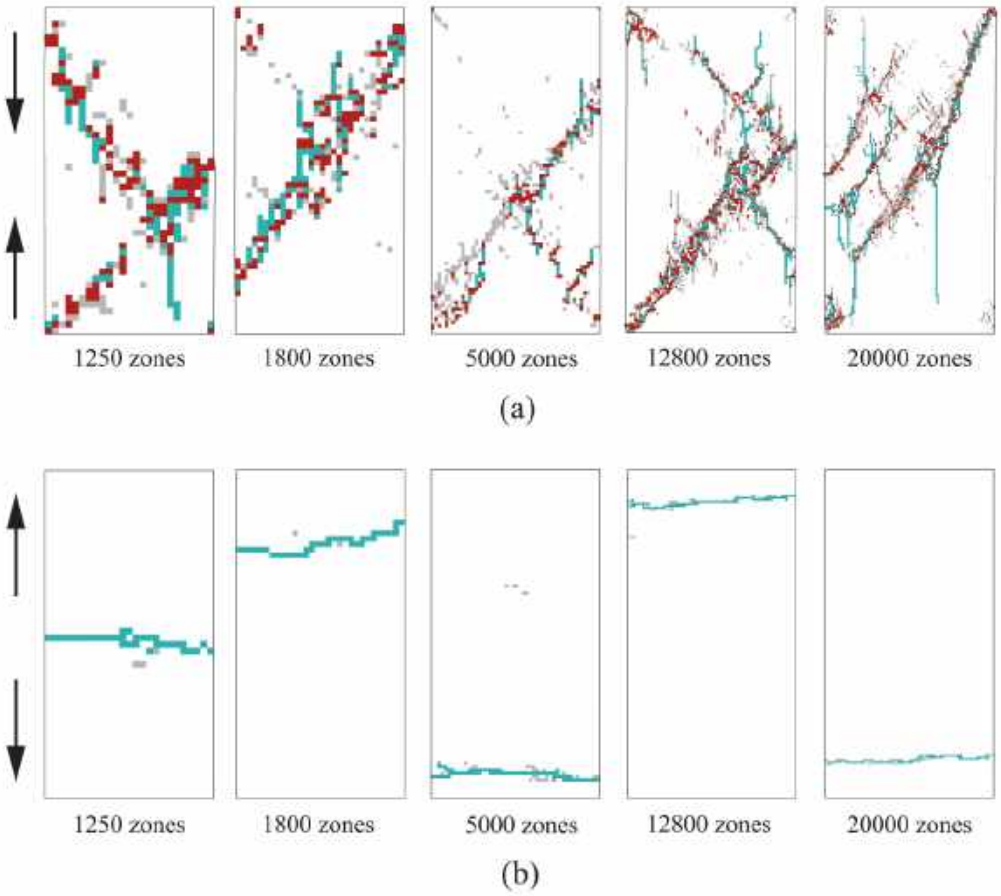

Figure 6 Fracture patterns of models with different number of zones: (a) under compression, (b) under tension

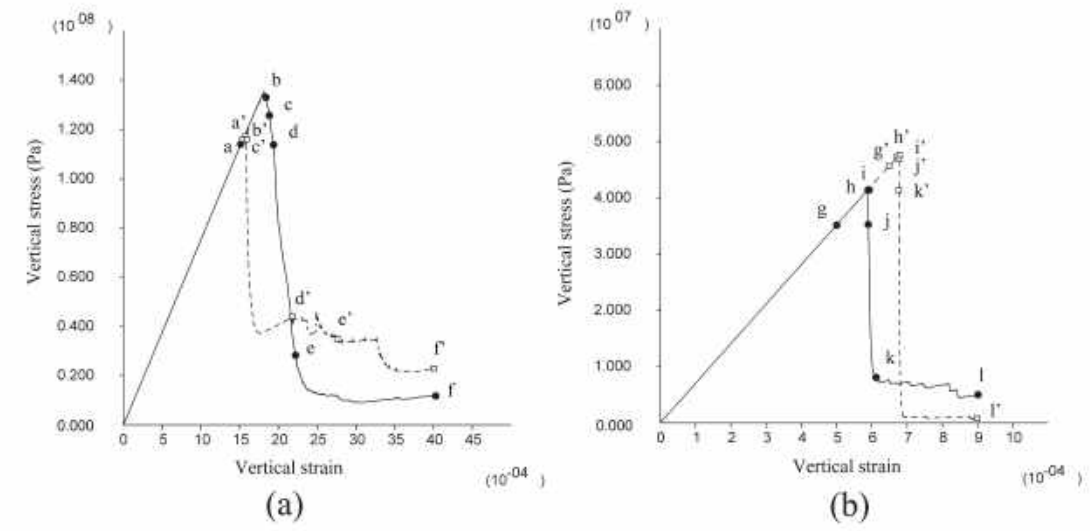

Figure 7 Stress strain curves for uniaxial test: (a) under compression with b=15, (b) under tension with b=5

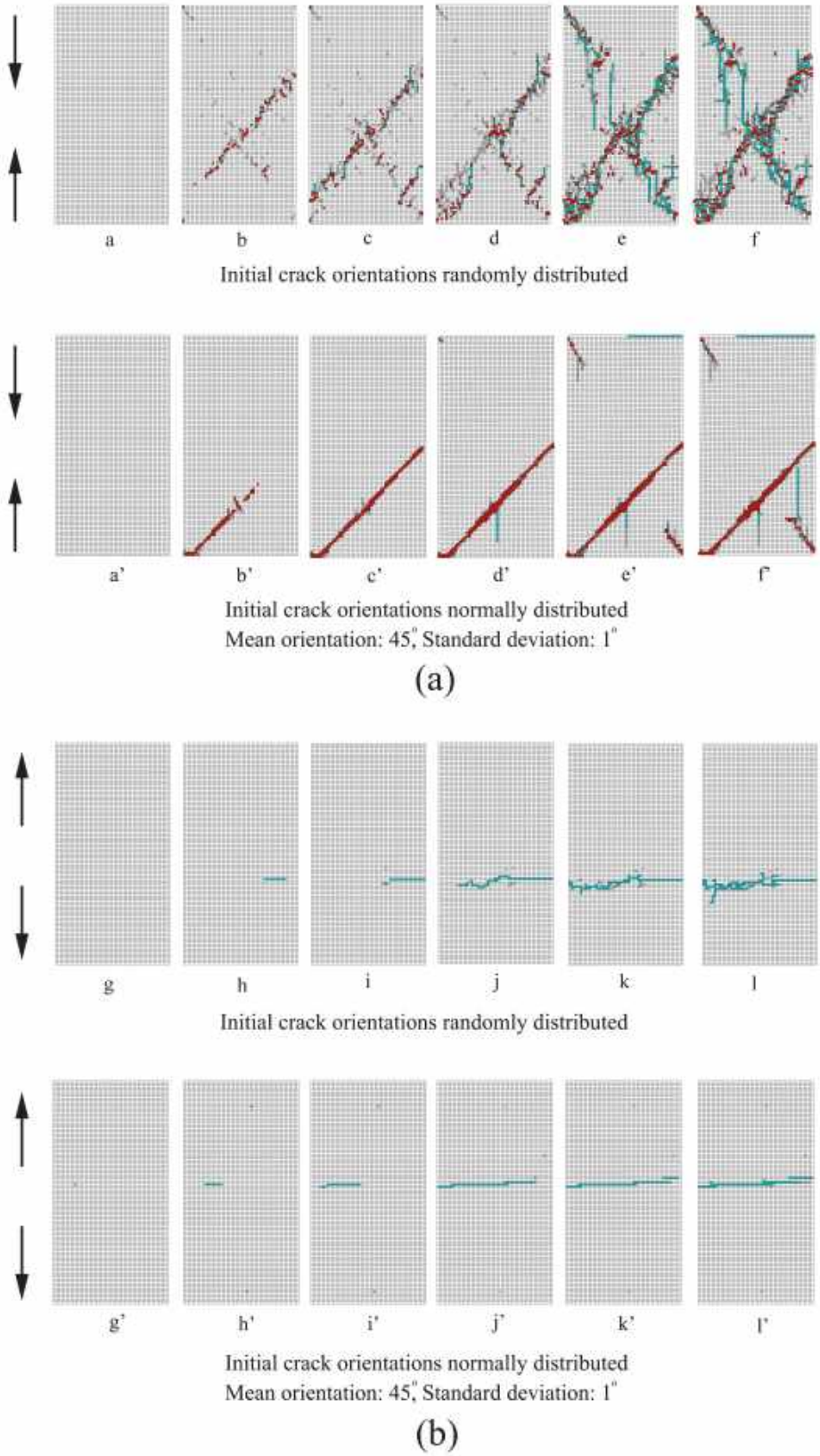

Figure 8 Fracture development under distinct loadings (a~f and g~l correspond to respective stress levels in Fig. 5; zone in red: failed in shear; zone in green: failed in tension; zone in grey: failed in past)

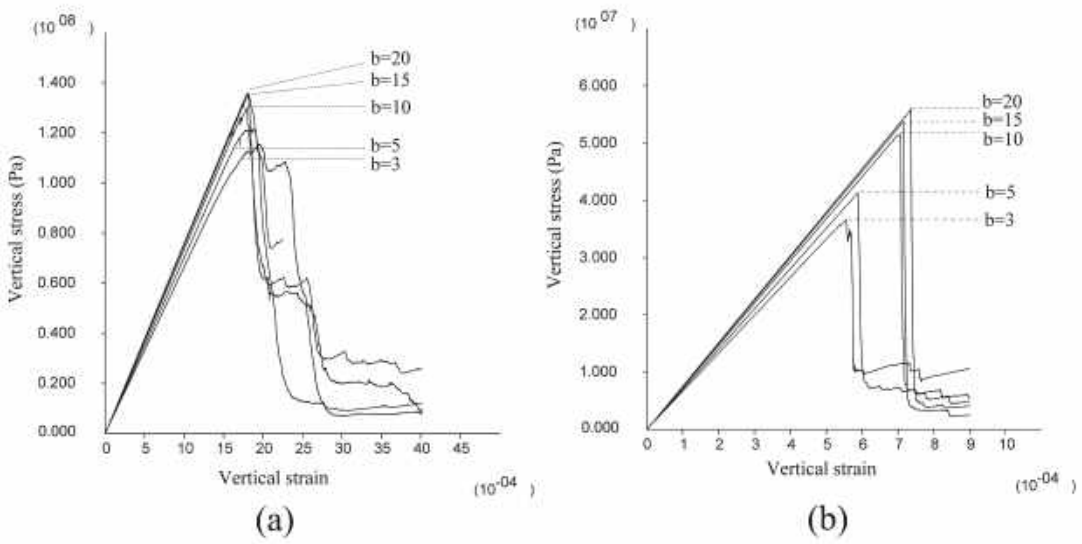

Figure 9 Stress strain curves for models with different shape parameter b

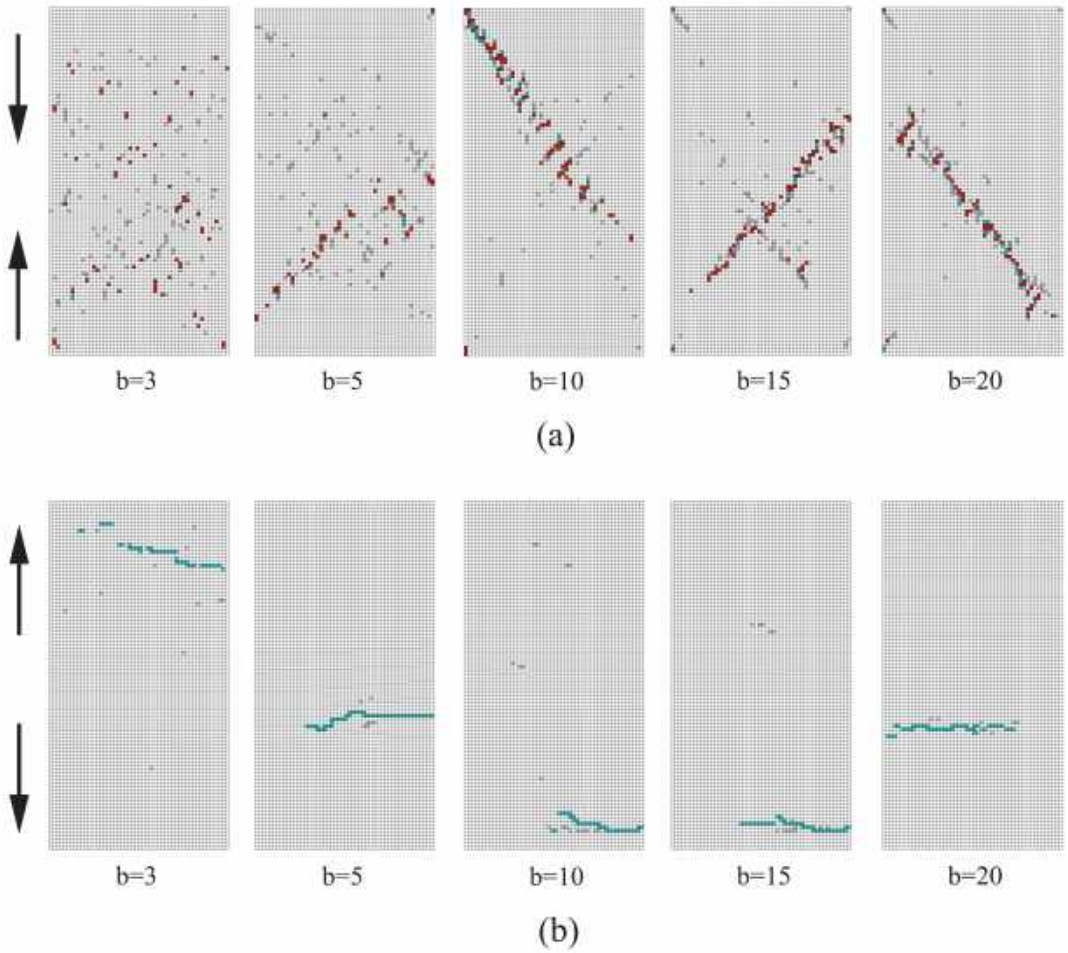

Figure 10 Fracture patterns of identical model with different heterogeneities: (a) under compression at 200 failed zones, (b) under tension at 50 failed zones

Comparisons have been made between mechanical responses of the model with different distributions of initial microcracks to study the effect of structural heterogeneity. In particular, tests are carried out on numerical models where microcrack orientations follow normal distribution with distinct mean values of 20^{o}, 30^{o}, 40^{o}, 45^{o}, 50^{o}, 60^{o} and 70^{o}, while other model parameters remain unchanged. Since each zone is considered to be a homogeneous body, the above mentioned cases also equal to mean microcrack orientations of 160^{o}, 150^{o}, 140^{o}, 135^{o}, 130^{o}, 120^{o} and 110^{o}, respectively. As is shown in Fig. 11, the strength of the model is the lowest around mean microcrack orientation of 50^{o} (130^{o}) under compression; while under tension, the strength becomes smaller when the mean microcrack orientation is approaching 0^{o} (180^{o}), i.e. perpendicular to the external load direction. Within the range tested in this study, the lowest strength is found at mean microcrack orientation of 20^{o} (160^{o}). The effect of microcrack lengths on the model's mechanical response is also investigated by assigning distinct mean values for the normally distributed initial microcrack lengths. Numerical test results of model with mean initial microcrack lengths of 0.2 mm, 0.4 mm, 0.5 mm, 0.6 mm, and 0.8 mm are included in Fig. 12. It is observed from the results that the strength of the model reduces with longer mean initial microcrack lengths, for both compressive and tensile loading cases (Fig. 12).

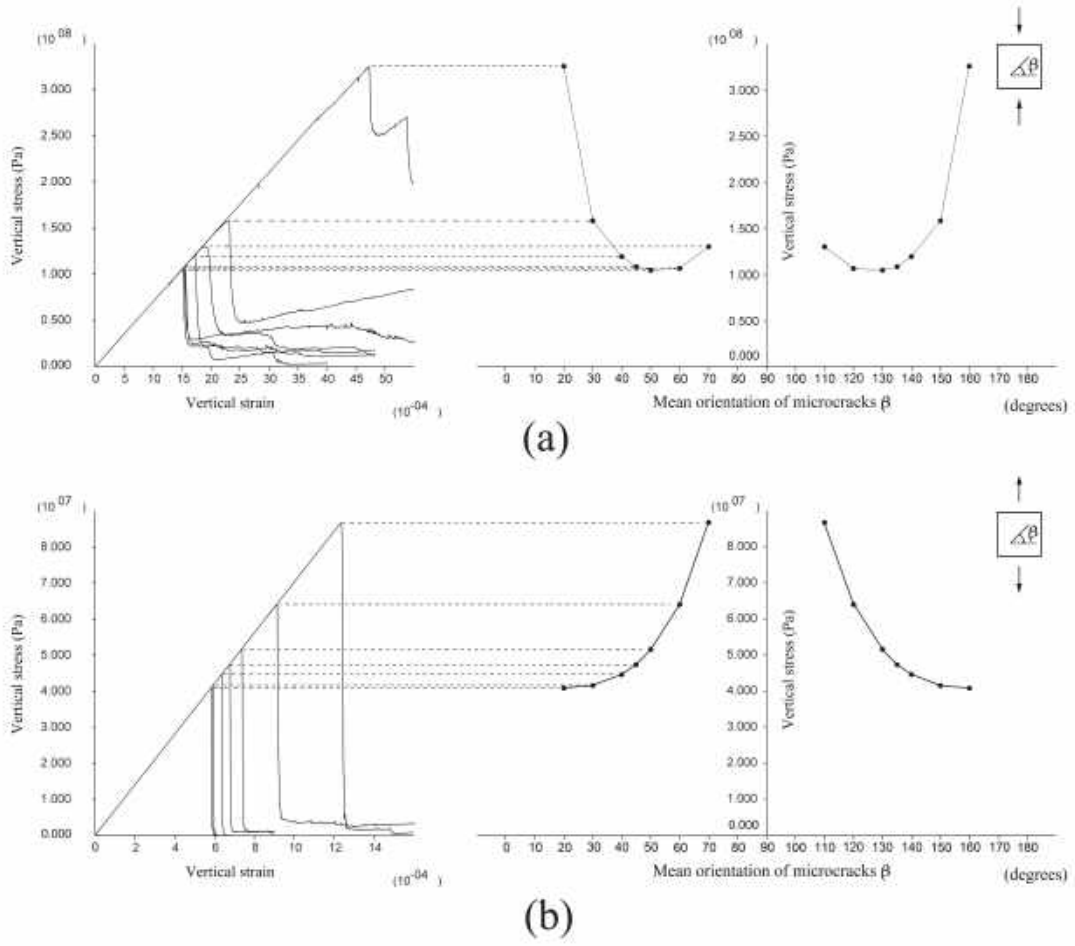

Figure 11 Stress strain curves for uniaxial test with different mean orientations of initial microcracks

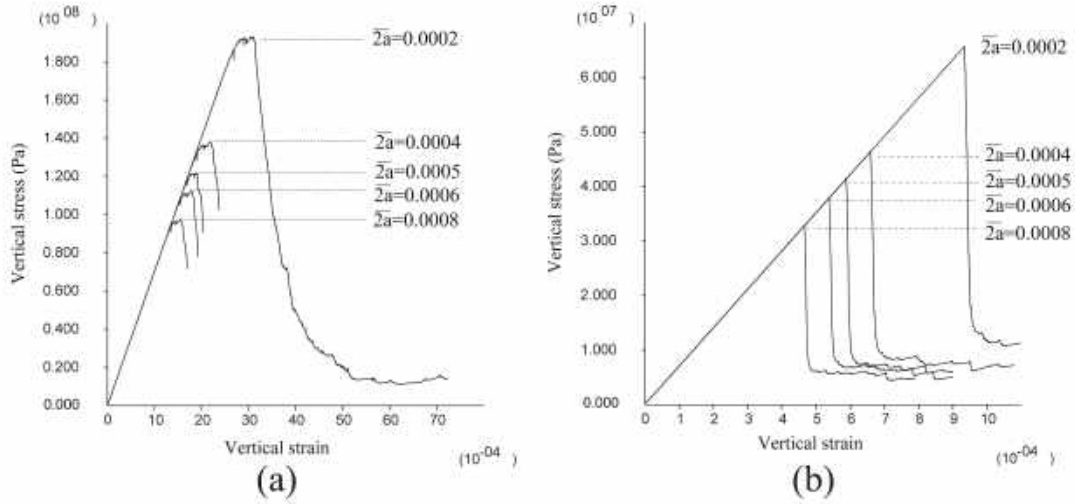

Figure 12 Stress strain curves for uniaxial test with different mean initial microcrack lengths

3.2 Uniaxial compression test and Brazilian test

Uniaxial compression test and Brazilian test are carried out on the model with data calibrated for Eibenstock II granite [40]. The parameters adopted in the simulation are listed in Table 1, where the bulk modulus (K) and shear modulus (G) of each zone are obtained from Young's modulus and Poisson's ratio ($\mathrm{K} = \mathrm{E}/3(1-2\mu),\ \mathrm{G} = \mathrm{E}/2(1+\mu)$). The calibrated numerical model for uniaxial compression test is established with 100 mm in length, 50 mm in diameter, and the size for each zone is 1 mm^2. The fracturing process of numerical model under uniaxial compression test is shown in Fig. 14, where distinct loading stages a, b, c and d correspond to the respective data points on the stress strain curve in Fig. 13. It is observed that due to the material and structural heterogeneity of the model, zone failure occurs at random locations at beginning of the loading stages (Fig. 14a). As external load increases, more zones start to fail, and coalescence of the failed zones is observed at several locations (Fig. 14b). Then the coalesced damage locations have formed visible inclined macroscopic fractures as shown in Fig. 14c. Finally, the shear band formed by the macroscopic fractures penetrates the model and failure of the model is observed (Fig. 14d). The model's heterogeneity is also clearly seen: the stress strain curve develops nonlinearly as damage locations increase before the total loss of load bearing capacity of the model (Point "a" to Point "c" in Fig. 13). The simulation result is compared with data obtained from lab test, where remarkable agreement is observed in both mechanical response (Fig. 13) and macroscopic fracture pattern (Fig. 14d, e).

Table 1 Calibrated material parameters

Young's modulus E (scale parameter)	22 GPa
Poisson's ratio μ (scale parameter)	0.26
Bulk modulus	Obtained by E and μ
Shear modulus	Obtained by E and μ
Shape parameter for E and μ	10
Coefficient of friction	0.3
Initial crack lengths (normal distribution)	0.0005 m (mean value)
Initial crack orientations (random distribution)	0^o ~360^o
Mode I fracture toughness	0.71 MPa·$m^{1/2}$
Mode II fracture toughness	1.846 MPa·$m^{1/2}$
Initial friction angle	30^o
Residual friction angle	30^o

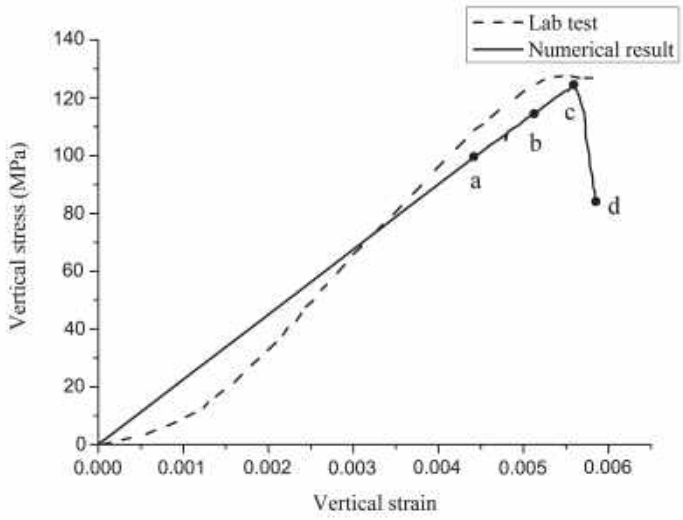

Figure 13 Stress strain curves for uniaxial compression test

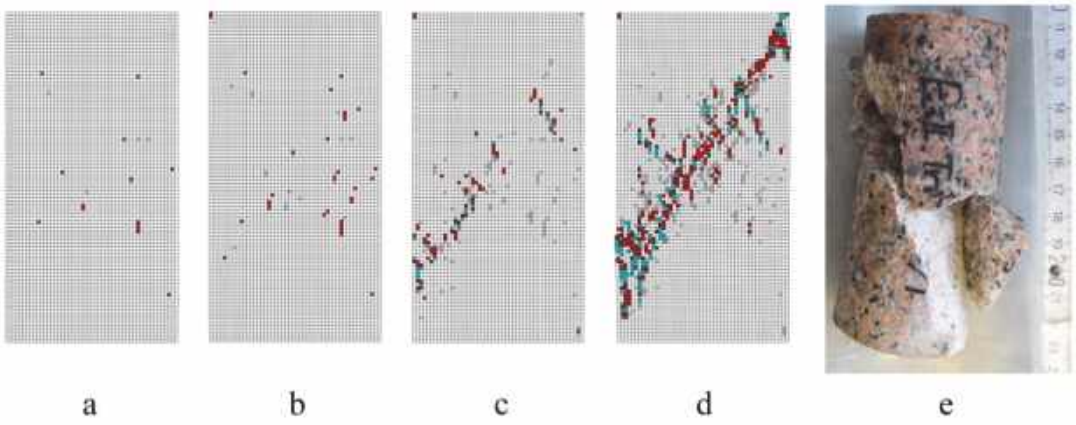

Figure 14 Fracturing process in uniaxial compression test (a~d: distinct loading stages in the simulation; e: fracture pattern of Eibenstock II granite in lab test)

The Brazilian test is carried out on a disc shaped numerical model with 50 mm in diameter, and 1 mm^2 in size for each zone. The material parameters of the model are identical with those in uniaxial compression test (Table 1). The vertical load and strain curve for the Brazilian test is shown in Fig. 15. The curve develops linearly up to Point “a” in Fig. 15, at which load level initial zone failures occur at upper and lower locations of the disc, as shown in Fig. 16a. The load increases as the loading plates keep pressing the disc (Point “b” in Fig. 15), where more zone failures have occurred in the same locations as Fig. 16b illustrated. At Point “c” in Fig. 15 (near the peak load), the microscopic fracture formed by the failed zones propagates towards the center of the disc, and a tensile fracture also appears near the center line of the disc (Fig. 16c). A sudden drop can be observed from the vertical load strain curve (Point “d” in Fig. 13)

after the macroscopic fractures connect and penetrate the disc (Fig. 16d), causing the failure of the model. The deviation of the microscopic fracture from the center line of the disc (Fig. 16d) is caused by the heterogeneity of the model, which reflects the fracture pattern observed in the lab test (Fig. 16e) accurately. It is known that the tensile stress along the loading line of the plane disc under diametrical compressive line load can be expressed as [39]

$$\sigma_x = \frac{2P}{\pi D}, \tag{12}$$

where P denotes the external line load; D denotes the diameter of the disc. A peak load of 590542 N is recorded in the simulation. Substituting the peak load into the above given equation, a tensile strength of 7.5 MPa is calculated, which is in agreement with the data obtained from lab test [40].

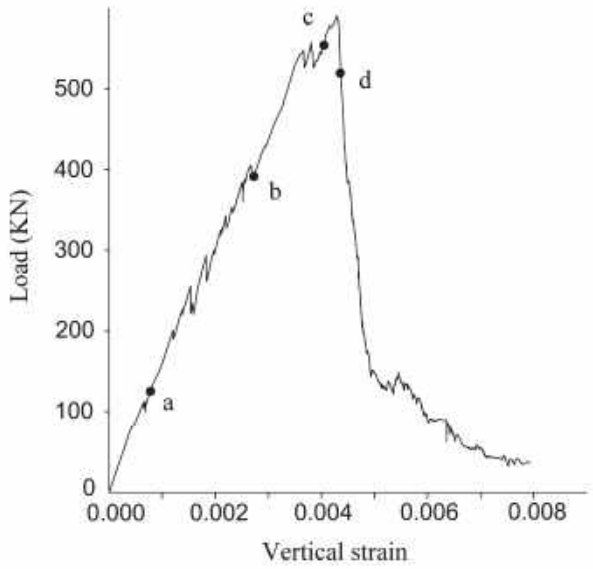

Figure 15 Load strain curve for numerical model in Brazilian test

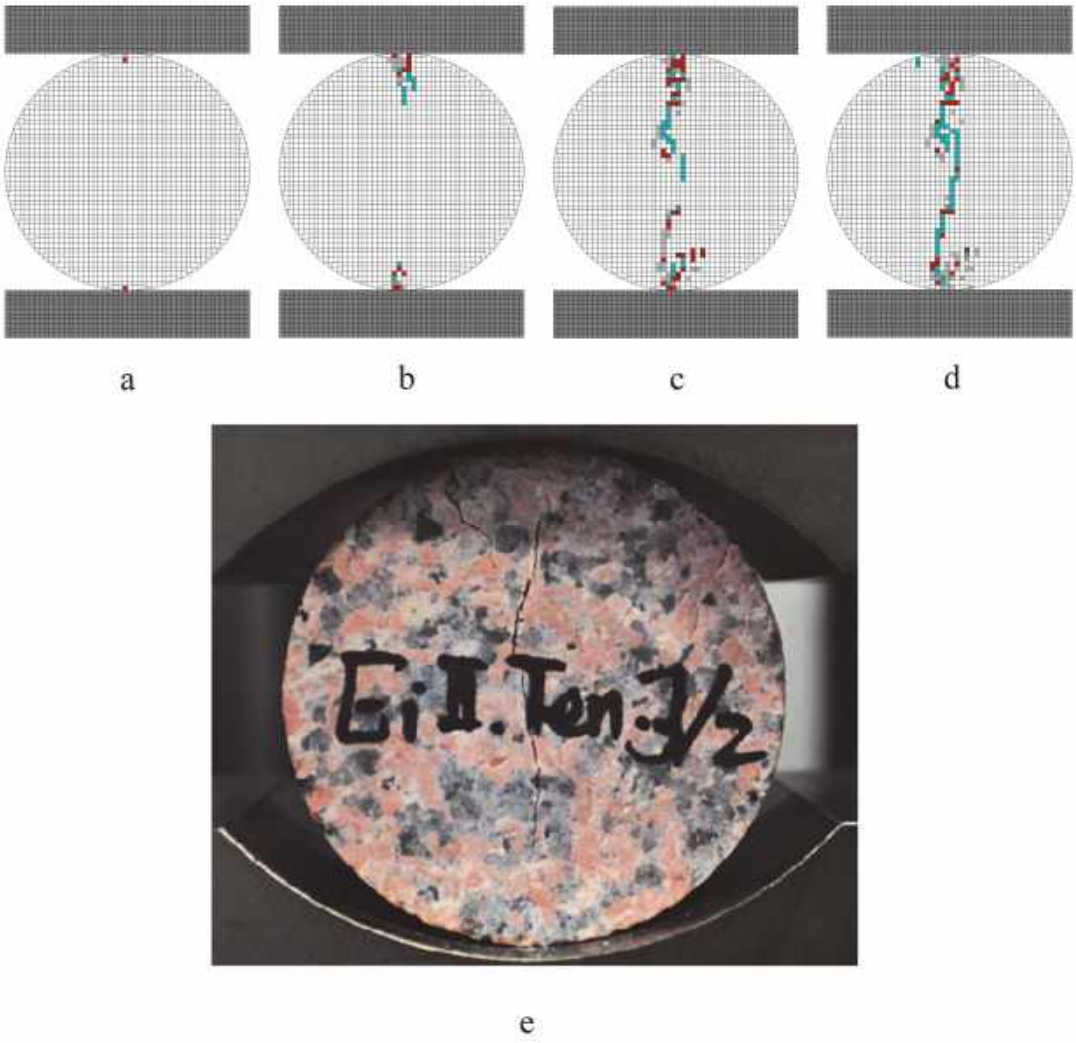

Figure 16 Fracturing process in Brazilian test (a~d: distinct loading stages in the simulation; e: fracture pattern of Eibenstock II granite in lab test)

3.3 Creep test

The time dependent model is established utilizing the identical material parameters and geometry as the time independent model introduced in Section 3.1. Under a constant compressive stress of 100 MPa, the model's creep curve and corresponding failed zone counts are obtained (Fig. 17). The three creep phases are observed from the creep curve: primary creep phase with a decreasing strain rate, secondary creep phase where the strain rate is steady, and tertiary creep phase with increasing strain rate. The number of failed zones shows a similar trend as the creep curve, where major zone failure events occur in the time range coinciding with the primary creep phase and tertiary creep phase, preceding the failure of the whole model. It is seen in Fig. 17 that the zone failure events are spatially diffused at the beginning of the primary creep phase due to the material and structural heterogeneity of the model. Coalescences of failed zones occur gradually with time and finally form shear bands which lead to the failure of the model. It is also worth noticing that most failed

zones are in shear failure at the beginning of the test (Point “A” in Fig. 17). Later on tensile cracks (zones failed in tension) emerge from the shear band tips and eventually form macroscopic tensile fracture along the direction of applied load, as illustrated by fracture pattern corresponding to Point “B” in Fig. 17.

To study the effect of external load level on lifetime of the model, more simulations are implemented with axial stress of 20 MPa, 40 MPa, 60 MPa, 80 MPa, 100 MPa and 110 MPa, respectively. From simulation results it can be concluded that the lifetime of the model is shorter under higher level of external load (Fig. 18). Especially, the axial strain curve shows no sudden increase for model under 20 MPa, which indicates that no major damage has occurred within the time span considered in the simulation. Therefore, a significantly long lifetime can be assumed under this loading condition. A more detailed investigation on factors influencing lifetime of the model is given in reference [41].

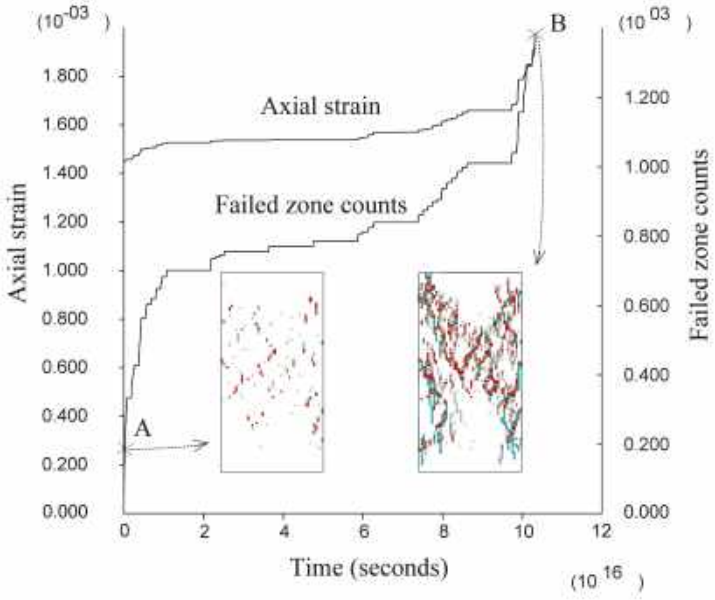

Figure 17 Creep curve and corresponding failed zone counts at constant uniaxial compressive stress of 100 MPa

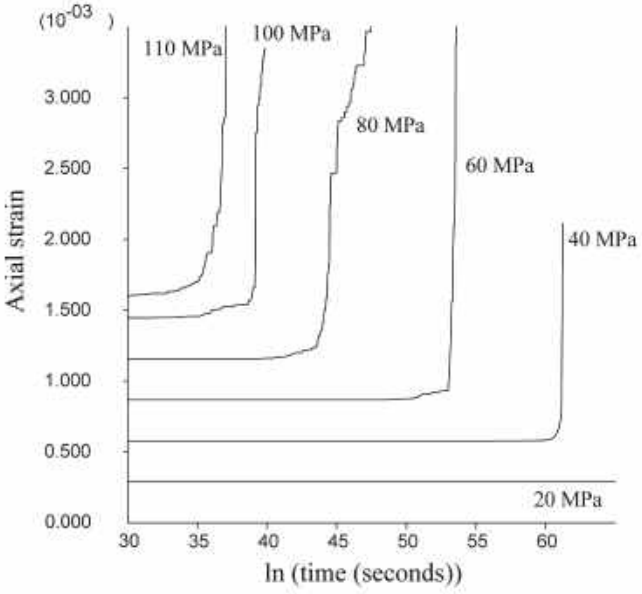

Figure 18 Creep curves of numerical model under different compressive stresses

4. Conclusions

Based on physical assumptions valid for rock-like material, a modeling scheme has been developed to simulate the fracturing process of brittle rocks. The numerical model includes material heterogeneity at element scale for the consideration of distinct mechanical responses of different microscopic compositions for rocks. Microcracks are included in the numerical model, based on the fact that microflaws are widespread in natural rock bodies, and should not be ignored when studying the fracturing process of rock materials. Heterogeneity results from microcracks and is represented in the numerical model by assigning the microcracks' initial length and orientation with values following certain random distributions. The kink scheme and wing crack propagation scheme are adopted to describe the mechanical condition on microcracks for time independent and time dependent behavior, respectively. Tests are carried out on numerical models with distinct loading types. Simulation results have been compared with those obtained from lab tests. The following conclusions can be drawn based on the scope of this study:

1. The established numerical model can reproduce the fracturing process of brittle rock material quiet well. Realistic initiation and coalescence of the microscopic damage are observed in the simulations.
2. Fracture patterns of numerical model under different loading conditions are in accordance with laboratory observations: shear bands are formed (partially mixed with axial splitting) when uniaxial compressive load is applied, while tensile macroscopic fractures are observed propagating perpendicular to the loading direction where uniaxial tensile load is applied.

3. The influence of heterogeneity on the mechanical behavior is studied, and observations include: the elastic modulus and strength of the model increase with decreasing material heterogeneity levels; the failed zones are located at more scattered locations when the heterogeneity levels are higher, which is the case for both material and structural heterogeneities. The influence of initial microcrack distributions are also analyzed: under compression, low strength value of the model is found at a mean microcrack orientation of 50º (130º), while under tension, the strength is lower when the mean microcrack orientation is approaching 0°(180º), i.e. perpendicular to the loading direction. Observations also show that the strength increases as mean initial crack length becomes shorter.
4. Typical lab test simulations are accomplished with calibrated numerical models. Accurate simulation results are obtained with respect to mechanical response as well as fracture patterns.
5. Three creep phases are observed using time-dependent numerical model under constant load, where zone failure events correspond to the strain curves at distinct creep phases. It is also observed that the lifetime of the model increases as external load increases, especially, a significantly long lifetime can be obtained at a certain low load level.

It is concluded that the proposed simulation scheme can render results of remarkable precision compared with observations in lab tests including fracture pattern. With reasonable calibration, the numerical model can be an indispensable means for the simulation of tests which are impossible, or difficult to practice in laboratory. However, simplifications are made in the simulation schemes, such as overlooking other possible wing crack growth modeling approaches [42], and the changing material properties at the interface of the zones on the controlling of stress field by stress intensity factor is not considered in detail. Improvements are in need for the current numerical model to be more practical. Possible future work is planned, such as developing constitute models for dynamic loadings; optimizing the model to facilitate simulations on large scale rock structures and extending the current model into 3 dimensions. More calibration work is also needed utilizing data obtained from lab tests.

Acknowledgements

This work was supported by the National Natural Science Foundation of China (NSFC, Grant No. 11402311 and No. 11472311).

References

[1] Atkinson BK. Fracture mechanics of rock. London: Academic Press INC. (London) LTD; 1987.

[2] Bobet A, Einstein HH. Fracture coalescence in rock-type materials under uniaxial and biaxial compression. Int J Rock Mech Min Sci 1998;35(7):863-888.

[3] Zhu WC, Tang CA. Micromechanical model for simulating the fracture process of rock. Rock Mech Rock Eng 2004;37(1):25-56.

[4] Yang SQ, Jing HW, Wang SY. Experimental investigation on the strength, deformability, failure behavior and acoustic emission locations of red sandstone under triaxial compression. Rock Mech Rock Eng 2012;45:583-606.

[5] Fortin J, Stanchits S, Vinciguerra S, Guéguen Y. Influence of thermal and mechanical cracks on permeability and elastic wave velocities in a basalt from Mt. Etna volcano subjected to elevated pressure. Tectonophysics 2011;503:60-74.

[6] Mayr SI, Stanchits S, Langenbruch C, Dresen G, Shapiro SA. Acoustic emission induced by pore-pressure changes in sandstone samples. Geophysics 2011;76(3):MA21-MA32.

[7] De Gennaro V, Perira J. A viscoplastic constitutive model for unsaturated geometerials. Comput Geotech 2013;54:143-151.

[8] Main IG. A damage mechanics model for power-law creep and earthquake aftershock and foreshock sequences. Geophys J Int 2000;142(1):151-161.

[9] Tang CA, Kaiser PK. Numerical simulation of cumulative damage and seismic energy release during brittle rock failure, part I: Fundamentals. Int J Rock Mech Min Sci 1998;35:113-121.

[10] Tang CA, Liu H, Lee PKK, Tsui Y, Tham LG. Numerical studies of the influence of microstructure of rock failure in uniaxial compression, part II: Effect of heterogeneity. Int J Rock Mech Min Sci 2000;37:555-569.

[11] Nemat-Nasser S, Hori M. Micromechanics: overall properties of heterogeneous materials. North-Holland. (Amsterdam); 1993

[12] Myer LR, Kemeny JM, Zheng Z, Suarez R, Ewy RT, Cook NGW. Extensile cracking in porous rock under differential compressive stress. Appl Mech Rev 1992;45:263-280.

[13] Golshani A, Okui Y, Oda M, Takemura T. A micromechanical model for brittle failure of rock and its relation to crack growth observed in triaxial compression tests of granite. Mech Mater 2006;38(4):287-303.

[14] Konietzky H, Heftenberger A, Feige M. Life-time prediction for rocks under static compressive and tensile loads: a new simulation approach. Acta Geotech. 2009;4:73–8.

[15] Lu YL, Elsworth D, Wang LG. A dual-scale approach to model time-dependent deformation, creep and fracturing of brittle rocks. Comput Geotech 2014;60:61-76.

[16] Chen W, Konietzky H. Simulation of heterogeneity, creep, damage and lifetime for loaded brittle rocks. Tectonophysics 2014;633:164-175.

[17] Anderson TL. Fracture mechanics. USA: CRC Press LLC; 1995. 2005.

[18] Atkinson BK. Fracture mechanics of rock. London: Academic Press INC. (London) LTD; 1987.

[19] Itasca Consulting Group. FLAC. 2nd ed. Minneapolis, Minnesota; 2005.

[20] Xu T, Xu Q, Tang CA, Ranjith PG. The evolution of rock failure with discontinuities due to shear creep. Acta Geotech 2013;8:567-581.

[21] Weibull W. A statistical distribution function of wide applicability. J Appl Mech 1951;18(3):293-297.

[22] Deng MY, Tao YZ, Xu J, Tang HM, Mu SG, Deng JF. The practical atlas of microscopic characteristics of magmatic and metamorphic rocks. China: Sinopec Press; 2014

[23] Erdogan F, Sih GC. On the crack extension in plates under plane loading and transverse shear. ASME J Basic Eng 1963;85:525-527.

[24] Baud P, Reuschlé T, Charlez P. An improved wing crack model for the deformation and failure of rock in compression. Int J Rock Mech Min Sci 1996;33(5):539–42.

[25] Wiederhorn SM, Johnson H, Diness AM, Heuer AH. Fracture of glass in vacuum. J Am Ceram Soc 1974;57:336–41.

[26] Atkinson BK. Subcritical crack propagation in rocks: theory, experimental results and applications. J Struct Geol 1982;4:41–56.

[27] Atkinson BK. Subcritical crack growth in geological materials. J Geophys Res 1984;89(B6):4077–114.

[28] Dill SJ, Bennison SJ, Dauskardt RH. Subcritical crack-growth behavior of borosilicate glass under cyclic loads: evidence of a mechanical fatigue effect. J Am Ceram Soc 1997;80(3):773–6.

[29] Ritter JE, Huseinovic A, Chakravarthy SS, Lardner TJ. Subcritical crack growth in soda–lime glass under mixed-mode loading. J Am Ceram Soc 2000;83(8):2109–11.

[30] Nara Y, Kaneko K. Sub-critical crack growth in anisotropic rock. Int J Rock Mech Min Sci 2006;43:437–53.

[31] Fuller Jr ER, Thomson RM. Lattice theories of fracture. In: Bradt RC, Hasselman DPH, Lange FF, editors. Fracture mechanics of ceramics. New York: Plenum Press; 1978. p. 507–48.

[32] Wiederhorn SM, Bloz LH. Stress corrosion and static fatigue of glass. J Am Ceram Soc 1970;53(10):543–8.

[33] Brown SD. Multibarrier kinetics of brittle fracture: I. Stress dependence of the subcritical crack velocity. J Am Ceram Soc 1979;62(9–10):515–24.

[34] Charles RJ. Static fatigue of glass I. J Appl Phys 1958;29(11):1549–53.

[35] Charles RJ. Static fatigue of glass II. J Appl Phys 1958;29(11):1554–60..

[36] Li X. Lifetime prediction for rocks – a numerical concept based on linear elastic fracture mechanics, subcritical crack growth, and elasto-plastic stress redistributions. Dissertation, TU Bergakademie Freiberg; 2013

[37] Nemat-Nasser S, Horii H. Compression-induced nonplanar crack extension with application to splitting, exfoliation, and rockburst. J Geophys Res

1982;87:6805–21.

[38] Horii H, Nemat-Nasser S. Compression-induced microcrack growth in brittle solids: axial splitting and shear failure. J Geophys Res 1985;90:3105–25.

[39] Timoshenko SP, Goodier JN. Theory of elasticity. 3rd ed. Singapore: McGraw - Hill; 1982.

[40] Tan X. Hydro-mechanical coupled behavior of brittle rocks – laboratory experiments and numerical simulations. Dissertation, TU Bergakademie Freiberg; 2013

[41] Li X, Konietzky H. Simulation of time-dependent crack growth in brittle rocks under constant loading conditions. Eng Fract Mech 2014;119:53-65.

[42] Zang A, Stephansson O. Stress Field of the Earth's Crust. Dordrecht: Springer Science and Business Media B.V. (Dordrecht); 2010.

Herausforderungen bei der Durchführung einer großräumigen Gebirgsvereisung am Beispiel des Gefrierschachtprojektes Ust-Jaiwa

Challenges in performing large-scale ground freezing at the Ust-Jaiwa freeze shaft project

Jürgen Franz, Deilmann-Haniel GmbH
Nikolai Hentrich Deilmann-Haniel GmbH
Deilmann-Haniel GmbH
Haustenbecke 1
44319 Dortmund

Abstract

The Ust-Jaiwa mine in the Perm Region of the Russian Federation is developed through the construction of two vertical shafts. The freezing method was employed in order to provide for both water cut-off and temporary support, and although this method has been established in mine development more than 100 years ago, breakdowns of the freeze system cannot be ruled out throughout its operation. Such breakdowns are mostly not related to design deficiencies but instead a result of insufficient ground investigation or technical failures of the freeze plant. This paper reports about challenges that were related to freeze plant breakdowns and shaft sinking through difficult ground conditions. The countermeasures that were developed throughout the period of construction are described and subsequently discussed. The consequent development of a thermal ground model proofed to be a sound basis for decision-making, so that problem solutions could be provided to the operation in a timely manner, and as such maintaining an uninterrupted and safe sinking operation.

Zusammenfassung

Die Erschließung des Bergwerks Ust-Jaiwa in der Region Perm der Russischen Föderation erfolgt über zwei vertikale Schächte, die im Gefrierverfahren abgeteuft wurden. Trotz der Etablierung dieses Bauverfahrens seit mehr als 100 Jahren kann es während der Bauausführung zu unvorhergesehenen Störfällen der Vereisungsmaßnahme kommen, die weniger in den Bereich der Dimensionierung der Vereisung fallen, sondern Folgen unzureichender Baugrunderkundung oder technischer Probleme der Gefrieranlage sind. Dieses Paper berichtet über Herausforderungen, denen als Folge von Komplett- bzw. Teilausfällen der Gefrieranlage und beim Durchteufen schwieriger Gebirgsverhältnisse zu begegnen war. Darüber hinaus werden die während des Bauablaufs entwickelten Gegenmaßnahmen beschrieben und deren Ergebnisse dargestellt und diskutiert. Die konsequente Weiterentwicklung eines thermischen Baugrundmodells erwies sich dabei als grundlegende Stütze der Entscheidungsfindung, so dass

der Baustelle schnell Lösungen zur Verfügung gestellt werden konnten, die einen sicheren Teufbetrieb ohne Unterbrechungen ermöglichten.

1 Einleitung

In der Region Perm der Russischen Föderation befindet sich eines der weltweit größten bekannten Rohkalivorkommen. Auf dem Gebiet des Lagerstättenteils Ust-Jaiwa entsteht das neue Bergwerk Nr. 5 des Unternehmens Uralkali. Es gehört zum Kalivorkommen von Beresniki und Solikamsk und damit zur Verkhnekamsk-Lagerstätte, die wirtschaftlich gewinnbare Vorräte für die nächsten 100 Jahre enthält. Die Deilmann-Haniel GmbH wurde Ende 2011 mit der Planung und dem Bau der Schächte für das Bergwerk Ust-Jaiwa beauftragt, wozu hauptsächlich das Abteufen von zwei Schächten mit einer Teufe von 465 m bzw. 422 m mit einem endgültigen Schachtdurchmesser von 8,0 m zählt.

Das Abteufen erfolgt für beide Schächte im Bereich des wasserführenden Gebirges bis zu einer Teufe von 245 m im Gefrierverfahren. Für das sukzessive Aufgefrieren der Schächte wurde eine Gefrieranlage mit einer maximalen Gefrierleistung von 3,0 MW installiert.

Während des Betriebs der Vereisung musste Herausforderungen begegnet werden, die sowohl aus dem Betrieb der Gefrieranlage als auch aus unzureichender Baugrunderkundung resultierten. Dabei ist zu bemerken, dass sich auch die operativen Schwierigkeiten während der Teufphase (Teil- oder Komplettausfälle der Gefrieranlage, Ausfall des Systems zur Überwachung der Gebirgstemperaturen, einzelne Gefrierrohrausfälle) direkt in geomechanische Probleme umsetzen, da die Vereisung der Gebirgsstabilisierung dient und die Aufrechterhaltung eines ausreichenden Frostkörpers von fundamentaler Bedeutung für den Erfolg der Baumaßnahme ist.

Die Entwicklung eines thermischen Baugrundmodells, welches über die komplette Bauzeit den betrieblichen Randbedingungen angepasst wurde, erwies sich dabei insbesondere beim Auftreten von Störfällen der Gefrieranlage als große Hilfe im Rahmen der Entscheidungsfindung für betriebliche Maßnahmen zur Fortsetzung eines sicheren Teufbetriebs. Bei Auftreten von unvorhergesehenen Gebirgsverhältnissen, begründet durch unzureichende Baugrunderkundung, wurde das thermische Modell mit mechanischen Modellen gekoppelt, um den Schachtvortrieb unter den tatsächlichen Randbedingungen während der Bauausführung zu simulieren und gegebenenfalls den Teufbetrieb den Erfordernissen anzupassen.

Im Folgenden werden zunächst die geologischen und hydrogeologischen Randbedingungen des Projekts beschrieben, und danach die Anwendung thermischer und mechanischer Baugrundmodelle zur Lösung der oben dargestellten Probleme beschrieben. Abschließend werden Schlussfolgerungen gezogen und ein Ausblick für weitergehende Arbeiten gegeben.

2 Geologie und Hydrogeologie

Die Geologie und Hydrogeologie der Region ist infolge der dort seit mehr als 100 Jahren stattfindenden Bergbauaktivitäten gut bekannt. Übergeordnet ergaben die Schachtvorbohrungen folgende Ergebnisse für die Planung des Schachtes und der Gefriermaßnahme:

- den quartären Ablagerungen folgende Bunte Schichten, die sich im Wesentlichen aus Sandsteinformationen zusammensetzen und bis in eine Teufe von ca. 70 m reichen,
- Terrigene-Karbonat-Schichten, die durch eine teilweise stark wasserführende Wechsellagerung aus Kalk-, Mergel- und Anhydritformationen charakterisiert sind und bis in eine Teufe von ca. 170 m reichen,
- Wechsellagerungen aus Dolomit-, Kalk- und Kalk-Mergel-Formationen bis zu einer Teufe von ca. 240 m, die von einer hohen Salinität der Gebirgswässer geprägt sind und daher im Folgenden als Salz-Mergel-Schichten bezeichnet werden,
- Wechsellagerungen aus Mergel- und Steinsalzformationen bis zu einer Teufe von 245 m,
- in größeren Teufen der Übergang zur Kali-Lagerstätte.

Zum Durchteufen der wasserführenden Gebirgsformationen, die im Bereich der Salz-Mergel-Schichten teilweise entfestigt auftreten, wurde das Gefrierverfahren ausgewählt.

3 Gefriersystem und Temperaturmesstechnik

Der Durchmesser des Gefrierkreises betrug an beiden Schächten 17 m. Auf jedem Kreis wurden 45 Gefrierlöcher mit einer Teufe von 245 m geplant, die somit einen theoretischen Abstand von 1,19 m zueinander aufwiesen. Die Bohrungen wurden unter Anwendung des Richtbohrsystems „Measurement While Drilling“ (MWD) abgeteuft. Zudem wurden an jedem Schacht vier Temperaturmesslöcher gebohrt und ausgebaut. Die Geometrie des Gefrierkreises und die Abweichungen der Gefrierlochbohrungen sind für einen Schnitt in 240 m Teufe am Schacht 2 in Fig. 3-1 dargestellt.

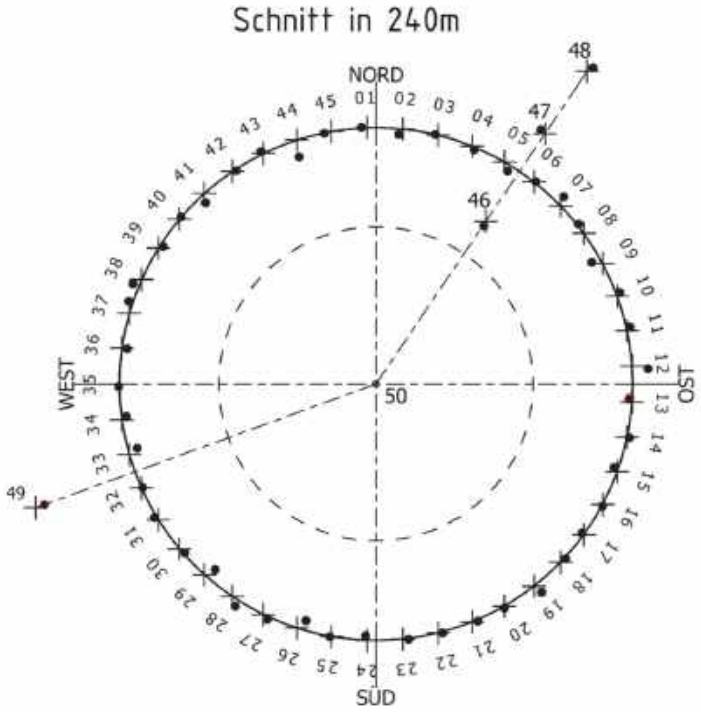

Fig. 3-1: Geometrie des Gefrierkreises und Ergebnisse der Gefrierlochbohrungen

Die eingesetzte Gefrieranlage umfasste insgesamt sechs Gefrieraggregate mit einer Kälteleistung von maximal 500 kW je Aggregat. Als Kälteträger wurde eine Kalzium-Chlorid-Lauge bei einer Vorlauftemperatur von -35°C eingesetzt.

Die Gebirgstemperaturen wurden in den Temperaturmessrohren durch LWL-basierte faseroptische Messkabel bestimmt. Die Datenausgabe erfolgte entlang des Kabels mit einem Datenpunktabstand von 0,5 m mit einer Messtoleranzgrenze von ±0,3 K. Die Speicherung der Messdaten erfolgte automatisch in vorgegebenen Zeitabständen auf einem vor Ort installierten Rechner.

4 Thermisches Baugrundmodell

Zur numerischen Simulation der Frostausbreitungsvorgänge am Projekt Ust-Jaiwa wurde ein thermisches Baugrundmodell entwickelt [1], welches im Verlauf des Projekts kalibriert und verifiziert wurde [2]. Zu diesem Zweck wurde das Programmpaket Geo-Studio 2012 (Programmteil TEMP/W) von Geo-Slope verwendet. Temp/W ist ein zweidimensionales Finite-Elemente-Programm zur Lösung von thermischen Fragestellungen in der Geotechnik [3].

Im Rahmen der Kalibrierung wurden für beide Schächte eine Vielzahl von Berechnungshorizonten ausgewertet und entsprechende numerische Modelle generiert. Auf die Nutzung rotationssymmetrischer Modelle wurde dabei verzichtet, da sämtliche Lageabweichungen der Gefrierrohre aus der Vertikalen explizit abgebildet wurden. Ein Beispiel für die Modellvernetzung zeigt Fig. 4-1.

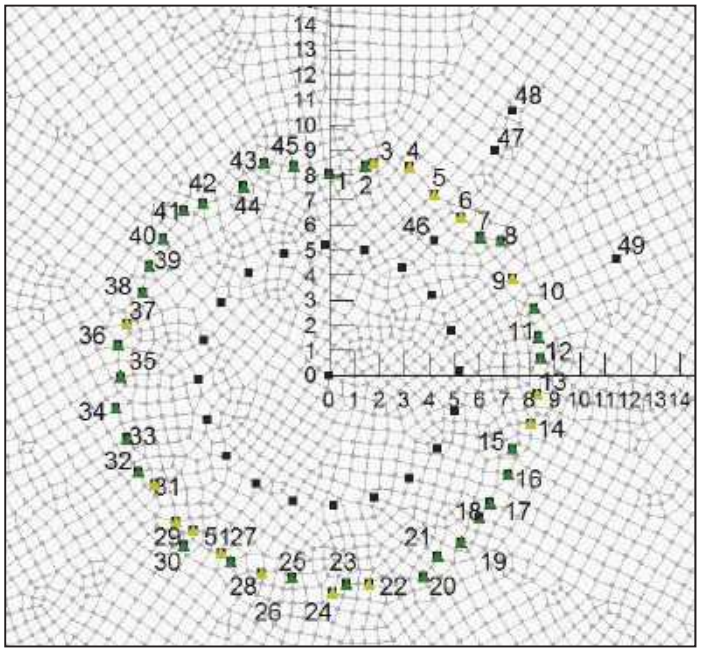

Fig. 4-1: Beispiel für die Modellvernetzung

5 Ausfall der Temperaturüberwachung und Störungen beim Betrieb der Gefrieranlage

Die Gefrieranlage wurde im August 2013 für das Aufgefrieren von Schacht 1 in Betrieb genommen. Der Beginn des Aufgefrierens von Schacht 2 erfolgte etwa zwei Monate später. In Fig. 5-1 sind die gemessenen Temperaturen des Messkabels 46 in einer Teufe von 60 m (blaue Linie) und die durch numerische Berechnungen prognostizierten Temperaturen (grüne Linie) dargestellt. Es ist erkennbar, dass die während des Gefrierprozesses aufgetretenen betrieblichen bzw. bautechnischen Änderungen der Randbedingungen im Modell gut nachgebildet werden konnten.

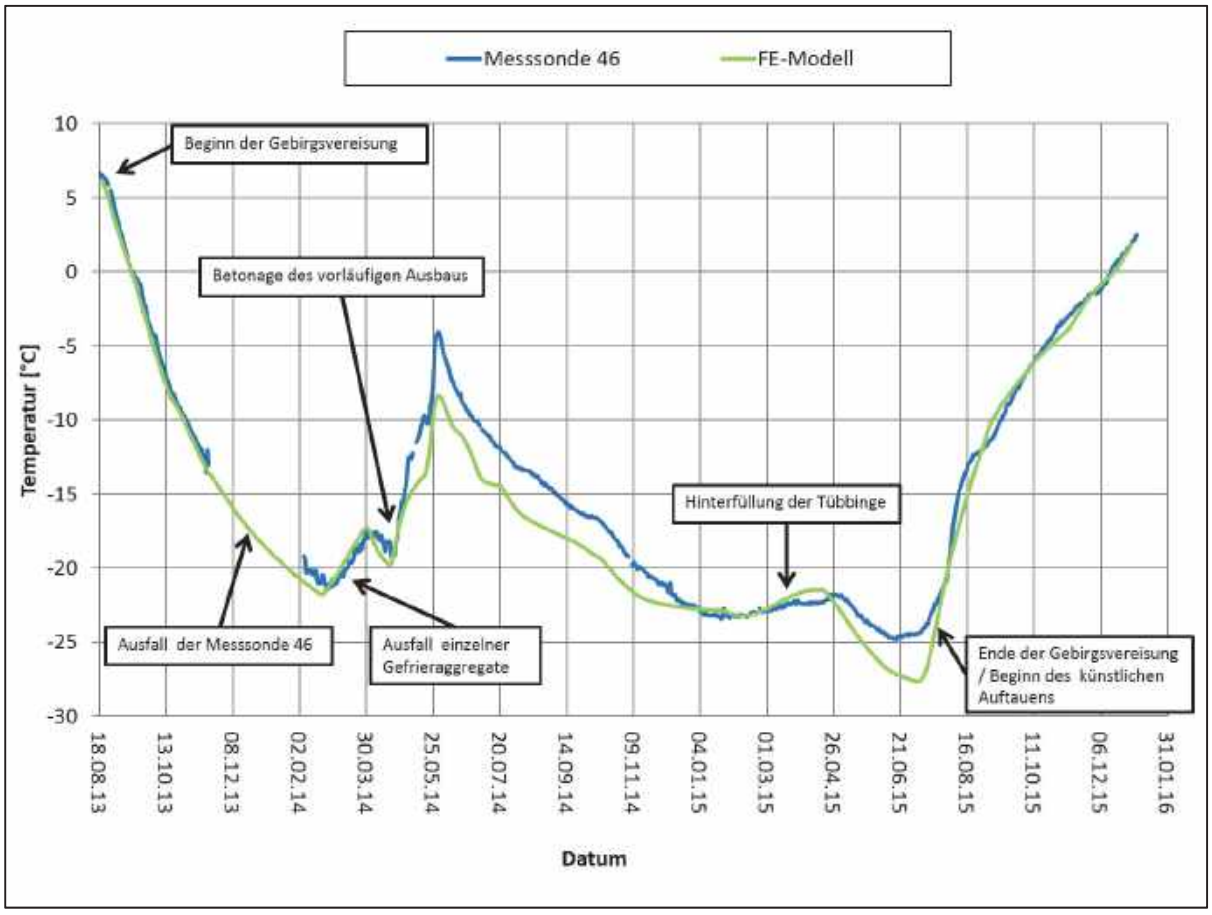

Fig. 5-1: Gemessene und prognostizierte Gebirgstemperaturen in einer Teufe von 60 m (Kabel/Messpunkt Nr. 46)

Die mit Beginn des Betriebs der Vereisung startenden Rückrechnungen thermischer Baugrundparameter anhand der kontinuierlich gesammelten Messwerte und die Kalibrierung thermischer Baugrundmodelle erwiesen sich bereits während der Aufgefrierphase am Schacht 1 als sehr wertvolles Steuerungsinstrument. Wie Fig. 5-1 entnommen werden kann, fiel das relativ zum Gefrierkreis innen liegende Messkabel Nr. 46 (vergleiche Fig. 3-1) bereits wenige Wochen nach Inbetriebnahme für etwa drei Monate aus, so dass das Wachstum des Frostkörpers in Richtung Schachtstoß nicht gemessen werden konnte. Da alle anderen Messkabel zu diesem Zeitpunkt jedoch in Betrieb waren, ist eine kontinuierliche Verifizierung der genutzten thermischen Modelle möglich gewesen, so dass durch Prognoserechnungen die Frostausbreitung alleine

durch Berücksichtigung der betrieblich eingestellten Vorlauftemperatur des Kälteträgers im Modell beobachtet werden konnte. Nach Inbetriebnahme des reparierten Messkabels zeigte sich zwischen der gemessenen und berechneten Gebirgstemperatur ein Unterschied von weniger als 2 K.

Ebenfalls konnte die Frostkörperentwicklung bei einem temporären Ausfall von zwei Gefrieraggregaten zwischen Mitte Februar und Ende März 2014 (siehe ansteigende Gebirgstemperaturen während dieser Zeitspanne in Fig. 5-1), und einer damit reduzierten Gefrierleistung bzw. einer Reduktion der Vorlauftemperatur, durch Prognoseberechnungen anhand des bestehenden thermischen Modells sehr zuverlässig analysiert werden, so dass der Teufbetrieb ungehindert fortgesetzt werden konnte.

6 Ausfall einzelner Gefrierrohre

Im betrieblichen Ablauf der Gefriermaßnahme kam es aus sehr verschiedenen Gründen zu Ausfällen einzelner Gefrierrohre, z.B. im Rahmen von Instandsetzungsmaßnahmen des Messsystems, der Gefrierköpfe oder durch Arbeiten im Gefrierkeller. Der Zeitraum der Ausfälle wurde in den thermischen Modellen durch entsprechende Änderungen der thermischen Randbedingungen berücksichtigt.

In Fig. 6-1 ist die Temperaturverteilung im Berechnungsmodell zu zwei unterschiedlichen Simulationszeitpunkten dargestellt. Der mit einem Radius von 5,20 m durch schwarze Quadrate markierte Kreis stellt den späteren Ausbruchsquerschnitt des Schachtes dar, und die Isolinien des Gefrierpunkts sind als unterbrochene blaue Linien abgebildet.

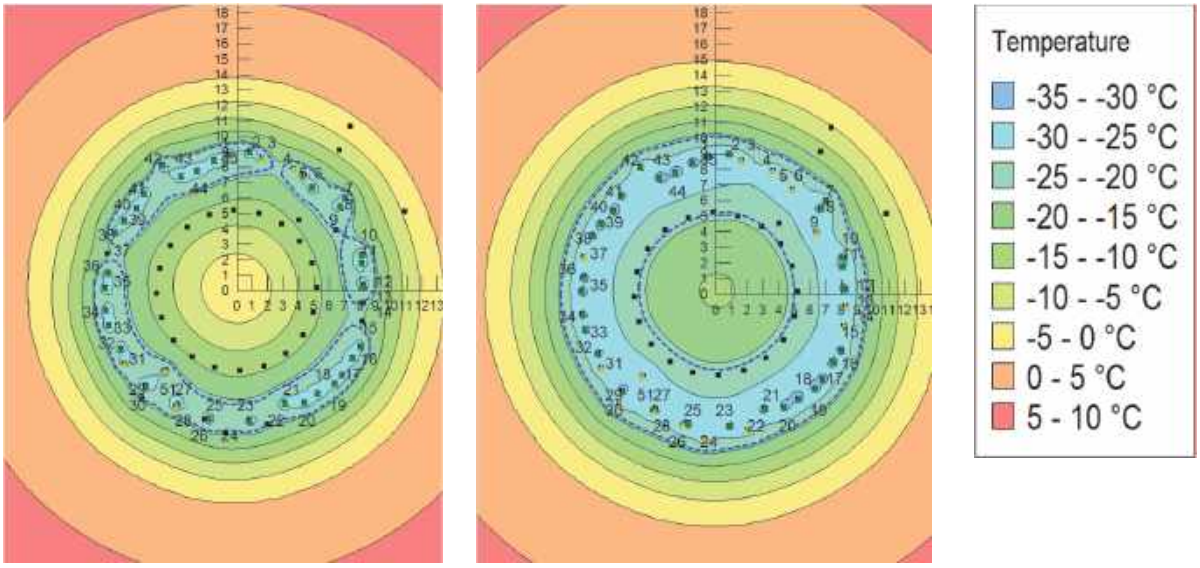

Fig. 6-1: Temperaturverteilung zu verschiedenen Simulationszeitpunkten

Der Plot auf der linken Seite in Fig. 6-1 zeigt, dass der Frostkörper Lücken aufweist und somit die Berücksichtigung von Lageabweichungen der Gefrierrohre aus der Vertikalen und die Berücksichtigung unterschiedlicher thermischer Randbedingungen in den einzelnen Gefrierrohren von großer Bedeutung ist, um Fehlinterpretationen der

Messdaten zu vermeiden. Insbesondere liegen die Fehlstellen des Frostkörpers in diesem Fall nicht an den Stellen, an denen die Temperaturüberwachungskabel liegen. Unter Annahme einer gleichförmigen Temperaturverteilung radial zum Gefrierkreis würden derartige Schwachstellen somit übersehen werden. Der Plot auf der rechten Seite in Fig. 6-1 zeigt im Vergleich den Frostkörper zum Zeitpunkt des Abschlusses des Aufgefrierens direkt vor dem Durchteufen.

7 Behandlung gebirgsmechanischer Herausforderungen auf der Basis des thermischen Baugrundmodells

Eine besondere Herausforderung stellte das Durchteufen der sogenannten entfestigten Salz-Mergel-Schichten dar, die nicht homogen in der Geologie auftreten und deren projektspezifische Existenz und Teufenlage somit nur durch eine Schachtmittelbohrung erkundet werden kann. Auch bei den für das Projekt Ust-Jaiwa niedergebrachten Schachtmittelbohrungen wurden in der Teufe zwischen 180 m und 230 m mehrere entfestigte Horizonte festgestellt, in denen erhöhte Anforderungen an den Frostkörper und den temporären Schachtausbau zu stellen waren. Aufgrund der erhöhten Salinität der Gebirgswässer liegt der Gefrierpunkt in den Salz-Mergel-Schichten bei etwa -22°C. Die Gebirgsfestigkeiten sind in hohem Maße temperaturabhängig, wie Tab. 7-1 zu entnehmen ist.

Tab. 7-1. Gebirgsparameter der Salz-Mergel-Schichten

Probenmaterial	E [MPa]	υ [-]	K [MPa]	G [MPa]	φ [°]	$c_{,c}$ [MPa]
Entfestigter Salz-Mergel	200	0.21	115	83	20.5	0.17
Entfestigter Salz-Mergel, T = -25°C	485	0.40	808	173	20.5	2.00
Salz-Mergel	1,350	0.21	776	558	33.0	2.00
Salz-Mergel, gefroren	1,350	0.40	1,125	519	33.0	4.15

Eine der baubetrieblich wichtigsten Fragen war die Beurteilung, in welchem Abstand der temporäre Betonausbau dem Schachtvortrieb nachfolgen musste, um gemeinsam mit dem Frostkörper die Schachtstabilität sicherzustellen [4]. Wie Fig. 5-1 aufzeigt, stellt der Einbau des vorläufigen Betonausbaus und die damit freiwerdende Hydratationswärme eine erhebliche thermische Belastung des Frostkörpers dar, so dass entsprechende Prognoserechnungen zum Zeitpunkt des Durchteufens der entfestigten Salz-Mergel-Schichten andeuteten, dass mit Frostkörpermächtigkeiten von weniger als 1,70 m zu rechnen war.

Die nachfolgenden geomechanischen Berechnungen unter Berücksichtigung der temperaturabhängigen Gebirgsfestigkeiten wurden mit dem Programm FLAC3D [5] durchgeführt. Wie Fig. 7-1 entnommen werden kann, vergrößert sich der Bereich der Plastifizierung im Berechnungsmodell mit größer werdender unausgebauter Stoßhöhe des Schachtes. Bei einer unausgebauten Stoßhöhe von ca. 3,0 m und weniger reduziert sich die Plastifizierung im Bereich des Frostkörpers erheblich, und auch die rechnerischen Verschiebungen im Bereich der Gefrierrohre sinken auf ein verträgliches Maß.

Auch bei dieser Problemstellung ist festzustellen, dass eine fachlich fundierte Prognose des Gebirgsverhaltens ohne die kontinuierliche Weiterentwicklung des thermischen Baugrundmodells äußerst schwierig gewesen wäre.

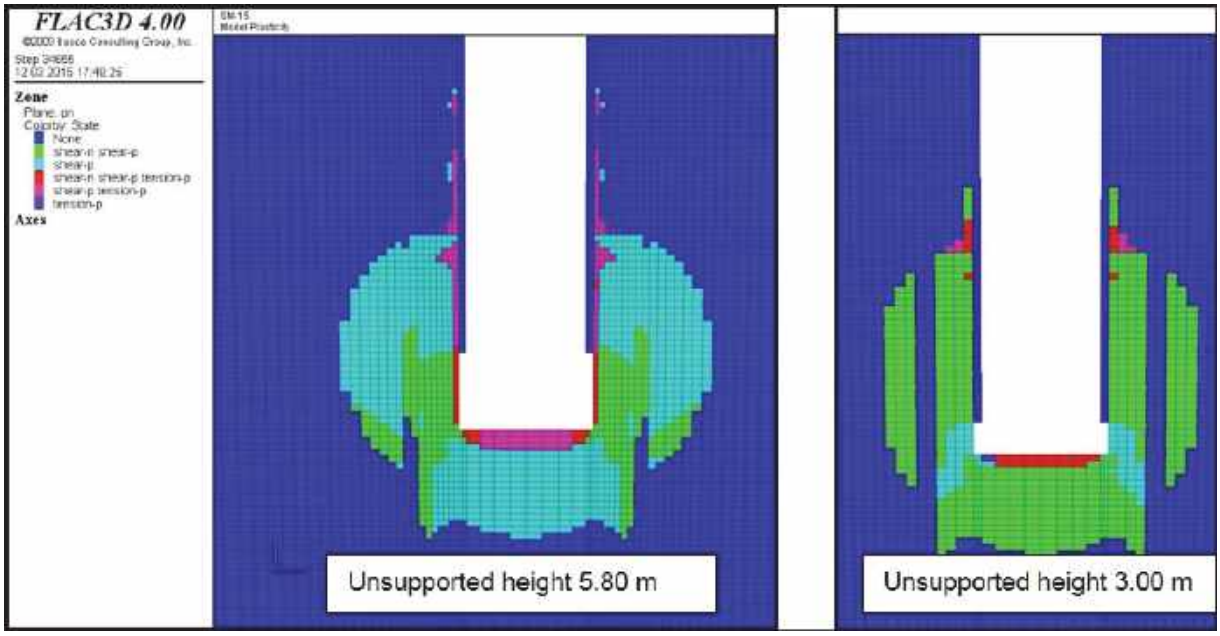

Fig. 7-1: Plastifizierte Zonen für unterschiedliche freie (unausgebaute) Stoßhöhen [4]

8 Zusammenfassung

Zur Erschließung der Lagerstätte Ust-Jaiwa wurden zwei vertikale Schächte im Gefrierverfahren abgeteuft. Nach einem etwa zweieinhalbjährigen Betrieb der Gefrieranlage und nach sicherem Durchteufen und Ausbauen der Gefrierschachtbereiche wurde die Vereisung im Juli 2015 am Schacht 1 und im Januar 2016 am Schacht 2 abgeschaltet. Obwohl das Gefrierverfahren seit mehr als 100 Jahren eine bewährte Methode zum Abteufen von Schächten in wasserführendem Gebirge ist, haben die Techniken zur Überwachung und Prognose von Frostausbreitungsvorgängen erst in jüngerer Vergangenheit wesentliche Fortschritte erzielt.

Die Entwicklung, Kalibrierung und Verifizierung eines thermischen Baugrundmodells, welches über die komplette Bauzeit den betrieblichen Randbedingungen angepasst wurde, erwies sich sowohl bei betrieblichen Störungen der Gefrieranlage oder einzelner Komponenten des Gefriersystems als auch bei der Behandlung von temperaturabhängigen geomechanischen Problemen als wertvolles Werkzeug bei der Bestimmung von Lösungen, die der Baubetrieb mit ausreichender Vorwarnzeit umsetzen konnte. Es wurde gezeigt, dass die Entwicklung des Frostkörpers auf Basis des verifizierten Modells sogar bei einem temporären Ausfall des der Überwachung der Gebirgstemperaturen dienenden Messsystems weiterhin analysiert werden konnte.

Die tägliche Überprüfung der betrieblichen Vorgänge und der daraus resultierenden Modellrandbedingungen erforderte in der Zeitnot des Baustellenalltags ein außerordentliches Maß an Teamarbeit zwischen Bauleitungspersonal und Planungsingenieuren. Nur dadurch war es möglich, die thermischen Modellrandbedingungen detailliert

zu pflegen, so dass heute für beide Schächte getrennt jeweils ein thermisches Simulationsmodell zur Verfügung steht, welches die gesamte Bauzeit umfasst.

Die während des Teufens der Gefrierschächte Ust-Jaiwa gesammelten Messdaten begründen die Anwendung gekoppelter thermisch-mechanischer Berechnungen, die derzeit im Rahmen von Untersuchungen zur Optimierung von Teufzyklen und Ausbauverfahren genutzt werden. Somit werden weitere Erkenntnisse erlangt, die bei zukünftigen Projekten genutzt werden können.

9 Literaturverzeichnis

[1] Hentrich, N.: „Numerische Simulationen zur Prognose der Frostkörperentwicklung und Optimierung einer fiktiven Gefriermaßnahme am Beispiel des Schachtprojektes Ust-Jaiwa“, Masterarbeit, Lehrstuhl für Geotechnik im Bauwesen, RWTH Aachen, 2014, unveröffentlicht.

[2] Franz, J. & Hentrich, N.: „Numerische Simulationen zur Prognose der Frostausbreitungsvorgängen am Beispiel des Gefrierschachtprojekts Ust-Jaiwa“. In: *Beiträge zum I. Internationalen Freiberger Schachtkolloquium*, Philipp, S. & Mischo, H. (eds.), Freiberg, Germany, September 30 - October 1, 2014, pp. 53-58. Technische Universität Bergakademie Freiberg, Institut für Bergbau und Spezialtiefbau, Freiberg, Germany.

[3] Geo-Slope International (2012): Geo-Studio 2012 Software Package, Calgary, Canada.

[4] Franz, J., Kisse, A., Hentrich, N.: „An investigation of shaft wall stability in low-strength rock mass conditions at the Ust-Jaiwa Freeze Shaft Project". In: *EUROCK 2015 & 64th Geomechanics Colloquium*, Schubert, W. (ed.), pp. 1053-1058, Salzburg, Austria.

[5] Itasca 2009. Fast Lagrangian Analysis of Continua in 3 Dimensions. Manual FLAC 3D 4.0.

About the behaviour of shafts and tunnels in a faulted rock mass

Zum Verhalten von Schächten und Tunneln in gestörtem Gebirge

Alexander Poisel
IGT consulting engineers
5020 Salzburg, Mauracher Str. 9, Austria

Rainer Poisel
Vienna University of Technology, Institute for Geotechnics
1040 Vienna, Karlsplatz 13, Austria

Abstract

At the construction lot SBT2.1 of the Semmering Base Tunnel (SBT) in Austria two shafts with a depth of about 400 m and a cavern at their bottom were excavated. During shaft excavation opposite vertical displacements were observed on the opposite walls depending on the dip direction of schistosity or fault zones. Moreover, a stress peak was observed on the opposite shaft side to the one the fault zone was entered. During excavation of the cavern longitudinal displacements against the dip direction of schistosity occurred. These observed displacements could be simulated in numerical calculations with the finite element method using a transversally isotropic material model. When approaching a fault zone, the results showed stress peaks in the competent rock in different distances to the fault zone. Consequently, experiences gained in tunnels may not be transferred to shafts automatically.

Zusammenfassung

Beim Baulos SBT 2.1 des Semmering Basis Tunnels wurden 2 Schächte mit einer Tiefe von ca. 400 m abgeteuft und eine Schachtfußkaverne vorgetrieben. Beim Abteufen der Schächte wurden in Abhängigkeit des Einfallens der Schieferung bzw. der Störungen auf gegenüberliegenden Seiten entgegengesetzt gerichtete Vertikalverschiebungen beobachtet. Darüber hinaus traten beim Eintauchen in Störungszonen auf den dem Störungsmaterial gegenüberliegenden Seiten Spannungskonzentrationen auf. Beim Vortrieb der Kaverne wurde eine Längsverschiebung gegen das Einfallen der Schieferung beobachtet. Die beobachteten Verschiebungen konnten durch Verwenden eines transversal isotropen Materialmodells in numerischen Untersuchungen mittels der Finiten Elemente Methode nachgebildet werden. Dabei zeigten sich bei Annäherung an eine Störung Spannungskonzentrationen im kompetenten Gebirge in unterschiedlicher Entfernung von der Störungszone. Die direkte Übertragung der Erfahrungen aus Tunnelvortrieben auf Schachtvortriebe ist daher nur eingeschränkt möglich.

1. Introduction

In this article the behaviour of shafts and tunnels in a faulted rock mass are discussed. The results of numerical calculations is analysed with regard to the observations made during the excavation works at the Semmering Base Tunnel.

At the construction lot SBT 2.1 “Tunnel Fröschnitzgraben” of the Semmering Base Tunnel (SBT), which is situated in Eastern Austria, two shafts with a depth of approximately 400 m were excavated. The excavation diameter amounts to 12 m at the shaft Fröschnitz 1 and 9 m at the shaft Fröschnitz 2.The shafts enable the supply to and disposal of materials from the tunnelling works of the two single-track running tunnels and the emergency station. In the final state they serve as air supply and extraction shafts in case of an incident (Poisel et al. 2016). At the bottom of the shafts caverns with diameters up to 20 m were excavated. These caverns serve as site facility area during construction and as an emergency station in the final state.

2. Semmering Base Tunnel - Geotechnical conditions, design and monitoring

The rock mass in the project area mainly consists of phyllites, sheared schists and gneisses. Generally, schistosity planes are dipping 20° to 40° westward. There are numerous strongly sheared zones as well as cataclastic fault zones up to a thickness of 10 and more meters. Their orientation is mainly parallel to the schistosity. The degree of fracturing of the rock mass differs frequently. Fig. 2.1 shows the general layout of the shafts and the caverns in a vertical section along the tunnel axis from East to West.

For the shafts and the caverns the geotechnical design was developed according to the principles of the NATM (Austrian Society for Geomechanics 2010b) and according to the “Guideline for the Geotechnical Design of Underground Structures with Conventional Excavation” (Austrian Society for Geomechanics 2010a). Both shafts were excavated conventionally by drill and blast with full face excavation. The support elements were systematic rock bolting and shotcrete lining with wire mesh reinforcement. The round length varies from 3.0 to 1.5 m. Several numerical calculations in 2D were carried out to determine the necessary support measures based on different geological and geotechnical circumstances. The caverns were also excavated by drill and blast. The support measures were also specified on the results of numerical calculations carried out in 3D.

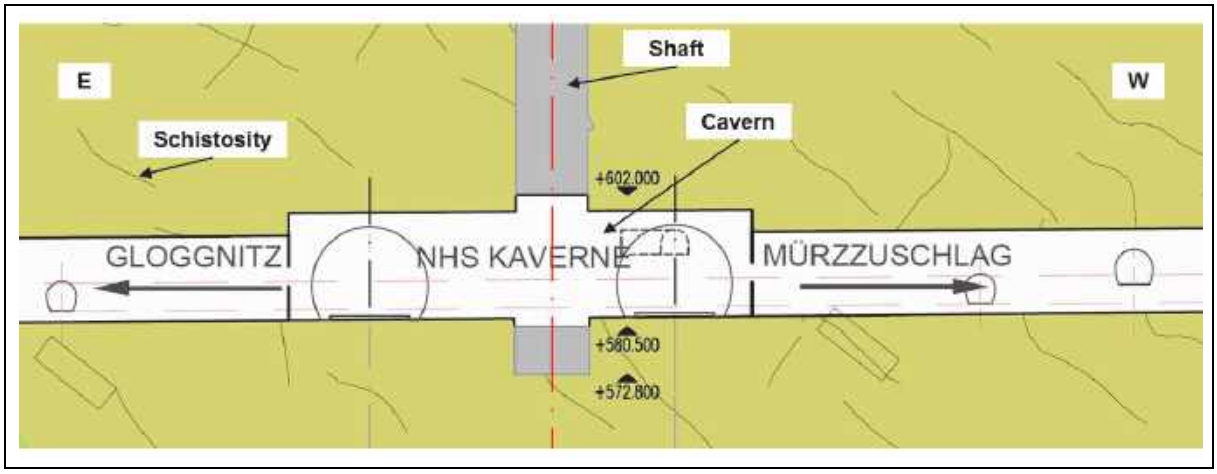

Fig. 2.1: Layout of shafts and caverns at the Semmering Base Tunnel

A Geotechnical Safety Management based on the observational method according to EC7 was implemented for the excavation works. Therefore, a continuous displacement monitoring was performed during the excavation works of both shafts and the caverns to get detailed information about the actual system behaviour. Monitoring sections consisting of 3D-monitoring points were installed with a vertical distance of approximately 20 m in good rock mass conditions and approximately 10 m in poor ones.

3. Monitoring results

3.1 Shaft

During the excavation of the two shafts at the Fröschnitzgraben radial displacements of a few millimetres occurred in good rock mass conditions. After about two days no further increase of displacements was monitored. Vertical displacements downwards were observed over the full shaft depth due to a gravitational slip of the shotcrete lining off the rock surface. These vertical displacements amounted up to 20 mm in total and lasted over several weeks.

Crossing a rock mass with lower strength due to high fracturing or especially a fault zone, however, the radial displacements increased and the decreasing of the displacement rates occasionally took more than one week. In addition, vertical displacement vector orientation represented a special issue. As an example, Fig. 3.1 shows the displacement vector orientation in the monitoring section MS-220 and MS-213 of shaft Fröschnitz 2 during the first two weeks after excavation. As is illustrated the monitoring points in the east half of the cross section showed slight displacements upwards and small radial ones. The displacement vectors of the monitoring points in the west half pointed very clearly downwards and showed higher radial displacements. Similar phenomena of different radial displacements have been observed in deep mine shafts. This was obviously caused by schistosity (Board 1989).

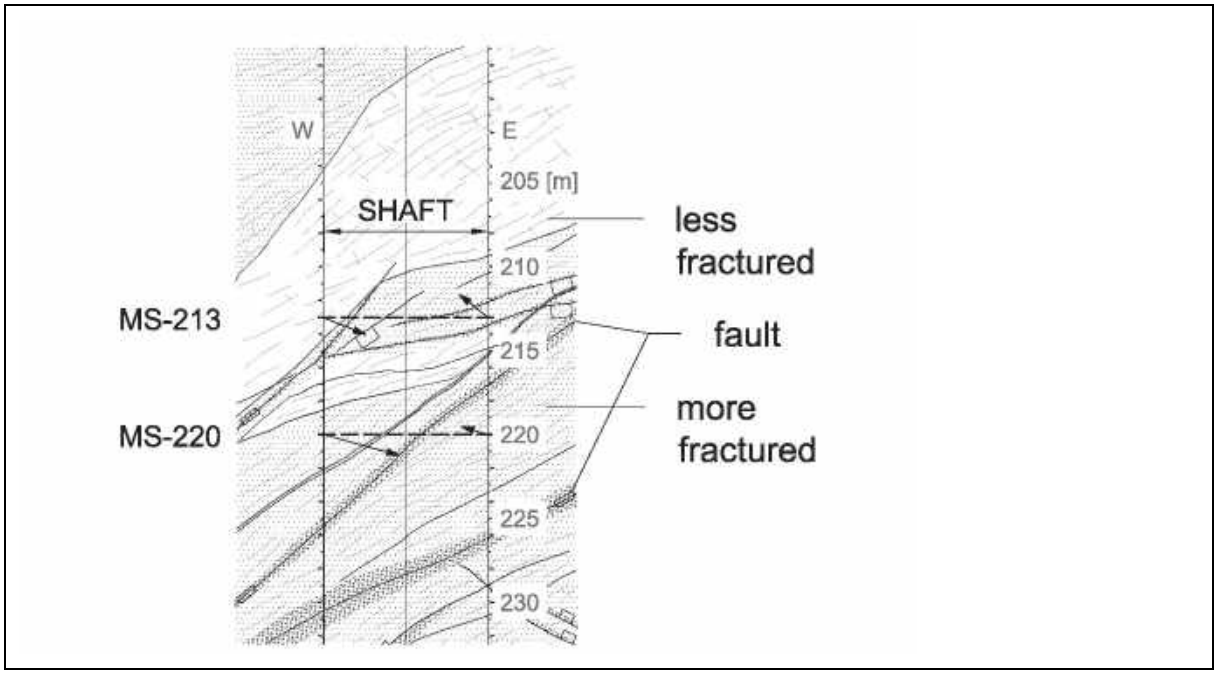

Fig. 3.1: Displacement vector orientation in monitoring sections MS-220 and MS-213 of shaft Fröschnitz 2 (vertical section).

When entering a fault zone not forecast the shotcrete outer lining, which was installed during excavation based on the prognosis of good rock mass conditions and an appropriate system behaviour, showed brittle fracture already after a short span of time. This failure first occurred on the opposite side to the fault zone entered. The area damaged started some meters above the fault zone and occasionally reached 10 m upwards the current shaft bottom, which corresponds approximately to one shaft diameter. It was assumed that a failure of the rock mass was caused by a stress concentration in the competent rock layers lying above the fault zone, due to redistribution of stresses from incompetent to competent rock. This failure mechanism “hard on soft” is often observed in rock mechanics, when competent rock masses are lying on a soft and incompetent base (Poisel et al. 1988). It was supposed that the failure of the rock mass subsequently led to an overloading of the shotcrete outer lining. Therefore, it was decided to strengthen the support measures at least one shaft diameter before entering a (predicted) fault zone.

3.2 Tunnel

The axis of the main cavern at the bottom of the shafts runs more or less east to west. The shaft Fröschnitz 1 is situated approximately in the middle of this cavern from where the excavation works started. Therefore, one excavation was driven east (east cavern) against the dipping of schistosity, and the other one was driven west (west cavern) with the dipping of schistosity. The excavation area of the top heading was approximately 120 m^2, which was divided in a left and a right part during excavation. Regarding the longitudinal displacements the following observations were made: In the west cavern the longitudinal displacements amounted approximately twice the one in the east cavern. In the west cavern the longitudinal displacements increased, until the excavation face reached a distance of app. 2 tunnel diameter to the monitoring section (Fig. 3.2).

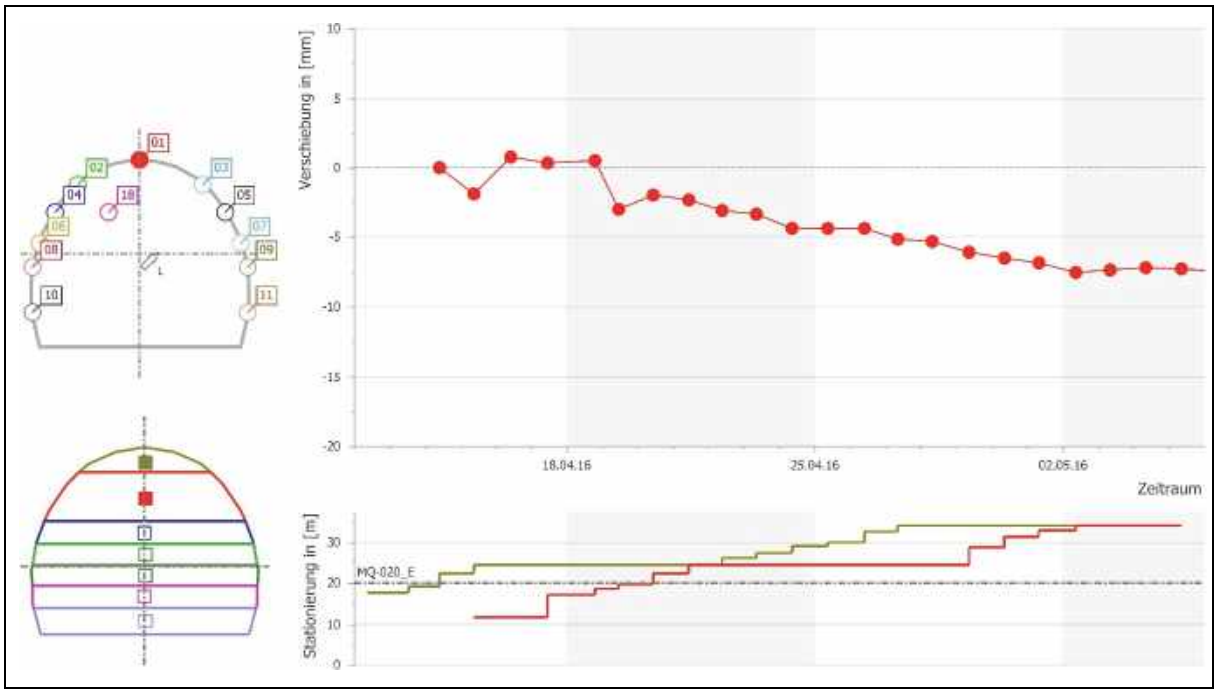

Fig. 3.2: MS-020 West cavern: Longitudinal displacement of crown over time

In the east cavern the longitudinal displacements increased only within the next few excavation steps (Fig. 3.3). It was concluded that this difference is caused by schistosity. In both drives the displacement vector orientation pointed against the direction of excavation.

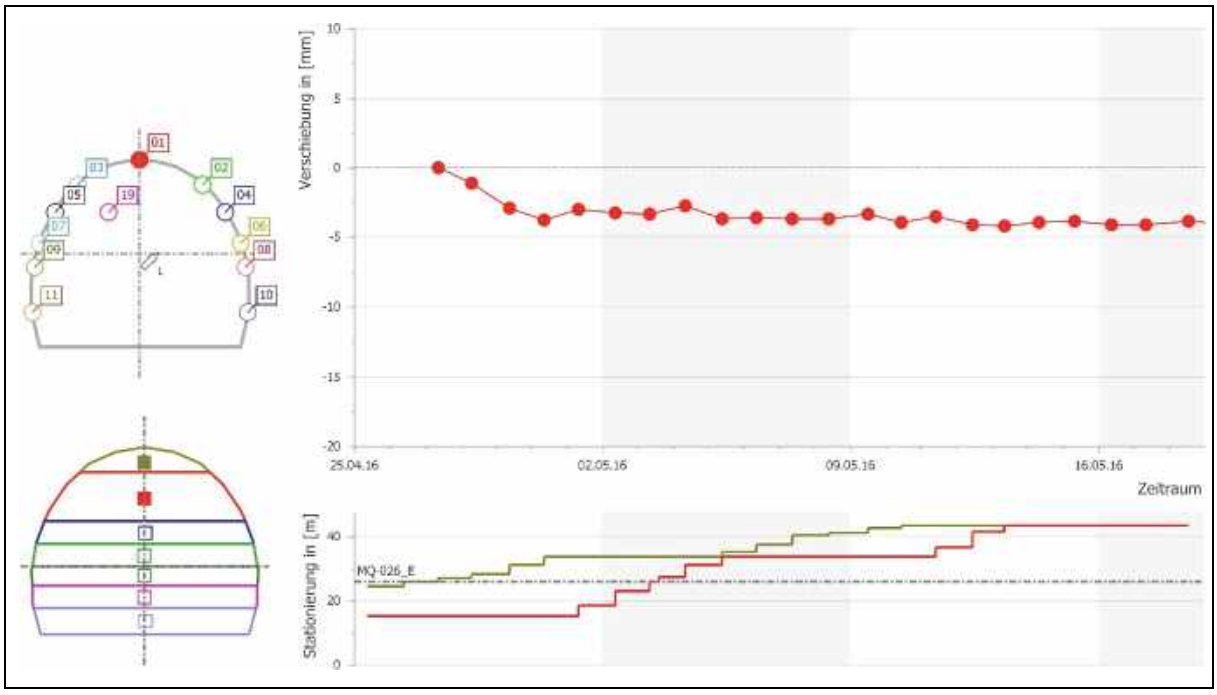

Fig. 3.3: MS-026 East cavern: Longitudinal displacement of crown over time

4. Numerical investigations of a tunnel in faulted rock

The influence of geological structures on the deformation pattern of tunnels was investigated frequently (Steindorfer 1998). These investigations revealed the influence of dominating discontinuity sets, like schistosity in the rock mass, on the displacement vector orientation in space. When the discontinuity set dips against the direction of excavation, the displacement vector in the crown tends to point slightly in the direction of excavation. In the other case, when the discontinuity set dips in the direction of excavation, the displacement vector in the crown tends to point slightly against the direction of excavation.

Approaching a fault zone with a tunnel excavation the development of longitudinal displacements represents a special issue (Budil 1996). In a homogenous rock mass longitudinal displacements in the direction of excavation are observed. If there is a rock mass with lower stiffness (fault zone – “soft” rock mass) in front of the tunnel face, the direction of the longitudinal displacements changes with ongoing excavation until the transition to the rock mass with lower stiffness is reached. There, the longitudinal displacements point against the direction of excavation due to a stress concentration between the tunnel face and the transition because of a redistribution of stresses from incompetent (“soft”) to competent (“stiff”) rock (Steindorfer 1998). For a transition from soft to stiff the longitudinal displacements increase with ongoing excavation, until the transition to the rock mass with higher stiffness is reached. Depending on the dipping of the fault zone with regard to the excavation direction the amount of the longitudinal displacements differs. If the fault zone dips with the excavation direction, the longitudinal displacements are higher than when the fault zone dips against the excavation direction. The maximum is even reached at an earlier excavation stage in the first case.

As a result of these investigation results and numerous case studies a method was developed to predict rock mass conditions in front of the tunnel face by analysing the alteration of the displacement vector orientation.

In addition Budil (1996) pointed out that there is a difference of vector orientation between numerical calculations and observed ones. In numerical calculations displacement vectors point in the direction of excavation in homogeneous rock mass conditions. Displacement vectors observed during excavation are normally oriented against excavation direction. This difference could be caused by multiple circumstances. This has to be taken into account when analysing the observed longitudinal displacements and comparing them with the calculated ones.

The numerical model applied to the shaft problem and described below (ZSOIL; see Chap. 5) provided the same results for a tunnel simulation as described above. For the tunnel simulation the dimensions of the modelled rock mass volume were 100 × 50 × 50 m in x-, z- and y-direction resulting in 60,840 3D FE elements (average element size 1.0 x 2 x 2 m) and 65,559 nodes. The negative y-axis represented the vertical direction (direction of gravity). In the centre of the model the tunnel running horizontally 25m below the upper boundary was modelled with a radius of 6m according to the one of the shaft. The tunnel excavation was modelled step by step, the round length was set at 1.5 m. The excavation direction points in the negative z- direction. The vertical in-situ stress on the upper boundary of the model was set at a dead weight

of 200 m. The displacements were fixed in x- and z-direction on the sidewalls and in y- direction on the lower boundary of the model. For all calculations an isotropic in-situ stress field was assumed. The following results are taken from an excavation step according to app. 3/4 of the tunnel length.

As described for the shaft model, in the tunnel model one weakness plane was defined for the multilaminate material model to take schistosity into account (calculation model 1, see 0). This weakness plane dips in the negative z- direction –in the direction of excavation– with an angle of 60° to the horizontal (+α…clockwise). In calculation model 2 (see 5.1.2) the fault zone crosses the tunnel at half of its length.

As is shown in Fig. 4.1 and Fig. 4.2, the displacement vector in the crown is oriented depending on the dip direction of schistosity as is described by Steindorfer when excavating under homogeneous rock mass conditions (calculation model 1, see 0). Analysing the longitudinal displacements in the invert another phenomenon is revealed with regard to the results of the shaft simulation. There are almost no longitudinal displacements in the invert of the tunnel when excavating with the dip direction of the schistosity (Fig. 4.1). When excavating against the dip direction of schistosity (Fig. 4.2) significant longitudinal displacements occur in the invert oriented against the excavation direction. As a matter of fact the face displacements are bigger than the one when excavating with the dip direction of schistosity.

Fig. 4.3 shows the displacement vectors when the tunnel excavation approaches a fault zone (calculation model 2, see 5.1.2). Increasing longitudinal displacements with decreasing distance to the fault zone are clearly detected. Within the fault zone the displacement vectors in the crown and the invert significantly point against the excavation direction.

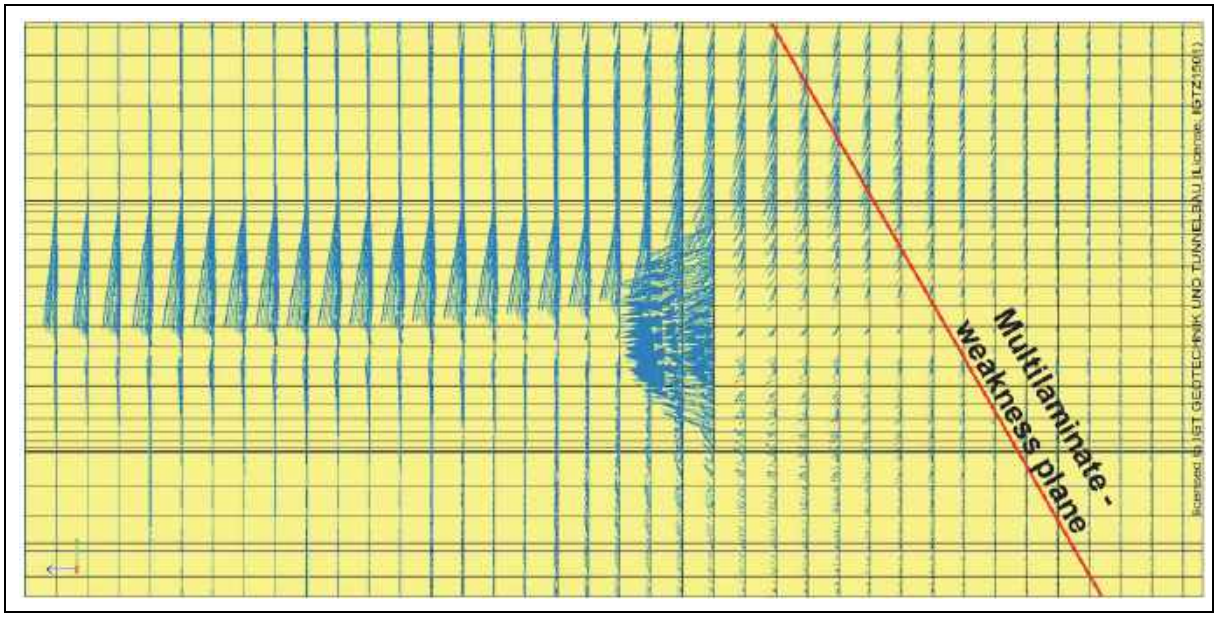

Fig. 4.1: Displacement vectors when excavating with the dip direction of schistosity

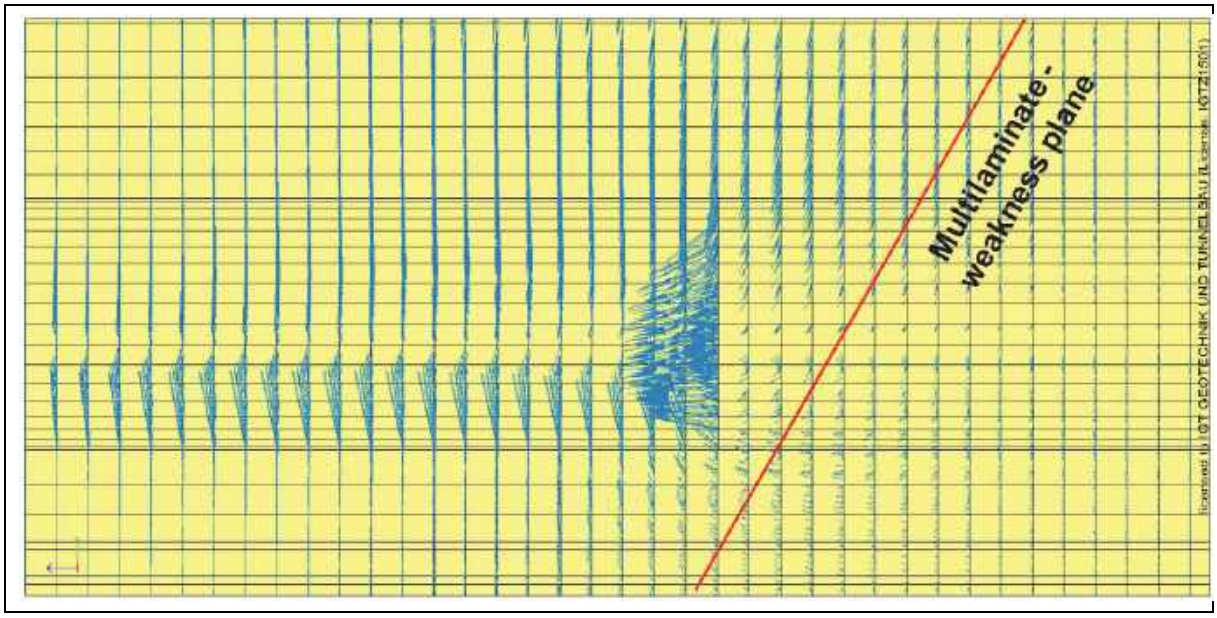

Fig. 4.2: Displacement vectors when excavating against the dip direction of schistosity

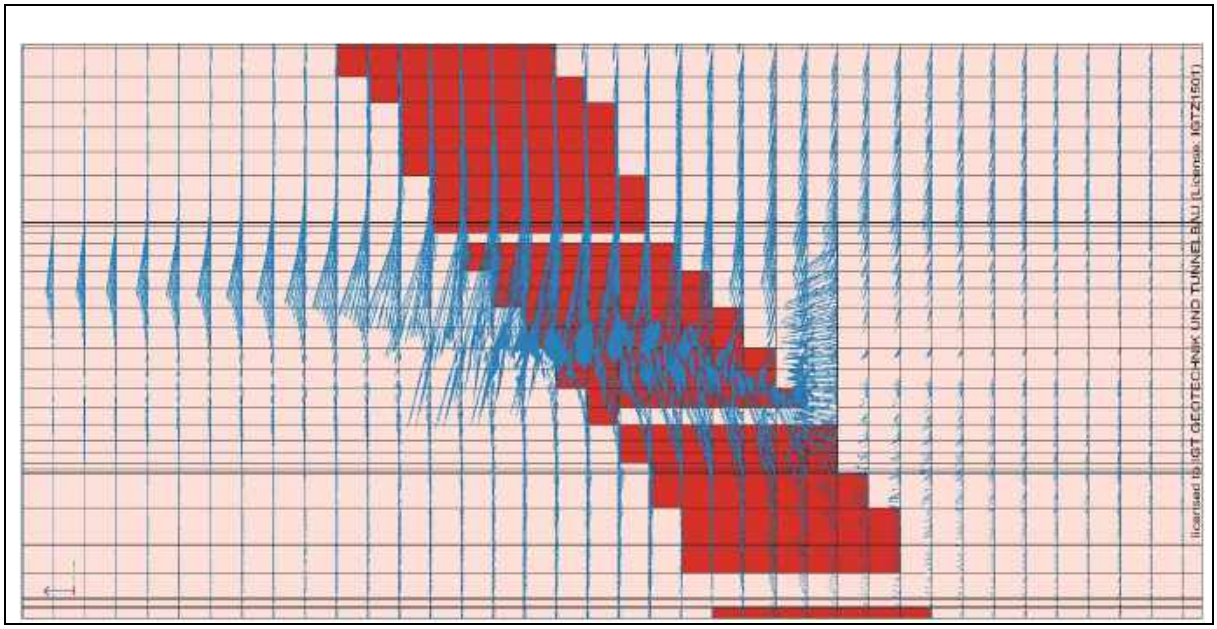

Fig. 4.3: Displacement vectors when approaching a fault zone (red elements)

Analysing the tangential stresses for a tunnel excavation (Fig. 4.4) it becomes obvious that a stress peak occurs immediately at the transition from the “stiff” to the “soft” rock mass, which matches with the investigation results of Steindorfer as described in chapter 4.

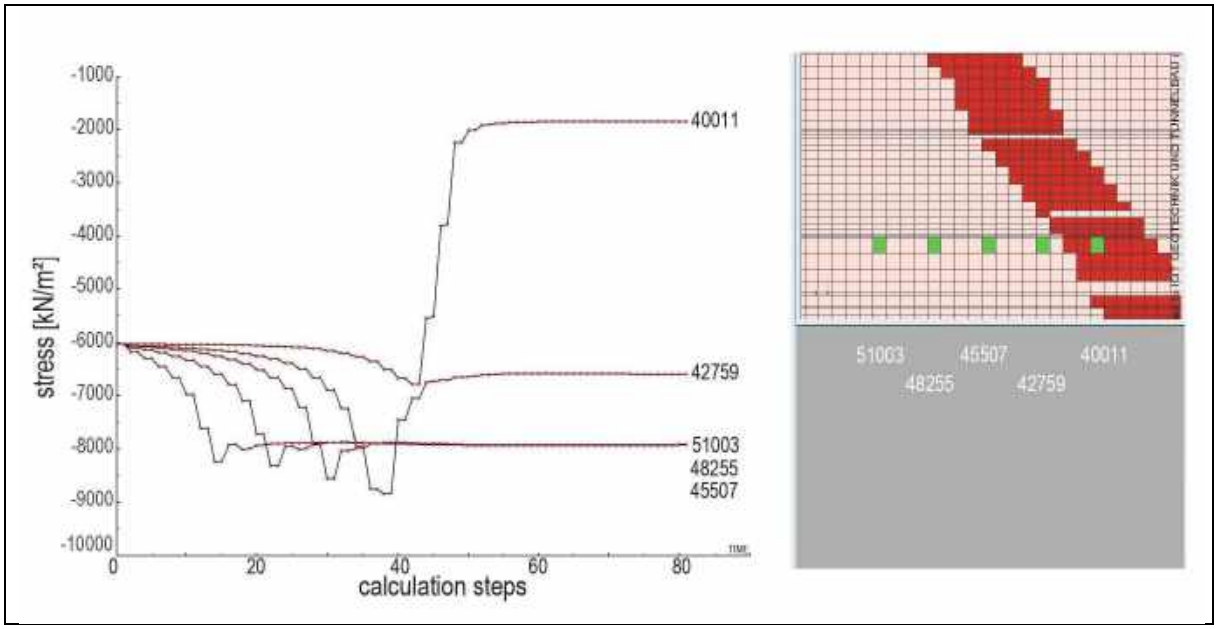

Fig. 4.4: Tangential stresses of selected elements plotted over time

5. Numerical investigations of a shaft in faulted rock

5.1 Shaft model

The dimensions of the modelled rock mass volume were 100 × 100 × 49.5 m in x-, z- and y-direction resulting in 83,952 3D FE elements (average element size 1.5 × 2 × 2 m) and 89,964 nodes. The y-axis represented the vertical direction (direction of gravity in negative y-direction). In the centre of the model the shaft was modelled with a radius of 6 m. The shaft excavation was modelled step by step, the round length was set at 1.5 m. The vertical in-situ stress on the upper boundary of the model was set at a dead weight of 200 m. The displacements were fixed in x- and z-direction on the sidewalls and in y- direction on the lower boundary of the model. For all calculations an isotropic in-situ stress field was assumed.

5.2 Calculations and Material properties

Subject of the investigations was the ground behaviour without any effect of support measures in accordance with the “Guideline for the Geotechnical Design of Underground Structures with Conventional Excavation” (Austrian Society for Geomechanics 2010a).

The rock mass for the different calculation models (model 1 and model 2 according to 0 and 5.1.2) consisted of different ground types (GT) according to the Austrian “Guideline for the Geotechnical Design of Underground Structures with Conventional Excavation” (Austrian Society for Geomechanics 2010a).

5.2.1 Calculation model 1

The rock mass for the calculation model 1 consisted of ground type 1. The material properties of this ground type 1 were set to the following parameters (Table 1).

Table 1: Material parameters of ground type GT 1 in model 1

		Young's modulus [GPa]	Cohesion [MPa]	Friction Angle [°]	Poisson's ratio [-]	Unit weights [kN/m3]
GT1	Matrix material	3.0	1.5	22.5	0.25	26
	Weakness plane		0.5	22.0		

A multilaminate material model was chosen in order to simulate anisotropic material behaviour. In the current model one weakness plane was defined in order to take schistosity into account. Within the shaft model the weakness plane dips against the positive x-direction with an angle of 60° to the horizontal (+α…anti clockwise). In this weakness plane Mohr-Coulomb plasticity condition and a tension cut-off condition must be fulfilled. As failure criterion of the core material the Mohr-Coulomb model was used.

5.1.2 Calculation model 2

In the calculation model 2 a fault zone was considered consisting of ground type 2 and a dipping angle equal to the one of the weakness plane (Fig. 5.1). The fault zone crosses the shaft at half of its length. The fault zone was modelled as continuum with a Mohr-Coulomb failure criterion. The material properties were set to the following parameters (Table 2):

Table 2: Material parameters of ground type GT 1 ad GT2 in model 2

		Young's modulus [GPa]	Cohesion [MPa]	Friction Angle [°]	Poisson's ratio [-]	Unit weights [kN/m3]
GT1	Matrix material	3.0	1.5	22.5	0.25	26
	Weakness plane		0.5	22.0		
GT2	Fault zone	1.0	0.5	20.0	0.30	26

On top of each model an element row was modelled as ground type GT0. The stiffness of this ground type was set at a very high value to eliminate boundary effects.

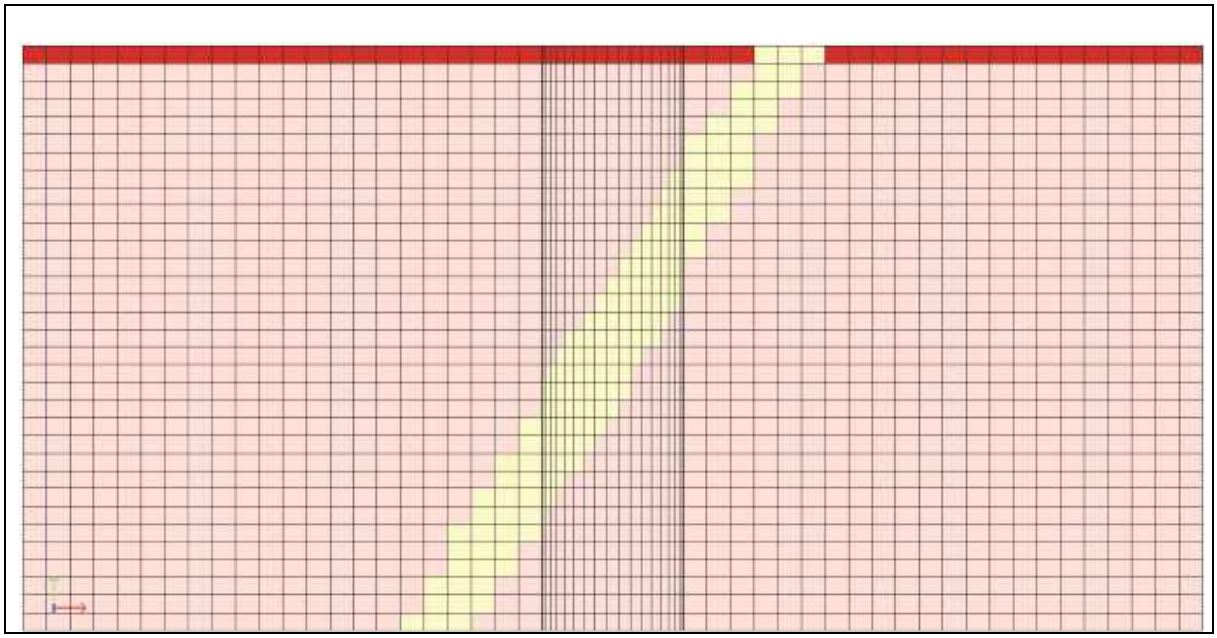

Fig. 5.1: Model 2 for shaft calculations

5.3 Results of the numerical calculations

The results discussed in the following chapters are taken from an excavation step at a depth of app. 275 m. In calculation model 2 this step corresponds to the depth of the shaft with the fault leaving the excavation profile.

5.3.1 Calculation model 1

The results (Fig. 5.2) reveal a displacement vector orientation in opposite direction to the excavation direction. On the right side, where the schistosity enters the shaft profile, a slight displacement occurs upwards. On the left side, where the schistosity leaves the shaft profile, a slight displacement downwards can be observed. Below the shaft bottom displacements occur upwards. Consequently the shaft bottom shows a heave. The radial displacements are nearly the same on both sides. Only small plastic zones occur within the rock mass outside the shaft profile. These results generally match with the observations made during the shaft excavation in a rock mass of lower strength. Therefore, a difference of the vector orientation is detected when compared with a tunnel being excavated in the dip direction of schistosity (Fig. 4.1). At the tunnel excavation the amount of longitudinal displacements is even bigger. No difference in the displacement pattern is observed, when gravity is eliminated within the rock mass volume.

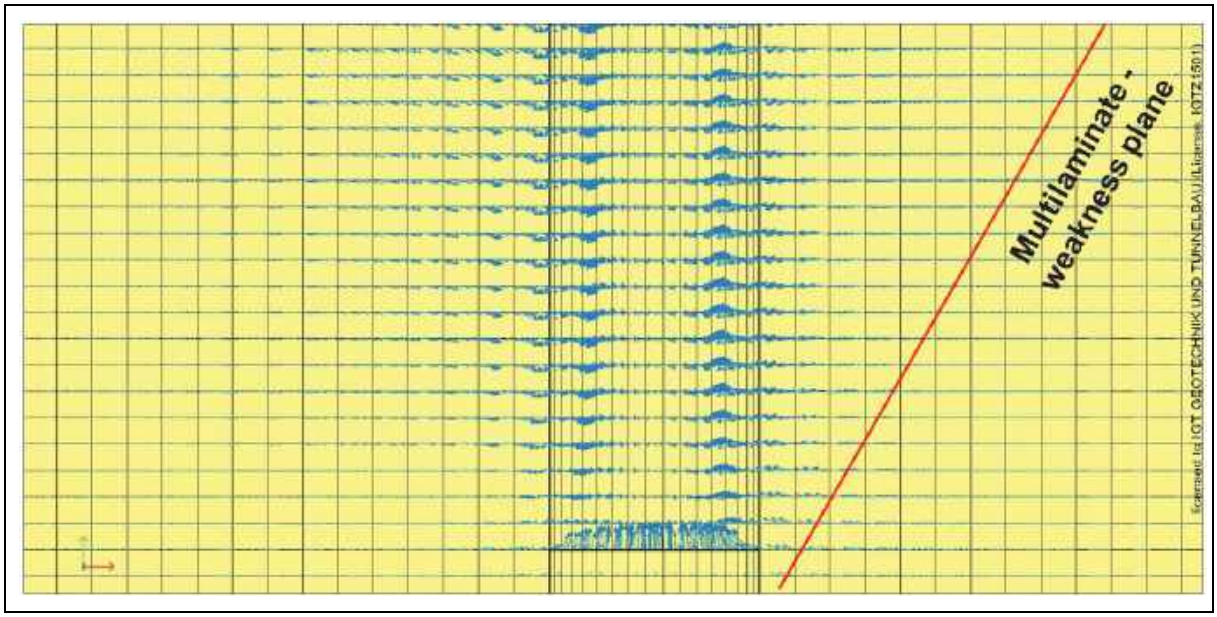

Fig. 5.2: Displacement vectors in x-y-plane for model 1

5.3.2 Calculation model 2

The results (Fig. 5.3) reveal that elements of GT2 show displacement vectors pointing significantly upwards, against the excavation direction, as in the tunnel model (Fig. 4.3). The orientation of the displacement vector of GT1 elements corresponds to the results of calculation model 1 (Fig. 5.2). On the left side of the shaft the displacement vectors point downwards in the direction of excavation. No increase of the longitudinal (vertical) displacements can be observed with the distance to the fault zone decreasing. This is different to the observations made at tunnel excavations (chapter 4 and Fig. 4.3). Therefore, the application of the prediction method for tunnel excavations to detect an alteration of rock mass conditions in front of the shaft bottom by analysing the displacement vector orientation has to be questioned.

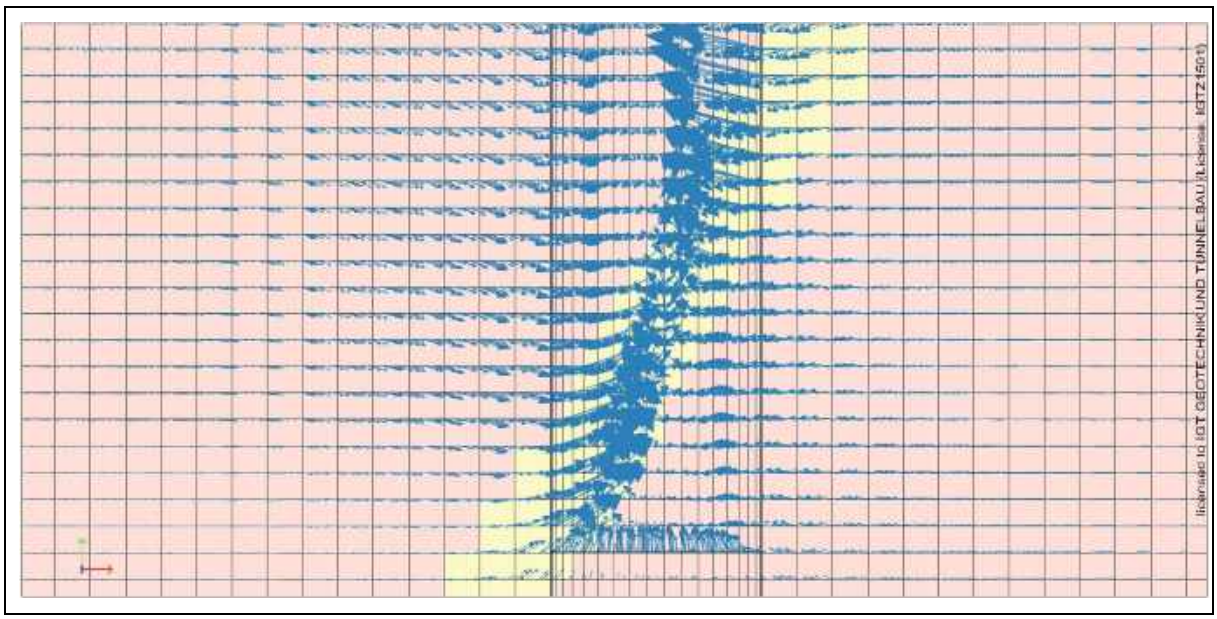

Fig. 5.3: Displacement vectors in x-y-plane for model 2

As is shown in Fig. 5.4, there is a stress peak of the tangential stresses in a certain distance to the transition from the “stiff” to the “soft” rock mass. This stress peak matches with the observations during shaft excavation when entering a fault zone not forecast, as described in chapter 0. As described above and shown in Fig. 4.4, a stress peak occurs immediately at the transition from the “stiff” to the “soft” rock mass in the tunnel model.

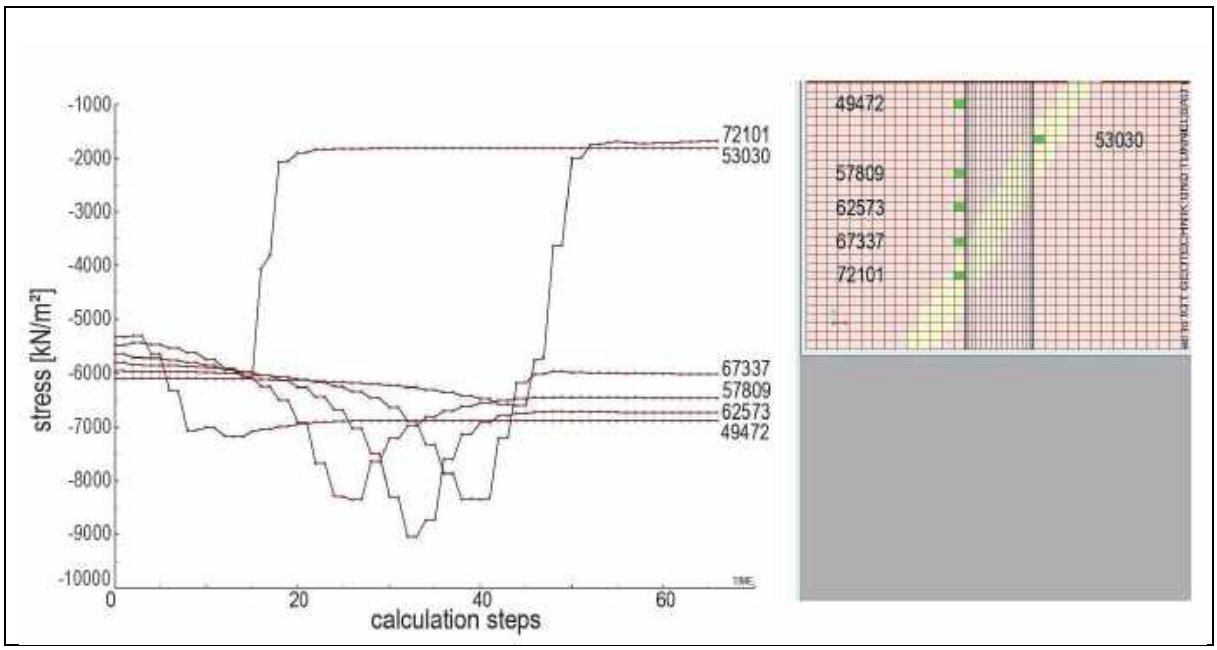

Fig. 5.4: Tangential stresses of selected elements plotted over time – shaft

6. Summary and conclusions

As mentioned in chapter 3, shafts and caverns excavated for the Semmering base tunnel in faulted rock showed displacement vector orientations against the dip of schistosity and of fault zones at the excavation boundary, where the geological structure enters the excavation. Additionally, it was observed that the shotcrete outer lining showed brittle fracture already after a short span of time, when entering a fault zone not forecast. This failure first occurred on the opposite side to the one the fault zone was entered. Therefore, it was decided to strengthen the support measures at least one shaft diameter before entering a (predicted) fault zone.

Numerical investigations assuming an isotropic in situ stress state helped to understand these observations. In accordance with monitoring results the numerical investigations showed opposite longitudinal displacements during shaft excavation due to a transversally isotropic material behaviour. However, in numerical simulations of a tunnel this opposite displacement orientation does not occur.

When approaching a fault zone, numerically determined tangential stresses revealed a maximum value on the opposite shaft side to the one the fault zone was entered. In the tunnel model, on the other hand, a stress peak occurs immediately at the transition from the “stiff” to the “soft” rock mass. The influence of anisotropic in situ stress states as well as of the geometric set up (shaft – fault zone) are being investigated.

Knowing these correlations help to be aware of approaching a fault zone and entering a zone of extraordinary stresses. However, correlations between displacement vector orientations and stresses in faulted rock seem to be different in tunnels and shafts and experiences gained in tunnels may not be transferred to shafts automatically.

REFERENCES

Austrian Society for Geomechanics. 2010a. *Guideline for the Geotechnical Design of Underground Structures with Conventional Excavation*. Salzburg: ÖGG

Austrian Society for Geomechanics. 2010b. *NATM - The Austrian Practice of Conventional Tunnelling*.

Board, M.P. & M.J.Beus.1989. *In Situ Measurements and Preliminary Design Analysis for Deep Mine Shafts in Highly Stressed Rock*, RI9231, U.S. Bureau of Mines, 46p.

Poisel, A., Schachinger T, Wagner, O.K., Wahlen, R., Steindorfer A. 2016. Deep shaft excavation – geotechnical monitoring and back analysis. *Proceedings of the ISRM international symposium EUROCK 2016*. Ürgüp, Vol. 2, 1255 – 1260

Poisel, R. Eppensteiner, W. 1988. A contribution to the systematics of rock mass movements. *Proceedings of the 5th international symposium of Landslides.* Lausanne, 2, 1353-1357.

Steindorfer, A. (1998): Short term prediction of rock mass behaviour in tunnelling by advanced analysis of displacement monitoring data, *Geotechnical Group Graz, Vol. 1*, 111 pp

Budil, A. (1996): *Längsverschiebungen beim Tunnelvortrieb*. Ph.D. thesis, Technical University Graz

Stability and deformation of backfilled shafts

Stabilität und Verformung von Schacht-Schottersäulen

Nguyen Quang Tuan[1,2], Heinz Konietzky[1]
[1]Institut für Geotechnik, TU Freiberg,
Gustav-Zeuner-Straße 1, Tel. 03731 39-2519 , Email: heinz.konietzky@ifgt.tu-freiberg.de
[2]Geotechnical Department, Thuy Loi University,
175 Tay Son str., Dong Da distr. Hanoi, Vietnam, Email: nqtuan@tlu.edu.vn

Abstract

Mine shafts are often backfilled with granular material after finishing the mining activities. The behavior of backfill is a key factor controlling the stability and deformation of shaft and connected openings. Many shaft failures documented are due to the instability of the backfill. Moreover, often the engineering practice requires structures to isolate the backfill material from the biosphere. Pressure exerted on these structures needs to be predicted. This paper documents the application of discrete element model to investigate the behavior of ballast column backfilled in mine shaft. The models can be used to predict the stability and deformation of backfill column in mine shaft, especially in terms of stresses and forces acting on the shaft walls, the shaft bottom and retaining structures.

Zusammenfassung

Nach Abschluss der Bergbauaktivitäten werden Schächte oft mit Schotter verfüllt. Das Verhalten des Schotters ist entscheidend für Stabilität und Deformation des Schachtes sowie der angrenzenden Grubenbaue. Viele Versagensfälle von mit Schotter verfüllten Schächten sind dokumentiert. In der Ingenieurpraxis wird häufig die Isolation des Versatzmaterials von der Biosphäre gefordert, wobei die Druckbelastung auf diese Strukturen prognostiziert werden muss. Dieser Beitrag dokumentiert die Anwendung der Diskreten Elemente Methode zur Beschreibung des Verhaltens von mit Schotter verfüllten Schächten. Die Modelle können Stabilität und Deformationen von Schottersäulen in Schächten prognostizieren, insbesondere in Bezug auf Spannungen und Kräfte, die an den Schachtwandungen, der Schachtsohle und Dammbauwerken angreifen.

1 Introduction

The closure of underground mines is connected to the closure of shafts. The number of shafts to be closed is quite high. For example, in the United Kingdom the number of abandoned shafts is estimated to be 100,000 (Dun 1982). About 10,000 shafts are registered in the Ruhr area, Germany (Hollmann et al. 2009).

Collected case histories (Salmon et al. 2015) have shown that, in reality, incidents of mine shafts are mainly caused by shaft filling material collapse. An overview about failure scenarios is shown in Fig. 1. It is obvious that the failure of filling material plays a dominant role for the safety of backfilled shafts.

Most important types of backfill material in hard rock mining are rock fill, slurry fill and paste fill (Hustrulid and Bullock 2001). Among those, rock fill is the first type used in mining to provide underground support and commonly used due to its availability at sites. It is beneficial from the economical point of view if waste materials are utilized.

Due to the shaft dimensions (large height to diameter ratio) the behavior of granular shaft column is characterized by silo and arching effects. Besides, the properties of granular material play a very important role. Also, the character of contact between the backfill and the shaft wall affects the behavior of the granular column inside the shaft. The silo effect has been investigated by numerous authors but research in the field of mining, especially in relation to shaft backfilling, is quite limited. Most studies were performed in civil and processing engineering. They are mainly based on conventional analytical theories accompanied by experiments. However, these conventional methods have several constraints in respect to silo flow of granular material.

Depending on the geometry of the shaft, on the filling process, on the mechanical properties of the fill material and on the shaft wall characteristics, a certain stress state will develop inside the fill column and backfill pressure will exert on shaft walls and/or any retaining structure. Often simple analytical models are used to predict the stresses or pressure distributions. Numerical methods can be used in combination with experiments to predict the behavior of the shaft fill column in more detail.

To some extend numerical simulations regarding the behavior of granular materials can be performed with the help of classical continuum mechanical methods. However, it is impossible to investigate such systems at the particle scale. It is also difficult to simulate the flow or movement of the whole system. Meshfree methods like particle-based techniques are an interesting alternative to overcome these difficulties.

This paper presents simulations of the behavior of ballast material inside mine shafts using PFC^{3D} (Itasca 2008), a three-dimensional code based on the Discrete Element Method. The applied procedure considers the mechanical properties of the ballast including grain-size distribution and particle shapes. The interaction between the particles is characterized by contact constitutive laws (sphere-to-sphere or sphere-to-wall). The linear contact model was used in this study. This model is defined by normal and shear stiffnesses k_n and k_s (Itasca 2008). It is assumed, that every contact in the model has the same stiffness, which is characterized by contact Young's modulus (E_c)

and the ratio of particle normal to shear stiffness k_n/k_s. Values of normal and shear stiffnesses for each particle are related to particle radius R and can be determined by using the following equations:

$$k_n = 4RE_c, \tag{1}$$

$$k_s = k_n. \tag{2}$$

The main research deals with the simulation of real shaft backfilling using ballast. A simple clump template was used to describe particle shape. Grain grading was also incorporated. The micro parameters of the numerical models were derived from calibrations of the models on the basis of the lab tests performed with specific ballast material. The numerical simulations depict the filling process, the effects of different dumping height, the initial compaction and the friction at the shaft walls on the stability and settlement of the ballast column. The silo effect was well replicated in the shaft backfill by the numerical simulations. Pressure values obtained from numerical models were compared with those calculated on the basis of Janssen's theory (Janssen 1895).

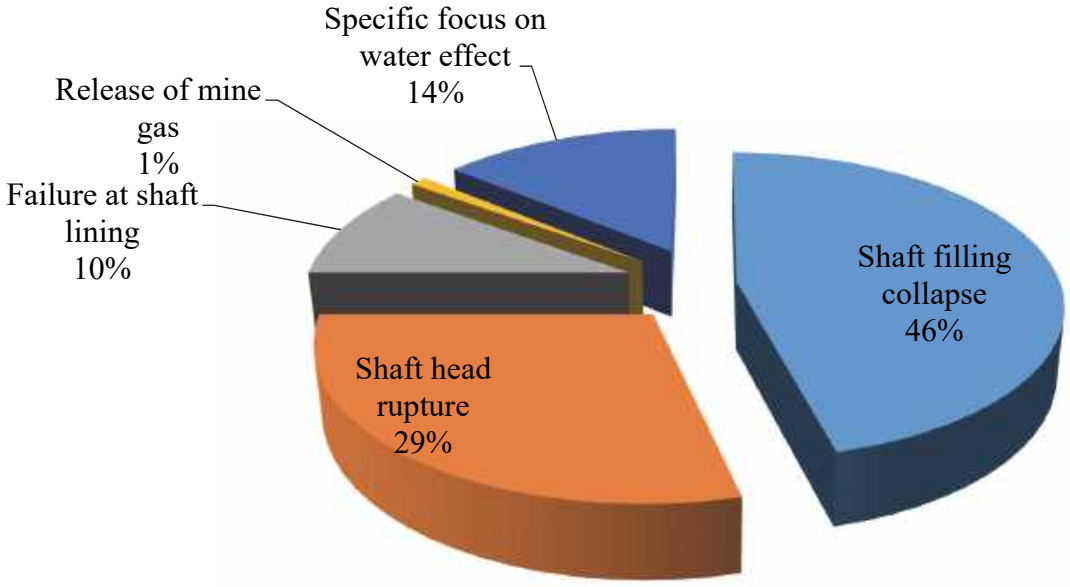

Fig. 1: Shaft failure modes (Lecomte et al. 2012; Salmon et al. 2015)

2 Classical theory of stress distribution in backfilled shafts

Due to the tube like shape, the granular column in a shaft is partially supported by the shaft wall. Therefore, pressure increases non-linearly with the height of the filling column. Conventionally, the pressure on the shaft is determined using Janssen's theory. A summary of Janssen's approach can be found in Pipatpongsa and Heng (2010). According to this theory, the vertical pressure (p_v) and the horizontal pressure (p_h) of backfill at depth z are determined by Eq.3 and Eq.4, respectively:

$$p_v = \frac{\gamma R}{2\mu_w K}\left[1 - e^{-2\mu_w K\frac{z}{R}}\right], \quad (3)$$

$$p_h = K p_v. \quad (4)$$

where: $\boldsymbol{K}$ is the lateral stress ratio, $\boldsymbol{\mu_w}$ is the friction coefficient between material and wall, $\boldsymbol{\gamma}$ is the bulk density of filling material and R is the radius of shaft/silo.

3 Small-scale shaft filling experiments and DEM simulations

To evaluate the suitability and feasibility of a DEM approach for the simulation of shaft backfilling problems, small-scale shaft experiments with backfilling of glass spheres were conducted and modelled.

In order to obtain appropriate micro parameters for the synthetic material, standard lab tests were performed in combination with DEM simulations. The tests performed in the lab comprise dumping tests, angle of repose tests, friction tests between glass spheres and the surface of the tube (small shaft), oedometer compression tests and direct shear tests. The calibration works helped to determine the micro parameters and to investigate the influence of different parameters on the overall mechanical behavior of the model.

The small-scale shaft experiments were simulated considering the filling process. Resulting stresses and pressures inside the shaft were observed under different loading conditions. The results of the simulations showed that DEM might be a suitable tool to investigate the problem of shaft backfilling. Once the micro parameters for the synthetic DEM material are derived, the shaft backfilling process including stability / instability and post failure behavior can be investigated (Tuấn and Konietzky 2015).

4 Rock ballast: Modelling of lab tests and calibrations

4.1 Ballast material for shaft backfilling

Typical ballast materials used for shaft backfilling in Germany were selected. These ballast types are equivalent to the track ballast which is widely used by Deutsche Bahn AG (railway company). The grading of rock ballast is presented in Fig. 2. This grading was also incorporated in the simulations. The grain density of ballast is 3060 kg/m^3. The ballast material was tested to determine mechanical behavior and properties. The lab tests include the repose test, the dumping test and the oedometer compression test to determine the bulk response. The lab test results were used to calibrate the PFC^{3D} models by applying suitable micro parameters.

4.2 Grain shape and clump logic

Shape and angularity of ballast particles are major factors influencing the material response. To reproduce the particle shape effect clumps were used. In this study a simple clump which consists of two overlapping spheres called ‘dyad’ was used for modelling (Fig. 2 c).

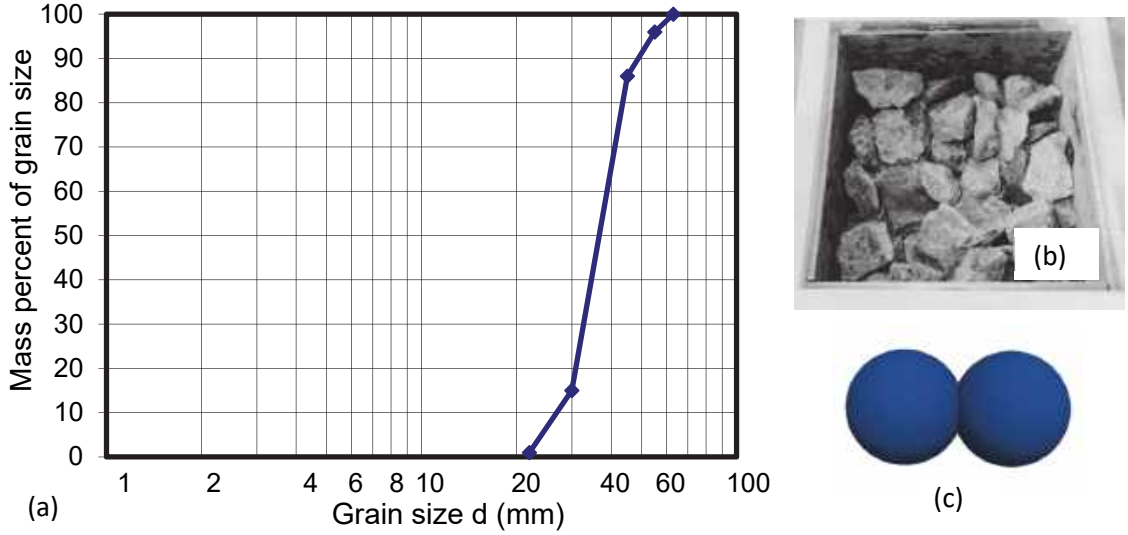

Fig. 2 (a) Grain-size distribution of shaft backfill, (b) ballast inside box, (c) ‘dyad’ clump as ballast particle in PFC^{3D}

4.3 Particle up-scaling and model symmetry

The huge number of particles creates tremendous problems in terms of computational time. It is therefore necessary to limit the number of particles especially for simulating large scale in-situ problems. Therefore, particle size up-scaling is applied to the bulk material. In this tudy, different up-scaling factors, defined as ratio between particle size in numerical model and real size, were used.

Considering geometry alone, axisymmetric conditions exist. Therefore, half or quarter models have been considered as an acceptable model approximation (Nguyen 2016). Symmetry planes with zero friction were used. Half and quarter models were used for modelling dumping tests, oedometer tests and the shaft backfilling to verify this simplification.

4.4 Ballast calibration

4.4.1 Repose test

The repose angle of rock ballast can be measured at the slopes of natural tailings. In practice the stable angle of ballast slopes after dumping in drifts varies between 42 and 45 degree (Breidung 2002).

Numerical modelling to simulate the repose test with rock ballast was performed to provide an initial basis for the micro friction calibration. As a result of these simulations, variation on angle of repose was obtained depending on micro friction coefficient of

particles. Fig. 3 shows that the angle of repose increases almost linear with increasing micro friction coefficient up to a certain limit, i.e. 43 degrees corresponding to a micro friction coefficient of 0.5. When micro friction is greater than this limit, there is almost no further increase of repose angle.

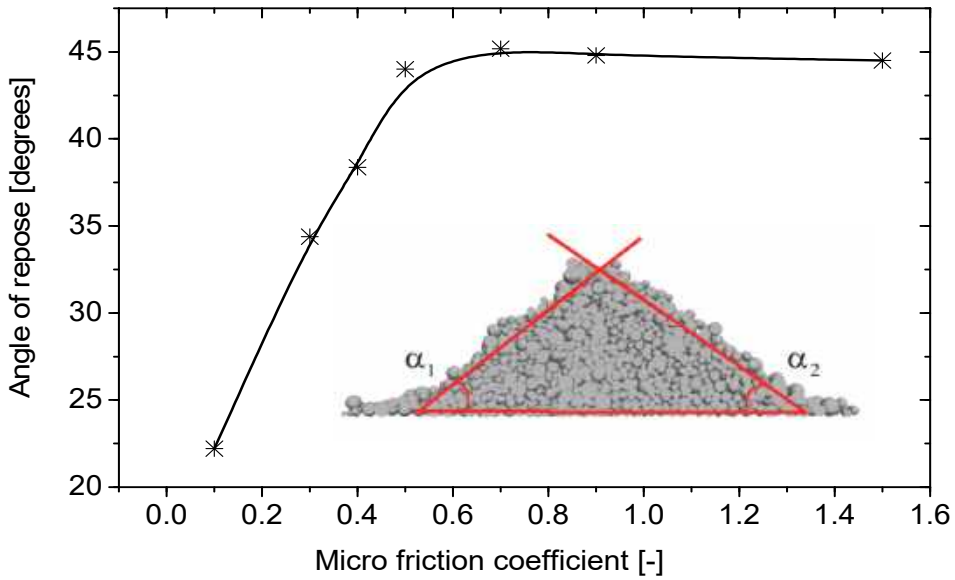

Fig. 3 Angle of repose versus micro friction coefficient and profiles to measure repose angle (based on 'dyad' particle simulation)

4.4.2 Dumping test

Dumping tests were used to determine the bulk density and porosity of rock ballast. In the lab, the ballast assembly was poured from above into the cylindrical oedometer cell. By this procedure, an oedometer sample was prepared for the compression test afterwards.

Due to the axisymmetric geometry of the model only one half of the domain was modelled to save computational time. The clumps were dropped by gravity from a funnel into a cylinder which has same geometry as the oedometer cell in the lab (0.8 m high and 0.505 m diameter). After the cell was filled, clumps above the oedometer sample height were removed and the total volume of the clumps was computed. The value of bulk density was obtained by dividing the total mass of ballast by the volume. The obtained porosity depends on the micro friction between particles as shown in Fig. 4.

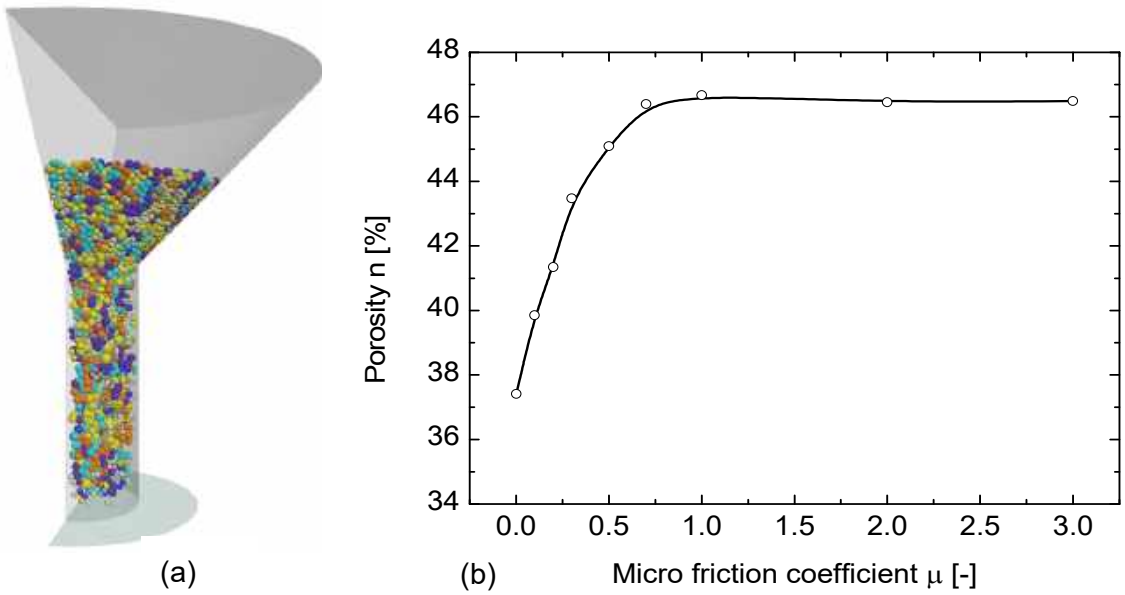

Fig. 4 (a) Numerical model of dumping test, (b) porosity versus micro friction coefficient

4.4.3 Oedometer compression test

Simulations of oedometer compression tests were performed to simulate the deformability of the material under compression. A specimen with porosity of 45 %, identical to the porosity of the real material, was prepared by dumping as mentioned above.

In the numerical model, one segment of the cylindrical wall, which is located at the middle height of the oedometer cell, was used to measure the normal pressure at the confining wall. This pressure is used as σ_h to calculate the backfill average pressure in the oedometer cell according to Eq. 5.

$$p = \frac{1}{3} \cdot (\sigma_v + 2\sigma_h). \quad (5)$$

The following micromechanical parameters were obtained from the calibration procedure on the basis of different lab tests. All further simulations are based on these values:

- Contact Young's modulus: E_c = 1.2 · 10^8Pa
- Ratio of particle stiffnesses: k_n/k_s = 30
- Friction coefficient of particles: μ = 0.75

A comparison between simulated and in the lab measured compaction behavior is shown in Fig. 5b.

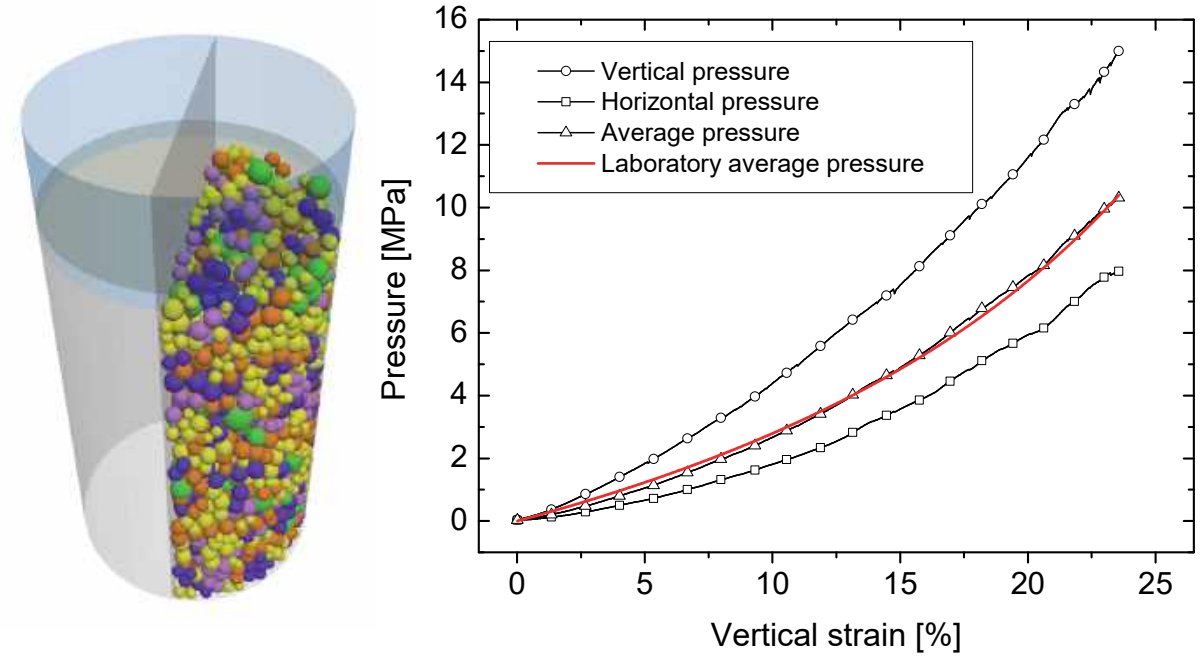

Fig. 5 (a) Numerical model of oedometer compression test, (b) comparison between lab and numerical simulation results (right)

4.5 Simulation of shaft backfilling

4.5.1 Shaft and drift geometry

The geometry of shaft and drift selected for simulations is typical for mine shafts. Different geometrical settings were considered. The main shaft was assumed to be vertical with cylinderical shape and diameter of 5 m. A shaft section with maximum height of 50 m was selected for the simulation. Two main schemes were considered. The first scheme considers a shaft without any connected drift and filling station. This scheme is useful to investigate the silo effect of granular backfill in a shaft. The pressure exerted by backfill, i.e. normal pressure on shaft wall and vertical pressure on shaft bottom, can be used to estimate pressure on retaining walls in drifts next to main boundary and pressure on plug, respectively. The second scheme was built to depict a real shaft connected to a large horizontal stope, working or cavern. This scheme is conservative to predict the stability of backfill column inside the shaft, especially in case of loading on top of backfill.

The walls of shaft and drift were modelled by wall elements. Based on symmetry conditions, only one-fourth of the domain was analysed to reduce the computational effort. The symmetry planes are modelled by flat walls which zero friction.

4.5.2 Backfilling process

The ballast column inside the shaft was formed by a dumping process which replicates the actual backfilling work (Fig. 6). A series of particle packages, called ‘cloud of ballast’, were generated randomly at certain height inside the shaft. The dumping process is driven by gravity. Since the clumps have a free fall, local damping was set to zero and viscous damping was used with the critical damping ratio of 0.1. The

compaction of the backfill column, stress state at any location or pressure on walls can be monitored during the simulation process.

4.6 Results

4.6.1 Pressure distribution and silo effect

One main objective of the study was the determination of pressure acting on the shaft wall and the shaft bottom. Simulations for different values of friction between shaft wall and ballast particles were carried out. The simulations document the significant influence of the wall-particle friction on the pressure at the shaft wall and shaft bottom (Fig. 7). As observed, the pressure of ballast exerted on the shaft walls becomes unaffected after a certain height of backfill. The friction of the shaft wall has almost no effect on the compaction of the backfill.

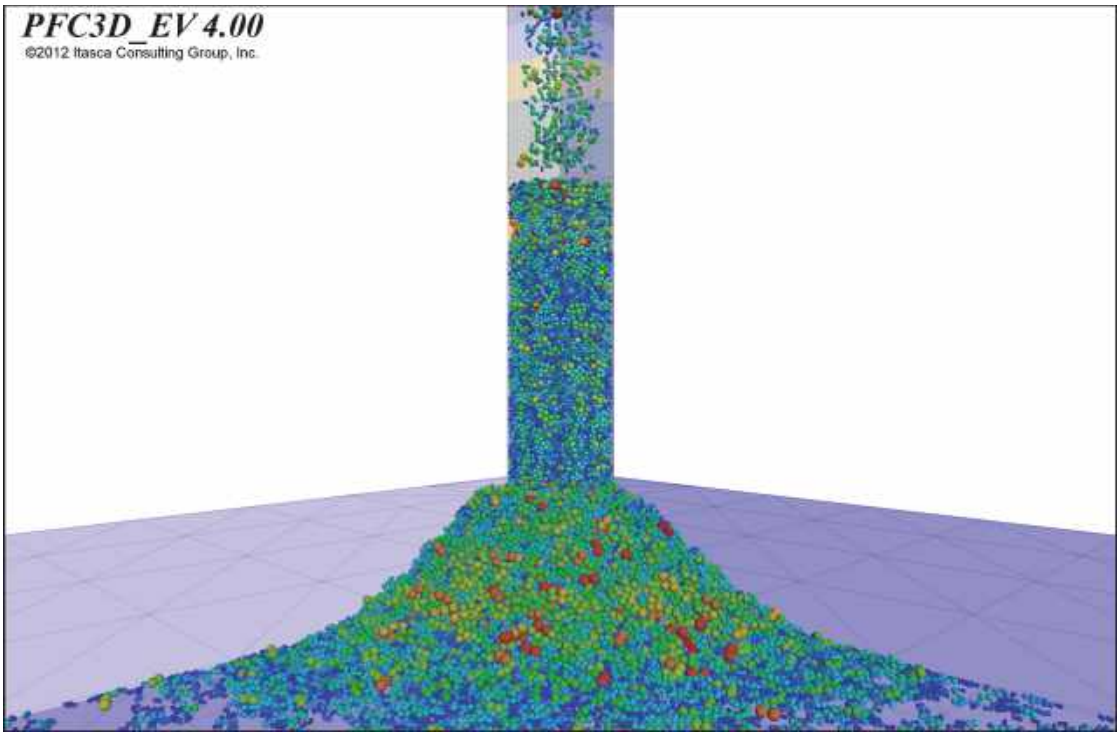

Fig. 6 Numerical model of shaft backfilling: dumping process inside the shaft.

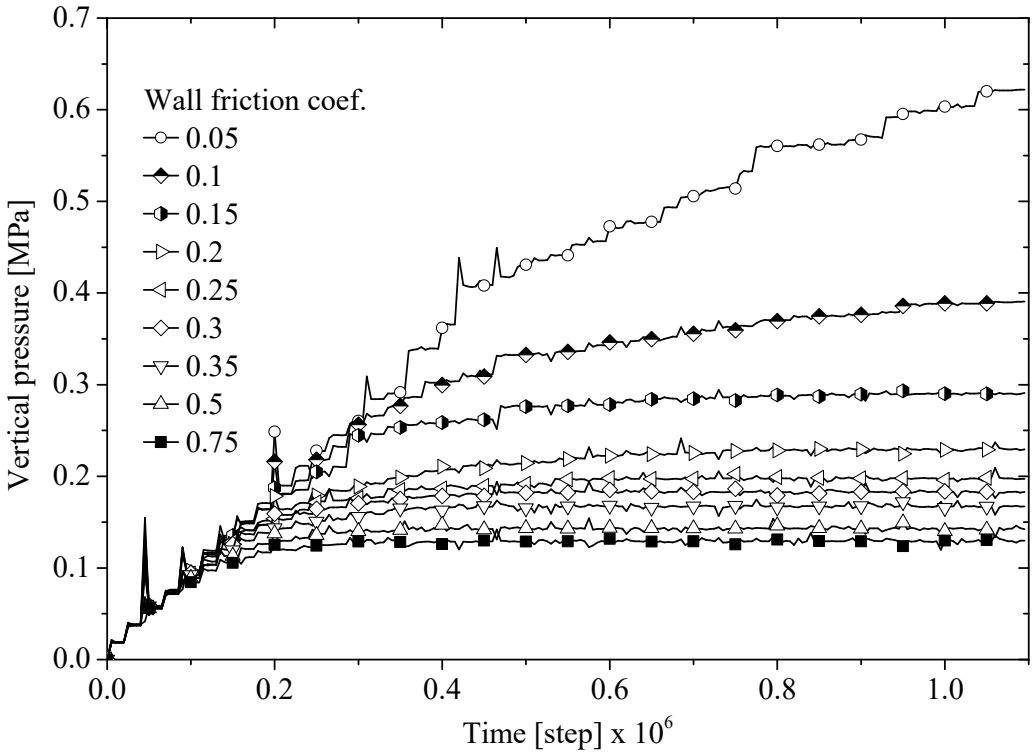

Fig. 7 Development of vertical pressure on plug during backfilling process for different wall friction coefficients; inter-particle friction coefficient = 0.75; upscaling factor = 7.0.

Higher wall-particle friction generates lower vertical pressure and the pressure distribution curves level off earlier. Greater values of friction coefficient produce more pronounced pressure fluctuations. Nevertheless, for wall-particle friction coefficients greater than 0.5, the vertical pressure on the plug at the bottom and the normal pressure at the shaft wall are almost identical. The variations of maximum pressure for different wall-particle friction coefficients are shown in Fig. 8. It can also be seen, that for the values of wall-particle friction coefficient greater than 0.5, the maximum pressure obtained are almost the same.

When we assume that the particle-particle contact friction is equal to wall-particle contact friction and equal to contact friction obtained from calibration, i.e. friction coefficient is 0.75, the depth of stress/pressure saturation is located at about 10 m. This depth is very close to measurement results obtained from a real shaft backfill project as reported by Breidung (2002). This indicates that the assumption about wall friction is quite reasonable.

We proved that the saturation pressure on shaft bottom can be predicted by Janssen's model. However, using Janssen's model of stress distribution, once the saturation or maximum stress is fitted, the data obtained deviate from fitted curve at certain depth. On the one hand pressure or stress at this certain depth is underestimated, on the other hand saturation depth is overestimated (see dashed curves in Fig. 9.

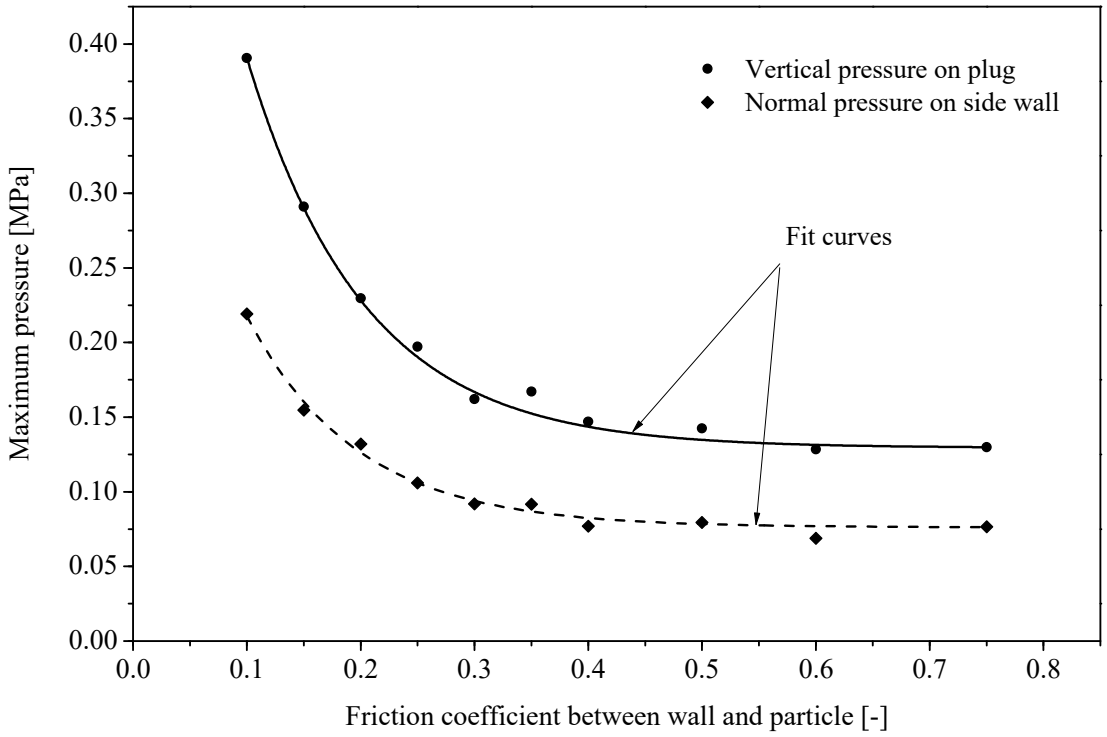

Fig. 8 Variation of maximum pressure calculated for different values of wall friction coefficient; inter-particle friction coefficient = 0.75; upscaling factor = 7.0

It can be clearly seen in Fig. 9, to a certain extent, the pressure on the shaft bottom is a linear function of depth. This gravitational overburden behavior is not well obtained by Janssen's model. Therefore, a new model is proposed to fit the results of numerical simulations, in which a depth range including the gravitational overburden effect, is invoked as follows:

$$\text{For } z < z_0,\ \sigma_v = \gamma z$$
$$\text{For } z > z_0,\ \sigma_v = \sigma_{z,0} + (\sigma_{z,max} - \sigma_{z,0})\left(1 - e^{\frac{2(z-z_0)\mu_w K}{R - z_0 \mu_w K}}\right). \quad (6)$$

Where:

- R is the radius of the cylindrical shaft
- z_0 is the depth of gravitational overburden zone
- $\sigma_{z,0} = \gamma z_0$ is the bulk density of the backfill used in the analytical calculations; based on the average porosity of the filling column obtained from the numerical model.
- $\sigma_{z,max}$ is the maximum/saturation vertical stress, $\sigma_{z,max} = \frac{\gamma R}{2\mu_w K}\left(1 - e^{\frac{-2\mu_w K z}{R}}\right)$.

In the new proposed model (Eq. 6), there are two unknown parameters, i.e. K and z_0. The physical explanation for introducing z_0 is that the contact friction between ballast

and shaft wall in the zone near the surface is not mobilized. Hence, this zone is not influenced by friction of shaft wall. In other words, this zone of ballast is not supported by the shaft side walls and the vertical stress is produced by pure gravitational load. z_0 and K are dependent on the relative size of shaft diameter to the size of ballast particles. The K value is the same for both Janssen's model and the new model. Practically, it was found that K is close to the coefficient of lateral active earth pressure, K_a, in theory of Rankine (1857):

$$K_a = \frac{1 - sin\emptyset}{1 + sin\emptyset} \tag{7}$$

The solid curve in Fig. 9 is a best fit for the simulation data using the new formula. The fitting parameters for this curve are K = 0.23 and z_0 = 4 m. By applying a similar approach we obtained the variation of stress saturation depth z_0 versus up-scaling factor as shown in Fig. 10. It is found that the value z_0 tends to increase linearly with particle size.

It can be seen that the new model captures closer the variation of vertical pressure with depth than the conventional model of Janssen. The new model allows a significant better prediction of the depth of stress saturation and describes the stress profile within this certain zone in a more realistic manner.

A series of simulations were performed with different grain size (up-sacling). Applying Janssen's model to this problem, the parameter K should be calibrated depending on the up-scaling factor. Calibrations of K for different up-scaling factors show that K decreases with increasing up-scaling factor (see Fig. 10a). Meanwhile, by applying a similar approach, we obtained the variation of stress saturation depth z_0 versus up-scaling factor as shown in Fig. 10b.

The pressures can be determined accurately by combination of numerical simulations and application of the new analytical model. Values of K and z_0 can be obtained by extrapolation. Then the pressure distribution can be predicted for real size of ballast, that means no upscaling or upscaling factor = 1.0. (see Fig. 11). This prediction is confirmed by in situ measurements of two real backfilling projects as reported by Breidung (2002).

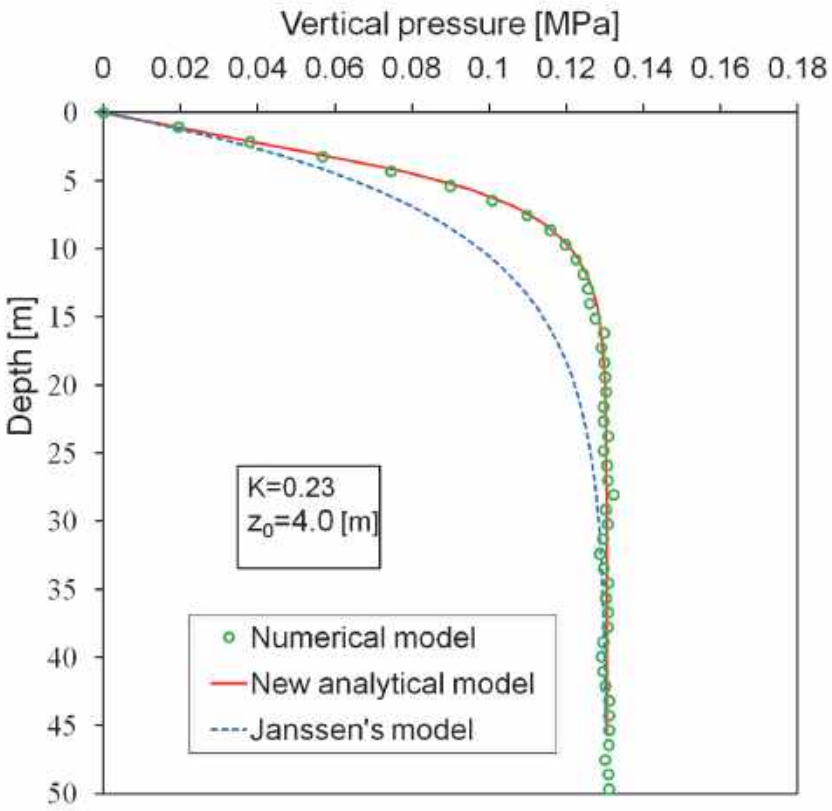

Fig. 9 Vertical pressure on shaft bottom as a function of depth and fitting curves by two models: conventional Janssen's model and new proposed model. Upscaling factor = 7.0, particle type yad_4, inter-particle friction coefficient = 0.75, wall friction coefficient = 0.75

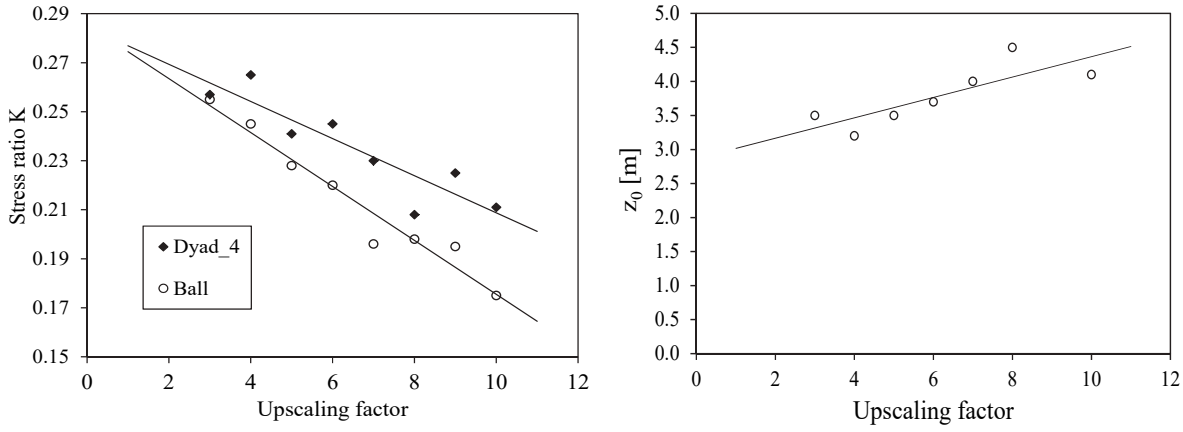

Fig. 10 Value of K and z_0 vs. grain size, upscaling factor for clump dyad_4

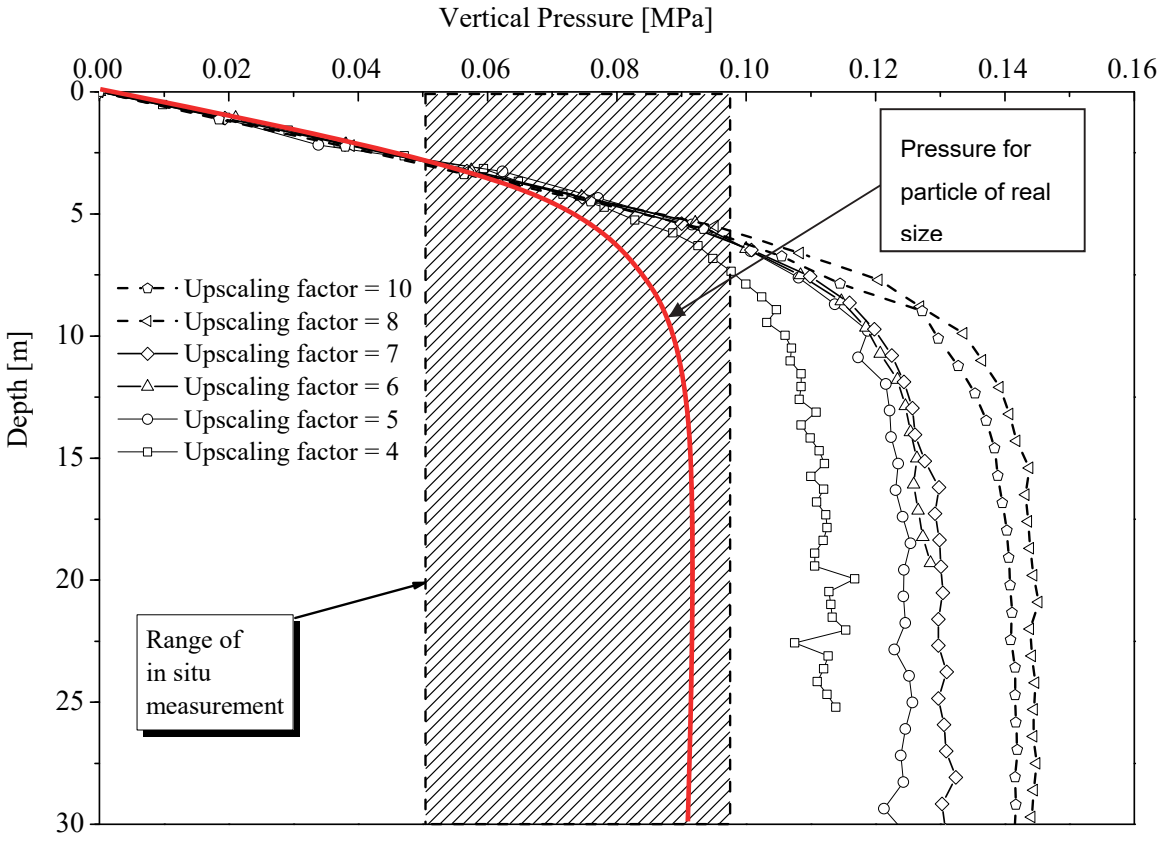

Fig. 11 Vertical pressure obtained from simulations with clump Dyad_4 for different up-scaling factors, wall friction coefficient = 0.75; inter-particle friction coefficient = 0.75.

4.6.2 Behavior of backfill column under additional load

Simulations were performed to evaluate the settlement and stability of ballast under additional loading on top of the ballast column. Such an additional load can be created by the weight of a sealing plug and/or a water column or other filling material above the plug. A top layer of 2 m thickness was selected and used as loading mass by increasing the density of those particles in such a manner that the desired mass (load) is created. A number of particles at different specified positions were selected as gauge particles to measure their displacements. The relations between pressure and amount of settlement were obtained during the loading process. Based on this curve, the peak pressure at which the backfill column becomes instable is determined. It was observed that after the load exceeds the peak value the whole backfill column sinks rapidly (Fig. 13). The whole system fails, and the settlement of loading mass reaches a large value while the material rushes into the cavern.

For example, Fig. 12 shows vertical stress depth profiles for a ballast column under different additional vertical load q on top of the column. The settlement versus load can be predicted as shown in Fig. 14. Two stages of the load-settlement curve can be observed. In the first stage, the column is compressed elastically and the load-settlement curve is almost linear. In the second stage, the backfill starts to move downward and the load-settlement curve becomes nonlinear. The column can reach a new stable condition after certain movement. In this stage, the whole column moves

and the backfill runs into the horizontal workings. The backfill might also totally fail and the settlement at the top of the column can reach very large values. Loading on top of the backfill column was simulated for a number of configurations, i.e. different height of backfill column and different wall friction. Hence, different scenarios can be predicted.

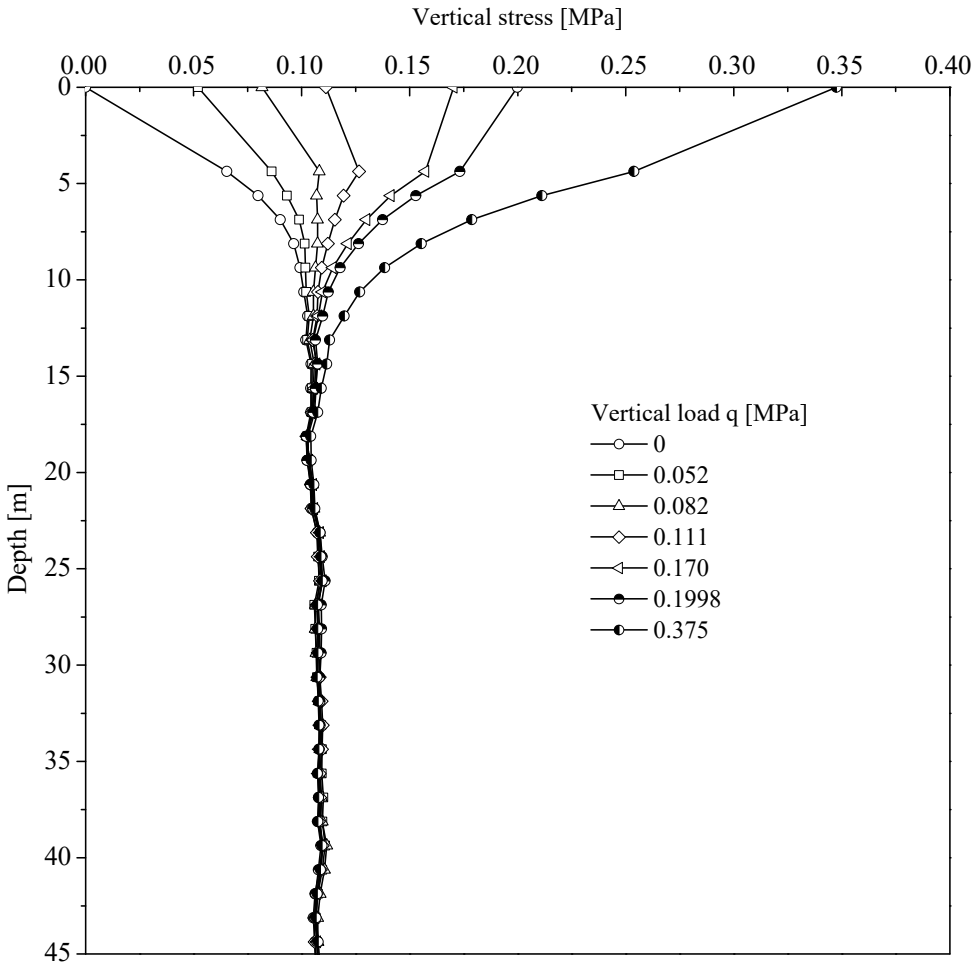

Fig. 12 Distribution of vertical stress under different additional vertical load, wall-particle friction coefficient = 0.5, inter-particle friction coefficient = 0.75.

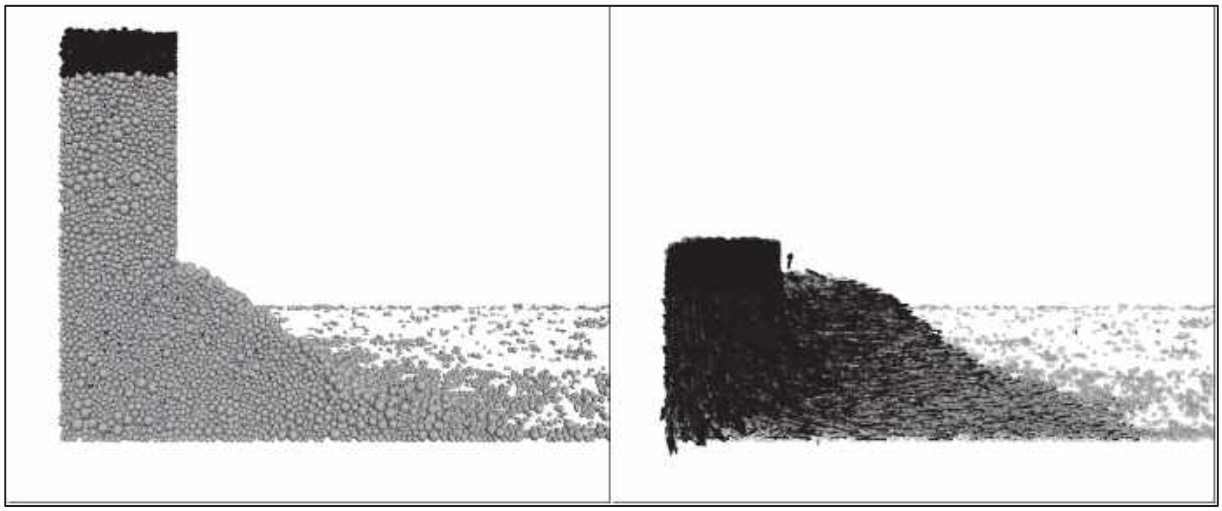

Fig. 13 Behavior of backfill with original height of 8 m from bottom under vertical loading (left: at the beginning, right: close to the final state after collapse).

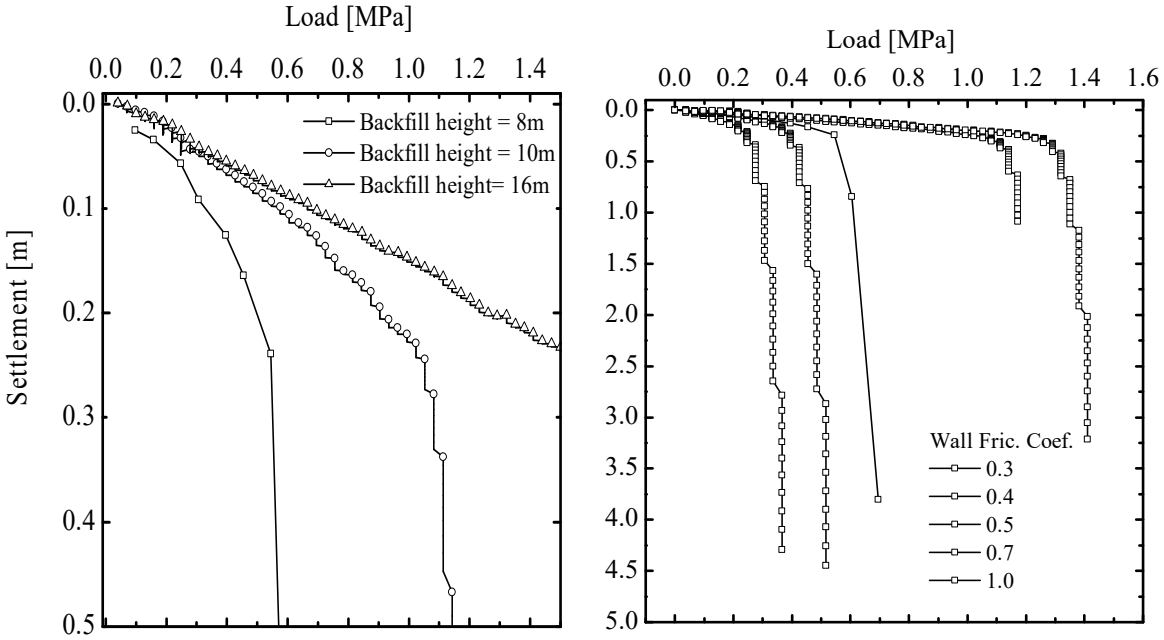

Fig. 14 Settlement of top of backfill under loading: (left) for different column height; (right) for column height of 8 m and different values of wall friction. Shaft is connected to cavern of 4 m height.

5. Conclusions

In this paper, experimental and numerical studies are presented to investigate the behavior of shaft backfilling. The shaft backfilling problem was successfully simulated by PFC^{3D} considering the dynamic filling process and the behavior of ballast column after filling under different loading conditions. The method of gravitational packing ('rainfall method') was used to avoid local high and unrealistic contact forces inside the backfill domain and to duplicate realistic porosity and packing structure. Symmetry was considered to reduce computational effort. Consequently, computational time was

reduced remarkably. The results of numerical studies were compared with analytical solution according to classical Janssen's silo theory. Following conclusions can be drawn:

- It was proven, that DEM is a suitable tool to simulate shaft backfilling with granular material.
- The developed procedure can be used for dimensioning of shaft backfilling incl. connected drifts.
- The influence of different micromechanical parameters on the backfill behavior is documented.
- Influence of up-scaling and symmetric models (reduction of calculation time) is documented.
- A new modified Janssen's silo model is proposed.
- Simulations reveal that under certain conditions settlements/failure of ballast columns have to be expected.

For further study, some of following issues shall be considered:

- Breakage of ballast grains should be incorporated into the modelling, for instance by applying the cluster logic.
- Behavior of the backfill should be investigated under flooding conditions.
- The convergence of the shaft should be modelled for long term considerations.
- The behavior of ballast backfill and sealing elements under seismic loading condition should be investigated.

Reference

Breidung, K. P. (2002). Forschungsprojekt Schachtverschluss Salzdetfurth Schacht II. Bad Salzdetfurth, Hannover.

Dun, R. B. (1982). The treatment of the disused mine shafts and adits. N. C. B. Mining Department. London.

Hollmann, F., et al. (2009). Zum Verhalten von Schachtfüllsäulen beim Ersaufen eines Grubengebäudes. ALTBERGBAU-KOLLOQUIUM Leoben

Hustrulid, W. A. and R. L. Bullock (2001). Underground Mining Methods - Engineering Fundamentals and International Case Studies, Society for Mining, Metallurgy, and Exploration (SME).

Itasca (2008). PFC^{3D} Version 4.0 - Manuals. Minneapolis, Minnesota, Itasca Consulting Group, Inc.

Janssen, H. (1895). "Versuche über Getreidedruck in Silozellen." Zeitschrift des Vereines Deutscher Ingenieure 39: 1045-1049.

Lecomte, A., et al. (2012). Case studies and analysis of mine shafts incidents in Europe. 3. International Conference on Shaft Design and Construction (SDC 2012), Londres, United Kingdom.

Nguyen, Q.T. (2016): Shafts backfilled with ballast: Stability and settlement predictions via DEM simulations, Veröfftl. Institut für Geotechnik (Ed. H. Konietzky), Heft 2016-1

Pipatpongsa, T. and S. Heng (2010). "Granular Arch Shapes in Storage Silo Determined by Quasi-static Analysis under Uniform Vertical Pressure." Journal of Solid Mechanics and Materials Engineering 4(8): 1237-1248.

Rankine, W. J. M. (1857). "On the Stability of Loose Earth." Philosophical Transactions of the Royal Society of London 147: 9-27.

Salmon, R., et al. (2015). Mine shafts: improving security and new tools for the evaluation of risks (MISSTER). Luxembourg European Commission.

Tuấn, N. Q. and H. Konietzky (2015). Simulation von Schottersäulen mittels DEM. 20. Fachtagung Schüttgutfördertechnik. Magdeburg. Schüttguthandling im Zeitalter von Industrie 4.0.

Rock slope stability considering surface load

Standsicherheit von Felsböschungen unter Berücksichtigung von Oberflächenlasten

Hang Lin , Hu Wang , Ping Cao
(School of Resources & Safety Engineering, Central South University, Changsha, Hunan, 410083, China)

Abstract

Under surface load, the failure mode of a 3D rock slope differs from that under pure gravity load; however, it is controlled by both, surface and gravity loads together. This study analyze the stability of a 3D mine pit slope under surface load, including the variation of the cohesion and friction angle of rock mass and the value of surface load, via two stability analyses, namely, the strength reduction method and the load increment method. Results demonstrate that failure mode determination of the slope under surface and gravity load is critical, and stability is improved by decreasing X-component load and by increasing Y- and Z-component loads. The three coordinate direction component loads can be changed by adjusting the structure of the foot; thus, this procedure can effectively improve the stability of slope under surface and gravity loads. This study confirms the practicability of the load increment method. These results can provide a reference for design and stability analysis of 3D slopes, particular for slopes under surface loads.

Zusammenfassung

Unter Oberflächenbelastung versagt eine numerisch simulierte 3D-Felsböschung nicht wie unter reiner Gravitationslast, sondern das Versagen wird durch die Kombination von Oberflächen- und Gravitationslast kontrolliert. Diese Arbeit analysiert die Stabilität einer 3D-Tagebauböschung unter Oberflächenauflast, einschließlich der Variation von Kohäsion und Reibungswinkel des Gebirges und der Magnitude der Oberflächenauflast, anhand von zwei Stabilitätsanalysen. Diese sind die Strength- Reduction-Method und die Load-Increment-Method. Die Ergebnisse zeigen, dass die Bestimmung des Versagenszustands der Böschung unter Oberflächen- und Gravitationslast kritisch ist. Die Stabilität wird durch Verringerung der Last in X-Richtung sowie Erhöhung der Last in Y- und Z-Richtung verbessert. Die drei Raumrichtungskomponenten der Auflast können durch Anpassung der Struktur des Sohlenfußes geändert werden. Durch dieses Vorgehen kann die Stabilität der Böschung unter Oberflächen- und Gravitationsauflast wirksam verbessert werden. Diese Untersuchung kann als Empfehlung für Planungs- und Stabilitätsuntersuchungen von 3D-Böschungen, insbesondere unter Berücksichtigung von Oberflächenlasten, dienen.

1 Introduction

Slope stability analysis methods, mainly 2D limit equilibrium method and strength reduction method (SRM), are based on plane strain models and have a clear concept with simplified calculation and well-developed theories [1 - 3]. However, the 2D slope stability analysis method cannot properly model the true 3D characteristics of a landslide [4]; and, the results are derived with a conservative solution. Numerous 3D stability analyses that use limit equilibrium method and SRM can be found in the literature [4 - 8]. The 3D limit equilibrium method remains limited to simple problems because of its difficulty in satisfying equilibrium conditions and determining slip surface [9]. And moreover, studies on slope stability analyses mainly focus on slope stability problems under gravity load, given that slope rock mass often shows a tendency to slide down along a potential slip surface [10]. In practical engineering, a slope is usually under transverse, concentrated, or surface load [9 - 12]. Lin et al [10] analyzed the stability of a slope under the surface load, and some valuable results were obtained.

Under surface load, the potential failure mode of the 3D rock slope does not slide down like under pure gravity load; however, it is controlled by surface and gravity loads together. Therefore, the potential failure mode and influence factor of stability analysis must be determined. This study analyzes the stability of a 3D mine pit slope under surface load via two stability analysis methods, namely, SRM and load increment method (LIM). Similarities and differences between these two methods were demonstrated. The stability analyses illustrates the governing factors of potential failure; thus, it provides a reference for design and stability analysis of 3D slopes, particularly for slopes under surface load.

2 Modeling and Methodology

2.1 Modeling

A numerical model was established, including the ground surface and the underground geotechnical materials by Dimine, via the generated ground surface model and drill hole data. Then, ANSYS was used to generate mesh, and the information of nodes and elements was transformed to FLAC3D for calculation. The numerical calculation model is shown in Fig. 1. The details are given in the work by Lin and Zhong [10]. The specific physical and mechanical parameters of the geotechnical materials were obtained through site investigation, as shown in Table 1.

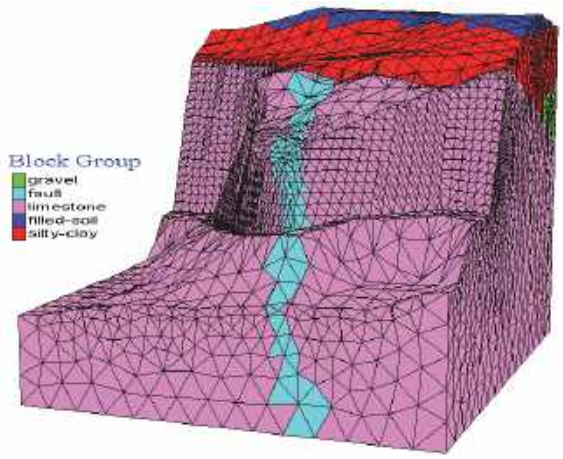

(a) Overall model

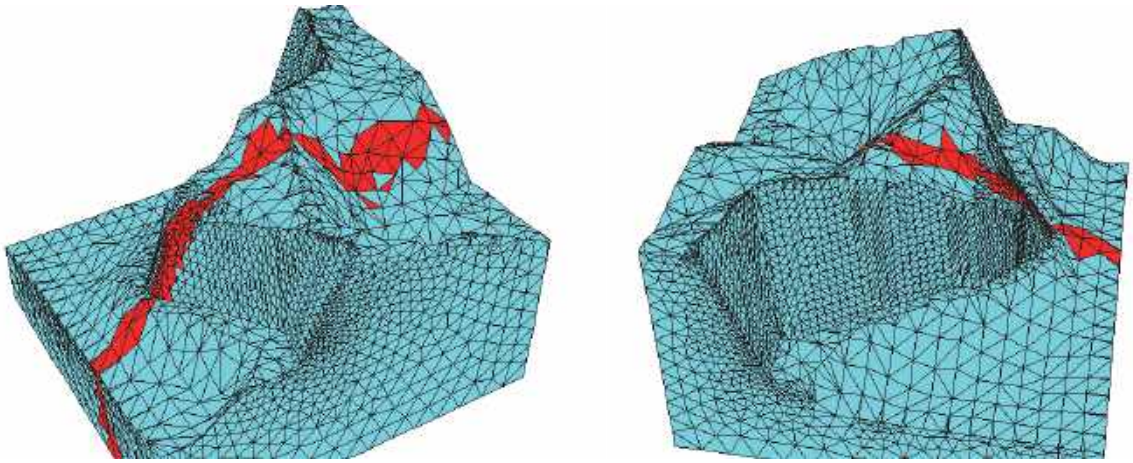

(b) Limestone distribution

Fig. 1 3D numerical calculation model of the slope

Table 1 Calculation parameters

	Poisson's ratio	Tensile strength[kPa]	Unit weight γ [kN/m^3]	Elastic modulus E [MPa]	Friction angle Φ [°]	Cohesion c [kPa]
filled soil	0.4	0	18.8	2.5	10	8
silty clay	0.38	0	19.0	9.0	19	50
gravel	0.3	0	20.0	15.0	32	0
limestone	0.22	1400	26.5	90000	36	300

2.2 Design Load and Boundary Conditions

The designed load value of foot A (Table 2) and the load distribution (shown in Fig. 2) indicate that the foundation of foot A was 3 m high. The total force from foot A was divided by the number of nodes along the loading places, and then the applied load was set in the calculation model with an initial height of 3 m, as shown in Fig. 2. The model was fixed in all directions at the bottom and side boundaries, and the gravitational load was considered as initial load. The Mohr–Coulomb criterion used in FLAC3D was based on the principal stresses and strains, which were the three components of the generalized stress vector and three corresponding strains for this model. A composite Mohr–Coulomb criterion with tension cutoff was used to describe the failure of the material.

Table 2 Load of foot A

Load (kN)		
X	Y	Z (direction of gravity)
641184	282135	306240

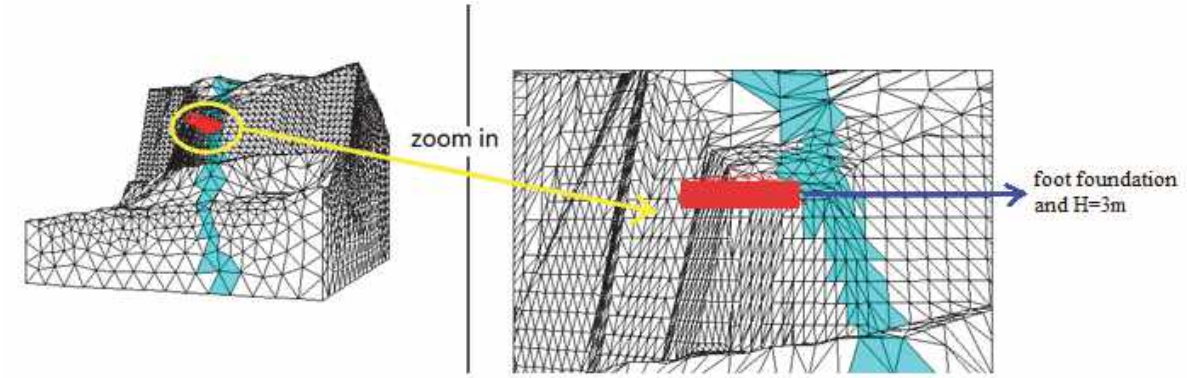

(a) view 1

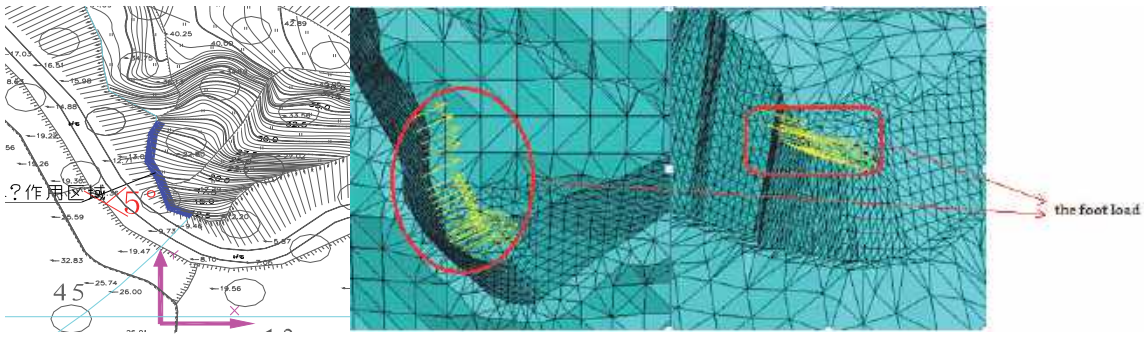

(b) view 2

Fig. 2 Applied load on the slope in the numerical model.

2.3 Methodology

In relevant lectures, factor of safety (FOS) was used to reflect the stability of slope. When FOS < 1, the slope was in an unstable state and for FOS = 1, the slope was in a critical state and when FOS > 1, the slope was stable. However, FOS could be obtained through many ways [3, 13, 14]. The two methods used in this study are introduced in detail as follows.

SRM

The SRM, which was proposed by Zienkiewicz and Humpheson [15] and developed later by Griffiths and Lane [2] and Matsui and San [16], is a primary finite element method (FEM) of slope stability analysis. The perfect application of SRM is Mohr-Coulomb criterion, which is one of the most widely used models in geotechnical engineering. In FEM calculation processing, c_0 and ϕ_0, which are the actual cohesion and friction angle of the slope, respectively, are divided by coefficient *K*. By changing *K* continuously until the slope is at a critical state of failure and FOS = 1 (as shown in Fig. 3a), corresponding c^{cr} and ϕ^{cr} are obtained. Then, the safety factor of the slope can be expressed as

$$F = \frac{F}{F^{cr}} = \frac{c^0}{c^{cr}} = \frac{\tan\phi^0}{\tan\phi^{cr}}, \tag{1}$$

where F^{cr} = 1, which corresponds to the critical state of slope.

LIM

The slope is under the load of the foot A; thus, we can make the slope reach a critical state by changing the load to determine FOS, which is similar to the tolerable safety factor. Calculation methods of LIM are summarized as follows: First, upper bound K1, lower bound K2, and precision η are given. Second, the load is multiplied by a coefficient (K1 + K2) / 2, and the numerical calculation starts. Third, the upper and lower bounds are reduced by dichotomy until the slope reaches a critical state (FOS = 1) and K2 − K1 < η (as shown in Fig. 3b). By this time, the FOS can be expressed as

$$\mathrm{F} = \frac{Load}{Load^{cr}}, \tag{2}$$

where $Load^{cr}$ is the load at the critical state of failure.

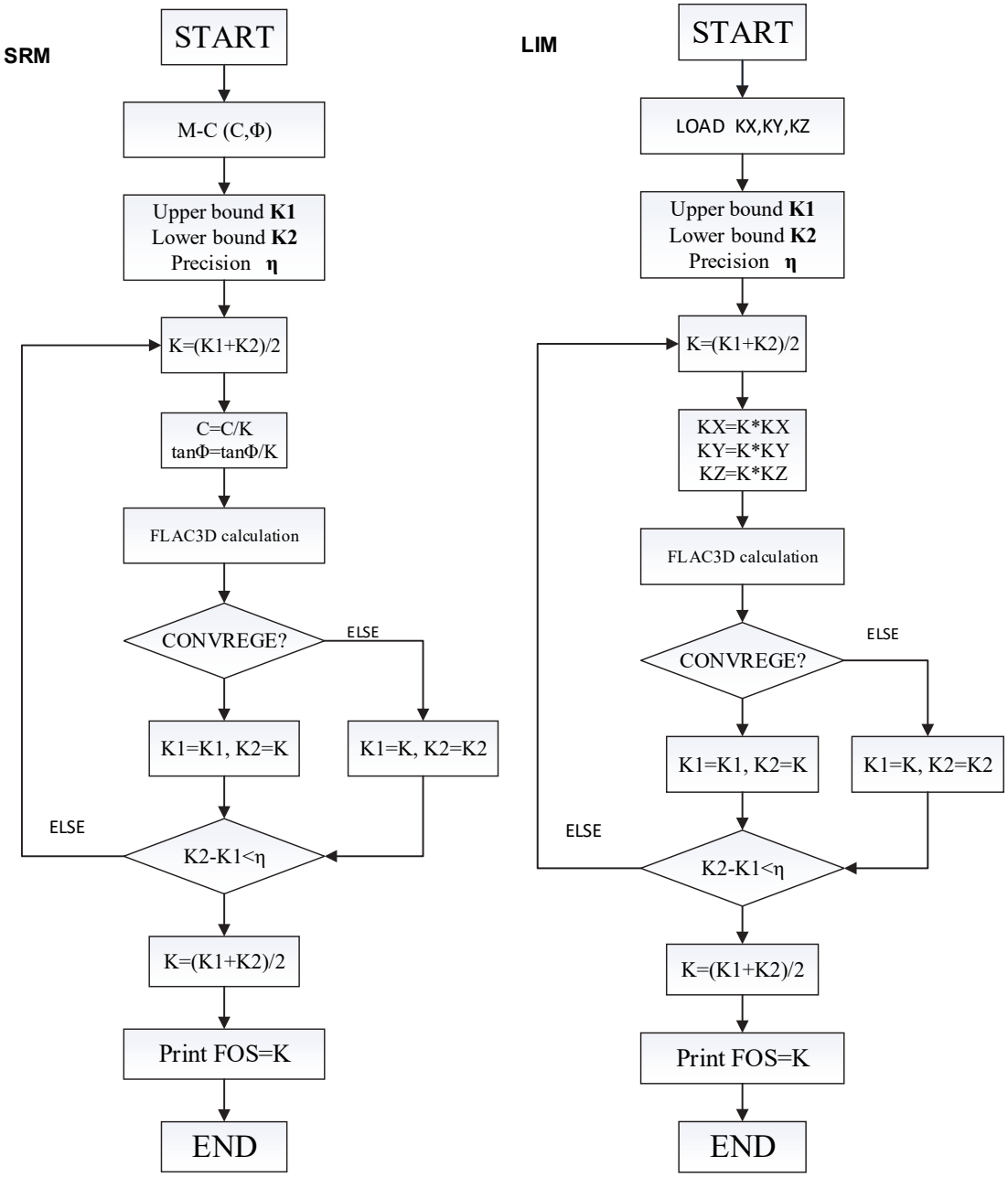

(a) **SRM** (b) **LIM**

Fig. 3 Flow diagram of SRM and LIM method

3 Results and Discussion

3.1 Slope stability analysis

The slope is in a relatively stable state under the initial gravitational load, with FOS reaching 2.53. However, when foot load is applied, the FOS of the SRM and LIM decreases significantly to 0.71 and 0.52, respectively, thereby indicating that the slope cannot resist the foot load.

As shown in Fig. 4a for SRM, the jutting rock mass in the foot A region is eventually destroyed by shearing force, and the general direction of displacement tendency is along the foot loading direction. The jutting rock mass under the foot load encompasses an upward sliding tendency. Tensile and shear failures occur in most parts of the jutting rock mass, as shown in Fig. 4a. The overall lateral shear failure occurs in the rock mass. For LIM, the displacement tendency and the plastic zone of the rock mass under the foot load show similar behavior, whereas the failure area is somewhat reduced (Fig. 4b).

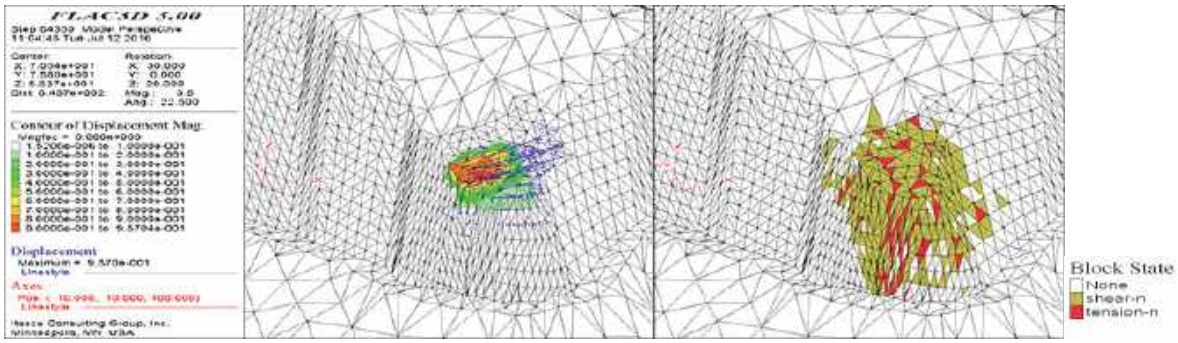

(a) **SRM**

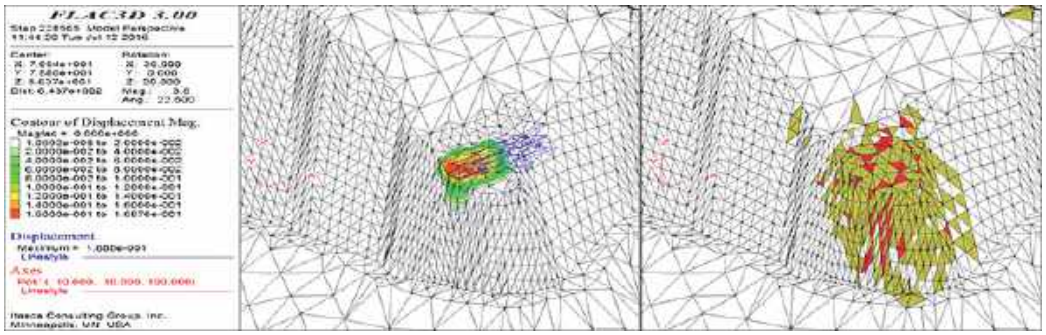

(b) **LIM**

Fig. 4 Rock mass displacement tendency and failure region distribution of the slope

3.2 Parametric study

According to the preceding analysis, the rock slope in the foot A region becomes unstable when the foot load is applied. Therefore, cohesion and friction angle of rock mass and the value of the surface load are changed to further study the influence of different factors on the rock slope of foot A and to provide a reference for the selection of reinforcement design schemes by obtaining the corresponding variation of the safety factor. Limestone is the main resisting material; thus, only its cohesion is changed.

Cohesion

Fig. 5 shows that the FOS of the slope at the foot A region changes with the variation of cohesion from 120 kPa to 1600 kPa. The FOS of the SRM and LIM reveals the same tendency, that is, the FOS increases with the increase of cohesion. The relations between cohesion and FOS are nearly linear and can be fitted by the linear equation with a high-fitting coefficient. If cohesion is < 700 kPa, then the slope is in an unstable state (FOS < 1). The FOS of LIM is less than that of SRM. Conversely, if cohesion is

> 700 kPa, then the slope is in a stable state (FOS > 1). However, the FOS of LIM is greater than that of SRM. The slope reaches a critical state when cohesion is approximately 700 kPa. The FOS of SRM and that of LIM are close to 1 and overlap at 1.

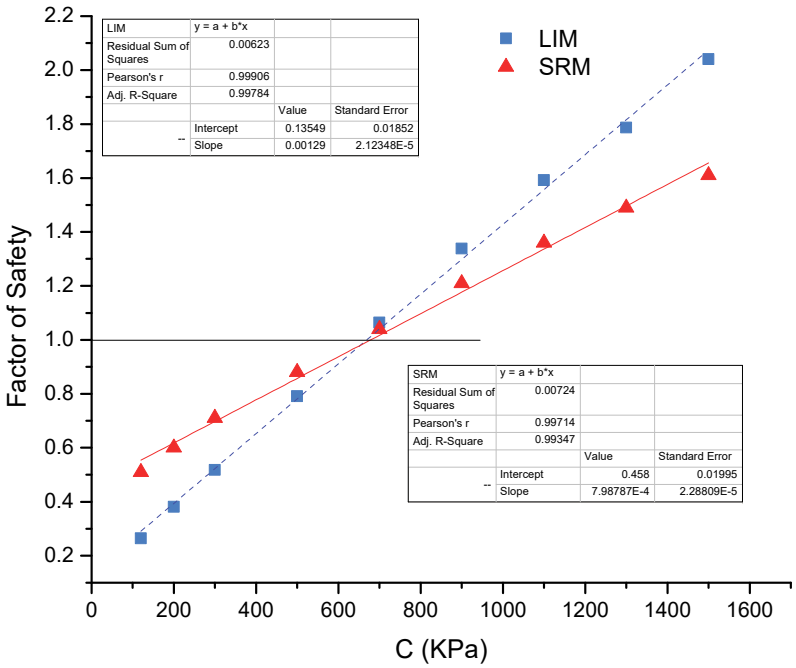

Fig. 5 Relation between FOS of the slope and cohesion

Internal Friction Angle

Fig. 6 shows that the FOS of the slope increases with increasing friction angle; however, it cannot reach 1, that is to say, the variation of friction angle is insufficient to bring the slope into a stable state. The FOS of SRM and LIM reveals the same tendency as the preceding analysis. The safety factor of the slope converges when approaching the critical state.

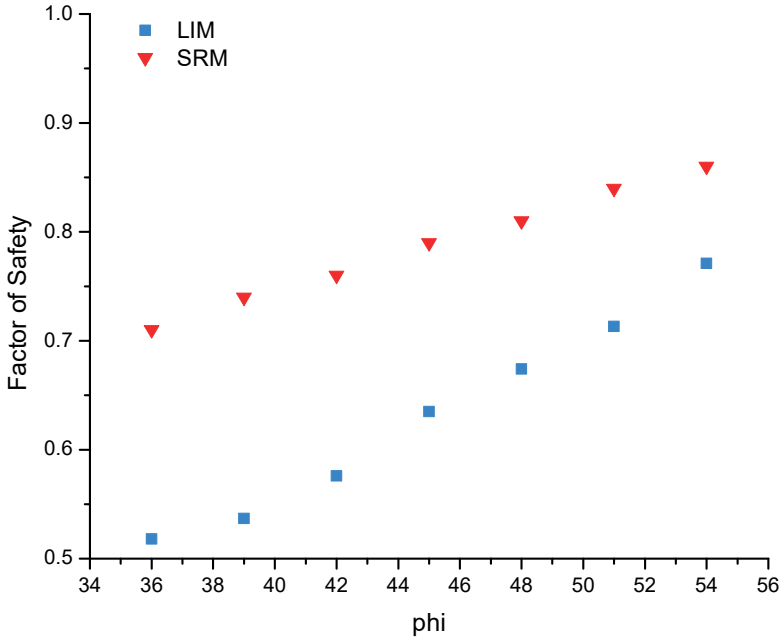

Fig. 6 Relation between the safety factor of slope and friction angle in degree

Loading

The three coordinate direction components of the foot load (Fx, Fy, and Fz) can be changed by adjusting the structure of foot A. The method used by Lin and Zhong [10] is the same method used in this study, and the variation coefficients of foot load in the X, Y, and Z directions are set as kx, ky, and kz, respectively.

The FOS of SRM and that of LIM initially increase and then decrease with the increase of kx (Fig. 7). If kx < 0.7, then the slope is in a stable state. For SRM, kx changes from 0.05 to 0.35, and the safety factor increases. However, when kx further increases, the safety factor decreases. Fig. 8a illustrates that the deformation of rock mass is along the resultant force of Y and Z direction loads when X direction load is small. As X direction load increases, the resultant force, which is influenced by it, restrains the failure mode; thus, the slope stability is improved. Finally, the failure mode is transformed into shear failure along X direction with the decrease of safety factor of slope. For LIM, the displacement tendency and plastic zone of rock mass (Fig. 8b) under the variation of X direction load have the same tendency. Similarly, when kx = 0.7, the results of SRM and LIM show that the slope is in a critical state (FOS = 1), and the safety factor of the slope converges when the critical state is approached.

Fig. 7 shows that the average displacement changes with variation of kx. In this study, the value of displacement is the number of nodes on the foot rock mass to which the load was applied after 5000 calculation steps. X-disp, y-disp, and z-disp represent the displacement of X-component, Y-component, and Z-component, respectively. Disp represents the total displacement. The displacements are close to 0 when FOS > 1, which corresponds to a stable state. When FOS < 1, the displacements present a continually increasing trend. Meanwhile, the total displacement value nearly coincides with the X-component displacement value, which indicates that the displacement is mainly controlled by X-component displacement. Thus the failure mode is controlled by X direction load, which matches the description of transformation of the aforementioned failure mode.

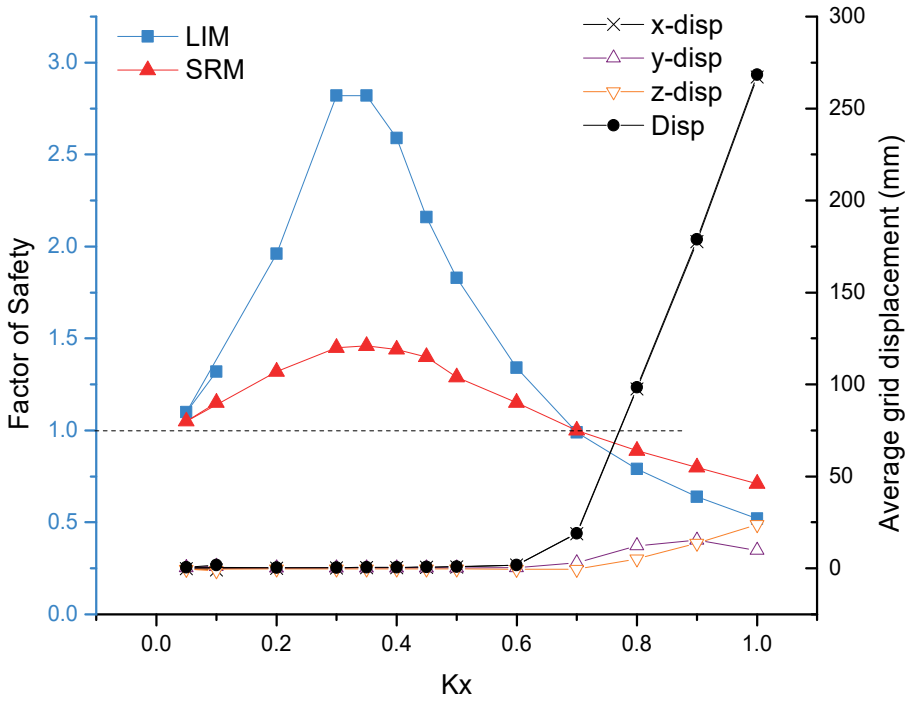

Fig. 7 Relation between safety factor of slope and kx (ky = kz = 1)

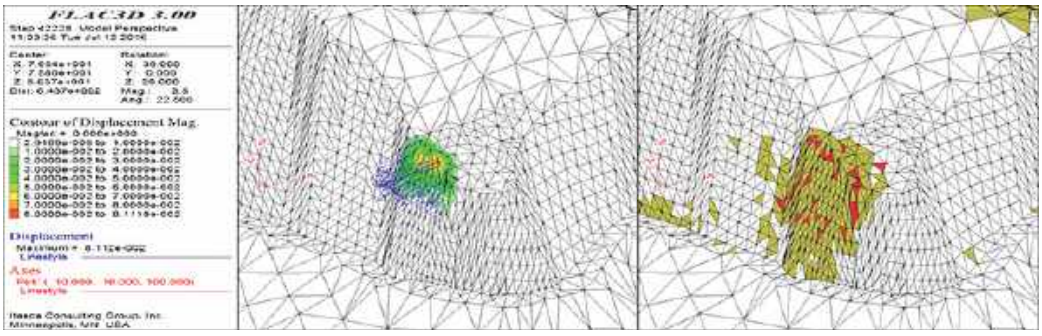

kx = 0.05

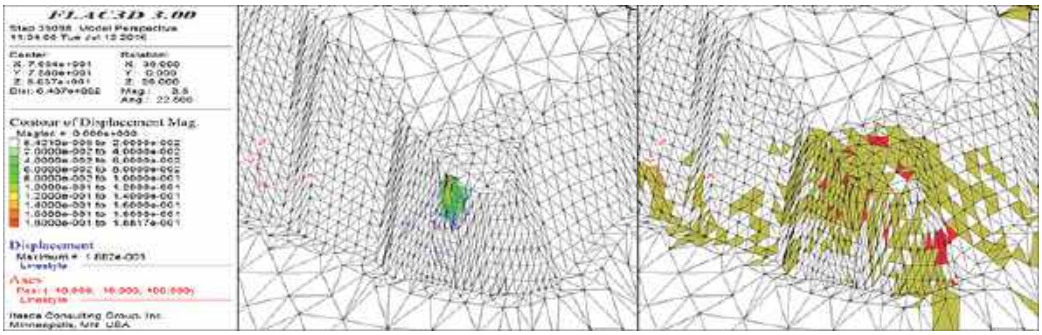

kx = 0.35

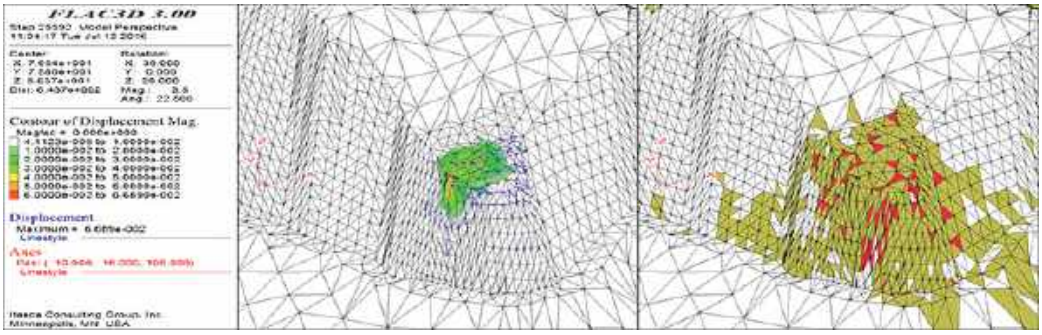

kx = 0.5

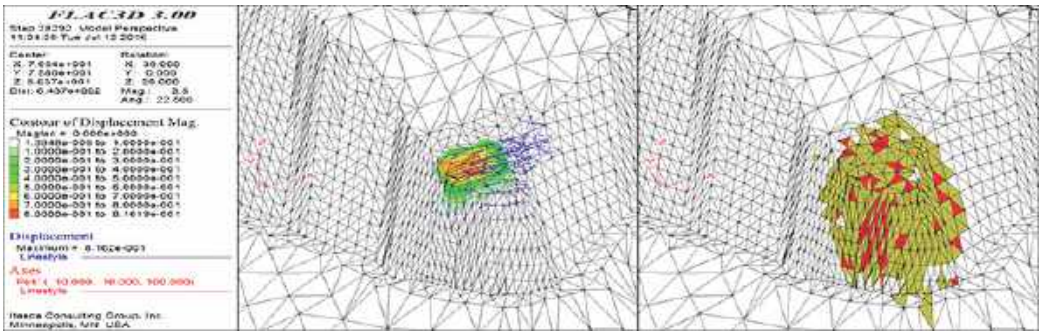

kx = 0.9

(a) **SRM**

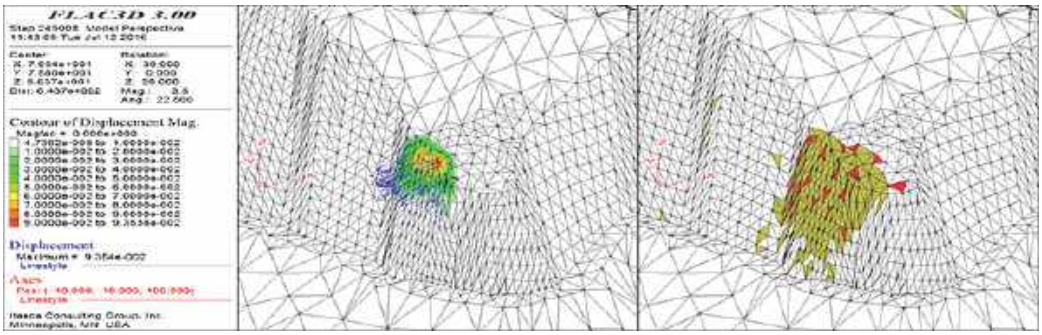

kx = 0.05

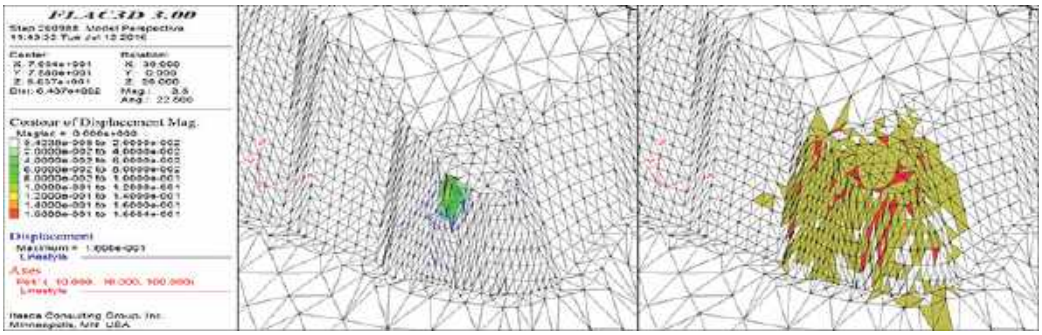

kx = 0.35

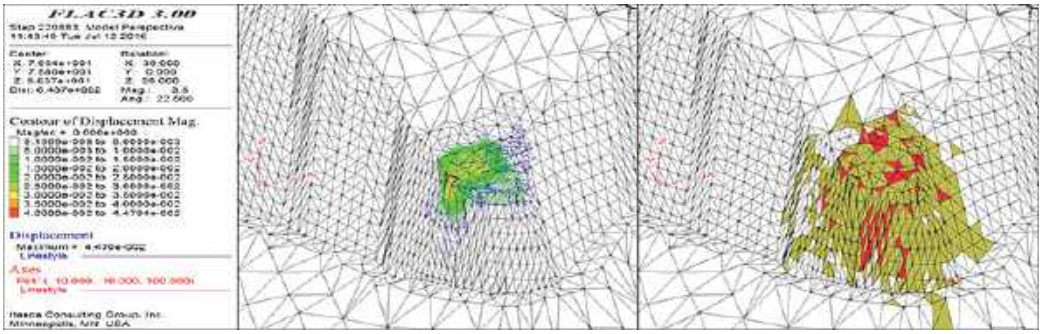

kx = 0.5

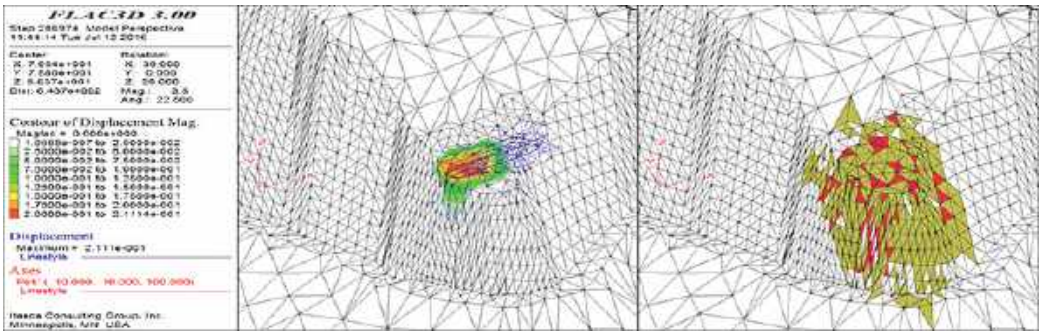

kx = 0.9

(b) **LIM**

Fig. 8 Total displacement and failure region with variation of kx (ky = kz = 1)

Fig. 9 shows the relationship between the safety factor of the slope and ky. The safety factor of the slope first increases and then decreases with the increase in ky; however, it remains smaller than 1. According to SRM (Fig. 9), when ky is within (0.1, 1), the safety factor of the slope is less than 0.7, which is the safety factor of the slope under the original state (ky = 1). The safety factor increases with the increase of ky from 0.1 to 2; however, it decreases when ky > 2. In this process, the failure mode of rock mass is changed from shear failure along the X direction, which is controlled by X-component and Z-component loads, to failure along the Y direction controlled by Y-component load (Fig. 10a). For LIM, the displacement tendency and plastic zone of rock mass (Fig. 10b) under the variation of Y direction load shows the same tendency. However, when ky > 3, the unstable region of LIM is smaller than that of SRM. This scenario may be a result of significant local instability with the increase of ky in LIM, and the unstable region is reduced. As a consequence, when ky is greater than 3, the gap between SRM and LIM is larger than that of ky less than 3.

The average displacement is not zero under ky variation, corresponding to a safety factor less than 1 (Fig. 9). The minimum average displacement corresponds to the maximum safety factor. When ky is increased from 0 to 3, the average displacement nearly coincides its X-component, thereby indicating that the displacement is mainly controlled by X-component load. When ky increased from 3 to 9, the average displacement nearly coincides its Y-component, thereby indicating that the displacement is mainly controlled by Y-component load. This conclusion is the same as the preceding analysis.

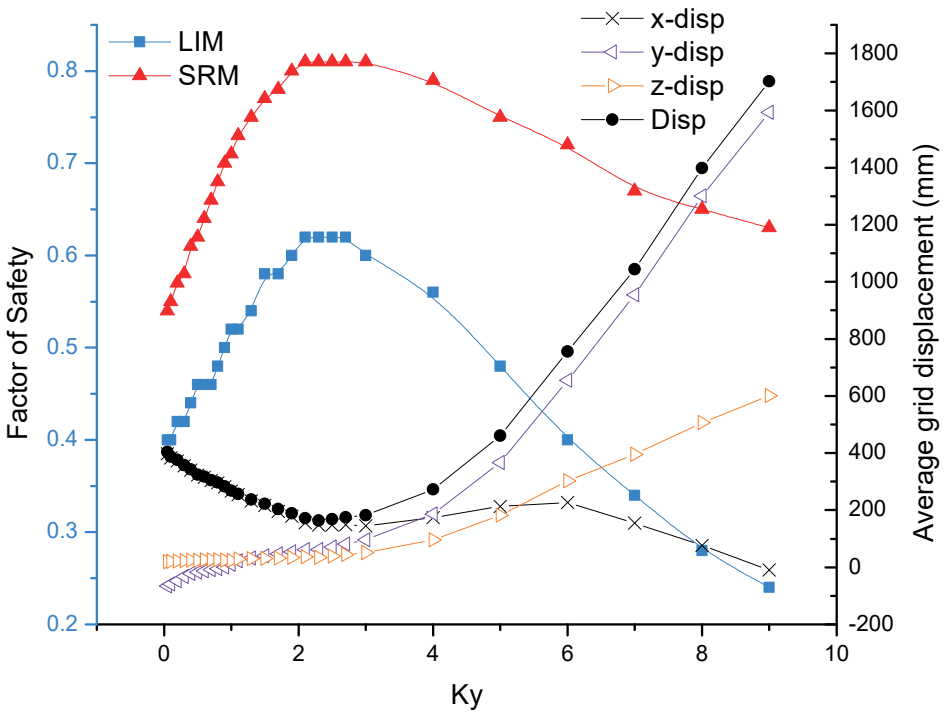

Fig. 9 Relation between safety factor of slope and ky (kx = kz = 1)

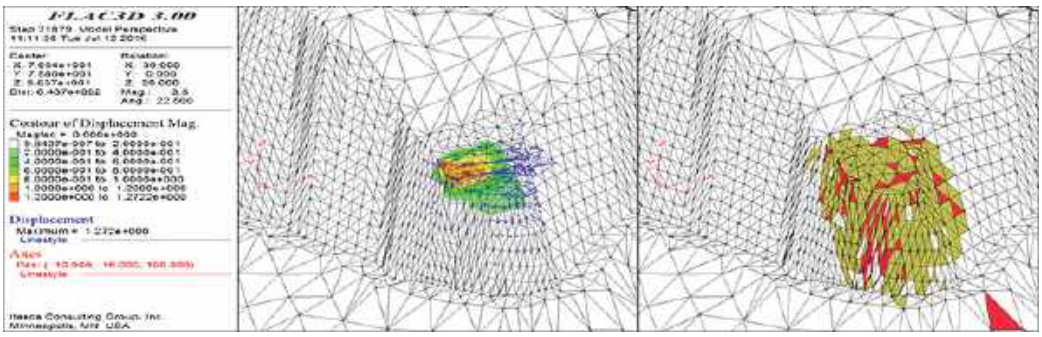

ky = 0.05

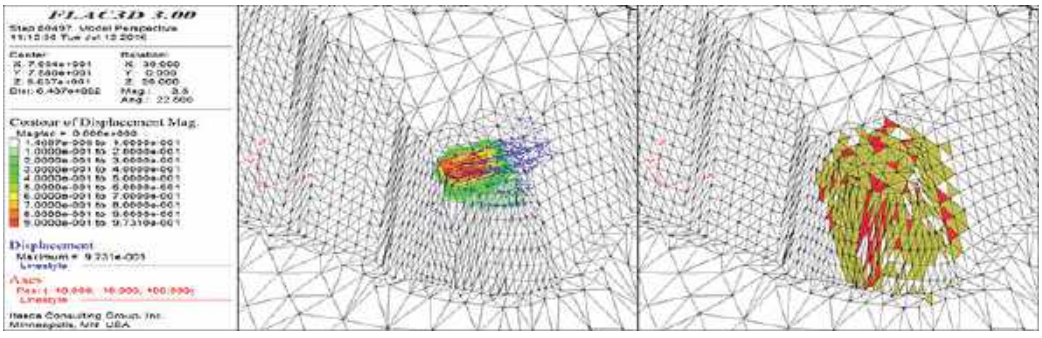

ky = 0.9

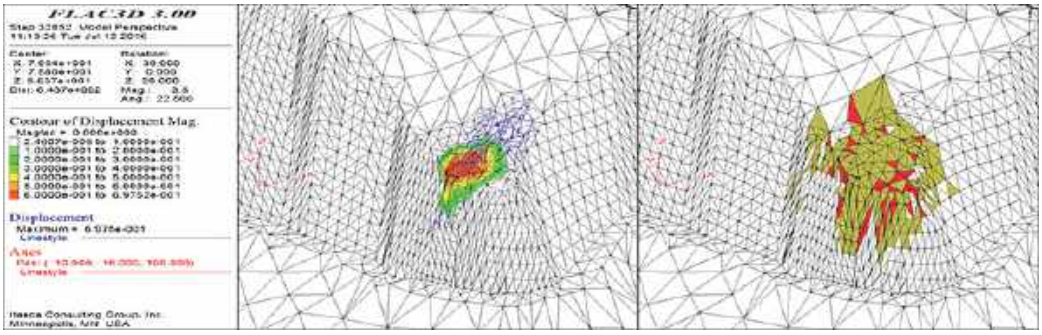

ky = 3.0

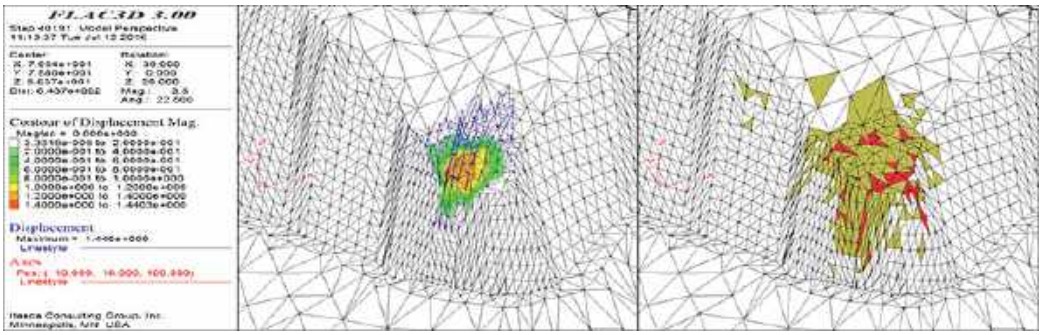

ky = 5.0

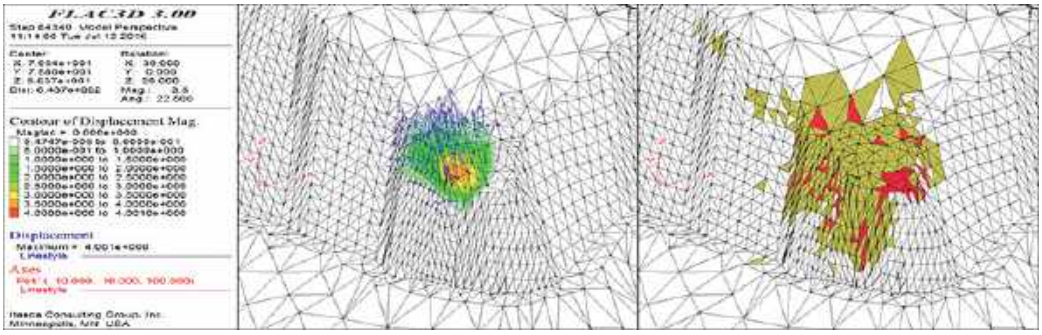

ky = 9.0

(a) **SRM**

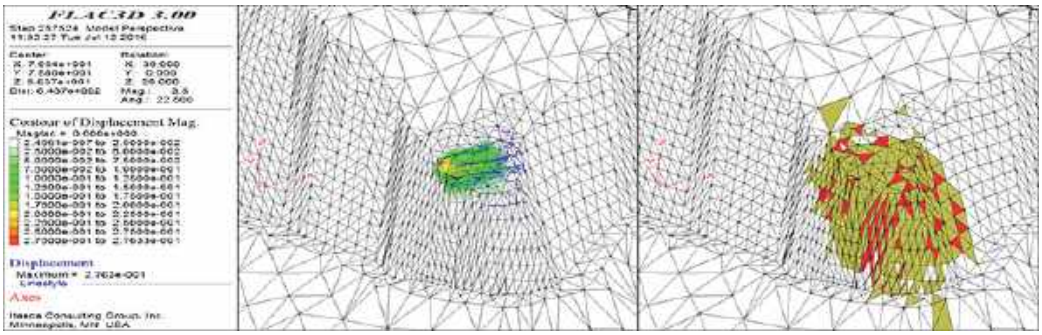

ky = 0.05

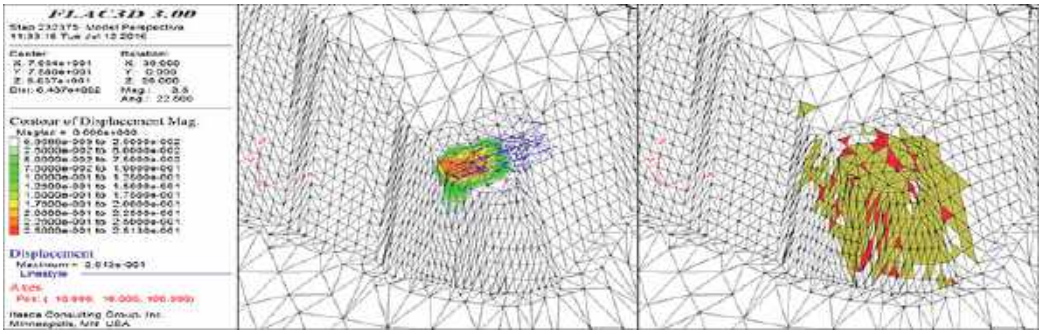

ky = 0.9

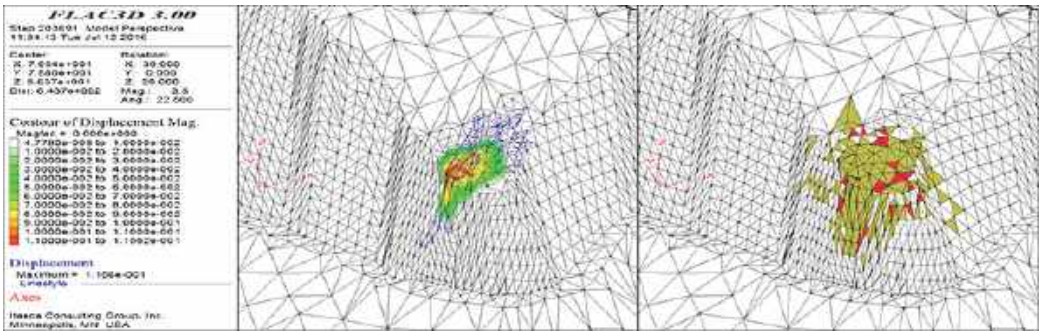

ky = 3.0

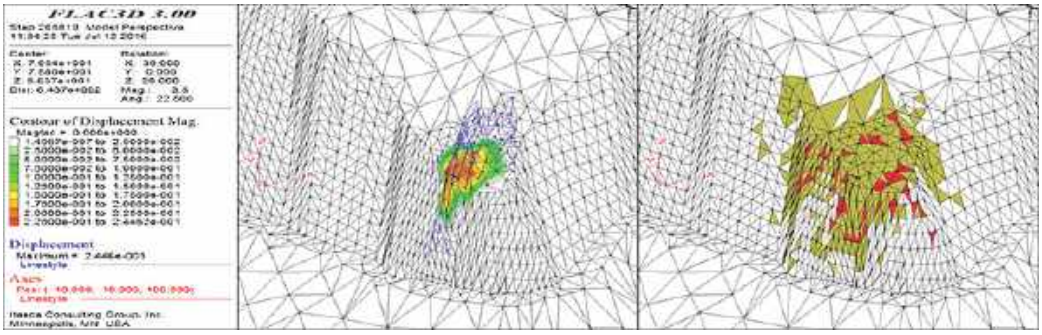

ky = 5.0

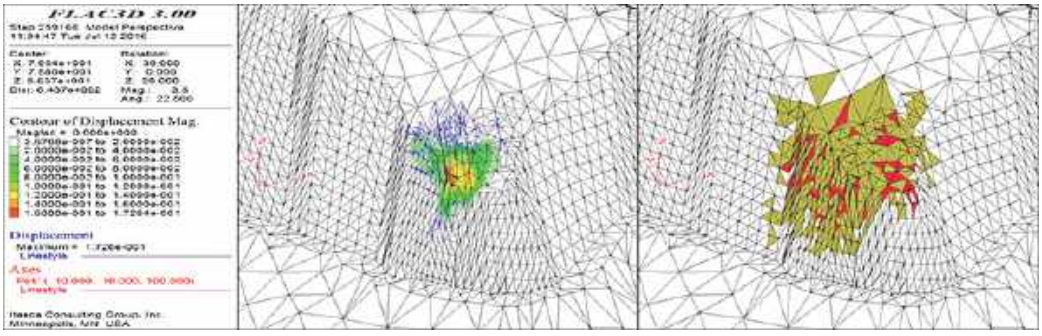

ky = 9.0

(b) **LIM**

Fig. 10 Total displacement and failure region with variation of ky (kx = kz = 1)

Fig. 11 shows the relationship between the safety factor of the slope and kz. The safety factor initially increases and then decreases with the increase of kz; however, it remains smaller than 1, and it reaches the maximum when kz = 2.5. When kz < 1, the safety factors of SRM and LIM are less than the safety factor of the slope under original

state (kz = 1), thereby indicating that the decrease of Z-component load reduces the stability of the slope. Fig. 12 illustrates that the failure mode of the slope changes when kz increases from 0.05 to 4.5. First, when kz < 2, the failure is controlled by X- and Y-component composition loads and slip along this load. Then X-, Y-, and Z-component determine the failure together. When kz > 3, the failure is eventually controlled by Z-component load. However, compared with that of SRM, the failure region of LIM is reduced relatively; thus, this failure region is affected by local instability, and the gap of the safety factor between SRM and LIM is large. Accordingly, if the load increase is sufficiently large to cause significant local instability, then the safety factor cannot indicate global stability. Thus, the local instability must be considered when LIM is used.

Similar, the average displacement is not zero under the variation of kz, corresponding to the safety factor less than 1 (Fig. 11). The minimum average displacement corresponds to a maximum safety factor. When kz < 2.3, the average displacement nearly coincides with its X-component, which indicates that the displacement is mainly controlled by X-component load. When kz > 2.3, the average displacement is controlled by Z-component displacement, thereby indicating that the displacement is mainly controlled by Z-component load. This analysis has the same conclusion as the preceding analysis.

Finally, on the basis of the foregoing analysis, the safety factor is improved by decreasing the X-component load and by increasing Y- and Z-component loads to ensure that the failure mode is controlled by X-, Y-, and Z-component loads together.

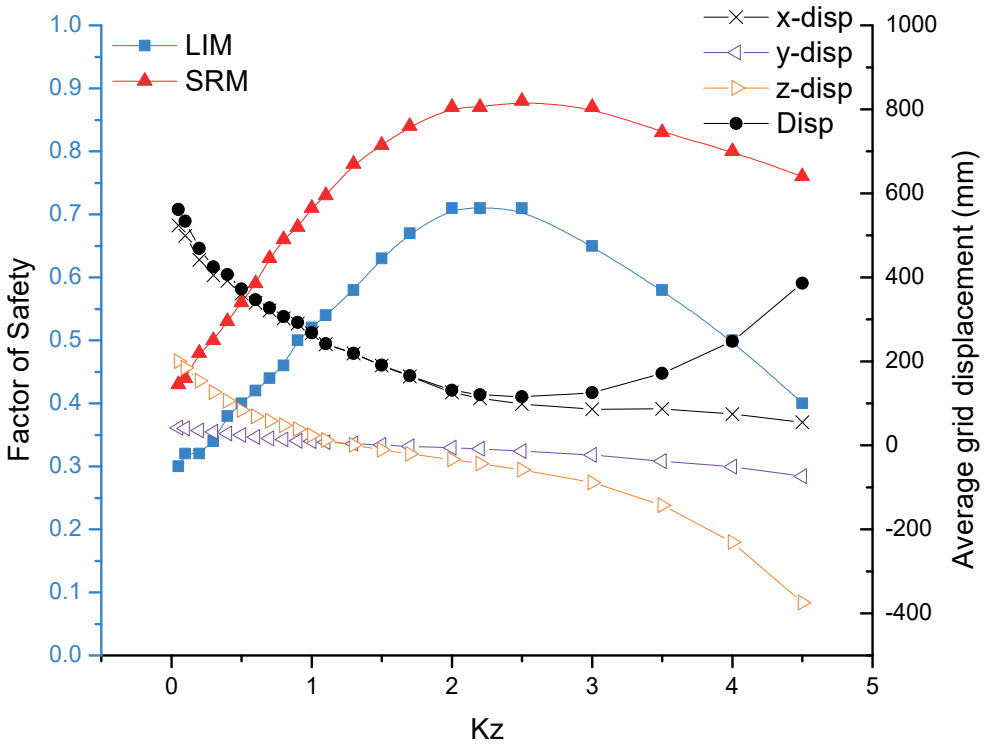

Fig. 11 Relation between safety factor of slope and kz (kx = ky = 1)

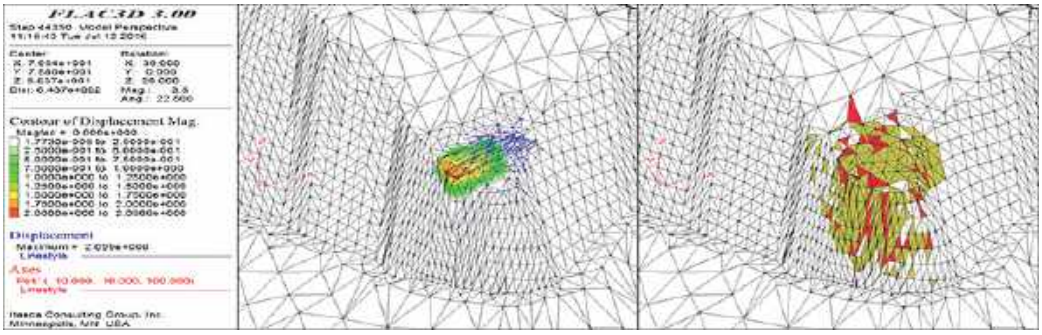

kz = 0.05

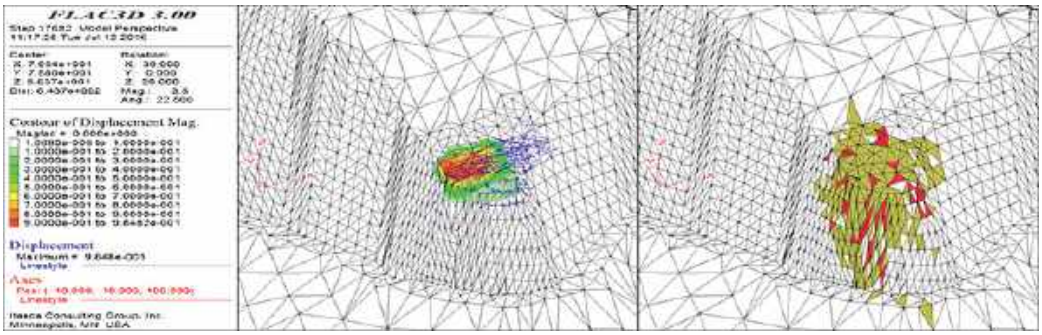

kz = 0.8

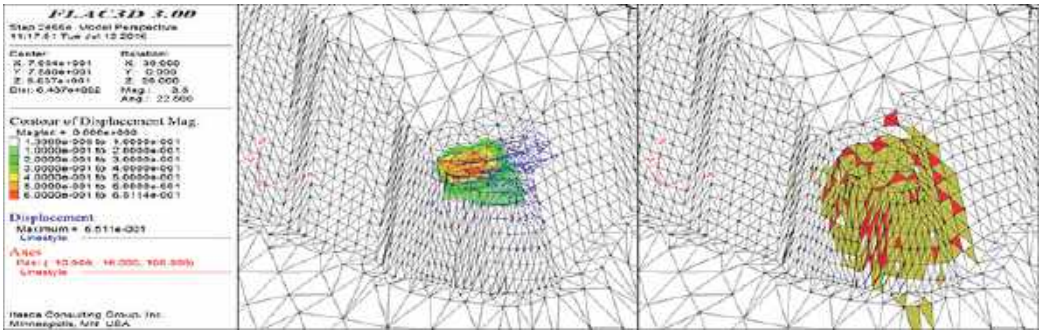

kz = 1.5

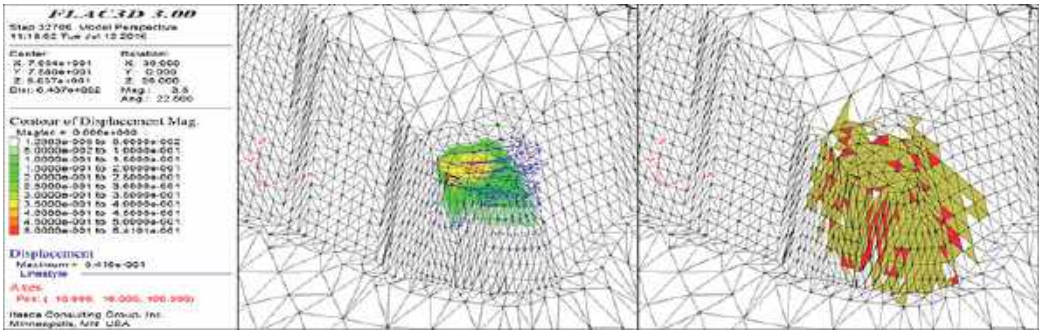

kz = 2.0

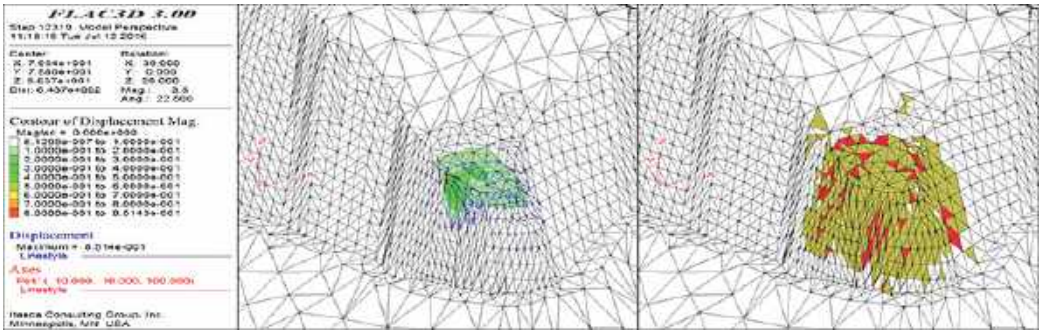

kz = 3.0

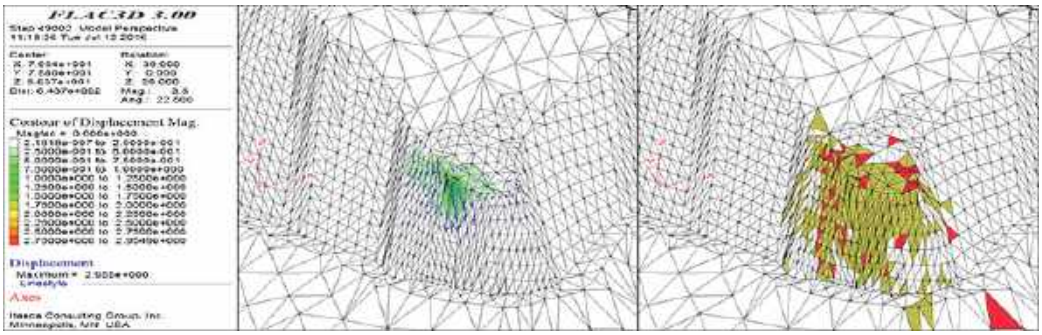

kz = 4.5

(a) **SRM**

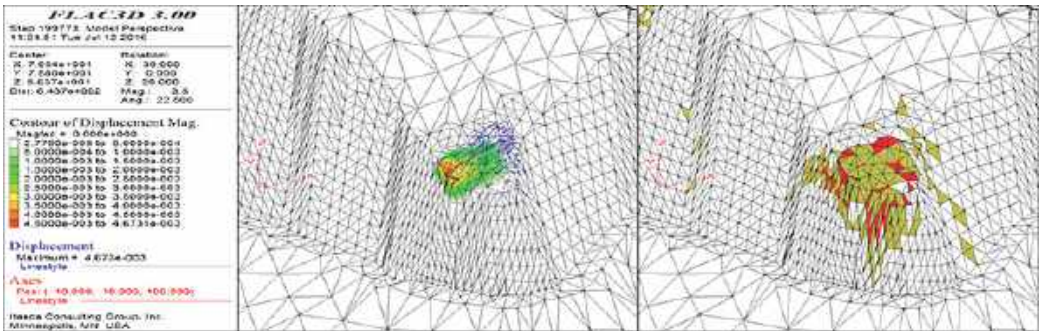

kz = 0.05

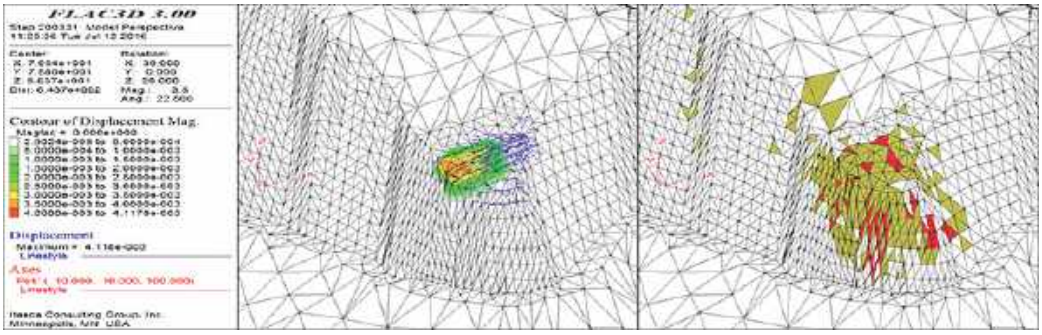

kz = 0.8

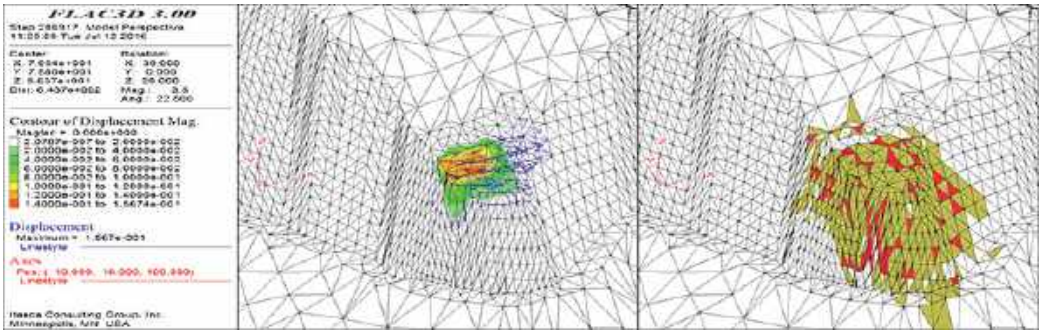

kz = 1.5

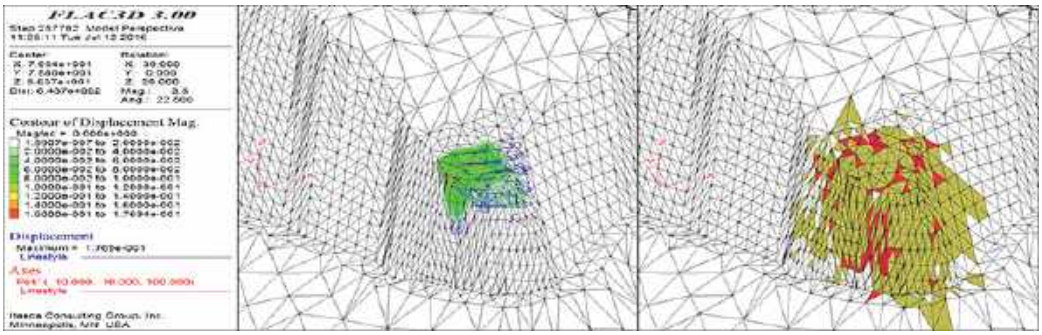

kz = 2.0

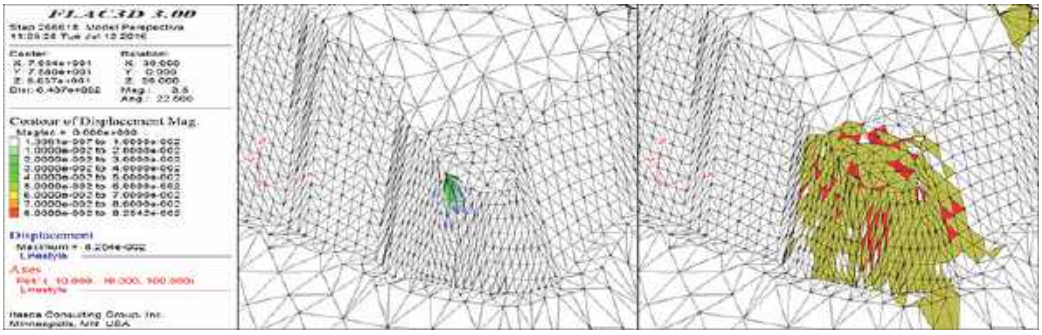

kz = 3.0

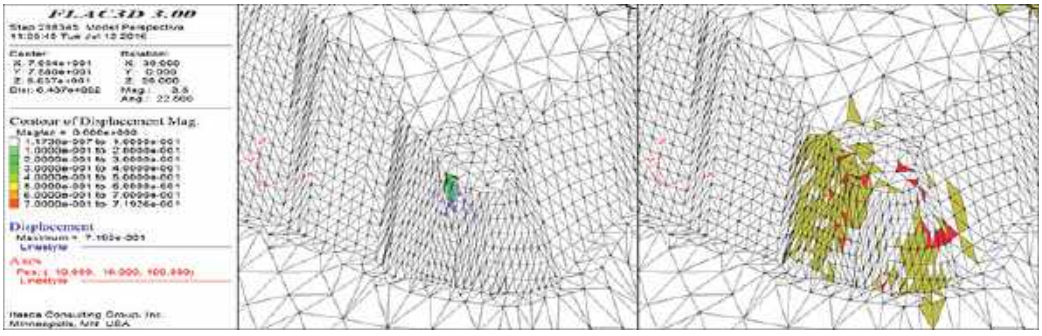

kz = 4.5

(b) **LIM**

Fig. 12 Total displacement and failure region with variation of kz (kx = ky = 1)

4 Conclusions

This study analyzes the stability of the 3D mine pit slope under surface load by using two methods, namely, SRM and LIM. Numerical analysis shows that safety factor, displacements, and failure region of LIM are close to those of SRM when the slope is in the critical state. When the slope is in an unstable state, the safety factor of LIM is less than that of SRM. The safety factor of LIM is greater than that of SRM when the slope is in a stable state. Therefore, reliable results are obtained when the slope is close to the critical state for LIM. The safety factor cannot represent the global stability partly because the local instability is caused by variation in load when it is increased sufficiently to influence the global stability. So the influence of the local instability on the safety factor in LIM must be understood.

Under surface load, the potential failure mode of the slope is transformed from sliding according to gravitational load to failure according to surface load. This potential failure mode is mainly controlled by surface load. Thus, it is a critical factor and has a significant influence on slope stability. For example, in this paper, the stability of the slope is predominantly affected by Y- and Z-component load unlike X-component load. The safety factor is improved by decreasing X-component load and by increasing Y- and Z-component loads. Consequently, if the structure of the foot is adjusted appropriately, then the stability of the slope can be improved.

5 Acknowledgment

This paper gets its funding from Project (51304240, 51474249) supported by National Natural Science Foundation of China; Project (No.2016CX019) supported by Innovation Driven Plan of Central South University. The authors wish to acknowledge these supports.

6 References

[1] Cheng YM, Lansivaara T, Wei WB. Two-dimensional slope stability analysis by limit equilibrium and strength reduction methods. Computers and Geotechnics. 2007;34:137-50.

[2] Griffiths DV, Lane PA. Slope stability analysis by finite elements. Geotechnique. 1999;49:387-403.

[3] Duncan JM. State of the art: Limit equilibrium and finite-element analysis of slopes. Journal of Geotechnical Engineering. 1996;122:894.

[4] Chen Z, Haberfield C, Yin J, Wang Y, Wang X. A three-dimensional slope stability analysis method using the upper bound theorem: Part I: theory and methods. International Journal of Rock Mechanics & Mining Sciences. 2001;38:369–78.

[5] Griffiths DV, Marquez RM. Three-dimensional slope stability analysis by elasto-plastic finite elements. Geotechnique. 2007;57:537-46.

[6] Cheng YM, Yip CJ. Three-dimensional asymmetrical slope stability analysis extension of Bishop's, Janbu's, and Morgenstern-Price's techniques. J Geotech Geoenviron Eng. 2007;133:1544-55.

[7] Leong EC, Rahardjo H. Two and three-dimensional slope stability reanalyses of

Bukit Batok slope. Computers and Geotechnics. 2012;42:81-8.

[8] Wei WB, Cheng YM, Li L. Three-dimensional slope failure analysis by the strength reduction and limit equilibrium methods. Computers and Geotechnics. 2009;36:70-80.

[9] Wei W. Three dimensional slope stability analysis and failure mechanism [ph.d]: Hong Kong Polytechnic University; 2008.

[10] Lin H, Zhong W, Cao P. Three-dimensional rock slope stability analysis considering the surface load distribution. European Journal of Environmental & Civil Engineering. 2015;20:1-22.

[11] Taiebat HA, Carter JP. Numerical studies of the bearing capacity of shallow foundations on cohesive soil subjected to combined loading. Geotechnique. 2000;50:409-18.

[12] Erickson HL, Drescher A. Bearing capacity of circular footings. Journal of Geotechnical & Geoenvironmental Engineering. 2002;128:38-43.

[13] Bishop AW. The use of the slip circle in the stability analysis of slopes. Géotechnique. 1955;5:7-17.

[14] Zuyu C. Stability analysis of soil slopes. Bejing: China Water Power Press; 2003.

[15] Zienkiewicz OC, Humpheson C, Lewis RW. Associated and non-associated visco-plasticity and plasticity in soil mechanics. Géotechnique. 1975;25:671-89.

[16] Matsui T, San KC. Finite element slope stability analysis by shear strength reduction technique. Soils & Foundations. 1992; 32:59-70.

Modeling of the Hydromechanical Behavior of Rock Salt using DEM

Modellierung des hydromechanischen Verhaltens von Steinsalz mittels der DEM

Christian Müller[1], Eric Kuate Simo[1], Thomas Frühwirt[2], Heinz Konietzky[2]
[1]DBE TECHNOLOGY GmbH, Peine
[2]TU Bergakademie, Freiberg

Abstract

In Germany, salt formations are considered to be suitable to host a deep geological repository for radioactive waste. However, local stress changes adjacent to man-made openings lead to the evolution of an excavation damaged zone (EDZ) during and after excavation. Such an EDZ can have a major impact on the operation and closure of a radioactive waste repository since it represents a region where progressive failure occurs. This decreases the material strength and thus increases the permeability of the original tight rock salt. The objective of this investigation is determined by the need to develop a modeling strategy that can be applied to simulate the permeability increase due to mechanical deterioration of rock salt, in particular that occurring in the EDZ. In order to simulate the shape and arrangement of crystal grains in rock salt, discontinuum approaches were applied using polyhedral elements (Voronoi polyhedra) for the simulation. To derive relevant input parameters used in the models and to validate the mechanical behavior of the models, a comprehensive geotechnical program was carried out. It includes compression tests in combination with acoustic emission testing. The calibration of the parameters to simulate the mechanical behavior provides good results, and it was shown that cracking in the EDZ was simulated in a realistic manner. In order to quantify the fluid flow in the fracture system generated, the hydraulic conductivity tensor was calculated which provides information on the direction and magnitude of the major and minor component of conductivity.

Zusammenfassung

In Deutschland werden Salzformationen als geeignete Wirtsgesteine für tiefe geologische Endlager für radioaktive Abfallstoffe angesehen. Lokale Spannungsänderungen können jedoch während und nach der Auffahrung von Grubenbauen zur Ausbildung einer Auflockerungszone (ALZ) führen. Solch eine Auflockerungszone kann wesentliche Auswirkungen auf den Betrieb und Verschluss eines Endlagers für radioaktive Abfälle haben, da sie einen Bereich darstellt, wo das Wirtsgestein geschädigt ist. Das verringert die Materialfestigkeit und erhöht somit die Permeabilität des ursprünglich dichten Wirtsgesteins. Das Ziel dieser Untersuchungen ist die Entwicklung einer Modellierungsstrategie, die dazu verwendet werden kann, den Permeabilitätsanstieg in

der Auflockerungszone von Steinsalz aufgrund von mechanischer Schädigung zu modellieren. Zur Simulation der Form und Anordnung von Kristallkörnern in Steinsalz wurden Diskontinuumsansätze eingesetzt, die polyedrische Elemente für die Simulation verwenden. Die hier verwendeten polyedrischen Diskreten Elemente werden Voronoi Polyeder genannt. Um relevante Inputparameter abzuleiten und um das mechanische Verhalten des Models zu validieren, wurde ein umfangreiches geotechnisches Laborprogramm durchgeführt. Es beinhaltet Kompressionsversuche in Kombination mit akustischen Emissionsmessungen. Die Kalibrierung der Parameter zur Simulation des mechanischen Verhaltens liefert gute Ergebnisse und es konnte gezeigt werden, dass die Rissbildung in realistischer Weise simuliert wurde. Um den Durchfluss der generierten Risssysteme zu quantifizieren, wurde der hydraulische Durchlässigkeitstensor ermittelt, der Informationen über die Richtung und die Größe der Durchlässigkeit gibt.

1 Introduction

Deep geological formations are regarded to be suitable to host repositories for radioactive waste. In Germany, the safety concept for a deep geological repository in salt formations considers not only the isolation capability of the geological barrier but also that of the geotechnical barriers in order to seal all man-made openings (e.g., shafts, chambers and drifts) (Krone et al. 2008). However, local stress changes adjacent to man-made openings lead to the evolution of an excavation damaged zone (EDZ) during and after excavation which can have a major impact on the operation of a radioactive waste repository. The EDZ is a region where progressive failure occurs. This decreases the material strength and thus increases the permeability of the originally tight host rock. Although this result in a macroscopic deformation, the relevant processes that induce an EDZ occur at the scale of the microstructure. The objective of this investigation is determined by the need to develop a modeling strategy that can be applied to simulate the permeability increase due to mechanical deterioration of rock salt, in particular that occurring in the EDZ (Müller et al. 2016). In order to simulate the shape and arrangement of crystal grains in rock salt, the discrete element method (DEM) was applied. The geometric properties of the grains were simulated by using polyhedral elements based on a Voronoi tessellation (*Neper*, Quey et al. 2011).

2 Calibration

The DEM was used in order to consider the microstructure of rock salt as a multi-body system consisting of individual grains. It differs fundamentally from the continuum approach used so far for salt mechanics problems. The basic approach of the DEM is an assemblage of rigid or deformable discrete elements and contacts among them establishing the medium. The approach allows an arbitrary displacement and rotation of the discrete elements, a separation of discrete elements along their contacts as well as a detection of new contacts (Cundall & Hart 1992). The explicit consideration of discontinuities is the main advantage over the continuum approach. However, in contrast to continuum mechanical approaches, the DEM considers the mechanical behavior an order of magnitude below the model dimensions. The relevant micromechanical processes are difficult to calibrate from classical, standardized laboratory tests where only the macroscopic behavior of the material is characterized. Thus, a first step for grain scale modeling is the calibration and validation of the DEM model. Combined uniaxial compression tests and acoustic emission (AE) measurements were conducted in order to allow both a calibration of the macroscopic deformation and a micromechanical validation of the relevant fracture processes.

2.1 Laboratory Testing

The compression test was performed on a cylindrical specimen with 100 mm in diameter and 250 mm in length. Axial deformation was measured directly on the specimen using three length extensometers with measuring points applied at the third points of the sample length. Lateral deformation was determined by a circumferential extensometer with a roller chain at the center of the specimen. The volumetric strain was calculated by summing up the strain along the principal directions using the information from the length and circumferential extensometers. A relatively fast constant loading velocity of 0.25 mm/min was applied, which is equal to an axial strain rate of 10^{-3} min^{-1}. Particularly emphasis is given to the development of microstructural damage along grain

boundaries occurring in the EDZ. Assuming that time-dependent creep (dislocation creep) has no impact on the formation of the EDZ, only short-term deformation processes must be taken into account, i.e., evolution of dilatancy due to microstructural deterioration, primary creep caused by strain hardening (dislocation glide), short-term laboratory compressive strength, and residual strength above the peak strength.

The objective of AE testing was to detect and locate fracture generation as well as to identify the focal mechanisms of events (Polarity analysis) by distinguishing events caused by tensile and closure mechanisms, and those with some component of shear motion of rock salt during the uniaxial compression test (Zang et al. 1998). AE events are transient elastic waves emitted by the rapid energy release within the material due to fracture generation. These waves can be detected by sensors mounted on the boundary surface of the specimen. Particularly in the domain of salt mechanics, AE testing is an interesting option to further investigate the development and interaction of fractures before and after the dilatancy boundary (e.g., Manthei 2004; Alkan et al. 2007). Acoustic measurements were performed using the acoustic emission system Vallen AMSY6 which is based on the so-called "hit-based" architecture using eight piezoelectric sensors fixed to the boundary surface of the specimen.

2.2 Calibration Method

The calibration of the DEM model is based on the principle of simulating a uniaxial compression test and varying the unknown input parameters of the DEM model until the behavior of the numerical sample matches the behavior of the physical sample. Numerical compression tests were performed on a cylindrical specimen with a diameter of 37.5 mm and a length of 75 mm that consisted of 1561 Voronoi elements. To allow a validation with laboratory experiments, additional output data was recorded as close as possible to laboratory conditions. The axial stress is the sum of forces at the top of the PVC spacer divided by the sample area. Axial deformation is calculated by measuring the vertical distance between gridpoints located at the third points of the sample length. Lateral strain was calculated at the center of the sample by measuring the horizontal displacement of gridpoints at the sample area.

The DEM code 3DEC was used for simulation allowing the translation, rotation as well as the deformation of discrete elements when subjected to mechanical load (Itasca 2013). Deformation is governed by continuum mechanical approaches using a finite difference scheme and 4 node tetrahedral elements.

The plastic deformation within the salt grains is mainly produced due to an accumulation of dislocations when recovery mechanisms do not occur. With increasing dislocation density and resulting increase of interactions between both free dislocations within each glide plane and different glide planes, they can constrain each other in their development. As a consequence, a larger yield stress is required to maintain plastic deformation. In order to simulate the deformation within the salt grains with an associated mechanism of hardening (dislocation glide), a continuum-based Mohr-Coulomb criterion with an additional strain hardening approach is applied. The model is based on a common Mohr-Coulomb model with nonassociated shear (shear yield function) and associated tension (tensile yield function) flow rules. In order to simulate the effect of hardening, the cohesion is increased after yield as a function of the plastic portion of

the total strain using the aforementioned approach. Since the structure of the salt crystal is not modified by the deformation processes, a constant-volume and crack-free deformation is assumed.

The bonds between the polyhedral elements can also be configured to simulate the cracking along grain boundaries. Contacts in 3DEC are penalty-based and are simulated by stiffness springs in normal and tangential direction. A Mohr-Coulomb criterion (shear yield function) including a tension cut-off condition (tension yield function) was used and the friction angle was set to zero to simulate ideal plastic material behavior. Thus, the maximum shear and tensile force is limited to the cohesion and the tensile strength of the contact. Once the onset of failure is identified at a contact, in either tension or shear, the tensile strength and cohesion are taken as zero. In order to simulate a Coulomb friction law after slip, the residual cohesion was set to zero and the friction angle contains an angle unequal zero. The dilation angle at slip was set equal the friction angle (associated flow rule).

2.3 Calibration Results

Fig. 2.1 shows laboratory results against numerical calculation results of the best design. When looking at the numerical results and the axial stress strain curves, the comparison to laboratory observations is satisfying as well. The numerical results show slightly lower strain accumulations compared to the laboratory results. Axial stresses reach approximately the axial compressive strength of the laboratory test with values of 27 MPa. The post peak behavior of the axial strain behavior is characterized by brittle failure with an abrupt decrease of axial stress as observed in the laboratory. However, the numerical sample shows a slightly stiffer behavior with lower lateral strain accumulations when compared to the laboratory. Maximum lateral strain with values of up to 0.25 as observed in the laboratory was not achieved in the numerical models. The simulated post peak behavior in lateral strain is characterized by a more or less sudden decrease in stress, whereas the behavior in the physical experiment is markedly ductile. The volumetric strain, which is directly calculated by using the axial and lateral strain results, does not fully correspond to laboratory tests. Compaction due to elasticity is much too low in 3DEC and the volume increase due to plastic deformation is not adequately simulated. Only marginal dilatancy is observed in the phase of pre-peak plastic behavior until immediately before peak load. However, starting from this initiation point the volumetric expansion rate is overestimated in the numerical calculation as compared the laboratory results.

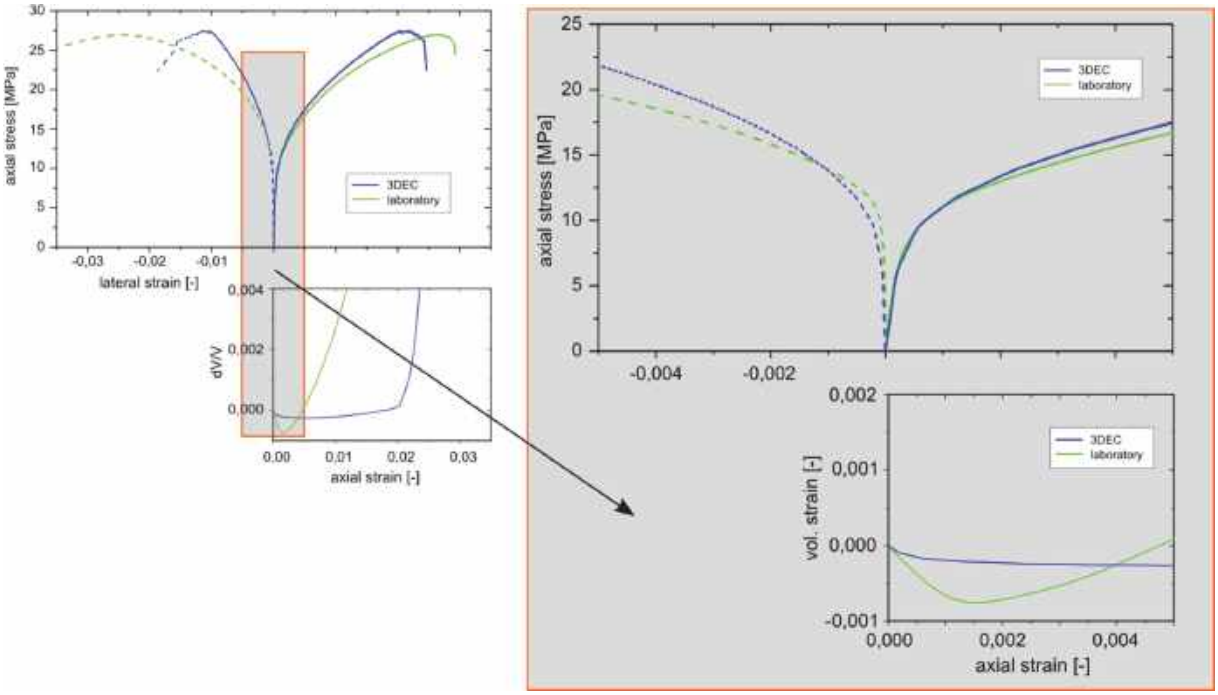

Fig. 2.1: Axial and lateral strain versus axial stress, together with volumetric strain versus axial strain of laboratory testing and numerical analysis.

AE testing results were used for a micromechanical characterization and validation of the relevant fracture processes (Fig. 2.2). AE measurements show that cracking starts at stress levels above 5 MPa and coincides with the strain hardening observed in graph of stress versus axial strain. AE activity reaches its maximum during early stages of loading and decreases gradually with increasing stress levels. However, a certain amount of AE energy is maintained throughout the entire testing, which indicates that AE events were released continuously. Furthermore it could be shown that cracking is mainly due to tensile cracking which is comparable to results published in literature (Fig. 2.3; Manthei 2004).

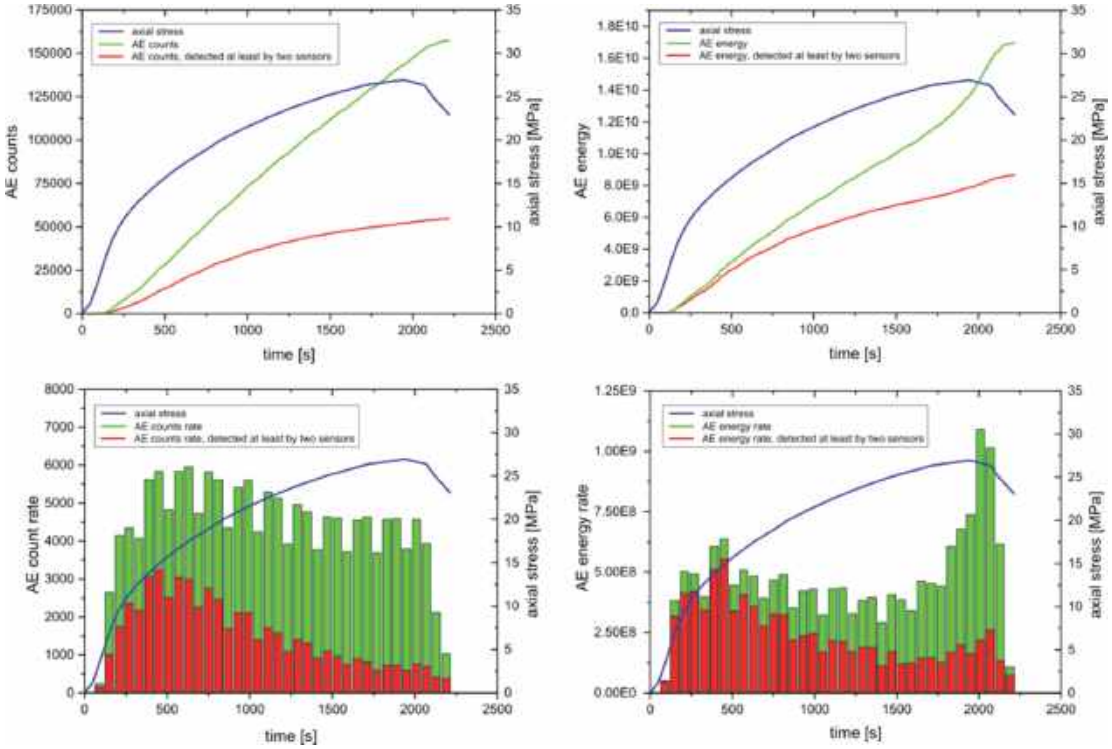

Fig. 2.2: AE events, AE rate, AE energy as well as AE energy rate versus time of loading

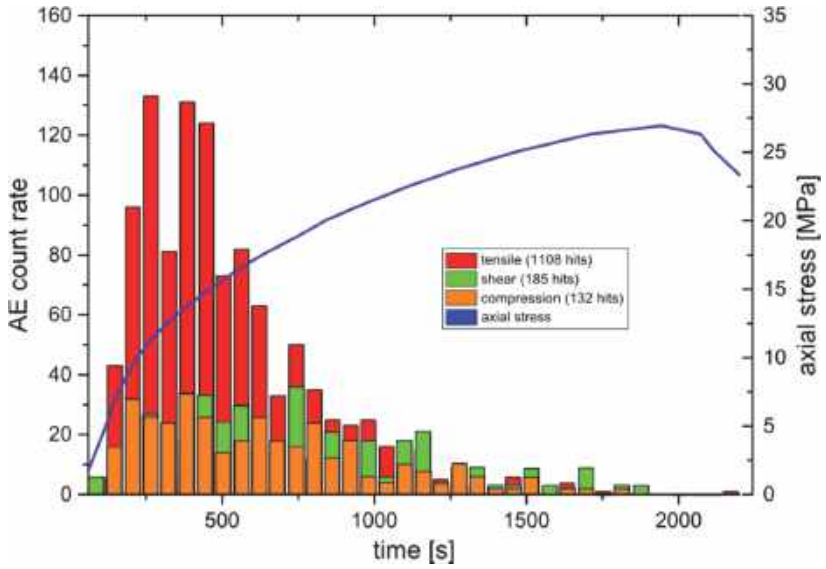

Fig. 2.3: Classification of located events due to their first motion polarity into three types (tensile, shear and compressional) after Zang et al. (1998).

Consequently, the results of the AE measurements were used to make a qualitative comparison with the fracture processes simulated. The classification of fracture events according to their type of fracture generation was conducted by determining the so-called failure states of contacts in a 3DEC model. The onset of failure is identified at stress levels above 3 MPa (Fig. 2.4). The number of tensile fractures increases rapidly and the maximum is reached between 10 and 12 MPa axial stress. At the beginning of loading, tensile fractures appear more frequently than shear fractures, which is in good

agreement with the laboratory results. After this, the number of tensile fractures decreases continuously. The number of shear fractures increases less rapidly up to 12 MPa and is maintained throughout the simulation. Overall, a good agreement was achieved in the numerical modeling with respect to fracturing as observed in the laboratory.

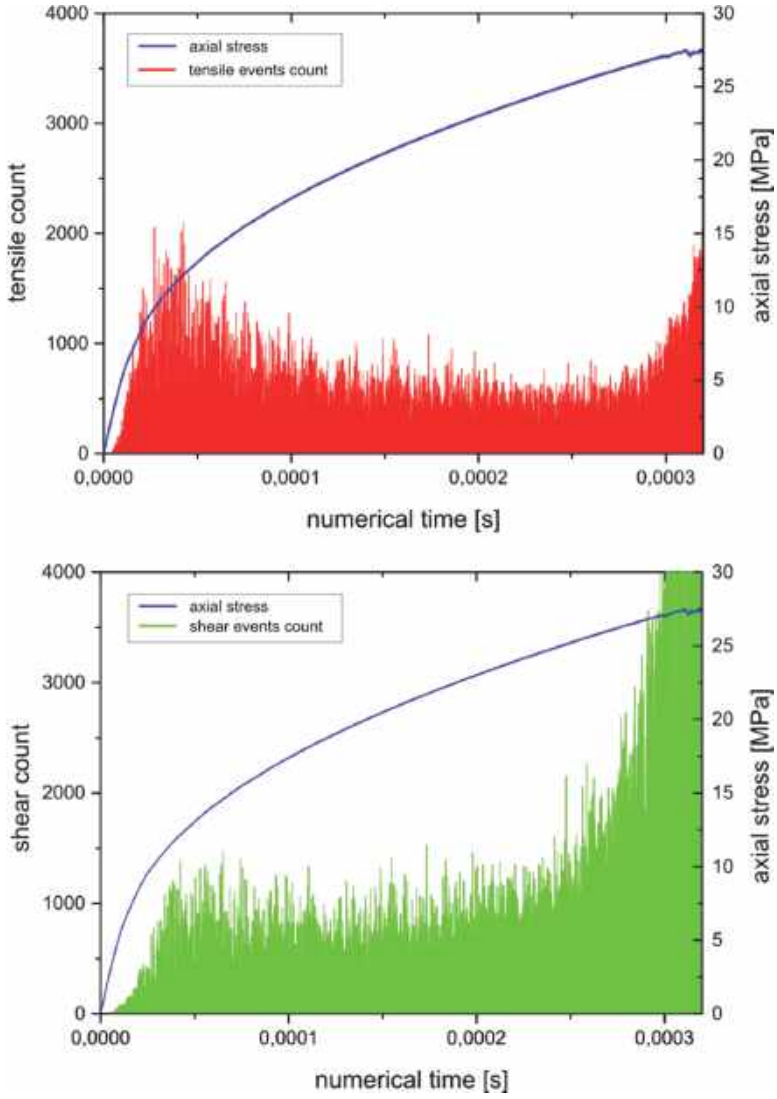

Fig. 2.4: Number of contacts failed in either tensile or shear against numerical calculation time.

3 Mechanical Modeling

This chapter contains the generation of realistic fracture networks occurring in the EDZ using the DEM approach. The excavation of a drift is first simulated with continuum mechanical approaches to determine the in situ stresses that occur in the region surrounding an excavation in a rock salt formation. The zone stresses are then transmitted as boundary stresses onto a DEM model to simulate the fracturing in the EDZ.

The numerical model consists of a rock model with an excavation and has model dimensions of 200 m in the length and 200 m in the height (Fig. 3.1). The drift is modelled with a simplified geometry by using a square of six meters length with rounded corners at the center of the model. The drift is located at a depth of 1250 m below ground level. The drift is assumed to be long enough so that stresses along the drift are constant and the deformations in the direction along the drift can be neglected. Thus, the simulation process can then be reduced to a two-dimensional model. The model is constrained at the left, right and bottom boundaries with roller boundary conditions. A roller boundary condition supposes that only the degree of freedom perpendicular to the boundary face is fixed while gridpoints are free to move along the two other degrees of freedom parallel to the boundary face. Since a two-dimensional model is considered, symmetric boundary conditions are placed at the front and back face of the model. When symmetric roller boundaries are applied, the displacement of boundary gridpoints is restricted to a movement within the boundary plane. The gridpoint displacement perpendicular to the boundary is disabled.

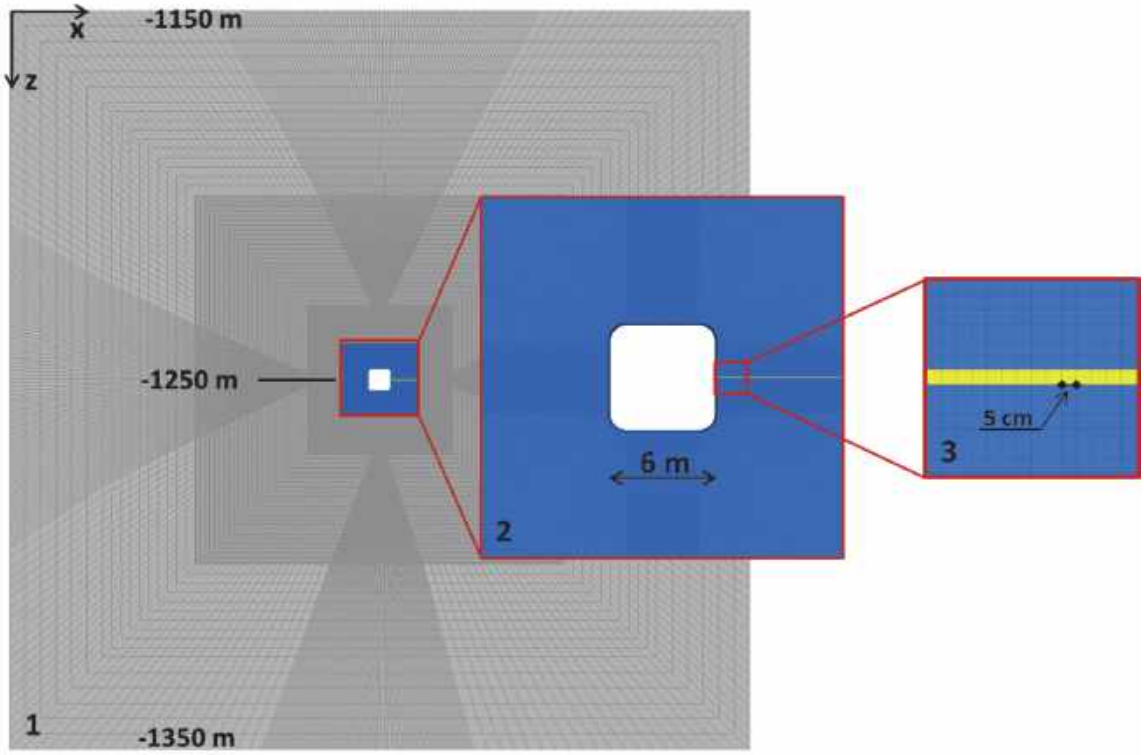

Fig. 3.1: Numerical model used to derive stress conditions.

The geology considered for this study is a generic rock based on the rock salt formations located in Germany. Rock salt exhibits a visco-plastic material behavior when it is subjected to mechanical loads. However, viscous or plastic behavior was neglected and the stress redistribution is solely based on the linear elastic solution. The simulation is performed with the finite difference based code Flac3D (Itasca, 2005).

Stresses derived from continuum modeling were transferred as boundary conditions on a discrete model consisting of Voronoi elements in order to simulate the fracturing in the EDZ (Fig. 3.2). Displacements in the large model (continuum model) and the

submodel (discontinuum model) were, however, not compared in this step. For simplification it was furthermore assumed, that the applied stresses in the submodel are equal on opposite sides. This results in a displacement field where the vertical plane of symmetry is in the center of the submodel. Thus, displacements simulated in the submodel do not correspond to the real displacement field where the convergence is aligned towards the drift across the entire submodel. However, compared to the continuum model the selected submodel is very small, so that differences in the displacement field are likely to have only a minor influence on the fracture processes in the investigated area. The discrete model has a length of 50 mm, consisting of 1954 polyhedral shaped elements. The average grain size of 4 mm is the same size as was used during the calibration of the constitutive material parameters. In order to avoid any numerical effects due to the boundary conditions, the discrete model is hosted in a continuum far field block. The model is constrained at the eight corners to avoid displacements which occur during the computational stepping necessary to reach the equilibrium. The outer corners are fixed with roller boundaries in all three directions.

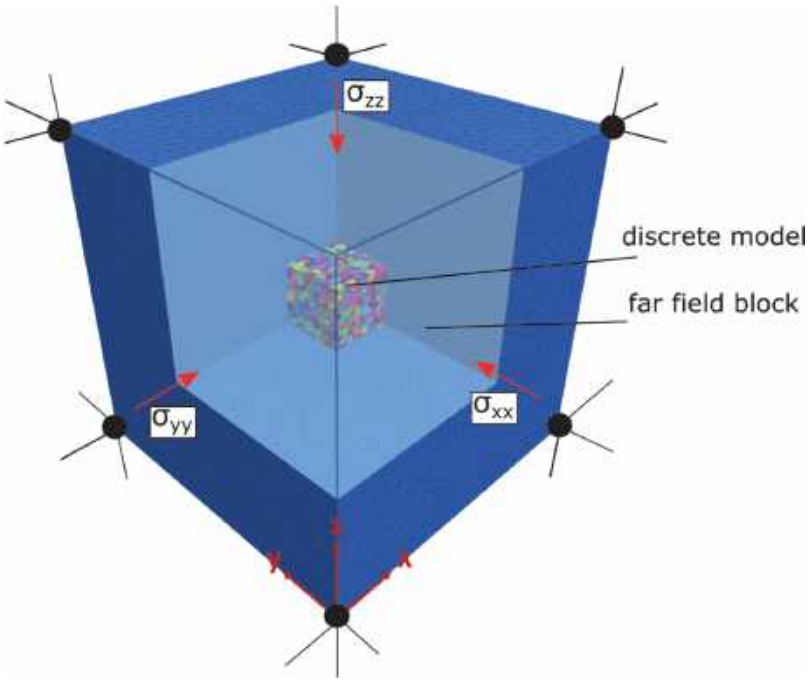

Fig. 3.2: Continuum far field block used to enclose the discrete model consisting of polyhedral elements. Parts of the far field are hidden for illustration.

Simulated fracture networks for different depths according to the continuum stress measuring points are shown in Fig. 3.3. The examinations of the crack patterns show that an important amount of cracks are more or less oriented along the y-z-plane due to the orientation quite perpendicular to the x-direction. Thus, it can be concluded that the resulting damage in the discrete model is anisotropic. This is in agreement with observations where the fractures of the EDZ are principally orientated along the direction of the minimum principle stress.

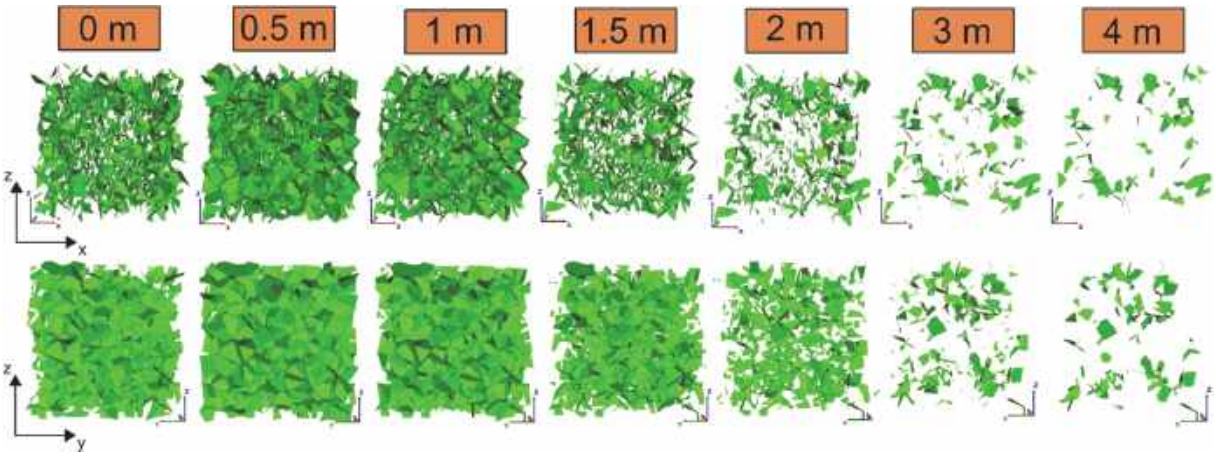

Fig. 3.3: Simulated fracture networks in the EDZ using the DEM.

To allow a validation, a simple comparison with the continuum mechanical solution was conducted. The octahedral shear stress was calculated for the monitored points in the continuum model and related to the dilatancy boundary proposed by Cristescu & Hunsche (1998). The dilatancy boundary gives information about the beginning of fracturing in the EDZ. It turns out that the damage extends to a depth of 2 m and the greatest damage is to be expected at a depth of nearly 1 m, which is in good agreement with the DEM solution (Fig. 3.4).

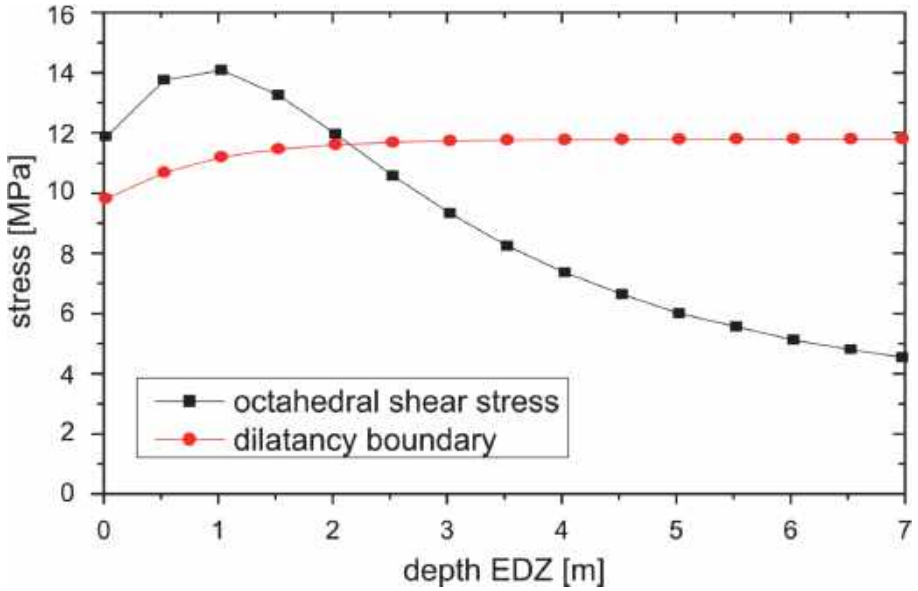

Fig. 3.4: Calculated octrahedral shear stress for the monitored points in the continuum model and dilatancy boundary after Critescu & Hunsche (1998).

4 Hydraulic Modeling

The permeability increase in the EDZ is mainly caused by microfractures, which can compromise the sealing function of the originally tight rock salt. Therefore, the specification of adequate permeability values is particularly important since it provides information about major pathways for fluid flow. The following chapter introduces a method

to upscale the information gained from discontinuum modeling to the macroscale since the larger number of fractures makes the discrete approach less efficient for large-scale modeling. By calculating the permeability tensor, it is investigated if the flow of a discontinuum model with fractures explicitly represented can be simulated using continuum modeling approaches (equivalent porous medium). The permeability tensor provides information about the direction and magnitude of the major and minor component of flow. This allows the specification of directionally dependent (anisotropic) permeability properties that can be used as input parameters for continuum models simulating the fluid flow at larger scales.

In order to check whether the discontinuum model with fractures explicitly represented behaves as a continuum, the calculated directional conductivity for different head directions must be approximated by an ellipsoid with the three principal conductivity values K_x, K_y and K_z (Long et al., 1982):

$$\frac{x^2}{1/K_x} + \frac{y^2}{1/K_y} + \frac{z^2}{1/K_z} = 1 \qquad (1)$$

In this case, the reciprocals of square roots of the directional conductivity $K_x^{-1/2}$, $K_y^{-1/2}$ and $K_z^{-1/2}$ are the semi axes of the ellipsoid. The major axis of the ellipsoid is in the direction of minimum conductivity for hydraulic conductivity measurement in the direction of the hydraulic gradient. After Bear (1972), the directional hydraulic conductivity K_J is a scalar physical quantity that describes the ratio between the magnitude of the discharge q_i in the direction of the gradient and the gradient itself:

$$K_J = \frac{|q|cos\theta}{|J|} \qquad |q|cos\theta = K_J|J| \qquad (2)$$

where $|J|$ is the magnitude of the hydraulic gradient and $cos\theta$ is the angle between the vectors q_i and J_i (Bear, 1972). The relationship between the directional conductivity and the hydraulic conductivity tensor is given by Long et al., 1982:

$$K_J(n_i) = n_j K_{ij} n_i \qquad (3)$$

Thus, measurements of the directional permeability under different head directions can be used to find the equivalent permeability tensor for a given discrete model with fractures explicitly represented. The directional permeability was evaluated by changing the hydraulic boundary conditions (e.g. Jackson et al., 2000; Blum et al., 2007). Hydraulic boundary conditions were changed using linearly varying heads according to the superposition principle to generate a unit hydraulic gradient vector in any direction. To obtain directional permeability values for different head directions, the gradient vector was rotated counterclockwise from 0° to 150° in 30° steps on the x-y plane starting in the direction of the x-axis and assuming a right-handed Cartesian coordinate system. This procedure was carried out for different inclination angles (angle between z-direction and the gradient vector) from 90° to 0° in 30° steps in order to characterize the fluid flow of the fracture system for various hydraulic gradients (Fig. 4.1).

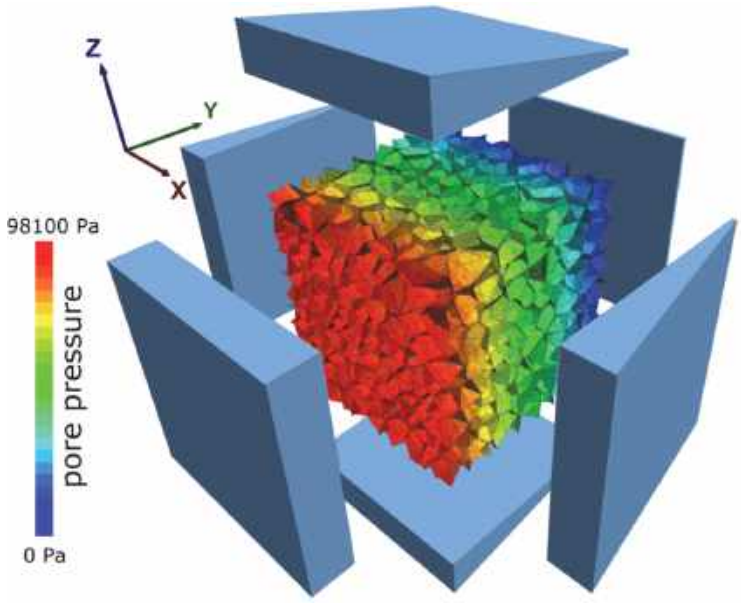

Fig. 4.1: Hydraulic gradient vector in y-direction as an example of the hydraulic head boundaries with linearly varying hydraulic heads along the six sides of the cube. A unit head gradient was employed (9.81 Pa/m).

When evaluating the directional permeability K_J, the components of the Darcy velocity vector q_i need to be determined. The approach used in this study consists of taking the average Darcy velocity vector q_i over the associated crack and matrix volume proposed by Oda (1985). Assuming the matrix (salt grains) is impermeable and the water flows only through intergranular cracks, the directional conductivity can be calculated by:

$$\overline{q_i} = \frac{1}{V}\left(\int_{V(crack)}^{\cdot} q_{i_{(crack)}} \cdot dV_{(crack)}\right) \tag{4}$$

Knowing the Darcy velocity vector q_i and the hydraulic gradient J_i, the directional permeability K_J can be calculated. In order to graphically check whether the DFN behaves as a continuum, the reciprocals of the square roots of the calculated directional permeability $1/\sqrt{K_J}$ were plotted in a polar coordinate system. Furthermore, an average hydraulic conductivity tensor based on the calculated directional permeability K_J was calculated using the method of least squares by minimizing the following expression:

$$\min f(k_{ij}) \coloneqq \sum_{n=1}^{N} (K_J^n - n_j K_{ij} n_i)^2 \tag{5}$$

where N denotes the number of hydraulic head directions. This is followed by a diagonalization of the calculated hydraulic conductivity tensor in order to determine the three principal values and the three corresponding directions.

The permeability of a DFN depends significantly on the geometry of the fractures (size, orientation and density) as well as the transmissivity of individual fractures. As men-

tioned earlier, the former was generated using Voronoi models to simulate the fracturing at grain scale. The fluid flow through these individual fractures has not been considered yet, and hydraulic information is needed to derive these properties. However, it is very difficult to obtain relevant hydraulic information, and there was no data available that was suitable for calibration. For a first estimate, the aperture was adjusted based on information coming from microscopic investigations. The fluid flow through individual fractures is based on the cubic law where the aperture is the main input parameter controlling the fluid flow. In literature, rock salt that was damaged during laboratory testing shows aperture values up to 100 μm but apertures below 10 μm were mainly measured. The maximum allowable hydraulic aperture after a contact has broken was set to 10 μm and the fluid flow in unbroken grain boundaries (contacts) was numerically inhibited. The hydraulic conductivity is thus solely controlled by the formation of new cracks along the grain boundaries.

The hydraulic conductivity tensor of the fracture patterns that were introduced in chap. 3 were calculated for the depths of 1 m (Fig. 4.2). At these depths the greatest damage is to be expected. Since the calculated numerical results (yellow dots) and the calculated ellipsoid fit together, the hydraulic behavior can be approximated by a symmetric conductivity tensor. Due to the geometry of the fracture pattern, the principle directions of the conductivity tensor are parallel to the orthogonal Cartesian coordinate system. The tensor ellipsoid clearly indicates the maximum permeability (minor axis of the ellipsoid) along the y-z-plane which is in the main direction of the fracture planes and in direction of the highest stress. There is only a small difference between the principle values of the conductivity tensor in the yz-plane and, thus, the conductivity can be assumed as an orthotropic property. The anisotropy factor, defined as the ratio between the maximum and minimum principle conductivity, resulted in a value of 1.73. In order to allow a comparison with values from the literature, the hydraulic conductivity (m/s) was converted into permeability values (m^2). This lead to permeability values in the order of 10^{-15} m^2. Wieczorek & Schwarzianeck (2004) specify permeability values between 10^{-16} and 10^{-15} m^2 near the drift surface.

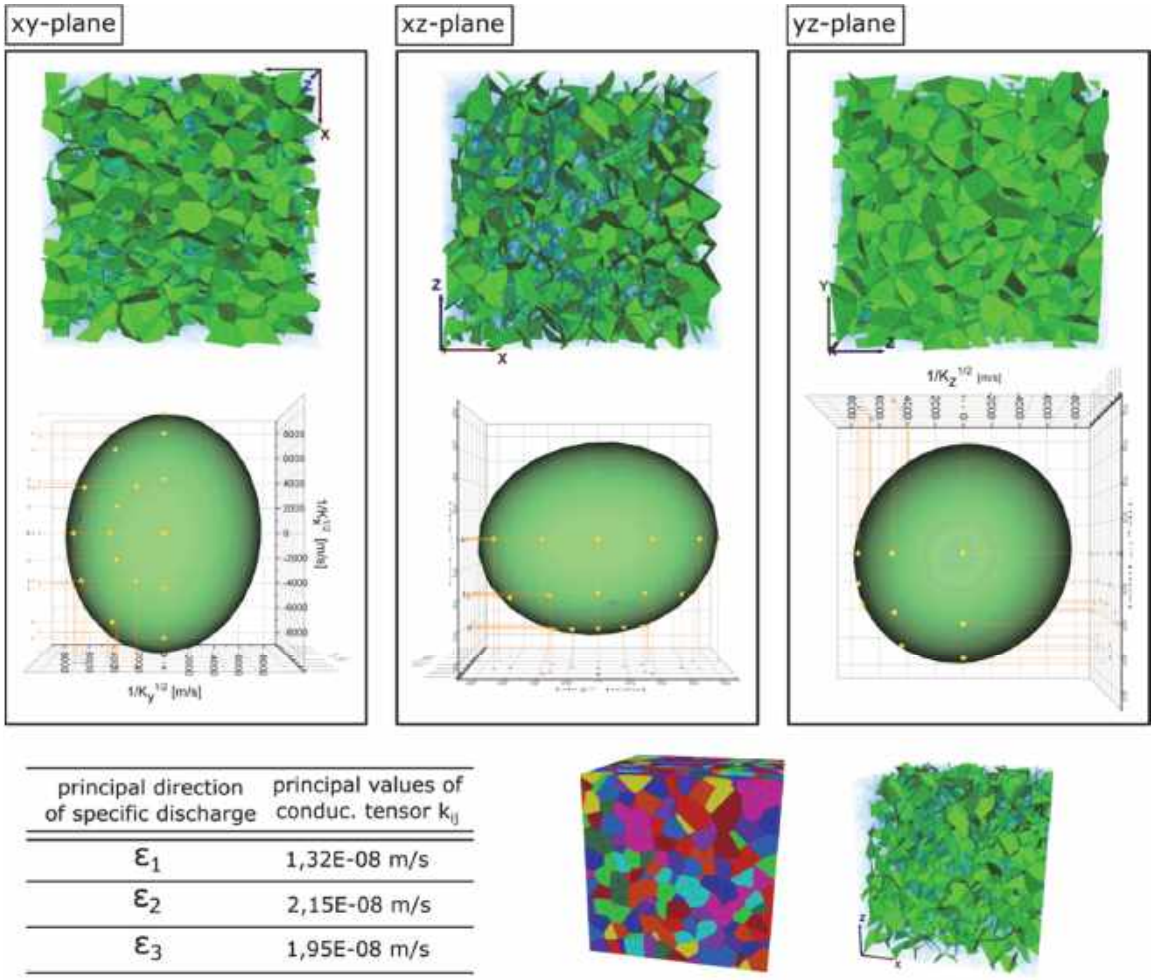

principal direction of specific discharge	principal values of conduc. tensor k_{ij}
ε_1	1,32E-08 m/s
ε_2	2,15E-08 m/s
ε_3	1,95E-08 m/s

Fig. 4.2: Calculated hydraulic conductivity tensor ellipsoid at a depth of 1 m from contour and corresponding principal values of the hydraulic conductivity.

5 Discussion and Conclusion

Discontinuum modeling methods have been used to investigate the fracturing and fluid flow in the EDZ of rock salt. Since the mechanical deterioration of rock salt occurs mainly through micro fractures, the mechanical and hydraulic behavior was investigated at grain scale where fracturing can be explicitly investigated.

To derive relevant input parameters used in the constitutive models and to validate the mechanical behavior of the models, a comprehensive geotechnical program was carried out. The calibration of the parameters to simulate the mechanical behavior provides good results, and it was shown that cracking was simulated in a realistic manner. However, the calibration process is based on uniaxial compression tests, and the parameters derived provide satisfactory results for only relatively small external loads. Furthermore, in literature it is described that incompatibilities in the plastic deformation of adjacent crystal grains cause local stresses at the grain boundaries, which led to the formation of intergranular microcracks (Bourcier et al. 2012). Local incompatibilities are the result of anisotropic crystal deformation taking place only on certain planes and in certain directions. Simple isotropic constitutive models were used for simulation that

cannot simulate the interaction between intra- and intercrystalline deformation adequately. Thus, the cooperative nature of crystal plasticity and cracking along grain boundaries was solely reached due to a suitable parameter combination. Moreover it was shown, that the predicted strain softening behavior for the lateral direction is not represented well in the numerical results. Based on the theory of linear elastic fracture mechanics (LEFM), the strain softening can be considered as a consequence of material damage that leads to a gradual degradation of material properties. In LEFM, the material fracture properties, i.e., tensile or cohesive strength, are usually decreased after contact breakage by a softening relationship of the normal stress acting on the fracture surface vs. crack-opening displacement. However, the constitutive models used are not based on LEFM and the degradation of material properties under tensile and shear failure are simulated by a sudden drop to residual values and are thus not characterized by strain softening.

In order to quantify the fluid flow, the hydraulic conductivity tensor was calculated which provides information on the direction and magnitude of the major and minor component of permeability. Model calibration is usually carried out by varying relevant input parameters until the laboratory or in situ conditions are achieved. However, hydraulic calibration was not possible and relevant input conditions could only be estimated based on (mechanical) apertures measured microscopically. Therefore, only a qualitative assessment about the permeability of the EDZ was possible. Further research should focus on the development of new constitutive models adapted to the DEM approach as well as additional hydraulic laboratory tests to allow a through validation of the calculation results.

Acknowledgements

The work was supported by the German Federal Ministry for Economic Affairs and Energy (BMWi) represented by the Project Management Agency Karlsruhe (Karlsruhe Institute of Technology, KIT) under contract no. FKZ02E11082.

References

Alkan, H., Cinar, Y., & Pusch, G. (2007). Rock salt dilatancy boundary from combined acoustic emission and triaxial compression tests. *International Journal of Rock Mechanics and Mining Sciences, 44*(1), 108-119.

Bear, J. (1972). *Dynamics of fluids in porous media.* American Elsevier Publishing Company, Inc.

Blum, P., Mackay, R., Riley, M. S., & Knight, J. L. (2007). Hydraulische Modellierung und die Ermittlung des repräsentativen Elementarvolumens (REV) im Kluftgestein. *Grundwasser, 12*(1), 48-65.

Bourcier, M., Dimanov, A., E., H., Raphanel, J., Bornert, M., & Desbois, G. (2012). Full field investigation of salt deformation at room temperature: Cooperation of crystal plasticity and grain sliding. In Bérest, Ghoreychi, Hadj-Hassen, & Tijani (Hrsg.), *Mechanical Behavior of Salt VII* (S. 37-43). Taylor \& Francis.

Cristescu, N., & Hunsche, U. (1998). *Time effects in Rock Mechanics.* Chichester: Wiley & Sons.

Cundall, P. (1971). A computer model for simulating progressive, large-scale movements in blocky rock systems. *Proc. Int. Symp. on Rock Fracture*, (S. 11-8).

Itasca. (2013). *3DEC - 3 Dimensional Distinct Element Code Users's Guide.*

Itasca. (2005). *FLAC – Fast Lagrangian Analysis of Continua Users's Guide.*

Jackson, C. P., Hoch, A. R., & Todman, S. (2000). Self-consistency of a heterogeneous continuum porous medium representation of a fractured medium. *Water Resources Research, 36*(1), 189-202.

Krone, J., Buhmann, D., Mönig, J., Wolf, J., Heusermann, S., Keller, S., et al. (2008). *Überprüfung und Bewertung des Instrumentariums für eine sicherheitliche Bewertung von Endlagern für HAW – ISIBEL.* Gemeinsamer Abschlussbericht FKZ 02E10065 und 10055, DBE TECHNOLOGY GmbH, BGR, GRS, Peine, Hannover, Braunschweig.

Long, J., Remer, J., Wilson, C., & Witherspoon, P. (1982). Porous media equivalents for networks of discontinuous fractures. *Water Resources Research, 18*(3), 645-658.

Manthei, G. (2004). Characterization of Acoustic Emission Sources in a rock salt specimen under triaxial load. *Journal of Acoustic Emission, 22*, 173-189.

Müller, C., Kuate, E.S., von Borstel, E.; Engelhardt, H.J. (2016).Improvement of the Excavation Damaged Zone in Saliferous Formations – Final report – FKZ02E11082

Müller, C., Frühwirt, T., Haase, D., Schlegel, R., Konietzky, H. (in preperation). Modeling Deformation and Damage of Rock Salt using the Discrete Element Method.

Oda, M. (1985). Permeability tensor for discontinuous rock masses. *Geotechnique, 35*(4), 483-495.

Wieczorek, K., & Schwarzianeck, P. (2004). *Untersuchung zur Auflockerungszone im Salinar (ALOHA2) Untersuchungen zur hydraulisch wirksamen Auflockerungszone um Endlagerbereiche im Salinar in Abhängigkeit vom Hohlraumabstand und Spanungszustand.* Tech.rep., Gesell. für Anlagen- und Reaktorsicherheit (GRS) mbH.

Zang, A., Wagner, F. C., Stanchits, S., Dresen, G., Andresen, R., & Haidekker, M. A. (1998). Source analysis of acoustic emissions in Aue granite cores under symmetric and asymmetric compressive loads. *Geophysical Journal International, 135*(3), 1113-1130.

Determination of the 3D in situ stress conditions for the geotechnical planning and the construction of the Brenner Base Tunnel

Ermittlung von 3D Gebirgsspannungszuständen als Basis für die geotechnische Planung und den Bau des Brenner Basistunnels

Roland Braun
Consultancy in Rock Mechanics
Caputh, Schmerberger Weg 113, 14548 Schwielowsee
Chris Reinhold
Brenner Basistunnel BBT SE
Amraser Str. 8, A-6020 Innsbruck

Abstract
This paper presents and compares the results of different procedures for the determination of the 3D in situ rock stress conditions at three positions along the Brenner Base Tunnel. The analyses showed for both the tectonic and the very varied topographical conditions clear differences in the stress regime and in the stress magnitudes and orientations. Independent of this, the maximum horizontal in situ stress component was in good agreement with the World Stress Map at all positions. This includes however only one stress component without any information about its magnitude and is therefore far from being a complete description of the in situ stresses.

A direct complete determination of the 3D in situ rock stress conditions was made with RACOS® stress analyses on core samples. Besides the complete determination of the in situ rock stress conditions these also enable information to be derived about the in situ structures. The results from this are very consistent with the relevant geological model. The comparison of the RACOS® data with the minimum in situ rock stress components determined directly with hydraulic fracs (HF) showed good agreement at all the positions in both magnitude and orientation. For the approximately vertical-horizontal orientated in situ stress conditions there were also almost identical intermediate and maximum components. In contrast, for inclined stress orientations, the intermediate and maximum stress components calculated for a vertical-horizontal approach on the basis of the HF data did not agree with the directly measured 3D RACOS® data, but only with their transformed vertical-horizontal components.

Zusammenfassung
In vorliegendem Artikel werden die Ergebnisse unterschiedlicher Verfahren zur Ermittlung von 3D Gebirgsspannungszuständen an drei Lokationen des Brenner Basistunnels vorgestellt und miteinander verglichen. Die Analysen ergaben sowohl für die tektonisch bedingten, als auch für die verschiedenartigen topographischen Zustände eindeutige Unterschiede des Spannungsregimes, der Spannungsmagnituden und deren

Orientierungen. Unabhängig davon wurde für den maximalen horizontalen Gebirgsspannungsanteil an allen Lokationen eine gute Übereinstimmung mit der World Stress Map festgestellt. Diese beinhaltet jedoch nur eine Spannungskomponente ohne Angaben zu deren Magnitude und reicht deshalb für eine vollständige Beschreibung der in situ Spannungen bei weitem nicht aus.

Eine vollständige direkte Ermittlung des kompletten 3D Gebirgsspannungszustandes erfolgte mit RACOS® Spannungsanalysen an Bohrkernen. Daraus lassen sich neben der vollständigen Ermittlung des Gebirgsspannungszustandes auch Aussagen zu den Gebirgsstrukturen ableiten. Die dabei erlangten Ergebnisse decken sich sehr gut mit dem jeweiligen geologischen Modell. Die Vergleiche der RACOS® Daten mit den bei hydraulischen Fracs (HF) direkt bestimmten minimalen Gebirgsspannungskomponenten zeigten an allen Lokationen eine gute Übereinstimmung sowohl der Magnituden als auch deren Orientierungen. Bei den näherungsweise vertikal-horizontal ausgerichteten in situ Spannungszuständen waren auch fast identische mittlere und maximale Komponenten zu verzeichnen. Bei gekippten Spannungsausrichtungen stimmten dagegen die auf der Basis der HF Messdaten für einen vertikal-horizontalen Ansatz berechneten mittleren und maximalen Spannungskomponenten nicht mit den direkt gemessenen 3D RACOS® Daten, sondern nur mit deren transformierten vertikal-horizontalen Komponenten überein.

1 Introduction

A significant prerequisite for the successful completion of the Brenner Base Tunnel is the guarantee of its constant stability during the investigation, construction and operational phases. In addition to the relevant technical and technological boundary conditions, the rock mass in situ structure, its strength and deformation behaviour, and, to a special degree, the 3D in situ rock stresses around the tunnel influence this. Around the Brenner Base Tunnel, a north-south crossing of the Alps, these are influenced by diverse geological/topographical and tectonic situations. From these there result very different in situ loadings, which were to be determined for the project planning before the construction of the tunnel. The analysis of the primary in situ rock stresses for the project was based initially on hydraulic fracs (HF) in 13 exploration boreholes. To verify and extend these results, RACOS® stress analyses were made on cores from three of these boreholes. In this paper the RACOS® procedure for the direct determination of the 3D in situ stress condition on cores is described and the results obtained with it at three locations are compared with those from HF and from a 2D numerical simulation (2DNS) in one position.

2 Tunnel project and rock mass

2.1 Description of the project

The Brenner Base Tunnel between Innsbruck (Austria) and Franzensfeste (Italy) is 55 km long. With the Innsbruck by-pass it forms the world's longest underground stretch of railway, with a total length of ca. 64 km between Tulfes and Franzensfeste. The tunnel is conceived as a twin-tube system each with a track in one of the directions. A special feature is the full length investigation drift, which is located midway between the two main tubes. This is driven in sections in advance to investigate the geological-geotechnical situation. The investigation results are used immediately in the planning of the main tunnels. In this way risks can be minimized and also construction cost and time can be optimized. Also, the investigation adit serves for drainage and maintenance in the operational phase. A detailed presentation of the project is given, amongst other places, in Bergmeister [1] or Reinhold [2].

2.2 Geological and tectonic situation

Geologically, the Brenner Base Tunnel passes through the central part of the Eastern Alps. From north to south along the line of the tunnel, the main geological zones with the corresponding main tectonic units are (see Figure 2.1):

1. Innsbruck Quarzphyllite (Unterostalpin),
2. Obere Schieferhülle dominantly with Bündnerschiefern (Tauernfenster-Penninikum) – partially folded with the Unteren Schieferhülle,
3. Untere Schieferhülle and Zentralgneiskerne (Tauernfenster-Helvetikum),
4. Obere Schieferhülle dominantly with Bündnerschiefern (Tauernfenster-Penninikum) – partially folded with the Unteren Schieferhülle,
5. Ostalpines Kristallin with thin Maulser Trias,
6. Maulser Tonalitlamelle / Periadriatische fault zone,
7. Brixner Granite (Südalpin).

Further, in the route corridor there are some fault zones of regional or greater importance. The significant fault zone of these is the so called “Periadriatische Naht“. It dived the Südalpen from the Ostalpen and the southern Kalkalpen from the Austrian Zentralalpen. The vertical and horizontal displacements along this fault zone are estimated to be around 100 km.

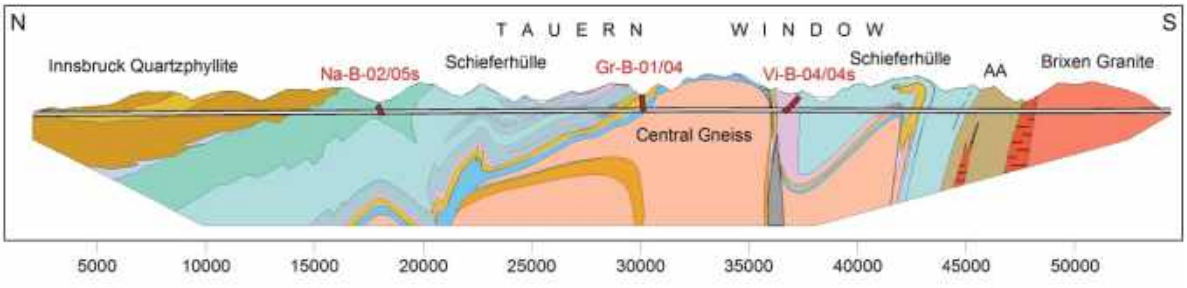

Fig. 2.1: Geological longitudinal section

2.3 Regional stress field

The stress field in the area of the Brenner Base Tunnel is mainly determined by two factors. One is the large scale tectonic stress field. For that, in Figure 2.2, are shown the maximum horizontal stress components in a part of the Alpine arch from a section of the World Stress Map. There it shows for the whole area including the project section a mainly N-S to NNW-SSE oriented constraint. This always acts perpendicular to the Alpine arch. Besides this, the local stresses in the area of the route corridor are strongly affected by the alpine topography and therefore by the relief of the terrain.

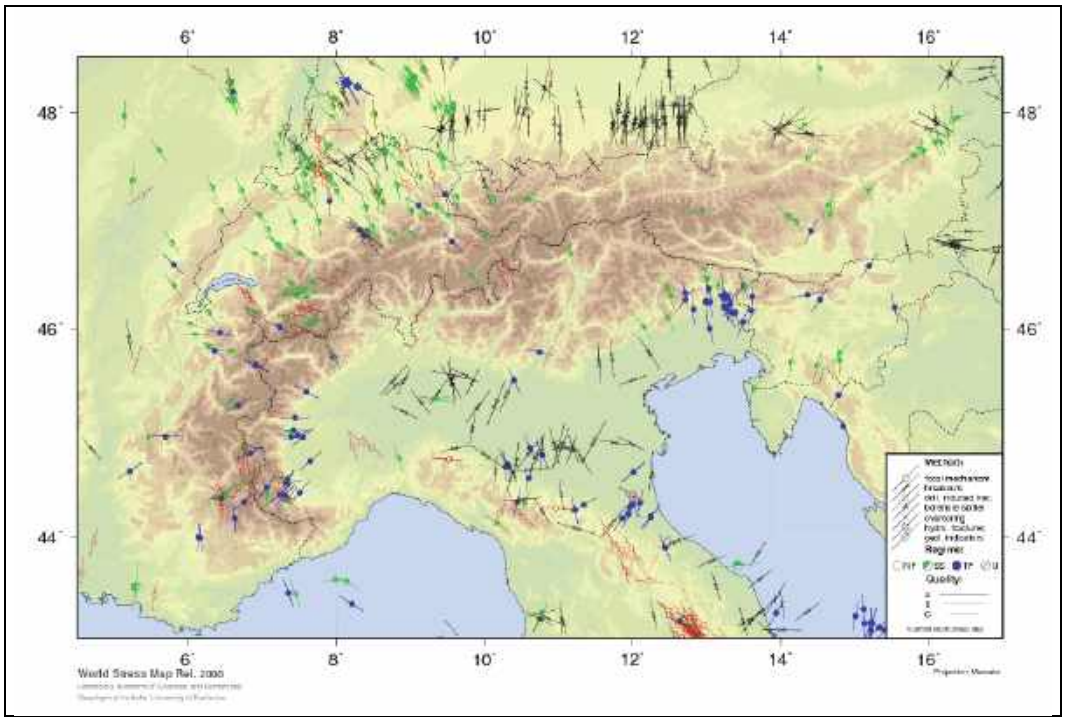

Fig. 2.2: Detail of the Alpine arch from the World Stress Map [3]

3 Significant in situ stress components

For considerations of stability the effective loading components in all three principal directions must be taken into account. Some comments on this are given below.

3.1 Direction-dependent loadings

For the 3D stability considerations required for the tunnel structures it is always necessary to consider the complete 3D in situ rock stress condition. Otherwise serious misjudgements of the stability situation can arise. Figure 3.1 shows the results of an example stability calculation with the BOREHOLE (vgl. Braun [4]) 3D elastic analysis package for a horizontal section of tunnel in a horizontal-vertical oriented in situ principal stressfield. Identical in each case are the mechanical properties of the rock, the overburden pressure σ_v and the minimum in situ rock stress measured by hydraulic frac σ_h. The usually not directly determined maximum horizontal stress σ_H is chosen freely.

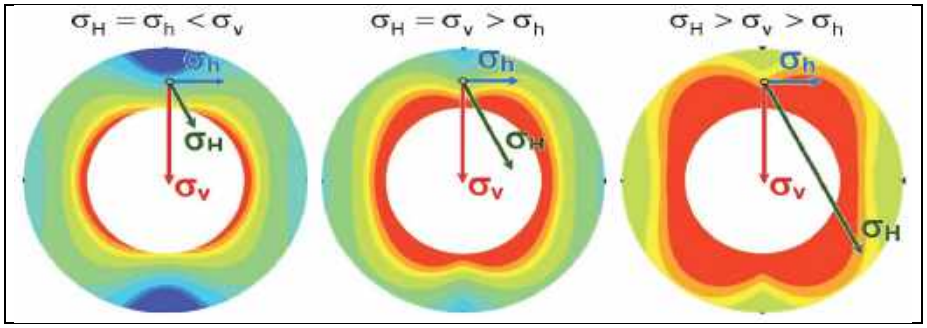

Fig. 3.1: Example of the effect of different horizontal-vertical 3D in situ stresses on the stability of a horizontal tunnel (the rock failure areas are shown in red). The arrow lengths show the magnitude of the corresponding in situ rock stress components.)

The example illustrates the marked influence of different magnitudes of the maximum horizontal stress component σ_H and thus of different stress regimes on the intensity of failure. In this case the shear stresses parallel to the tunnel axis are especially destructive. Therefore all loading magnitudes and orientations are always to be determined exactly and not just estimated.

3.2 Total and effective loadings

The interpretation of in situ stress analyses for the purposes of stability requires consideration of various loading components. One of these is the external (total) in situ rock stress, which results from the average density and the thickness of the overlying rocks and from tectonic influences, the in situ deformation properties of the rocks and from its horizontal constraint. The internal component is the hydraulic pore pressure. For that it is necessary to take into account that, depending on the rock structure and its deformation properties, its mechanical effectiveness is reduced by the factor of the pore pressure effectiveness (Biot-coefficient) between 0 and 1 (see Braun [5]). For deformations, instabilities and rock failure the 3D combination of the external and internal components is the relevant one. This is described as the effective stress and it is shown in its relationship in Figure 3.2.

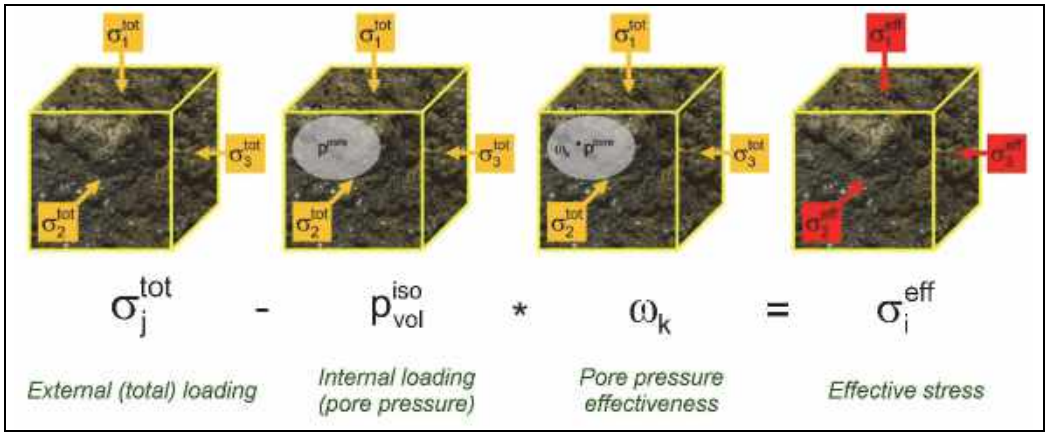

Fig. 3.2: Combination of the various in situ loading components

4 Applied in situ stress analyses

Because of the need for anticipatory in situ rock stress investigations classical in situ measurements at the excavation face (flat jack etc.) cannot be considered at first. For this reason, in this case, the analyses carried out of primary in situ rock stresses were based on hydraulic fracs (HF) in 13 exploration boreholes, RACOS® stress analyses of core from 3 of these boreholes and one stress modelling on the basis of rock parameters (2DNS) for the borehole Na-B-02/05a. With HF the minimum was determined directly and with RACOS® all three principal in situ stresses. The other, with HF and 2DNS not directly determined, direction-dependent in situ rock stresses were calculated with specific approaches. It should be noted that with HF the total and with RACOS® and also mainly with 2DNS the effective in situ stresses were determined.

4.1 Hydraulic fracturing (HF)

Hydraulic fracturing determines directly the minimum total in situ rock stress component. For this purpose a section of borehole is isolated with hydraulic packers and then pressurized with a fluid. This continues until, in intact unfissured rock, a crack forms in the borehole wall and widens, or in fissured rocks existing cracks/fissure open hydraulically. The stable pressure (closure pressure) after the injection corresponds as the normal to the surface of the crack or fissure directly to the minimum total in situ stress. The determination of the geographical orientation (accounting for the geometrical data of the borehole) is based on crack traces on special (geographically oriented) impression packer. As a further parameter, the total overburden pressure can be derived from the density log of the borehole. This is however not necessarily identical with a principal stress component. Under the assumption of a horizontal-vertical orientation of the principal stresses and the use of a rock tensile strength for a homogeneous isotropic rock mass the maximum horizontal stress component can also be calculated. The rock tensile strengths can be derived from laboratory tests and/or from the use of various pressures during fracking. In the project area of the Brenner Base Tunnel it must be taken into account that for the largest part of the route there is metamorphic rock with pronounced anisotropy. Further, because of the tectonic situation and the topographical conditions it is only in a few areas that there are horizontal-vertical principal stresses. Therefore, in general, only the minimum total stress component can be determined.

Further, with the HF procedure the mechanical operating pore pressure is not considered. With use of an inversion calculation procedure no assumption about pore pressure is required for the calculation of the horizontal stress through an extended evaluation of the crack formations and orientations in several hydraulic fracs at different depths in a borehole. However this inversion procedure only works reliably when the overburden pressure is a principal stress component and thus when there is a vertical-horizontal principal stress orientation. Also, for 3D considerations the vertical principal stress component must have the intermediate or the maximum magnitude (see Baumgartner [6]).

4.2 RACOS® Analyses

The effective 3D in situ principal stresses are determined directly with RACOS®. The basis for this are analyses of the deformation and breakage of the core due to unloading following its removal from the surrounding rock. For this optimally oriented rectangular blocks are taken (see Figure 4.1 left). There then follows in the laboratory a hydrostatic reloading with simultaneous measurement of the spatial propagation velocities of compressional and shear waves (see Figure 4.1 right).

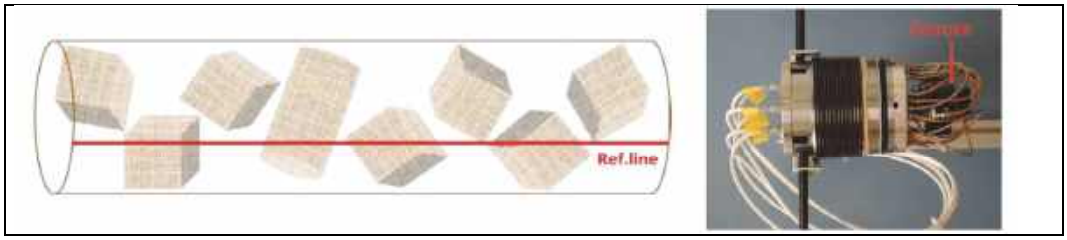

Fig. 4.1: Preparation and testing of the core samples

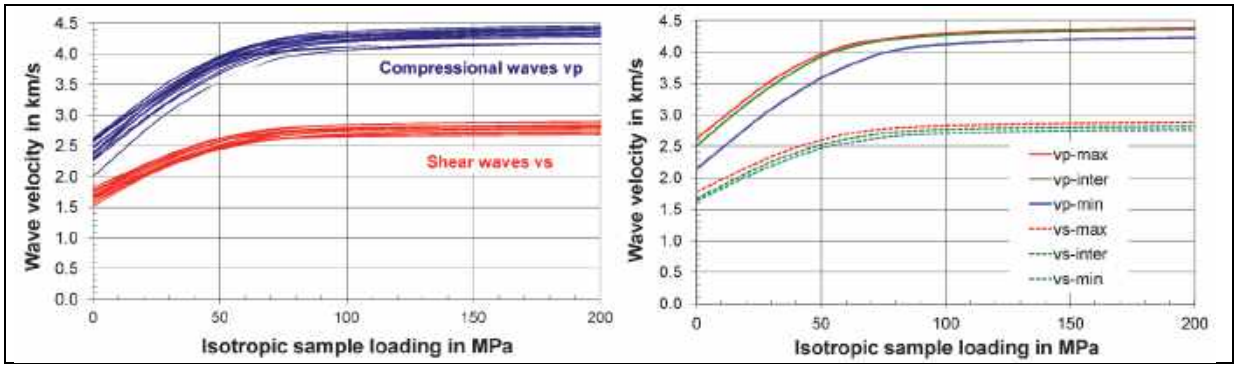

Fig. 4.2: Direction and load dependent measured data (left) and their 3D principal components (right)

The determined direction and loading dependent measurement values (see Figure 4.2 left) are then combined statistically with reference to their three principal normal's (see Figure 4.2 right). Their spatial orientation is initially referred to a reference line on the core. With orientated coring the geographical 3D orientation is then available directly. In other cases the corresponding reorientation is carried out using comparisons of specific data. That can be comparing recognizable structural elements on the core, or geophysical parameters (compressional wave velocity etc.) which have been measured on it, with the in situ rock structure. Further, an orientation is also possible using that

of the visco-remnant magnetization in the recent terrestrial magnetic field. There then follows the determination of the magnitudes and anisotropies of the propagation velocity of elastic waves relevant for the rock texture. For this the hydrostatic pressure is determined (see Figure 4.3 left) which there occur no loading related changes of the mean velocity of elastic waves (dvp-mean) and/or of their direction dependent deviators (dvp-diff). Above this value (Correction load) the propagation velocity of elastic waves is characterized only by the rock facies, whereas below it loading-related structural changes are also contained. For the determination of the purely loading-related rock behaviour the measured compressional and shear wave velocities are calibrated with this correction value for the influence of the rock fabric (see Figure 4.3 right). In the figure, as an example, the compressional wave velocity is shown, as the loading magnitudes and directions are generally derived from this. This is based on the fact that the effective principal stresses act parallel to the principal propagation directions of the compressional waves.

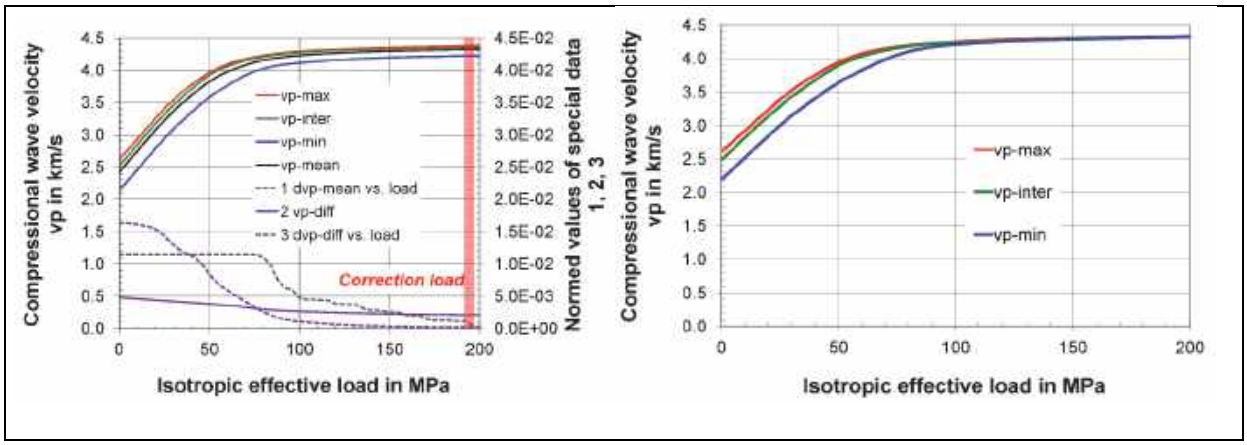

Fig. 4.3: Determining the calibration load (left) and the thus corrected load-dependent compression wave velocity (right)

The then remaining velocity anisotropies (see Figure 4.3 right) result from the structural changes of the rock following unloading from a triaxial in situ rock stress and/or other loosening resulting from technical effects during coring or sample preparation. On unloading additional seismic anisotropies can occur resulting from directional differences in the deformation behaviour of the rock (anisotropic constitutive law). On hydrostatic reloading these latter anisotropies will be compensated again. Furthermore, the loading independent facies related anisotropies are negated by the previously mentioned calibration of the measurement data. There remain the velocity anisotropies from the loosening caused by stress deviators. There is generally not a steady line for the relation between hydrostatic loading and the measured principal propagation direction of compressional and shear waves. (see Figure 4.4). Rather the closure/compensation of loosening and cracks resulting from coring is documented on reloading by often sudden changes of the azimuth and dip of the calibrated elastic waves. These effects are most clearly recognized for the shear waves. The orientation of the calibrated compressional wave velocity in the moment of compensation of an unloading-related plane of weakness shows the orientation of the normal to that plane and so the effective principal stress component. The magnitude of this is the hydrostatic reloading pressure which closed the crack. In this regard, it should be noted that the minimum component

of the compressional wave velocity is usually perpendicular to the maximum breakage (loosening) and so parallel to the greatest change of loading.

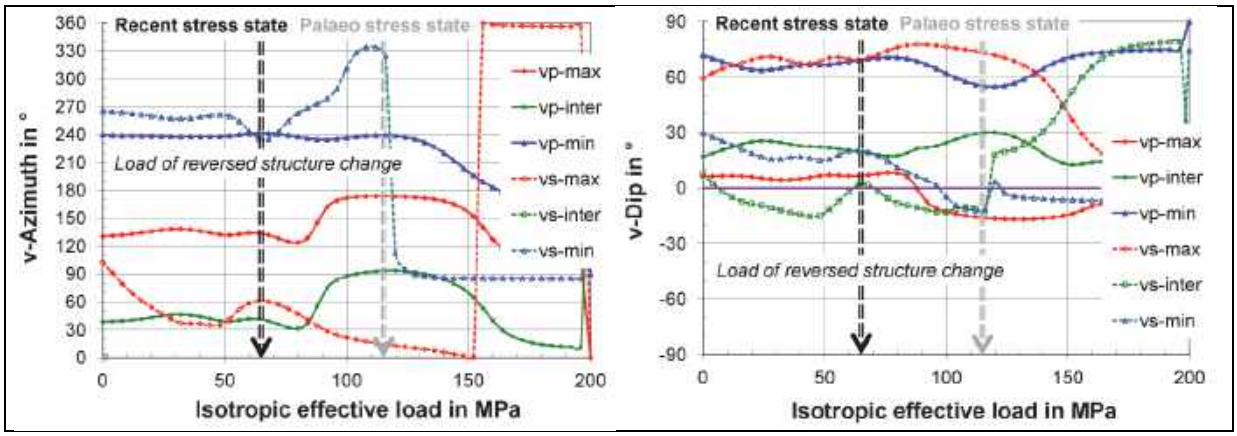

Fig. 4.4: Example of identification of effective stress components based on the load-dependent principal directions of the propagation of elastic waves

In this way, on the basis of the orientation of a principal compressional wave velocity, the magnitude and orientation of the corresponding principal stress component can be determined directly. This method can be applied for the recent and also for paleo in situ rock stress conditions. In this example (see Figure 4.4) the directly determined effective stress component on crack closure (Load of reversed structure change) corresponds to the maximum loading (parallel to the minimum compressional wave velocity).

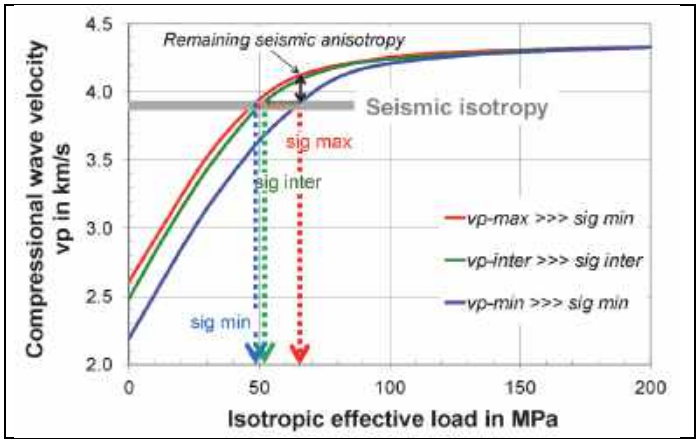

Fig. 4.5: Derivation of the effective 3D stresses

The determination of the other two 3D principal stress components is based on a comparative consideration of the calibrated loading-dependent compressional wave velocities. This is based on the approach that on coring and therefore unloading from an anisotropic in situ rock stress field, there occur direction-related differences in the intensity of deformation/loosening, and so seismic anisotropy which does not result from an anisotropic constitutive law. On hydrostatic reloading it is true that the magnitudes change, but there remain, in comparison with the directly determined comparison value, differences in the compressional wave velocities in the individual directions (shown in Figure 4.5 as "Remaining seismic anisotropy"). The seismic isotropy of the in situ initial

condition of interest can then only be reached through additional triaxial stress components. These document the effective stress anisotropy at coring.

The determination of the corresponding loading components is calculated in RACOS® on the basis of the experimentally determined relations between compressional wave velocity and hydrostatic loading. The simplest way to determine the principal effective in situ rock stress components is to drop a perpendicular to the isotropic loading axis from the intersection of the comparison value of the isotropic compressional wave velocity with the other direction-related principal velocity components. In doing this, the spatial orientation of the individual principal stress components can be derived from the relevant principal propagation directions of the compressional waves. To check the validity of the determined effective stress tensor its vertical component is compared with the effective overburden pressure. This is the result of the overburden load of the rock mass, the pore pressure and the pore pressure effectiveness (see Figure 3.2). A load smaller than the real overburden pressure indicates rock damage from drilling or sample preparation. In contrast, sudden changes in the orientation of elastic waves at higher pressures suggest the presence of possible paleo conditions. All this applies to effective rock stresses. The calculation of the 3D total stress is made by linking the determined effective stress, the pore pressure and the 3D pore pressure effectiveness (see Fig 3.2). The latter is calculated from the measured rock 3D compressional and shear wave velocities, and the derived values of these for the rock solid, and the densities. The results are generally presented in tables and in Schmidt plots (see the example in Fig. 4.6).

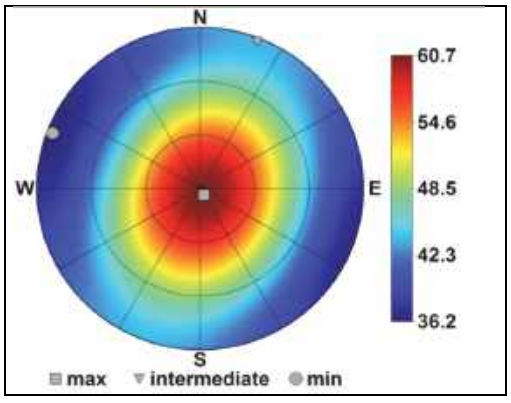

Fig. 4.6: Presentation of determined effective stresses in a Schmidt plot

These plots are for visualizing 3D data on a 2D disc. The direction (azimuth) of the parameter is given around the perimeter. It starts with 0° (North) and continues clockwise. The inclination with reference to horizontal (dip) is taken from the radius. The outer circle shows a zero dip and the centre point vertical, with a dip of 90°. The magnitudes of the parameter (in this case effective stress) are shown by a colour scale.

In summary, RACOS® is based on special laboratory tests on cores and specific links between their results (see Fig. 4.7).

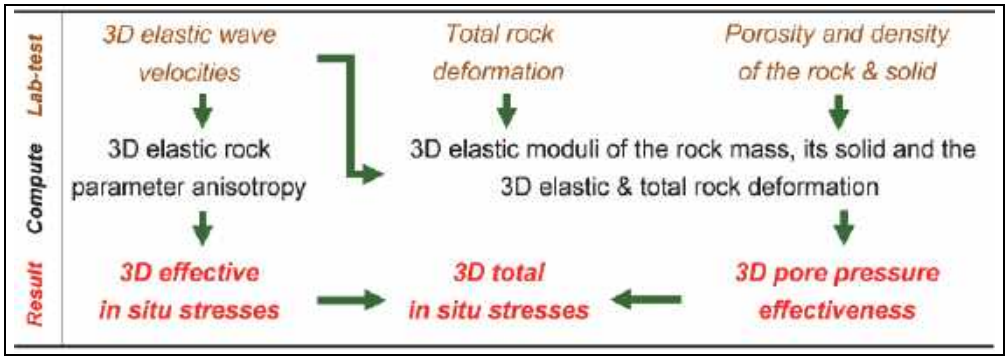

Fig. 4.7: Overview of the RACOS® procedures

4.3 Numerical simulations (2DNS) to obtain in situ stresses

The computational establishment of the stress condition in rock mass conditions such as those found at the Brenner Base Tunnel is a complex task. The stress condition there, besides the topographical influences, is also strongly affected by the tectonic situation and the geological history. As was shown in Section 3.1, for considerations of stability the 3D principal normal stress components and their orientation are always necessary. These can only be captured at all by elaborate 3D calculations. The additional inclusion of tectonic stresses in 3D numerical calculation models is not reasonably possible. Too many assumptions must be made about the boundary conditions. Numerical stress analyses can therefore only be applied in support with simple boundary conditions. In situ or laboratory tests for stress analysis cannot be replaced by numerical calculations. In the current case the stress situation could only be understood with a numerical calculation model for borehole Na-B-02/05s. In the area of this borehole there are relatively simple boundary conditions. The numerical simulation to obtain the stress conditions and to verify the measurements for borehole Na-B-02/05a was made with a 2D model. The calculation program was Version 8 of Rocscience‘s Phase2. The rock was modelled as elastoplastic with a Mohr-Coulomb failure criterion.

Because of the topography there the model used a section perpendicular to the valley and so parallel to the tunnel route (see Fig. 4.8). From a geotechnical point of view the area can be divided into three sections: Quarzphyllite (IQP-QP) in the northern part, Kalkschiefer (SH-KS) in the southern part and a zone of alternating Schwarzphyllite-Calcite-Quarzite (SH-SK). Borehole Na-B-02/05s was drilled there. The relevant parameters of the geological conditions were based on investigation data for this zone. The calculation of the in situ rock loading was made purely gravitationally with densities determined from cores. It has not yet been possible to obtain the the stress situation for boreholes GR-B-01/04 and Vi-B-04/04s. Because of the topographical situation in the areas of these two boreholes (see Fig. 5.1) 3D consideration is imperative. Further, the stress situation in the areas of these two boreholes is strongly tectonically influenced. This is clearly seen from the following results.

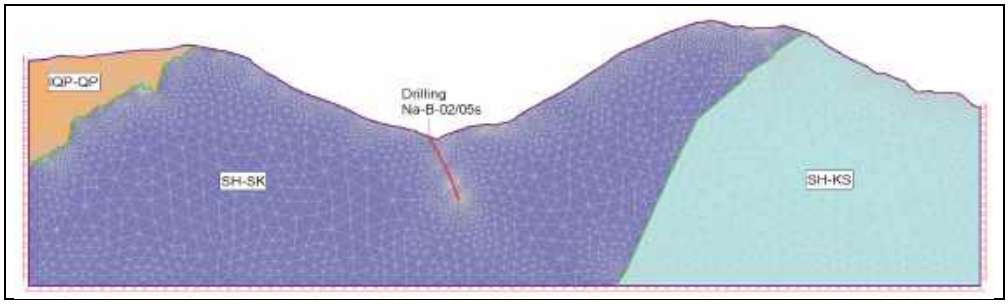

Fig. 4.8: Numerical model for determination of rock stresses, borehole Na-B-02/05s

5 Comparison of analysis results

In the course of the investigations to date of the Brenner Base Tunnel between 2004 and 2012 hydraulic fracs (HF) were carried out to determine the in situ stressfield in 13 locations. Fig. 5.1 shows the elevation model of the project area, the route of the Brenner Base Tunnel and the positions of the boreholes for the hydraulic fracs carried out to date. From these, three positions were selected for the RACOS® stress analyses (Na-B-02/05s, GR-B-01/04, Vi-B-04/04s) and one for the numerical modelling (Na-B-02/05s). In the following the analysis results obtained for these positions with the individual methods are documented and compared.

5.1 Na-B-02/05a

Location: Borehole Na-B-02/05a was drilled in Navistal, a deeply-cut, WSW-ENE striking v-shaped valley. The existing faults/fissures/cracks there document themselves in the direction of the maximum compressional wave velocity. In the RACOS® analysis zone this was almost horizontal towards the west and so approximately parallel to the Navistal (see Fig. 6.1 left). The minimum velocity component as normal to these fault planes indicated their ca. 50° dip to the south. The borehole itself ran SSE, and thus approximately perpendicular to the course of the valley and with a dip of 70° in the analysis zone.

Stress analyses: In borehole Na-B-02/05a 8 hydraulic fracs were made at vertical depths (TVD) from 232 to 416 m. The analysis here is of a frac at TVD = 416 m. The RACOS® analyses were carried out on a piece of core from the Kalkschiefer at TVD = 432 m. A 2D numerical simulation was also made for this area. That simulation was made for a plane calculation section perpendicular to the valley and thus parallel to the tunnel. The results of all the investigations are summarized in Table 5.1. These also contain a horizontal-vertical transformation of the RACOS® data. The coloured cells contain the directly measured data. Of these σ_{min} corresponds to the closure pressure of the hydraulic frac. Figure 5.2 also shows the location and the trace of borehole Na-B-02/05a, as well as the principal stress directions determined with RACOS® and HF.

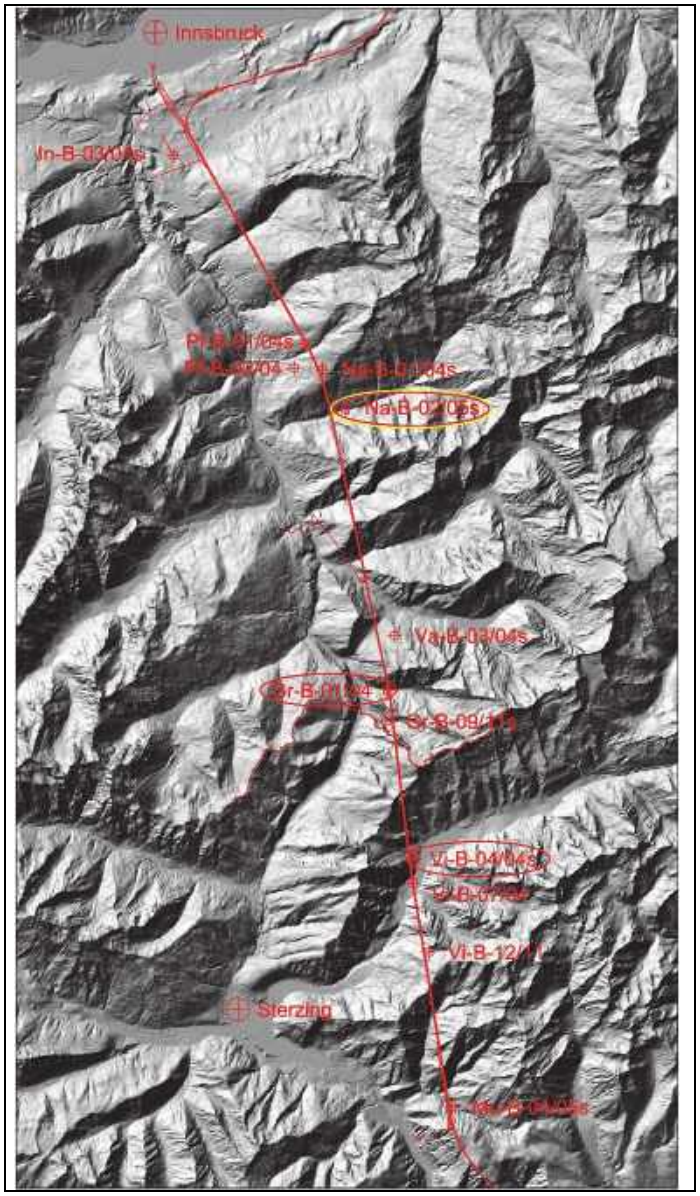

Fig. 5.1: Route of the Brenner Base Tunnel, with the locations of the previously executed hydraulic fracturing tests, the (outlined in red) RACOS® analyses and the numerical simulation (yellow outline) in the elevation model of the project area

The small difference between the minimum magnitudes for the effective stress determined in RACOS® and the total stress measured with the hydraulic frac results from the small pore pressure effectiveness and/or pore pressures in the surrounding tight rock (see the relationships in Fig. 3.2). The overburden pressure with a dip of 90° is almost identical for all three analyses (HF, horizontal-vertical transformation of the RACOS® data and 2DNS). However the determined vertical stresses indicate an (unrealistic) average density of the overlying rocks of 3.52 g/cm^3. It is therefore to be assumed that this rock load documents a (preserved) condition during the development of the deeply-incised Navistal. For an average real density of the overlying rock of 2.75 g/cm^3 the overburden pressure corresponds to a vertical depth of 552 m and so to a height difference of the vertical stress due to the valley formation of 120 m. This present condition corresponds only to a small extent to the actual height difference of > 600 m and is therefore only a residue of earlier vertical in situ rock loading. This shows the marked

influence of the rock mass topography. Further, the RACOS® measurement data show a recognizable inclination of σ_{max} and σ_{inter} around the axis of σ_{min}, so that the maximum and intermediate principal normal stress in the rock mass are deviated in their working from horizontal/vertical. This must be considered in stability analyses.

Table 5.1. Compilation of stress analysis data for borehole Na-B-02/05s

Parameter*		Hydraulic Frac $\sigma_{i\text{-}HF}^{tot}$ (TVD 416 m)	RACOS® $\sigma_{i\text{-}R}^{eff}$ (TVD 432 m)		Numerical 2D Simulation
			measured	transformed	
σ_{max}	Magnitude in MPa	22.0	22.0	20.9	22.6
	Azimuth in °	340	358	358	358
	Dip in °	0	22	0	0
σ_{inter}	Magnitude in MPa	14.7	13.8	14.9	15.4
	Azimuth in °	70	167	0	0
	Dip in °	90	68	90	90
σ_{min}	Magnitude in MPa	9.4	9.0	9.0	-
	Azimuth in °	250	267	268	-
	Dip in °	0	4	0	-

*: In this case the overburden pressure does not correspond to a principal normal stress component. Accordingly, the calculated HF - data for σ_{max} & σ_{inter} do not describe real principal stresses, but only approximately their horizontal-vertical transformations.

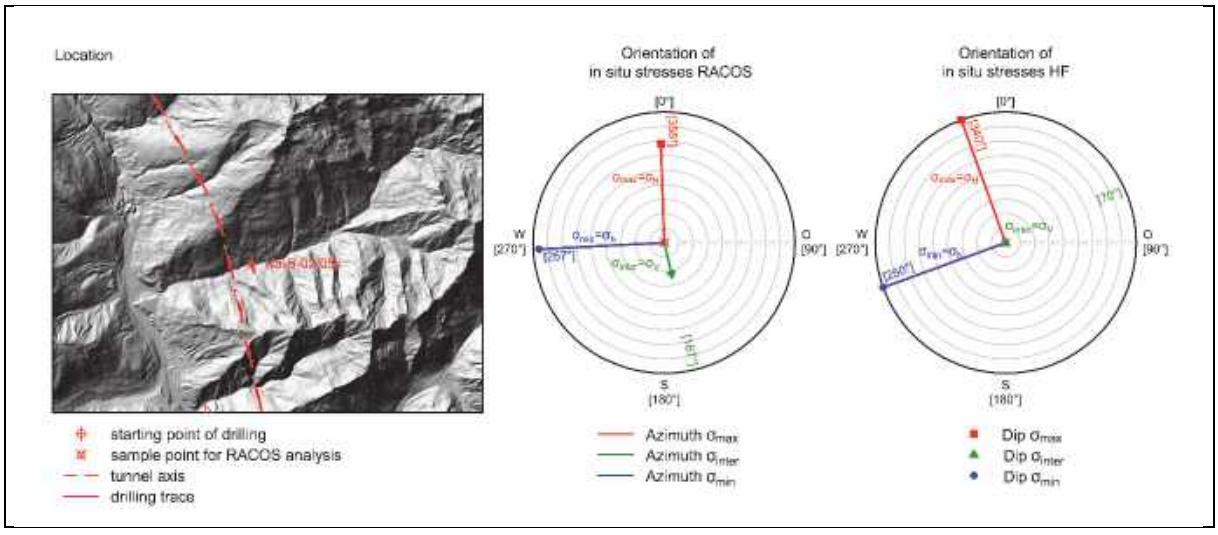

Fig. 5.2: Overview of location Na-B-02/05s and the principal stress directions determined there

Stress regime: Because of the determined in situ rock stresses the stress regime in the area of borehole Na-B-02-05s corresponds to a strike slip with $\sigma_H > \sigma_v > \sigma_h$. This clearly resulted from the uplift and the upfaulting of the Alps with a N-S compression and resulted in a slight inclination of the N-S loadings.

5.2 GR-B-01/04

Location: Borehole GR-B-01/04 was drilled in the approximately eastward striking Venntal. The faults there are documented in the direction of the maximum compressional wave velocity. In the RACOS® analysis zone this is ENE-WSW and so almost parallel to the valley (see Fig. 6.1 central). The minimum velocity component indicates for the normal to these fault planes a dip of 40° to the NW. The borehole itself ran SE, and so almost perpendicular to the line of the valley, with a dip of 74° in the analysed section.

Stress analyses: In borehole GR-B-01/04 9 hydraulic fracs were made at vertical depths (TVD) from 501 to 785 m. This evaluation is for a frac at TVD = 501 m. The RACOS® analyses were made on a piece of core from the Kalkmarmor from a depth TVD = 502 m. The results of all the investigations are summarized in Table 5.2. These include a horizontal-vertical transformation of the RACOS® data. Figure 5.3 shows the location and the alignment of borehole Gr-B-01/04, as well as the principal stress directions determined with RACOS® and HF.

Table 5.2. Compilation of stress analysis data for borehole Gr-B-01/04

Parameter*		Hydraulic Frac $\sigma_{i\text{-}HF}^{tot}$ (TVD 501 m)	RACOS® $\sigma_{i\text{-}R}^{eff}$ (TVD 502 m)		Numerical 2D Simulation
			measured	transformed	
σ_{max}	Magnitude in MPa	13.8	16.0	12.7	-
	Azimuth in °	163	153	0	-
	Dip in °	0	47	90	-
σ_{inter}	Magnitude in MPa	13.3	10.5	12.6	-
	Azimuth in °	73	23	351	-
	Dip in °	81	31	0	-
σ_{min}	Magnitude in MPa	6.9	6.7	7.9	-
	Azimuth in °	253	276	261	-
	Dip in °	9	27	0	-

*: In this case the overburden pressure does not correspond to a principal normal stress component. Accordingly, the calculated HF - data for σ_{max} & σ_{inter} do not describe real principal stresses, but only approximately their horizontal-vertical transformations.

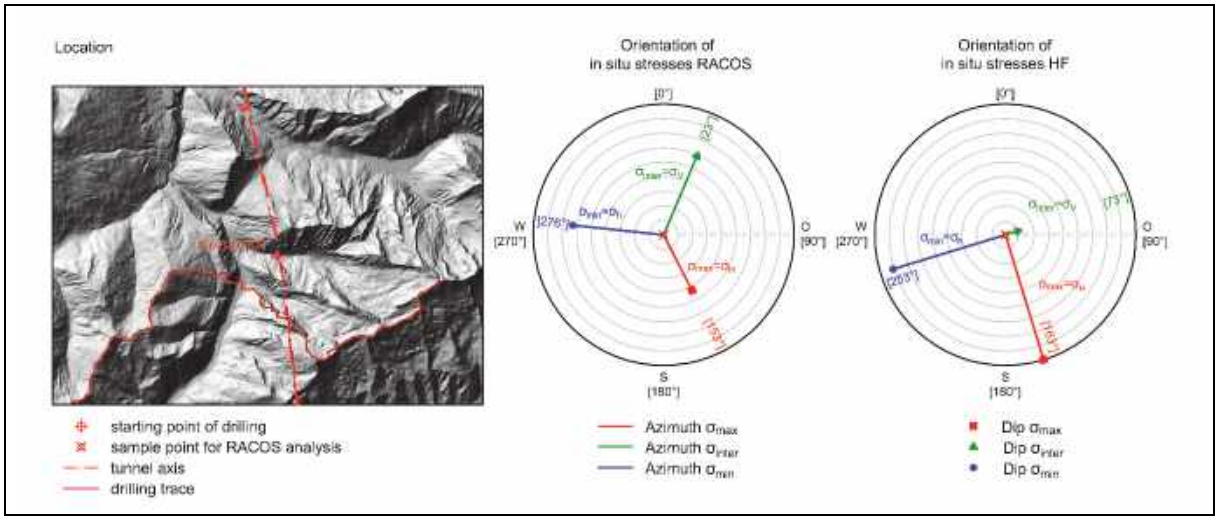

Fig. 5.3: Overview of location Gr-B-01/04 and the principal stress directions determined there

Because of the almost identical minimum magnitudes of the effective stresses determined with RACOS® and the total stress measured by hydraulic frac, a mechanical pore pressure effect can be largely excluded. Therefore the effective stress resulting from a vertical-horizontal transformation of the RACOS® measurement data corresponds approximately to the total overburden pressure and so to an average density of the overlying rocks of 2.58 g/cm^3. For the calculation of the two in situ rock stress values which are not directly measurable with hydraulic fracturing (HF) 2.65 g/cm^3 was assumed, which is a somewhat higher average density than that found with RACOS®. The vertical total loading determined with this is therefore slightly larger. The intermediate stress magnitude, which was also calculated, is, in contrast, clearly larger and the maximum stress component considerably smaller than the data measured in RACOS®. However the magnitudes differ only slightly in comparison with the horizontal-vertical transformation of the RACOS® measured values. It can be concluded from this that the calculations in this case on the basis of hydraulic fracs only describe the horizontal-vertical loading components. They do not take into account any inclination of the real principal stresses. This may lead to significant miscalculations in stability analyses.

Stress regime: Because of the transformed maximum horizontal stress in the direction N351°E with an approximately N-S orientation, the only slightly larger vertical stress and a much smaller E-W striking minimum component the original stress regime corresponds to a transition from normal fault with $\sigma_v > \sigma_H > \sigma_h$ to strike slip with $\sigma_H > \sigma_v > \sigma_h$. This is connected with thrusts/uplifts and N-S striking shear fracturing. However the whole rock mass was subsequently faulted again and again and has a steeply dipping folded structure. From this resulted a clearly identifiable inclination of the principal stresses. This affects above all the now much larger maximum component with a recent azimuth of SSE and a dip of 47°.

5.3 Vi-B-04/04s

Location: Borehole Vi-B-04/04s was drilled from an elevated area (not from a valley). The maximum compressional wave velocities, to document the direction of faulting there, is almost vertical in the RACOS® analysis section and the only slightly smaller intermediate component is approximately horizontal in the direction E-W (see Fig. 5.4). The approximately horizontal in the direction N-S measured minimum compressional wave velocity indicates steeply inclined E-W striking layer interfaces/faulting. The borehole direction was N350°E and so approximately in the direction of the layer surface normals, however with a much greater dip.

Stress analysis: In borehole Vi-B-04/04s 8 hydraulic fracs were made at vertical depths (TVD) from 572 to 717 m. The evaluation here refers to a frac at TVD = 642 m. The RACOS® analyses were made on core from strongly foliated Quarzphyllite from a depth of TVD = 642 m. The results of all the analyses made are summarized in Table 5.3. These also include a horizontal-vertical transformation of the RACOS® data. In Figure 5.4 are shown the location and the alignment of borehole Vi-B-04/04s, as well as the principal stress directions determined with RACOS® and with HF.

Table 5.3. Compilation of stress analysis data for borehole Vi-B-04/04s

Parameter+		Hydraulic Frac $\sigma_{i\text{-}HF}^{tot}$ (TVD 642 m)	RACOS® $\sigma_{i\text{-}R}^{eff}$ (TVD 642 m)		Numerical 2D Simulation
			measured	transformed	
σ_{max}	Magnitude in MPa	28.0	27.2	27.1	-
	Azimuth in °	-	348	349	-
	Dip in °	-	6	0	-
σ_{inter}	Magnitude in MPa	20.0	23.2	23.2	-
	Azimuth in °	-	258	259	-
	Dip in °	-	2	0	-
σ_{min}	Magnitude in MPa	16.7	17.2	17.3	-
	Azimuth in °	-	150	0	-
	Dip in °	-	84	90	-

+: In this case only indistinct impressions of the frac cracks were obtained with the packer. Therefore no reliable derivation could be made on this basis about the orientations of the measured σ_{min} or of the calculated σ_{max} & σ_{inter} from HF.

Because of the evident small difference between the minimum magnitude of the effective stresses determined with RACOS® and the total stress measured with a hydraulic frac, a mechanical pore pressure effect in the depth zone of 642 m is largely excluded. Further, the minimum in situ rock stress in RACOS® dipped very steeply and corresponds approximately to the overburden stress. This implies a mean density of the overlying rocks of 2.75 g/cm^3.

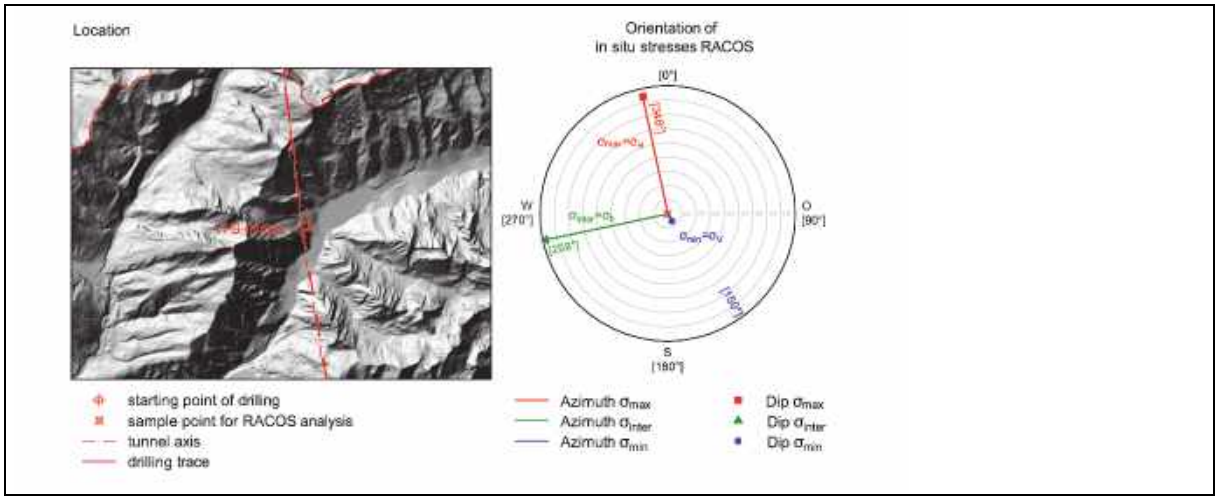

Fig. 5.4: Overview of location Vi-B-04/04s and the principal stress directions determined there

Stress regime: Because of the arrangement of the stress components the stress regime corresponds to a thrust fault, with $\sigma_H > \sigma_h > \sigma_v$. The northward acting horizontal maximum component results clearly (analogously with Na-B-02/05s and GR-B-01/04) from the upfolding of the Alps with a N-S compression. At this location there is an intermediate component oriented E-W which is also horizontal and which is clearly relevant for the almost vertical layer interfaces which have the same strike. To that extent, this configuration is less that of a classical thrust and has more to do with a local tectonic, possibly in connection with horizontal and vertical displacements of blocks along the Periadriatischen Naht. The smallest principal stress component corresponds to the overburden pressure.

6 Data evaluation and interpretation

The comparative in situ rock stress analyses were made for three very different locations, depths and geological contexts of the Brenner Base Tunnel.

For the northern tunnel area the analyses were carried out for borehole Na-B-02/05a in the Navistal at a vertical depth of TVD = 416m & 432 m in Kalkschiefer. The faulting identified in the compressional wave velocities runs E-W parallel to the Navistal and dips ca. 50° to the south (see Fig. 6.1 left). This matches the geological model, which foresees East-West striking fault systems in the side valleys of the Wipptal. These East-West striking fault systems were already encountered in the surface mapping. The maximum principal stress was found there in an approximately horizontal N-S orientation (see Fig. 6.2 left). With the steeply dipping intermediate principal stress and the horizontal E-W acting minimum component this corresponds to a tectonic strike-slip regime. The overburden pressure in this valley incision does not only result from the density of the overlying rock, but still includes residual loadings from the time before the formation of the valley. A comparison of the 8 hydraulic fracs made in the borehole shows almost no increase with depth of the horizontal stresses, and so much less than the increase in overburden pressure.

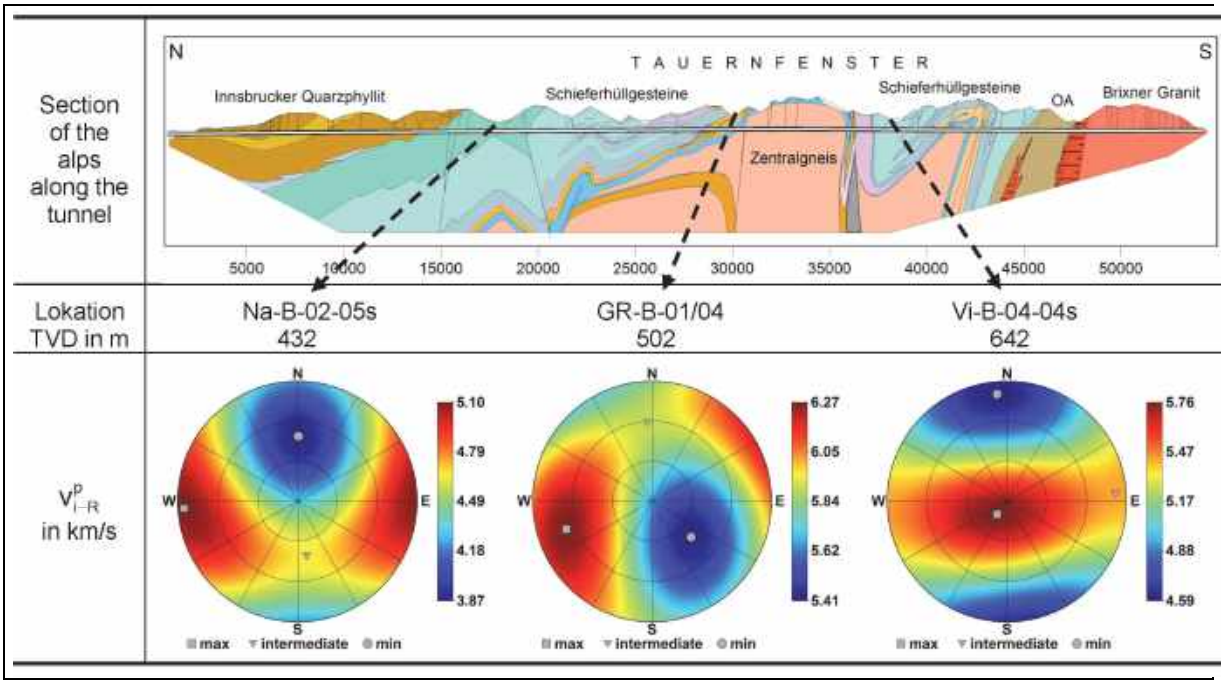

Fig. 6.1: Comparison of the rock structures in the analyzed locations based on the 3D propagation velocities of compressional waves determined in RACOS® (v^P_{i-R})

For the middle part of the tunnel the analyses were made at a vertical depth TVD = 50 m - 502 m in Kalkmarmor in borehole GR-B-01/04, which was drilled in Venntal. The structures identifiable in the compressional wave velocities strike parallel to the Venntal, approximately in the direction ENE-WSW with a dip of 40° to the NW (see Fig. 6.1 centre). This corresponds essentially with the main foliation direction of the marble in this area. The maximum principal stress found there acts SSE with a dip of 47° (see Fig. 6.2 centre). As a result of the local structural folding the inclined principal stresses have horizontal and vertical components, which document a transition from normal fault to strike slip with an approximately N-S oriented maximum horizontal stress. In comparison of the 9 hydraulic fracs made in the borehole the horizontal stresses increase more strongly with depth than the overburden pressure. However, in this location there is a pronounced inclination of the principal stresses, which is not considered sufficiently in the calculations for hydraulic fracs. In a comparison of all the locations and depths the smallest gradient for the minimum principal stress was in borehole GR-B-01/04.

For the southern tunnel area the analyses were carried out at a vertical depth TVD = 462 m in strongly foliated Quartzphyllite at borehole Vi-B-04/04s, which was drilled in an elevated area. The layering/faults recognizable in the compressional wave velocities dip very steeply (81°) to the south and strike E-W (see Fig. 6.1 right). This reflects in this area to the orientation of the foliation. The maximum principal stress was found to have an approximately horizontal N-S orientation (see 6.2 right). In addition, at this location there is an intermediate principal stress oriented horizontal E-W which is clearly relevant for the layer surface which strikes in the same direction and is almost vertical. The smallest principal stress corresponds there to the overburden pressure. Because of the steeply dipping structures this stress configuration is less of a classical thrust, but rather results from a specific local tectonic along the Periadri-

atischen Naht. At the location Vi-B-04/04s, in comparison with all the investigated locations and depths, the greatest gradient was found of the (in this case vertically oriented) minimum principal stress. A comparison of the 8 hydraulic fracs made in the borehole showed that the horizontal stresses increase with depth more slowly than the overburden pressure does.

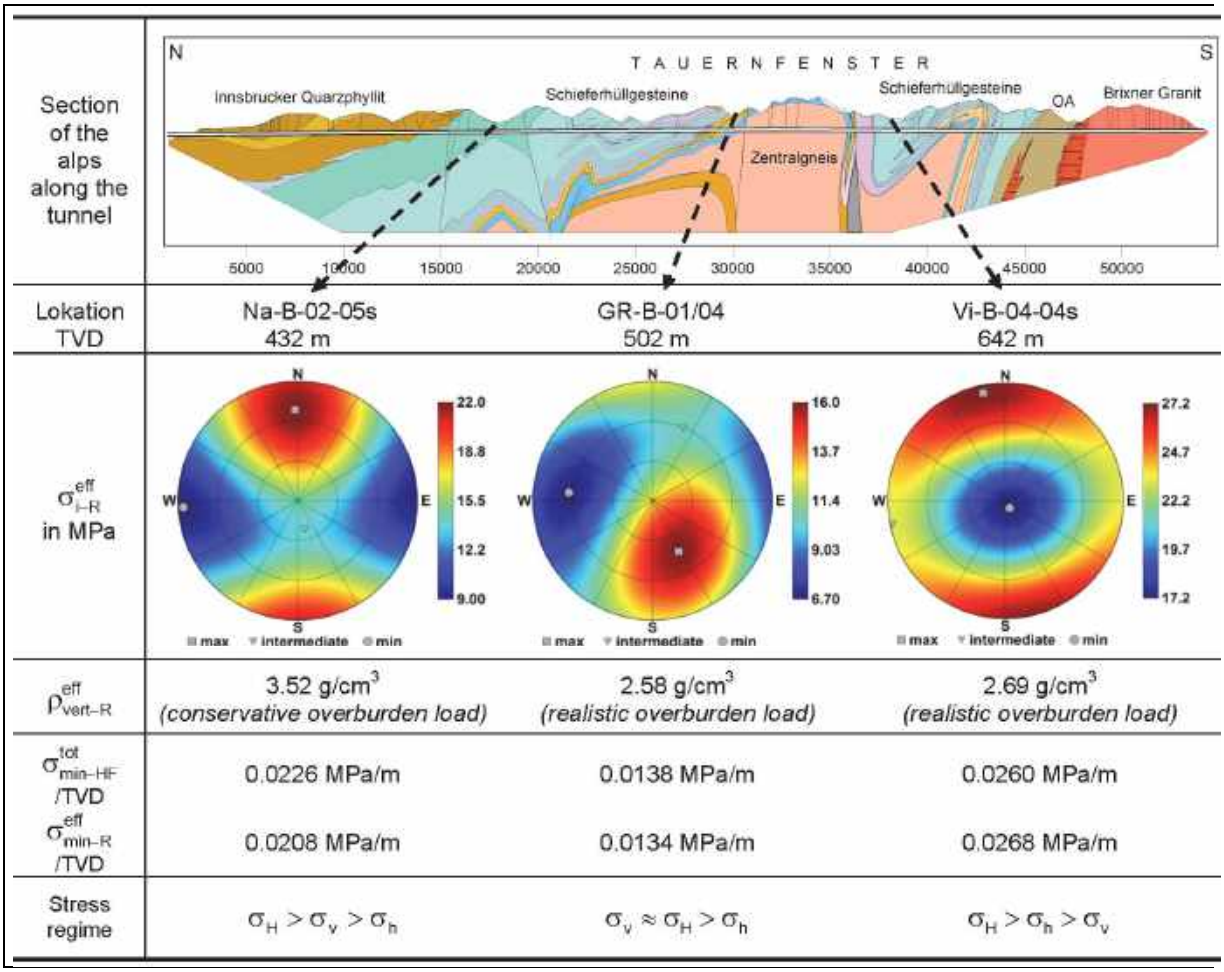

Fig. 6.2: Comparison of effective 3D rock stresses ($\sigma^{eff}_{i\text{-}R}$) determined with RACOS® for the analyzed locations, the effective overburden densities ($\rho^{eff}_{vert\text{-}R}$) plus the depth-related total ($\sigma^{tot}_{min\text{-}HF}$ / TVD) and effective ($\sigma^{eff}_{min\text{-}R}$ / TVD) gradients of the minimum in situ stress components and the horizontal-vertical stress regime

The orientation of the maximum horizontal in situ stress components determined in all locations corresponds to the results shown in the World Stress Map (see Fig. 2.2). In a comparison of the directly measurable in situ rock stresses the closure pressure of a hydraulic frac as the minimum total principal normal stress is very similar to the corresponding effective component in RACOS®. Thus a mechanically effective pore pressure plays hardly any role in the investigated area.

The complete 3D in situ stress condition is determined directly with RACOS®. In contrast, the additional stress calculations on the basis of hydraulic fracs clearly only document the vertical-horizontal portions of the loading in the case of inclined principal stresses. This can lead to significant misjudgements in stability analyses. In contrast,

with a vertical-horizontal orientation of the principal normal stresses there is good agreement between the results of the two procedures and data from the 2D modelling.

7 Closure

Three different procedures were used to determine the in situ stresses for the Brenner Base Tunnel; the widely-used hydraulic fracking (HF), the numerical simulation of in situ rock loadings (2DNS) and the newly-developed RACOS® stress analysis on core.

In HF the determination of the minimum total in situ rock stress is on the basis of crack-opening tests in boreholes and so immediately on site. However these direct measurements only include the magnitude and orientation of one principal normal of the 3D in situ rock stress condition. The determination of the other two components - which are essential for stability analysis - is by additional analytical/numerical calculations. For these the overburden pressure based on density logs is often taken as the vertical principal stress. Thus the complete HF approach is referred to a horizontal-vertical orientation of the 3D in situ stress condition. Even a demonstrated inclination of the minimum principal stress did not enable any conclusion to be reached about the spatial orientation of the stress tensor. Also, in this approach the mechanical effectiveness of the pore pressure is not considered. So the determined/calculated total stress components from HF do not allow any conclusions to be reached about the effective in situ rock stresses, which are those relevant to stability analysis. However, in the locations investigated in this case the mechanically effective pore pressure played only a small role, so that the effective and total stresses are approximately equal.

The 2DNS were based on experimentally determined rock parameters. Once again, the overburden pressure is defined as a principal stress component. The horizontal-vertical calculation approach which results does not consider in any way tectonic and/or topography related deviations in the orientation of the principal stresses. Thus, also, their magnitudes are not determined uniquely.

The RACOS® stress analyses include a direct determination of all three effective principal stress components and thus the real magnitudes and orientations of the 3D in situ rock stress situation. With a transformation of these data into a vertical-horizontal system comparisons can be made with the corresponding data from hydraulic fracs and the numerical analyses. Moreover, the 3D pore pressure effectivenesses are also determined, so that for a known hydraulic pore pressure, effective and total stresses can be directly spatially linked. Further advantages of RACOS® are the additional possibilities for structural in situ rock analysis on the basis of the measured spatial propagation of compressional waves. Thus the determined in situ rock stresses can be directly related to the in situ rock structure. Also, all measurement and analysis data are reoriented geographically.

Therefore the RACOS® stress analyses offer universal possibilities for the determination and comparison of 3D in situ rock stresses. Even with any inclination of the principal stress components these do not contain any unknown deviations of the magnitude and orientations, and so have no associated erroneous consequences for stability analyses. This is particularly advantageous for rock mass areas with very different structures and faults.

The only prerequisite for RACOS® is a consolidated core from the location of interest and information about the borehole path. Thus the investigations can be made without any further on-site activity at any time after the coring was carried out.

Symbols and abbreviations

HF	Hydraulic Fracturing
2DNS	2D numerical Simulation
σ_H	maximum horizontal principal stress
σ_h	minimum horizontal principal stress
σ_V	vertical principal stress
σ_{tot}	total stress
σ_{eff}	effective stress
p^{iso}_{vol}	isotropic pore pressure
ω_K	principal pore pressure effectiveness (3D BIOT coefficient)
σ_{max}	maximum stress component
σ_{inter}	intermediate stress component
σ_{min}	minimum stress component
TVD	true vertical depth
$\sigma_{i\text{-}HF}$	Stress (i = min / inter / max) determined with Hydraulic Fracturing
$\sigma_{i\text{-}R}$	Stress (i = min / inter / max) determined with RACOS®
v_P	Compressional wave velocity (i = min / inter / max) determined with RACOS®

References

[1] Bergmeister, K. (2011): *Brenner-Basistunnel – Der Tunnel kommt*. Tappeinerverlag, Lana

[2] Reinhold, C. (2014): *The Brenner Base Tunnel – project and status of realisation*. Veröffentlichungen des Institutes für Geotechnik der TU Bergakademie Freiberg, Heft 2014-2, Herausgeber H. Konietzky, ISSN 1611-1605

[3] World Stress Map Rel. 2008: The World Stress Map Project - A Service for Earth System Management, http://dc-app3-14.gfz-potsdam.de/pub/stress_data/stress_data_frame.html

[4] Braun, R. (2015): *Borehole stability – Aspects of the Influence of the 3D Effective Stresses*. OIL Gas European Magazine 3/2015. Pp OG133-OG137

[5] Braun, R. (2007): *A Commonly Neglected Factor in Rock Mass and Borehole Stability*. OIL GAS European Magazine, 2/2007, pp. OG79 – OG82.

[6] Baumgärtner, J. (1987): *Anwendung des Hydraulic-Fracturing-Verfahrens für Spanungsmessungen im geklüfteten Gebirge, dargestellt anhand von Messergebnissen aus Tiefbohrungen in der Bundesrepubilk Deutschland, Frankreich und Zypern*. Berichte des Institutes für Geophysik der Ruhr-Universität Bochum, Reihe A, Nr.21, April 1987

Modelling of interaction of bentonite based sealing element and host rock

Modellierung der Wechselwirkung von Bentonit basierten Dichtelement und Wirtsgestein

R. Blaheta, M. Hasal, Z. Michalec
Institute of Geonics of the Czech Academy of Science (CAS)
Studentska 1768, Ostrava, Czech Republic

Abstract

The motivation of the presented work is to increase the understanding of hydro-mechanical processes in bentonite based sealing structures and the surrounding host rock. With this aim a series of SEALEX experiments were realized by IRSN in Tournemire underground rock laboratory in France. The experiments were simulated within the DECOVALEX 2015 project; see e.g. (Millard et al. [1] and [2]). This paper briefly describes the hydro-mechanical model, which was developed at the Institute of Geonics CAS within the DECOVALEX 2015 project and used for simulation of the SEALEX PT-A1 experiment, see [1] and [2]. The modelling realised within DECOVALEX 2015 is extended by considering the composition of the sealing plug from prefabricated bentonite/sand made blocks and investigation the effects of gaps between the blocks. The modelling described in [1] and [2] used 3D simulations of the HM processes in horizontal plug installation with originally asymmetric technical gap between the plug and surrounding rocks. For investigation of the role of gaps, a simplified 2D axisymmetric model is used.

Zusammenfassung

Die Motivation der vorliegenden Arbeit ist es, das Verständnis der hydromechanischen Prozesse in den Bentonit basierten Dichtungsstrukturen und in dem umgebenden Wirtsgestein zu erhöhen. Mit diesem Ziel wurde von IRSN eine Reihe von SEALEX Experimenten in dem unterirdischen Felslabor in Tournemire in Frankreich realisiert. Die Experimente wurden gemäß dem DECOVALEX 2015 Projekt simuliert; siehe z. B. (Millard et al. [1] und [2]). Dieser Forschungsbericht resümiert das hydromechanische Modell, das im Institut of Geonics der Tschechischen Akademie der Wissenschaften (CAS) im Rahmen des DECOVALEX 2015 Projektes entwickelt wurde, und zur Simulation des SEALEX PT-A1 Experiment angewendet wurde, siehe [1] und [2]. Die Modellierung innerhalb von DECOVALEX 2015 wird unter Berücksichtigung der Zusammensetzung des Verschlussstopfens aus vorgefertigten Bentonit/Sand Blöcken realisiert. Die Untersuchungen werden um die Auswirkungen von Lücken zwischen den Blöcken erweitert. In [1] und [2] werden 3D-Simulationen der HM Prozesse in einer horizontaler Stopfen-Installation mit ursprünglich asymmetrischer technischer Lücke zwischen dem Stopfen und dem umliegenden Gestein beschrieben. Zur Untersuchung der Rolle von Lücken wird ein vereinfachtes 2D-achsensymmetrisches Modell benutzt.

1 Introduction

The need for understanding the performance of engineered barriers for underground repositories of spent nuclear fuel motivates investigations of hydro-mechanical processes in bentonite based sealing structures and surrounding host rocks. The performance of sealing plugs was tested in a series of SEALEX experiments and further analysed through numerical simulations of the monitored processes. The SEALEX experiments (SEALing performance EXperiments) were realized by the French Institute of Radiation Protection and Nuclear Safety (IRSN) in Tournemire underground rock experimental station in France (see Barnichon [3]) and the simulations were done e.g. within the DECOVALEX 2015 project, see (Millard et al. [1] and [2]).

The preparation of the SEALEX PT-A1 experiment can be seen in Fig. 1.1. The plug from pre-compacted disk blocks made from bentonite-sand mixture (BSM) was installed into a horizontal borehole and consequently flooded by water from both sides (see Fig. 1.2). The installed sensors (Fig. 1.3.) monitored relative humidity and pressure evolution. Further available data concerned the amount of injected water as well as results of laboratory testing the BSM made of MX80 bentonite and quartz sand in dry weight proportions 70/30.

Fig. 1.1: Preparation of the plug from eight BSM blocks and its horizontal installation.

The applied mathematics group from the Institute of Geonics CAS took part in the modelling reported in (Millard et al. [1] and [2]). The modelling had some specific features caused by the horizontal installation of the plug (see Fig. 1.1) with a significant asymmetric initial gap between the plug and the rock. The hydro-mechanical relations had to be formulated with respect to larger deformation due to bentonite swelling. The model described in Section 2 then includes flow in variable saturated BSM taking into account that the permeability and also the retention characteristics would depend on BSM deformation. The modelling used 3D finite elements implemented via the COMSOL Multiphysics software [4], see Fig. 1.4.

The sealing structure was constructed from eight pre-compacted bentonite disk shape blocks (see Fig.1.1, Fig.1.2) and in this paper; we extend the results from (Millard et al. [1] and [2]) by investigating the role of the gaps between the blocks and showing that

the gaps contribute significantly to the plug saturation in early stages of water injection. For this modelling, we use an axisymmetric model described in Section 3. The inter-block gaps are modelled explicitly using the fracture flow interface offered by COMSOL Multiphysics [4], [5]. The modelling includes time variable fracture flow parameters provided by a local model of one inter-block gap. Finally, the results of computations with and without considering the inter-block gaps are presented in Section 4.

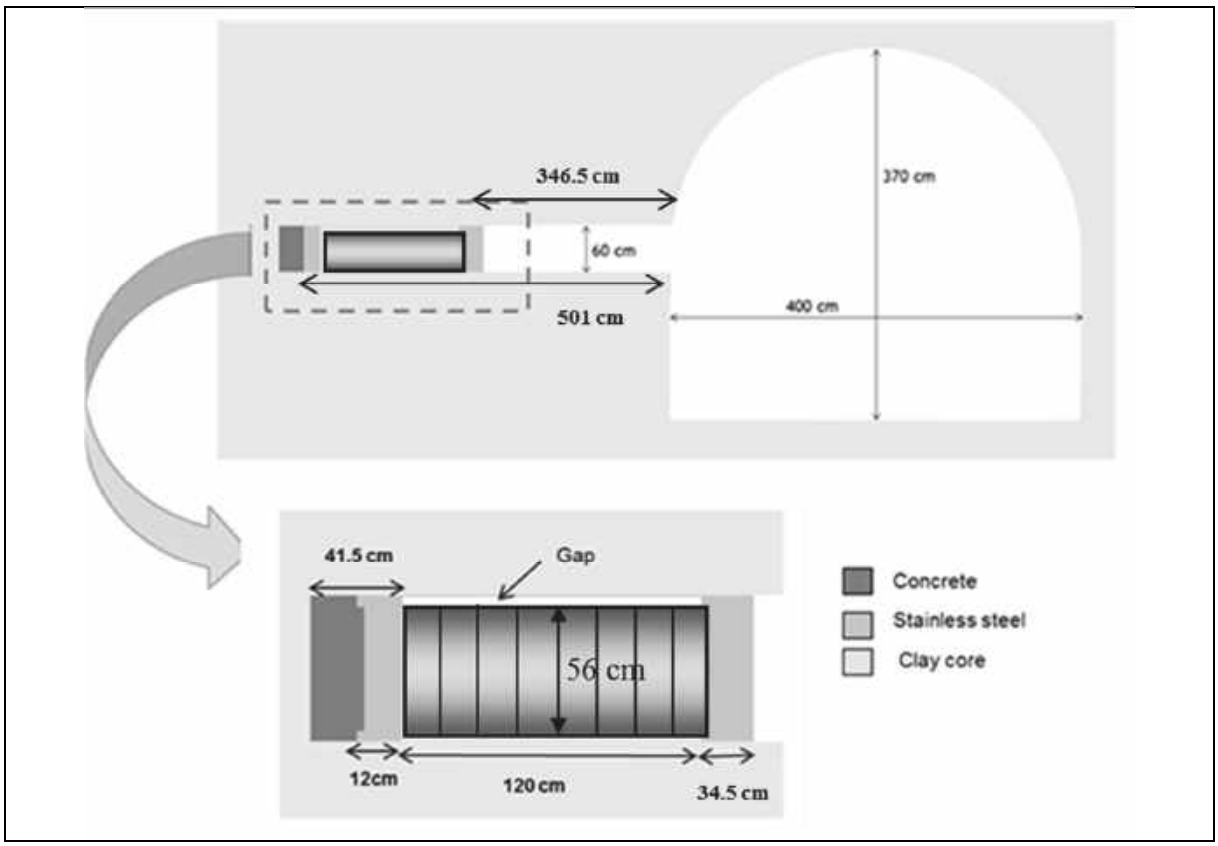

Fig. 1.2: Scheme and dimensions of the experimental installation.

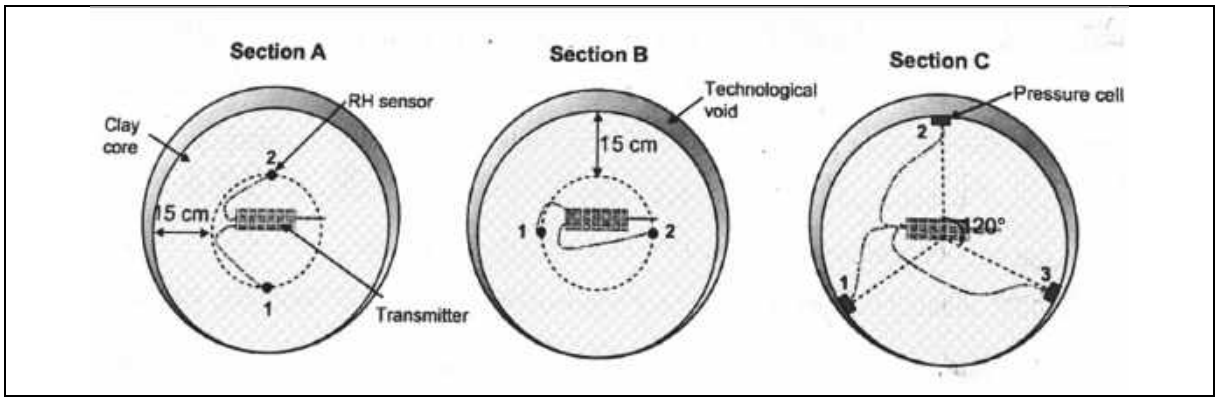

Fig. 1.3a: Installation of sensors for relative humidity and stress measurement.

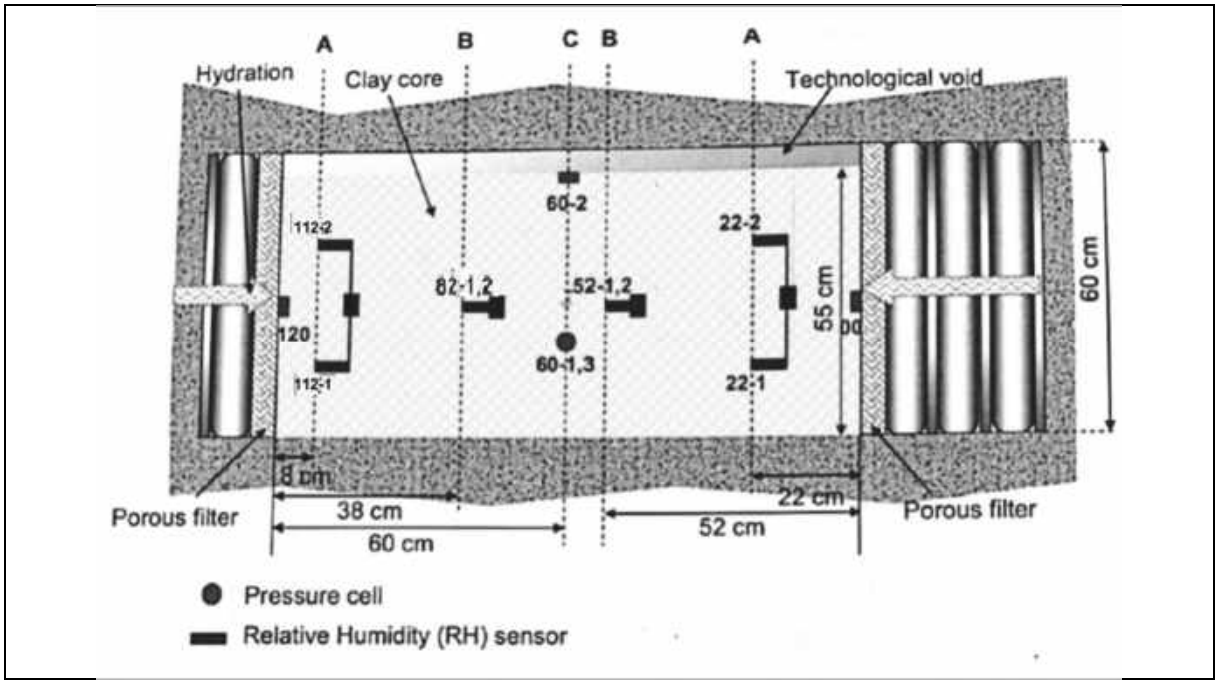

Fig. 1.3b: Installation of sensors for relative humidity and stress measurement.

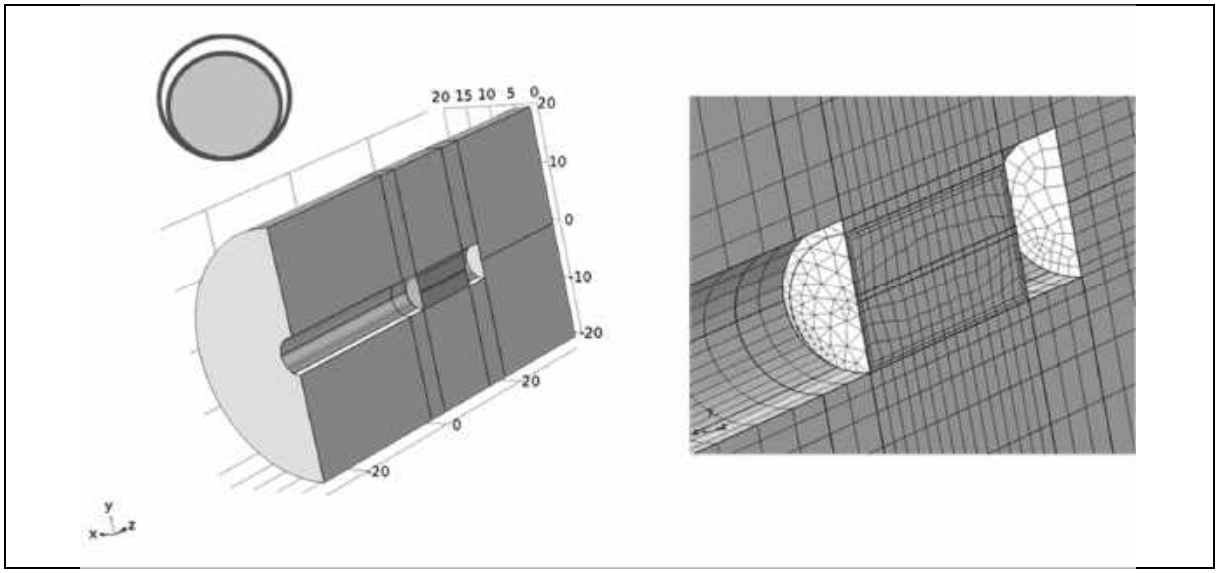

Fig. 1.4: 3D finite element discretization used by the Institute of Geonics CAS for modelling the SEALEX experiment with initial asymmetric technological gap between the plug and the surrounding rock.

2 Hydro-mechanical (HM) model

To describe the hydro-mechanical processes in BSM, we developed a HM model based on Richards' equation [6], [7] and nonlinear elasticity within the Decovalex 2015 project. The modelling of HM processes in BSM, gap and rocks is described in this section.

Modelling HM processes in the BSM

1. In variably saturated BSM the flow is described by Richards' equation [6], [7]. This equation can be generalized to include the vapour diffusion, but this generalization is not used as it was found not significant for the isothermal processes. The used equation is as follows:

$$\rho_w(\phi C_m + S C_s)\frac{\partial p}{\partial t} = \nabla \cdot \left(\rho_w \frac{k_{rel}(S) k_{sat}}{\mu} \nabla p\right) + Q,$$

where p [MPa] is the fluid (pore) pressure, ρ_w = 1000 kg/m^3 is the density of water, S is the saturation, C_S [MPa^{-1}] is the storativity and $C_m = \partial S/\partial p$ [MPa^{-1}] is the specific moisture capacity. The storativity C_S is kept to be C_s = 4.4 · 10^{-4} MPa^{-1} which is the compressibility of water at 20°C. This term stabilizes the equation in (nearly) fully saturated region with C_m = 0. The term $\partial S/\partial p$ depends on the exploited water retention function. The term Q [kg/(m^3·s)] denotes fluid source (positive) or sink (negative).
The dynamic viscosity is μ = 1.002 · 10^{-9} MPa·s for water at 20°C. The saturated permeability depends on deformation, see the Kozeny–Carman equation described in the sequel. It has the value k_{sat} = 1.5e-20 m^2 for the BSM with the dry density ρ_d = 1670 kg/m^3. The relative permeability is expressed by generalized Irmay's formula

$$k_{rel}(S) = k_{rel}(S_e) = (S_e)^4\,, \qquad S_e = \frac{S - S_{res}}{S_{max} - S_{rel}},$$

where S_e, S_{max}, S_{res} and S_{rel} are the effective, maximum, residual and relative, saturation, respectively. The exponent was obtained by a model calibration by simulation of an infiltration laboratory experiment.

With respect to large deformations, which occur during the BSM swelling and closing the gap between the plug and the surrounding rock, a special attention has to be paid to the retention curve for BSM. It will depend on the volumetric deformation ε_V or equivalently on the dry density ρ_d, which is connected with ε_V through the relation $\rho_d = \rho_{d0} / (1 + \varepsilon_V)$. Here, ρ_{d0} denotes the dry density for the initial (not deformed) state.

It is suitable to describe the retention curve as the relation between the suction and the mass water content w, which unlike the saturation, does not depend on the deformation. The retention curve for ρ_d = 1670 kg/m^3 is constructed from the laboratory measurement data as a bilinear dependence between the natural logarithm of suction and the mass water content, see Fig. 2.1. For other values of dry density this curve is modified in such way that the first branch follows the maximal mass water content $w_{max} = w_\phi + w_{res}$, where w_ϕ corresponds to water filling of the pore space (depending on dry density) and w_{res} is the residual mass water content, which is an amount of extra water absorbed in the bentonite.

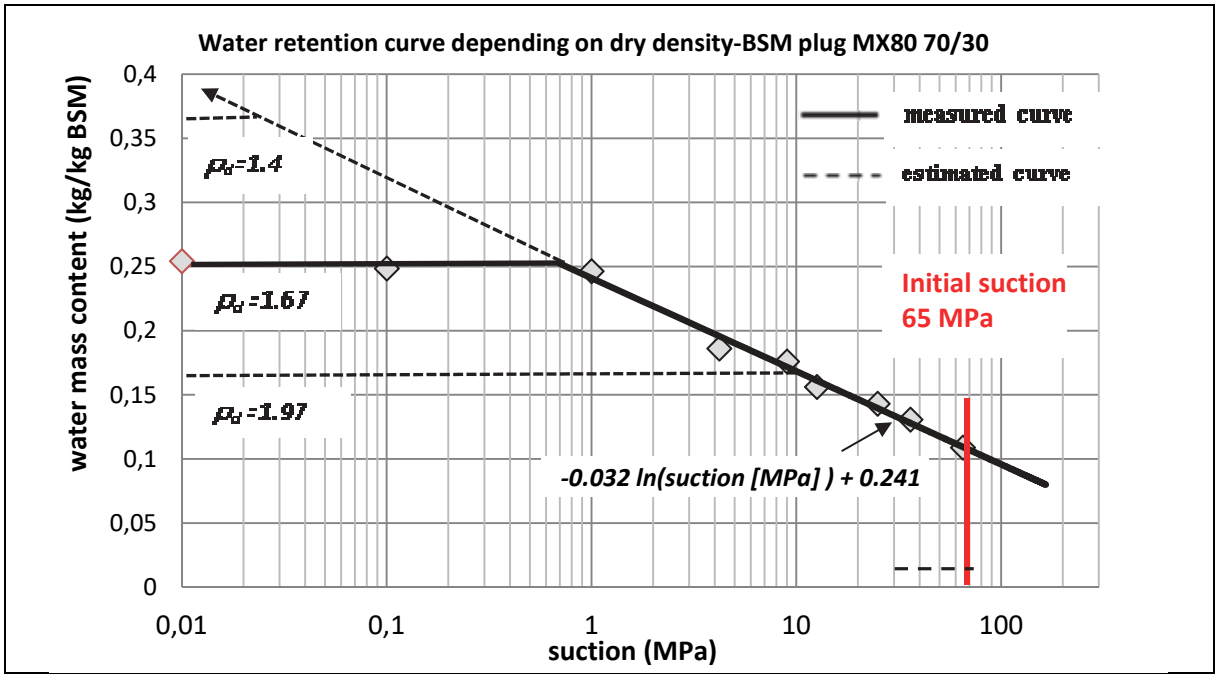

Fig. 2.1: The BSM retention curves ln(s)-w or dry density ρ_d = 1400, ρ_d = 1670 and ρ_d = 1970 kg/m^3.

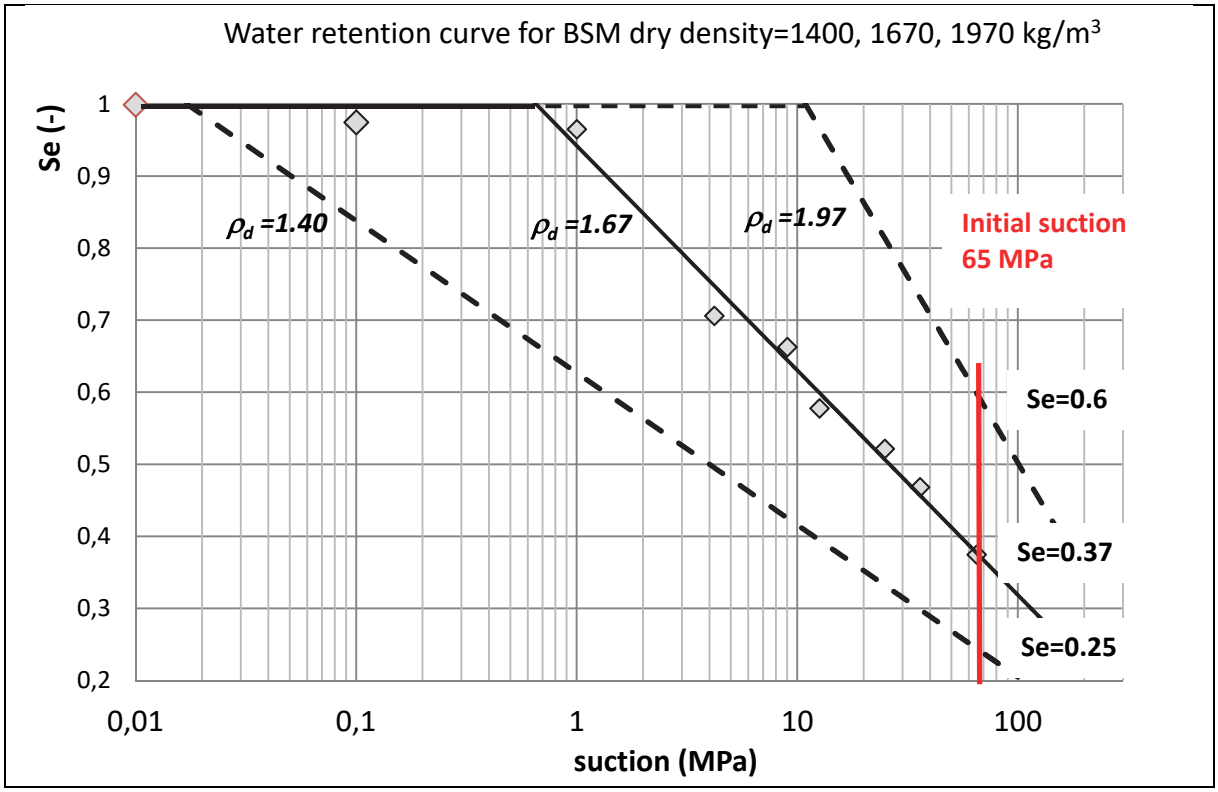

Fig. 2.2: The BSM retention curves ln(s)-Se for dry density ρ_d = 1400, ρ_d = 1670 and ρ_d = 1970 kg/m^3.

For BSM we take w_{res} = 0.022. The second branch of the retention curve remains unchanged as the micro pores are not significantly affected by the deformation (see eg. Wang [8]). The relation

$$S_e = \frac{w - w_{res}}{w_{max} - w_{res}}$$

enables also to express the retention curve as the dependence between the natural logarithm of suction and effective saturation S_e, see Fig. 2.2.

2. The mechanical behaviour of BSM is given by the stress *(σ)* - strain *(ε)* relation, which is in the form of elasticity with variable elastic tensor $\boldsymbol{C}$,

$$\sigma = \boldsymbol{C}\colon \varepsilon, \qquad \boldsymbol{C} = \boldsymbol{C}(\varepsilon_v) = \boldsymbol{C}(\rho_d).$$

The material is assumed to be isotropic with constant Poisson ratio $\nu = 0.3$ and the elastic modulus depending on dry density. The relation $E = 3(1 - 2\nu)$ between the elastic and bulk modulus then suggests the exponential dependence on the dry density,

$$E = 0.0348\exp(3.54\rho_d)\ MPa.$$

The above elastic modulus was constructed from data of unloading branch of the loading/unloading oedometer tests providing the values E = 12.8 MPa for ρ_d = 1670 kg/m^3 and E = 37 MPa for ρ_d = 1970 kg/m^3. The use of the unique analytical expression for a wide range of dry densities of course requires some compromise. The elasticity with variable modulus is then implemented in an incremental way.

3. The Biot's interconnection of hydro and mechanical processes is used only for the saturated case, i.e.

$$\sigma'_{ij} = \sigma_{ij} - \alpha\,\gamma(p)p\delta_{ij}, \quad Q_\varepsilon = \alpha \cdot \rho_w \gamma(p)\frac{\partial \varepsilon_v}{\partial \mathrm{t}},$$

$$\gamma(p) = \begin{cases} 1 & \text{for } p \geq 0, \\ 0 & \text{otherwise.} \end{cases}$$

Above, Q_ε is the contribution to the source term in the Richards equation and α is the Biot-Willis constant, σ and σ' are the total and effective stresses, respectively.

4. The mechanical deformation is completed by swelling strain, which is depending on the increment of mass water content w. We use the expression

$$\varepsilon_{swell} = \mathrm{c} \cdot (\rho_d/\rho_w)(w - w_{initial})$$

where the coefficient c depends on several parameters as initial dry density, effective saturation and stress level. For the considered problem with initial dry density ρ_d = 1970 kg/m^3 the value c = const =0.45 was found convenient.

5. The deformation changes the saturated permeability via the Kozeny–Carman equation

$$K_{sat} = K_{sat}(\varepsilon) = K_0 \frac{\phi^3}{(1-\phi)^2} \frac{(1-\phi_0)^2}{\phi_0^3},$$

where K_0 = 1.5e – 20 m^2 for ρ_d = 1670 kg/m^3, i.e. for ϕ_0 = 0.389.

Modelling of the gap behaviour

The gap, which appears in between BSM and rock, is not treated as a free space but as a saturated porous material with a very low initial dry density, which gradually increases as the gap is closing. Such approach is not so far from reality, as detailed observations show that the gap is soon filled with a gel which gradually becomes a compacted form of the bentonite, see e.g. (Saba [9]). The initial dry density was set to ρ_d = 100 kg/m^3 or a bit higher in case of difficulties with numerical stability. Note that $\rho_d = \rho_s (1 - \phi)$ provides initial porosity ϕ_0 = 0.963 for ρ_d = 100 kg/m^3.

For the considered applications, it is important that the gap remains fully saturated and serves as a transport zone for water before closing. After closing it obtains the same hydraulic properties as the standard solid BSM. The flow is therefore driven by

$$C_s \frac{\partial p}{\partial t} = \nabla \cdot \left(\frac{k_{sat}}{\mu} \nabla p \right) + \alpha \rho_w \frac{\partial \varepsilon_v}{\partial \mathrm{t}},$$

where the Biot-Willis constant is taken α = 1 and the saturated permeability changes with porosity by using Kozeny- Carman's formula already used for the BSM. The mechanical behaviour of the gap is described as nonlinear elasticity using the same relations as for the BSM.

Note that we identify the moment when the plug fil the full gap, and after that moment, we avoid the flow in the gap by interconnecting the flow models in the plug and the host rock. This interconnection uses the COMSOL extrusion coupling operator.

Modelling HM processes in the host rock (argillite)

As the argillite is substantially stiffer than the plug, it is modelled as rigid without computing its deformation. The flow in argillite is described again by Richards' equation with the use of van Genuchten´s formulas (Bear [7])

$$w = \begin{cases} w_{max} \left(1 + |0.02 \cdot p[MPa]|^{1.9}\right)^{-0.474} & if \;\; p < 0, \\ w_{max} & if \;\; p \geq 0, \end{cases}$$

$$k_{rel} = S_e^{1/2}\left[1 - \left(1 - S_e^{1/0.474}\right)^{0.474}\right]^2,$$

with parameters w_{max} = 0.033, w_{res} = 0.002 and k_{res} = 0.03.8e – 21 m^2.

3 Axisymmetric model

For testing the effect of inter-block gaps, we use a simplified axisymmetric model of the plug saturation experiment with a hypothetical axisymmetric installation of the cylindrical plug into horizontal circular borehole (with a symmetric gap between the plug and the rock), see Fig. 3.1.

The modelling of saturation has two phases, see Fig. 3.2. In Phase I, the plug (experiment) is not installed, the borehole is open for 150 days and the surrounding rock is slightly desaturated. Only the flow in rock (the argillite) is computed in Phase I with an initial condition given by full saturation with a constant pressure p = 0.6 MPa.

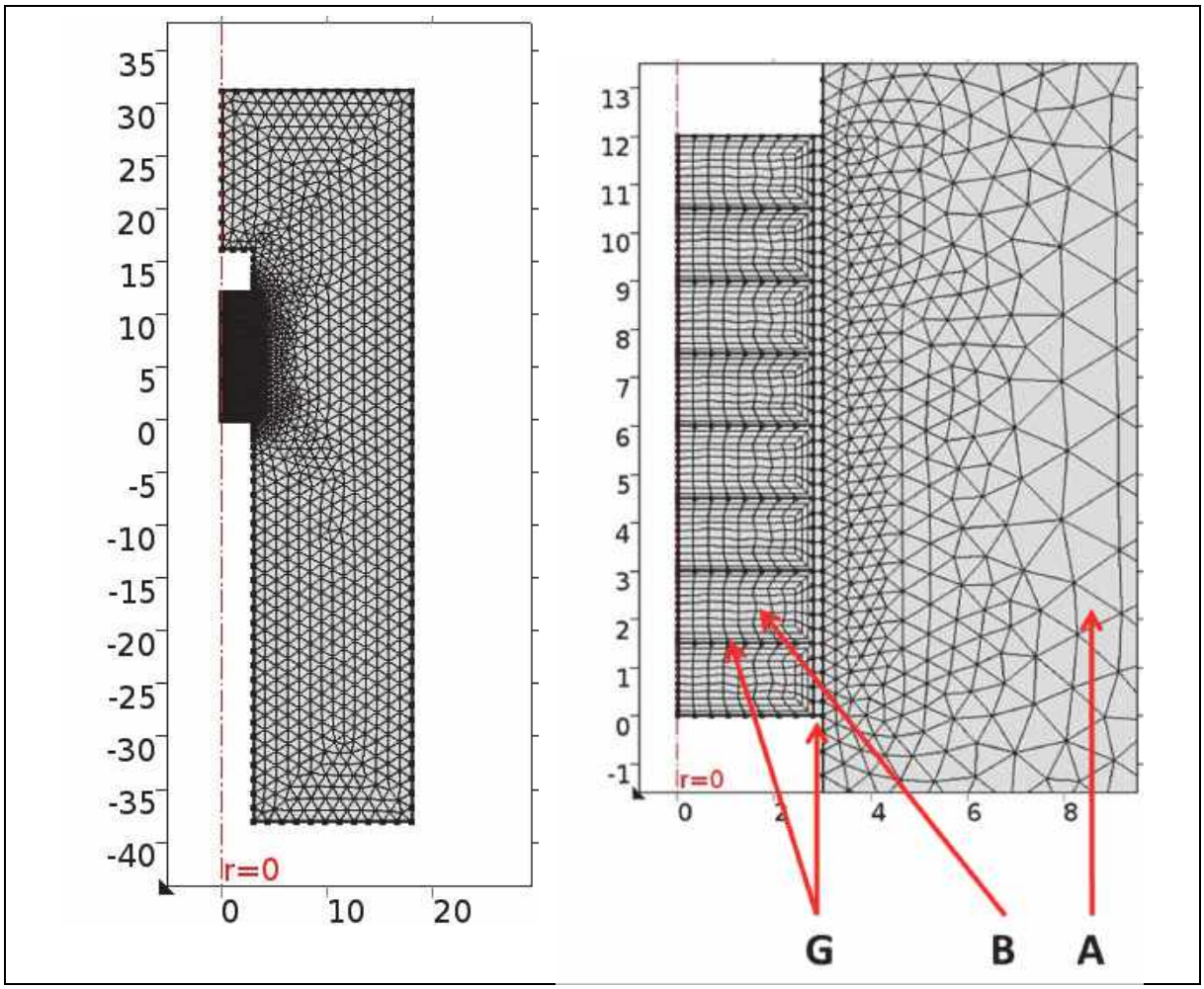

Fig. 3.1: Mesh for the axisymmetric finite element model of SEALEX experiment (left) and its detail (right). Model uses three materials: Argillite rock (A), BSM plug (B) and gap modelled as a special material (G).

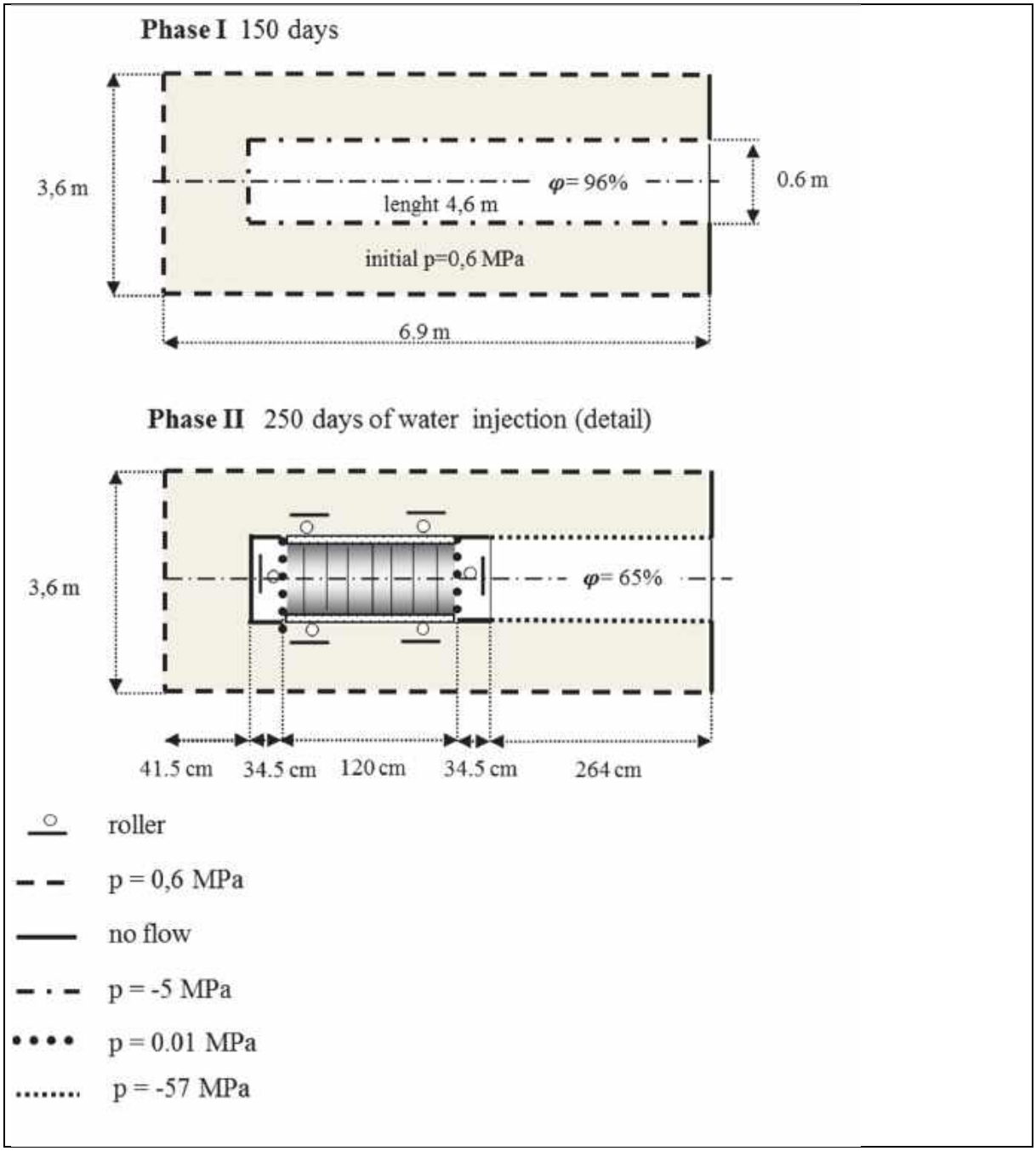

Fig. 3.2: Phases of modelling and the used boundary conditions.

In Phase II, the plug is installed and gradually saturated. The initial conditions for the flow are taken from Phase I in argillite, suction of 65 MPa is considered in the BSM (corresponding to its initial saturation) and pressure of 0 MPa is prescribed in the gap. The boundary conditions for Phase II can be seen in Fig. 3.2.

For Phase II we shall consider two variants of simulations. In Variant 1, the plug is assumed to be homogeneous; in Variant 2, the decomposition of the plug into eight BSM blocks is considered.

There are two possibilities for modelling the inter-block gaps. The first one is to prepare a detailed model in which the gaps are subdomains with specific properties. These properties can be the same as it was described in the previous section for the gap between the plug and the rock. In this way, the gaps have initially very low dry density and high porosity. Correspondingly, the gaps provide a high permeable path for the water saturation of the BSM. In the beginning, the fractures have also a low elastic modulus which contributes to fracture closing. In the course of closing, the gaps become less permeable and stiffer. In the final stage, the gaps obtain HM characteristics similar to the characteristics of the surrounding BSM.

A difficulty of the above approach to the modelling lies in the necessity of introducing the fractures into the finite element mesh and performing demanded computations with nonlinear phenomena on highly locally refined mesh. An alternate approach is the modelling of gaps as objects of lower dimension, see e.g. [10], [11]. Such modelling can be implemented through the fracture flow interface offered by COMSOL Multiphysics.

The “Fracture Flow Interface” (FFI) in COMSOL Multiphysics [5] allows introducing 2D or 1D objects into 3D or 2D porous media flow models. The lower dimensional fracture is then characterized by its aperture *a* [m], the fracture storage coefficient C_{sf} [MPa^{-1}], the fracture permeability K_f [m^2], and the source term Q_f [kg/(m^3·s)].

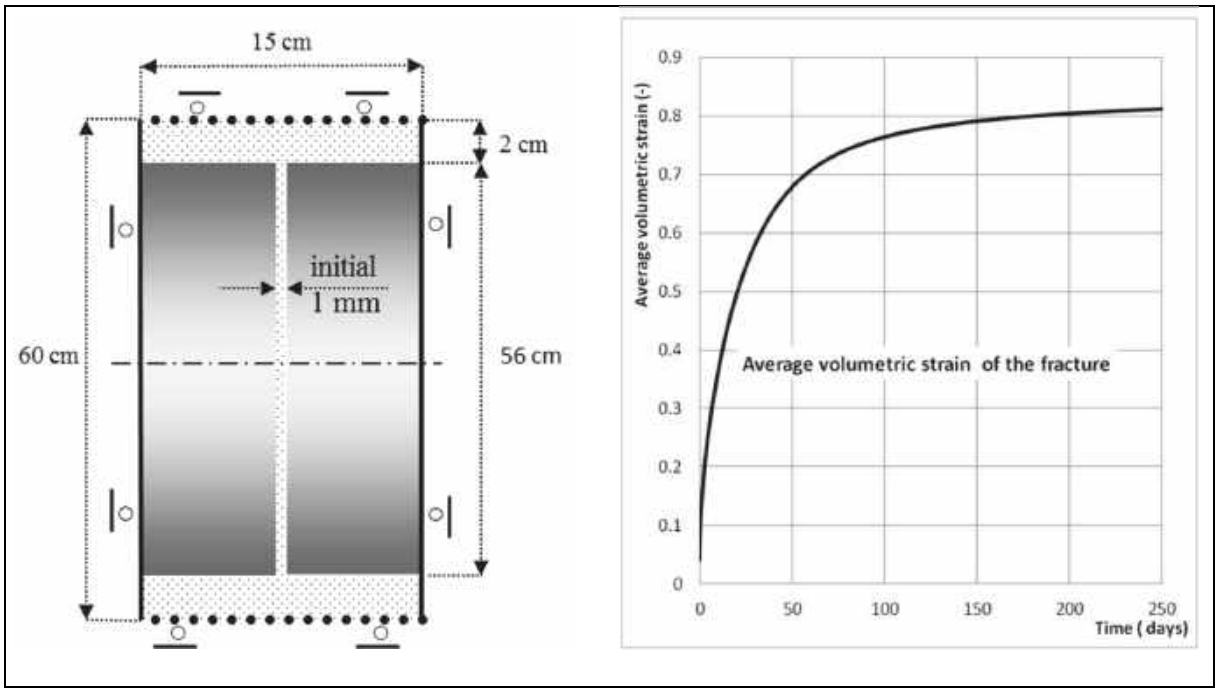

Fig. 3.3: The 2D axisymmetric model of a single fracture for computation of average volumetric strain of the gap and consequently the change of average gap aperture.

In our model, introducing FFI change the saturation of the surrounding BSM and accordingly also change the elastic properties, which depend on the dry density.

The standard FFI assumes that the fracture characteristics do not change in time. To simulate the fracture closing and the change of its permeability in time, we have to provide FFI time dependent aperture data, which are obtained by solving an auxiliary local problem, see Fig. 3.3. The auxiliary local problem uses the material models for BSM and the gap as described in Section 2. The initial fracture gap aperture is assumed to be 1 mm.

4 Numerical results

The results of the described modelling are illustrated by the evolution of saturation in different positions of the BSM plug, see Fig 4.1 and 4.2.

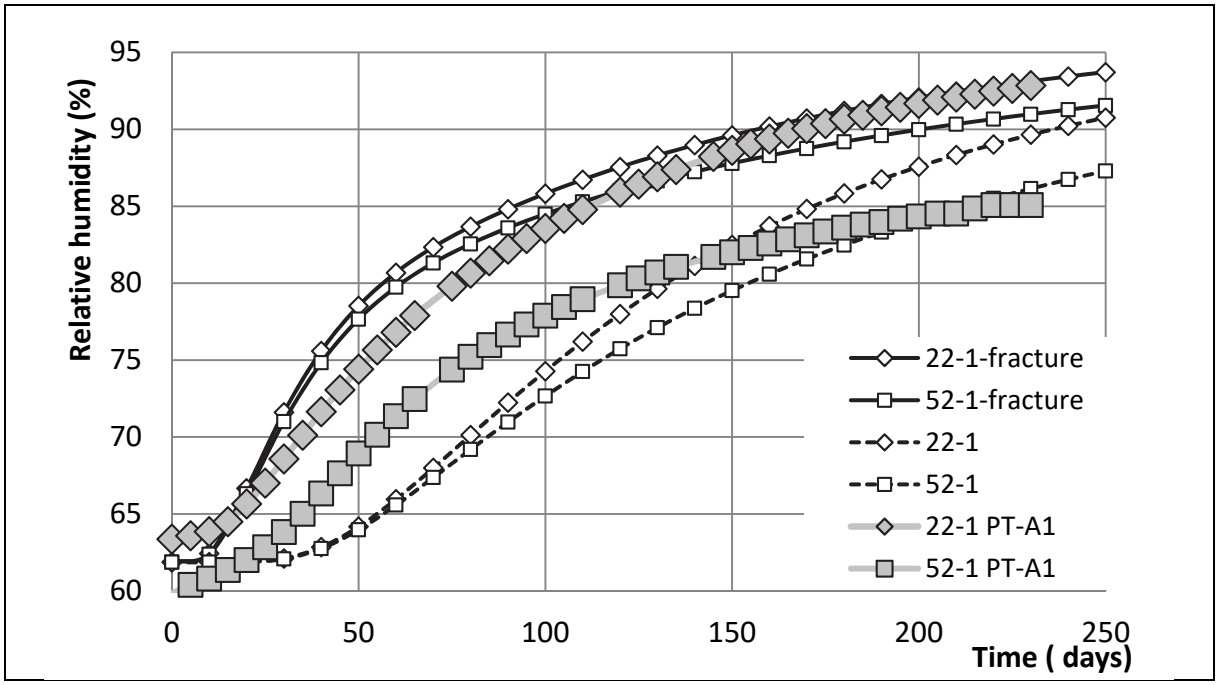

Fig. 4.1: Development of relative humidity in the position 52-1 (middle of the plug, see Fig. 1.3 and in the position 22-1 (22 cm from the right end). Curves with suffix PT-A1 represent measurements during the experiment, suffix fracture means that the inter-block fractures are included in the model; no suffix means that inter-block fractures are not modelled.

In Fig. 4.1 it can be seen that including the inter-block gaps substantially speeds up the saturation in the initial period (i.e. the period up to about 200 days). We can also compare the computed results with the measured data, showing good agreement despite of the fact that we use axisymmetric idealization. In Fig. 4.2 this trend is also confirmed in other sensor locations except from the location 112-2, which is only 8 cm from the saturated end of the plug.

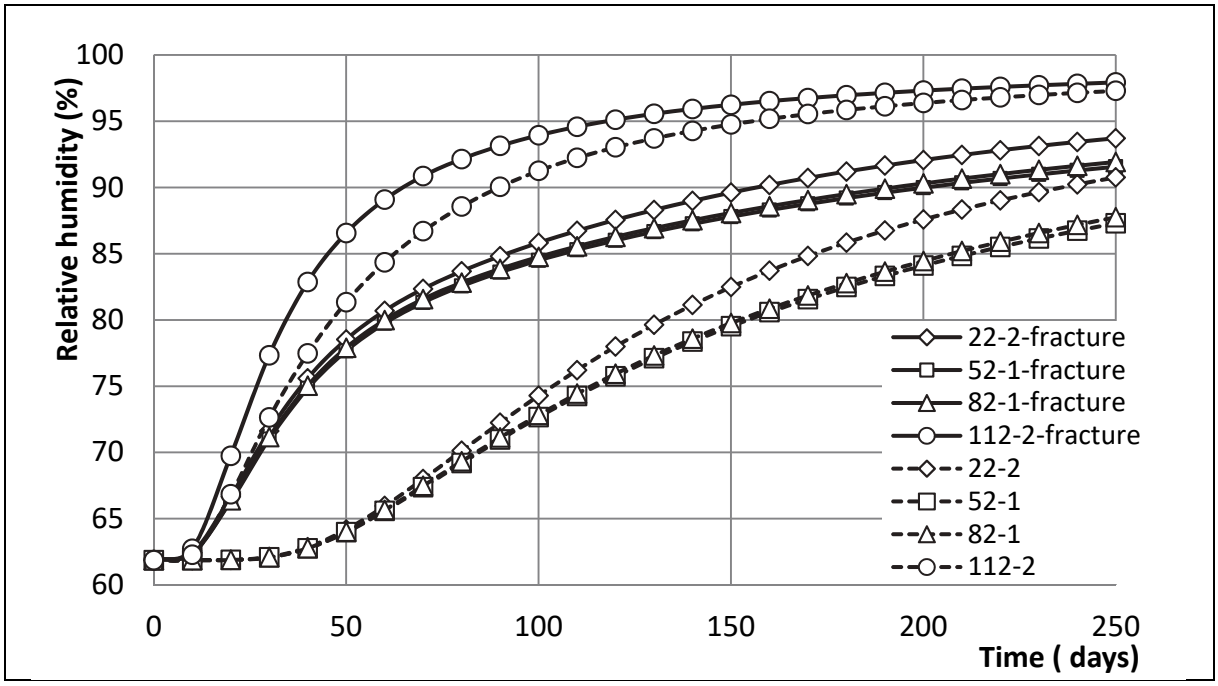

Fig. 4.2: Development of relative humidity in four sensor positions (see Fig. 1.3). The simulations with (suffix fracture) and without (no suffix) of the inter-block fractures in the model.

5 Conclusions

The paper provides an overview of the hydro-mechanical model, which was developed to simulate processes in swelling bentonite-sand sealing structures with special emphasis on the modelling of the SEALEX experiment within the DECOVALEX 2015 project.

This model has several special features:

- the use of strain dependent retention curves within Richards' equation based flow model,
- a procedure for construction of the retention curves for different dry densities. This construction respects the double structure of the BSM when only macro pores are substantially affected by compaction,
- modelling of the gap between BSM and rock as a special material with the described properties.

The model is further extended by considering the inter-block gaps. The adopted modelling approach then combines the use of local and global models. The local model considers an individual gap between the blocks and uses the same approach as used for modelling the gap between the plug and rocks. The global model idealizes the gaps as lower dimensional objects. These objects are equipped with specific flow parameters and the time evolution of gap conductivity is arranged through evolving aperture computed by the local model.

Including of inter-block gaps increases the accuracy of the model in early phase of saturation (about up to 1 year). This fact is confirmed by comparison with the mea-

surements. In later phase of saturation the results computed with and without considering the inter-block gaps become similar. The accuracy of the model can be further increased by using 3D model and fractures with properties varying in both time and space.

The model was implemented within the COMSOL Multiphysics software.

Acknowledgement

The presented work was partly conducted within the context of the international DECOVALEX 2015 project. The authors are grateful to the Funding Organizations who supported the work. The views expressed in the paper are, however, those of the authors and are not necessarily those of the Funding Organizations.

The further research is supported by Radioactive Waste Repository Authority of the Czech Republic (RAWRA/SURAO) and the project LQ1602 IT4Innovations excellence in science by the Ministry of Education, Youth and Sports of the Czech Republic**.**

References

[1] A. Millard, N. Mokni, J.D. Barnichon, K.E. Thatcher, A.E. Bond, A. Fraser-Harris, C. McDermott, R. Blaheta, Z. Michalec, M. Hasal, T.S. Nguyen, O. Nasir, R. Fedors, H. Yi, O. Kolditz, Comparative modelling of laboratory experiments for the hydro-mechanical behavior of a compacted bentonite-sand mixture. Submitted to Environmental Earth Sciences.

[2] A. Millard, N. Mokni, J.D. Barnichon, K.E. Thatcher, A.E. Bond, A. Fraser-Harris,C. McDermott, R. Blaheta, Z. Michalec, M. Hasal, T.S. Nguyen, O. Nasir, R. Fedors, H. Yi, O. Kolditz, Comparative modelling approaches of hydro-mechanical processes in sealing experiments at the Tournemire URL. Submitted to Environmental Earth Sciences.

[3] J.D., Barnichon, P. Dick, C. Baue, The SEALEX in situ experiments: Performance tests of repository seals. In: Harmonising Rock Engineering and the Environment – Qian & Zhou (eds), Taylor & Francis Group, London 2012, pp. 1391-1394.

[4] COMSOL Multiphysics web page https://www.comsol.com/comsol-multiphysics.

[5] COMSOL Multiphysics, Discrete Fracture, www.comsol.com/model/discrete-fracture-691.

[6] A. Szymkiewicz, Modelling Water Flow in Unsaturated Porous Media. Springer-Verlag Berlin Heidelberg 2013.

[7] J. Bear, A.H.D. Cheng, Modeling Groundwater Flow and Contaminant Transport, Springer, Dordrecht 2010.

[8] Q. Wang, Hydro-mechanical behaviour of bentonite-based materials used for high-level radioactive waste disposal. Dissertation Universite Paris-Est; Tongji University Shanghai, 2012.

[9] S. Saba, Hydro-mechanical behaviour of bentonite-sand mixture used as sealing materials in radioactive waste disposal galleries. Dissertation Universite Paris-Est, 2013.

[10] V. Martin, J. Jaffré, J. E. Roberts, Modeling Fractures and Barriers as Interfaces for Flow in Porous Media. SIAM J. Sci. Comput., 26(5), 1667–1691.

[11] J. Březina, J. Stebel, Analysis of Model Error for a Continuum-Fracture Model of Porous Media Flow. In High Performance Computing in Science and Engineering, T. Kozubek et al. eds., Lecture Notes in Computer Science, Volume 9611, Springer 2016.

The geothermic Fatigue Hydraulic Fracturing experiment at Äspö Hard Rock Laboratory, Sweden

Das geothermische Fatigue Hydraulic Fracturing Experiment im Kristallinlabor Äspö, Schweden

Arno Zang, Ove Stephansson
GFZ German Research Center for Geosciences
Telegrafenberg, 14473 Potsdam

Abstract

In this article, the concept of Fatigue Hydraulic Fracturing is described, and its geothermal application is discussed. The basic idea behind fatigue fracturing is to vary the effective stress magnitude at the fracture tip to optimize fracture initiation and growth. The optimization can include lowering seismic radiated energy and/or generating various fracture networks with different permeability paths. Historically, we start referring to results from mechanical laboratory core testing and discrete element modeling of fluid-induced seismicity and permeability evolution in crystalline rock. Second, an in situ experiment in Äspö Hard Rock Laboratory is described where three different fluid injection schemes (continuous, cyclic and pulse injection) are performed. Under controlled conditions, hydraulic fractures are extended to about 3 to 7 m in length from a 28 m long, horizontal borehole drilled from a tunnel at 410 m depth. The facture process is mapped by an array of acoustic emission and micro-seismic monitoring instruments. First results indicate that in the same rock type, e.g. Ävrö granodiorite, the fracture breakdown pressure is lower and the number of fluid-induced seismic events are less in the fatigue testing scheme as compared to continuous fluid injection applied in conventional hydraulic fracturing.

Zusammenfassung

In diesem Artikel wird das Konzept des Fatigue Hydraulic Fracturing (FHF) beschreiben und seine mögliche Anwendung in der tiefen Geothermie. Das Grundprinzip der FHF Methode ist die Reduktion der Spannungen an der Rissspitze z.B. durch zyklische Fluidinjektion. Das Risswachstum kann hierdurch optimiert werden in Form von Reduktion induzierter Seismizität und/oder Erhöhung der Gesteinspermeabilität. Historisch beginnen wir mit der Diskussion der Ergebnisse aus Labortests und der Modellierung fluid-induzierter Seismizität und Risspermeabilität basierend auf hydro-mechanisch gekoppelten, Diskrete-Element-Rechnungen. Danach wird ein in situ Experiment im schwedischen Kristallinlabor Äspö beschrieben, in dem drei unterschiedliche Fluid-Injektions-Szenarien getestet werden. Unter kontrollierten Bedingungen werden hydraulische Brüche von einem 28 m langen, horizontalen Bohrloch in 410 m Tiefe aus-

gebreitet. Das Bruchwachstum von etwa 3 bis 7 m Länge wird mit akustischen Emissions-Sensoren, mikro-seismischen Bohrlochsonden und Geophonen überwacht. Erste Resultate bestätigen, dass der Bruchentstehungsdruck in Ävrö-Granodiorit niedriger ist und weniger induzierte seismische Ereignisse auftreten bei Anwendung der FHF Methode im Vergleich zum konventionellen Hydraulic Fracturing mit kontinuierlich ansteigendem Fluidinjektionsdruck.

1 Introduction

Hydraulic fracture growth through naturally fractured rock is an area of interest and current research for petroleum, mining and geothermal applications. In particular in the development of enhanced geothermal systems (EGS), hydraulic fracturing is used to form fracture networks connecting injection and production well for heat exchange purposes. However, hydraulic fracturing imposes environmental risks, one of which is induced seismicity associated with the permeability enhancement process (Giardini 2009, Ellsworth 2013, Rubinstein and Mahani 2015). Of particular interest are, therefore, fracturing concepts that limit the number and magnitude of seismic events. In this context, the fatigue hydraulic fracturing concept and the multi-stage hydraulic stimulation concept have been proposed. The key point in fatigue hydraulic fracturing is the frequent lowering of the injection pressure to allow stress relaxation at the fracture tip (Zang et al. 2013). Reducing the maximum injection pressure e.g. by cyclic fluid injection will lower the breakdown pressure, and as a consequence will affect the damage zone surrounding the fracture and the radiation pattern of seismic events associated with fracture growth (Fig. 1.1). For multi-stage stimulation, instead of massive stimulation, injection rate and pressure are controlled, and the reservoir is formed stage by stage (Meier et al. 2015, Zimmermann et al. 2015).

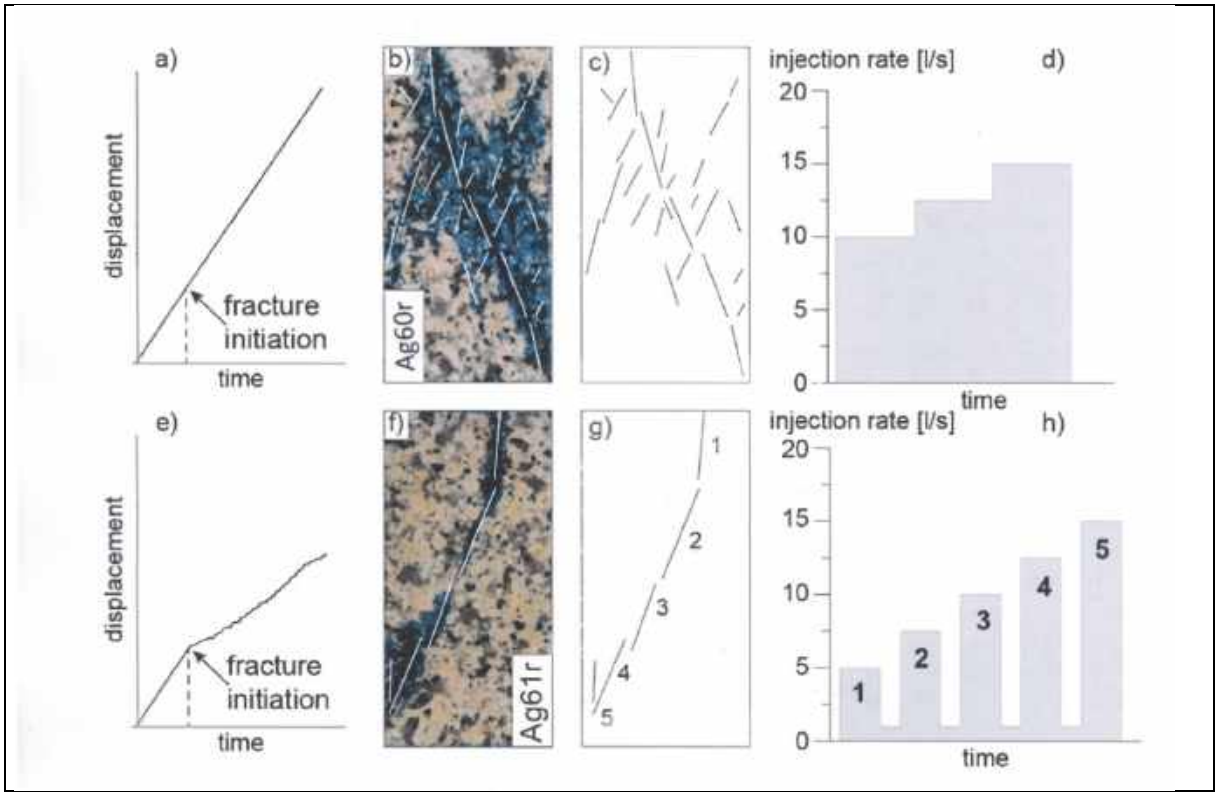

Fig.1.1: Two laboratory triaxial indenter tests on Aue granite with different load-time curves are compared. In a-c, the data from a mechanical, constant displacement-rate test is shown indicating a broader fracture damage zone. In e-g, the results from the crack-rate-controlled test are shown with frequent loading cycles resulting in a narrower damage zone. The concept of fatigue hydraulic fracturing is based on frequent lowering of crack tip stresses. In hydraulic fracture growth, this can be achieved by cyclic fluid injection (h) which is different from continuous fluid injection as used in conventional hydraulic fracturing (d); Zang et al. 2013.

The multi-stage stimulation method has been successfully applied in commercial shale gas development (Johri and Zoback 2013) while the fatigue hydraulic fracturing method using different fluid-injection schemes (e.g., cyclic, pulse pressurization) is still at the concept proof stage and its validation in the field has yet to be achieved. A general understanding of fatigue failure is that damage accumulates in rocks during cyclic loading, consequently leading to strength decrease. However, the mechanism of rock fatigue failure has not yet been fully understood (Erarslan and Williams 2012). More important, the fatigue cycling process during mechanical loading (Erarslan and Williams 2012) can be very different from fatigue hydraulic fracturing where a high-pressurized fluid is operated in cycles at the fracture tip (Zang et al. 2013).

Modeling hydraulic fracture growth and associated induced seismicity is a highly non-linear and complex process (Smart et al. 2014). Based on laboratory triaxial indenter tests results Yoon et al. (2014) developed and calibrated a hydro-mechanically coupled modeling tool which is able to study the application of fatigue hydraulic fracturing for dynamic cyclic and pulse fluid injection schemes. During cyclic injection the fluid pressure in the discrete element simulation runs is found to be lower compared to constant injection rates as operated in conventional hydraulic fracturing (Fig. 1.2). This is true for both, intact and naturally fractured crystalline reservoirs (Yoon et al. 2014), and fractured reservoirs with multiple stimulated wells (Yoon et al. 2015).

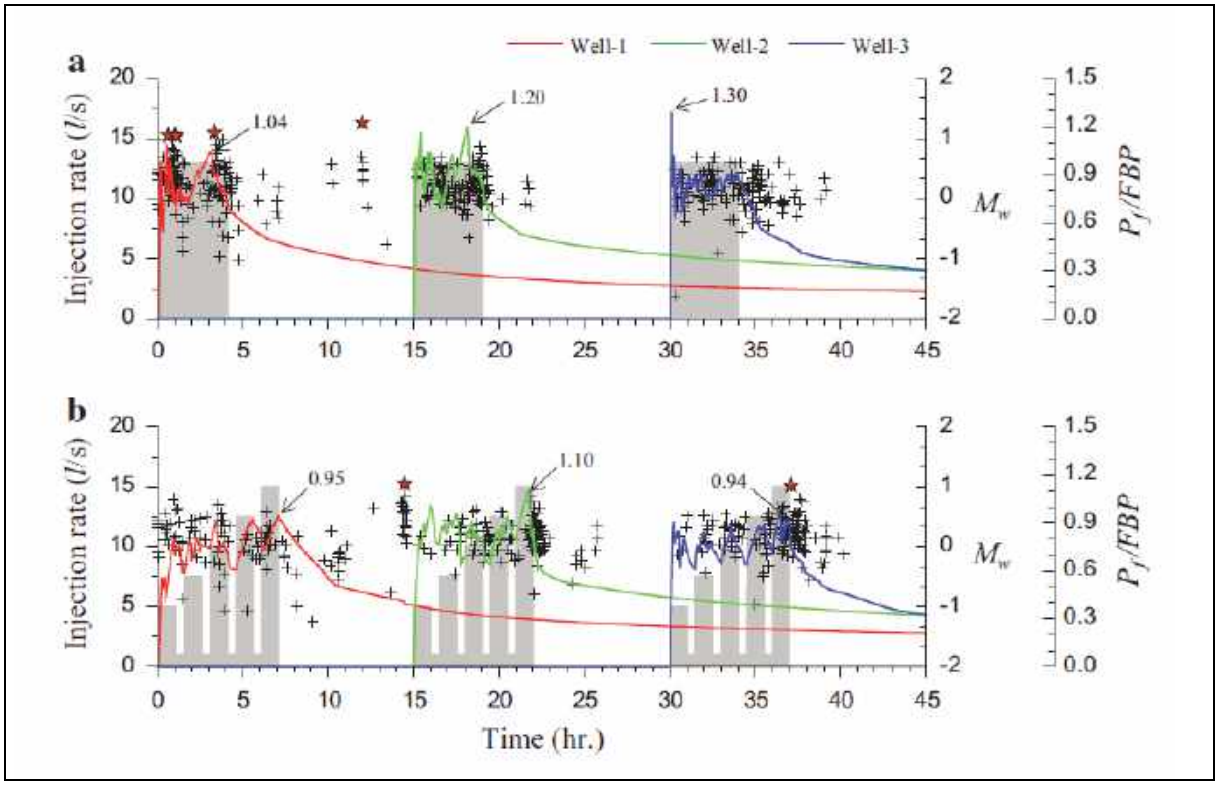

Fig.1.2: Two different fluid-injection schemes and their impact on induced seismicity evolution are compared for a naturally fractured reservoir with three injection wells. In (a) a constant fluid injection rate is modeled, and in (b) a five-cycle fatigue injection scheme is modeled. Total number of seismic events and their magnitude change according to injection style. Fluid pressure at the injection well is normalized to the fracture breakdown pressure (FBP) of the rock, after Yoon et al. 2015.

There are different scales involved in hydraulic treatment of rock mass. Hydraulic fracture operations in hydrocarbon (Suckale 2009), shale gas (Warpinski et al. 2012) and geothermal exploitation (Zang et al. 2014) involves rock volumes up to several hundreds of meters. Hydraulic fractures at mine scale normally extend over few tens of meters only (Niitsuma et al. 1993, van As et al. 2002). In the following, we describe a field test operated in May and June 2015 in Äspö Hard Rock Laboratory, Sweden to upscale laboratory results of cyclic fluid injection into crystalline cores (Zhuang et al. 2016) to field-size acoustic emission response of crystalline rock mass at 410 depth subjected to different water-injection schemes (Zang et al. 2016).

2 In Situ Experiment

Validating the FHF concept requires three steps: (1) determination of the fracture breakdown pressure, (2) detection and comparison of fluid-induced seismicity events, and (3) information on the permeability enhancement process. In the following, we compare the conventional hydraulic fracturing injection scheme with the cyclic fatigue hydraulic fracturing scheme tested in the field under controlled conditions. Äspö HRL has been selected as test site because geology, hydraulics and rock mechanics are well known from a large number of tests, including hydraulic fracturing stress measurements (Klee and Rummel 2002) and integrated stress determination (Ask 2006). The stress conditions from Klee and Rummel 2002 are assumed to be valid, i.e. if the borehole is drilled in the direction of minimum horizontal stress, such stress conditions would favor the propagation of radial and parallel fractures (Fig. 2.1). This is because once open, hydraulic fractures start to grow and orient themselves rapidly in the plane containing the maximum and intermediate principal stress.

A high-resolution borehole camera, scanning the entire borehole (diameter 102 mm), and the drill cores (diameter 86 mm) were used to select suitable test sections. In phase I of the experiment, a conventional flow test with continuous increase of fluid pressure in the testing interval is carried out. For this, a continuous flow rate versus time is used until the fracture breakdown pressure FBP is reached (Fig. 2.1, HF). After the fracture is formed the flow in the injected part of the borehole is tested and determined. In phase II, the hydraulic test is modified and a different water injection scheme is used (i.e. cyclic) with frequent stages of pressure decrease before the FBP is reached allowing stress relaxation at the fracture tip (Fig. 2.1, FHF). After the flow test, an impression packer is used to map fracture orientation at the borehole wall from cyclic testing. Phases I and II of the in situ experiment are repeated in different rock types, and are operated with fracturing equipment of two different companies (MeSy Solexperts Bochum, Germany and ISATech Prague, Czech Republic).

All phases of the hydraulic fracturing in situ experiment were monitored with acoustic emission (AE), micro-seismic borehole sensors and geophones, as well as electromagnetic sensors. In total, 39 sensors are operated in the near-field, close to the testing borehole (depth level 410 m), and 36 sensors were deployed in the far-field above (depth level 280 m) and below the test section (depth level 450 m). In the following, we report on data obtained from the AE monitoring system operated by the Gesellschaft für Materialprüfung und Geophysik (GMuG) mbH Bad Nauheim, Germany. This network is designed to monitor in the frequency range from 1 kHz to 100 kHz. The in situ AE monitoring system consists of eleven AE sensors and four accelerometers

(Fig. 2.2a). AE sensors employed are uniaxial side view sensors for borehole installation. For this three inclined monitoring boreholes are drilled left and right of the hydraulic testing borehole F1. Additional sensors are installed in short boreholes in the tunnel roof (Fig. 2.2b).

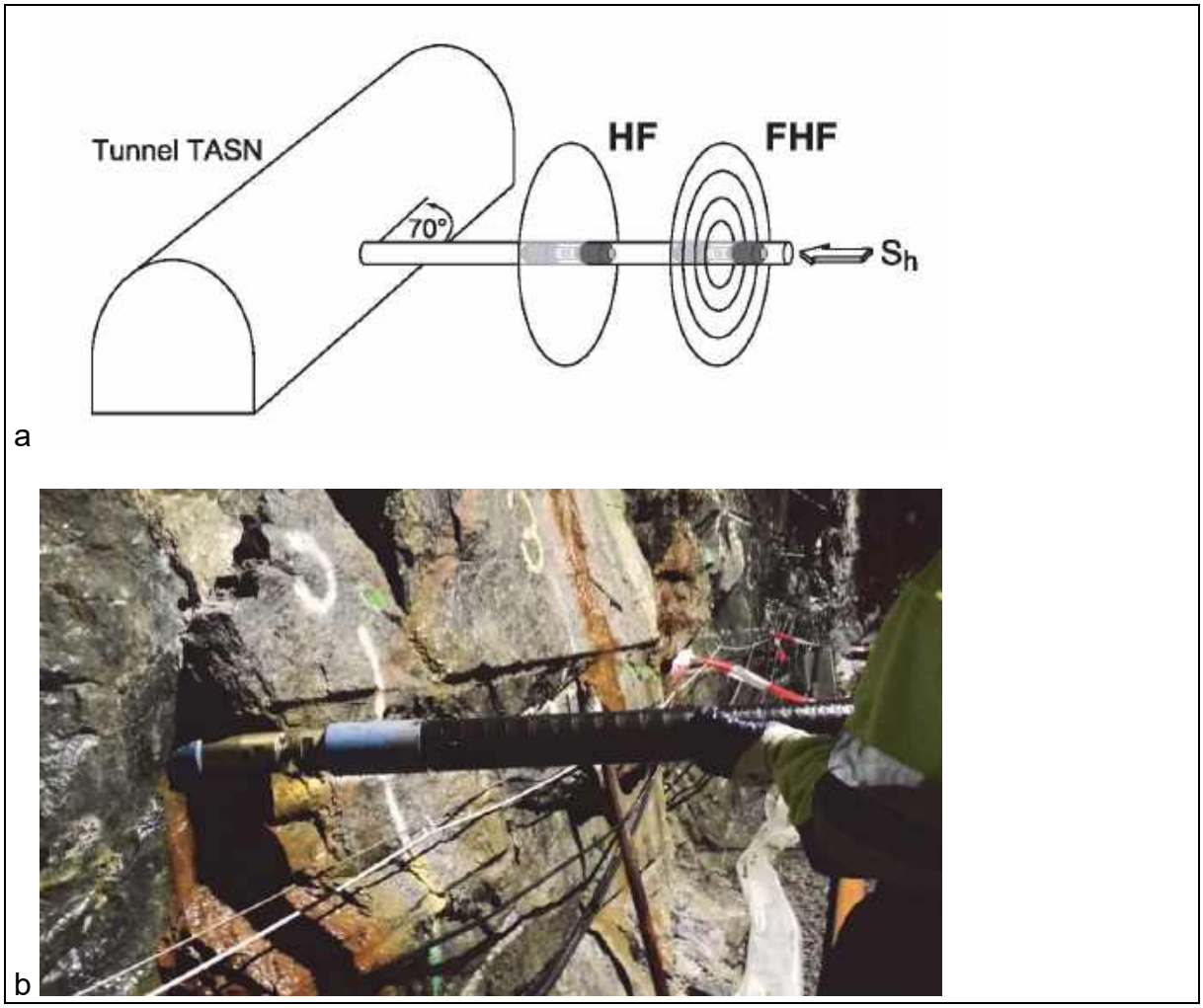

Fig. 2.1: (a) Two different fluid-injection schemes and their impact on induced seismicity evolution are compared in naturally fractured granitic rock mass at Äspö HRL. At depth level 410 m, conventional (HF) and fatigue hydraulic fracturing (FHF) are performed in a sub-horizontal borehole (diameter 4 inch) drilled from an experimental tunnel to total length of 28 m. (b) Fractures are designed by different water-injection schemes using a modified straddle packer system. The fracture process is mapped by acoustic emission and micro-seismic sensors.

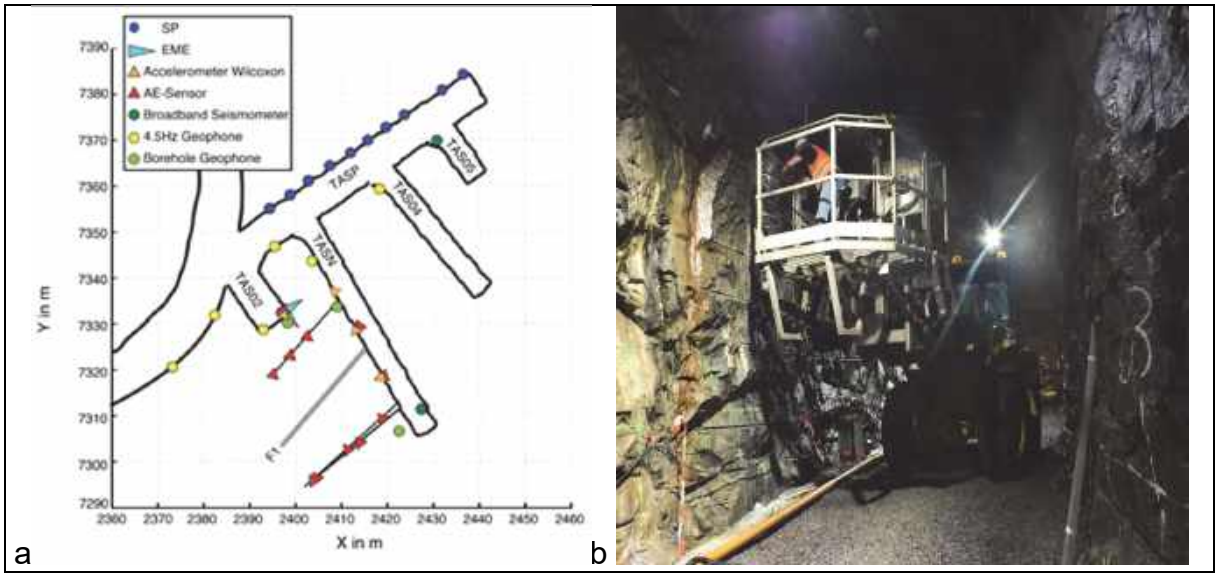

Fig. 2.2: (a) Near-field multi-sensor array design at depth level 410 m in Äspö HRL to monitor hydraulic fracture growth with different water-injection schemes. The hydraulic testing borehole F1 is drilled sub-horizontal, parallel to the minimum horizontal compressive stress. Three inclined monitoring boreholes on both sides of the testing borehole are equipped with AE sensors. (b) Additional sensors are installed in the tunnel roof; Zang et al. (2016).

Data was recorded using the measuring system GMuG AE system that is suitable both for continuous recording of data and recording in trigger mode with 1 MHz sampling frequency per channel. Below, we report on data registered with the in situ triggering system. Very sensitive trigger conditions were chosen in situ to maximize the sensitivity of the network. Once a trigger is detected, data is recorded on all synchronized channels. A ring buffer for pre-trigger recording is implemented. Picking of P- and S-wave onsets is based on a Hilbert transform and modified short term/long term average algorithm. Localization of AE events is based on gradient descent and a modified least square algorithm. For localized events the AE magnitude is estimated using the Eisenblätter and Spies (2000) relative magnitude approach. For more details on in situ trigger data processing, see Zang et al. (2016).

Velocities for both P- and S-waves were obtained from active ultrasonic transmission tests. This calibration procedure involves an ultrasonic pulse transmitter which is inserted into the fracturing borehole before the experiment. Active pulses were sent from one-meter intervals and recorded at the sensors of the AE network. The retrieved velocity values used for localization of AE events in a homogenous, full space velocity model are 5800 m/s and 3200 m/s for P- and S-wave, respectively.

3 In Situ Testing Results

Some results from three hydraulic in situ tests in Ävrö granodiorite are listed in Table 3.1. Experiment HF1 and HF2 are conventional hydraulic fracturing tests with continuous increase in injection pressure. In experiment HF3, the fatigue concept is tested by cyclic fluid injection. FBP is determined from the initial fracturing cycle of the conventional HF. The reopening pressure FRP is determined from the first re-fracturing cycle of HF. The magnitude of the minimum horizontal stress, Sh is determined from the

instantaneous shut-in pressure. The vertical stress is computed from the overlying rock density to be 10.9 MPa.

Table 3.1: Results from three in situ hydraulic fracturing experiments in Ävrö granodiorite, Zang et al. (2016). Listed is the mid test interval in borehole F1, the injection style, the fracture breakdown pressure (FBP), the fracture reopening pressure (FRP), and the horizontal minimum stress (Sh) determined from instantaneous shut-in pressure (ISIP).

Experiment	Test interval	Injection style	FBP (MPa)	FRP (MPa)	Sh (MPa)
HF1	25.0	continuous	13.1	8.9	8.3
HF2	22.5	continuous	10.9	6.7	8.6
HF3	19.0	cyclic FHF	9.2	8.8	9.2

In situ triggered AE data were used to obtain information about the fracture growth, its location, orientation and extension in near real time. During the experiment all events that were located automatically during fracturing, shut-in or bleed-off were then manually reviewed and plotted on site. During post processing a seismic catalogue was created that is free of noise events. In total, this catalogue contains 196 relocated AE events which occurred during the fracturing time periods. More information on this data set is found in Zang et al. (2016). Below, some results from hydraulic testing in Ävrö granodiorite are summarized using this catalogue.

In Figure 3.1, results from one conventional (HF2) and one cyclic fatigue hydraulic fracturing test (HF3) in Ävrö granodiorite are compared. Hydraulic data are indicated on the left ordinate, i.e. injection pressure and flow rate. Relative AE magnitude from the in situ triggered and localized data is indicated on the right ordinate. Both data sets are shown versus experimental time on the abscissa.

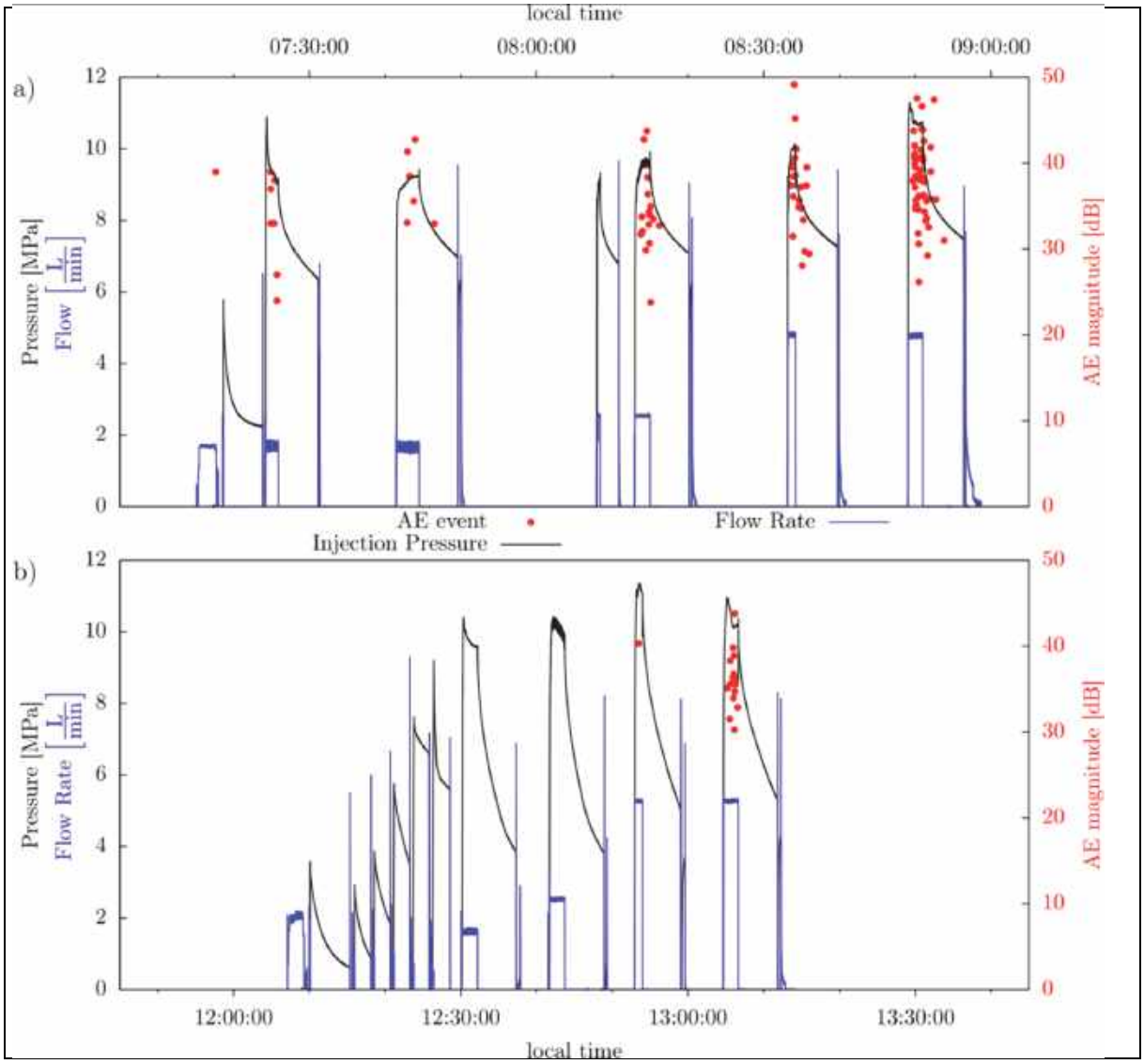

Fig. 3.1: Injection pressure and flow rate (left ordinate) and relative AE magnitude (right ordinate) for two in situ experiments with different fluid-injection schemes: (a) continuous water injection in conventional hydraulic fracturing (HF2), and (b) cyclic water injection in the fatigue treatment (HF3); Zang et al. (2016).

Initial fracturing cycle and first refrac of HF2 test (Fig. 3.1a) indicate pressure values of 10.9 MPa and 6.7 MPa. After five cycles of fatigue testing (Fig. 3.1b), the FBP is determined to be 9.2 MPa. This value is 15% lower compared to the FBP value from conventional HF2. While AE events are observed during all re-fracturing phases (except refrac 2) of the conventional HF2 (Fig. 3.1a), in experiment HF3 with cyclic water injection, AE events occur in the third and fourth re-fracturing stage only (Fig. 3.1b). No AE activity is observed in the five cycle fatigue treatment and before the FBP occurred despite the steady increase of flow rate in the last three re-fracturing cycles. The in situ trigger level of the AE system and the procedure in AE localization technique were the same in all experiments, HF1-HF3.

In Figure 3.2, relocated AE events for experiments HF1-HF3 are shown in map view and side view. For experiments HF1 and HF2 the AE events cluster and outline near

vertical fracture planes. AE activity migrates with time away from the borehole in the direction of maximum and intermediate principal stress (perpendicular to the testing borehole F1). For the cyclic HF3 experiment, no clear fracture plane could be outlined by AE hypocenter results, and no clear migration of AE hypocenters is visible. The maximum fracture extension from AE analysis is 5.3 m, 6.7 m and 2.3 m for HF1, HF2 and HF3, respectively (Zang et al. 2016). The AE fracture outline was compared to impression packer results. While in conventional HF1 and HF2 single hydraulic fractures were confirmed from AE data and impression packer results, in the cyclic experiment HF3 two fracture planes were identified by borehole impression packer. Further analysis is needed to conclude on the nature of the cyclic FHF.

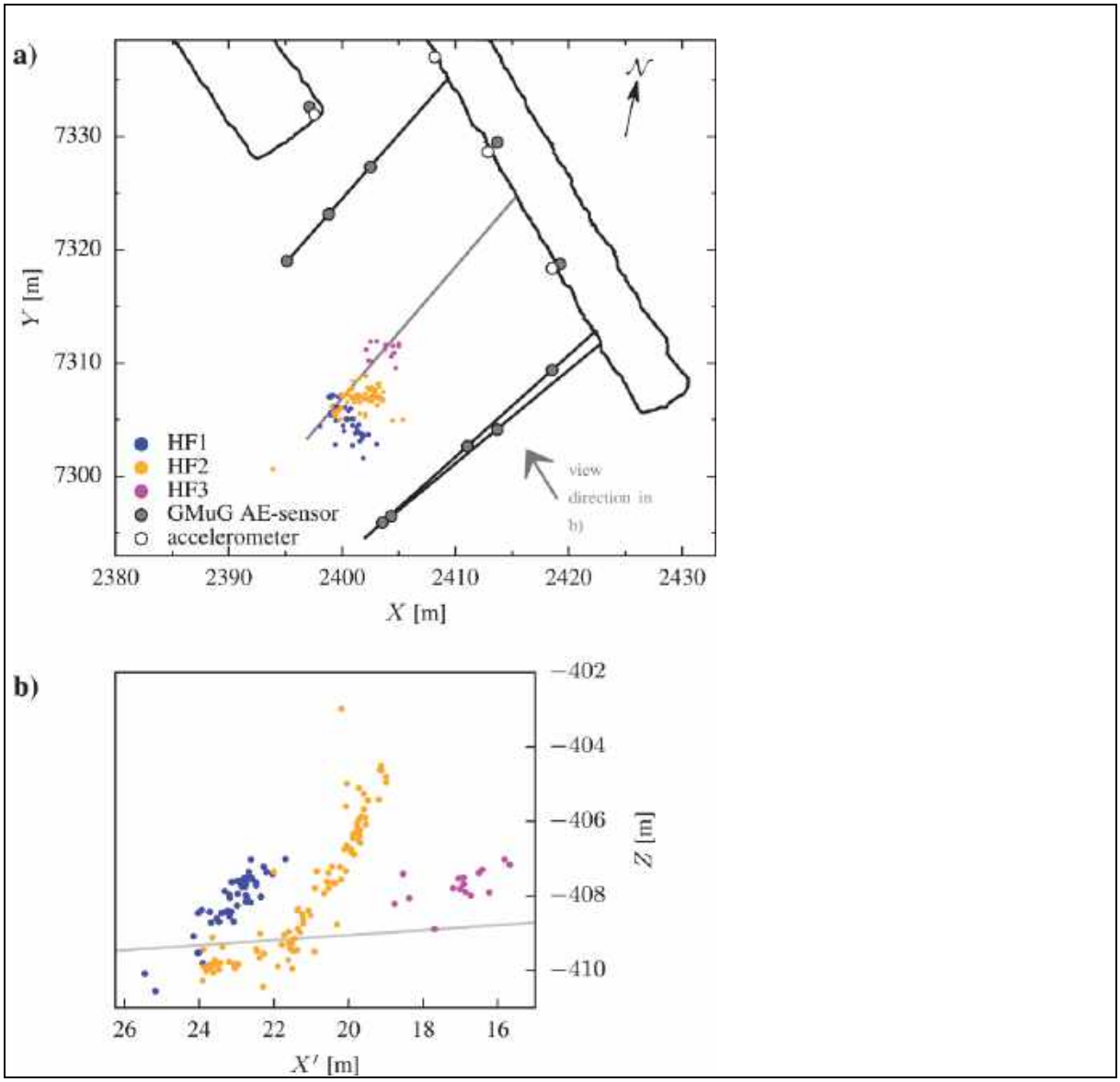

Fig. 3.2: Comparison of relocated acoustic emission events for three hydraulic fractures HF1-HF3 generated in Ävrö granodiorite (a) in map view, and (b) in side view. Solid black line outlines the tunnel at the experimental site. Thin black lines outline the long monitoring boreholes and solid grey line outlines the hydraulic testing borehole. Circles symbolize the sensors locations (grey – AE sensor, white – accelerometer); after Zang et al. (2016).

4 Discussion

Results from the in situ field test indicate that the fracture breakdown pressure of rock (Ävrö granodiorite) in the fatigue test was lower compared to the conventional test (30 % lower HF1 versus HF3, 15 % lower HF2 versus HF3). During five cycles of fatigue hydraulic loading (HF3) with a 20 % pressure increase in each cycle, no seismicity was observed. However, most of the conventional hydraulic fracturing stages (HF1, HF2) were accompanied by in situ triggered and relocated AE events.

The in situ test results in granitic rock are in line with laboratory results on rock cores (diameter 100 mm, length 200 mm) and concrete blocks (one cubic meter in size) performed by Jirakova et al. (2015). In their study, the authors found a fracture breakdown pressure 18 % lower using cyclic instead of continuous water injection. The same tendency of lower fracture breakdown pressure using cyclic water injection was found by Zhuang et al. (2016) when testing Pocheon granite cores from Korea (diameter 50 mm, length 100 mm). In their study, the conclusion was that hydraulic fracturing in the field can be conducted with smaller injection pressure (82 % of conventional value) when it is subjected to fatigue cycles. A reasonable number of laboratory cycles applied were varied from 2 to 27, 2 to 65, and up to 150 cycles.

We encourage further upscaling of the fatigue hydraulic fracturing concept to the wellbore scale. However, based on the findings from laboratory and the in situ test testing, a careful design of the fatigue hydraulic fracturing treatment at wellbore scale is needed. Appropriate numbers of operational injection parameters need to be assigned (e.g., number of cycles, injection duration, interval duration, rate increment per cycle, number of fracturing stages). Only in this way, the fracture optimization process can be guaranteed. The most ambitious task will be to design the test procedure to create low seismicity fracture networks with high permeability pathways.

Our present knowledge about fatigue hydraulic fracturing treatment seems to show that reduction of breakdown pressure and seismicity can be obtained with the pump capacity and testing time that is normally applied in conventional testing for fracture extension operations, leak-off testing and hydraulic stress measurements. The new approach is to allow the stresses at the fracture tip to fully relax and thereafter generate a new loading state that permits the fracture to seek and find the optimum and least energy consuming fracture extension at the new stress state at the fracture tip. Laboratory experiments on crystalline rock and results from the Äspö experiments have shown that the resting time after venting the pressure system has been enough to release the old and generate the new stress situation at the fracture tip to enhance the fracture propagation. If this also holds for fatigue hydraulic fracturing at wellbore scale needs to be tested in the field. If the procedure is functioning it is likely that existing industrial pump capacities can be applied and it is a matter of modifying the scheme of pumping to reach lower breakdown pressure and reduced seismicity.

5 Conclusion

Based on the analysis of three hydraulic fractures propagated at 410 m depth in Ävrö granodiorite and mapped with acoustic-emission monitoring, the following conclusions are drawn. (1) Compared to conventional hydraulic fracturing, the formation breakdown

pressure in fatigue hydraulic fracturing is lower. Also, the total number of acoustic events is lower in the cyclic water-injection test. (2) The in situ acoustic emission monitoring system recorded events in the frequency range above 1 kHz for three fractures in Ävrö granodiorite. Acoustic emission relocations outline the fracture location, orientation and expansion. The fracture location and orientation is in good agreement with impression packer results for the two conventional tests. The double fracture in the cyclic test needs further interpretation. (3) To bridge the gap between hydraulic fracturing results on laboratory cores tested and borehole size stimulation tests in geothermal applications, mine-scale hydraulic testing is seen valuable. The fracture monitoring system, however, has to be adapted to the frequency range expected, and complementary sensor arrays need to be in operation.

A more detailed picture of the hydraulic fracture growth process will follow when post-processing of the continuous waveform recordings of the experiment is completed. This picture will include information on local fracture modes (tensile, shear), their evolution in space and time, as well as numbers of hydraulic fracture apertures. Final goal is to evaluate the energy partition of the fracture process (hydraulic energy, seismic radiated energy, fracture surface energy and dissipated energy).

Acknowledgements

Nova project 54-14-1 was financially supported by GFZ German Research Center for Geosciences (75 %), KIT Karlsruhe Institute of Technology (15 %) and Nova Center for University Studies, Research and Development (10 %). An additional in-kind contribution of SKB for using Äspö Hard Rock Laboratory as test site for geothermal research is greatly acknowledged.

6 References

Ask D (2006) New developments in the Integrated Stress Determination Method and their application to rock stress data at the Äspö HRL, Sweden. Int. J. Rock Mech. & Min. Sci. 43, 107–126

Eisenblätter J, Spies T (2000) Ein Magnitudenmaß für die Schallemissionsanalyse und Mikroakustik, Deutsche Gesellschaft für Zerstörungsfreie Prüfung, 12, *Kolloquium Schallemission, Jena*

Ellsworth WL (2013) Injection-induced earthquakes. Science 341, http://dx.doi.org/10.1126/ science.1225942

Erarslan N, Williams DJ (2012) Mechanism of rock fatigue failure damage in terms of fracturing modes. *International Journal of Fatigue* 43, 76-89

Klee G, Rummel F (2002) Rock stress measurements at the Äspö HRL. Hydraulic fracturing in boreholes KA2599G01 and KF0093A01, International Progress Report IPR-02-02, SKB.

Giardini D (2009) Geothermal quake risk must be faced. Nature 426, 848–849

Jiráková H, Frydrych V, Vintera J, Krásný O, Vaněček M (2015). Results of the rock hydraulic fracturing research project. *Tunel - Un- dergr. Constr. Mag. Czech Tunneling Assoc. Slovak Tunneling Assoc.* **24**(4), 57–64

Johri M, Zoback MD (2013) The evolution of stimulated reservoir volume during hydraulic stimulation of shale gas formations. *In: Proceedings of the unconventional resources technology conference, Colorado, 12-14 August 2013*

Meier PM, Rodríguez AA, Bethmann F (2015) Lessons learned from Basel: new EGS projects in Switzerland using multistage stimulation and a probabilistic traffic light system for the reduction of seismic risk. *In Proceedingsof World Geothermal Congress 2015, Melbourne, 19-25 April 2015*

Niitsuma H, Nagano K, Hisamatsu K (1993) Analysis of acoustic emission from hydraulically induced tensile fracture of rock. Journal Acoustic Emission 11, S1-S18

Rubinstein JL, Mahani AB (2015) Myths and facts on wastewater injection, hydraulic fracturing, enhanced oil recovery, and induced seismicity. *Seismological Research Letters* **86**(4), 1060–1067

Smart KJ, Ofoegbu GI, MorrisAP, McGinnis RN, FerrillDA (2014) Geomechanical modeling of hydraulic fracturing: Why mechanical stratigraphy, stress state, and pre-existing structure matter. *Am. Assoc. Pet. Geol.Bull.* **98**(11), 2237–2261

Suckale J (2009) Induced seismicity in hydrocarbon fields. Advances Geophys. 51, 55–106

van As A, Jeffrey RG (2002) Hydraulic fracture growth in naturally fractured rock: mine through mapping analysis. In: Hammath et al. (eds) Proceedings 5th North American Rock Mechanics Symposium, NARMS-TAC, University of Toronto, Canada, pages 1461-1469

Warpinski NR, Du J, Zimmer U (2012) Measurements of hydraulic fracture induced seismicity in gas shales. SPE Production and Operations, August, 240–252

Yoon J-S, Zang A, Stephansson O (2014) Numerical investigation on optimized stimulation of intact and naturally fractured deep geothermal reservoirs using hydro-mechanical coupled discrete element fracture network model. Geothermics 52, 165-184

Yoon J-S, Zang A, Zimmermann G (2015) Numerical investigation on stress shadowing in fluid injection-induced fracture propagation in naturally fractured geothermal reservoir. Rock Mechanics and Rock Engineering, Vol. 48, 1439-1454

Zang A, Yoon J-S, Stephansson O, Heidbach, O (2013) Fatigue hydraulic fracturing by cyclic reservoir treatment enhances permeability and reduces induced seismicity. Geophysical Journal International 195, 1282-1287

Zang A, Oye V, Jousset Ph, Deichmann N, Gritto R, McGarr A, Majer E, Bruhn D (2014) Analysis of induced seismicity in geothermal reservoirs - An overview. Geothermics 52, 6-21

Zang A, Stephansson O, Stenberg L, Plenkers K, Specht S, Milkereit C, Schill E, Kwiatek G, Dresen G, Zimmermann G, Dahm T, Weber M (2016) The geothermic fatigue hydraulic fracturing experiment at Äspö Hard Rock Laboratory, Sweden – Monitoring design, hydraulic testing and first results. Geophysical Journal International (submitted)

Zhuang L, Kim KY, Jung SG, Diaz MB, Min KB, Park S, Zang A, Stephansson O, Zimmermann G, Yoon JS (2016) Laboratory study on cyclic hydraulic fracturing of Pocheon granite in Korea, 50th US Rock Mechanics / Geomechanics Symposium, Houston, Texas, USA, 26-29 Jun. 2016, ARMA 16-163

Zimmermann G, Hofmann H, Babadagli T, Yoon J-S, Zang A, Deon F, Urpi L, Blöcher G, Hassanzadegan A, Huenges E (2015) Multi-fracturing and cyclic hydraulic stimulation scenarios to develop enhanced geothermal systems - Feasibility and mitigation strategies to reduce seismic risk. *In Proceedings of World Geothermal Congress 2015, Melbourne, 19-25 April 2015*

Rock Mass Scale Effects on Tool Wear in Hardrock Tunnelling – practically significant and scientifically neglected?

Gebirgsmaßstäbliche Einflussfaktoren auf den Werkzeugverschleiß im Felstunnelbau – baupraktisch relevant und wissenschaftlich vernachlässigt?

Ralf J. Plinninger,
Jan Düllmann
Dr. Plinninger Geotechnik
Kirchweg 16, D-94505 Bernried / Germany

Abstract

The investigation of rock abrasiveness and the assessment of tool wear represent important tasks in the course of any recent tunnel project. This especially applies to mechanized tunneling (TBM, shield, roadheader), where wear plays an important role for the working cycle and consequently for construction time and costs. Starting from a normative "vacuum", increasing knowledge and standardization work has led to an increasing application of laboratory scale tests, such as the CERCHAR method (CAI) or the Rock Abrasiveness Index (RAI). However, it must be taken into account, that larger scale - rock mass - factors, such as discontinuities, rock type distribution and stress conditions do additionally influence tool wear. Indeed, the negative consequences of adverse rock mass conditions may be of a much higher degree, than an increase in intact rock abrasiveness. The proposed paper is intended to give an overview of the current state of knowledge and to resume in practical suggestions for investigation, description and contractual aspects of such effects in rock tunneling.

Zusammenfassung

Die Untersuchung der Abrasivität des anstehenden Gebirges und die Bewertung des zu erwartenden Werkzeugverschleißes stellen heute im Vorfeld jeglicher Tunnelbaumaßnahme wichtige Aufgaben dar. Dies gilt insbesondere für maschinelle Vortriebsverfahren (TBM / SM / TSM), bei denen die Auswirkungen von Verschleiß eine besondere Relevanz für Arbeitszyklus, Bauzeit und -kosten besitzen. Ausgehend von einem normativen „Vakuum“ in diesem Bereich haben mit zunehmendem Erkenntniszuwachs und dem Einsetzen entsprechender Gremienarbeit auf Laboruntersuchungen basierende Kennwerte, wie der CERCHAR-Abrasivitätsindex (CAI) oder der Abrasivitätsindex RAI zunehmenden Eingang in entsprechende Regelwerke gefunden. Dennoch ist festzustellen, dass über den Maßstab des intakten Gesteins hinaus auch größermaßstäbliche Faktoren, wie z. B. Trennflächengefüge, Gebirgsaufbau oder Spannungszustand signifikanten Einfluss auf den Werkzeugverschleiß nehmen. Die Folgen dahingehend widriger Verhältnisse können sogar um ein Vielfaches gravierender sein, als

eine Erhöhung der Abrasivität des intakten Gesteins alleine. Der vorgeschlagene Beitrag stellt praxisorientiert den derzeitigen Stand der Erkenntnisse dar und gibt Anregungen für die Erkundung, Bewertung und bauvertragliche Berücksichtigung derartiger Situationen im Felstunnelbau.

1 Tool Wear – Contractual Risk

Disregarding the chosen construction method – either mechanical or conventional tunneling, the wear of rock excavating tools has always been a highly relevant factor, influencing construction performance and expenses. However, wear phenomena do not only directly affect related wage and material costs for the exchange of worn tools, but are additionally able to affect in many ways the whole working cycle, including standstills and overall machine availability.

For tunnel works, which are based on a construction contract between a client (for instance public authority) and a contractor (usually construction company) it is therefore important to clearly define relevant geological-geotechnical causes for tool wear and to fairly distribute the risks connected with this topic. For instance, tunneling contracts in Germany and Austria usually locate the ground related causes for wear in the risk sphere of the client, while the choice of an appropriate construction method, choice of excavation equipment and associated performance and wear estimates are located within in the risk sphere of the contractor.

Starting from a normative "vacuum" in this field of engineering geology, laboratory procedures, such as the CERCHAR test (see Figure 1.1) or mineralogical and geotechnical indices, such as the Equivalent Quartz Content or the Rock Abrasivity Index (RAI) have in the meanwhile seen an increasing use and are undergoing further standardization. With the introduction of the Supplementary Volume for the national German Standard for Construction Works, VOB, in 2015, the CERCHAR test and the so determined CERCHAR Abrasivity Index, CAI have been referred to as standard method for the assessment of hardrock abrasivity, also in the field of tunneling (DIN 18312 standard).

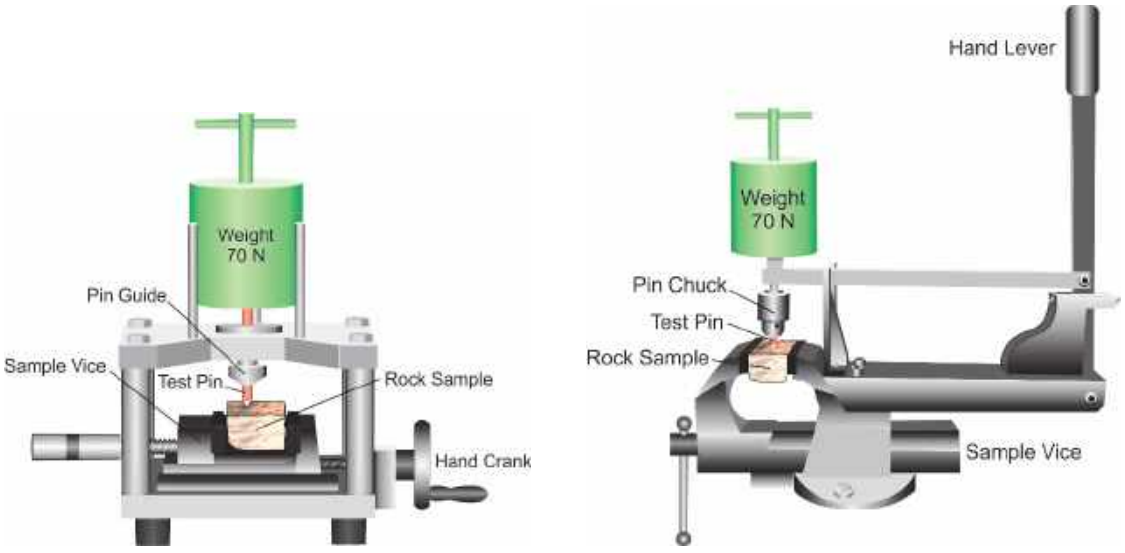

Fig. 1.1: Typical testing layouts for the CERCHAR test.

Although the investigation of rock abrasivity in a laboratory scale is an important and positive step towards an optimized wear prediction and a fair building contract, it has to be concluded, that the final aim cannot be reached by those methods alone, as relevant influencing factors in the rock mass scale must remain neglected.

2 Defining „Tool Wear“ and „Abrasivity“

Based on the now retracted (because not updated) German Standard DIN 50320, the term **"tool wear"** can be defined as progressive loss of material from the surface of a tool, caused by mechanical contact and relative movement between tool and rock mass.

This wear can be caused by various processes which usually do represent interactions between more continuous and abrading modes (→ "abrasive wear") and suddenly occurring events with more or less catastrophic failure of tool parts (→ "tool failure", see Fig. 2.1).

Fig. 2.1: Worn point attack picks of a roadheader, whose replacement was both caused by continuous abrasion, as well as partial failure of tool components (Photo: Plinninger).

However, a definition in the form, that “tool wear” does only include continuous abrasive processes cannot be derived from the relevant standards and literature. On the contrary, the gross wear parameters commonly used in civil engineering and tunneling, such as the "drill bit lifetime" according to German Standard DIN 20301 [drilled meters / bit], the "specific tool wear" [picks / m³ (solid)] or the "cutter life" [m³ (solid) / disc] do indeed strongly suggest that an appropriate “tool wear” definition must be able to describe the full life time cycle of a tool between insert of the new tool and replacement of the worn tool - regardless of the type of wear that took place.

While the tool wear has to be seen as one result of the tribological contact between the tool and the rock mass, the term **"abrasivity"** is intended to describe the geogenic causes for tool wear. According to Plinninger (2002) it might be defined as the ability of a rock mass, rock or mineral to cause wear on a rock excavating tool (Fig. 2.2).

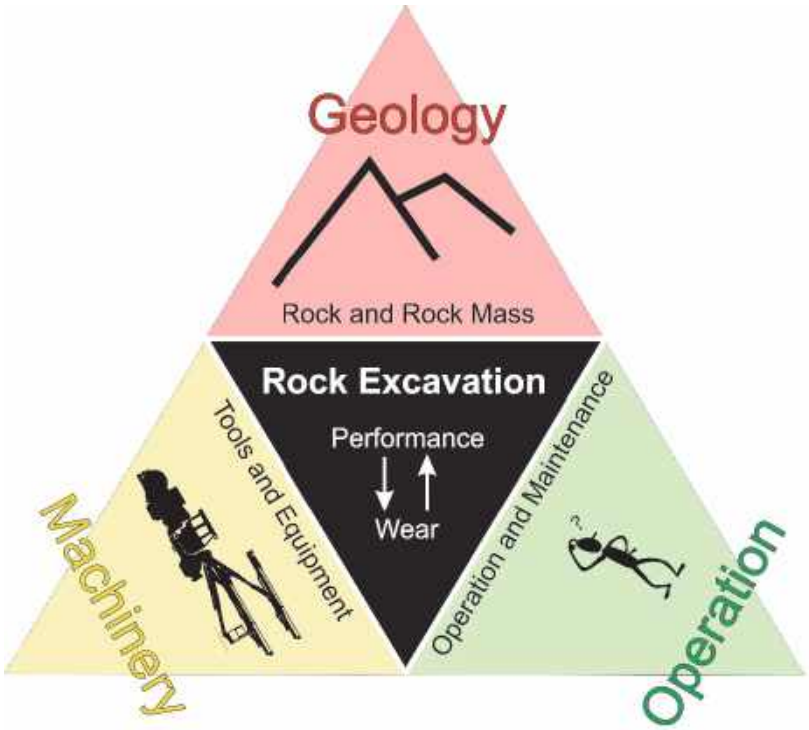

Fig. 2.2: Visualization of the influencing factors in rock excavation (according to: Plinninger, 2002, Fig. 26, p. 30, redrawn).

However, the abrasivity of a rock mass, rock or mineral is by no means an absolute measure, but depending on the specific type and characteristics of the rock tool, as well as the system conditions (pressure, temperature conditions, etc.).

Although the objective and definition of the term “abrasivity” (explicitly including rock mass properties) clearly suggest a holistic meaning of the term, it must be noted that sudden, catastrophic failure of tools and tool components sometimes are excluded in the evaluation or back-analysis of projects. Even if this approach may contribute to the fact that the (so adjusted) wear rates can much better be explained and be predicted by the results of small-scale laboratory experiments, this method on the other hand leads to an obvious underestimation of the economic and scientific importance of catastrophic wear processes, often associated with rock mass scale properties.

The experiences and theories presented in the following Section 3 are intended to show some examples for such effects.

3 Rock Mass Scale Effects on Tool Wear

3.1 Mixed Face“ Conditions

The term „mixed face condition“ is used in the field of TBM tunnelling since the 1980s (see for instance Beckmann & Simons, 1982). While there is no definition available from the applicable German national standards, the term is defined in the Austrian Tunnelling Standards ÖNORM B 2203-1 (conventional tunnelling) and ÖNORM B 2203-2 (TBM/Shield Excavation) as follows:

- for conventional excavation: "conditions with simultaneous appearance of rock types with significantly differing excavatability at one face, requiring excavation with blasting on the one hand and excavation with excavator or roadheader on the other hand side";
- for mechanical (TBM, shield) excavation: „excavation under conditions with simultaneous appearance of coherent layers of rock types with significantly differing excavatability".

Although these definitions leave a considerable space for interpretation especially in the field of mechanized tunnelling, the consequences of such conditions have lucidly been presented for a variety of excavation methods:

For the application of **roadheaders**, effects of typical "mixed-face" conditions have been presented by Plinninger, Thuro & Bruelheide (2001) and Plinninger (2011).

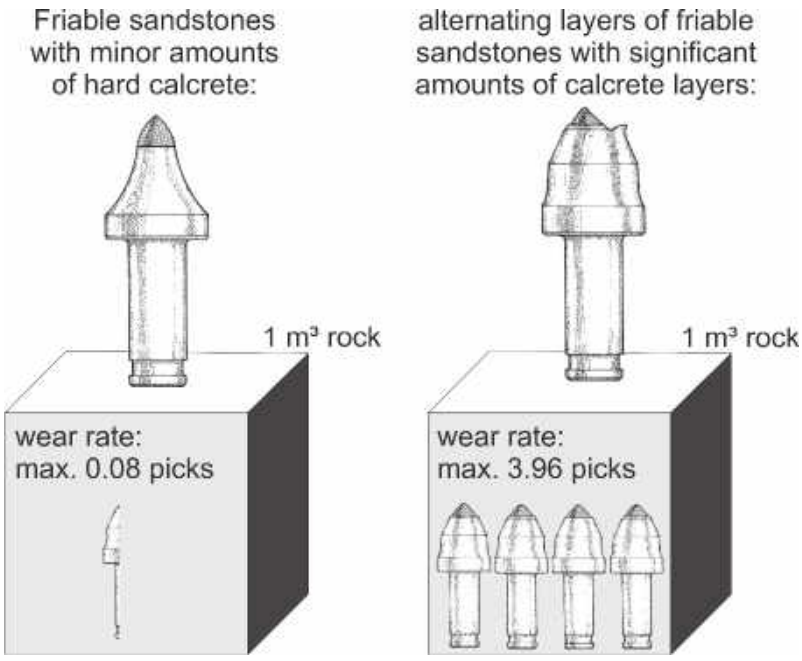

Fig. 3.1: Comparison of tool wear forms and specific pick consumption in homogeneous and “mixed face” conditions during roadheader excavation at Nuremberg Metro (according to: Plinninger, Thuro & Bruelheide, 2001, redrawn).

Investigations during roadheader application for the Nuremberg Metro in alternating layers of friable sandstones and very strong calcrete layers showed a clear relationship

between the thickness and frequency of the concretions on the one hand and the wear form / wear rate on the roadheader's point attack picks on the other hand (Figure 3.1).

It should be noted in this context, that referring to the already mentioned Austrian Standard ÖNORM B2203-1, such conditions would have been defined as "mixed face" conditions only if a combined excavation of blasting AND roadheader would have been applied - a circumstance, which also casts doubt on the general applicability of this definition.

In the field of **mechanized tunneling** Alber (1999) describes a situation where a flat lying boundary between a dolomite of approx. 35 MPa intact rock strength and a shale of approx. 13 MPa has been excavated by a TBM. To avoid disk damage and vibrations in this section, the contact pressure had to be reduced to a level of 0.105 MN/disc, until the different penetrations could be absorbed by the TBM without damage (Fig. 3.2). After passing through this zone, the contact pressure again increased to a "normal level" of about 0.145 MN/disc.

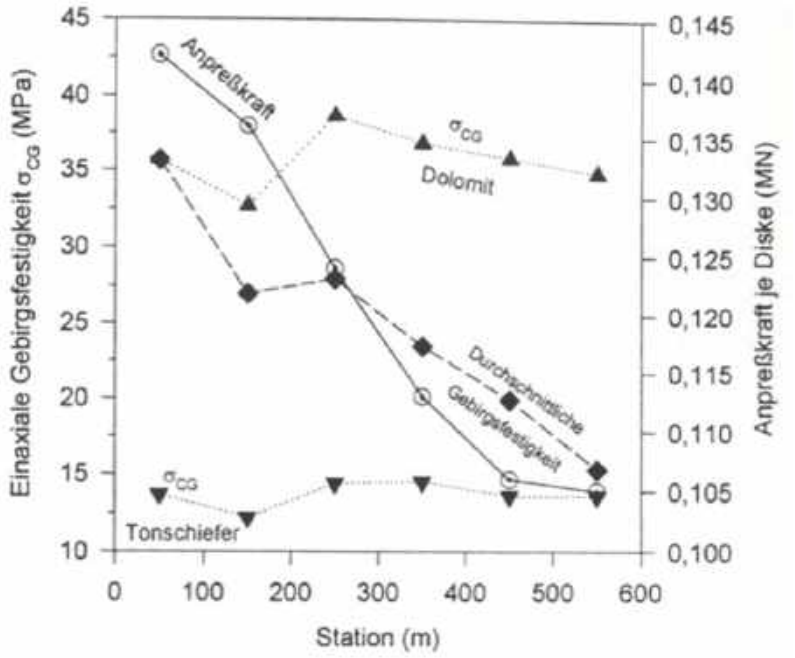

Fig. 3.2: Schematic plot of rock UCS, mean UCS and thrust evolution for a TBM drivage under „mixed face" conditions (from: Alber, 1999, Fig. 4.12, S. 59).

Comparable conclusions can also be drawn from the relatively new results published by Entacher, et al. (2013) from load measurements on TBM disc cutters in crystalline rock with different fracture spacing. In the diagrams presented in this paper, the peak stresses of the discs show significant matches with the boundaries of zones with differing fracture spacing (A / B-boundary lines in Fig. 3.3).

In such heterogeneous ground conditions, the thrust applied on the cutterhead by the TBM cannot be uniformly distributed amongst the discs. The dynamically and unevenly distributed disc loads and associated high peak stresses at single discs are the reasons for disc damages and vibrations as already described by Alber (1999).

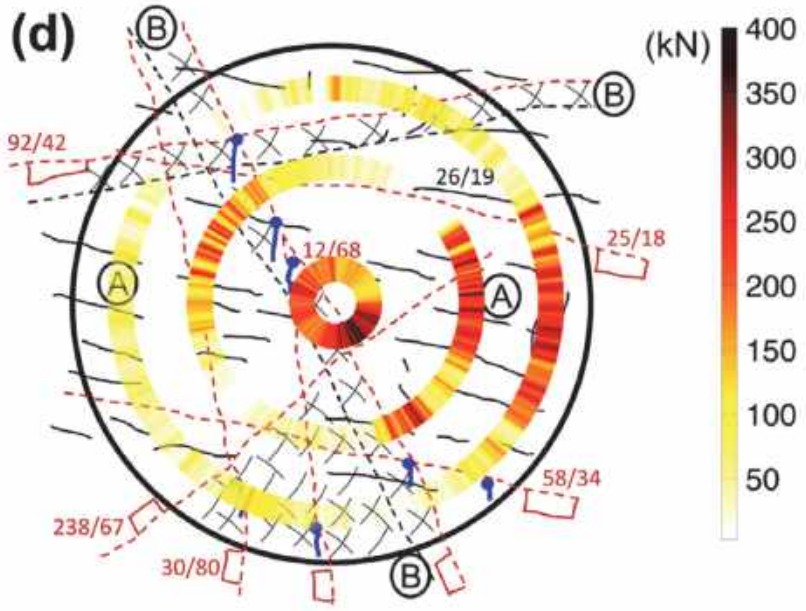

Fig. 3.3: Measured Normal forces FN compared with the corresponding geological mapping (from: Entacher et al, 2013, Fig. 24, S. 495).

A geometric assessment of the "mixed-face" phenomenon shows that the scale of excavation plays an essential role: During blasthole drilling the contact between tool and rock ranges in a scale of some centimeters and thus more on the scale level of intact rock. During roadheader application, but even more for full-face tunnel boring machines, which excavate areas of up to approx. 150 m² in a single turn, the sequence of different rock types and rock layers plays a much more significant role.

According to Plinninger (2002), the percentage of homogeneous rock conditions (no "mixed-face" condition) can be determined by the scale of rock excavation (d) and the layer thickness (m) under the assumption of a rock mass composed of two concordantly alternating rock types as given in the following equation and presented in Fig. 3.4:

$$H = (1 - \frac{d}{t}) \cdot 100$$

with: H Amount of homogeneous rock conditions [%]
d Diameter of rock excavation at a single time [m]
t Layer thickness [m]
Remark: For all cases $d \geq m$ $H = 0$ %

Based on these considerations, it is clear that an assessment of "mixed-face conditions" must always be based on the background of the specific excavation method. It is also evident, that for full-face excavation techniques, the subject of inhomogeneous ground conditions and "mixed-face" conditions must have a much greater significance than for example blasthole or exploratory drilling.

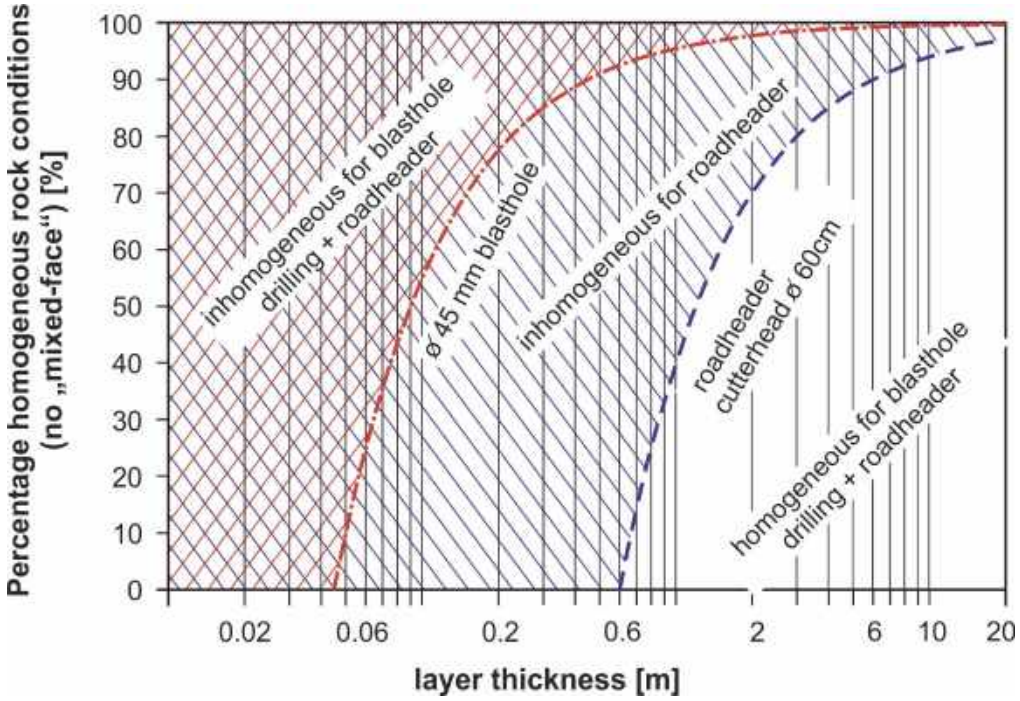

Fig. 3.4: Correlation of the amount of homogeneous / non-mixed-face conditions vs. layer thickness for several rock excavation techniques, including ∅ 45 mm blasthole drilling and roadheader application by use of a ∅ 60 cm cutterhead (according to: Plinninger, 2002, Fig. 27, p. 32, redrawn).

3.2 Unstable Face Conditions / „Blockiness“

The terms of an "unstable", “collapsing”, "blocky" face or "blockiness" describe conditions in mechanized tunneling, where the rock mass collapses at the face in front of the cutterhead, forming larger rock bodies besides or instead of the “normal” rock chips that form during cutting (see for instance Austrian Standard ÖNORM B2203-2). Such rock blocks or plates can reach significant sizes of up to several cubic meters (see Fig. 3.5).

Fig. 3.5: Cubic decimetre to cubic meter large gneiss blocks in front of the cutterhead of a hard rock TBM. Discs and cutterhead can be seen on the right edge of the image (Photo: Plinninger).

Depending on the strength and abrasiveness of the blocks, such conditions may present unusual and severe demands for the TBM and its tools. Loose blocks, which are larger than the cutterhead openings have to be crushed between face and cutterhead until they are small enough to pass these openings and be mucked out. As a TBM cutterhead is usually not designed for such "crushing", head structure, front plating and cutters are facing dynamic, locally extremely high impacts and shock loads instead of the more or less continuous rolling movement during regular excavation. Increased failures of tools and tool components (ring fractures, screw breaks, etc.) are frequently observed consequences of such conditions.

The most relevant geological causes for "unstable", "blocky" or "collapsing" face conditions are mechanically effective discontinuities, like joints and bedding planes, which may lead to structural outbreaks under unfavorable orientations. In addition, high rock stress conditions can also lead to rock spalling or rock bursts with often typical, concave or arched profiles at the face and thin, sharp-edged, platy debris.

Although a strictly deterministic assessment of the quantitative impact of such conditions on the lifetime / consumption of disc cutters seems difficult at the present state of knowledge, back-analysis of past projects provide clear correlations between blocky conditions at the tunnel face and the increased occurrence of brittle fracture of tools and tool parts (see for instance Weh, 2007).

3.3 Stress Conditions

The stress conditions in the rock mass at the face have an additional influence on rock excavation and tool wear. Since in situ primary and secondary stress conditions can only be determined with great effort and the impact on the excavation process might only be identified indirectly - by comparison of different conditions - the issue of stress influences is still discussed controversially and mostly based on model calculations as presented in Figure 3.6 (from Alber, 2008).

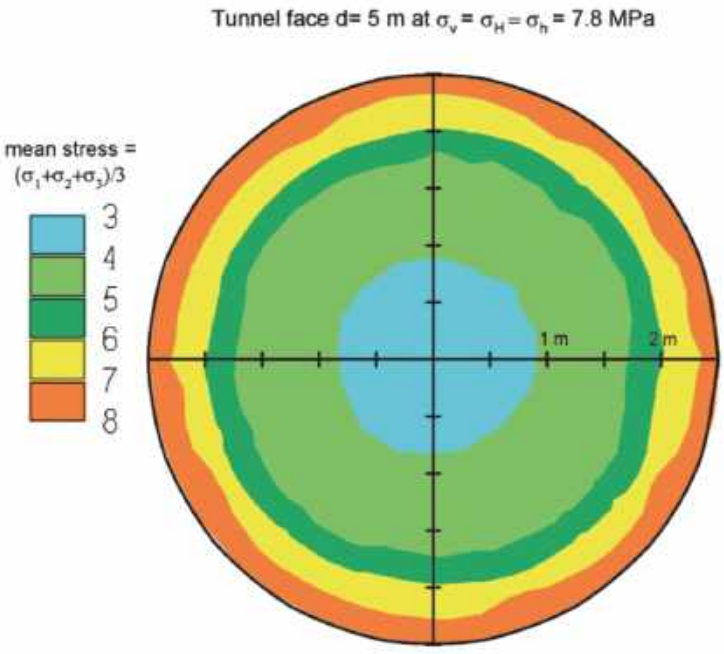

Fig. 3.6: Modelling of stress distribution on a TBM tunnel face (from: Alber, 2008, Fig. 7, p. 35)

In the referring literature (including Rutschmann, 1974, Alber, 2008, Lagger, et al, 2015) considerations have been presented, which postulate that stress conditions, depending on level, orientation and rock mass properties may either have a positive (by forming of new discontinuities), neutral or negative influence (by increasing the resistance against excavation) effects on rock excavation and tool wear.

4 Tool Failure as a result of Adverse Rock Mass Conditions

Due to the significant technical and economic relevance, it seems necessary from the authors point of view to respond in detail to the phenomenon of failure of tools and tool parts, which is predominantly influenced by the prevailing rock mass conditions. In the following Sections, features and relevance of such wear processes are described for tools with hard metal inserts (Section 4.1) and steel tools (Section 4.2). Section 4.3. gives an insight into the potential impact of tool failure for wear estimates.

4.1 Failure of Hard Metal Inserts

For button drill bits and point attack picks, the hard metal insert(s), usually cemented tungsten carbides, represent the main part of the rock tool. Although these hard metals

have a high material hardness and an associated, high resistance capacity against abrasive wear, the material properties on the other hand lead to relatively high brittleness. This results in the effect, that even during more or less continuous abrasion material removal from the tool surface mainly takes place as a result of "microcracking", i.e. microscopic outbreaks from the hard metal surface.

If the tool is subjected to high impact, the danger exists, that large parts of the insert are broken or the entire hard metal pin is ripped out of the steel body by breakage of the bedding. If that happened, the missing hard metal insert is no longer able to effectively protect the tool body from abrasion, which in most cases requires early replacement of the tool. Although brittle fractures of this category per definition are macroscopically visible, the application of scanning electron microscopy gives a further impression on the devastating extent of further damage (Fig. 4.1).

Fig. 4.1: Shell-shaped brittle fractures in the hard metal insert of a point attack pick, about 16-fold magnification. The loss of material (based on the volume of the cemented carbide insert) in this case was about 40% (from: Plinninger, 2002, Figure 23, p. 23).

If the insert is not removed entirely, the differently oriented, typically shell-shaped fractures can also significantly weaken the remaining insert. Since such already prescribed fracture surfaces can easily be activated during subsequent loading, such damage may drastically increase the likelihood of complete wear after only a little period of time.

4.2 Failure of Steel Tools

Homogeneous steel tools, as for instance disc cutters or steel bodies of drill bits and point attack picks can also be affected by brittle material failure - although steel is able to perform significantly tougher than hard metals. Such phenomena, for instance fracturing of disc cutters (see Fig. 4.2) have to be rated as one the most expensive problems during operation of a hardrock TBM.

Fig. 4.2: Broken 17“-cutter disc of a hardrock TBM (Photo: Plinninger).

The occurrence of brittle fractures of any type (hard metal insert or steel parts) is influenced by geological features, mainly the rock´s compressive strength and the discontinuity system at the face, as well as by the layout of tools and machines, as for instance the arrangement, type and quality of the tools, the type of excavation process taking place as well as applied forces.

4.3 Impacts of Tool Failure on Wear Estimation

While the more or less continuous abrasion of rock tools can reasonably well be predicted on the basis of laboratory methods, catastrophic macroscopic tool failures are mainly related to rock mass scale effects as presented earlier in this paper. Such conditions cannot be investigated in the laboratory and therefore cannot be included in such prediction models. If adverse rock mass conditions (including "mixed face", "blockiness", etc.) occur, which are able to cause tool failure, wear estimates based on the assumption of continuous material removal will therefore provide wrong – too optimistic – results, which is explained in the followings diagrams (Figure 4.3 and 4.4).

Figure 4.3 represents the hypothetical decrease of a point attack pick´s mass for a pick which is worn by continuous abrasive wear and is replaced at the end of its (relatively long) service life time because the carbide insert becomes unusable.

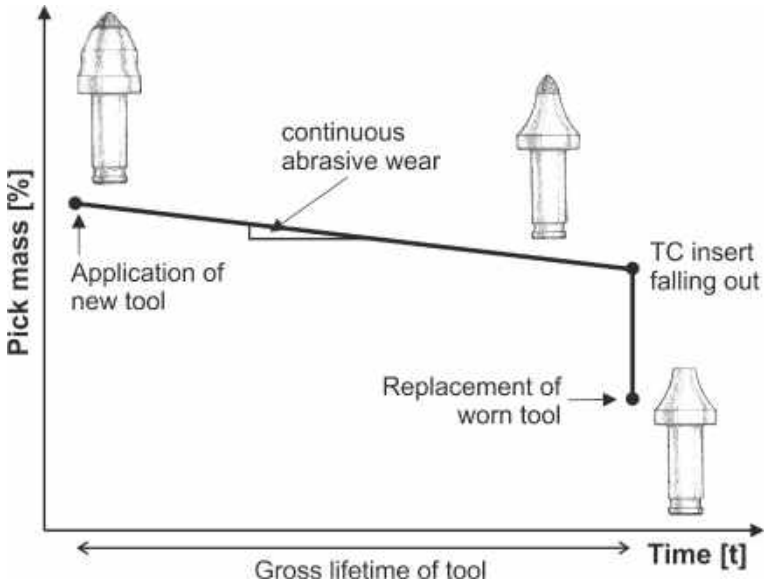

Fig. 4.3: Hypothetical mass loss diagram for a point attack pick that is undergoing continuous abrasive wear („Case A“).

In contrast to this, Figure 4.4 depicts a pick, that has to be replaced at any time during operation as a result of catastrophic failure of the hard metal insert.

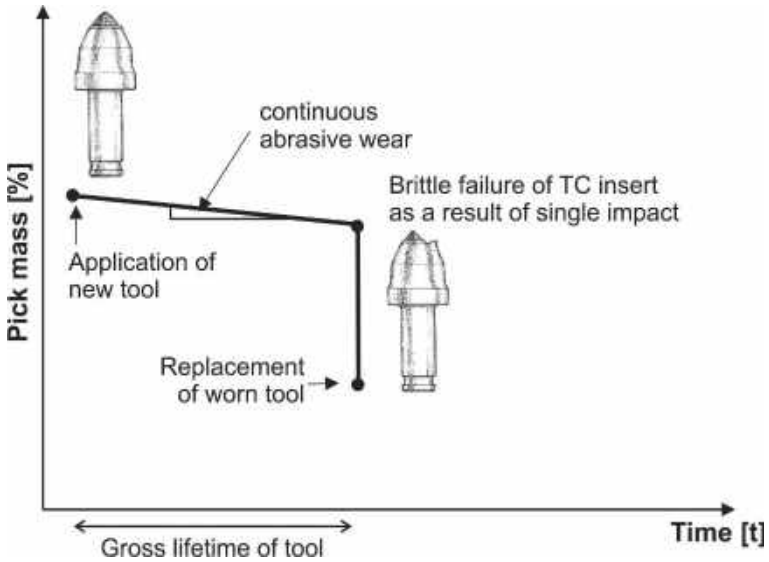

Fig. 4.4: Hypothetical mass loss diagram for a point attack pick, that has to be removed after catastrophic failure of the hard metal insert („Case B“).

In both cases, the same wear rates are determined, if only abrasive wear is considered. Although these rates might deterministically be derived from rock scale laboratory investigations, such as the CERCHAR test, such properties are of no use for an appropriate assessment of tool lifetime in “Case B". In case of tool failure it appears essential for the assessment of the actual tool wear rate, to add a probabilistic assessment of the likelihood and frequency of impacts / loads which might cause brittle material failure and cause an immediate replacement of the tool.

5 Conclusions and Suggestions

From the presented experiences and theories, the following conclusions may be drawn:

1. The term "abrasivity" should in a holistic way describe the potential of a rock mass to cause any form of tool wear to a rock tool. To restrict the term solely on the ability of intact rock to cause more or less steady, continuous abrasion, underestimates the task of the geologists and geotechnical engineer to determine and to describe all relevant ground parameters required for an appropriate wear assessment.
2. Tool removal as a result of catastrophic failure of tool parts (inserts, shank, etc.) is nevertheless still "tool wear", although it might be useful to separately describe and classify such phenomena and to separate them from abrasive wear phenomena during back-analysis.
3. Beyond the scale of intact rock, wear-relevant rock mass conditions, such as "mixed-face" conditions, "blockiness" or unusual stress conditions can have a significant effect on rock excavation and the wear of rock tools.
4. The occurrence of such adverse ground conditions has in principle to be located within the risk sphere of the client / owner.
5. To ensure a fair risk distribution and to allow a bidder / contractor to compensate for such effects, information on type, probability and frequency of such adverse rock mass conditions should be included in the Geotechnical Reports and specific positions should be implemented in the referring Bill of Quantities.

A view over the borders of Germany shows that some of the mentioned phenomena are already incorporated into the standards of other countries. For instance, the Austrian tunneling contract standard ÖNORM B2003-2 defines rock mass sclae factors like "mixed-face conditions" or "blockiness" as "difficulties" which either cause higher costs or reduce the performance of excavation. Consequently, the regulations of the ÖNORM B2003-2 do demand estimates on distribution, bandwidth and local association for such difficulties in the tender documents - a noble aim, which even in Austria is still not common status.

Literature

[1] Alber, M. (1999): Geotechnische Aspekte einer TBM-Vertragsklassifikation.- Dissertation an der Fakultät für Bauingenieurwesen und Angewandte Geowissenschaften der Technischen Universität Berlin, Dezember 1998, 116 S, Berlin.

[2] Alber, M. (2008): Stress dependency of the Cerchar Abrasivity Index (CAI) and its effects on wear of selected rock cutting tools.- in: Tunnelling and Underground Space Technology, 23, 4: 351 - 359.

[3] Beckmann , U & Simons, H. (1982): Tunnel-boring machine payment on basis of actual rock quality effect.- Tunnelling ´82: 261-264, Institution of Mining and Metallurgy, London.

[4] DIN – Deutsches Institut für Normung e.V. (2012): VOB 2012: Vergabe- und Vertragsordnung für Bauleistungen, Ausgabe 2012, Ergänzungsband 2015. Beuth Verlag, Berlin, 2015.

[5] Entacher, M., Winter, G. & Galler, R. (2013): Cutter force measurement on tunnel boring machines – Implementation at Koralm tunnel.- Tunnelling and Underground Space Technology, 38: 487-496 (Elsevier).

[6] Lagger, M. & Henzinger, M., Radončić, N. & Schubert, W, (2015): Influence of the primary stress state on the disc cutter penetration.- in: Schubert, W. (2015, Hrsg.), Proceedings EUROCK 2015 & 64th Geomechancis Colloquium: 1139 – 1144, Salzburg.

[7] ÖNORM B 2203-1: Untertagebauarbeiten – Werkvertragsnorm, Teil 1: Zyklischer Vortrieb. Ausgabe vom 01.12.2001.

[8] ÖNORM B 2203-2: Untertagebauarbeiten – Werkvertragsnorm, Teil 2: Kontinuierlicher Vortrieb. Ausgabe vom 01.01.2005.

[9] Plinninger, R.J. (2002): Klassifizierung und Prognose von Werkzeugverschleiß bei konventionellen Gebirgslösungsverfahren im Festgestein.- Münchner Geologische Hefte, Reihe B, 17 - Angewandte Geologie, XI + 146 S., München.

[10] Plinninger, R.J. (2011): Teilschnittmaschinen als alternatives Vortriebsverfahren im innerstädtischen Tunnelbau – Chancen und Risiken.- in: Tiedemann, J. (Hrsg., 2011): Veröffentlichungen zur 18. Tagung für Ingenieurgeologie, Berlin: 139-145.

[11] Plinninger, R.J., Thuro, K. & Bruelheide, T. (2001): Erfahrungen bei Fräsvortrieben im Nürnberger U-Bahn-Bau. - Felsbau 19,1: 1-8, Essen (Glückauf).

[12] Rutschmann, W. (1974): Mechanischer Tunnelvortrieb im Festgestein.- 200 S., Düsseldorf (VDI).

[13] Weh. M (2007): TBM-Hartgesteinsvortriebe auf den Abschnitten Raron und Steg am Lötschberg: Erfahrungen und vertragliche Konsequenzen,- Kolloquium „Anspruchsvolle maschinelle Vortriebe im Fels“, ETH Zürich, 31.05.2007

Roof Bolting in Potash Mining – Monitoring of Long-Term Performance

Systematische Firstsicherung im Kalibergbau – Beobachtungen zur Langzeitbeanspruchung der Ankerung

Thomas Frühwirt
TU Bergakademie Freiberg, Institut für Geotechnik
Matthias Nitschke, Jan-Peter Schleinig
K+S Aktiengesellschaft, Kassel
Jens Sippel
K+S KALI GmbH, Werk Werra

Abstract

In order to enhance the knowledge on long-term performance of mining roofs, reinforced by pre-stressed rock bolts, a research project was set up to develop an approach for in situ measurement of the load bearing behavior of installed rock bolts in an active mine site. Costum-made rock bolts combined with a data processing and logging unit were developed, constructed and tested at laboratory and pilot plant scale. Following an in situ testing phase of prototypes, a measurement site in an active mine was set up. The measurement site has been chosen by typical geological, geometrical and technological conditions. The custom-made bolts were installed manually as part of the regular bolting pattern and were pre-tensioned to five different levels. After approximately 16 months of continuous monitoring, axial forces in all measuring rock bolts are currently in an interval of -20 % to +50 %, comparative to the initial pre-tension level. Thus, all rock bolts in the monitored panel are completely active and fulfill all technological requirements.

Zusammenfassung

Für den sicheren untertägigen Abbau von Kalisalzen ist es notwendig, das vorhandene Wissen und das Verständnis zur Beanspruchung geankerter Hohlraumfirsten weiterzuentwickeln. In einem Forschungsprojekt wurde daher ein Messsystem entworfen, mit dem die Beanspruchung von Ankern im eingebauten Zustand ermittelt werden kann. Dieses Messsystem besteht aus instrumentierten Standard-Gebirgsankern und den zugehörigen Messverstärkern, Datenloggern und einer Auswertesoftware. Nach intensiver Entwicklungs- und Testphase wurde ein untertägiger Feldversuch eingerichtet. In fünf Vortrieben wurden Gebirgsanker mit unterschiedlichen Vorspannkräften gesetzt. Nach ca. 16-monatiger Beobachtungsphase zeigt sich, dass die Kräfte aller instrumentierten Anker in einem Bereich von -20 % bis +50 % bezogen auf die initiale Vorspannkraft liegen. Die untersuchten Gebirgsanker erfüllen daher ihre Funktion mit allen untersuchten Vorspannkräften.

1 Introduction / Motivation

In order to prevent roof fall in mining rooms, developed by the room-and-pillar method, systematical roof bolting is applied in potash mines in Germany. The application of pre-stressed expansion-shell type rock bolts is state-of-the-art and has been extensively tested in underground mining conditions. To continuously provide safe and economic mining activities, regular consideration of established approaches and working principles are mandatory and considerable efforts are currently made to enhance the knowledge. It is possible to gain deeper insight by using up-to-date monitoring approaches and techniques, especially regarding in situ processes.

The motivation for the current study was to enhance the knowledge on long-term performance of mining roofs reinforced by pre-stressed rock bolts. This aim can most effectively be reached by in situ measurements of the load bearing behavior of installed rock bolts in an active mine site.

2 Systematic Approach

Neither the monitoring equipment for this task, nor experiences gained from comparable measuring approaches were available. Thus, a research and development project was set up, consisting of a three stage approach:

Stage 1 – Development and construction of custom-made roof bolts which represent an efficient measurement device. Verification and documentation of capacity and quality control of the newly developed equipment by accompanying tests at laboratory, as well as pilot plant scale.

Stage 2 – In-situ installation of prototypes of gauged rock bolts in a long-term accessible mining room. Long-term measurement for one year.

Stage 3 – Setup of a monitoring domain in a representative panel. The monitored part of the mining field should represent typical geological, geometrical and technological conditions. Realization and regular inspection of a long-term measurement with a measuring time for at least one year.

3 Instrumentation / Gauged Rock Bolts

The measurement device developed in stage 1 consists of individual strain gauges which are mounted radially opposite on standard rock bolts. These rock bolts are regularly used for the reinforcement of the roof. It is crucial for the success of the measurement that the custom-made rock bolts are able to represent standard rock bolts, used in the regular bolting pattern. Thus, this study focusses on standard bolts with a minimum modification regarding its geometry and mechanical behavior during the installation of the measurement equipment. Only minimal alteration of the mechanical properties is induced by machining the thread of the rebar-like bolt rod. Therefore the load-bearing core of the rock bolt rod is not influenced by gauge installation. The strain gauges are encapsulated and protected against the extreme mining environment (Fig. 3.1).

Fig. 3.1: Prototype of gauged rock bolt rod equipped with encapsulated strain gauges and 30 m electrical cable.

Each gauged rock bolt is connected to a portable data processing and logging unit. This unit is designed to read and record data from multiple instrumented rock bolts automatically. Its core components are a measuring amplifier and a high capacity data logger which are operated by battery power packs. Its stable housing made of high-grade steel (degree of protection: IP 66) makes it ideal for the use in extreme mining conditions. Since all electrical components have been optimized for maximum power effectiveness the data processing and logging unit can be operated in a self-sustaining mode for minimum one year featuring data logging at stepless variable intervals of 1 hour to 24 hours. The logging unit is equipped with a communication interface and an USB-port which enables plug-and-play communication with a laptop and easy download of measurement data. Subsequent processing of the measurement data, including calculating and plotting of axial loads and strains of the rock bolt is provided by a newly developed software package based in Microsoft Visual Basic environment.

To meet the visco-plastic behavior of the salt rock expansion-shell rock bolts used in potash mining typically have a large axial deformation capacity. The requirements are defined in the guideline “Grundsätze der systematischen Ankerung zur Firstsicherung im Kali- und Steinsalzbergbau (Ankerleitlinie)” [1] and provided by the gauged standard rock bolts. In order to follow the deformation of the bolt rod of up to 10 % special non-foil strain gauges are used and an appropriate application technique had to be developed and optimized. In an extensive testing program comprising tests at laboratory as well as at pilot plant scale the capability of the instrumented rock bolts to fully follow the elasto-plastic-hardening material behavior of the bolt rod up to an axial deformation limit of 10 % is well documented and proven. Tests at different time scales ranging from minutes to months revealed that the gauged rock bolts can accurately monitor relatively quick loading scenarios as well as withstand long-term constant loads without exhibiting drift of measurement data. Each individual instrumented rock bolt is subjected to a multipoint calibration in laboratory environment prior to its installation in situ.

Following stage 2 of the systematic approach, in 2013 two prototypes of gauged rock bolts have been installed in the roof of a long-term accessible mining field in the Werra

mine additionally to the regular bolting pattern. The measurement was conducted for one year. Prior to the campaign the complete newly developed measurement system, consisting of the gauged rock bolts as well as the data processing and logging unit, was tested regarding its reliability under extreme mining conditions. Quality control was ensured due to the close proximity to a conventional roof monitoring station. Monitoring of the behavior of the rock bolts has been performed reliably and continuously at this station by more than two years now.

4 Measuring Site for In Situ Experiment

A mining panel in the Werra mine of K+S KALI GmbH was chosen for the in situ experiment (Fig. 4.1). This part of the mine is developed by the room-and-pillar method and is considered representative for mining conditions in potash mining of flat dipping seams. It is expected that the local situation at the monitored site will be influenced in the future due to subsequent mining of adjacent panels.

The roof in this mining field is thinly stratified with accompanying carnallitic and kieseritic layers interbedded with thicker rock salt layers. The accompanying beds show distinct tendency to detach inhomogeneously.

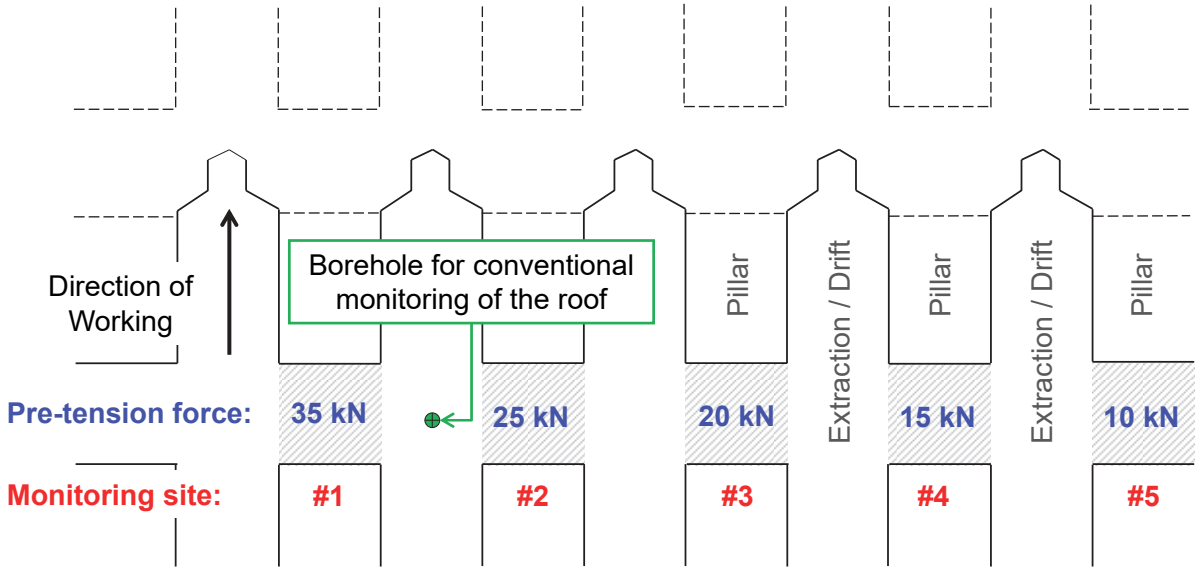

Fig. 4.1: Ground view of the measuring site in the mining field worked in a room-and-pillar scheme.

Fig. 4.1 shows the measuring site comprises five cross cuts and was established immediately after excavation. The roof of the cross cuts is reinforced by a regular bolting pattern with a uniform pre-tension force in each of them. The instrumented bolts were installed manually as part of the regular bolting pattern and were pre-tensioned with 10 kN, 15 kN, 20 kN, 25 kN and 35 kN (Fig. 4.2, left picture). The torque to reach the particular levels of pre-tension force was evaluated empirically. The behavior of the roof of each cross cut is accompanying monitored by using tell-tales, test holes and the measurement of convergence. Fig. 4.2 shows the working activities during the installation of the measurement device.

Fig. 4.2: Working activities during the installation of the measurement device. Left picture: Pre-tensioning of the custom-made bolts using a torque wrench. Right picture: Setup of the data processing and logging unit.

5 Results and Discussion

Fig. 5.1 shows representative results for the development of the force in rock bolts which have been pre-tensioned to five different levels. The measurement has been continuously active for approximately 16 months and revealed that all instrumented rock bolts are working reliably. All gauged bolts reflect a comparable general trend, showing a moderate increase of axial force due to loading by roof convergence. This major, long-term progress is superimposed by abrupt reduction of rock bolt force on a characteristic, shorter time-scale. It is observed in the instrumented bolts that axial force is reduced to a minimum level of approximately 20 % below the initial pre-tension level. However, in none of the observed events a reduction of bolt force to zero, causing a complete loss of pre-tension force, has been detected. Partly reduction of the bolt force causes a shortening of the pre-strained rod driven by elastic effects.

The overall behavior of rock bolt axial force reflects a saw-tooth shape, caused by moderate loading of the bolts due to convergence of the roof at a long-term time-scale and a superimposed short-term reduction of axial force. Generally the available measurement results show that the axial forces of all rock bolts are remaining at their pre-tension level with a slightly increasing trend.

Subsequent processing and analysis of the measurement data revealed that the maximum convergence of the roof in the monitored mining field was approximately 3 mm during the complete measuring time of approximately 16 months.

Considerable efforts were taken to correlate abrupt events of reduction of rock bolt force to mining activities, e.g. blasting. During the mining process the distance between the mining front and the monitoring site has increased. However, during the first two to three months of the measurement, the mining working activities were proximal to the monitoring site. In this early stage of the measuring time, the correlation between the time of blasting and the force monitored by the instrumented bolts was recognized. The reduction of the rock bolt force was observed preferentially at shift change, when the multishot rounds were fired. Later, when mining working activities have moved to greater distances related to the measuring site, abrupt reduction of the rock bolt force was observed, too. However, no significant connection between the mining activities and the rock bolt performance could be derived.

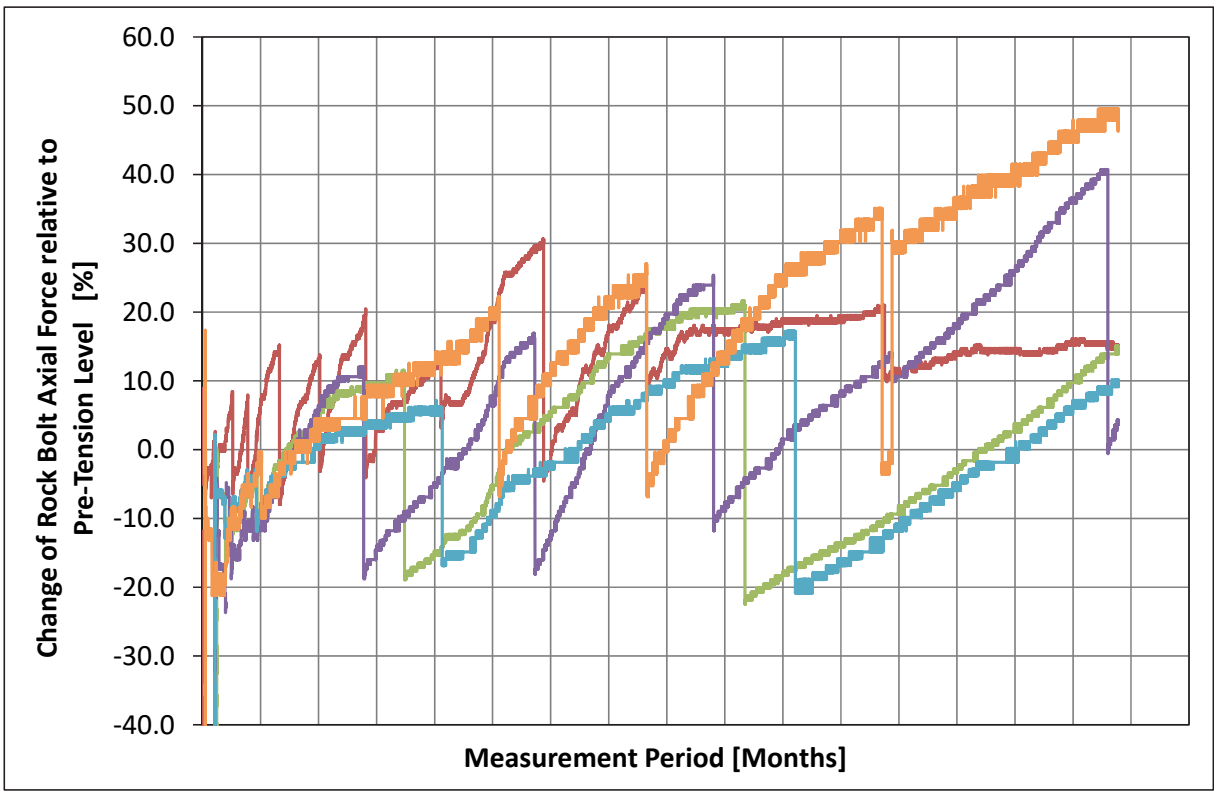

Fig. 5.1: Representative results for the development of force in rock bolts pre-tensioned to different levels.

6 Quality Management

During the conceptual design of the measurement system and the development of the custom-made rock bolts, design-engineering measures have been taken in order to reduce potential errors in the measurement data and to guarantee long-term stable data recording. The efficiency of this procedure has been extensively tested and documented at laboratory and pilot plant scales in stage 1 and 2 of the project.

To ensure and document the quality of the generated in situ measurement data, a quality management system has been established, in order to include the extreme mining conditions. Each local measurement site consists of a cross drift reinforced by rock bolts with the same pre-tension level. Two custom-made rock bolts are integrated in each of them. Data of these two gauged rock bolts are processed and read simultaneously. Therefore the mechanical damage of one of the custom-made rock bolts can immediately be recognized and compensated. To this day no incident has been recorded.

Furthermore each of the custom-made rock bolts is equipped with two hermetically sealed gauges. Both gauges are calibrated using a multipoint regression technique in the laboratory before installation. One of the gauges is read out automatically at the chosen measurement interval of 30 min. Its measurement data are processed and stored in order to record timelines as shown in Fig. 5.1. The other gauge is quarterly read out manually. As both gauges are attached to the same bolt rod and therefore are

monitoring the behavior of the same rock bolt, their readings are expected to be identical. Regular checkups confirm this requirement and no anomalies have been detected so far.

After a measurement period of approximately one year the pre-tension force of three instrumented rock bolts has been manually increased using a torque wrench. The procedure was similar to the installation of the rock bolts. However by means of checking the measurement system, higher torques were applied. Thus, the magnitude of the displayed rock bolt force and the sensitivity of the custom-made bolts were checked and verified.

These measurements were set up to guarantee the high quality of the data which were determined using the custom-made rock bolts and its components. In addition, the basic monitoring approach of using custom-made rock bolts was checked for suitability. Parallel observation of roof behavior through conventional pilot holes, tell tales as well as traditional convergence measurement points in the close proximity of the gauged rock bolts, were used to interpret the data gained from the custom-made rock bolts. General spatio-temporal trends of convergence represent good agreement across all monitoring systems and confirm the reliability of the newly developed measurement equipment.

7 Conclusion

The measurement is still active and currently running for a period of approximately 16 months without interruption or deficiency. Several independent measurements have been taken to ensure the high quality of the gained data and prevent measurement errors. As proven by quality management all instrumented rock bolts work perfectly and the derived timelines for rock bolt axial forces and strains are reliable. Axial forces in all gauged rock bolts are currently in an interval of -20 % to +50 % related to initial pre-tension level.

Therefore it can be concluded that all rock bolts in the monitored panel are fully active and fulfill the requirements derived from working safety as well as from a geomechanical position, independent of their level of initial pre-tensioning during installation.

The monitoring program will be continued and subsequent studies on this topic will be conducted in the future to enhance the understanding of the revealed processes.

References

[1] Verband der Kali- und Salzindustrie e.V. (2016): Grundsätze der systematischen Ankerung zur Firstsicherung im Kali- und Steinsalzbergbau (Ankerleitlinie).

Herausforderungen Tunnelbau bei 110 % Neigung am Beispiel der neuen Standseilbahn Schwyz-Stoos

Challanges for tunneling at 110 % inclination using the example of the new funicular Schwyz-Stoos

Thomas Kobler
Amberg Engineering AG
CH-8105 Regensdorf

Zusammenfassung

Mit einer Neigung von 47° respektive 110 % wird die neue Standseilbahn auf den Stoos die steilste Standseilbahn der Welt. Für die Ausführung heisst dies Tunnelbau in extremer Schräglage. Die Bahnstrecke führt dreimal durch einen Tunnel. Die Ausbruchfläche der Tunnels beträgt knapp 30 m^2. Der Ausbau erfolgt einschalig mittels Spritzbeton, Bewehrungsnetzen respektive Stahlfasern und Ankern. Die Tunnels werden sprengtechnisch von oben nach unten erstellt. Der etwas flachere Stossfluhtunnel wird im Vollausbruch erstellt und das Ausbruchmaterial mittels Windenbahn nach oben geschuttert. Bei den beiden anderen Tunnels wird vorgängig ein Raisebohrloch (∅ 1.4 / 1.8 m) erstellt. Bei der anschließenden sprengtechnischen Aufweitung erfolgt die Schutterung dann durch dieses Rollloch. Für die Vortriebsarbeiten wurde eine spezielle Vortriebsinstallation entwickelt. Auf dieser sind alle notwendigen Installationen vorhanden und das ganze kann im Tunnel auf Schienen hin und her verfahren werden. Die Baustelle ist nur über eine Materialseilbahn und eine Windenbahn erschlossen.
Die größten Herausforderungen stellen sicherlich die extreme Steilheit des Geländes und die schwierige Erschließung dar.

Abstract

With an inclination of 47 ° and 110 %, respectively, the new funicular on the Stoos will be the steepest funicular in the world. That means tunneling under extreme oblique conditions. The railroad track contains three tunnels. The cross section of the tunnels is nearly 30 m^2. The support is single-leaf with shotcrete, reinforcement meshes and steel fibers, respectively, and anchors. Tunnels were constructed using blasting from top to down. The slightly shallower tunnel is constructed via full face tunneling and excavated rock mass is transported downwards with a winch system. The other two tunnels are constructed via Raise-boring- technology (∅ 1.4 / 1.8 m). Subsequently widening is performed by blasting and head is moved through the chute. A special excavation technology was developed. On a special excavation device which can be moved on rails along the tunnel all necessary tools are installed. The construction site is accessed via a cable car for material transport and a winch system. The biggest challenges are the extreme steepness of the terrain and the complicated development.

1 Einleitung

Die Standseilbahn Stoos im Kanton Schwyz (Schweiz) ist der Zubringer für die rund 150 Einwohnerinnen und Einwohner des Dorfes Stoos. Sie stellt auch deren Grundversorgung sicher und fährt jährlich 7000 Tonnen Material aus dem Tal zur Bergstation. Seit 1933 fährt die Standseilbahn täglich mindestens 28 Mal rauf und runter. Nach mehr als 80 Jahren Betrieb läuft die Konzession für die bestehende Bahn nun aus und kann nicht mehr verlängert werden. Im Herbst 2013 starteten deshalb die Bauarbeiten für einen Neubau. Moderne Kabinen mit horizontalem Ein- und Ausstieg, 50 Prozent mehr Kapazität und automatischer Niveauausgleich lösen die bisherige Technik ab.

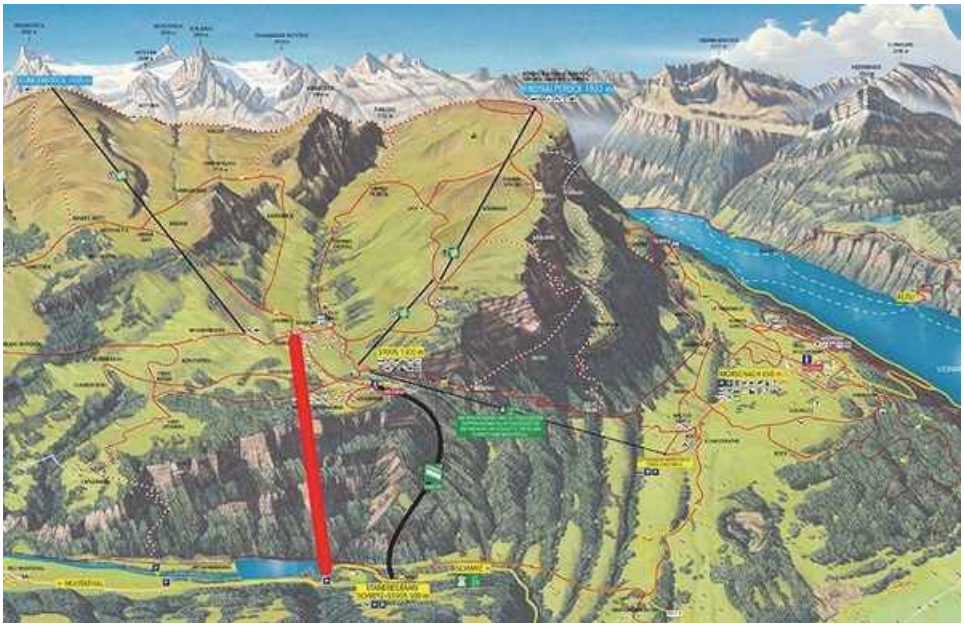

Fig. 1.1:

Die Standseilbahn überwindet auf einer Länge von 1740 m eine Höhendifferenz von 744 m. Im Steilhang weist das Trassee eine Neigung von bis zu 110 % auf. Im Grundriss ist die Linienführung gerade. Als Seilbahntyp ist eine Standseilbahn im Pendelbetrieb mit 2 Fahrzeugen für Personen- und Güterverkehr vorgesehen. Beide Fahrzeuge verkehren auf einem gemeinsamen Gleis zwischen den Endstationen mit Abt'scher Ausweiche in der Mitte der Streckenführung.

2 Projekt

Anschließend an die neue Talstation im Schlattli wird die Muota mit einer ca. 100 m langen Brücke überquert. Dabei steigt die Neigung des Trassees von 0 % auf ca. 65 % an.

Fig. 2.1: Brückenmontage

Anschließend folgt eine ca. 250 m lange Trasseestrecke bis zum Portal Nord des Tunnels Zingelifluh (Tunnel 1). Dieser ist rund 250 m lang und weist eine Neigung zwischen 90 % und 110 % auf. Nach einer kurzen (ca. 70 m) langen offenen Strecke folgt der Tunnel Ober Zingeli (Tunnel 2) mit einer Länge von rund 90 m. Die Neigung variiert hier zwischen 101 % und 85 %. Nach dem ca. 155 m langen Abschnitt mit der Ausweiche führt die Linienführung mit dem dritten Tunnel durch die Stoosfluh. Hier variiert die Neigung zwischen 66 % und 20 % am stärksten. Danach folgt noch eine Flachstrecke und am Schluss wieder eine Brücke in die Bergstation.

Der Ausbruchquerschnitt in den Tunnels beträgt 27 m^2 bei einer Profilbreite von 4,60 m und einer Höhe von 6,45 m (senkrecht zur Schienenoberkante). Die Tunnels werden einschalig mit Spritzbeton, Bewehrungsnetzen respektive Stahlfasern und Ankern ausgebaut. Vom Bauherrn wird eine Dichtigkeitsklasse 2 gefordert. D. h. einzelne Feuchtstellen ohne tropfendes Wasser sind an der trockenseitigen Bauwerksoberfläche zugelassen. Dies wird durch die in der Regel 10 cm starke Spritzbetonschicht erreicht. Bei lokalen Wasserzutritten werden zusätzlich Noppenfolien eingebaut um das Bergwasser gezielt ableiten zu können.

Das Gebiet Stoos – Schlattli wird geologisch der helvetischen Drusberg-Decke zugerechnet und besteht zur Hauptsache aus Kalk- und Mergel Gesteinen der Kreide- und Tertiärzeit. Die Drusbergdecke ist im Bereich Stoosfluh als Antiklinale mit einem nahezu flach liegenden oberen Faltenschenkel ausgebildet. Talwärts schließt eine stark geknickte Synklinale an. Die Tunnel Zingelifluh (Tunnel 1) und Ober Zingeli (Tunnel 2) kommen fast ausschließlich im Kieselkalk zu liegen, einem typischerweise im dm-Bereich gebankten, sehr harten Kalk. Oft wird die Bankung von senkrecht darauf stehenden Kluftflächen durchtrennt („Mäuerchenkalk“). Der Stoosfuhtunnel liegt in den Drusberg-, Schrattenkalk- und Garschellaformationen. Vor allem der Schrattenkalk ist sehr karstanfällig.

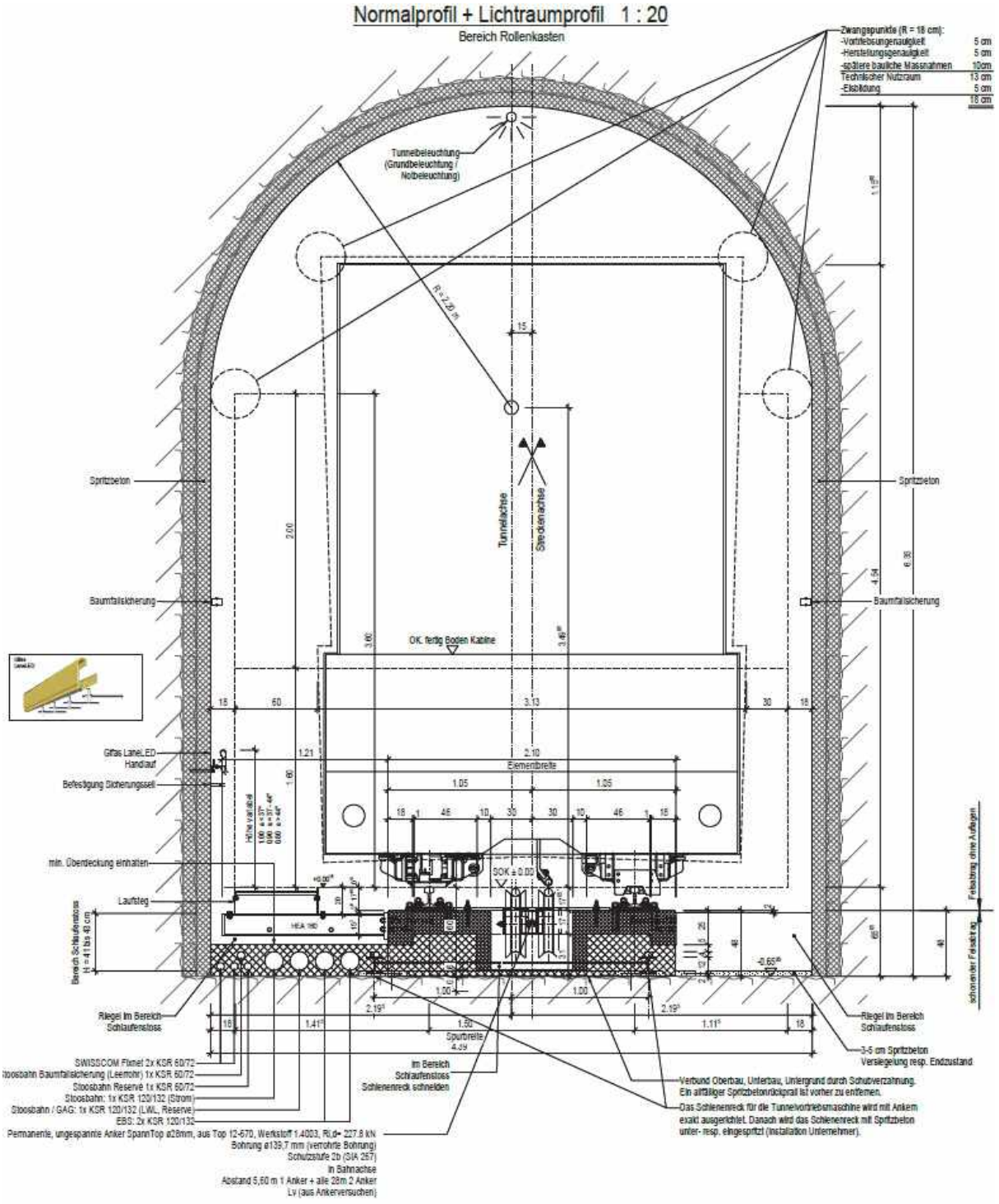

Fig. 2.2: Normalprofil Tunnel

3 Baustellenerschließung

Das Dorf Stoos kann über keine öffentliche Straße erreicht werden. Es gibt eine teilweise sehr steile und schmale Privatstraße respektive Kiesweg. Diese darf durch die Baustelle aber nur für Ausnahmetransporte genutzt werden. Ansonsten erfolgt die gesamte Baustellenerschließung über eine temporäre Materialseilbahn. Diese führt von der Talstation bis an den Beginn der Flachstrecke. Die Transportkapazität beträgt maximal 7,5 Tonnen.

Fig. 3.1: Materialseilbahn

Die Materialseilbahn überwindet auf nur 1300 m Streckenlänge eine Höhendifferenz von rund 700 m und bewältigt dabei eine Steigung von über 110 %. Der Antrieb der Bahn wird auf der Bergstation mit einem 500 kW starken Elektromotor sichergestellt, der mit Hilfe von zwei Hydraulikpumpen und 4 Radialkolbenmotoren die beiden 2 m großen Antriebsräder bewegt. Der Laufwagen, welcher auf den Tragseilen die Lasten

transportiert, hat einen eigenen Dieselmotor, welcher die Hydraulik für das Heben und Senken der Lasten antreibt. Über ein Funksystem können die beiden Aufzugswinden auf dem Laufwagen synchron oder einzeln angesteuert werden. Lasten bis zu 7,5 Tonnen können so punktgenau an einem beliebigen Ort unter der Seillinie (Bahnachse) im Gelände angehoben und abgesetzt werden. Durch ein speziell entwickeltes Funksystem ist es auch möglich, über die ganze Distanz von 1300 m, den Seilbahnantrieb auf der Bergstation zuverlässig von der Talstation oder von einem beliebigen Standort im Gelände aus zu bedienen. Über eine große Transportdistanz, wie zum Beispiel ein Transport von der Tal- zur Bergstation, wird die Seilbahn im Automatikmodus betrieben. Vor allen Stützenmasten wird der Laufwagen automatisch auf eine geringere Geschwindigkeit verzögert. So wird ein sicheres Überfahren der Masten gewährleistet.

Materialtransporte in Bereiche außerhalb der Materialseilbahnachse erfolgen mittels Helikopter.Für den Personenzugang und den Materialtransport in den Tunnels ist eine Windenbahn installiert.Ansonsten erfolgt der Zugang zu den einzelnen Bauabschnitten zu Fuß über vorrangig ausgebaute Wanderwege.

4 Bauausführung

In der durchgeführten Submission wurde dem Unternehmer keine Vortriebsmethode vorgegeben. Dadurch konnten die verschiedenen Anbieter ihre Erfahrungen und ihr vorhandenes Inventar optimal offerieren. Aus Sicht Bauherr / Projektverfasser waren verschiedene Vortriebsmethoden und auch verschiedene Vortriebsrichtungen denkbar.

Der Ausbruch der drei Tunnels erfolgt effektiv aufgrund der unterschiedlichen Neigungen auf zwei leicht unterschiedliche Arten. Der eher flache Stoosfluhtunnel (Tunnel 3) wird im Vollausbruch von oben nach unten ausgebrochen. Bei den anderen beiden Tunneln wird vorgängig ein Rollloch (∅ 1,8 m Tunnel 2 respektive ∅ 1,4 m Tunnel 1) mittels Raisedrillverfahren erstellt. Danach erfolgt die sprengtechnische Aufweitung von oben nach unten.

5 Spezielle Herausforderungen

Die größte Herausforderung im gesamten Projekt stellt die enorme Steilheit des Geländes und die damit verbundenen Schwierigkeiten der Baustellenerschließung dar.

Die Arbeiter haben täglich mindestens eine halbe Stunde Arbeitsweg. Während dem größten Teil ihrer Arbeit sind sie an einem Seil vor Absturz gesichert.

Fig. 5.1: Zugang Baustelle

Für den Vortrieb wurde durch den Unternehmer eine spezielle Vortriebsmaschine entwickelt und gebaut. Alle notwendigen Vortiebsgeräte (Bohrlafette, Baggerarm, Personenkorb etc.) und die Hilfsinstallationen (Lüftung, Pumpen etc.) sind auf einem auf Schienen verfahrbaren Stahlgerüst montiert. Die ganze rund 60 Tonnen schwere Einheit lässt sich mittels zweier Seilwinden verfahren. Damit kann die gesamte Vortriebsinstallation während der Sprengung in Sicherheit gebracht werden. Nach jedem 3 m langen Abschlag werden die Schienen wieder verlängert.

Pro Abschlag von 3 m Länge werden rund 70 Bohrlöcher gebohrt und mit etwa 120 kg patroniertem Sprengstoff geladen und gesprengt. Das anschließende Schuttern funktioniert in den Tunnels 1 und 2 durch das Rolloch gut. Um die Materialaufgabe ins Loch zu vereinfachen wird die Ortbrust praktisch horizontal ausgeführt. Im obersten Tunnel ohne Rolloch war das Schuttern sehr zeitaufwendig. Die Transportkapazität der Windenbahn war das einschränkende Element. Aus Platzgründen konnte nur ein Schutterkübel eingesetzt werden. D. h. während der Bahnfahrt konnte weitergearbeitet werden.

Fig. 5.2: Bohren / Laden

Die Tunnelbauarbeiten werden ganzjährig im Dreischichtbetrieb ausgeführt. Die Hauptinstallationen der Baustelle befinden sich auf ca. 1200 m über Meer und das ganze Projektgebiet liegt in einem Nordhang. Deshalb müssen die gesamten Installationen auch wintersicher (Schnee und negative Temperaturen) ausgebildet werden.

Fig. 5.3: Wintersichere Baustelleninstallation

Eine weitere Herausforderung stellte die Raisebohrung dar. Zum einen waren da die sehr eingeschränkten Platzverhältnisse bei der Installation und zum anderen wurden hohe Genauigkeiten für die Pilotbohrung gefordert. Das Rollloch soll auf der ganzen Strecke innerhalb des Tunnelprofils liegen.

Fig. 5.4: Montage Raisebohrkopf

More papers

Improved Support method for the deep roadway in weakened rocks under high stress: a case study

Verbesserte Ausbaumethoden für tiefliegende Strecken in geringfestem Gebirge unter hohen Spannungen: eine Fallstudie

Ping CAO[1*], Ri-hong Cao[1], Yongfang Zhong[1], Yusheng Mu[2], Qibo Gao[2]
[1] School of Resources and Safety Engineering, central South University, Changsha 410083, China
[2] Jinchuan Group Co.Ltd., Jinchang, Gansu 737100, China

Abstract

Roadway instability has always been a major concern in the field of mining and rock engineering. This paper aims at providing a practical and efficient strategy to support the roadways under high in-situ stress. A case study on the stability of deep roadways was carried out in an underground mine in Gansu Province, China. Currently, the depth of roadway in this mine has reached 1000m, and the surrounding rock strata are extremely fractured. A series of engineering disasters, such as large deformations, side wall collapses, and severe floor heaves, have taken place in the past. This resulted in the roadway needing frequent maintenance and repair during its service period, with the repair cycle generally being 3 to 6 months. Aiming to solve these problems, an improved support method was proposed, which included optimal bolt parameters and arrangement, floor beam layout by grooving, and full length grouting. For implementation and verification, field experiments, along with deformation monitoring, were conducted in the 958 level roadway of Mining II areas. The results show that the proposed strategy can successfully solve the problems of floor heave and prevent large deformations in side walls. The improved support can significantly reduce surrounding rock deformation, avoid frequent repair, and maintain the long-term stability of the roadway. Compared to the original support, the new support method can greatly save investment of mines, and has good application value and popularization value.

Zusammenfassung

Instabilitäten von Strecken sind schon immer von besonderem Interesse im Bergbau und der Geotechnik. Ziel dieses Artikels ist es, eine praktische und effektive Methode zum Ausbau von Strecken unter hohen Spannungen vorzustellen. Eine Fallstudie wurde durchgeführt zur Stabilität von tiefliegenden Strecken in einem Bergwerk in der Provinz Gansu, China. Gegenwärtig haben die Strecken in dieser Gruben eine Teufe von 1000 m erreicht und das umgebende Gebirge ist extrem geklüftet. Eine Vielzahl von Schadensfällen, wie unverträglich große Deformationen, Stoßversagen und starke Sohlhebungen wurden in der Vergangenheit beobachtet. Das führte zwangsläufig zu häufigen Unterhaltungsarbeiten an den Strecken mit einem Reparaturzyklus von 3 bis 6 Monaten. Um diese Probleme zu lösen, wurde eine verbesserte Ausbaumethodik

vorgeschlagen, die optimale Ankerparameter und –anordnung, in Nuten verlegte Balken in der Sohle sowie vollvermörtelte Anker beinhaltet. Für die Einführung und Verifikation dieser Methode wurden Feldexperimente mit Deformationsmessungen auf der 985er Sohle des Bergbaugebietes II durchgeführt. Die Ergebnisse zeigen, dass die vorgeschlagene Strategie erfolgreich zur Lösung der Probleme der Sohlhebung und zur Vermeidung von Stoßabschalungen eingesetzt werden kann. Der verbesserte Ausbau kann die Deformationen im umgebenden Gebirge deutlich verringern, die häufigen Wartungsarbeiten vermeiden und die langzeitliche Standsicherheit gewährleisten. Verglichen mit dem ursprünglichen Ausbau kann die neue Ausbaumethode zu erheblichen Kosteneinsparungen für die Grube führen und hat somit großen Anwendungswert.

1 Introduction

With rapid economic developments, the global demand for mineral resources is increasing. After many years of exploitation, shallow mineral materials have dried up in many areas of the world, thus the deep mining engineering is the inevitable trend of the future (Gurtunca R G 1998; X.B.LI 2001; Diering D H 1997). Currently, the underground coal/metal mining has become deeper and deeper in order to keep pace with the increasing demand for mineral materials worldwide (Yu-Yong Jiao 2013). For instance, the depth of the Anglo gold mine (Republic of Ghana) has reached 3700 m, and there are three gold mines whose mining depth has been over 2400 m in Kolar (India). In addition, the depths of nonferrous metals mining are over 1000 m in Canada, Australia, United States and many other countries.

As mining and underground constructions migrate to deeper grounds, the depth of the roadway and crustal stress are ever-increasing (Vogel M 2000; Li CC 2010). With the increase in stress, the surrounding hard rock shows the mechanical properties of a soft rock, such as expansion and creep, which have been well researched and discussed in the literature (Bell FG 1993; Okamoto R 1981; Ordaz J 1981). Due to the deterioration of physical and mechanical parameters of the rock, the behavioral characteristics of a deep roadway under high in-situ stress are primarily characterized by a high rate of initial deformation and long-term rheological deformation. Under high tectonic stresses, many roadways may experience a number of engineering disasters such as roof caving, floor heave, and side wall collapse, which not only increases the security risks of deep roadway, but also significantly restricts the operations of the mines. Due to high crustal stress and complex geological environment, the instability of deep roadways has been a focus in the fields of mining and rock engineering (Hoek E 1995; Baotang Shen 2014; H. Kang 2013; C Wang 2000).

With the purpose of providing a safe environment for workers and keeping high productive efficiency for the mines, the selection of supporting methods should consider the aspects such as engineering conditions, the production cost, the advantages and limitations of supporting types. Originally based on wood structures, the roadway support technology has been gradually improved to rigid metal arches, yieldable steel sets and the rock bolt (Yu-Yong Jiao 2013). In recent decades, the U-shaped steel retractable bracket and bolt applications are the most representative and have received widespread recognition among many countries. In the countries like the United States, Canada and Australia, bolting, and bolting combined with shotcrete lining are commonly applied as the main support methods for the roadway.

It is worth noting that the roadway is more seriously damaged under high stress (Yu-Yong Jiao 2013; Wang C 2000; Baotang Shen 2014). In particular, in regions of high horizontal stress, floor heave is very obvious, and severe ones can lead to instability and failure of the whole roadway. However, the supporting types like yieldable U-shaped steel, shotcrete lining, and bolt do not create better control of floor heave of roadway. Currently, in many mines, floor grouting is used to control the deformation of the floor heave, and it can improve the rock mechanical properties of roadway floor. However, numerous engineering practices have proved its poor effect on squeezing failure (Wang WJ 2005). Moreover, in the ultrabasic rock, where the water invading

rocks results in strength deterioration and expansion of volume, the application of grouting support is not recommended (Wu Aixiang 2003; Fu J 2011).

This paper reports a case study on deep roadway stability at Jinchuan mine in Gansu Province, China, where the surrounding rock strata were extremely weak and the roadway are suffering from the problems of severe floor heave and side wall collapse. The systematic study includes loosing circle measurements, optimal roadway support design, field experiment and monitoring of the roadway deformation. Our results show that the new support technology not only provides a better control of the surrounding rock convergence, but also limits floor heave, greatly extending the roadway repair cycle and savings for mining investment.

2 Deep roadway at Jinchuan

2.1 Engineering geology

Jinchuan Group Co. Ltd., the largest nickel production base of China, occupies an important position in China's economy. Jinchuan mine is located in Gansu Province, China (Fig. 1), whose terrain is relatively flat with the altitude of 1500 - 1800 meters, and temperate continental climate. Jinchuan Mine can be divided into 4 parts, Mining area I, Mining area II, Mining area III and Mining area IV. The lithology of the rock mass is very complex, and mainly includes striation migmatite, marble, homogeneous mixing rock, ultrabasic rock, granite, biotite plagioclase gneiss, and garnet-bearing gneiss. The lithology distribution of each Mining area is shown in Fig. 2.

Fig. 1. Location of Jinchuan Mine

After decades of exploitation of Jinchuan Mine, the shallow resources have been depleted and the depth of mining is growing ever deeper, with the Mining II area being

the most obvious. Currently, it has already reached a depth of 850 level, about 1000 meters from the surface. As can be seen from Fig. 2, the rock mass of the Mining II area consists mainly of marble, ultrabasic rock and homogeneous mixing rock. Among these, ultrabasic rock is widely distributed, and is often intrusive of other lithology with irregular shape.

Fig. 2 The lithology distribution of each Mining area

In Mining II area, the UCS of most rocks is larger than 130 MPa, but because the rock joints in the mining region are extremely developed and very complex, the rock mass is in a broken state after cutting by various structured surfaces (shown in Fig. 3), under such broken state, the mechanics properties of rock mass degrades severely. In addition, the current mining area contains many ultrabasic rocks such as lherzolite, and consequently grouting cannot be applied to reinforce the surrounding rock in Mining II area. Moreover, as mining and underground constructions migrate to deeper grounds, the in-situ stress also escalates, especially in the form of horizontal ground stress. According to the measurement, the maximum horizontal stress is close to 40 MPa at 1000 m depth(Wu Aixiang 2003).

Fig. 3 Rockmass strata around the deep roadway

2.2 Patterns of roadway failure under high in-situ stress

In recent years, the development of rock roadway support technology has also promoted the progress of Jinchuan. The yieldable U-shaped steel, shotcrete lining, bolt, and metal mesh support has been applied in Jinchuan Mine. But the failure of the roadways in Jinchuan Mine could occur at any part of the periphery, in its roof, floor and both sides. After the field investigation, we found that large deformations occurred mainly in side walls and floor, while side wall convergences led to squeeze damage occurring in the roof of the roadway. Under high horizontal stress, the side wall suffered severe damage (Fig. 4), with displacements of more than 1000 mm even though the U-shaped steel and metal mesh were employed in this region (Figs. 4a and b). Plastic sliding was also very common at the lower rib of the roadway, which directly resulted in severe deformation of U-shaped sets and shortcrete lining (Figs. 4c and d).

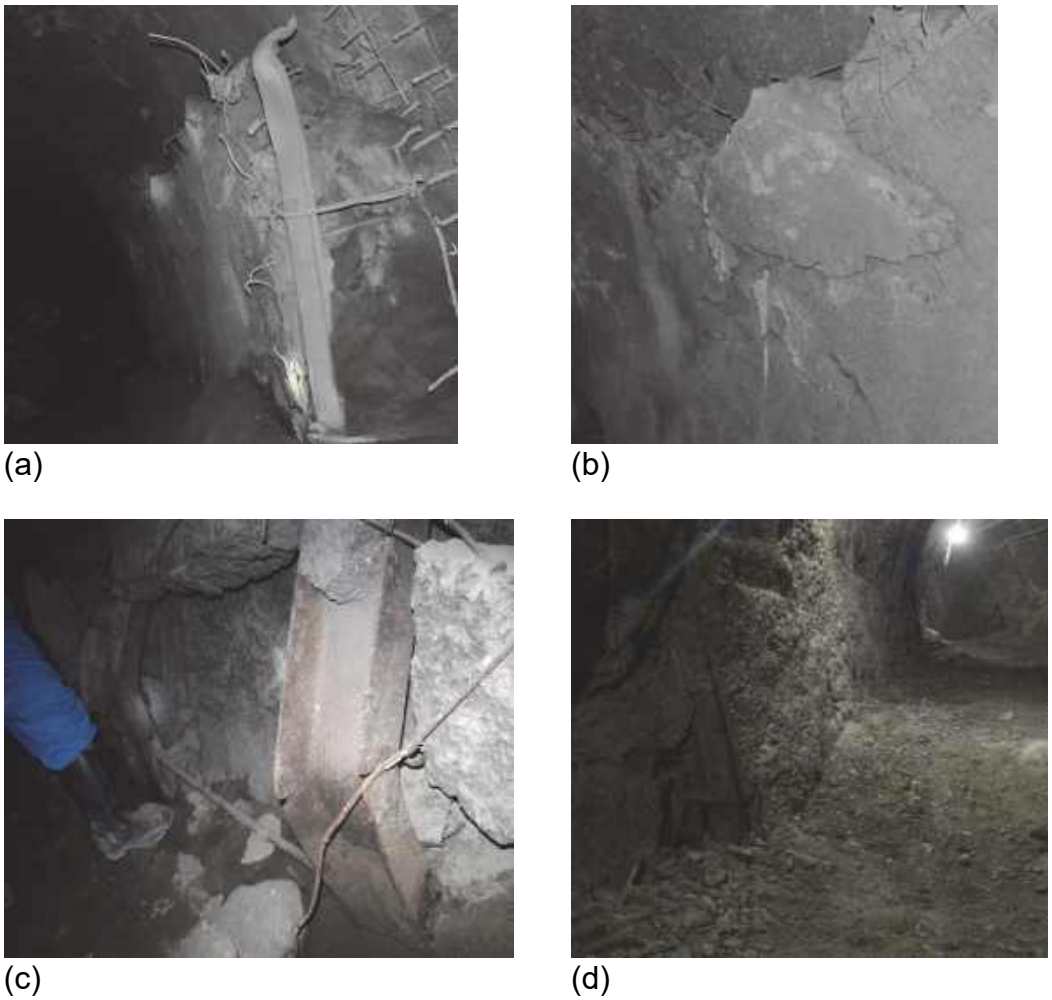

(a) (b)

(c) (d)

Fig. 4 Failure patterns of side wall

Unfortunately, an additional deformation characteristic of Jinchuan deep roadway is the severe floor heave. As shown in Fig. 5, the roadway is supported by bolt and U-shaped steel sets. When repairing this section of the roadway, measurements revealed that the roadway floor heave reached 1200 mm (Fig. 5a). From the failure characteristic of floor, the pattern of floor heave of Jinchuan deep roadway belongs mostly to the extrusion flow model. In this situation, due to the large deformation of side wall,

the rock mass of floor is squeezed by side wall and uplifted to form obvious floor heave (Fig. 5b). Thus, there is an urgent need for special measures which can prevent the occurrence of plastic sliding and excessive floor heave.

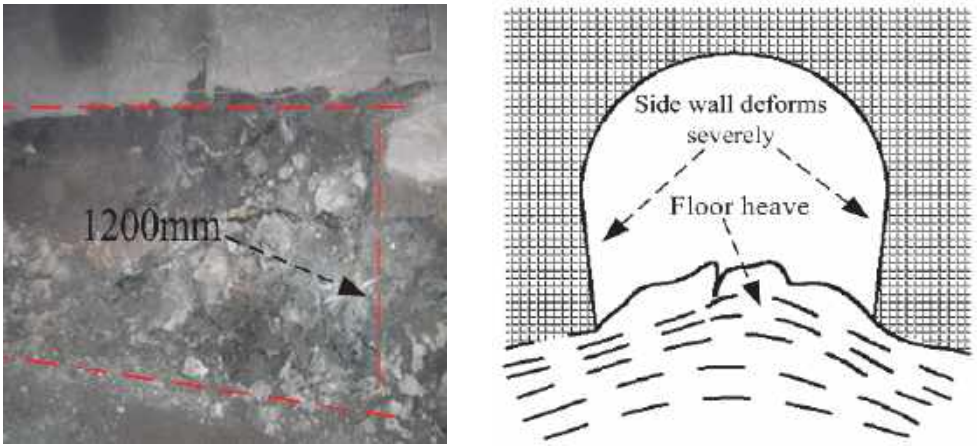

(a) (b)

Fig. 5 The severe floor heaves of the roadway

The cross sectional shape of Jinchuan roadway is a semi-arched and straight wall (it can be seen from the above Figures), with the width of 5200 mm and height of 4700 mm. Even though the roadway section of Jinchuan is big enough, but the side walls converged badly and extreme floor heave is obvious, thus causing great difficulties to pedestrians and transportation. Without constant repair, the rock mass would squeeze into the roadway and lead to overall failure.

3 The proposed supporting strategy

3.1 Bolt parameters optimization

The field investigation found that the deep roadway of Jinchuan has been severely damaged. In most cases, however, the rib bolts were not yielded nor suffered tensile failure(Fig. 6). Only a small number of anchor plates were torn into the rockmass. This was because the crushing zone extended wider than the length of conventional bolt. Hence, the bolts can only stay in the crushing zone and the effectiveness of the bolt in controlling rock deformation was very limited.

Fig. 6 The failure characteristics of bolt in original support

In order to guarantee the effectiveness of bolt in supporting the rock deformation, the depth of crushing zone should be determined before a reasonable length can be decided. Then, the loosing circle measurements were conducted as a part of this study. The loosing circle measurements took place in the transportation roadway numbered 958 at two locations (M1 and M2). The acoustic test method was employed, and at each location measurements were taken in roof, side wall and floor, respectively, the results from successful measurements at two locations are shown in Fig. 7. Based on the measurement results, it was confirmed that, at the periphery of roadway, the depth of loosing circle was closed to the length of conventional bolt (2250 mm) or even deeper than it. At M1 (Fig. 7a), the crushing zone(loosing circle) in the roadway spandrel and lower rib extended 2400 mm and 2450 mm respectively, which were deeper than the length of bolts. And in the location of M2 (Fig. 7b), the measurement results had the similar trend but showed a little differences in values compared to the M1.

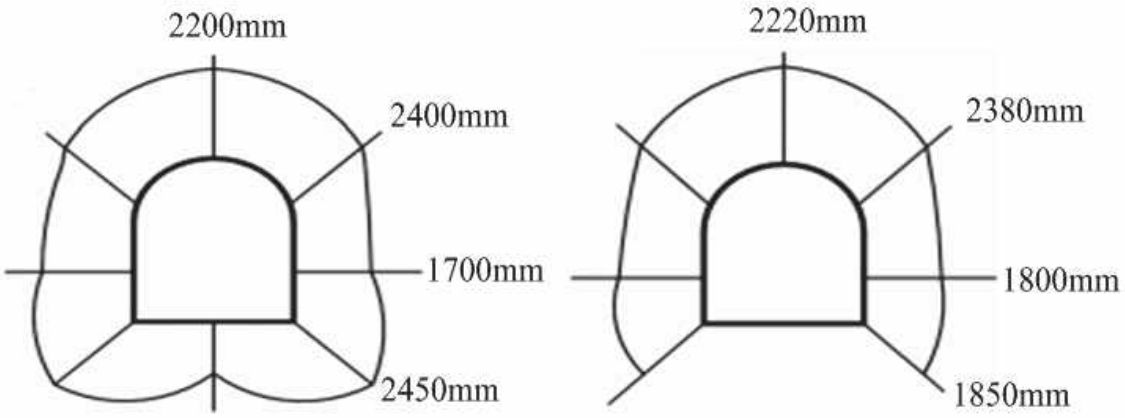

(a)M1 (b)M2

Fig. 7 Loosing circle measurement results

In the supporting design, the length of bolt should be determined based on the depth of loose circle as follows:

$$L = L_1 + L_p + L_2$$

Where L represents the length of the bolt(mm); L1 is the exposed length, the value of L1 is in the range of 50 ~ 100 mm; LP is the depth of loose circle (mm); L2 stands for the length of bolt anchored in stable rock, generally 300 ~ 400 mm.

According to the measurement results and combined with the actual situation of the project construction, the bolt length of spandrel and lower ribs had been adjusted to 3000 mm. Then, the bolt could anchor into stable rocks and form an effective reinforcement in the deeper and larger region of loose zone. The proposed design included six original bolts and two long bolts in the roof and three original bolts and one long blot in each side wall. The long bolt had a length of 3000 mm and the original bolt is 2250 mm, both are 25 mm in diameter, as shown in Fig. 8.

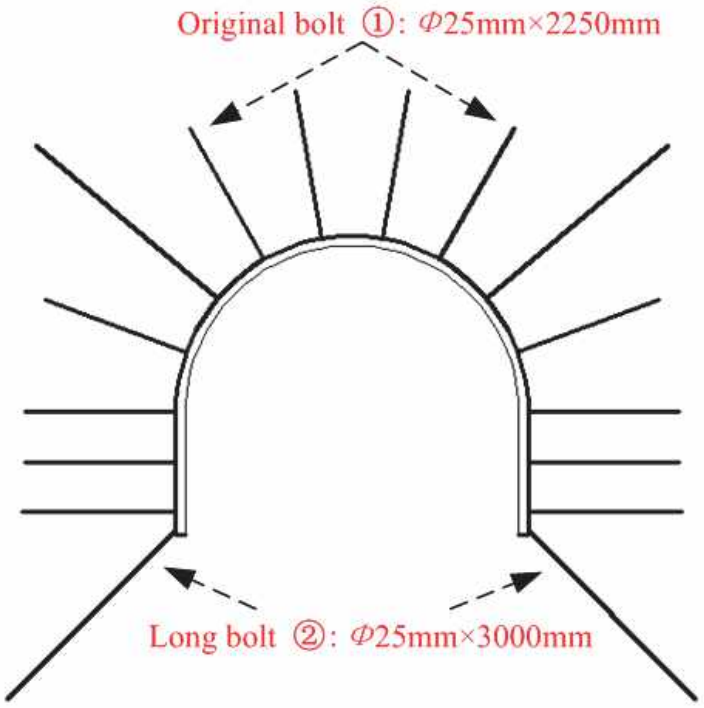

Fig. 8 Improved bolt layout diagram

3.2 Controlling for large deformation near roadway floor

As can be seen from the above failure patterns, under the high in-situ stress, there were lack of effective measures to restrict the large deformation at the lower ribs and roadway floor, thus leading to overall failure unavoidably as a consequence of side wall convergence and floor heave. In this study, a new support method is proposed to prevent serious deformation in lower ribs and floor. As shown in Fig. 9, the floor beams laid out by the method of floor grooving have been used to limit rock massive deformation and plastic sliding at lower ribs.

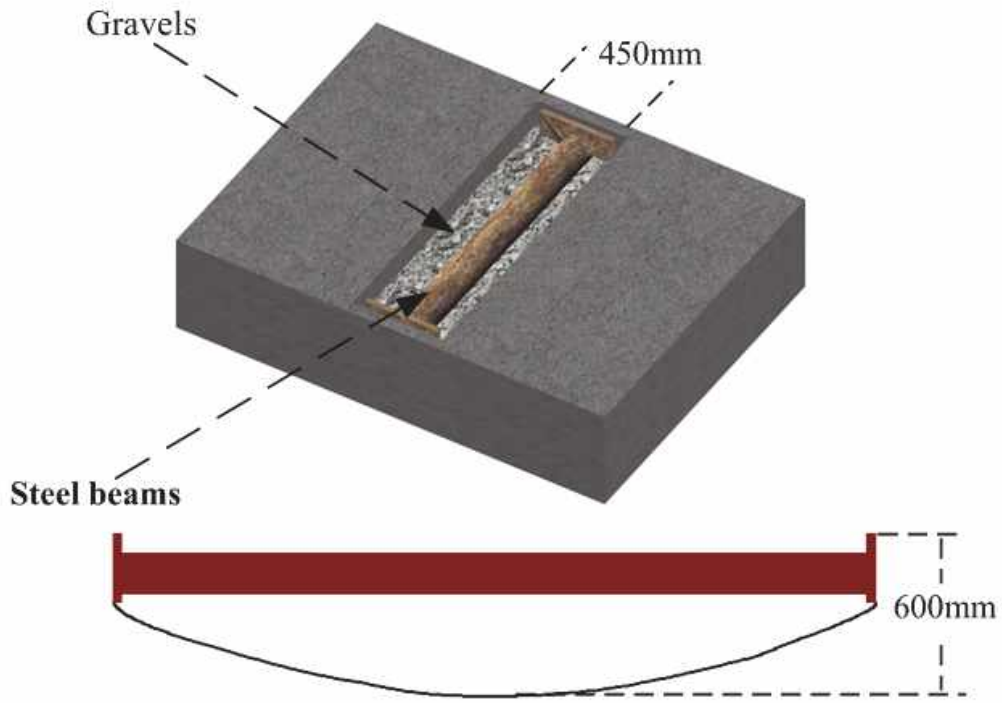

Fig. 9 Floor beam layout diagram

There was a need in excavating a groove before installing the steel beams, and the width of groove was about 450 mm. While, the depths of the groove in each place were different and it should be over 600 mm for the central part. Before the steel beam was placed down, the bottom of groove should be covered with a certain amount of gravels that were less than 25 mm, and the groove should be back-filled by gravels after the steel beams has been placed down. Steel beams made up of ordinary carbon round steels were placed in the middle of the groove, with 16 mm in thickness, 219 mm in the outer diameter, and 4500 mm in length. The stability coefficient of compression was 0.88, with the yield strength reaching 238 MPa, and the axial bearing capacity was 1900 kN.

Under high in-situ stress, floor heave was inevitable to some extent. In the past, the steel beam were placed on the floor directly (Fig. 10a), and after a few months, they would be jacked up by the uplift rocks (Fig. 10b). While, in this way, steel beams were placed in the middle of the groove (Fig. 10c), and the bottom of groove was covered with gravels, when the floor rose, the rock would squeeze gravels and the gravels would move to the reserved space. So, the uplift rock would not collide with the steel beam directly. Thus the steel beams would not be jacked up and lead to support failure (Fig. 10d).

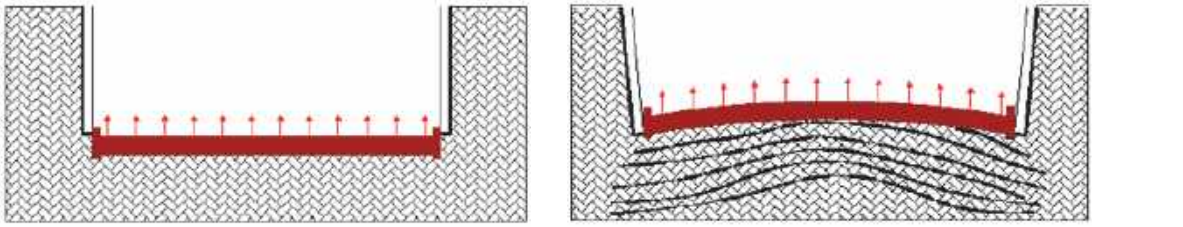

(a) Conventional layout (b) After a few months(conventional layout)

(c) Improved layout (d) Several months later (Improved support)

Fig. 10 Performance of floor beam in different layout

The improved support system and original support method were shown in Fig. 11 (a) and (b) respectively. In proposed strategy, the spacing between the original bolts/long bolts along the roadway axis was 0.8 m which was equal to the original one. The bolt parameters in the improved/original support design were given in Table 1. Compared to the original one, the major improvements of improved support system lied in: (1) bolt parameters and arrangement had been adjusted, and all bolts were fully grouted using resin chemicals for the entire length, (2) increasing the original spacing among the yieldable U-shaped steel arch and adding a floor beam (layout by grooving) every two U-shaped steel arch, (3) the double metal meshes and shotcrete lining were replaced by a single one.

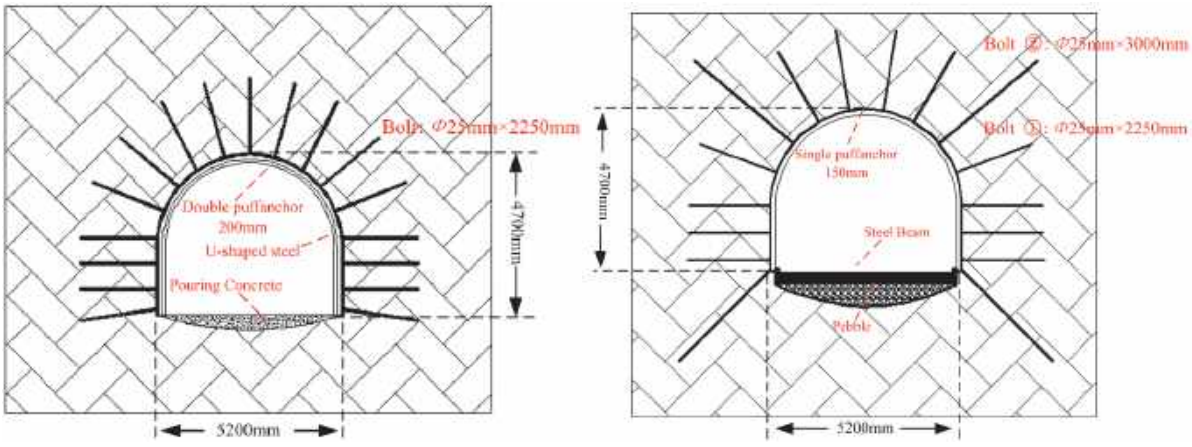

(a) Original support (b) Improved support

Fig. 11 Two kinds of support system diagram

The components consumption of the two support methods are listed in Table 1. The comparison of the material consumption per meter between the original and the improved strategy is provided in Table 2. As we can see, for the improved method, there

was a net cost reduction compared with the original one because of the adjustment of support parameters.

Table.1 The component comparison of the roadway supports

Support method	Bolt		metal meshes and shotcrete lining	Steel arch spacing	Steel beam spacing
	Length	Spacing			
Original support	2250 mm(17)	800 mm	Double(200 mm)	600 mm	—
Improved support	2250 mm(12) 3000 mm(4)	800 mm	Single(150 mm)	800 mm	1600 mm

Table.2 The cost comparison of the roadway supports (per meter)

Support method	steel arch (RMB)	Steel beam (RMB)	Bolt (RMB)	Cement+Steel mesh (RMB)	Labor Costs (RMB)	Other materials (RMB)	Total (RMB)
Original	6137	—	792.0	2107.5	456.2	2019.6	11512.3
New support	4600	1780	962.5	1375.6	812.5	911.68	10442.3

4 Analysis of the numerical simulation

4.1 Numerical model and calculation parameters

To make a comparison of the effect of the two supporting scheme, numerical calculation is carried out to analyze the roadway stability. The numerical model showed in Fig. 12, is established according to the actual standard size of the Jinchuan deep roadway: semicircle arch radius is 2500 mm, the height of straight wall is 2200 mm. The entire model's dimensions are 22 m in length, 30 m in width and 30 m in height.

Displacement boundary is set at the sidewall, roller boundary is set at the surrounding, and free surface is set at the top of the physical model so that vertical movements are allowed during the loading process. Unbalanced force ratio must meet the convergence criteria (node average maximum internal forces and unbalanced force ratio) of 10^{-5}. Rock mechanics parameters and calculation parameters of each support opponents are listed in Table 3.

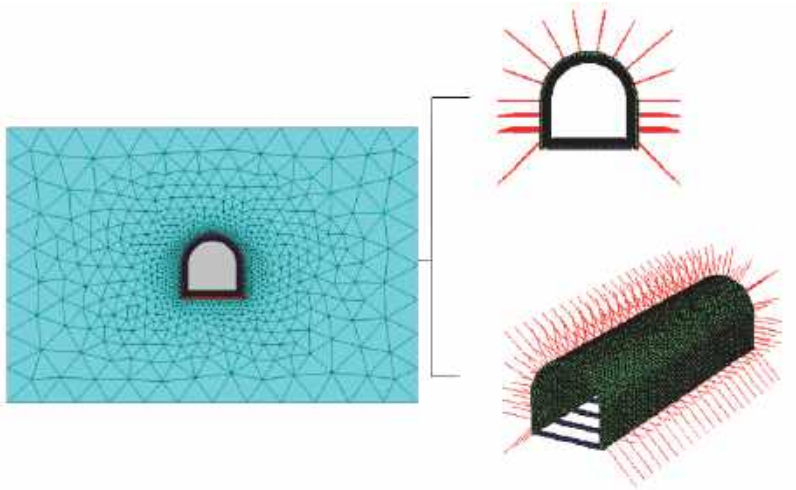

Fig. 12 Materials and mesh of engineering geological mode

Table 3 Calculation parameters

Classification	Density kg/m^3	Elastic Modulus GPa	Poisson's ratio	Cohesion MPa	Friction angle °
rock	2700	3.1	0.28	0.5	32
Bolt	7800	210	0.3	—	—
U-shape steel	7800	210	0.3	—	—
Steel beam	7800	210	0.3	—	—
Concrete	2500	34.5	0.17	2.59	52.4

4.2 Surrounding rock convergence

The displacement of roadway under two types of supporting are showed in Fig. 13. From the aspect of horizontal displacement, the roadway is damaged seriously under previous supporting (Fig. 13a). For example, the lateral displacement of the rock mass in foot position is as much as 600 mm, which conforms to the present actual situation in which foot rock mass deformation resulted in the collapse of side wall. In contrast, under the new support (Fig. 13b), the horizontal displacement of roadway which takes place mainly in the middle of two sides is controlled well in around 100 mm at high stress loading.

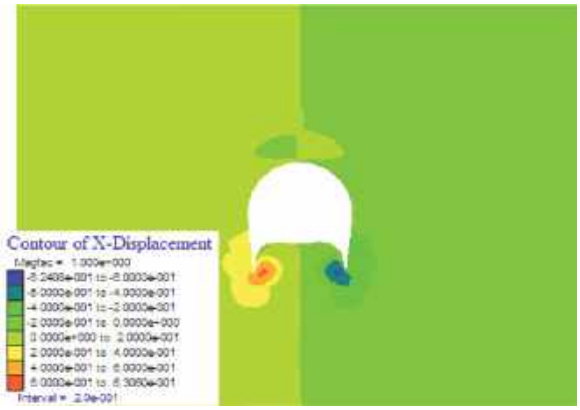

(a)Horizontal convergence of original support

(b)Horizontal convergence of new support

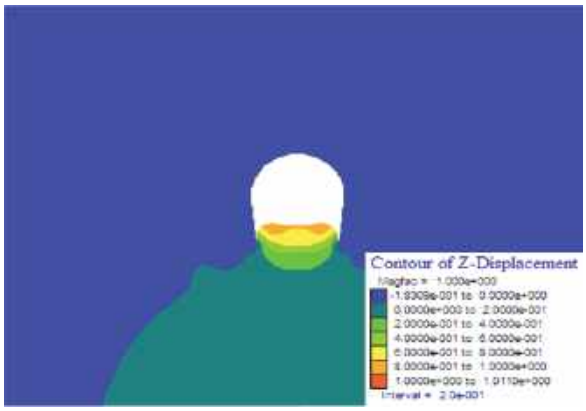

(c)Vertical convergence of original support

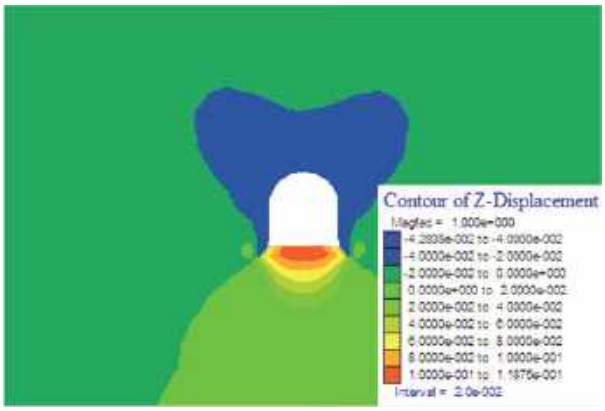

(d)Vertical convergence of new support

Fig. 13 The distribution of displacement around the roadway

In aspect of vertical deformation, the differences between two schemes are more obvious. The support comprise of double puff anchor and U-shaped steel cannot provide restrictions for foot rock, leading to serious floor heave which is nearly 1000 mm as shown in Fig. 13(c). To the contrary, the roadway floor heave is only about 10 mm in the new supporting (Fig. 13(d)). The comparison above illustrate that the new support system which combine long bolt in foot position with steel beam has provided effective control to surrounding rock near the floor, avoiding the large-scale convergence in foot position and preventing the overall damage.

4.3 The comparison of plastic zone distribution

With excavation of roadway, stress become concentrated and the surrounding rock enter the plastic state. And the plastic zone will also continue to develop along with time. Figure 14 shows the plastic zone distribution of roadway under two kinds of supporting.

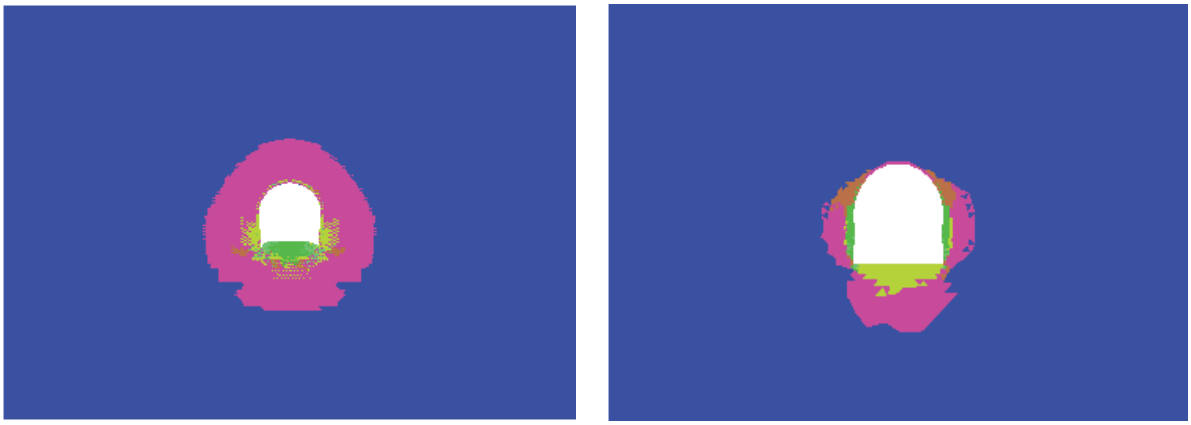

Original support New support

Fig. 14 The distribution of plastic area around the roadway

It can be found out from the figure that under the original support, roadway plastic zone fully extended to more than 4m. Even the plastic zone of roof, floor and side wall showed a trend of penetration. Oppositely, the plastic zone of roadway is much smaller, and the plastic zone in roof and foot position controls well under the new support. What's more, in foot position of roadway, the depth of plastic zone did not reflect the trend of the plastic slip.

5 On-site experimentation

In order to test the effectiveness of the improved support method and compare it with the original one, the field industrial experiment and monitoring were carried out in the transportation roadway of 958 working face in Jinchuan Mine which was damaged seriously (as shown in Fig. 15).

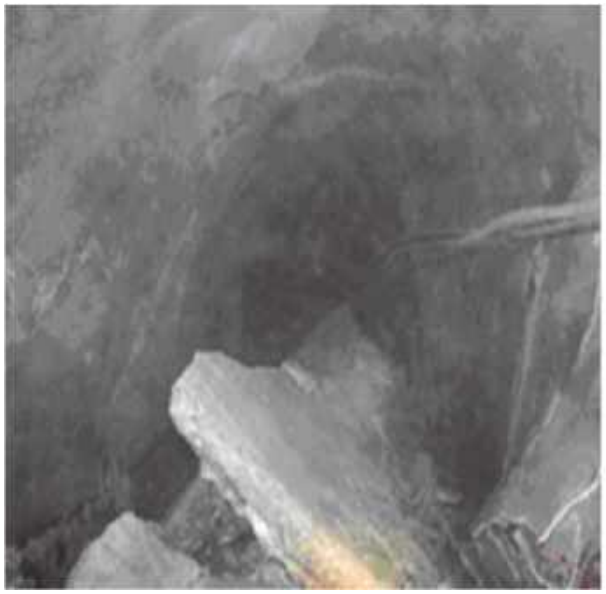

Fig. 15 A image of test roadway

Considering the differences of lithology and geographical environment, a 50 m long section of roadway was chosen as a trial of the improved support, whereas the remaining part of the roadway was supported by the original support method. The improved support method was experimented there as shown in Table 1.

The improved support method was conducted according to the design drawings (Fig. 11b) and supporting parameters (Table 1), and the layout of steel beam was presented in Fig. 16. As can be seen from the Fig. 16, the plate of the steel beams were in close contact with both ends of the side walls. In order to fix the steel beams, both ends of the steel beams would be filled with concrete. At the same time, the gap between the plate and the side wall would also be filled up.

Fig. 16 The layout of floor beam in field experiment

The roadway stability status of different support method and different periods has been demonstrated in the Fig. 17. And the (a) and (b) showed the roadway stability situation of original and new support respectively. The experimental section was observed to have a much better roadway profile than the roadway which was supported by the original method. The floor heave of the roadway was very obvious as shown in Fig. 17a which were photographed 4 months after the installation of the original support(U-shaped steel combined double metal meshes and shotcrete lining).

Floor of the roadway was uplifting which was clearly visible and accompanied by the phenomenon of cracking. The investigation showed that, the floor heave reached 900 mm. In addition, there were many cracks in both walls and especially in the lower rib of roadway, which occurred serious convergence and resulted in cracks produced in the shotcrete lining.

In contrast, the roadway maintained in a good condition as shown in Fig. 17b which were photographed 12 months after installation of the improved support. It could be seen that the deformation of the surrounding rock was well controlled by the new support, and the floor with no sign of uplifting phenomenon. Thelower rib did not show obvious deformation or large-scale convergence. It is clear that the new support is more suitable for roadways excavated in such high in-situ stress area.

(a)Original support (4 months later)

(b) Improved support(12 months later)

Fig. 17 Performance of two kinds of support method for test roadway

6 Conclusions

Taking the example of transportation roadway of the deep mining working face numbered 958 in Jinchuan Mine, Gansu, China, an efficient and economic supporting strategy has been put forward.

The result of the numerical result and field experiment showed that the deformation of the surrounding rock was satisfactorily controlled by the improved support method. After 280 days, the roadway maintained in a good condition with no obvious floor heave and no cracks in side walls. The successful application of this indicates that the implementation of the strategy was an ideal solution to supporting the roadways under high in-situ stress.

However, it also should be noted that the target object of our improvement in this research mainly aims to overcome the problems of side wall collapse, floor heave and large deformation under high in-situ stress, especially for the roadway support in ultrabasic rocks in which the grouting reinforce measures can't be used. At the same time, this case study also demonstrates that the deep roadway stability under high stress can be significantly improved by careful investigation and design.

Acknowledgments

This paper gets its funding from Project (51174228, 51304240, 51474249, 51404179) supported by National Natural Science Foundation of China; Project supported by the Program for New Century Excellent Talents in University. The authors wish to acknowledge these supports.

7 References

Bell FG, et al (1993) Volume change in weak rocks: prediction and measurement. In: Proceedings of the International Symposium on Geotechnical Engineering of Hard Soil—Soft Rocks. Athens, Greece. 20-23 September. Rotterdam: A. A. Balkema, P, 925-32.

Baotang Shen (2014) Coal Mine Roadway Stability in Soft Rock: A Case Study. Rock Mech Rock Eng 47: 2225-2238

C Wang (2000) The optimal support intensity for coal mine roadway tunnels in soft rocks.International Journal of Rock Mechanics & Mining Sciences 37: 1155-1160

Diering D H (1997) Ultra-deep level mining:future requirements. Journal of the South African Institute of Mining and Metallurgy 97(6): 249-255

Fu J, Feng CH, Shi JJ (2011) Investigation into the deformation of a large span roadway in soft seams and its support technology.Int J Min Sci Technol 21: 531-535.

Gurtunca R G, Keynote L (1998) Mining below 3000m and challenges for the South African gold mining industry.In:Proceedings of Mechanics of jointed and Fractured Rock.Rotterdam:A.A.Balkema, 3-10

H. Kang, Y. Wu, F. Gao , et al (2013) Fracture characteristics in rock bolts in underground coal mine roadways. International Journal of Rock Mechanics & Mining Sciences 62: 105-112

Hoek E, Kaiser PK, Bawden WF (1995)Support of underground excavation in hard rock. Rotterdam: Balkema.

Li CC (2010) A new energy-absorbing bolt for rock support in high stress rock masses. Int J Rock Mech Min Sci 47: 396–404

Okamoto R, Sugahara H, Hirano I (1981) Slaking and swelling properties of mudstone. In: Proceedings of the International Symposium on Weak Rock. Tokyo, Japan. 21-24 September. Rotterdam: A. A. Balkema p. 213-8.

Ordaz J, Gomez De Ruiz Argandona V (1981) Swelling characteristics of some mudrocks from Asturias (Spain). In: Proceedings of the International Symposium on Weak Rock. Tokyo, Japan. 21-24 September. Rotterdam: A. A. Balkema p. 231-5.

Vogel M, Andrast H P (2000) A1P transit-safety in construction as challenge, health and safety aspects in very deep tunnel construction.Tunneling and Underground Space Technology 15(2): 147-151

Wang C, Wang Y L S (2000) Deformational behaviour of roadways in soft rocks in underground coal mines and principles for stability control. International Journal of Rock Mechanics and Mining Sciences 37: 937-946.

Wang WJ, Feng T (2005) Study on mechanism of reinforcing sides to control floor heave of extraction opening. Chinese Journal of Rock Mechanics and Engineering 24(5): 808-811.

Wu Aixiang, Han Bin, Liu Tongyou , et al (2003) Study on deformation and support of roadway in weak rockmass in Jinchuan nickel mine.Chinese Journal of Rock Mechanics and Engineering 22(sup2): 2595-2560.

X.B.LI, et al (2001) Experimental investigation on the breakage of hard rock by the PDC with combined action modes. Tunneling and Underground Space Technology 16(2):107-114.

Yu-Yong Jiao, et al (2013) Improvement of the U-shaped steel sets for supporting the roadways in loose thick coal seam. International Journal of Rock Mechanics & Mining Sciences 60: 19-25.

Current state of the mining-induced consequences at the coalfield Lugau/Oelsnitz

Stand der Bergbaufolgen des ehemaligen Steinkohlereviers Lugau/Oelsnitz

Stefan Harms, Heinz Konietzky
Geotechnical Institute, TU Bergakademie Freiberg, Germany
Rolf Stoll
Glauchau, Germany

Abstract

The black coal basin Lugau/Oelsnitz is affected by mining-induced surface movements since the beginning of the 20th century. It was started to flood the mine after closure of the mining of hard coal in 1972. For examinations of the mine water, the facilities of two mine water monitoring stations were carried out. This study presents the current state of the mine water rising, the surface movement as well as the chemical composition of the mine water and the data processing.
Different water levels appear in the mine water monitoring stations available in the district. The chemical amounts of the mine water in the borehole Oelsnitz show other values than in the drilling Gersdorf. Surface movements are provable by measurements and have not subsided.

Zusammenfassung

Das Steinkohlerevier Lugau/Oelsnitz ist seit Beginn des 20. Jahrhunderts von bergbaubedingten Bodenbewegungen betroffen. Nach Stilllegung des Abbaus von Steinkohle im Jahre 1972 wurde begonnen die Grube zu fluten. Für Untersuchungen des Grubenwassers erfolgte die Einrichtung von zwei Grubenwassermessstellen. In dieser Arbeit wird der aktuelle Stand des Grubenwasseranstieges, der Bodenbewegungen sowie des Wasserchemismus betrachtet und dessen Bearbeitung gezeigt.
Es zeigen sich unterschiedliche Wasserstände an den im Revier vorhandenen Grubenwassermessstellen. Die chemischen Anteile des Grubenwassers in der Bohrung Oelsnitz zeigen andere Werte als in der Bohrung Gersdorf. Bodenbewegungen sind durch Messungen nachweisbar und sind nicht abgeklungen.

1 Introduction

In the southwestern region of the Erzgebirge Basin, which originated during the phase of the Variscan tectogenesis, lies the bituminous coalfield Lugau/Oelsnitz.

According to Beyer (1974), the basin was filled with abrasion masses during the Lower Carboniferous, the Upper Carboniferous and the Rotliegend. Exploitable coal deposits were found mainly in the Upper Carboniferous partially also in the Lower Carboniferous. The geology of this area is well documented, e.g. by Berger, Steinborn, Görne, & Junghanns (2010).

From January 7, 1844 to March 31, 1971, coal was won. During these 127 years of mining about 142 x 10^6 t were extracted (Beyer, 1974). The closure of the coal production was accompanied by the termination of the evacuation of accumulated mine water. Since then, the mine was flooded, according to Beyer (1974) and Böttcher, Schubert, Stoll, & Thiele (2010), by means of natural underground and aboveground inflows.

Figure 1.1 illustrates the location of the coalfield Lugau/Oelsnitz. Two mine water monitoring wells were established. These locations are also shown in the Figure.

A composition of available considerations to the process of flooding was carried out by Stoll, Beyer, & Richter (2013).

Fig. 1.1: Location of the coalfield Lugau/Oelsnitz (source of satellite image: GeoBasis-DE/BKG, GeoContent™, DigitalGlobe™ and Google).

2 The mine water level rising

From 2003 to 2004, a deep drilling was sink to a depth of 633.80 m. A mine water monitoring well was installed at this borehole. Since 2006, the measured levels of the mine water are continuously recorded (e.g. every 24 hours). Furthermore, an annual chemical analysis is performed since 2007. Publications to this topic are Böttcher, Schubert, Stoll, & Thiele (2010) and Köhler, Eckart, Klinger, & Abraham (2010).

An additional monitoring well was installed nearby the former Kaisergrube in 2013 in Gersdorf.

Pumping tests for hydrogeological investigations (Böttcher, Schubert, Stoll, & Thiele, 2010) reflected in the graph of the mine water ascent in the Oelsnitz borehole as sloping peaks.

To obtain a continuous and an uninterrupted view of the mine water rise, the data from both boreholes were interpolated. This can be realised with a polynomial for a series of measurements, since the grid points x_i (time of measurement) are pairwise different. A polynomial f of degree n was searched, which best fits the measurement series with its values of the function:

$$f(x) = p_1 x^n + p_2 x^{n-1} + \cdots + p_n x + p_{n+1} .$$

This gives a system of equations with the Vandermonde matrix $\boldsymbol{V}$, the vector of polynomial coefficients $\boldsymbol{p}$ and the vector of polynomial values $\boldsymbol{f}$:

$$\begin{pmatrix} x_1^n & x_1^{n-1} & \cdots & 1 \\ x_2^n & x_2^{n-1} & \cdots & 1 \\ \vdots & \vdots & \ddots & 1 \\ x_{n+1}^n & x_{n+1}^{n-1} & \cdots & 1 \end{pmatrix} \begin{pmatrix} p_1 \\ p_2 \\ \vdots \\ p_{n+1} \end{pmatrix} = \begin{pmatrix} f_1 \\ f_2 \\ \vdots \\ f_{n+1} \end{pmatrix}.$$

A solution is highly computationally intensive. According to Björck (1996), this problem can be solved numerically by using the method of least squares.

Figure 2.1 shows the interpolated graph (red) of the measurements at the mine water measuring point Oelsnitz (black). A polynomial of 10th degree adapts the curve best.

The values of the mine water measuring point Gersdorf (black) fits best with a polynomial of 7th degree (red). This is shown in Figure 2.2. The juxtaposition in Figure 2.3 presents both graphs of the mine water rise in the boreholes of Oelsnitz and Gersdorf. It can be noticed that the measurements in the borehole Gersdorf are continuously 22 – 23 m above the mine water level in the borehole of Oelsnitz.

Already Beyer (1974) prognosticated the mine water ascent. These predictions were revised and updated by Felix, Eckart, & Görne (2010).

Due to the mentioned aboveground inflows, Böttcher, Schubert, Stoll, & Thiele (2010) examined the Relationship between the infiltration of precipitation and the increase of the mine water level.

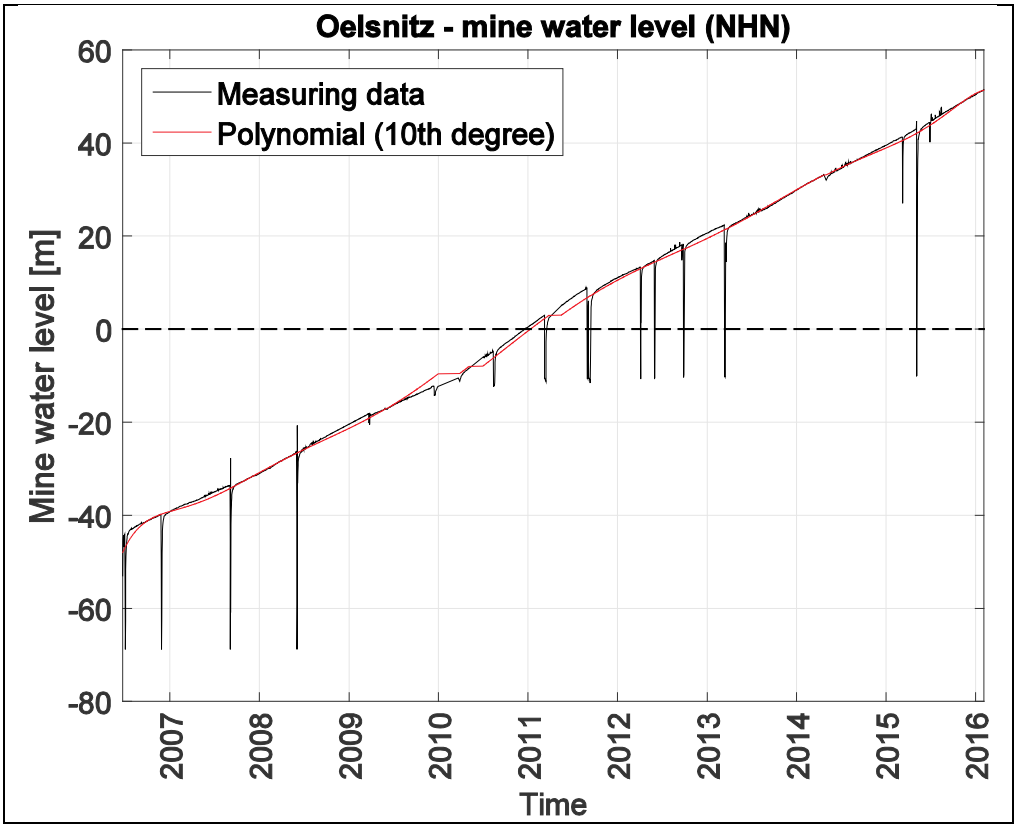

Fig. 2.1: Measuring data of the mine water monitoring station in Oelsnitz (black) and interpolated graph (red) (measurement data provided by LfULG).

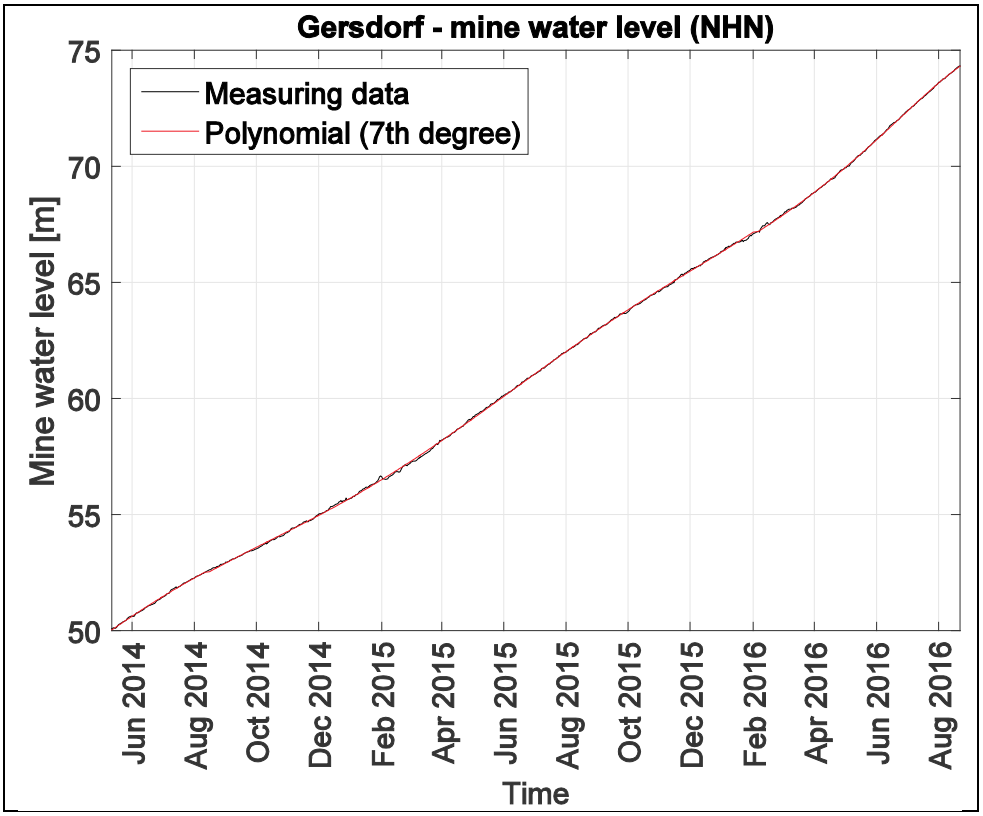

Fig. 2.2: Mine water measurements of the borehole Gersdorf (black) with interpolation (red) (measurement data provided by LfULG).

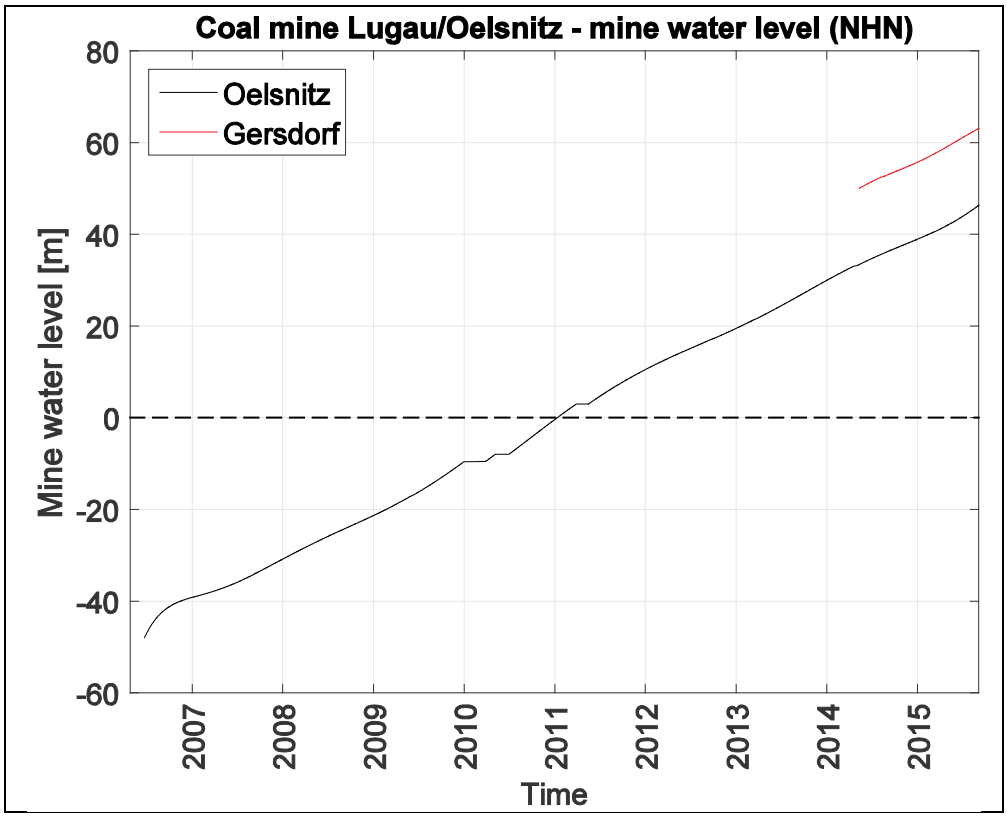

Fig. 2.3: The rise of the mine water level measured in the boreholes of Oelsnitz (black) and Gersdorf (red) (measurement data provided by LfULG).

3 Chemical composition of the mine water

The data of hydrochemical tests of the mine water were processed and sorted chronologically. Investigations of the borehole Gersdorf are only available from year 2014.

In Figure 3.1 (top), the variation over time of the content carbon and carbonic acid is shown. Contents of carbon in the water analysis of samples from the drilling Oelsnitz vary over the years and reveal a reducing under the value of 50 mg/l. The comparison between both values of carbon in 2014 indicates that the sample from the borehole Gersdorf is approx. 300 mg/l higher. The same applies in the graph of carbonic acid. However, the value of carbonic acid of the sample from the borehole Gersdorf is 15 mmol/l higher.

Decisive values for the salt content are sodium and chloride, as shown in Figure 3.1 (bottom). The contents of the mine water from the borehole Oelsnitz are risen over time. According to Menzel (2014), the salinity had an amount of 2.8 % in 2013. Seawater from the Baltic Sea has an average salt content of 2 %. That indicates the high salinity of the mine water from the borehole Oelsnitz. The mine water from the borehole Gersdorf has clearly lower values of ions.

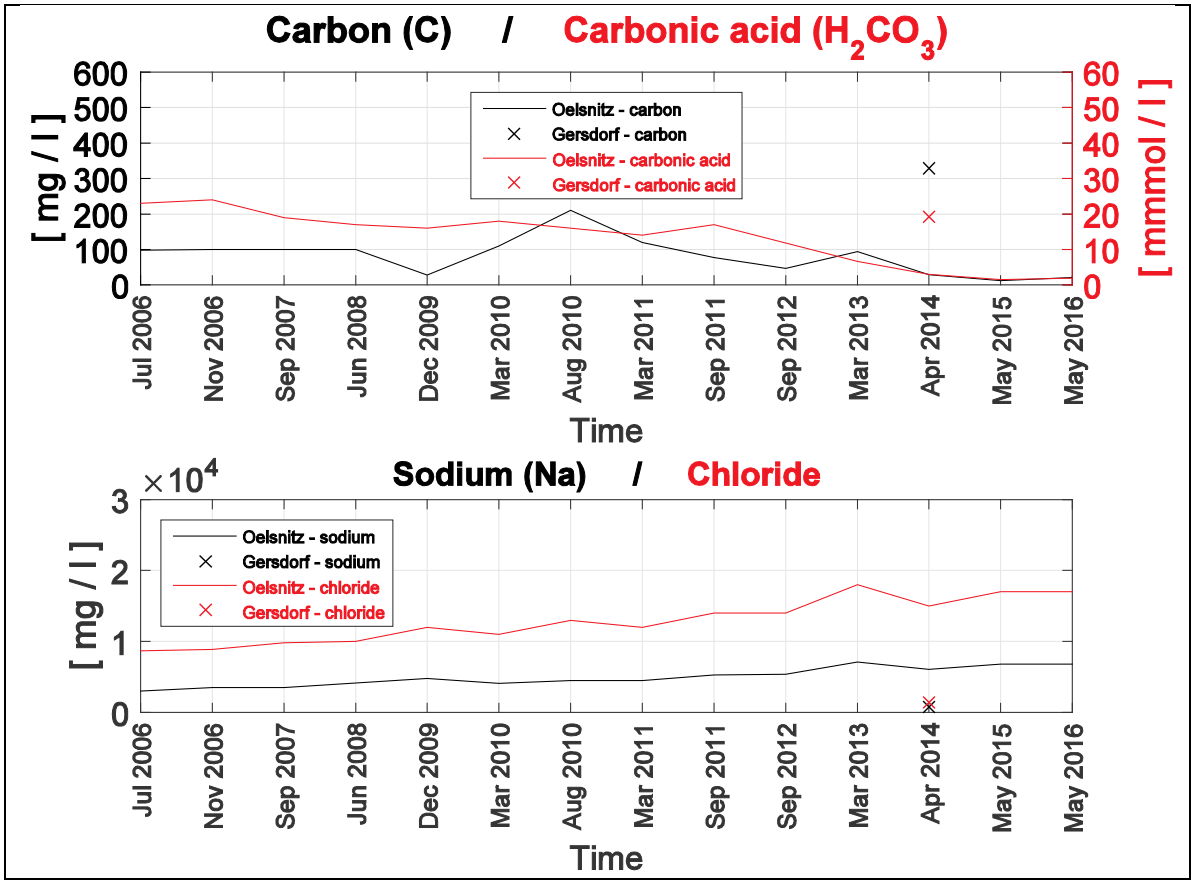

Fig. 3.1: Comparison of the carbonic and carbonic acid contents (top) as well as the sodium and chloride contents (bottom) of the mine water in both boreholes (measurement data provided by LfULG).

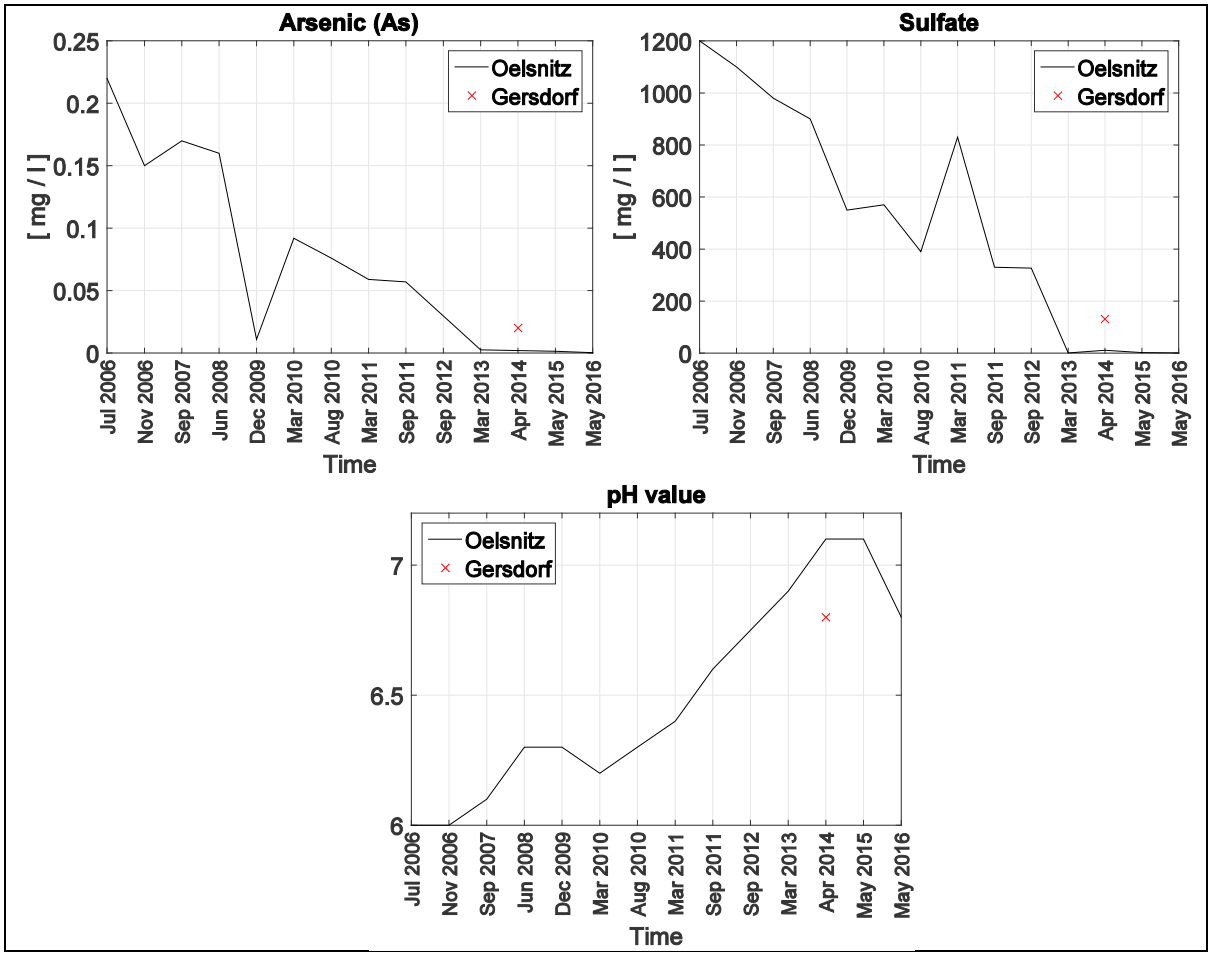

Fig. 3.2: Comparison of the arsenic content (top left), the sulfate content (top right) as well as the pH factor (bottom) of the mine water in both boreholes (measurement data provided by LfULG).

Figure 3.2 (top left) illustrates the chronological sequence of arsenic. The amount of the borehole Oelsnitz start with an initial value of 0.22 mg/l in 2006 and approaching zero after ten years. A same low arsenic value was tested at the sample from the borehole Gersdorf.

Sulfate values was influenced from a large decrease since 2013 in the measurements on samples from the borehole Oelsnitz (Figure 3.2 (top left)) and approaching zero in 2016. The value of sulfate from the sample from the borehole Gersdorf in 2014 is with 130 mg/l well above the 2014 analysed value of 11 mg/l from the borehole Oelsnitz.

The pH value in Figure 3.2 (bottom) indicates that the mine water from the borehole Oelsnitz was slightly acidic from 2006 to 2012 and has gone in a neutral state since 2013.

A neutral condition was determined also at the samples from the drilling Gersdorf.

4 Subsidence and uplift

For the former coalmine area, leveling data from 1972, 1996, 1997, 2002, 2006 and 2014 are available. It has been tested, which points were repeatedly surveyed at each leveling. Residual points were omitted in further considerations.

This was necessary to obtain a consistency in the calculation of the subsequent interpolation. The leveling of 1996 was not applicable, since a few number of points conformed with the remaining data.

To allow a better representation of subsidence and uplift, only altitude differences are used instead absolute altitudes.

Using the Delaunay triangulation (Delone & Raikov, 1948,1949), any point set can be utilized to create a triangular mesh, as visualized in Figure 4.1. In this case, these points are the repeatedly measured benchmarks. The resultant vertices $p_1, p_2, p_3, \dots, p_n$ of the originated triangles were weighted with barycentric coordinates b_1, b_2, b_3. An interpolation of the elevation data could be performed by defining additional points $v_1, v_2, v_3, \dots, v_n$ inside the triangles and weighted these points by barycentric coordinates. Every point in the mesh has unique barycentric coordinates. The interpolated altitudes could be calculated by using the dot product of the barycentric coordinates (indicated as vectors) and the altitudes of the vertices.

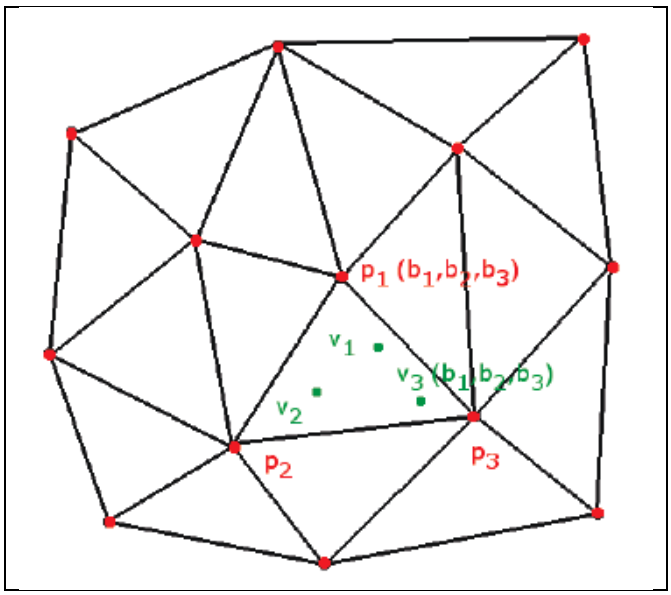

Fig. 4.1: Schematic of a triangular mesh using the Delaunay triangulation.

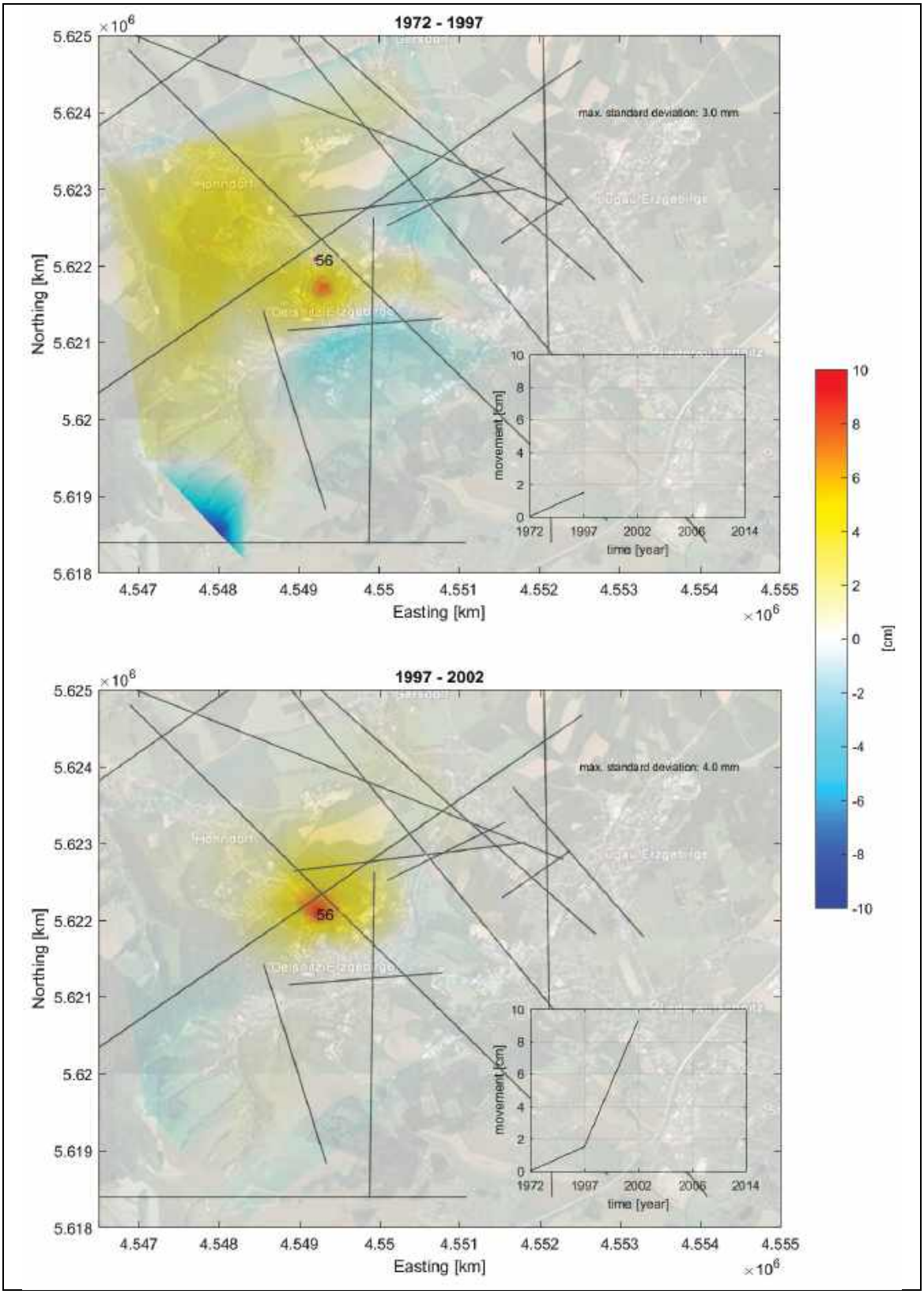

Fig. 4.2: History of the surface movements at the former coalfield Lugau/Oelsnitz with illustration of the local faults (grey) and an graph of the subsidence and uplift rates of a geodetic point (part 1) (source of satellite image: GeoBasis-DE/BKG, GeoContent™, DigitalGlobe™ and Google ; measurement data provided by Sächsisches Oberbergamt).

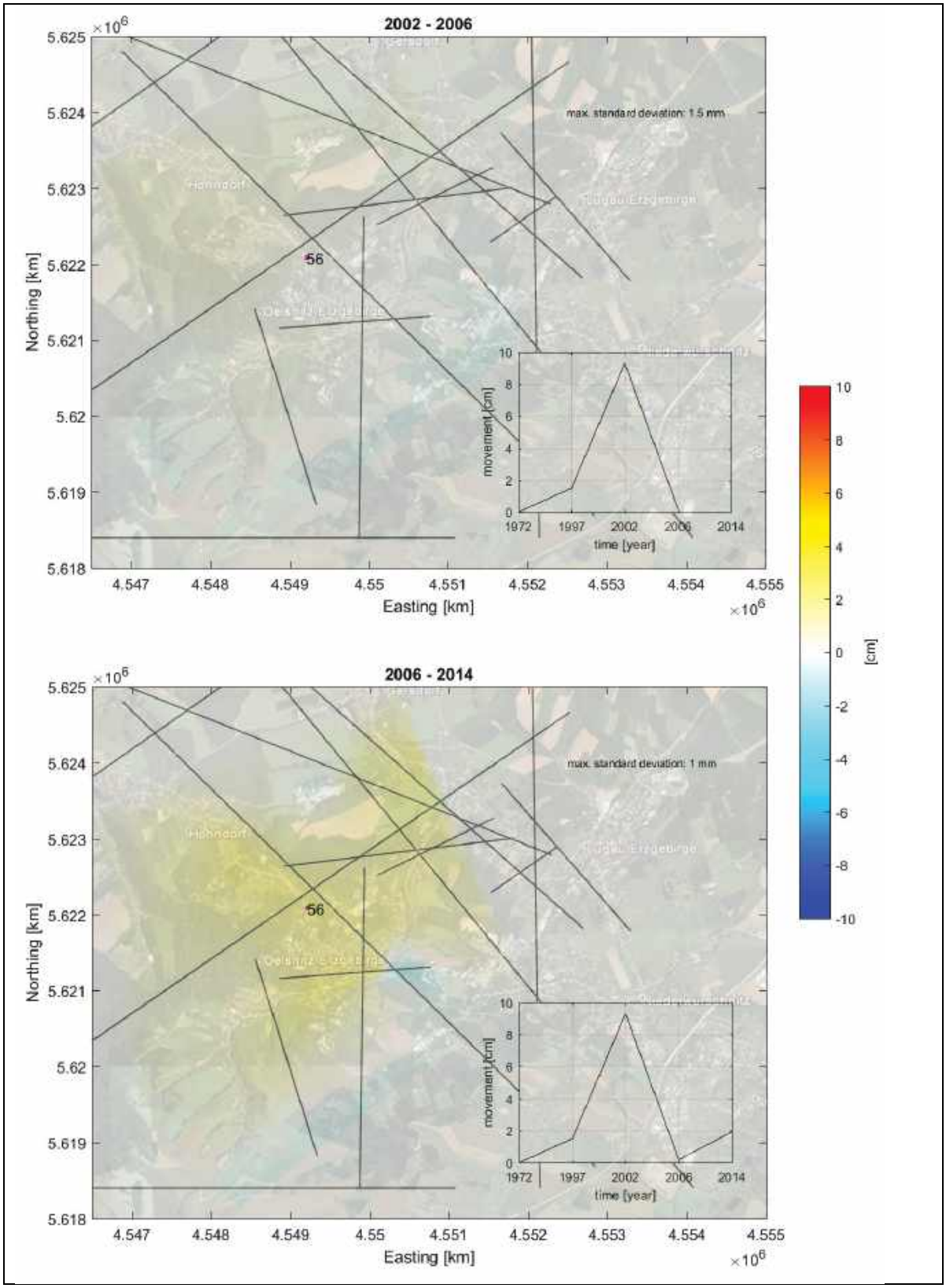

Fig. 4.3: History of the surface movements at the former coalfield Lugau/Oelsnitz with illustration of the local faults (grey) and an graph of the subsidence and uplift rates of a geodetic point (part 2) (source of satellite image: GeoBasis-DE/BKG, GeoContent™, DigitalGlobe™ and Google ; measurement data provided by Sächsisches Oberbergamt).

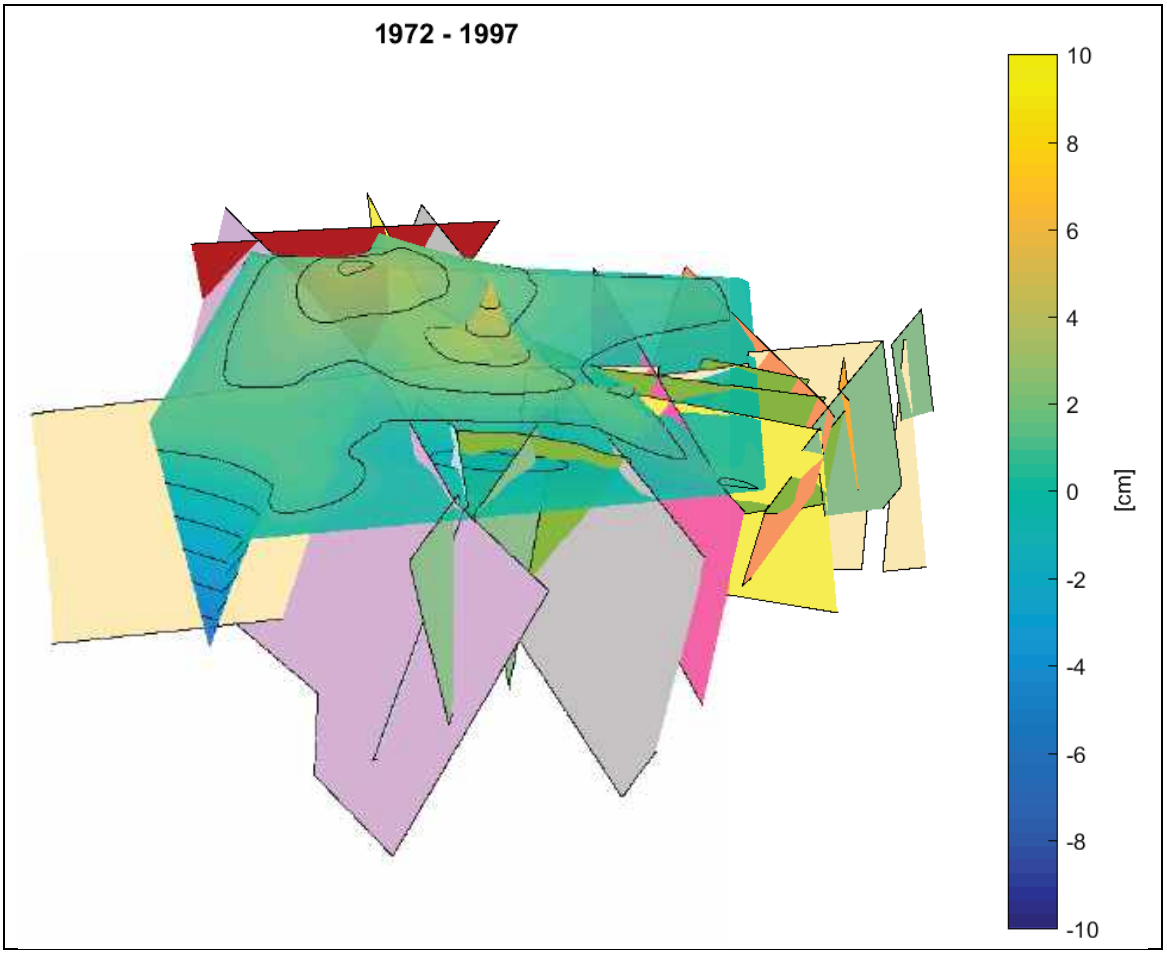

Fig. 4.4: Animated three-dimensional model to illustrate the surface movements and the locations of the local faults (measurement data provided by Sächsisches Oberbergamt).

Figure 4.2 and 4.3 shows the chronological sequence of subsidence and uplift in the former mining area. To illustrate the geological situation, the fault zones were mapped. In addition, the calculated maximum standard derivation of the leveling is illustrated. An additional chart displays the ratio of subsidence and uplift of a geodetic point. Color values were assigned to the values between the maximum and minimum altitude differences. The surface movements are in a range from approx. -10 to +10 cm and have not subsided.

Furthermore, an animated three-dimensional model could be created to become a closer look at the changes in the surface of the earth in conjunction with the local fault zones. An excerpt of this model is shown in Figure 4.4. Other authors as (Löbel & Döhner (2010) worked also on the mining induced surface movements in this region. There are considerations in this article to the period from 1900 to 1972.

5 Conclusions

The differences in the mine water levels and in the hydrochemical analysis of water samples lead to the presumption of separated mine waters of the boreholes Oelsnitz and Gersdorf. Including the geological situation with a high amount of fault zones in the former black coalmine area, it is supposed that mine barriers might occur and they might split the mine into two parts

Because of the surface movements up to approx. -10 and +10 cm in parts of the former coal basin and similar observations on other disused mining areas where flooding also occur, a connection between mine water ascent and surface movements cannot be excluded. The analysed and processed data in this study can be used for geomechanical researches regarding subsidence and uplift due to mine water rising.

Acknowledgements

The authors would like to thank the Landesamt für Umwelt, Landwirtschaft und Geologie von Sachsen (LfULG), the Sächsisches Oberbergamt and the Institute for Mine Surveying and Geodesy (TU Bergakademie Freiberg) for providing the data. The authors further thank the City of Oelsnitz/Erzgebirge for supporting this work.

References

Berger, H.-J., Steinborn, H., Görne, S., & Junghanns, C. (2010). Stratigraphie und Tektonik im Steinkohlerevier Lugau/Oelsnitz. *Geoprofil 13 (Sächsisches Landesamt für Umwelt, Landwirtschaft und Geologie)*, pp. 15-43.

Beyer, C. (1974). *Bergschadenskundliche Analyse "Lugau-Oelsnitz" (Unveröffentlicht).* Produnktionsbereich Zwickau & VEB Steinkohlenwerk Oelsnitz. Zwickau: VEB Baugrund Berlin.

Björck, A. (1996). *Numerical Methods for Least Squares Problems.* Philadelphia: SIAM.

Böttcher, F., Schubert, H., Stoll, R., & Thiele, M. (2010). Tiefbohrung in Oelsnitz/Erzgeb. *Oelsnitzer Stadtteilschriften 2010*, pp. 10-26.

Delone, B., & Raikov, D. (1948,1949). *Analytic Geometry (2 vols.).* State Technical Press. (in Russian).

Felix, M., Eckart, M., & Görne, S. (2010). Das Grubenwasseranstiegsmodell im Steinkohlerevier Lugau/Oelsnitz. *Geoprofil 13 (Sächsisches Landesamt für Umwelt, Landwirtschaft und Geologie)*, pp. 99-104.

Görne, S., Felix, M., & Berger, H.-J. (2010). Dreidimensionale Modellierung von Geologie und Bergbau als Grundlage für die Bewältigung der Bergbaufolgen im Lugau/Oelsnitz Revier. *Geoprofil 13 (Sächsisches Landesamt für Umwelt, Landwirtschaft und Geologie)*, pp. 71-78.

Köhler, U., Eckart, M., Klinger, C., & Abraham, T. (2010). Die Tiefbohrung Oelsnitz 1A/2003 im Zentrum des Bergbaureviers und ihr Ausbau zur Grubenwassermessstelle. *Geoprofil 13 (Sächsisches Landesamt für Umwelt, Landwirtschaft und Geologie)*, pp. 79-98.

Löbel, K.-H., & Döhner, S. (2010). Bergbaubedingte Senkungen und Hebungen. *Geoprofil 13 (Sächsisches Landesamt für Umwelt, Landwirtschaft und Geologie)*, pp. 55-69.

Menzel, A. (2014). *Entwicklung der Wasserbeschaffenheit des aufsteigenden Grubenwassers in Oelsnitz/Erzgebirge und Einschätzung der Umweltfolgen im Falle eines oberflächigen Austritts (Thesis).* Dresden: TU Dresden, Fakultät für Umweltwissenschaften, Institut für Abfallwirtschaft und Altlasten.

Stoll, R., Beyer, K., & Richter, H.-L. (2013). Zum Grubenwasseranstieg im ehemaligen Steinkohlenrevier von Lugau-Oelsnitz. *Turmstütze, Zeitschrift der Bergbaumuseums Oelsnitz/Erzgebirge und seines Fördervereins, Heft Nr. 31 Ausgabe 2*, 22-27.

Prediction of Classification of Rock burst Intensity Using the Cloud Model-Based Approach

Klassifizierung der Vorhersage der Gebirgsschlagsintensität basierend auf dem Cloud-Modell

Ke-ping Zhou
School of Resources and Safety Engineering, Central South University,
Changsha, Hunan 410083, China
E-mail: kpzhou@vip.163.com

Abstract

Rock burst is one of the common failures in deep rock mass engineering excavation. This study focuses on the prediction of rock burst classification by adopting the method of cloud model. Some main factors of rock burst including the rock brittleness coefficient (σ_c/σ_t), the stress coefficient (σ_θ/σ_c) and the elastic energy index (W_{et}) are chosen to establish evaluation index system. The weights are obtained by rough set method (RS) through 246 sets of rock burst samples from underground rock projects in China and abroad.
The 246 sets of rock burst samples are discriminated by normalizing data and establishing RS-cloud model. The discriminant results of the RS-cloud model are compared with those of Bayes, KNN and RF methods. The results show that the RS-cloud model has higher accuracy and Kappa than Bayes, KNN and RF methods. Hence, the RS-cloud model, with high discriminant ability and simple process, is a feasible and appropriate way to predict rock burst classification.

Zusammenfassung

Gebirgsschlag ist einer der häufigsten Versagensfälle beim Holraumbau im unterirdischen Felsbau. Diese Studie beschäftigt sich mit der vorhersagenden Klassifizierung der Gebirgsschlagsintensitäten unter Anwendung der Cloud-Modell-Methode. Einige der Hauptfaktoren für Gebirgsschlag, wie die Gesteinssprödheit (σ_c/σ_t), der Spannungskoeffizient (σ_θ/σ_c) sowie der elastische Energieindex (W_{et}) werden verwendet, um ein bewertendes Index-System abzuleiten.
Die Wichtungen werden mittels der Rough-Set Methode bestimmt. Dazu stehen 246 Datensätze von weltweiten Gebirgsschlägen zur Verfügung. Die Datensätze werden normalisiert und mittels der RS-Cloud-Methode klassifiziert. Die Ergebnisse wurden mit den Ergebnissen aus weiteren Verfahren (Bayes, KNN und RF) verglichen. Die Ergebnisse zeigen für die RS-Cloud-Methode höhere Präzisions- und Kappa-Werte. Folglich ist das RS-Cloud-Methode aufgrund der einfachen Durchführbarkeit und genaueren Ergebnisse ein geeignetes Verfahren zur Gebirgsschlagsklassifizierung.

Introduction

Rock burst is known as a dynamic, spontaneous and uncontrolled geological hazard commonly occurs in deep rock excavations. As a result of the stress redistribution in the rock mass due to the excavation of surrounding rock under high stress, rock burst can be described by several phenomena, such as bursting, stripping and ejecting. Rock burst is believed to be a result of the sudden release of the stored elastic strain energy from the hard brittle surrounding rock [1]. It is also assumed that the occurrence of rock burst shows a trend of high frequency in underground engineering [2], with the increase of buried depth and the level of stress. With the increase of global mining activities into deeper levels, the problem of rock burst is increasingly prominent. Since rock burst often occurs suddenly and intensely, which threatens the safety of operating personnel and equipment, it is of great significance to predict and control the hazard of rock burst.

The mechanism of rock burst has been studied by many scholars, and distinct prediction methods were proposed regarding the intensity of rock burst. Early research focused on the prediction of rock burst with the influence of a single factor. For instance, RUSSENES [3], TURCHANINOV [4] and HOEK [5] put forward strength criteria based on analyzing the relationship between surrounding rock stress and the occurrence of rock burst. WANG et al. [6] believed that lithology, together with the uniaxial compressive strength and the tensile strength, affect the occurrence of rock burst and proposed the relevant criteria. KIDYBINSKI [7], and SINGH [8] put forward the criterion of elastic strain energy based on the transformation of energy.

Based on the former research, it has become clear that rock burst is a complex nonlinear dynamic phenomenon and its occurrence is affected by many factors. In recent years, scholars carried out intelligent integrated prediction research of rock burst with various factors by intelligent methods. WANG et al. [9] predicted the grade of intensity of rock burst successfully with three factors by using the fuzzy mathematics comprehensive evaluation method. ZHOU et al. [10] combined the methods of Rough set (RS) and TOPSIS to establish an RS-TOPSIS model for rock burst prediction and applied the model to practical engineering projects. HU et al. [11] applied the improved matter-element extension model established based on the theory of matter-element extension to practice. DONG et al. [12] established the random forest model for rock burst forecast and obtained good results. ZHOU et al. [13] applied the k-nearest neighbor (KNN) algorithm to discriminate the grade of rock burst. GONG and LI [14] applied Bayes theory to build the Bayes model for rock burst prediction and applied the method to the underground engineering. However, uncertainties exist in rock burst prediction due to the influence of the choice of the models and parameters, and classification of rock burst is still a huge challenge.

In this paper, the classification of rock burst is investigated using the cloud model which is based on the uncertainty artificial intelligence [15]. The RS-cloud model for rock burst prediction is established using the rough set (RS) to calculate the weights of indicators [16]. The established model is applied to practical engineering and good results are obtained. We believe that the model provides a feasible approach for rock burst prediction.

1 Methodology of the cloud model

1.1 Indicator analyses and weight calculation

The evaluation indexes of evaluation index system of rock burst should be able to reflect the main characteristics of rock burst and properties of surrounding rock, and the relative data should also be obtained easily [10]. The rock brittleness coefficient (σ_c/σ_t), the stress coefficient (σ_θ/σ_c) and the elastic energy index (W_{et}) are common indicators, which can fully reflect the characteristics of a rock burst. The occurrence of rock burst and its intensity are also affected by lithology conditions, the ground stress field as well as rock elastic strain energy. The above three indices (σ_θ/σ_c, σ_c/σ_t and W_{et}) are chosen as the indicators of rock burst in deepness to establish evaluation index system.

The Rough Set (RS) theory [16] is a data mining method proposed by polish mathematician Z. Pawlak. The theory is capable of finding the hidden information with incomplete data. It has unique advantages in terms of determining evaluation factor's weight. The main processes are: ① Building the knowledge base (information table, columns represent the parameters, rows represent objects) according to the attribute of indicators; ② Simplifying the decision-making table and eliminating duplicate rows in the table; ③ Obtaining the importance of properties and ④ Normalizing the importance of each property.

1.2 The normal distribution characteristic of parameter

All parameters of rock burst indicators are random variables and many random variables either follow or can be transformed to follow a normal distribution according to the central limit theorem [17]. Thus, it can be found that each indicator parameter follows a normal distribution for the same level of rock burst by analyzing the statistical information in the database (available at http://www.ascelibrary.org). The three-sub-graph of probability distribution of σ_c/σ_t, σ_θ/σ_c and W_{et} belonging to light rock burst grade in database are shown in Fig.1. It is easy to find that all indicators basically follow normal distribution. Therefore, it is feasible to apply the normal distribution method to discribe the rock burst intensity.

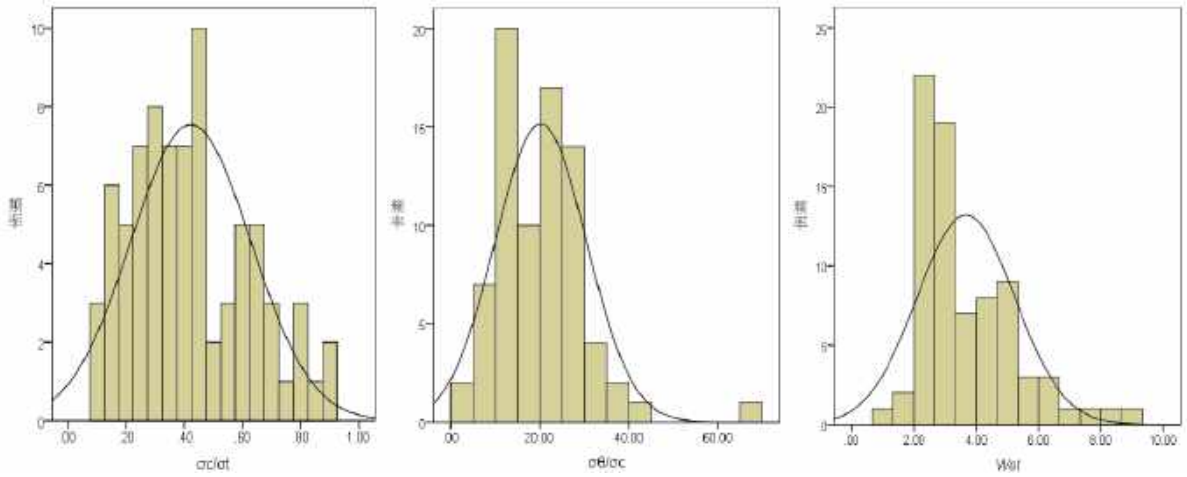

Fig. 1: Diagrams of probability distribution

1.3 The theory of cloud model

The Cloud model is a mathematical model proposed by LI [15] to deal with the transformation of uncertainty knowledge between quality and quantity on the basis of random mathematics and fuzzy mathematics.

Let U be a quantitative set which is expressed by precise values, $U = \{x\}$. C is a qualitative concept of U. For any element x of U, there is a stable tendency random number $\mu(x) \in [0,1]$, which is called the certainty degree of x to U, and the distribution of certainty degree on U is called the cloud. There are three numerical characteristics to express the transformation of cloud including expectation E_x, entropy E_n, and hyper entropy H_e. E_x represents the mean value of the set; entropy E_n represents the range of cloud droplets which may be accepted by qualitative concept in domain space, hyper entropy H_e is entropy of entropy E_n, reflecting the degree of dispersion of the cloud droplets [18].

Since the boundary value indicates the value of the transition from one level to another, the membership belonging to two levels are equal.

$$\exp[-\frac{(C_{\max}-C_{\min})^2}{8E_n^2}]=0.5\,. \tag{1}$$

Based on the principles of cloud model and concept of cloud numerical characteristics, the numerical characteristics can be calculated according to Eq. 2.

$$\begin{cases} E_x=(C_{\max}+C_{\min})/2 \\ E_n=(C_{\max}-C_{min})/2.355 \\ H_e=k \end{cases}. \tag{2}$$

In the above expression, C_{max} and C_{min} are the maximum and the minimum threshold corresponding to the grade standards, respectively. k is a constant which can be adjusted according to the fuzzy degree of variables, and it is given a unified value of 0.01 in this paper. Then the certainty degree of x to C can be calculated by Eq. 3.

$$\mu(x)=\exp(-(x-E_x)^2/2\times(E_n^{'})^2)\,, \tag{3}$$

where $E_n' \sim N(E_n, H_e^2)$.

Cloud models are produced by cloud generators. The forward cloud generator is denoted with CG in Fig. 2, which is the transformation between the qualitative knowledge and the quantitative representation. The forward cloud generator is used to generate the cloud drops through the three given cloud numerical characteristics. Given the three numerical characteristics of cloud and the specified value of x, the combination to generate the cloud drops drop(x, $\mu(x)$) is called the X-condition cloud, which is denoted by XCG in Fig. 2. The combination of the two kinds of generators can be used to derive various kinds of clouds to bridge the gap between the qualitative concept and the quantitative knowledge [19].

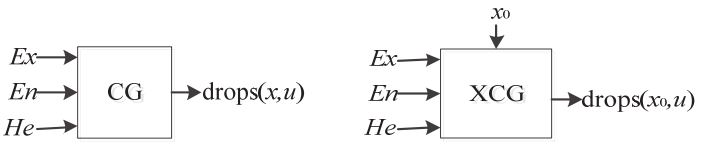

Fig. 2: Process of forward cloud generators and X-condition cloud generators

1.4 Implementation of the approach

Rock burst is usually divided into four grades [13]: class I (No rock burst activity), class II (Light rock burst activity), class III (Medium rock burst activity), and class IV (Violent rock burst activity). The process to classify the rock burst using the CM is listed as follows:

(a) Calculating the numerical characteristics of the cloud model for each indicator corresponding to each class of rock burst intensity according to Eq. 2;

(b) Establishing the cloud model by using the cloud generators and calculating certainty degree of each indicator corresponding to each rock burst intensity according to the measured data collected from underground engineering projects;

(c) Calculating the weight of each index by applying the method of RS and integrating certainty degree as follows, where $\mu(x)$ represents the certainty degree of each index, ω_j is the weight of each index;

$$U = \sum_{j=1}^{m} \omega_j \mu(x) . \tag{4}$$

(d) Discriminating the class of rock burst according to the maximum certainty degree principle.

1.5 Establishment of the cloud model

Since the indicators have different units, the data of indicators must be preprocessed before establishing the cloud model. The data normalization [20] is applied to remove the influence of different units of indicators. The normalization should be implemented before cloud transformation using Eq. 4. If the indicator value decreases with the increasing favorable of the indicator effect, data can be normalized by Eq. 5. Otherwise, the data can be normalized by Eq. 6.

$$x_{ij}^{'} = \begin{cases} 1, & x_{ij} \le x_{i\min} \\ 0.25 \times (j - \dfrac{x_{i\max} - x_{ij}}{x_{i\max} - x_{i\min}}), & x_{i\min} < x_{ij} < x_{i\max} \\ 0, & x_{ij} \ge x_{i\max} \end{cases} . \tag{5}$$

$$x_{ij}^{'}=\begin{cases}1, & x_{ij}\geq x_{i\max}\\ 0.25\times(j-\dfrac{x_{ij}-x_{i\min}}{x_{i\max}-x_{i\min}}), & x_{i\min}<x_{ij}<x_{i\max}\\ 0, & x_{ij}\leq x_{i\min}\end{cases}. \quad (6)$$

Here j is the grade of rock burst, $x_{ij}^{'}$ is the normalized data of indicator, x_{ij} is the original data of this indicator, $x_{i\max}$ and $x_{i\min}$ are the maximum value and the minimum value of the indicator, respectively.

After the data normalization, the factor values are transformed in the interval [0, 1]. The four ranking grades (I, II, III, IV) of the indicators (Table 1) are thus quantitatively expressed by four data intervals [0.0, 0.25), [0.25, 0.5), [0.5, 0.75), [0.75, 1.0], respectively. The three numerical characteristics of the cloud model can be calculated based on the normal cloud theory (Eq. 2). The cloud model is established by using the forward cloud generator. As is shown in Fig. 3, the *x*-axis is the index value, *y*-axis represents the membership of the value.

Table 1: Classification of evaluating indicators

Ranking grade	σ_c/σ_t	σ_θ/σ_c	W_{et}
I	40.0 - 55.0	0 - 0.3	0 - 2.0
II	26.7 - 40.0	0.3 - 0.5	2.0 - 4.0
III	14.5 - 26.7	0.5 - 0.7	4.0 - 6.0
IV	0 - 14.5	0.7 - 1.0	6.0 - 10.0

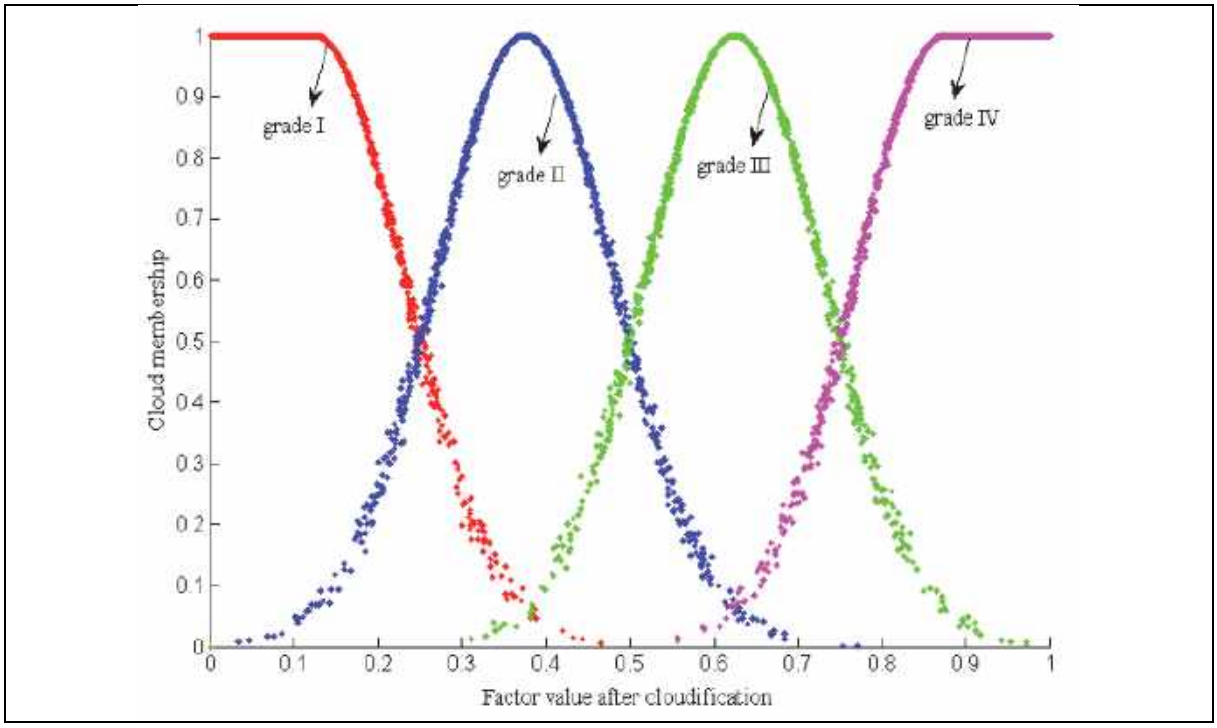

Fig. 3: The normal cloud model of indicators after data normalization

2 Results and discussion

2.1 Predicted results achieved by different models

The RS−cloud model, the KNN model, the Bayes model and the RF model are used to predict the intensity of the rock burst cases collected from the original database. 100 cases are chosen randomly as the training set and the reserved 146 cases are considered as testing data set when the cases are classified by Bayes, KNN and RF models. The prediction results of each method are shown in Table 2, where, *k* is 5 in KNN method, and NTree is 500 in RF method.

Table 2 Predictive results of four classification across four classifiers

Class label	Samples	Bayes		KNN		RF		CM	
		correct	missed	correct	missed	correct	missed	correct	missed
I	43	19	24	21	22	32	11	30	13
II	78	70	8	57	21	54	24	58	20
III	81	22	59	45	36	44	37	51	30
IV	44	24	20	25	19	36	8	34	10

The numbers of the predicted cases are given for each class of rock burst intensity in Table 2. The numbers in correct columns are the successfully predicted samples, and the numbers in missed columns are sample numbers predicted incorrectly. Compared with KNN, RF and CM models, Bayes model has a strong discriminant ability for the slight rock burst (II), but it achieved lower discriminant accuracy rate for the other three levels of rock burst. The discriminant accuracy rate of Bayes, KNN and RF models is related to the training samples. Generally, if the training sample set is more comprehensive, the discriminant accuracy is higher. CM has a superior discriminant ability for each level for rock burst without training set. Hence, the cloud model is a feasible method of the four classifiers for the prediction of rock burst classification.

2.2 Model performance evaluation

In order to analyze the prediction performance of four classifiers, two global classification metrics (classification accuracy and the Cohen's Kappa index) are used [21]. For each model, a confusion matrix is presented.

The accuracy of classifiers is evaluated according to classification accuracy rate. Let x_{ij} (i and j = 1, 2…m) be equal to the joint frequency of observations assigned to class i by prediction and to class j by observation data, respectively. Classification accuracy is a primary evaluation criterion and can be calculated as Eq. 5. The Cohen's Kappa index measures the proportion of correctly classified units after removal of the probability of chance agreement. The Cohen's Kappa is a robust index, and it takes into account the probability that a pixel is classified by chance. Therefore, the Kappa is always slightly lower than classification accuracy and can be given by Eq. 6.

$$\text{Accuracy} = (\frac{1}{n}\sum_{i=1}^{m} x_{ii}) \times 100\% \tag{5}$$

$$\text{Kappa} = \frac{n\sum_{i=1}^{m} x_{ii} - \sum_{i=1}^{m}(x_{i+} \cdot x_{+i})}{n^2 - \sum_{i=1}^{m}(x_{i+} \cdot x_{+i})} \tag{6}$$

Here x_{ii} is the element on the main diagonal, n is the number of samples, m is the number of class values, and x_{i+}, x_{+i} are the rows and columns total elements, respectively.

The value of kappa ranges from -1 (total disagreement) through 0 (random classification) to 1 (perfect agreement). It can be divided into six groups to represent different levels of consistency (as shown in Table 3). The value of kappa below 0.4 indicates poor agreement, while the value larger than 0.4 indicates good agreement.

Table 3: Relative strength of agreement associated with kappa statistic

Strength of agreement	Kappa value
total disagreement	-1.0~0.0
Slight	0.0~0.2
Poor	0.2~0.4
Moderate	0.4~0.6
Substantial	0.6~0.8
Perfect	0.8~1.0

The results of accuracy and Kappa of each model are shown in Table 4. The accuracy of sets with four models falls into the range [0.5488 – 0.7033], as shown in Table 4. Obviously, the CM predictor achieved the highest average accuracy rate of 70.33 %.The average accuracy rates of RF model and KNN model is 67.48 % and 60.16 %, respectively. Bayes had the lowest accuracy with a rate of 54.88 %. On the other hand, the Kappa values of the CM, RF, KNN and Bayes models are from poor to substantial (only the value of Kappa of Bayes model is poor with a value of 0.37) on the basis scale, as shown in Table 3. It is obvious that the Kappa of CM model is the highest with a value of 0.60. The RF, KNN and Bayes models rank in a successive way. The comprehensive analysis results of four models show that two global classification metrics (accuracy and Kappa) of CM model higher than others, which means the CM model has superior performance than RF, KNN and Bayes models. Hence, the cloud model is feasible and applicable for the prediction of rock burst classification.

Table 4: Performance metrics of each method

classification metrics	Bayes	KNN	RF	CM
Accuracy	54.88 %	60.16 %	67.48 %	**70.33 %**
Kappa	0.37	0.45	0.56	**0.60**

*Bolded values indicate the highest value.

3 Conclusions

Models for predicting rock burst play a significant role in underground mining and civil engineering projects. In this study the cloud model is adopted to predict the classification of rock burst. Based on the analysis results and comparison of the

performances of four classifiers, conclusions are made as follows:

(1) From the study of the four classifiers, the classification accuracy of Bayes, KNN, RF and CM models are 54.88 %, 60.16 %, 67.48 % and 70.33 %, respectively, the Cohen's Kappa index using Bayes, KNN, RF and CM models are 0.37, 0.45, 0.56 and 0.60, respectively. Thus, the method introduced in this study is applicable for rock burst classification.

(2) The predicted results of four models show that the classification accuracy and the Kappa index of CM are higher than those of Bayes, KNN and RF models. Since CM can predict rock burst without training set, it has superior capability for rock burst classification.

4 Acknowledgments

The research is partially supported by the National Natural Science Foundation Project (No. 51474252, 51274253) of China, the Innovation Driven Plan Project (No. 2015CX005) of Central South University of China and the Fundamental Research Funds Project (No.2016zzts095) for the Central Universities of Central South University of China.

References

[1] ZHU Si-tao, FENG Yu, JIANG Fu-xing. Determination of Abutment Pressure in Coal Mines with Extremely Thick Alluvium Stratum: A Typical Kind of Rockburst Mines in China [J]. Rock Mech Rock Eng, 2016, 49(10): 1943–1952.

[2] ORTLEPP WD, STACEY TR. Rockburst mechanisms in tunnels and shafts [J]. Tunneling and Underground Space Technology, 1994, 9(1): 59-65.

[3] RUSSENES BF. Analysis of rock spalling for tunnels in steep valley sides [D]. Norwegian Institute of Technology, 1974: 244-247(in Trondheim).

[4] TURCHANINOV A, MARKOV GA, GZOVSKY MV, et al. State of stress in the upper part of the Earth's crust based on direct measurements in mines and on tectonophysical and seismological studies [J]. Phys. Earth Planet. Inter. 1972, 6(4): 229–234.

[5] HOEK E, BROWN ET. Practical estimates of rock mass strength [J]. Int J Rock Mech Min. 1997, 34(8): 1165–1186.

[6] LU Jia-you, WANG Chang-ming. Study on back analysis for stress of rock mass from information of rockbursts [J]. Journal of Yangtze River Scientific Research Institute, 1994, 11(3): 27-30.

[7] KIDYBINSKI A. Bursting liability indices of coal [J]. Journal of Rock Mechanics and Mining Sciences, 1981, 18(6): 295–304.

[8] SINGH SP. Classification of mine workings according to their rockburst proneness [J]. Mining Science and Technology, 1988, 8(3): 253–262.

[9] WANG Yuan-han, LI Wo-dong, LI Qi-guang. Method of fuzzy comprehensive evaluations for rockburst prediction [J]. Chinese Journal of Rock Mechanics and Engineering, 1998, 17(5): 493–501.

[10]ZHOU Ke-ping, LEI Tao, HU Jian-hua. RS-TOPSIS Model of rockburst prediction in deep metal mines and its application [J]. Chinese Journal of Rock Mechanics and Engineering, 2013, 32(2): 3706-3710.

[11]HU Jian-hua, SHANG Jun-long, ZHOU Ke-ping. Improved matter-element extension model and its application to prediction of rockburst intensity [J]. The Chinese Journal of Nonferrous Metals, 2013, 23(2): 496-501.

[12]DONG Long-jun, LI Xi-bing, PENG Kang. Prediction of rock burst classification using Random Forest [J]. Transactions of Nonferrous Metals Society of China, 2013, 23(2): 472-477.

[13]ZHOU Jian, LI Xi-bing, Hani S. Mitri. Classification of Rockburst in Underground Projects: Comparison of Ten Supervised Learning Methods [J]. Journal of Computing in Civil Engineering, 2015: 1-19.

[14]GONG Feng-qiang, LI Xi-bing, ZHANG Wei. Rockburst prediction of underground engineering based on Bayes discriminant analysis method [J]. Rock and Soil Mechanics, 2010, 31(Z1): 370-377.

[15]LI De-yi, DU Yi. Artificial intelligence with uncertainty [M]. Beijing: National Defense Industry Press, 2005.

[16]Salvatore Barbagallo, Simona Consoli, Nello Pappalardo, Salvatore Greco, Santo Marcello Zimbone. Discovering Reservoir Operating Rules by a Rough Set Approach [J]. Water Resources Management, 2006, 20(2): 19–36.

[17]JU Pei, ZHAI Ying-hu. Lithology identification analysis based on normal distribution theory and fuzzy synthetic evaluation method [J]. Science Technology and Engineering, 2012, 12(21): 5253–5256.

[18]ZHOU Ke-ping, LIN Yun, DENG Hong-wei, LI Jie-lin, LIU Chuan-ju. Prediction of rock burst classification using cloud model with entropy weight [J]. Transactions of Nonferrous Metals Society of China, 2016, 26(7): 1995-2002.

[19]LIU Zao-bao, SHAO Jian-fu, XU Wei-ya, MENG Yong-dong. Prediction of rock burst classification using the technique of cloud models with attribution weight [J]. Nat Hazards, 2013, 68(3): 549–568.

[20]LIU Zao-bao, SHAO Jian-fu, XU Wei-ya, XU Fei. Comprehensive Stability Evaluation of Rock Slope Using the Cloud Model-Based Approach [J]. Rock Mech Rock Eng, 2014, 47(6): 2239–2252.

[21]ZHOU Jian, LI Xi-bing, Hani S. Mitri. Comparative performance of six supervised learning methods for the development of models of hard rock pillar stability prediction [J]. Nat Hazards, 2015, 79(6): 291–316.

Optimization and analysis on excavation procedure for biased tunnel in weak surrounding rock

Optimierung und Analyse der Ausbruchssequenz eines Tunnels in geringfestem Gebirge in Hanglage

Ren-dong HUANG, Xin-li ZHANG, Han WU, Jie WANG
School of Resources & Safety Engineering, Central South University
Changsha

Abstract
In consideration of the geological conditions of Dongtou mountain biased tunnel in soft surrounding rock, the construction process is simulated based on MIDAS/GTS software. Firstly comparing excavated shallow part with excavated deep part by the annular pilot heading conservation core soil method，the deformation and stress changes of rock mass and supporting structure of Dongtou mountain tunnel in different excavation sequences are obtained. Actual tunnel excavation sequence is optimized by comparison. Monitoring the data from tunnel excavation process for condition one and condition two are compared and analyzed. The results show that Dongtou mountain tunnel can effectively reduce the tunnel deformation and stress changes by excavating right side tunnel first and then left by taking the annular pilot heading conservation core soil method. The conclusions provide a reliable basis for the smooth construction of Dongtou mountain tunnel, which can also be considered as references for the design and construction of tunnels under similar geological and topographical conditions.

Zusammenfassung

Unter Beachtung der geologischen Bedingungen des Dongtou-Gebirges wurde der Tunnelvortriebsprozess eines Tunnels in Hanglage mittels der Software MIDAS/GTS simuliert. Zunächst wird verglichen die Auffahrung des flachliegenden mit dem tiefer gelegenen Teils mittels „pilot heading conservation core“ Methode, wobei die Deformations- und Spannungsänderungen im Gebirge und den Ausbauelementen des Dongtou-Tunnels bei unterschiedlicher Vortriebssequenz ermittelt wurden. Durch vergleichende Betrachtung wurde die optimale Ausbruchssequenz ermittelt. Weiterhin wurden die Monitoring-Daten für die Ausbruchssequenzen nach Variante 1 und 2 verglichen und analysiert. Die Ergebnisse zeigen, dass Deformationen und Spannungsänderungen beim Auffahren des Dongtou-Tunnels in effektiver Weise reduziert werden können, wenn zuerst der rechtsliegende Tunnel aufgefahren wird und danach der linksseitige bei Anwendung der „pilot heading conservation core“ Methode. Diese

Schlussfolgerung liefert die Basis für die problemlose Auffahrung des Dongtou-Tunnels und kann als Referenz für die Auffahrung von Tunnel unter ähnlichen geologischen und topographischen Bedingungen angesehen werden.

1 Introduction

With the rapid development of traffic facilities in our country, the application of tunnel engineering is more and more extensive, and the deformation of surrounding rock is usually larger when the tunnel is excavated [1] in areas of weak rock mass. The basic characteristics of weak surrounding rock is mainly characterized by low strength, easy weathering, large pore ratio, small bulk density, easy water seepage and so on. This has obvious influence on expansibility and timeliness [2], and often has a serious impact on the construction safety and construction period. Factors affecting the deformation of soft surrounding rock include geological factors, design factors, construction factors, meteorological factors etc. Also the influence of the excavation process on the stability of the construction is particularly important [3]. Therefore, it is significant to take appropriate technical methods for the tunnel construction and to select a reasonable excavation sequence. It is important to fully understand the mechanical characteristics and deformations of surrounding rock and support to ensure the stability of the tunnel including surrounding rock mass.

At present, the research on the construction technology of tunnels in weak surrounding rock is mainly focused on the simulation and analysis of the excavation process, and the conclusions of the studies are different. For example Zhou [4] analyzed the construction process of Yuanmo Bridge tunnel of highway in Yunnan in two dimensions using ANSYS program with bench method, and the results show that excavating the shallow buried side firstly is more reasonable in the biased state. While LIU[5] analyzed the construction process of Lishi loess arch tunnel segment in Shanxi Province based on ANSYS program, and the results show that it is better to first excavate deep buried side by three-heading excavation method and bench method. LIU conducted the analysis by three-dimensional simulations of the excavation process of portal section of shallow tunnel with unsymmetrical loadings of Laozhai tunnel in Guizhou province of Xiamen-Chengdu expressway by using FLAC^{3D} and came to the same conclusion as Zhou. Based on that, SHI carried out three-dimensional numerical simulations in respect to the excavation process of Liang Cun tunnel by using different excavation sequences via MIDAS / GTS program with CRD method, and the conclusion is that, firstly excavating shallow buried side is more reasonable.

The actual situation in respect to biased tunnels is unclear, and only a few detailed investigations on the excavation scheme for shallow embedded bias tunnels are available. The excavation methods and analysis methods are not exactly the same, so the conclusions are also different, while the simulation results for each typical tunnel are very valuable. Firstly, in combination with the Dongtou Mountain Tunnel project, the deformation of surrounding rock under different excavation procedure and supporting stress is simulated by MIDAS/GTS software and presented in this paper. Also, the simulated results were analyzed and compared to optimize the excavation procedure. Finally, combined with the field monitoring results of the surrounding rock under the

two excavation procedures, the characteristics of the deformation and supporting structure of Dongtou mountain tunnel are comparatively analyzed and verified. The conclusion can provide reference for the design and construction of similar projects.

2 General situation of the construction

Dongtou Mountain tunnel is located in Chengdu county, Shaoyang, with undulating terrain and developed vegetation, which shows a low-hilly landscape. Dongtou Mountain Tunnel is a separated tunnel with curvilinear distribution, and the tunnel deviates from the axis about 309 m. Its total length is 1315 m and midline elevation is 445 m to 697 m. Maximum height difference is about 252 m, and the natural slope gradient is about 20°to 40°.

The surrounding rock is weak. The cover soil of the tunnel is mainly clay and gravel with small thickness. Most of the bedrock in this area is exposed, and outcropping lithology is carbonaceous slate and sandy slate. Weathered carbonaceous slate in the tunnel region is characterized by joints and can be considered as fractured rock. It is easy for the roof without support to collapse, and the side wall could lose stability easily. The surface water does normally not enter the tunnel and only rainfall water close to the two entrances is used to generate a temporary water flow during the rainy season. Groundwater is mainly coming from fissures in the bedrock. The inclination direction of rock stratum is unfavorable for water discharge. Underground water-inrush appears like rain or flashy flow.

3 Numerical simulation of tunnel excavation

3.1 Software Introduction

Midas / GTS（Geotechnical and Tunnel Analysis System）is a finite element software mainly developed for rocks and soils, underground constructions, mines, tunnels and other projects [8]. The principle of this software is based on the finite element strength reduction theory. At the same time, it can define multiple construction stages conveniently, analyzing the inner force of the supporting structure for different surrounding rock types at different construction stages, verifying whether the structural safety factors is meeting the corresponding design specifications or not. Quantitative characterization for the influence of tunnel construction on the surrounding rocks/soil is possible. In addition, through the analysis of simulation, more reasonable construction methods and support parameters are put forward to guide the design and construction of the site. This paper focus on the Dongtou Mountain Tunnel excavation procedures and protecting measures, especially considering different excavation and supporting situations in the same section. Using two-dimensional simulations is the simplest and most effective method.

The number of soil constitutive models provided by MIDAS /GTS is up to 16. Included are the commonly used Mohr-Coulomb model, but also user-defined models can be

applied. The elastic plastic plane strain model is adopted in the calculation of the soil mass, and the characteristics of surrounding rock of tunnel are considered as homogeneous and elasto-plastic using Mohr-Coulomb constitutive model. Deformation and stress of surrounding rock are affected by multiple factors. Considering the boundary condition of $(\sigma_{pp})_{p=rl} = -P_l$, the stresses in surrounding plastic zone in rock mass is as follows:

$$\sigma_{\rho p} = B - (P_l + B)(\frac{\rho}{r_l})^{\frac{2\sin\varphi_p}{1-\sin\varphi_p}}, \tag{3-1}$$

$$\sigma_{\theta p} \approx \frac{1+\sin\varphi_p}{1-\sin\varphi_p}\left[B-(P_l+B)(\frac{\rho}{r_l})^{\frac{2\sin\varphi_p}{1-\sin\varphi_p}}\right]-\frac{2c_p\cos\varphi_p}{1-\sin\varphi_p}. \tag{3-2}$$

The formula for the radial displacement of the plastic zone of surrounding rock is

$$u_{\rho p}=\frac{(1-\mu_p^2)\ \rho}{E_p}\left\{\begin{array}{l}\left[B-(p_l+B)(\frac{\rho}{r_l})^{N_\varphi-1}\right](N_\varphi-\frac{\mu_p}{1-\mu_p})-\frac{2c_p\cos\varphi_p}{1-\sin\varphi_p}+\\ \frac{4\sin\varphi_p(P_l+B)}{(1-\sin\varphi_p)^2(N_\varphi+N_\psi)}\left[\left(\frac{\rho}{r_l}\right)^{N_\varphi-1}-(\frac{r_p}{r_l})^{N_\varphi-1}\left(\frac{r_p}{\rho}\right)^{1+N_\psi}\right]+\\ \frac{2(c_p\cos\varphi_p-B\sin\varphi_p)}{(1-\mu_p)(1-\sin\varphi_p)(1+N_\psi)}\left[1-\left(\frac{r_p}{\rho}\right)^{1+N_\psi}\right]+\frac{(1-2\mu_p)\ P_0}{(1-\mu_p)}\end{array}\right\}, \tag{3-3}$$

where σ_p and σ_θ are radial stress and circumferential stress, respectively. ρ is the distance from the point to the tunnel axis. φ_p and c_p are internal friction angle and cohesion of the rock or soil mass, respectively. ψ_p is dilatancy angle of surrounding rock; B is a constant.

3.2 Calculation model and calculation parameters

The numerical model is based on the V rock (the surface rock and soil mass is VI rock) of Dongtou Mountain Tunnel entrance, left line ZK37 + 300 tunnel segment. A pure gravitational stress field of the rock mass is considered in calculating the initial stress field. The model dimension is 140 meters in the horizontal direction and 50 meters in the vertical direction, as shown in Figure 3-1.The Mohr-Coulomb constitutive model is used to model the surrounding rock. The supporting structures of shotcrete, anchor bolt and steel bar are considered as linear elastic material. Vertical and horizontal boundaries are fixed in normal direction.

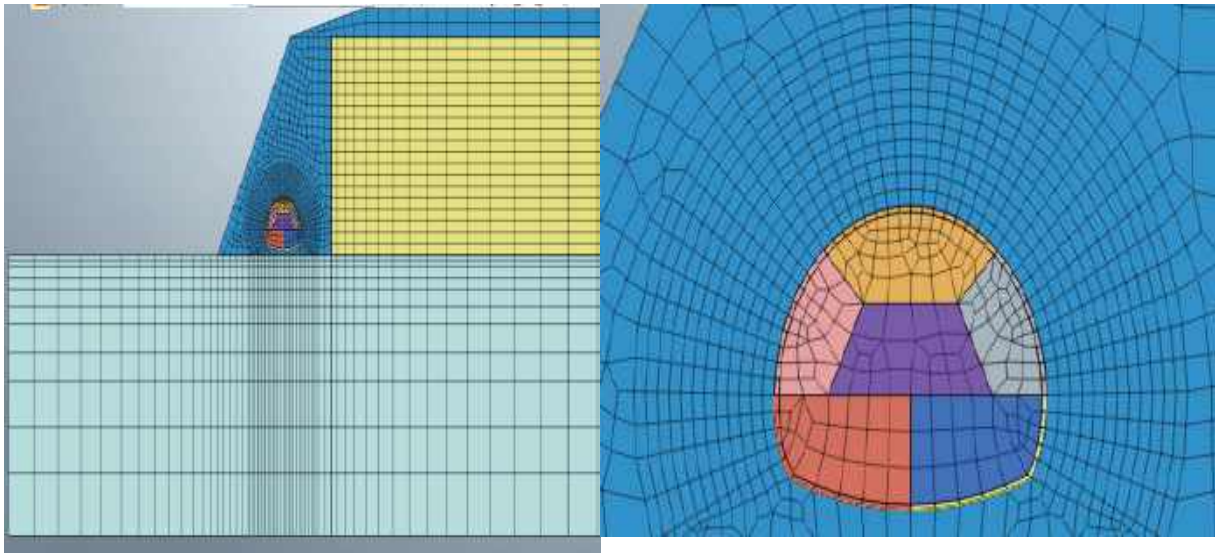

(a) (b)

Fig. 3-1 Calculation model

The physical and mechanical parameters of surrounding rock and supporting structure are given in Table 3-1.

Table 3-1 Model parameters

project	Elastic modulus E GPa	Poisson's ratio u	internal friction angle ϕ °	Cohesion C kPa	Tensile strength MPa	Density kg/m^3
VI Grade Rock	0.8	0.45	20	50	0.3	1.5 x 10^3
V Grade Rock	1.2	0.4	24	100	0.4	1.8 x 10^3
IV Grade Rock	2	0.33	35	600	0.5	2.4 x 10^3
22 mm diameter hollow grouting anchor	200	0.3	-	-	-	7.8 x 10^3
I18 steel arch	210	0.3	-	-	-	7.8 x 103
C20 shotcrete	21	0.2	-	-	-	2.2 x 10^3

3.3 Excavation Procedure simulation by the annular pilot heading conservation core soil method of tunnel

The annular pilot heading conservation core soil method is applied to excavate the weak surrounding rock of Dongtou Mountain Tunnel [9]. Different excavation sequences of the left and right sides of the tunnel are simulated. In order to analyze the deformation characteristics of the tunnel, several observation points were used, as shown in Figure 3-2.

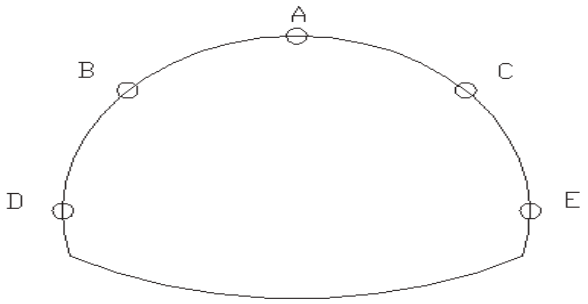

Fig.3-2 Schematic diagram of characteristic points

The excavation steps are illustrated in Figure 3-3 and Table 3-2:

Table 3-2 Excavation sequence for condition one and condition two

steps	1	2	3	4	5	6
Condition one	Upper left side of the annular pilot heading conservation	Central section of the annular pilot heading conservation	upper right side of the annular pilot heading conservation	Central core soil	left side of the lower bench	right side of the lower bench
Condition two	upper right side of the annular pilot heading conservation	Central section of the annular pilot heading conservation	upper left side of the annular pilot heading conservation	Central core soil	right side of the lower bench	left side of the lower bench

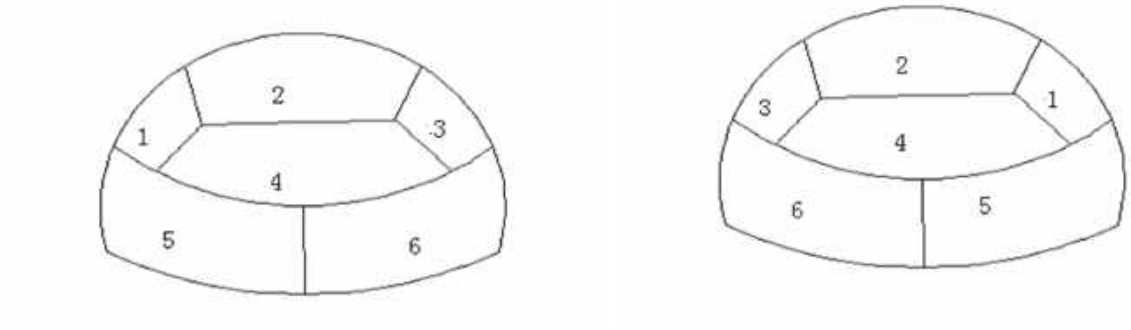

(a) Steps for condition one (b) Steps for condition two

Fig.3-3 Excavation sequence for condition one and condition two

4 Simulation results and analysis

The simulation results are shown in Figure 4-1.

condition one condition two

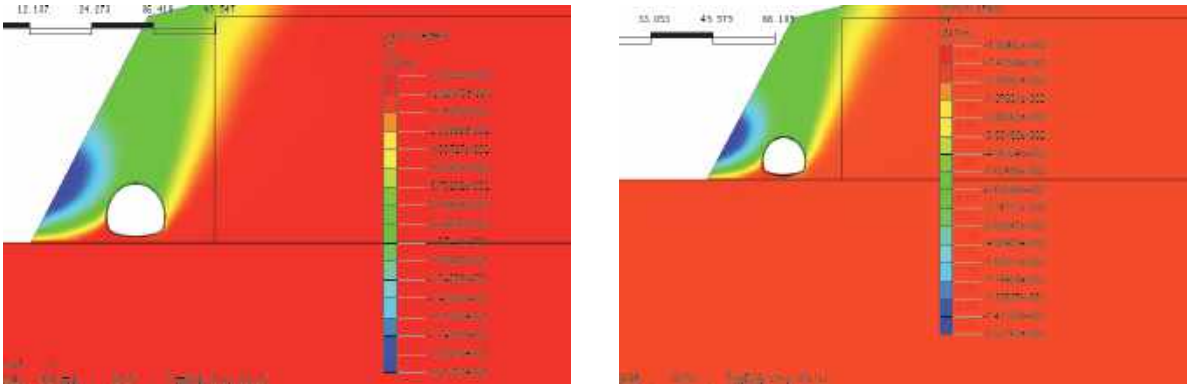

(a) Vertical displacement [m] of surrounding rock

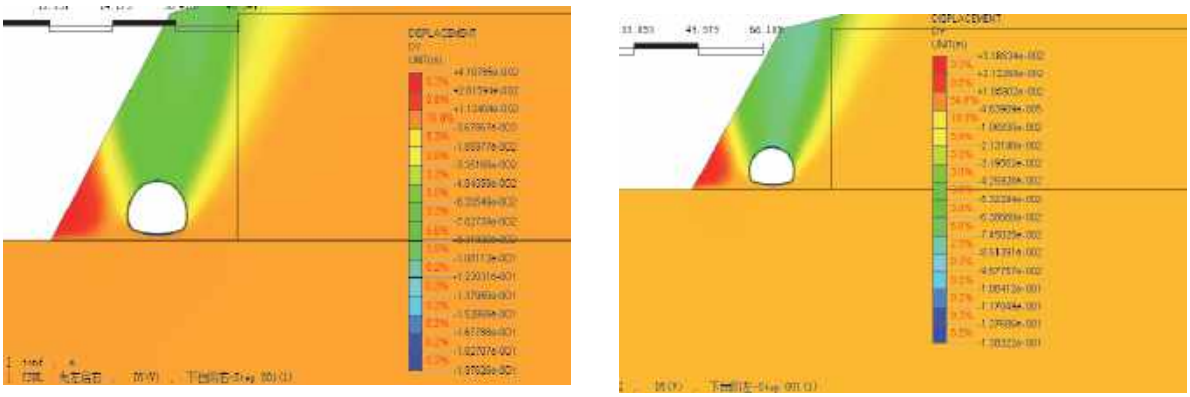

(b) Horizontal displacement [m] of surrounding rock

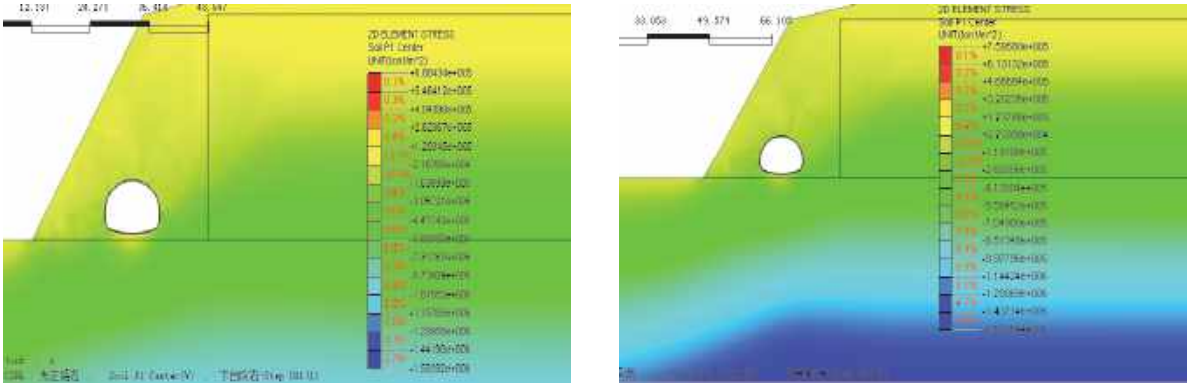

(c) Maximum principal stress [Pa] of surrounding rock

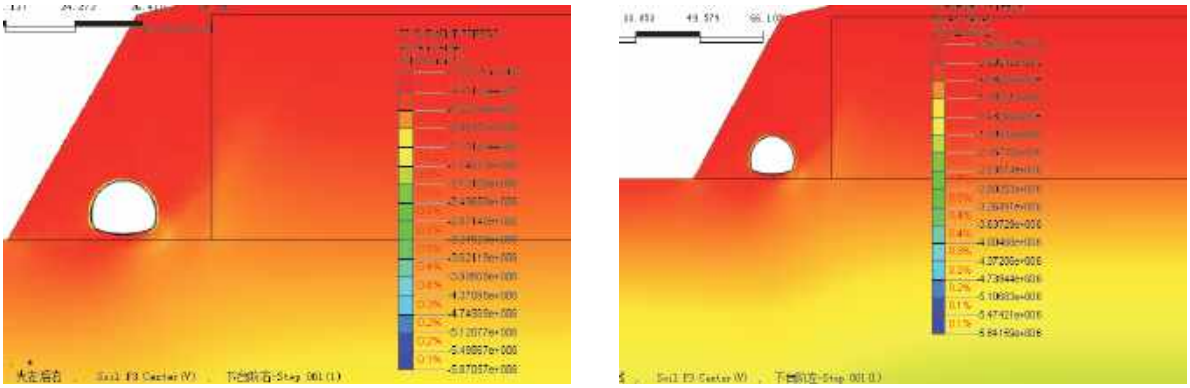

(d) Minimum principal stress [Pa] of surrounding rock

Fig. 4-1 Filled contour plots for deformation and stress for condition one and condition two

4.1 Displacement analysis

Observed displacements of selected observation points for the two different construction schemes [10] are shown in Figure 4-2.

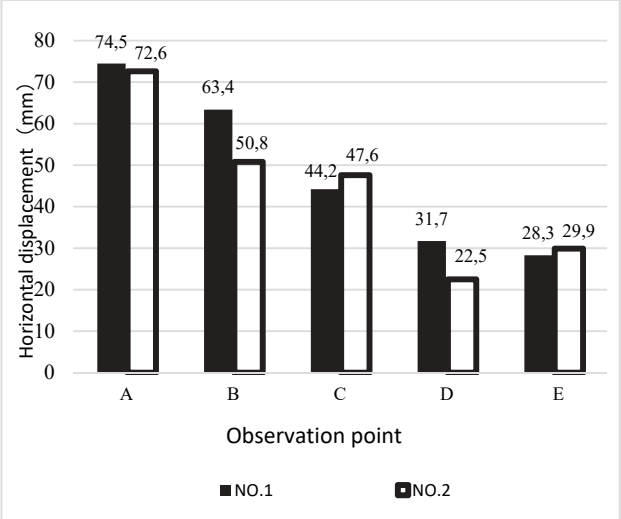

(a) Histogram of vertical displacement

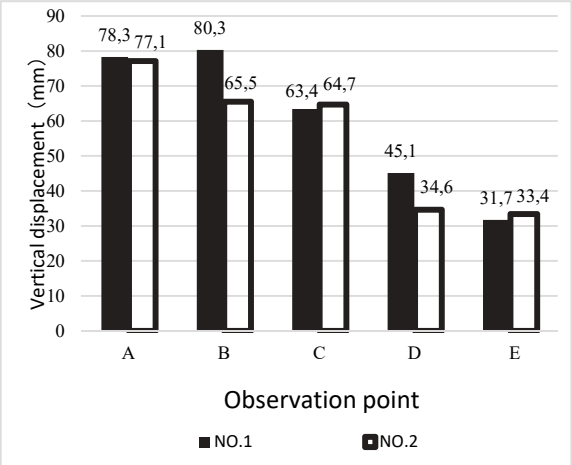

(b) Histogram of horizontal displacement

Fig. 4-2 Deformation and stress histogram of selected observation points for condition one and condition two

Under condition one and condition two, both, the vertical displacements and horizontal displacements at the left side of the Dongtou Mountain Tunnel are larger than those at the right side. In addition, vertical and horizontal displacements at point A are nearly unchanged in both cases. Compared with condition one, the vertical and the horizontal displacements at the left side of the tunnel are significantly reduced under condition two. The vertical displacement of point B is decreased by 14.8 mm, while the horizontal displacement is decreased by 12.6 mm and vertical displacement of point D is decreased by 1.2 mm. Under condition two, the tunnel at the right side has larger vertical and horizontal displacements, but the variation is small. Meanwhile, vertical displacement and horizontal displacement of point C increases by 1.3 mm and 3.4 mm, respectively. Vertical displacement and horizontal displacements of point C increases by 1.6 mm and 1.7 mm, respectively. Thus, it can be concluded that the left confining deformation affected by the excavation sequence is larger and less confining deformation is produced by the excavation sequence at the right side.

4.2 Stress analyses

The simulations show, that maximum principal stress of the tunnel in case of condition one appears at the left arch waist position with value of 0.083 MPa. The maximum principal stress for condition two is 0.11 MPa.

The above shown results indicate that without any auxiliary measures, changing the excavation sequence can reduce displacements at the left side of the tunnel, where the rock mass experience large deformations. Also, this would have only little effect on the deformation of surrounding rock at the right side. Therefore, when using the circular excavation method to excavate reserved core soil, changing the excavation sequence can effectively reduce the deformation of the tunnel [11], which is very effective and economical.

5 Comparative analysis of monitoring data under different excavation processes

Unfavorable excavation processes often lead to large deformations for biased tunnels in weak surrounding rock. So large deformations can eventually lead to suspension of construction work in early stages under condition one. Due to the numerical simulation results condition two is considered as optimized excavation method. Therefore, the project was switched to condition two. Monitoring data of deformation of the surrounding rock under the same lithology are collected and the tunnel vault settlement as well as the cumulative convergence curve are drawn. Analyzing the deformation characteristics of surrounding rock as function of time and space under different conditions, it was proven that condition two is advantageous for the engineering construction.

It is found that the section of ZK37 + 270 - ZK37 + 420 is a weak rock mass with V grade. The monitoring data at section ZK37 + 300 are chosen to reflect the deformations of the surrounding rock under condition one. At the same time, the section ZK37 + 325 under the condition two is selected to set measuring points and to carry out field measurements. The monitoring instruments and the arrangement of measuring points at the two sections are exactly the same.

5.1 Monitoring instruments and arrangement of measuring points

The chosen measuring instruments are listed in Table 5-1.

Table 5-1 Dongtou Mountain Tunnel monitoring instruments

horizontal clearance convergence		crown settlement	
Measuring instruments	testing accuracy	Measuring instruments	testing accuracy
JSS30A convergence gauge	0.1mm	level, micrometer, steel tape	0.1mm

Dongtou Mountain Tunnel crown settlement and horizontal convergence measurement arrangement is shown in Figure 5-1.

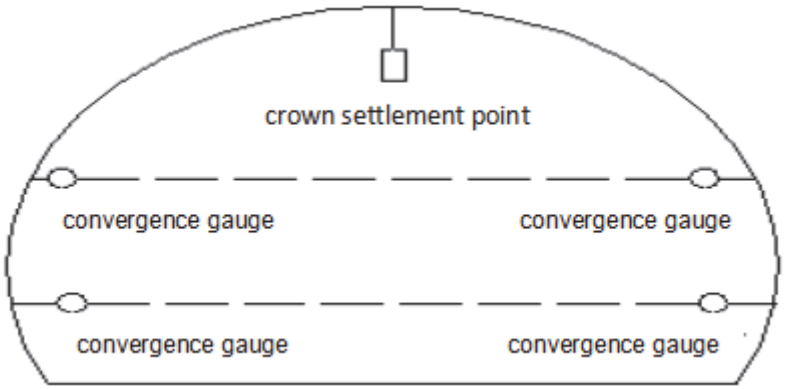

Fig.5-1 Arrangement of horizontal convergence and vault settlement measurements for Dongtou Mountain Tunnel

The distance between the monitoring sections of Dongtou Mountain Tunnel is 10 m.

5.2 Comparison of field monitoring data for condition one and two

At the time of excavation the section ZK37 + 300, blasting produced some perturbations to this section [13]. The field monitoring data of crown settlement and peripheral convergence under condition one and two are collected and sorted as follows.

（1）Monitoring results of crown settlement

According to the field monitoring data and the simulation results for point A in sections ZK37 + 300 and ZK37 + 325 the cumulative crown settlement curve is plotted as shown in Figure 5-2.

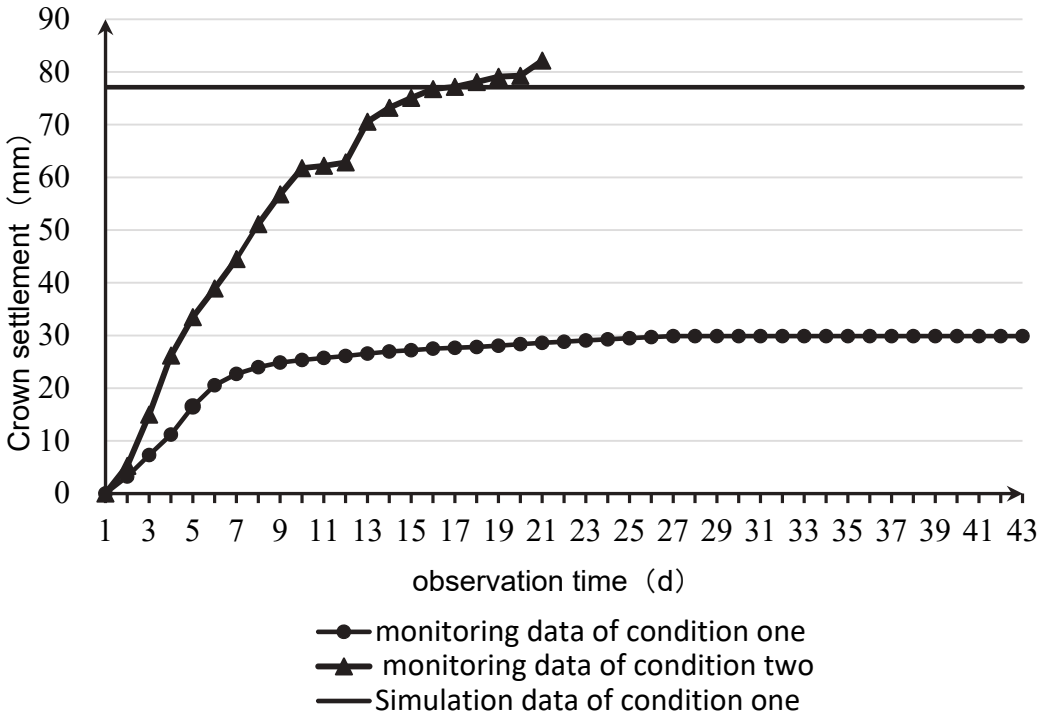

Fig.5-2 Crown settlement versus time for condition one and two

It is shown that during the period from March 23 to April 12 in 2015, the crown settlement at section ZK37 + 300 is 82.14 mm. During the period from July 28 to September 10, 2015, the crown settlement of section ZK37 + 325 is 29.86 mm. The deformation rate increases rapidly in early stage of excavation. With the completion of the initial support, the settlement rate becomes slow [14], and the crown settlement is similar to the simulation results.

（2）Monitoring results for peripheral convergence

Analyzing the monitoring data for peripheral convergence of the five measurement points, it can be concluded that the convergence of points B and C are larger. The data for these two measuring points are shown in Figure 5-3.

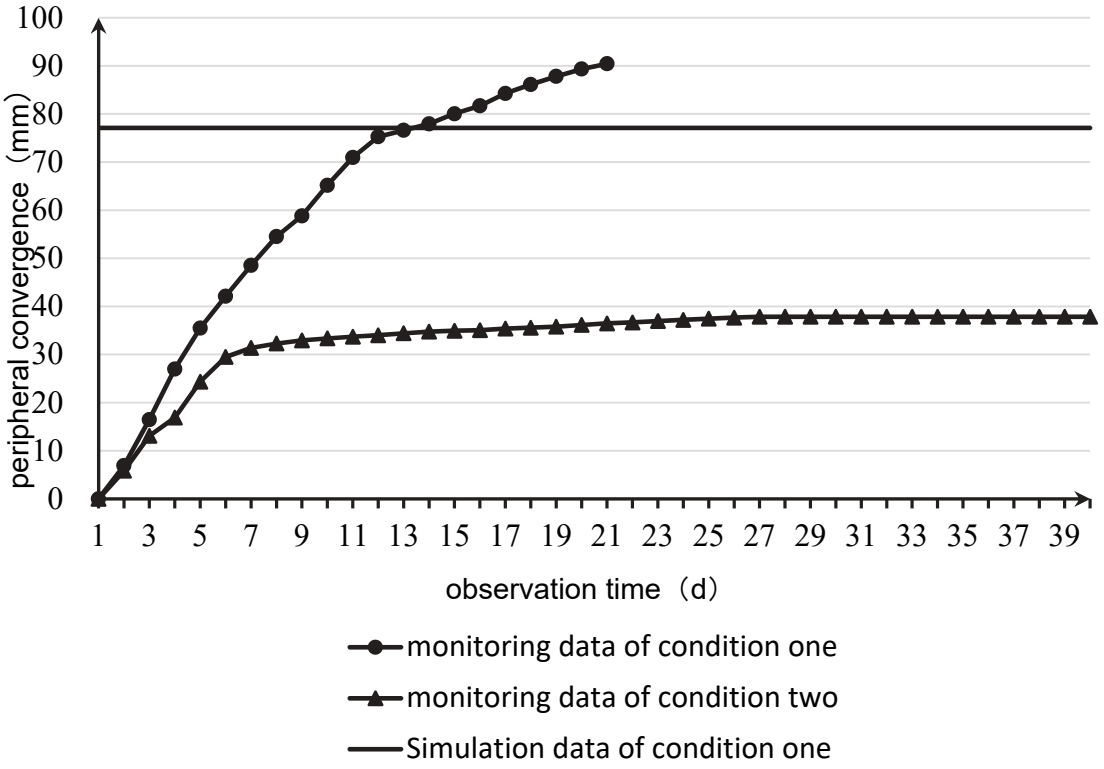

Fig.5-3 Peripheral convergence versus time for condition one and two

Under condition one, the convergence from March 23 to April 12, 2015 at section ZK37 + 300 was 90.43 mm. Under condition two at section ZK37 + 325 section from July 28 to September 10, 2015, the cumulative deformation was 37.84 mm. In the early stage of excavation, the deformation rate increases rapidly. With the completion of the initial support, the convergence rate becomes slow [14], and the accumulated convergence is close to the simulation results.

To summarize: in the process of tunnel excavation, the crown settlement and the horizontal convergence at condition one are strongly increased by the impact of construction disturbance, they are changing rapidly and lasting for a longer period in the early stage. With completion of initial support, the rate of crown settlement and horizontal convergence at condition two are reduced. The measured results are similar to the numerical simulation results for condition one. Therefore, it is verified that the excavation scheme of condition two is beneficial for Dongtou Mountain Tunnel [15].

6 Conclusions

(1) The two-dimensional numerical simulation analysis of the excavation procedure of biased tunnel in weak rock by using Midas/GTS shows close agreement with displacement monitoring data, which verifies the simulation approach.

(2) When using the annular pilot heading conservation core soil method to excavate Dongtou Mountain Tunnel, excavating the right side first and then excavating the left buried side, can effectively reduce the deformations and induced stresses of the tunnel. Therefore, it is reasonable to excavate the deep buried side first.

References

[1] TURKMEN S, OZGUZEL N. Grouting a tunnel cave-in from the surface: a case study on Kurtkulag-Irrigation tunnel, Turkey, Tunnelling and Underground Space Technology, 2003,18: 365-375.

[2] LEI J, ZHANG J, LIN C. Analysis of Stress and Deformation Site –monitoring in Fault Zone of Wushaoling Tunnel under Complex Geological Conditions . Rock and Soil Mechanics, 2008, 29 (5): 1367-1371.

[3] LUNARDI P. Tunnel design and construction - Geotechnical control deformation analysis method. (ADEC0-RS). Beijing: China Railway Publishing House, 2005.

[4] ZHOU Y, ZHAO Y, CHENG C. Optimum analysis on the construction process for double-arch tunnel with unsymmetrical loadings. Chinese Journal of Rock Mechanics and Engineering, 2002, 21(5): 679–683.

[5] LIU Y，JIANG S, ZHAO S. Optimizing analysis for construction schemes of shallow multi-arch loess tunnel. Chinese Journal of Underground Space and Engineering, 2005, 1(6): 944–947.

[6] Liu X, Zhang Y. Analysis of Reasonable Excavation Sequence and Stress Characteristics of Portal Section of Shallow Tunnel with Unsymmetrical Loadings. Chinese Journal of Rock Mechanics and Engineering, 2011, 30 (S1): 3066-3073

[7] SHI X, ZHANG J, LIU B. Study on the construction process of CRD method for large section shallow buried bias tunnel. Modern tunnel technology, 2015, 52(3): 193-199.

[8] LI M, ZENG P. Numerical Simulation Analysis of Pile-anchor Retaining in Deep Foundation Based on MIDAS. Research of Soil and Water Conservation, 2012, 19(1): 250-253.

[9] Kang T. Application of Core-keeping Ring Cut Method in Yangtaishan Tunnel. Tunnel Construction, 2009, 29(2): 114-116.

[10] ZHANG D, WANG J, ZHANG Y. Deformation of Soft Rock Tunnel and Technology of Construction Safety Control. Highway Engineering, 2011, 36(2): 124-128.

[11] LV G, SUI B, WANG Y, WU J. Study on numerical and stability analysis shallow buried tunnel excavation under unsymmetrical pressure. Journal of Shandong University: Engineering Science, 2013(43): 68-73.

[12] XU L, S, JIANG S. Monitoring during the Access Construction of YangPeng Right Tunnel. Chinese Journal of Rock Mechanics and Engineering, 2002, 21(5): 675-678.

[13] LIU X, ZHANG Y. Analysis of influence of topographic factors and surrounding rock classification on the tunnel with unsymmetrical loadings. Journal of Xi′an University of Architecture and Technology: Natural Science, 2010, 42(2): 205-209.

[14] HOEK E, BROWN T. Underground engineering of rock (Translated), Beijing: China Metallurgical Industry Press, 1986

[15] SHI Y, DING X, HAN C. Control measures for settlement deformation of soft rock tunnel. Chinese and Foreign Highway, 2009, 29(4): 397-400.

ADVERTISING

Central South University; School of Resources and Safety Engineering

Careers for talents around the world

Central South University (CSU) is situated in the famous historical cultural city of Changsha, Hunan province, P. R. China. The university was established in April 2000, by merging three separate universities: Hunan Medical University (HMU), Changsha Railway University (CRU), and Central South University of Technology (CSUT). Central South University is a national key university under the direct administration of the Ministry of Education of China. The University is among the first group admitted into both “Project 211”, a project of building national key universities and colleges for the 21st century, and “Project 985”, a joint constructive project of building world-class universities co-sponsored by the Chinese central government and local governments. As one of the leading universities, CSU is also among the first group admitted into “Project 2011” (institutions of higher learning innovation ability enhancement).

The School of Resources and Safety Engineering of CSU has one first-level national key discipline and three second-level national key disciplines. The School has three undergraduate programs (Majors): Mining engineering, Safety engineering, and Underground space engineering, and three post-doctoral research stations. For the purpose of serving the national innovation-driven development strategy, cultivating leading scholars for the disciplines, implementing the strategy of strengthening the university by talented scholars, and converging high-level innovation research teams, the School is now recruiting talents worldwide. Qualified scholars are warmly welcomed to join us!

1. Research subjects and specialties:

Mining engineering, Safety science and engineering, Geotechnical engineering, Engineering mechanics, City planning, Digital mine technology, Mine automation, and Big data for mining, etc.

2. Designations for scholars:

1. **“Disciplinary Leading Talent”:** Distinguished professors for the “Chang Jiang Scholars Program”, Obtainers of the National Science Funds for Distinguished Young Scholar of China (Class A).
   The age should be under 50.
2. **“Innovative Young Talent”:** Selected candidates of “Thousand Young Talents project”, Young scholars for the “Chang Jiang Scholars Program”, Top young scholars for the “10 thousand people plan”, Obtainers of the National Science Foundation for The Excellent Young Scholars of China.
   The age should be under 40.
3. **Doctors/ Post-Doctors** from well-known colleges or universities in China and overseas.
   The age should be under 35.

3. Salary and financial aid

The salary and financial aid is implemented according to the corresponding administrative regulations for the talent employment of CSU.

A brief list of the salary and financial aid for the recruited scholars

Scholar categories	Annual salary	One-off settling-in allow-ance or subsidy for house purchase (after tax)	Research fund	Other preferential treatments
“Disciplinary Leading Talent”	600,000 RMB	1,000,000 RMB	4,000,000 - 6,000,000 RMB	• Appointing the scholar as the Professor (of the second grade) • Arranging proper work for the scholar’s spouse. • Providing a two-year transitional housing for the scholar who owns no house within the urban district of Changsha city. • Providing a one-off quota for the scholar to employ 1 - 2 new teachers and recruit 1 - 2 PhD students.
"Thousand Young Talents" project	500,000 RMB	600,000 - 800,000 RMB	2,000,000 - 4,000,000 RMB	• Appointing the scholar as a Distinguished Professor. • Arranging proper work for the scholar’s spouse. • Providing a two-year transitional housing for the scholar who owns no house within the urban district of Changsha city. • Providing a quota for the scholar to recruit 1 PhD student.
Young scholar for the "Chang Jiang Scholars Program", Top young scholar for the "10 thousand people plan", Obtainer of the National Science Foundation for The Excellent Young Scholars of China	350,000 RMB	600,000 - 800,000 RMB	2,000,000 - 4,000,000 RMB	• Appointing the scholar as a Distinguished Professor. • Arranging proper work for the scholar’s spouse. • Providing a two-year transitional housing for the scholar who owns no house within the urban district of Changsha city. • Providing a quota for the scholar to recruit 1 PhD student.
Post-doctoral researchers	120,000 RMB			Providing 20,000 RMB as a start-up research fund

4. Documents needed for application

1. One resume.
2. A list of undertaken research projects, published papers (indicate the index condition of the papers: SCI, EI, SSCI, CSSCI, the journal impact factor, and other-citing times), and received awards. (The information needed must be within recent 5years).
3. Copies of certificates of academic degrees, all the research projects, awards, and patents.

4. Five representative papers (full text).
5. Hard copies of certificates (proofs) for working overseas, or working in important positions in China (when applicable).
6. A work plan for the applied position of corresponding category in CSU.

5. Contact information

Central South University, School of Resources and Safety Engineering
Address: No. 932 Lushan South Road, Changsha, Hunan, P. R. China
Postal code: 410083
Contact person: Mrs. Guo
Email: guoq@csu.edu.cn
Telephone: +86-0731-88879612
Fax: +86-0731-88879612